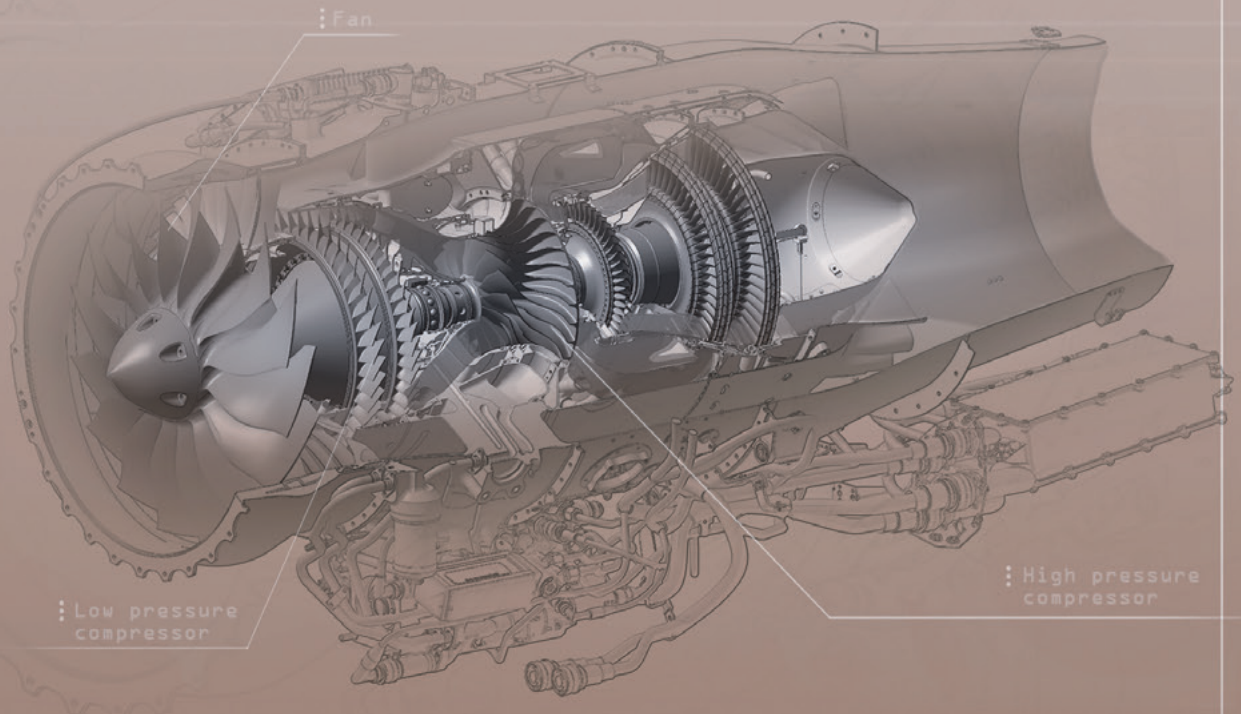
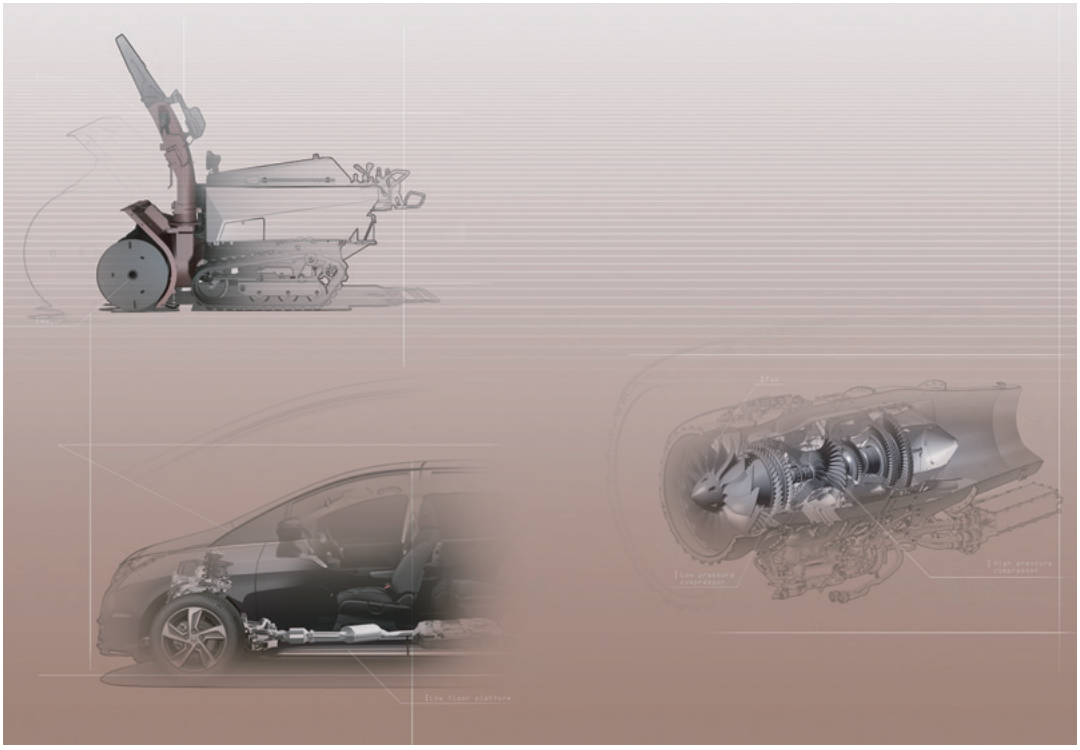
Honda R&D

Technical Review



October 2014
Vol.26 No.2



Comment on the Cover

Honda conducts more types of research and development than most of us know about—even those of us who work here. Now and then, something comes to light that surprises us and gets our hearts racing.

It makes me wonder: what other amazing things will I see in my lifetime?

At Honda, we are always working on spectacular new breakthroughs.

I designed the cover to give an advanced, high-tech impression through close-ups of products and components discussed in these papers.

Please enjoy this collection. Each paper is a dream in progress.



Automobile R&D Center
Masahiro Sagawa

Technical Review

October

2014

Honda R&D

CONTENTS

Introduction of new technologies

Development of HF120 Turbofan Engine . . . . . Etsuo NODA 1

HF120 Turbofan Engine Development Test for Type Certificate
. . . . . Ryosuke SHIBATA・Katsumasa ISHIKAWA・Ryo KODAMA
Shuu TAGUCHI・Hidehiko NAKATA 7

Verification of High Altitude Performance and Characteristics for HF120 Turbofan Engine
. . . . . Katsumasa ISHIKAWA・Norio KASAI
Norifumi IKEDA・Ikuo TAKAMATSU 14

Aerodynamic Technologies for High-efficiency and High Specific-flow-rate Fan and Centrifugal Compressor
. . . . . Hisato TANAKA・Mineyasu OANA 22

Structural Design and Verification of HF120 Turbofan Engine
. . . . . Junichi IKEDA・Takafumi TANAKA・Ryuji SANO 28

Application of CFRP Stator to HF120 Turbofan Engine
. . . . . Michihide ANAKURA・Shuu TAGUCHI・Shuichiro YOSHIDA 33

Development of High Reliability Control Software for HF120 Turbofan Engine
. . . . . Makoto TEZUKA・Shohei SUGIMOTO・Keisuke KAWAI
Hideaki JINNO・Yuta AKAI 38

Styling Design of 2014 Model Year ODYSSEY
. . . . . Katsuaki HAYASHI・Ryusaku SENDA・Wataru MURAKAMI 45

Development of New 50 cc Scooter Dunk . . . . . Makoto MITSUKAWA・Shuji HIRAYAMA
. . . . . Mamoru OTSUBO・Yasushi TATEISHI 53

Development of HSL2511 Large-sized Snow Thrower
. . . . . Kenta KOHIGASHI・Tsutomu MIZOROKE・Takashi HASHIZUME
Shohei URANO・Jun SONG 65

Development of High-Access Survey Robot for TEPCO's Fukushima Daiichi Nuclear Power Station
. . . . . Hisashi SUGIURA・Takafumi FUKUSHIMA・Mitsuhide KURODA
Ryusuke ISHIZAKI・Takashi MATSUMOTO 73

Study on Application of Engine Load Estimation Method Using Crank Angular Velocity Variation to Spark Advance Control
. . . . . Hirotaka KAWATSU・Ryosuke IBATA
Tetsuya KANEKO・Kenji NISHIDA 86

Simulation of Oil Separating Behavior for Engine Breather System . . . . . Makoto HAGA・Takumi KASAHARA 98

Model-Based Development Technologies to Support Increasingly Complex Power Train Systems
. . . . . Hidekazu ARAKI・Kanako SAITO・Ryosuke OHGUCHI
Masayuki FUNAKOSHI・Kensuke YAMAMOTO 107

Driving Simulator for Power Plant Controller Development
. . . . . Satoshi KODO・Shigeki FUJIMOTO
Takashi ONO・Tetsuya SUZUKI 117

Development of 8-Speed DCT with Torque Converter for Midsize Vehicles
. . . . . Shoji MACHIDA・Noriyuki YAGI・Kazunori MIYATA
Masayuki SADAKIYO・Tomoya OKAJI・Tomonori YAMANE 125

Technology to Predict Input Force to Engine Mount at Rapid Start of MT Vehicle
. . . . . Yasufumi JO・Takahiko MURATA
Masaki OKUMOTO・Satoshi YAMASHITA 132

Development of Active Control Engine Mount System for Reduction of Resonance Vibration at Engine Restart
. . . . . .Tatsuhiro YONE・Hideyuki OKAMOTO・Takashi YAMAGUCHI
Shintaro FURUI・Hirotomi NEMOTO 138

Control Parameter Optimization for Reduction of 2nd Order Vibration in Hybrid Drive Mode
of SPORT HYBRID i-MMD . . . . . Tatsunori TSURUTA 144

Design of Floating Seat for Control of Seat Resonance Frequencies
. . . . . Kengo YABE・Toru INAGAKI・Takashi KONDO 151

Predictive Simulation of Flow-induced Noise using CFD . . . . . Katsutomo KANAI・Hideki KATSUYAMA
Yuichi FUSHIMI・Norikazu YAMAMOTO 156

Development of Component Based Middleware for Intelligent Robot Software
. . . . . .Makoto SEKIYA・Norio NEKI
Zenta MIYASHITA・Nobuyuki ONO 165

System Design Process in Compliance with ISO26262 Using Model-Based Design
. . . . . Hiroki SAGAMI・Shinji HIRONAKA
Ryoji MORI・Takuyuki MUKAI 173

Development of Configuration Management System for ISO26262
. . . . . Hitoshi TAKUMI・Yasuo KUROSAKI・Hiroshi ISHIDA 181

Development of MEA with Built-in Oxygen Sensor for Measurement of Oxygen Concentration
around Fuel Cell Cathode Electrode Layer. . . . . Masahiro MOURI 190

Verification Test Results for Solar Hydrogen Station in Japan . . . . . Nobuyoshi YOSHIDA・Aoi MIYAKE 200

Project for Locally Rooted Design Development in Field Tests of Next-Generation Personal Mobility
. . . . . Tadahiro YAGUCHI・Kazunori HARADA 207

Technical papers

Study of Optimization of Reciprocating Parts for General-purpose Engine with Aluminum-alloy Connecting Rods
. . . . . .Masami OKUBO・Masato SUZUKI 214

Advanced Ignition Control Technology for HCCI Combustion
. . . . . Kiminori KOMURA・Masanobu TAKAZAWA・Teruyoshi MORITA 220

Identification of Brake-drag Mechanism in Coasting-down Mode and Proposal of Brake-drag Stabilization
and Reduction Methods
. . . . . Yasushi KOBAYASHI・Yuta HIGUCHI・Naoki NAKAMURA 229

Development of Feedback Active Noise Control Technology for Noise in Multiple Narrow Frequency Bands
by Multiplexing of Single-frequency Adaptive Notch Filters
. . . . . .Kosuke SAKAMOTO・Toshio INOUE 237

Development of Multiscale Computational Model for Carrier Mobility in GaAs Nanopillars with Twin Boundaries
. . . . . .Mitsumoto KAWAI 244

Development of HF120 Turbofan Engine

Etsuo NODA*

ABSTRACT

General Electric Company and Honda have jointly developed the HF120 turbofan engine to be installed in the HondaJet. Both GE and Honda brought their leading technologies to the HF120 program and targeted top-class light weight, low fuel consumption, and low emissions as key design goals for the small turbofan engine. The HF120 improved specific fuel consumption by 3% and thrust-weight ratio by 17% compared with an earlier HF118 turbofan engine that Honda had developed independently. In addition, the HF120 complied with emissions regulations for larger turbofan engines that currently do not apply to small engines in its class. Notable features of the HF120 include wide chord swept fan, carbon composite fan stator vane, high-efficiency centrifugal compressor, effusion-cooled combustor, and air-blast fuel nozzle. The HF120, with these and other technologies, received a Type Certificate from the United States Federal Aviation Administration in December 2013.

1. Introduction

The HF120 turbofan engine (HF120) to be installed in the HondaJet (Fig. 1) was jointly developed with General Electric Company (GE), starting from 2006 and received a Type Certificate issued by the United States Federal Aviation Administration (FAA) in December 2013. This paper provides a brief overview of the HF120 featuring top-class technologies in a small turbofan engine. These include light weight, low fuel consumption and low emission.



Fig. 1 HondaJet

2. Development Goal

One basic goal for the GE Honda joint venture team was to upgrade the HF118 turbofan engine (HF118)[1), 2)] independently developed by Honda and to achieve top-class low fuel consumption and high thrust-weight ratio in the engine class of comparable thrust. Although the small engine class to which the HF120 belongs is not subject to emissions regulations, one of the additional intentions was to conform to the regulations on NOx, CO and THC applicable to engines with 6000 lbf or more of thrust (larger engine)[3)].

3. Engine Overview

Shown in Fig. 2 and Table 1 are the HF120's external appearance and major specifications, respectively[4), 5)]. This engine belongs to a thrust class intended for business jet aircraft such as the HondaJet with the capacity of 6 to 8 people and features a conventional dual-shaft turbofan engines.



Fig. 2 HF120 engine

* Aircraft Engine R&D Center

Table 1 HF120 engine specifications

Model	HF120
Takeoff thrust	2095 lbf
Length	59.5 inch
Width	25.8 inch
Height	30.5 inch
Weight	466 lbs
Low-pressure rotor speed	19055 rpm
High-pressure rotor speed	49200 rpm
Interstage turbine temperature	860°C

4. Engine Performance

4.1. Specific Fuel Consumption and Thrust-Weight Ratio

Shown in Figs. 3 and 4 are the trends of specific fuel consumption (SFC), and thrust-weight ratio with respect to engine takeoff thrust. Both SFC and thrust-weight ratio improve with increase in takeoff thrust.

Figure 5 shows the achieved fuel consumption and thrust-weight ratio for the HF120 in comparison to certain competing engines of 2500 lbf or less. The figure indicates respective improvement in fuel consumption and thrust-weight ratio by 3% and 17% compared to the HF118. The HF120 also secures a competitive edge over the reference competing engines.

4.2. Exhaust Emissions

Figure 6 shows the amount of emissions of the HF120, when the limit of each item in the regulation is considered to be at its allowed limit. The limit for each item is calculated by engine thrust and cycle pressure ratio. Smoke is subject to emissions regulations for all turbofan engines, but there are no current regulations concerning NOx, CO and THC for the small engine class including the HF120.

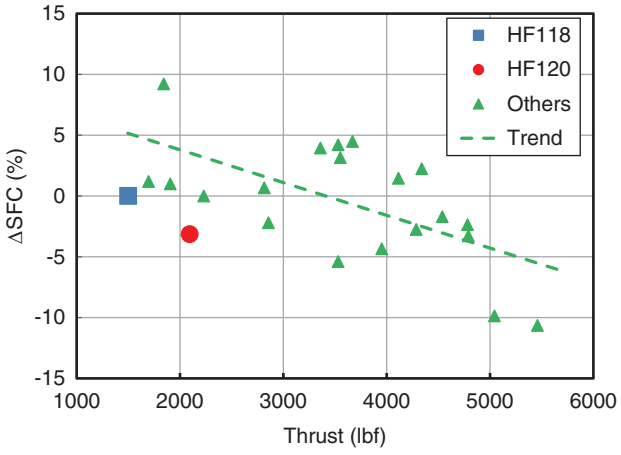


Fig. 3 Trend of SFC

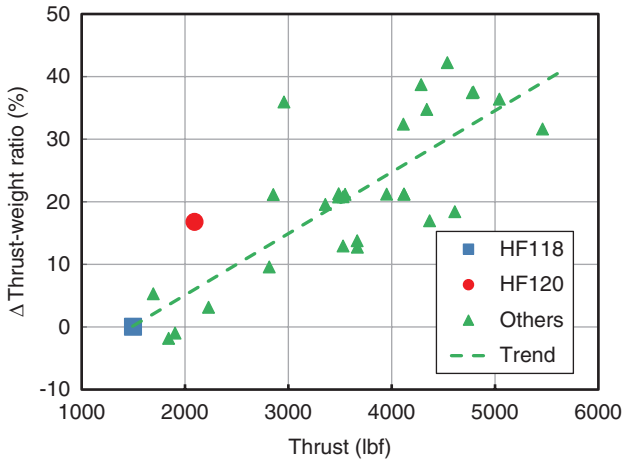


Fig. 4 Trend of thrust-weight ratio

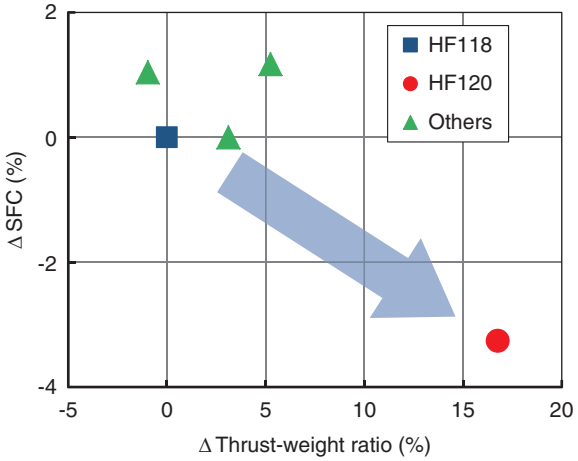


Fig. 5 Advantage of SFC and thrust-weight ratio

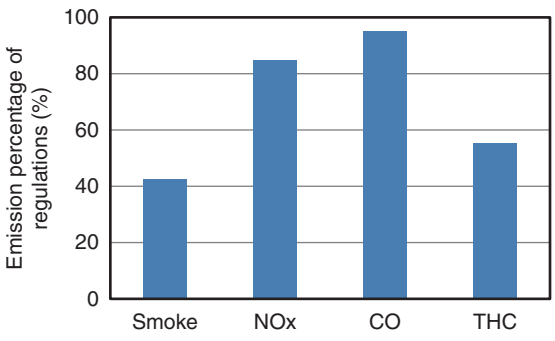


Fig. 6 Emission results

5. Engine Structure and Operating Principle

The HF120 engine's basic structure (Fig. 7) and the operating principle of many turbofan engines are illustrated below.

Air intake from the engine inlet is compressed by the fan and divided between the engine core and bypass duct.

Air taken into the engine core is compressed more by the low-pressure and high-pressure compressors and then sent to the combustor.

The high-pressure air is mixed with fuel sprayed from fuel nozzles within the combustor to generate high-temperature gas via steady combustion.

Energy is extracted from the high-temperature gas by the high-pressure and low-pressure turbines, and through a dual-structured rotating shaft, the high-pressure turbine drives the high-pressure compressor while the low-pressure turbine drives the low-pressure compressor and fan.

The air flowing through the bypass duct and the high-temperature gas after passing through the turbines are accelerated by the exhaust nozzle and emitted into aft area of the engine, which causes reactive force generating thrust.

For the HF120, a mixer blends the air and high-temperature gas upstream of the exhaust nozzle in an attempt to reduce exhaust noise and improve cruise fuel consumption.

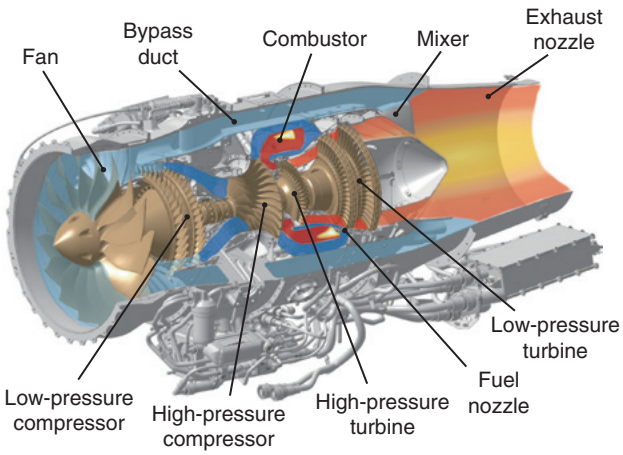


Fig. 7 HF120 engine features

6. Engine Characteristics

For overall component design, GE and Honda divided certain responsibilities. The high-pressure compressor, combustor and control system were assigned to Honda, while the low-pressure compressor, high-pressure turbine and mixer went to GE. The fan, low-pressure turbine and other components were jointly designed by GE and Honda. For example, Honda was mainly responsible for fan aerodynamic design and GE was responsible for structural analysis for bird strike testing.

6.1. Fan

Shown in Fig. 8 are the fan's major components. A wide chord swept design was introduced into the fan rotor for enhanced aerodynamic performance, and the blades and disk were integrally machined from forged titanium material for light weight and strength. In addition for weight reduction, carbon composite material was incorporated in the fan stator vane with sheet metal bonded to its leading edge for stronger resistance to erosion.

6.2. Compressor

Shown in Fig. 9 are the compressor's major components. The low-pressure compressor adopted a two-stage axial-flow design to provide a better cycle pressure ratio and to downsize high-pressure components. The high-pressure compressor features a centrifugal rotor made from heat-resistant, high-strength titanium and a

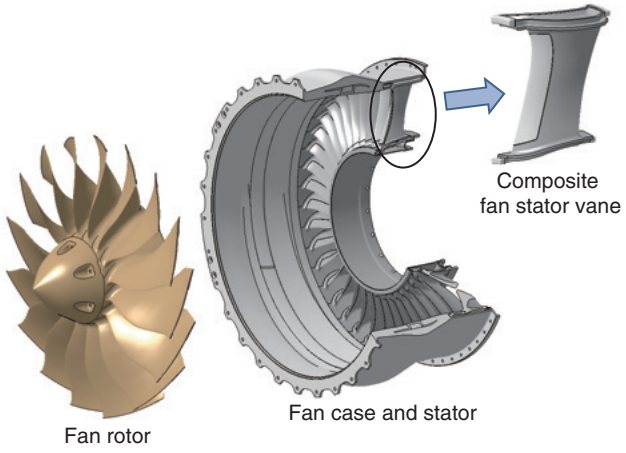


Fig. 8 Fan components

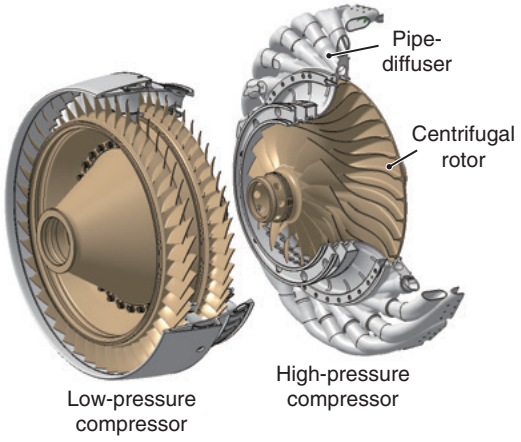


Fig. 9 Compressor components

pipe-diffuser structure that were highly streamlined by aerodynamic design using CFD in an attempt to improve fuel consumption.

6.3. Combustor

Shown in Fig. 10 are the major components of the combustor. A reverse annular layout was introduced in the combustor liner to reduce engine axial length. Effusion cooling by drilling a number of inclined narrow holes by laser beam (Fig. 11) was provided to cool the combustor liner wall and to simplify the structure. Typical fuel nozzles employ dual systems for the fuel lines in order to accommodate both the low flow rate and high flow rate regions. The HF120 utilizes a technology to consolidate them into a single system by using an air-blast fuel nozzle in an attempt to simplify and reduce weight. In addition, spray performance such as fuel atomization and flow pattern within the combustion chamber is adjusted accordingly to meet general emissions limits for larger engines.

6.4. Turbine

Shown in Fig. 12 are the turbine's major components. The high-pressure turbine featuring axial-flow and a single-stage uses a third-generation single-crystal alloy for the blade material to elevate permissible gas temperature at the turbine inlet in an attempt to reduce engine size and weight.

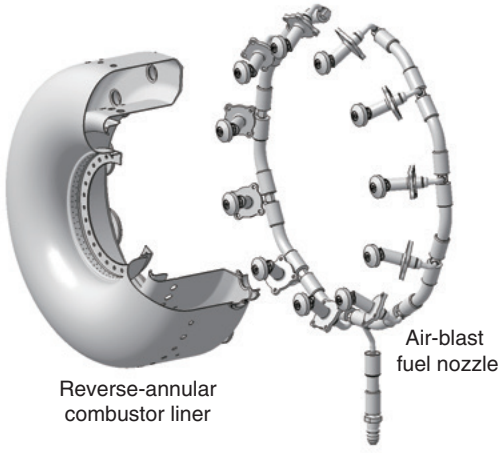


Fig. 10 Combustor components

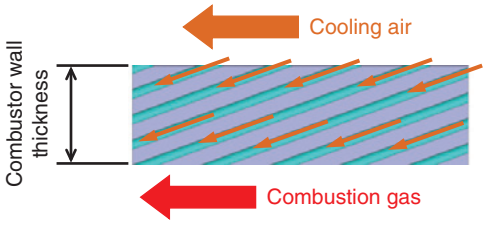


Fig. 11 Effusion cooling schematic

A low-pressure turbine (featuring a two-stage axial-flow layout) is designed to counter-rotate relative to the high-pressure turbine in an attempt to utilize swirl flow at the exit of high-pressure turbine and raise turbine efficiency.

6.5. Shaft System

Shown in Fig. 13 is the HF120's main-shaft cross-section. The low-pressure shaft's initial bending mode was set below idle speed and its secondary bending mode was set above redline to avoid any shaft resonance point within the engine's operating range. This setting was enabled by selecting a shaft structure that provides support for an overhung fan side. Shown in Fig. 14 is the Campbell diagram of the low-pressure shaft. Support of the high-pressure shaft turbine side was provided by a differential bearing that is held by the rotating low-pressure shaft, in an attempt to simplify bearing support of the structural members, the lubrication system, and the engine's design.

6.6. Control

A Full Authority Digital Engine Control (FADEC) regulates the engine by redundant digital electronic control

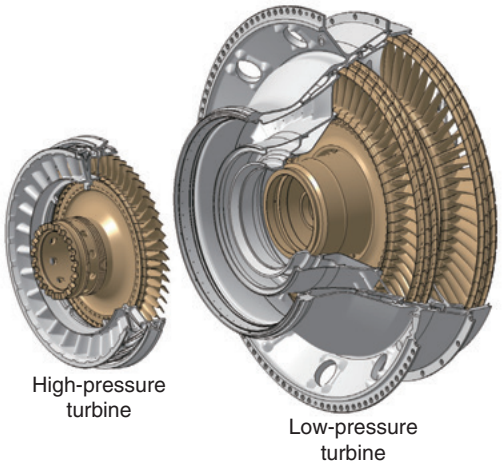


Fig. 12 Turbine components

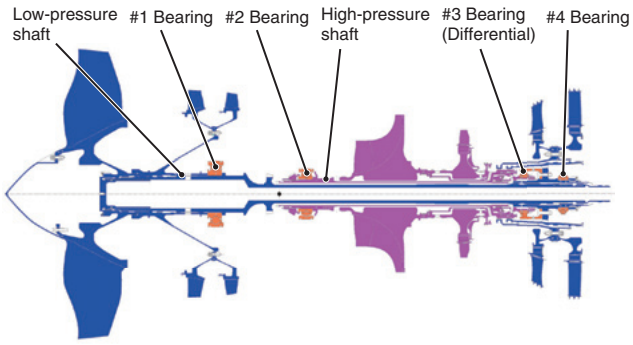


Fig. 13 Main-shaft cross-section

equipment. The major regulated items include fuel flow and bleed valve opening, providing thrust control to accommodate various flight conditions and pilot operations as well as adequate control to help prevent engine stall and lean blowout during acceleration and deceleration (Fig. 15).

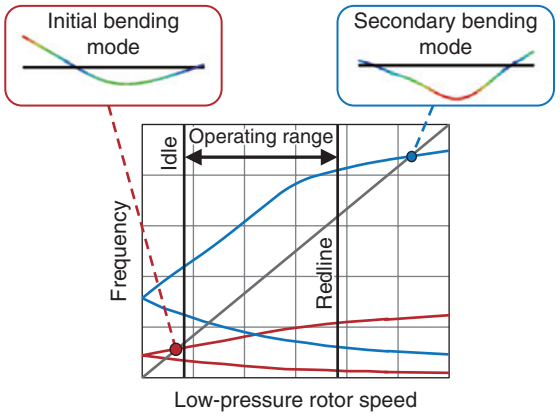


Fig. 14 Campbell diagram

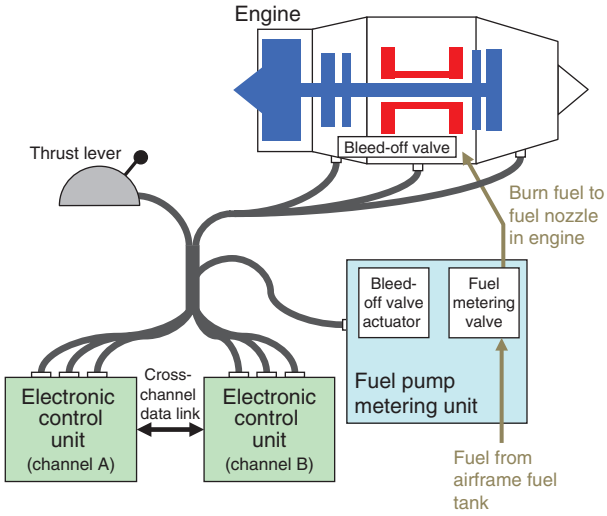


Fig. 15 FADEC system overview

7. Engine Type Certificate

Initial application for the HF120's FAA Type Certificate was made in February 2007 in parallel with developing the engine's detailed design, manufacturing all parts, and completing overall engine assembly. Ground testing for the first engine was initiated in October 2009, and flight testing and certification testing started in earnest in 2010. The engine certification process included various types of tests, such as endurance, foreign object ingestion, and icing. For component testing, endurance, fire, environment and other tests were performed. Certification reports (totaling 190) were submitted to the FAA. The FAA Type Certificate was issued on December 13, 2013 (Fig. 16). The European Aviation Safety Agency (EASA) Type Certificate is expected to be received at the end of 2014.


Department of Transportation
Federal Aviation Administration
Type Certificate

Fig. 16 FAA Type Certificate for HF120

8. Conclusion

Joint development with GE of the HF120 turbofan engine has been completed. The engine's FAA Type Certificate was issued in December 2013. Fuel consumption and thrust-weight ratio have been improved by 3% and 17%, respectively. For emissions, the HF120 satisfied the emissions regulations for NOx, CO and THC that currently only cover larger turbine aircraft engines.

References

(1) Sonoda, T., Noda, E.: HF118 Turbofan Engine for a Small Business Jet, Journal of the Japan Society of Mechanical Engineers, Vol.108, No.1039, p.456-457 (2005)
(2) Sonoda, T., Noda, E.: Development of Honda's HF118 Turbofan Engine for Business Jets, Journal of the Gas Turbine Society of Japan, Vol.34, No.3, p.165-171 (2006)
(3) Federal Aviation Administration: FUEL VENTING

AND EXHAUST EMISSION REQUIREMENTS FOR TURBINE ENGINE POWERED AIRPLANES, CFR. title 14, part 34
(4) http://www.gehonda.com/products/hf120/, 2014/4/25
(5) http://rgl.faa.gov/Regulatory_and_Guidance_Library/rgMakeModel.nsf/0/00BA6F1FAC1A32A186257C780058D54E?OpenDocument&Highlight=hf120, 2014/4/25

■ Author ■



Etsuo NODA

HF120 Turbofan Engine Development Test for Type Certificate

Ryosuke SHIBATA* Katsumasa ISHIKAWA* Ryo KODAMA*
Shuu TAGUCHI* Hidehiko NAKATA*

ABSTRACT

Honda and General Electric Company have performed component certification tests, engine certification tests, as well as associated engineering tests, to verify conformity with regulations in order to obtain United States Federal Aviation Administration Type Certificate for the HF120 turbofan engine. The results of these tests confirmed that the HF120 turbofan engine satisfies the airworthiness requirements and exhaust emission regulation requirements of the United States Federal Aviation Regulations Title 14 of the Code of Federal Regulations Parts 33 and 34.

A total of 190 certification test plans and reports were submitted in the development of the HF120 turbofan engine, and on December 13, 2013, a Type Certificate was received from the United States Federal Aviation Administration.

1. Introduction

Honda initiated aircraft engine research and development in the late 1980s. In December, 2003, Honda developed the HF118 turbofan engine (HF118), and installed it on a HondaJet proof of concept vehicle and started flight tests. In October, 2004, Honda and General Electric Company (GE) established a joint venture company, realizing Honda's dream of entering aviation industry. In February 2007, an application was made to the Federal Aviation Administration (FAA) for Type Certificate of the HF120 turbofan engine (HF120), which is the mass-production engine successor to the HF118. Since submitted application to FAA in 2007, GE and Honda continued detail design work. The first engine test was started from October, 2009. A series of certification tests and engineering tests was started from 2010.

2. Classification of Tests

Federal Aviation Regulations (FAR) require substantiating engine compliances with the regulatory requirements for Type Certificate by test and/or analysis. Certification tests involve conducting substantiation tests with FAA representatives present to demonstrate engine compliance with regulatory requirements. Analysis substantiation is verification with a high confidence level analysis model. The analysis model is verified by well correlated component or engine test results.

The next section explains the outline of various tests for acquisition of the turbofan engine Type Certificate.

2.1. Component Tests

Component tests are mainly classified into three types: a component test when the engine operating conditions can be well simulated on the component level, like a fire test; a component test with more severe conditions when the engine endurance test can not fully demonstrate a hardware capability, like an engine sensor test; and a component test to substantiate the correlation between an analysis and a test when a FAR requirement is complied with or supported by the analysis.

A total of forty-one component certification tests were conducted through the HF120 development program. Oil tank fire test, and Power Take Off (PTO) and Accessory Gear Box (AGB) endurance test are introduced herein as representative of the component tests.

2.2. Engine Tests

The engine tests consist of tests to confirm performance, function, and operability, such as steady-state tests and acceleration and deceleration tests to evaluate acceleration rate, surge, and flameout; tests to confirm engine soundness under severe conditions such as vibration tests, overheating tests, lubricant shut off tests and the like; tests in which foreign objects that could possibly be ingested during flight such as rainwater, hailstones, birds, ice and so on are actually fired into the engine; engine starting tests under

* Aircraft Engine R&D Center

crosswind or tailwind conditions and high-altitude restart tests; fan blade containment tests in which a fan blade is purposely broken to confirm that there is no concern with airworthiness of the engine; and exhaust gas measuring tests. A total of 29 itemized engine certification tests were performed in the development of the HF120. Many of the engine tests were performed by GE, but the various engineering tests were also performed by Honda

As examples of these tests, this paper describes surge and stall tests, High Pressure Centrifugal Compressor (HPCC) impeller vibration response stress measurement tests, bird ingestion tests, and blade containment tests, including engineering tests.

Note that the bird ingestion tests were performed with the approval of the Honda Bioethics Committee.

3. Component Tests and Results

The oil tank fire test, and PTO and AGB endurance test are introduced in this chapter.

3.1. Oil Tank Fire Test

3.1.1. Certification requirement

The relevant FAR[1] requires that hardware which contains or conveys flammable fluid during normal engine operation must be fireproof or fire resistant. Fireproof is determined by neither having leakage of flammable fluid nor supporting fire during hardware exposure to fire. To substantiate compliance with this requirement, the oil tank fire test was conducted.

3.1.2. Method of substantiation

Substantiation that the oil tank complies with this FAR requirement was demonstrated by the component test. The test components are shown in Fig. 1. The HF120 oil tank is integrated into the intermediate case (IMC). The sight gauge for oil level monitoring and oil tank cap are mounted on the outer surface of the IMC.

Prior to the fire test, a flame impingement location was defined as the area which includes the oil tank cap and sight gauge with or without flammable fluid, wall thickness, seal configuration, with or without fire protection feature, and with or without cooling flow.

Figure 2 shows the post-test condition of the area where flame was applied. No oil leakage and no flame growth were observed during the test and immediately after the completion of the test. Thus, the compliance with FAR requirement for fireproof of the oil tank was demonstrated.

In addition, the fire test sequence was as follows. First, a burner was calibrated prior to the test to confirm that flame temperature was 2000 ºF and more and heat flux was 4500 BTU/h and more. Then the oil temperature inside of tank was increased up to the steady upper limit and flame applied to the defined impingement location for 5 minutes with simulated cooling flow and pressure at engine minimum idle condition, and for another 10 minutes with simulated cooling flow and pressure at engine windmill condition. After the completion of a total of 15 minutes flame impingement, the burner was calibrated to confirm that the calibration results were the same as the pre-test calibration results.

Windmill is a condition when the engine main shafts rotate by air from engine inlet while engine is not operating. The reason to include testing under windmill conditions was to verify no flame enhancement under the windmill condition. Figure 3 shows fire test configuration.

3.2. PTO and AGB Endurance Test

3.2.1. Certification requirement

The relevant FAR[2]-[4] requires demonstrating the engine drive train endurance. Acceptance criteria for this requirement is that all test components are in a serviceable condition after the test completion. To demonstrate the endurance, drive train hardware endurance test was conducted. This test was the first certification test conducted by Honda.

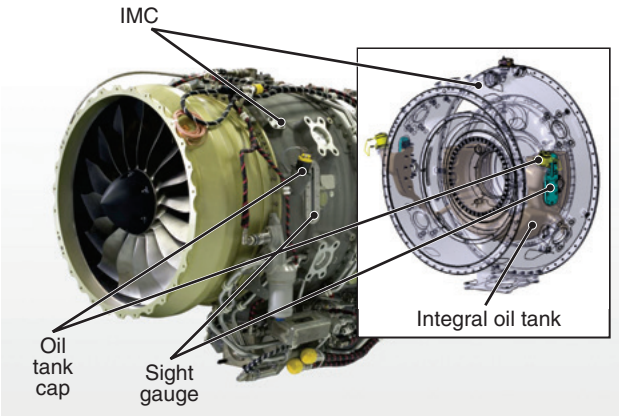


Fig. 1 HF120 oil tank system



Fig. 2 Fire exposure area of oil tank after test

3.2.2. Method of substantiation

Substantiation that PTO and AGB comply with this FAR requirement was demonstrated by the component test. The test components of PTO assembly, AGB, radial drive shaft and bevel gear for this test are shown in Fig. 4.

The endurance test was divided into the following two tests;

(1) Static Torque Test: Figure 5 shows the test configuration. In this test, the maximum allowable static torque was applied on each accessory pad, and it was confirmed that no fracture occurred on each axis.

(2) 150-hour Endurance Test: Figure 6 shows the endurance test setup. In accordance with the engine endurance test conditions in the FAR requirement, the test was conducted with a 25-cycle test, resulting in a total 150-hr and overload test. Oil temperature was kept at the steady upper limit of 290 ºF and more throughout the test. In addition, tests with the oil temperature transient upper limit of 330 ºF and more and with the minimum oil pressure were also conducted. The load on each accessory pad, which simulated the engine maximum load, was applied by hydraulic motor.

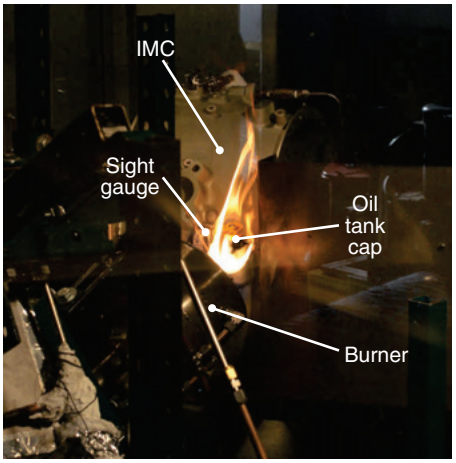


Fig. 3 Oil tank fire exposure

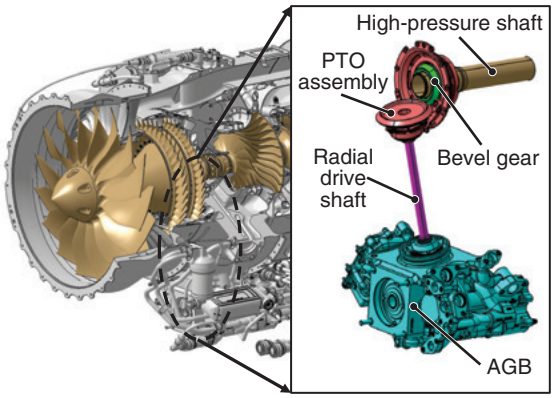


Fig. 4 Test components for PTO and AGB endurance test

As a result of the post-test tear down inspections, all test components were in a serviceable condition. Thus, compliance with the FAR requirements for engine drive train endurance was demonstrated.

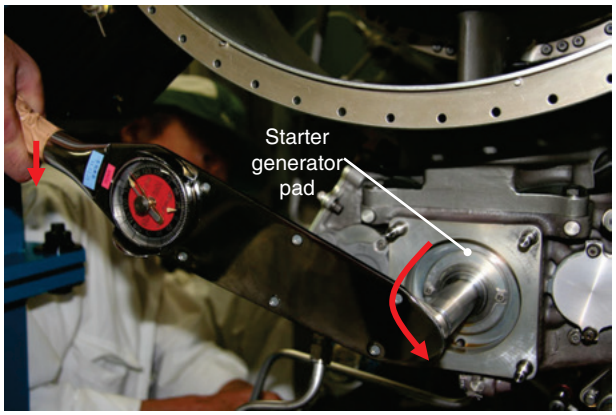


Fig. 5 Static torque test

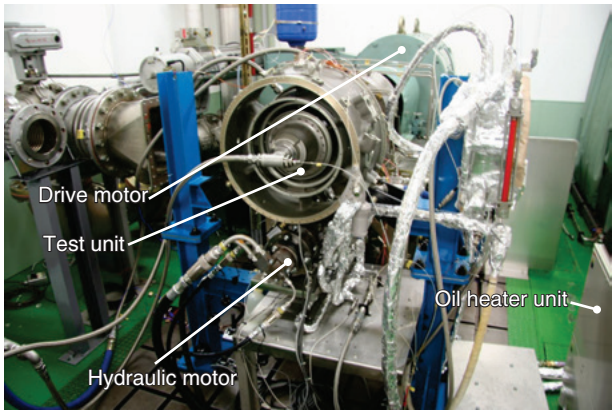


Fig. 6 PTO and AGB endurance test setup

4. Engine Test and Results

This chapter explains the surge and stall test, HPCC impeller vibration stress measurement test, bird ingestion test, and blade containment test.

4.1. Surge and Stall Test

4.1.1. Certification requirement

The operating limitations for an aircraft engine is defined as the operating envelope as functions of flight altitude and Mach number. FAR[5] requires demonstration that an engine surge or stall that cause flameout, structural damage, component over-temperature or failure of engine to recover thrust does not occur within the operating envelope. Here, the terms surge and stall refer to the phenomena of instability of the airflow flowing through the compressor. The components that were evaluated were fan rotor, low-pressure compressor (LPC), and high-pressure centrifugal compressor (HPCC).

4.1.2. Method of substantiation

Compliance with the applicable regulations was demonstrated through a combination of engine certification tests and engine model analysis. The process involved is described below. Note that the engineering and certification tests described in this section were performed by GE.

4.1.3. Engineering and certification tests

The first step was to obtain the high-altitude performance of the test components at the GE Altitude Test Facility (ATF) with the aim of improving the accuracy of the engine model used in the analysis. At this facility, high-altitude flight conditions can be simulated by setting the engine inlet pressure and temperature, and the airspeed relative to the engine.

Next, engine tests were performed as certification tests to verify compliance with the regulations in the condition where external disturbances from a crosswind are present. Stall characteristics under crosswind were obtained using a large blower at the GE outdoor test facility shown in Fig. 7. As a result, it was confirmed that under the conditions of blowing a crosswind of up to a maximum of 40 kt at the engine, no surge or stall occurred. The degree of crosswind influence obtained from these test results was reflected in the analytical model, and the fact that surge and stall would not occur within the operating envelope was proven by analysis.

Also, for the HPCC, taking into account factors such as deterioration of performance and engine manufacturing variations, an engine operating line was defined by the analytical model, and by engine tests it was verified that surge or stall would not occur.

Furthermore, in order to decide engine start limit conditions, engineering tests were performed using the facility shown in Fig. 7. In start capability verification tests for ground conditions, tests were performed with crosswind and tailwind. For altitude conditions, restart characteristics tests were performed using the ATF.

From the results of these tests, a range of start capability and wind speed limits for no occurrence of surge or stall were set. In this way, the engine tests used in combination with the analytical model verified by the tests confirmed that surge and stall would not occur within the operating envelope, and it was demonstrated that the certification requirements of Federal Aviation Regulations were satisfied.

4.2. HPCC Impeller Vibration Stress Measurement Test

4.2.1. Certification requirement

With regard to the rotating blades, stationary blades, rotating discs, and rotating shafts that constitute the engine components, the FAR[6] requires a vibration survey up to the maximum permissible engine rotational speed plus 3%, and in cases where signs of a new vibration response are observed within this plus 3% region, a further vibration survey to a 2% higher rotational speed region, and with regard to all observed responses it must be verified that the stress levels of the combined static and dynamic stress are less than the material fatigue limits. This section describes the vibration stress measurement test of the HPCC impeller.

4.2.2. Method of substantiation

The HPCC impeller vibration stress, measured using strain gauges in the engine certification tests, was evaluated with respect to the fatigue limit and verified conformity with the regulations.

The HPCC impeller is shown in Fig. 8. Since the blade vibration response stress is evaluated from the response of strain gauges attached to the impeller blade surface, it is necessary to output the stress signal to the outside using slip rings.

The HF120 has a twin-shaft structure in which there

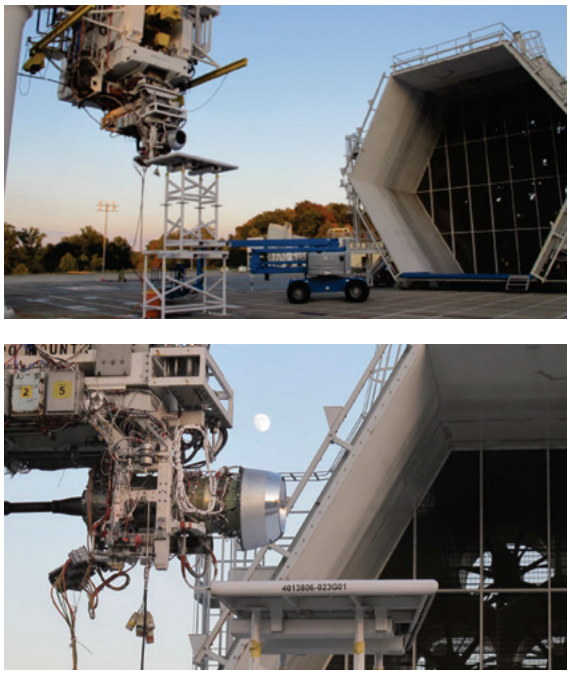


Fig. 7 Crosswind test setup

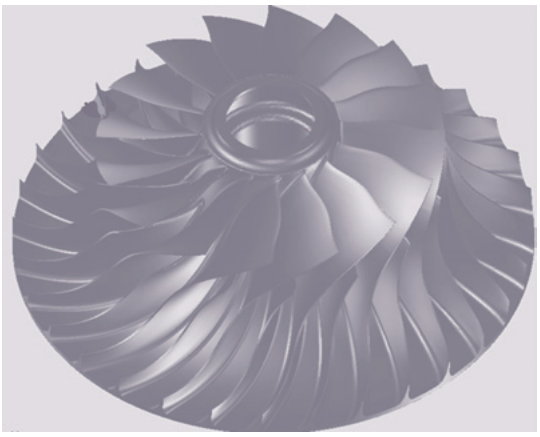


Fig. 8 HPCC impeller

is a high-pressure shaft section and a low-pressure shaft section. In order to access the HPCC impeller, the test was performed using a core-engine configuration comprising only the high-pressure section having the HPCC.

In this configuration, since the HPCC upstream fan rotor and LPC are not present, separate equipment was used to simulate the HPCC inlet conditions by feeding pre-compressed, heated air into the core engine intake.

In the evaluation of the strain gauge vibration response stress, since it is necessary to accurately measure a large number of vibration modes, it is desirable to efficiently obtain data from as many modes as possible in one strain measurement channel. Accordingly, instead of measuring all modes where the stress gradient is large and also the location where maximum stress is different for each mode, the strain gauge measuring points were chosen where the stress gradient is small and in locations with a possibility of multiple modes, making it possible to measure more accurately. For the choice of strain gauge location and the calculation of maximum vibration stress values, a ratio of subject point to measured point is used for each mode. In this case, a strain distribution based on a Finite Element Method (FEM) analysis was used. Furthermore, to verify the analysis probability, an individual vibration test was performed on the actual part. Figure 9 shows an example of typical mode deformation results for the HPCC impeller obtained in the individual vibration test.

Once these were prepared, the maximum vibration stress values during actual engine operation were obtained and combined with the static stress, and evaluated against fatigue limits obtained from a Goodman diagram.

4.2.3. Certification test

The engine test was performed by GE. A schematic of the engine test is shown in Fig. 10. Test results were obtained as a Campbell diagram, and from this Campbell diagram the blade surface strain gauge response levels, as well as the response rotational speeds and frequencies over the entire rotational speed operating range, can be read. For these results, combined with the FEM analysis, the vibration modes of the response and of the excitation source were identified and the maximum vibration responses were calculated. With regard to the maximum vibration stress values for all modes of the HPCC impeller obtained in these certification tests, combined with the static stress, the stress levels are less than the material fatigue limits, verifying that they satisfy the requirements of FAR.



Fig. 9 HPCC impeller mode shape

4.3. Bird Ingestion Test

FAR bird ingestion requirements that are applicable to the HF120 engine include specific bird numbers and size, etc. This section explains medium-sized bird ingestion tests.

4.3.1. Certification requirement

The FAR[7] for medium-sized bird ingestion tests requires verification that sustained thrust loss after the ingestion is not greater than 25%, that after bird ingestion a prescribed operating pattern is completed, that the engine can be shut down without issues, and that engine function and operability are acceptable.

4.3.2. Method of substantiation

Conformity with the regulations of medium-sized bird ingestion test was proven by engine certification tests. Also, the accuracy of the analytical model used to determine design specifications and the feasibility of the setup of test conditions are key points in the success of the certification tests. Therefore, engineering tests were performed by Honda in advance for the purpose of verification of the accuracy of the analytical model and confirmation of the feasibility of the certification tests. The certification tests were conducted by GE.

4.3.3. Core shot engineering test

The core shot test is a bird ingestion test aimed at the inner diameter side of the fan rotor. Figure 11 (a) shows the fan rotor bird ingestion target and Fig. 11 (b) shows a schematic of the test equipment. When a bird is ingested into the inner diameter side of the fan rotor of the HF120, surge is caused by blockage of a portion of the flow, and the pressure balance of the flow field fluctuates widely. At this time, some of the main aerodynamic parts may sustain damage having an effect on the thrust. Also, since the behavior inside the engine after bird ingestion is complex and changes within a short time, engineering tests using measuring technologies were run in order to gain detailed understanding of the events were conducted. As a result, it

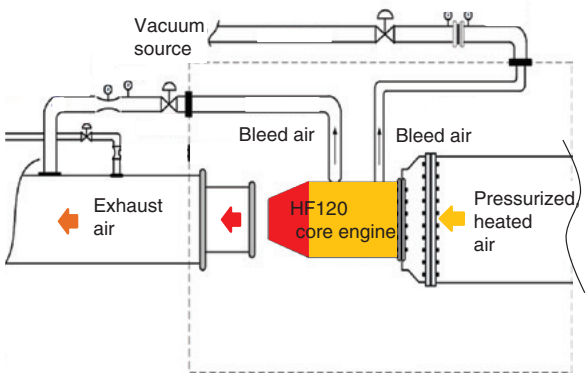


Fig. 10 HPCC stress survey core engine test

was possible to confirm the mechanism of the changes in thrust during the core shot.

Preliminary engine tests were conducted with the certification test specifications which were selected with this knowledge, and the thrust after bird ingestion was within the requirements.

4.3.4. Tip shot engineering test

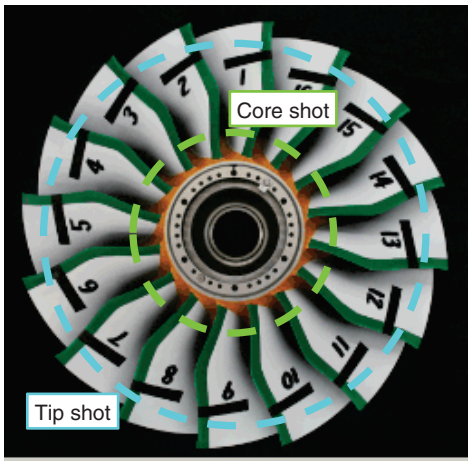
The tip shot is a bird ingestion test aimed at the outer diameter side of the fan rotor [Fig. 11(a)]. In this case, blade deformation is caused by bird collision with the fan rotor, affecting the thrust. For this evaluation, rather than using an engine test, a unit test was used in which appropriate test conditions could be set. The fan rotor was rotated at a specific rotational speed in the unit test rig shown in Fig. 12, and a tip shot test performed by letting a bird be ingested at the outer diameter side.

The post tip shot fan rotor was installed in the engine and the thrust before and after deformation was evaluated. The results provided an indication of satisfying the certification requirements.

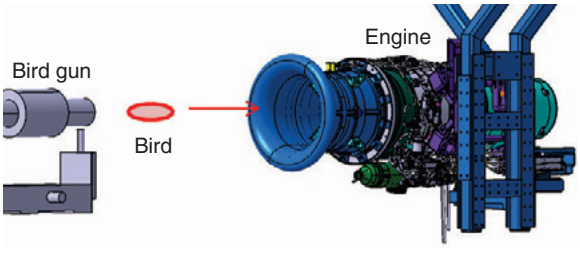
4.3.5. Certification test

The certification test was performed at the GE outdoor test site. The thrust after core shot satisfied the requirements, and the operation after ingestion was completed without issue. In this way, it was demonstrated that the FAR requirements were satisfied.

Regarding the tip shot, GE also performed a thrust verification test and it was confirmed that the requirements were satisfied.



(a) Fan rotor target location



(b) Core shot test setup

Fig. 11 Target location and core shot test setup

4.4. Fan Blade Containment Test

4.4.1. Certification requirement

The relevant FAR[8] requires substantiating that the engine is capable of containing damage from a fractured blade inside of the engine without catching fire and without damage to the engine mount system, and that the engine retains shut down capability after a blade fracture event occurs. FAR requires the most critical blade to be fractured. The most critical blade is a fan rotor blade in HF120. To verify conformance to this requirement, a fan blade containment test was conducted with an intentionally fractured blade during engine operation.

4.4.2. Method of substantiation

Fan blade containment compliance with the FAR requirement is demonstrated by engine certification test. Also, in the fan blade containment certification tests, as in the case of the bird ingestion tests, the accuracy of the analytical model used to determine design specifications and the feasibility of the setup of test conditions are key points in the success or failure of the certification tests. Engineering tests were therefore performed by Honda in advance for the purpose of verification of the analytical model and confirmation of the feasibility of the certification tests. The certification tests were then performed by GE.

4.4.3. Engineering test

In the engineering test, a fan rotor blade was broken off by wireless remote control from the test bench monitoring room. At the time the blade broke, the engine was running at the maximum permissible rotational speed.

Figure 13 shows a photo of the external appearance of the fan case after the engineering test. No evidence could be seen of the broken blade penetration on the fan case, and it was confirmed that damage was restricted to the interior of the engine. Neither catching fire, nor failure of the mount system was observed, and the engine had safe self shut-down after a blade fell. These results provided confirmation of satisfying the Federal Aviation Regulations requirements.

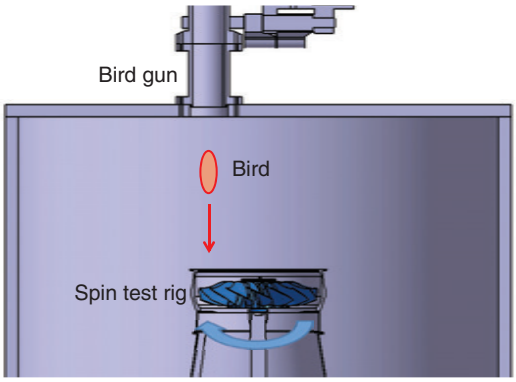


Fig. 12 Tip shot test setup

Also, detailed data such as strain data for each of the parts, necessary for verification of the analysis probability, was obtained.

4.4.4. Certification test

The certification test was conducted at the GE outdoor test facility. Figure 14 shows the blade containment test setup, the orange colored blade is the blade that was designed to fall. Figure 15 shows the fan rotor and fan case appearance after test completion. Same as the engineering test, no trace of fractured blade penetration appeared on the fan case, indicating that a fallen blade is contained inside the engine. The certification test also demonstrated safe self-shutdown after a blade fell, no catching fire, and no failure of the mount system, same as the engineering test, therefore substantiating compliance with FAR requirement.

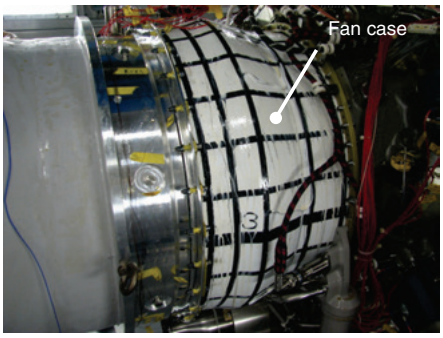


Fig. 13 Fan case after blade containment test

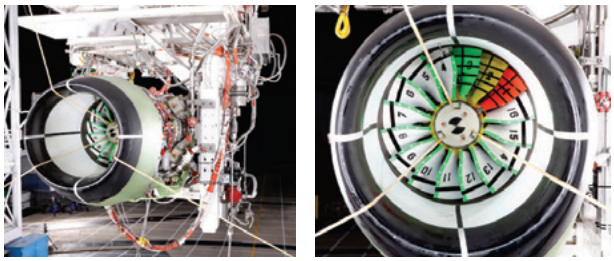


Fig. 14 Blade containment test setup

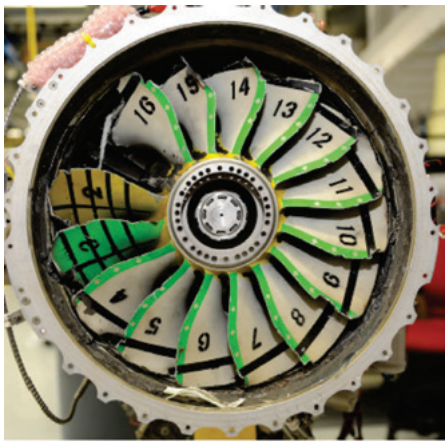


Fig. 15 Fan rotor and fan case after blade containment test

5. Conclusion

Through the HF120 development program, forty nine component certification tests and twenty nine engine certification tests were conducted, including the tests described in this paper. 190 certification test plans and reports were submitted to the FAA through the HF120 development program. GE and Honda finally received HF120 turbofan engine Type Certificate from the FAA in December 13, 2013.

A majority of the certification test was conducted by GE, while Honda conducted PTO and AGB endurance certification test and a number of engineering tests. These activities provided us not only technological outcomes but precise knowledge and experience.

References

(1) Fire protection, 14 Code of Federal Regulations Part33 Amendment 30 Section 33.17
(2) Accessory attachments, 14 Code of Federal Regulations Part33 Amendment 30 Section 33.25
(3) Endurance test, 14 Code of Federal Regulations Part33 Amendment 30 Section 33.87
(4) Teardown inspection, 14 Code of Federal Regulations Part33 Amendment 30 Section 33.93
(5) Surge and stall characteristics, 14 Code of Federal Regulations Part33 Amendment 30 Section 33.65
(6) Vibration test, 14 Code of Federal Regulations Part33 Amendment 30 Section 33.83
(7) Bird ingestion, 14 Code of Federal Regulations Part33 Amendment 30 Section 33.76
(8) Blade containment and rotor unbalance tests, 14 Code of Federal Regulations Part33 Amendment 30 Section 33.94

■ Author ■


Ryosuke SHIBATA


Katsumasa ISHIKAWA


Ryo KODAMA


Shuu TAGUCHI


Hidehiko NAKATA

Verification of High Altitude Performance and Characteristics for HF120 Turbofan Engine

Katsumasa ISHIKAWA* Norio KASAI*
Norifumi IKEDA* Ikuo TAKAMATSU*

ABSTRACT

The HF120 turbofan engine co-developed with General Electric Company was tested to verify its high altitude characteristics. Ownership of the tests was cooperatively shared between General Electric Company and Honda with General Electric Company leading the tests at the Altitude Test Facility and Honda leading the tests on the Flying Test Bed. A small business jet aircraft modified to replace an engine on one side with an HF120 turbofan engine was used for the Flying Test Bed. A data measurement system that can handle the large amounts of data acquired during flight tests was installed inside the aircraft to verify the engine conditions comprehensively.

The high altitude characteristics required for aircraft engines were verified from multiple aspects by taking advantages of the two different types of test environments of Altitude Test Facility and Flying Test Bed.

The combination of performance test data and engine model simulation verified that overall steady state performance meets the requirements throughout the engine operating envelope. Acceleration and deceleration characteristics have been verified to meet the requirements. Surge and stall characteristics have been verified to secure the required surge margin. The air start envelope has been verified through numerous air start demonstrations.

1. Introduction

The high altitude region where an aircraft engine can operate is defined as the operating envelope using pressure altitude and Mach number. Table 1 shows the minimum and maximum range of the HF120 turbofan engine (HF120) flight pressure altitude, Mach number, atmospheric pressure and atmospheric temperature. The normal operation of the engine under such atmospheric conditions has been demonstrated by testing. The Altitude Test Facility (ATF) simulates high altitude conditions at a ground test facility while the Flying Test Bed (FTB) lets an engine installed in a real aircraft perform testing at high altitude flight conditions. This paper provides a description of how the HF120's high altitude characteristics were verified using these facilities.

Table 1 HF120 operating range

	Min.*	Max.*
Pressure altitude (ft)	-1000	46000
Mach number (-)	0	0.85
Atmospheric pressure (kPa)	14.1	105.0
Atmospheric temperature (°C)	-77	55

* Min. and max. actual limitations are defined by operating envelope.

2. Characteristics of ATF and FTB

Figure 1 shows the HF120 installed in the ATF owned by General Electric Company (GE)[(1)]. The ATF is designed to simulate high altitude atmospheric conditions

* Aircraft Engine R&D Center

with accuracy and stability. As a ground test facility, the ATF provides a relatively high degree of freedom for instrumentation and other related equipment. Furthermore, the ability to directly measure thrust, which is difficult using the FTB, and the absence of constraints such as test time and weather make it possible to acquire detailed data under varied conditions.

However, the requirements for an ATF are demanding, needing a large-scale facility including equipment to cool and depressurize the copious amount of engine air inflow. For this reason, only a handful of engine manufacturers have ATFs.

Figure 2 shows the FTB with the HF120 installed. The FTB has a test engine installed on an existing aircraft, which can be tested under actual flight conditions. In addition to testing with aircraft movement, other items to be evaluated uniquely in FTB tests include vibration measurement during landing.

When performing an FTB test, partial alteration of the airframe is necessary to install the test engine. Also, atmospheric conditions at high altitude change occasionally, requiring certain flexibility in the test conditions.

HF120 high altitude characteristics were verified by utilizing the features of these two different test facilities that complement each other.

The ATF tests were led by GE and performed at the GE-owned ATF. Honda engineers provided their technical support on site.

The FTB tests were led by Honda and performed in cooperation with Atlantic Aero, Inc. (AA) in the United States. The test vehicle used was a small business jet aircraft with an engine on one side replaced by the HF120. The aircraft alteration plan was developed by Honda, carried out by AA, and an experimental Airworthiness Certificate was obtained. GE was responsible for supporting engine assembly and part of the instrumentation.

Collaboration with these companies started in the planning phase and continued while ATF and FTB tests were performed. Data acquired during these tests was shared between GE and Honda and analyzed in coordination between the U.S. and Japan.



Fig. 1 ATF test setup and HF120



Fig. 2 FTB and HF120

3. Test Items

Table 2 shows the list of evaluation items for verifying high altitude characteristics. Among the evaluated items were overall engine high altitude characteristics as well as subsystems relating to such as fuel, lubrication and vibration. A broad range of items were tested.

This chapter focuses on overall engine high altitude characteristics and describes some key points in the overview and technical assessment of each item.

3.1. Overall Steady State Performance, Acceleration and Deceleration

Engine performance during steady state flight conditions were evaluated using certain thrust and fuel consumption parameters. The evaluation not only covered the overall steady state performance but also included component characteristics such as the compressor, turbine and combustor.

For acceleration and deceleration, parameters such as acceleration and deceleration time, controllability, surge and stall, and lean blowout margin were evaluated. Surge and stall, in this context, refers to an unstable phenomenon of airflow passing through the compressor.

As examples of overall steady state performance tests, surge and stall tests are used to describe the selection method of the test points.

Individual characteristics of the ATF and FTB were taken into account in selecting test points, and each evaluation item was technically reviewed. Fundamentally, detailed and extensive amounts of data were collected by ATF tests, then major points at actual flight conditions were validated, and items unique to FTB tests were evaluated by subsequent FTB testing.

Figure 3 shows the HF120 operating envelope and representative test points used in evaluating overall steady state performance and surge and stall characteristics.

3.2. Windmill and High Altitude Air Start

Windmill refers to the condition of shaft rotation triggered by inflow aerodynamic forces while the engine is not operating. Since the rotating shaft is kept at a low speed under this condition compared to normal operation, lubrication and shaft vibration were evaluated under such

Table 2 Evaluation items

Category	Evaluation item
Overall engine characteristics	Performance
	Acceleration and deceleration time
	Controllability
	Surge and stall margin
	Lean blowout margin
	Windmill
	Air start
	Maneuver (FTB only)
Sub systems	Fuel system
	Control system
	Start system
	Lubrication system
	Secondary air system
	Thermal system
	Vibration and dynamics

circumstances.

High altitude air start testing is intended to verify the envelope where an aircraft engine can restart at high altitude conditions. The envelope is bound by altitude and Mach number. Figure 4 shows test points and air start envelopes for the high altitude air start test. HF120 high altitude air start, as indicated in this figure, can be defined by three types of envelope: starter-assisted air start (SAAS) envelope, steady state windmill (SSWM) envelope, and quick windmill relight (QWRL) envelope.

3.3. Maneuver

Maneuver here refers to aircraft behavior and is evaluated in flight tests under various conditions such as attitude change, acceleration change and rolling pitch and yaw fluctuation. Items being evaluated include lubrication function and vibration properties. In addition, disturbance from engine inlet air and its impact on overall steady state performance and acceleration and deceleration characteristics were also tested while flying with different angles of attack or angles of sideslip relative to the aircraft flying direction.

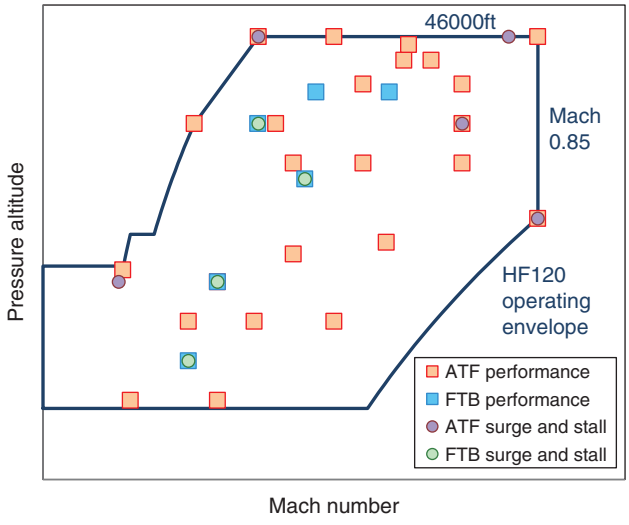


Fig. 3 HF120 operating envelope and test points

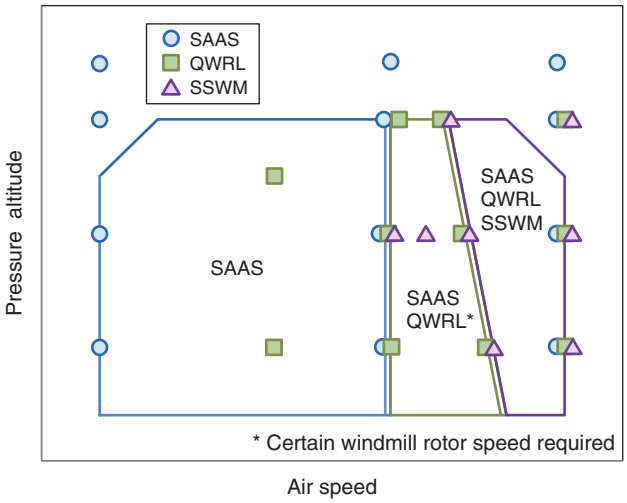


Fig. 4 HF120 air start test points and envelope

4. Test Facility and Operation

This section reviews the FTB test facility and test operation led and executed by Honda.

4.1. Data Measurement System

An instrumentation system was developed to measure various engine and airframe data with high precision in order to carry out the FTB tests.

Among the engine parameters measured were the temperatures, the pressures at representative positions, and the rotating speeds. In addition, high speed data sampling equipment to determine the vibrations and to detect any minor compressor stalls was installed as well as a system capable of measuring the clearance between rotor and casing, and bearing thrust loading.

To measure aircraft parameters, a boom installed on the nose of the aircraft measured flight conditions while a gyroscope installed inside the aircraft provided aircraft angle and angular velocity.

The items accumulated through this measurement system included over 400 channels in total, and all equipment including necessary instrumentation was installed inside the small business jet aircraft. The aircraft was extensively modified to accommodate the associated instrumentation layout and sensor signal routing. When carrying out this modification, aircraft cabin volume, electric power and

payload limitations were reviewed. Figure 5 shows the FTB data measurement system schematic.

Additionally, a video camera was mounted to monitor and record engine inlet external appearance in preparation for potential foreign object ingestion during flight testing (Fig. 6).

4.2. Control System

Figure 7 shows the FTB control system schematic. The HF120 Engine Control Unit (ECU) installed in the aft cargo room is a digital unit that controls fuel flow by receiving input values from engine sensors, various aircraft data and thrust lever angle (TLA) signals from the aircraft, and is a redundant system. The ECU can also detect engine and sensor malfunctions, and transmit data to the aircraft to indicate the engine condition. This data communication employs the Aeronautical Radio, Incorporated 429 (ARINC429) standard. In addition, as a backup for the ARINC communication system, the capability to output engine speed, temperature and oil pressure from the ECU analog circuit to the cockpit was provided.

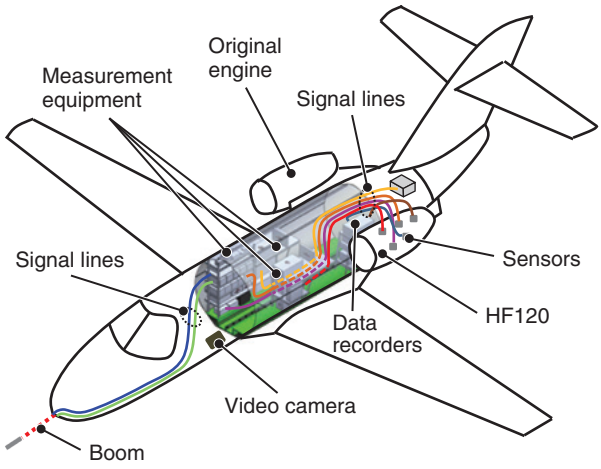


Fig. 5 FTB measurement system



Fig. 6 Engine monitoring camera view

TLA signals that belong to a different system from ARINC429 are recognized by the ECU via a Rotary Variable Differential Transformer (RVDT).

Moreover, the ECU has a Controller Area Network (CAN) data communication capability installed in it, and can input as well as output ECU internal parameters. Data from over 400 channels can be recorded at a high sampling rate when the Data Acquisition Panel (DAP) computer used in development is connected to the ECU via CAN communication. Also, ECU internal control settings can be overridden in real time during engine operation. This process is called adjustment by which testing under various control settings can effectively be applied without engine shutdown or ECU resetting.

The FTB had a computer called Interface PC installed in the cabin to connect the HF120 ECU to existing aircraft systems. The Interface PC was configured to mutually convert, send and receive aircraft data and ECU data.

In addition, the system also had information such as engine bleed level and landing gear weight-on-wheels (WOW) converted into the ARINC429 format by the Interface PC, so that it could be transmitted to the ECU.

4.3. Engine Mount and External Loading Simulation System

4.3.1. Engine mount

In order to switch the existing engine to the HF120, a new engine mount was manufactured and evaluated.

One of the key requirements for the engine mount to comply with is no engine separation under the maximum expected loads. The types of loads to be reviewed are the maximum impact load generated by loss of a fan blade, fatigue load generated by windmill after loss of a fan blade, and acceleration-induced load during maneuver testing. The engine dynamics model was used to evaluate the engine mount strength under these loading conditions, and it was analytically demonstrated that the engine would not be separated under any expected loading conditions.

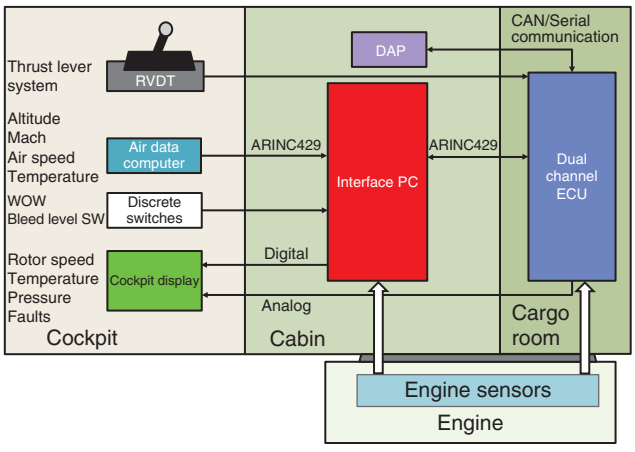


Fig. 7 HF120 FTB control system schematic

4.3.2. Fuel system

Because the existing fuel delivery system did not meet certain HF120 requirements, certain fuel piping and pumps in the FTB were replaced with units conforming to the HF120. This modification provided an independent fuel delivery system for both right and left sides, and the capability to install two engines having different fuel delivery requirements on a single aircraft.

4.3.3. External load simulation system

High pressure bleed air from the compressor is used for cabin pressurization and anti-icing systems when operating a business jet aircraft. Figure 8 shows the bleed air system configured to simulate this condition.

Electric power for instruments, air conditioners and electric lights is extracted from a generator mounted on the engine. This extracted electric power was regulated by variable load bank equipment during FTB testing. The load bank equipment was placed in the aft cargo room and structured to prevent overtemperature during operation by a cooling duct located on the side of the aircraft. Figure 9 shows photos of the variable load bank equipment.

Since the bleed air and the extracted electric power can induce external loads on the engines and affect engine characteristics, they are set as part of the test conditions.

By executing what was described in Sections 4.1 through 4.3, a flight testing system was formulated which efficiently evaluated the engine characteristics at multiple flight conditions from diverse perspectives.

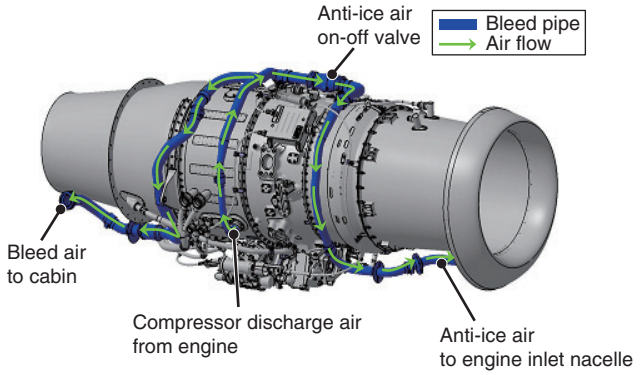


Fig. 8 Bleed air system

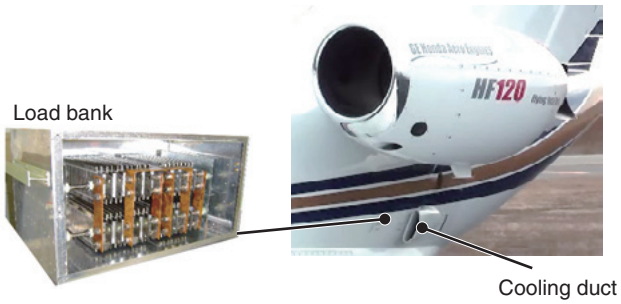


Fig. 9 Load bank and cooling duct

4.4. Operation during Flight Test

Two flight test engineers and two pilots were on board during the FTB tests. The engineers constantly monitored the engine data, aircraft data and control data. The engineers gave instructions to initiate the tests one by one while communicating with the pilots through an intercom system, then executed the flight tests accurately and effectively by assessing the test results.

5. Verification Results of High Altitude Characteristics

Four examples of verified HF120 high altitude characteristics are provided as below.

5.1. Verification of Overall Steady State Performance

Overall steady state performance contributes a great deal to aircraft performance during takeoff, climb, cruise, descent and landing throughout the entire operating envelope.

In order to evaluate a wide range of conditions with efficiency, characteristics of each engine component, such as the compressor or the turbine, were used to formulate a numerical computational model (hereinafter referred to as the model) to derive overall steady state performance. The effects of sensors or introduced parts were taken into account. The comparison between test results from typical flight conditions and values derived from the model validated the model.

Figure 10 shows the model validation process. If any difference is found through comparison of the test results with model derived values, the model will be adjusted until the discrepancy falls within an allowable tolerance. Major parameters used here are low pressure shaft speed (N1), high pressure shaft speed (N2), fuel flow rate, and interstage turbine temperature (ITT).

In order to validate the model, the impacts of changes made to test the engines were examined. These effects are primarily attributable to variation of components in the test engine, as compared to product engines, and sensor(s) installed inside the engine. These effects were derived from component test results or computational fluid dynamics analysis results.

A production engine model was obtained by comparing the model derived values with the test results, and then removing the test engine specific effects from the model.

Figure 11 shows model derived values (solid lines) and ATF test results (plotted points). As this chart displays multiple data with different test conditions, estimated values and test results were found to be consistent.

In this manner, overall steady state performance has been confirmed to meet the requirements throughout the

operating envelope by using the model verified by high altitude test results.

5.2. Acceleration and Deceleration Response Test

The acceleration and deceleration response testing was performed by varying altitude, Mach number and engine external loading conditions. For example, rapid acceleration is needed to generate the thrust demanded by pilot in circumstances such as a go-around.

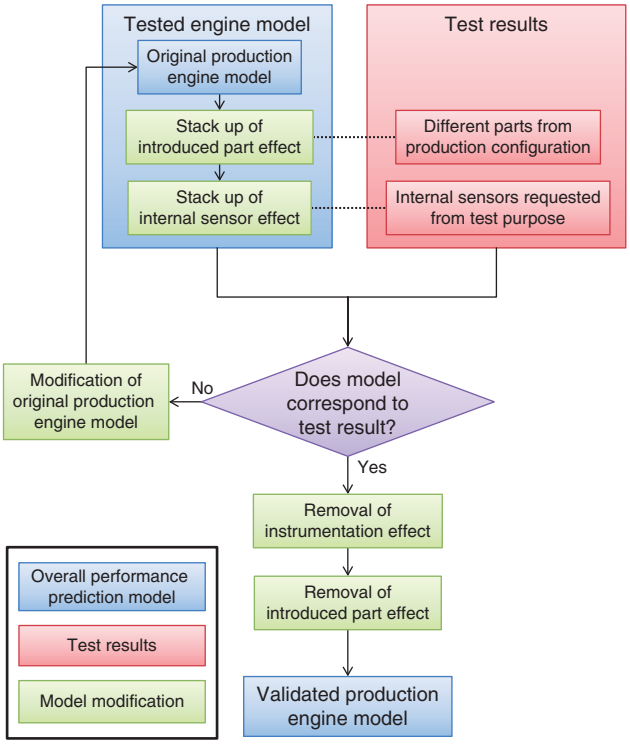


Fig. 10 Validation process of performance prediction model

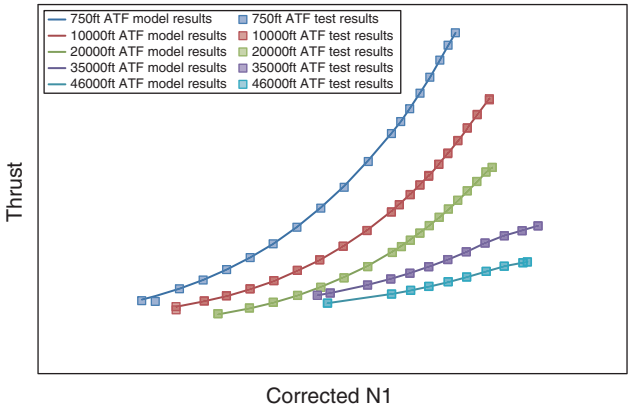


Fig. 11 Comparison between ATF model results and ATF test results

Figure 12 shows an example of engine behavior during quick acceleration. The acceleration response test focused on evaluating whether the acceleration time and the ITT values fall within the requirements while the deceleration response test focused on evaluating deceleration time. With other evaluations, it was demonstrated that both acceleration and deceleration meet the requirements within the operating envelope shown in Fig. 3.

5.3. Surge and Stall Test

A testing to check compressor surge margin was performed. This section describes the surge test for the high-pressure compressor. In order to confirm the surge margin during normal acceleration, the fuel flow command during acceleration was set higher than usual to intentionally trigger compressor surge. The higher fuel flow was set especially at the target engine speed so as to prevent engine overtemperature.

Figure 13 shows an example of a surge that actually occurred. Rapid decrease in high pressure compressor exit pressure (P3) indicates that a surge occurred.

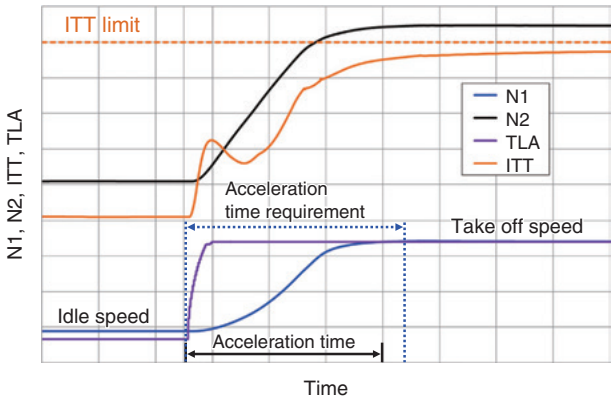


Fig. 12 Quick acceleration from idle

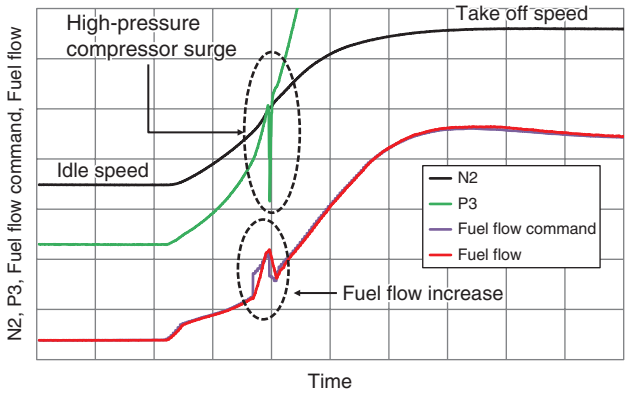


Fig. 13 High-pressure compressor surge test

Figure 14 shows the simple schematic of the high-pressure compressor surge line and the operating line. While the operating line during acceleration tends to get close to the surge line from the steady state operation line as indicated by arrows (A) and (B), it eventually reaches the takeoff running point. In addition, the higher the acceleration rate becomes, the closer the operating line moves to the surge line. In this figure, (A) indicates normal rapid acceleration operation which corresponding to Fig. 12, carrying a certain margin relative to the surge line by component test data. On the other hand, (B) represents the operating line when fuel flow was intentionally enriched to trigger a surge, and this surge was observed after the operating line surpassed the surge line by component testing.

The engine surge line was identified by varying engine inlet ambient conditions, the speed region and other parameters. By comparing this line with the operating line during normal acceleration, and then reviewing operating line shifts as a function of flight conditions, external loading conditions and others, it was verified that the HF120 has sufficient surge margin.

5.4. High Altitude Air Start Test

High altitude air start testing was executed by varying altitude and Mach number. As described in Chapter 3, three types of engine start sequence were defined.

First, Fig. 15 shows SAAS. The N2 threshold indicates the lowest speed limit capable of commanding fuel flow. In this figure, the pre-start N2 is less than the threshold and the starter is necessary for air start. Afterwards, the starter assist raises N2. Once N2 reaches a certain speed, relight provides ITT increase, which is followed by subsequent N2 increase, finally reaching steady state idle conditions. During this period, ITT limit is not exceeded and the air start is completed in a normal manner.

Next, Fig. 16 shows SSWM. It is a steady state windmill condition prior to start, with ITT and N2 statically determined. Since N2 is higher than the threshold, the subsequent relight is successful without relying on the starter. With no ITT overtemperature observed, the air start is finally completed.

Lastly, Fig. 17 shows QWRL. As shown in the figure, air start was initiated within a short time after engine shutdown operation. Hence, N2 exceeds the threshold, similar to SSWM, and no starter assist is necessary. Also in

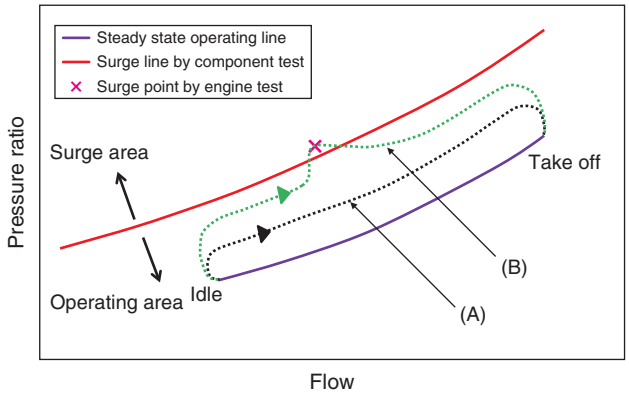


Fig. 14 Simple schematic of high-pressure compressor surge and operating line

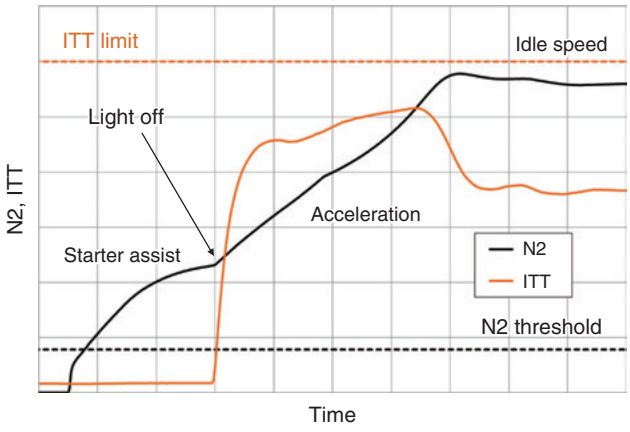


Fig. 15 SAAS

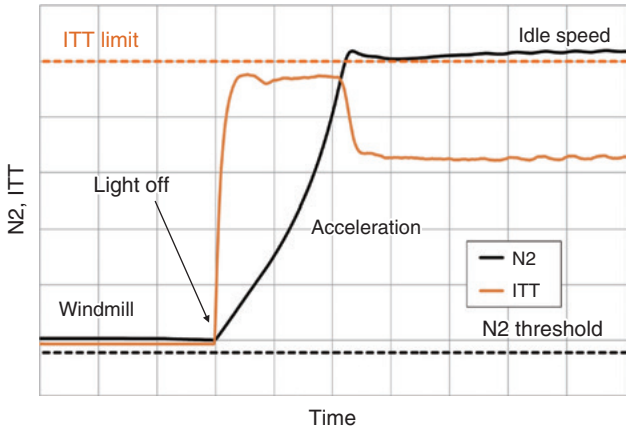


Fig. 16 SSWM

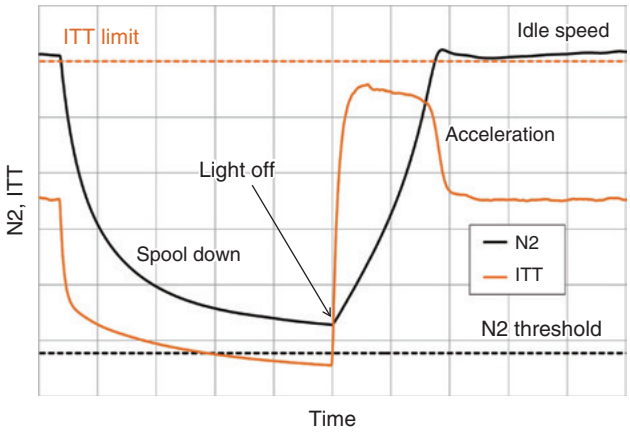


Fig. 17 QWRL

this case, no ITT overtemperature is observed, and the air start is finally completed.

ATF and FTB tests were performed over 300 times in total combined to validate the air start envelope shown by solid lines in Fig. 4.

6. Conclusion

HF120 high altitude characteristics were tested by employing an ATF simulating high altitude conditions using a ground test facility and an FTB capable of flight tests. The FTB tests had the engine on one side of a small business jet aircraft replaced by the HF120, and the developed flight testing system capable of measuring data of over 800 channels in order to evaluate multiple test items. The ATF and FTB test results were used to validate the high altitude characteristics of the HF120 within the operating envelope.

References

(1) http://world.honda.com/news/2009/c091019GE-Honda-HF120-engine/, 2010/3/25

■ Author ■


Katsumasa ISHIKAWA


Norio KASAI


Norifumi IKEDA


Ikuo TAKAMATSU

Aerodynamic Technologies for High-efficiency and High Specific-flow-rate Fan and Centrifugal Compressor

Hisato TANAKA* Mineyasu OANA*

ABSTRACT

This paper describes the development of aerodynamic technologies for a high-efficiency and high specific-flow-rate fan and centrifugal compressor during the preceding research for the HF120 turbofan engine in order to achieve low specific fuel consumption and high thrust-weight ratio.

For the fan, a swept fan blade design was selected to decrease the pressure loss from shock waves. Computational Fluid Dynamics analysis provided an estimate of the decreased pressure loss from shock waves at swept fan leading edge and flow passage, and the efficiency enhancement throughout the span. Small-scale rig testing indicated that the newly designed fan improves efficiency by 1.5% or more and inlet specific flow rate by 2% in comparison with the fan of the HF118 turbofan engine, in three typical operating conditions: takeoff, climb and cruise.

For the centrifugal compressor with increased aerodynamic loading from higher exit specific flow rate, a new blade configuration was designed to raise aerodynamic loading at the forward area of the blade where the boundary layer is thinner, followed by a confirmation of high efficiency via Computational Fluid Dynamics analysis. Small-scale rig testing indicated enhancement of exit specific flow rate by 7% and efficiency by 0.8% in cruise condition in comparison with the centrifugal compressor of the HF118 turbofan engine. The aerodynamic technologies described in this paper have been incorporated into the fan and centrifugal compressor of the HF120 turbofan engine.

1. Introduction

In 1986, Honda initiated fundamental research and development of a small-sized aircraft jet engine. In 2003, Honda completed stand-alone development of the HF118 turbofan engine (HF118)[(1)]. In 2006, Honda and General Electric Company (GE) of the US initiated joint development of the HF120 turbofan engine (HF120), successor to the HF118. In 2013, the United States Federal Aviation Administration awarded Type Certificate to the HF120.

Figure 1 shows HF120 engine features. The HF120 aims for lower specific fuel consumption and a higher thrust-weight ratio than those of the HF118.

To achieve low specific fuel consumption with low fuel flow rate and high thrust, enhancement of efficiency of aerodynamic parts is one of the key elements. Also, enhancement of specific flow rate by decreasing the frontal projected area of aerodynamic parts and increasing the air flow rate is important to achieving high thrust-weight ratio with less engine weight and high thrust.

Most HF120 thrust is proportional to the flow rate of the fan located at the front region of engine. Most of the HF120's total pressure ratio is produced by the centrifugal compressor. Thus, the fan and the centrifugal compressor have crucial roles among the aerodynamic parts of this engine.

This paper describes the aerodynamic technology of the design concept, the performance prediction method with computational fluid dynamics (CFD), and performance

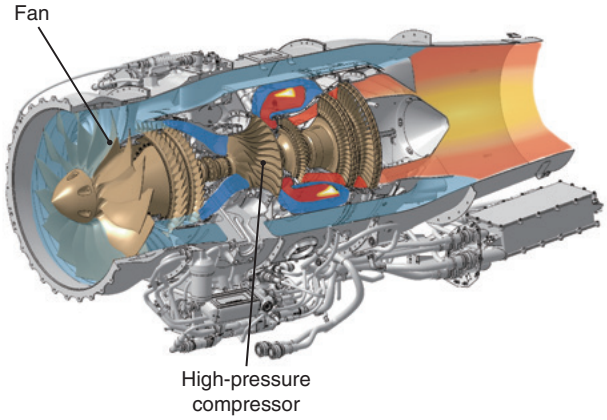


Fig. 1 HF120 turbo fan engine features

* Aircraft Engine R&D Center

substantiation testing by small-scale rig, enabling a high-efficiency and high specific-flow-rate fan and centrifugal compressor.

Honda is responsible for aerodynamic design of the fan and centrifugal compressor in the HF120 engine, and the technology described in this paper is incorporated into engine design.

2. Development Target

The HF120 concept was to enhance specific fuel consumption and thrust-weight ratio over those of the HF118. Numerical targets to preceding development of the fan and centrifugal compressor were to enhance efficiency by 1.5% and 0.5%, respectively, and 2% and 6%, respectively, for specific flow rate.

For specific flow rate calculation, frontal projected area is defined using outer diameter, which greatly affects engine weight. For the fan, inlet specific flow rate is defined using the inlet area. For the centrifugal compressor, exit specific flow rate is defined using the exit area. The HF118 engine's outer diameter at the axial location of the centrifugal compressor is larger than the engine inlet's outer diameter, so reducing the centrifugal compressor's exit diameter is crucial to enhancing thrust-weight ratio (Fig. 2).

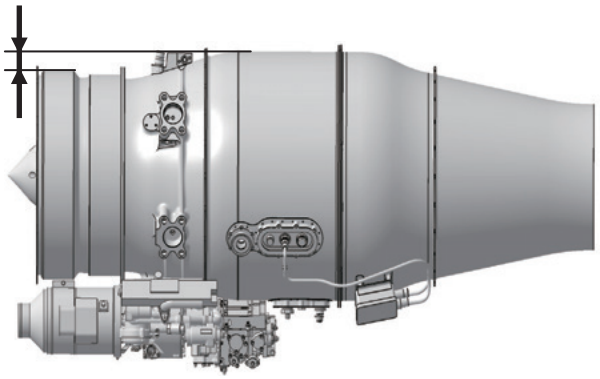


Fig. 2 Engine side view of HF118

3. Aerodynamic Technology – Fan

3.1. Fan Design Concept

Conventional fan rotor design placed emphasis on controlling centrifugal stress of rotating blades by designing the blade sections at various radial locations and stacking them in the radial direction by matching the position of their center of gravity. Figure 3(a) is a front view of the HF118 radial fan, designed using this conventional method.

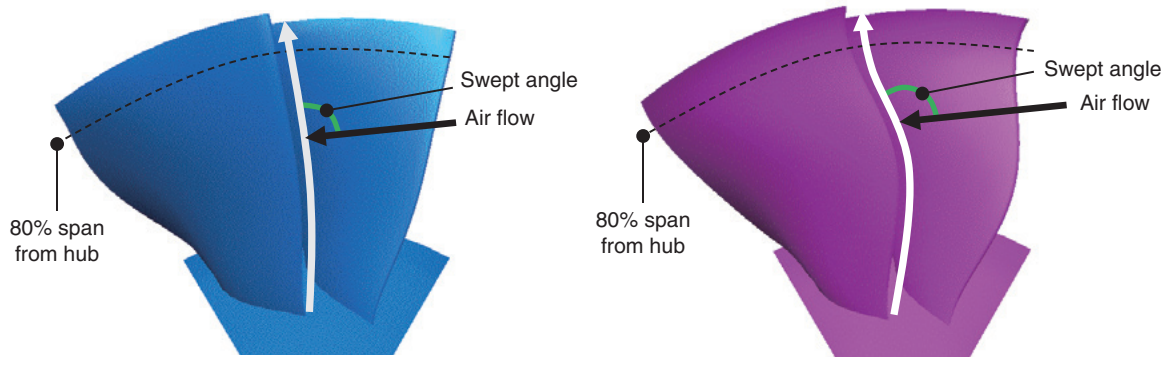
The relative velocity of inlet air to the fan rotor is supersonic. The shock waves generated at the fan rotor can cause pressure loss. Shock waves whose angles against air flow are 90 degrees are the strongest and create the maximum pressure loss and large loss of efficiency. The swept angle, defined as the angle between inlet air and the leading edge of the fan rotor, of the radial fan rotor is almost 90 degrees from hub to tip, and there is a large pressure loss on the leading edge of the fan rotor.

To decrease this large pressure loss on the leading edge of the fan rotor, a swept fan with various swept angles apart from 90 degrees from hub to tip was designed. Figure 3(b) shows the configuration of this swept fan. Unlike the radial fan, the positions of the center of gravity of each blade section are not always matched, but combining with studies of blade shape and thickness at each section enabled the resulting centrifugal stress to be within permissible limits.

3.2. Fan Performance Prediction

Performance prediction was produced with our in-house CFD analysis tool on the swept fan rotor[2].

Figure 4 shows analysis results of the radial fan and the swept fan at the cruise condition that is one of the typical operating conditions. These are relative Mach number contours on a cylindrical surface at 80% span from the hub, which are shown by the dashed lines in Fig. 3. The contour line density of the swept fan at the shock wave points in the green circle near the leading edge and the blue circle in the flow passage is lower than that of the radial fan. This result indicates that the shock waves in these areas are weakened and the pressure loss is reduced.



(a) Radial fan (b) Swept fan

Fig. 3 Front view of fan rotor

Figure 5 shows span-wise efficiency distribution in the cruise condition. Efficiency of the swept fan at 80% span point increased by 2% due to the weakened shock wave described in Fig. 4. There is no large difference between the efficiency of the radial fan and the swept fan at 90% and greater span area because of leakage flow at the tip gap. Efficiency is enhanced as the design intention in a broad area (0% to 80% span).

Calculated efficiency by integrating efficiency distribution and multiplying correlation factor between CFD analysis and testing shows that the fan efficiency is enhanced by around 1.5%, which means the target efficiency is achievable.

Additionally, specific flow rate is expected to be enhanced by 2%, making the target achievable, since not only pressure loss is reduced by a weakened shock wave at the swept fan, but also the development of the boundary layer behind the shock wave is decreased.

3.3. Fan Performance Substantiation

After fan performance prediction with CFD analysis, aerodynamic performance tests are done using a small-scale prototype to reduce engineering time on manufacturing as well as time up to substantiation testing.

Special consideration was made on processing accuracy of the prototype, because the accuracy of the small-scale prototype is tighter than that of the full-scale model by scale ratio. The geometry accuracy of the prototype fan blades was verified to satisfy the aerodynamic requirement through evaluation with a 3D coordinate measuring machine.

Measurement accuracy was secured by the combination of pressure and temperature measurement at multiple points on both circumferential and span-wise direction at fan exit and other measurement methods.

The small-scale swept fan prototype is shown in Fig. 6, and the small-scale rig test facility is shown in Fig. 7.

Figure 8 shows a small-scale rig test efficiency map of the radial fan and the swept fan in three typical operating conditions: takeoff, climb, and cruise. This map indicates that the peak efficiency of the swept fan is increased by 1.5% or more at every operating condition, which means the target efficiency is achieved in wide operating conditions, by incorporating the developed aerodynamic technology.

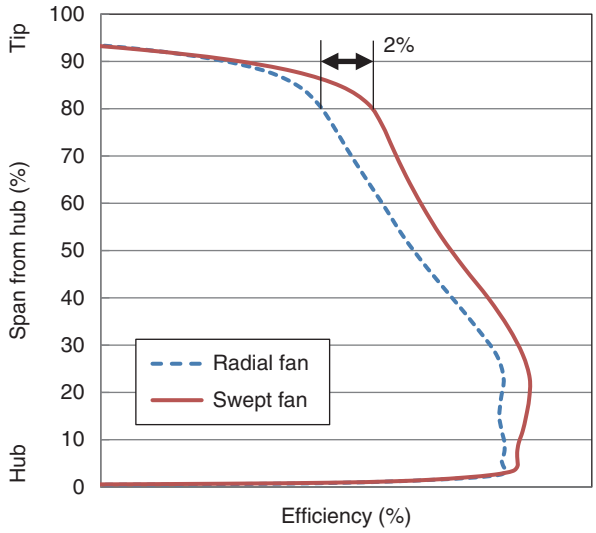
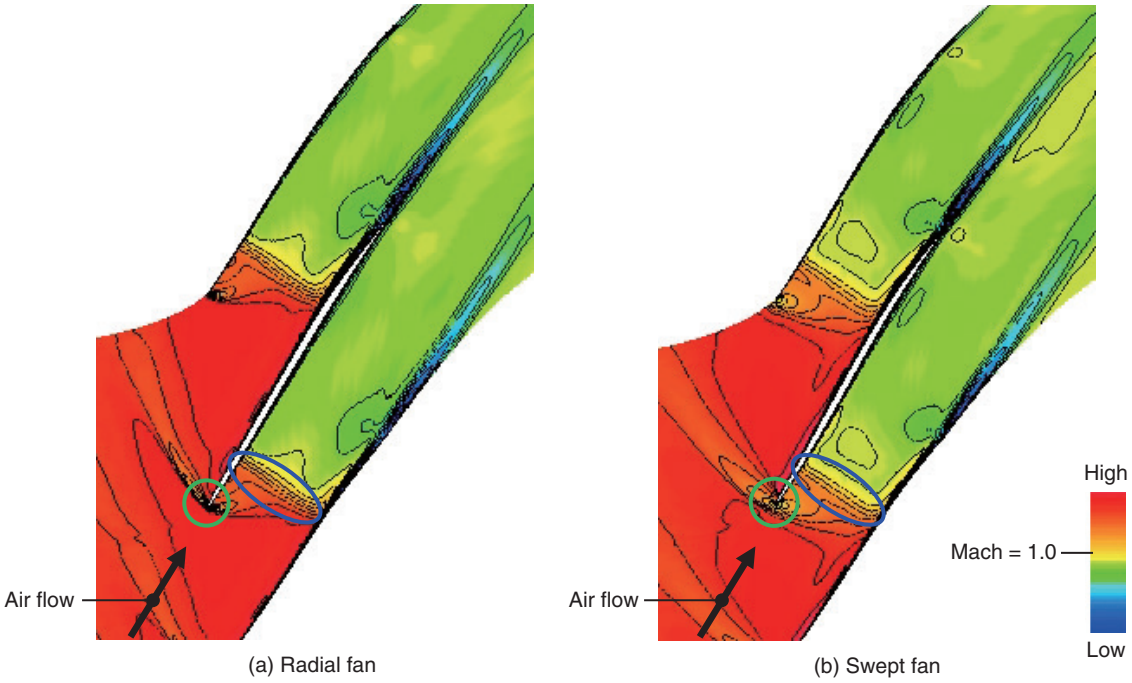


Fig. 5 Span-wise efficiency distribution of fan rotor exit



(a) Radial fan (b) Swept fan

Fig. 4 Mach contours of fan rotor at 80% span from hub

Inlet specific flow rate is also increased by 2%, thus satisfying flow rate target. Small-scale rig tests in various engine conditions were also conducted and all results satisfied the requirements in each condition.

With these results, confidence in design and analysis were substantiated.



Fig. 6 Swept fan of small-scale rig

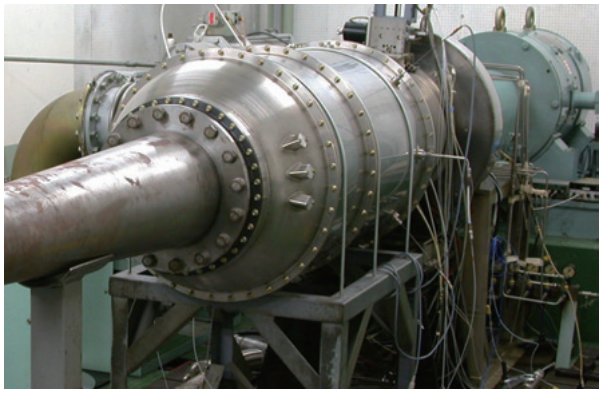


Fig. 7 Small-scale rig of fan

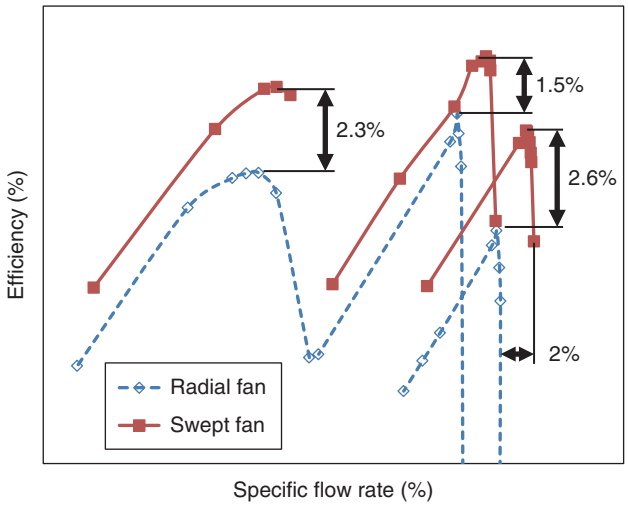


Fig. 8 Fan efficiency of small-scale rig

4. Aerodynamic Technology - Centrifugal Compressor

4.1. Centrifugal Compressor Design Concept

The high specific-flow-rate centrifugal compressor, as researched prior to the HF120, was designed with a smaller outer diameter than the conventional Honda centrifugal compressor of the HF118[3], as shown in the schematic view in Fig. 9. Therefore, the specific flow rate of the compressor is increased and aerodynamic load on the rotor should be significantly increased. However, such increase of aerodynamic load can cause drastic pressure loss induced by flow separation, and result in lower efficiency.

Therefore, the number of blades was increased to prevent load from exceeding the threshold, and the configuration of the blade was changed to increase aerodynamic load on the front portion of the rotor where the boundary layer is thinner to decrease pressure loss and increase efficiency.

Figure 10 shows a schematic of aerodynamic load distribution in airflow direction at the tip of the rotor. The goal of this design was to increase aerodynamic load on the high specific flow compressor in the 10% to 60% area in the flow direction from the front end of the centrifugal impeller.

4.2. Centrifugal Compressor Performance Prediction

A CFD analysis tool was utilized for centrifugal compressor performance prediction to verify the feasibility of the targeted 6% specific flow increment. Figure 11 shows span-wise efficiency distribution of both conventional and high specific-flow-rate centrifugal compressor. The high specific-flow-rate centrifugal compressor shows enhanced efficiency at the 90% span point (near the tip) of

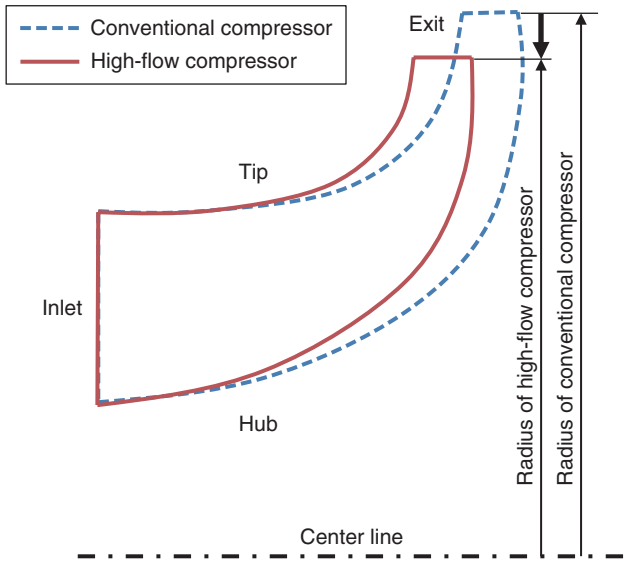


Fig. 9 General side-view of conventional and high-flow centrifugal impeller

1.5%, and retained at least equivalent or more efficiency at other points, although the aerodynamic load is increased.

Calculated efficiency by integrating efficiency distribution to span-wise direction, and multiplying by the correlation factor between CFD analysis and testing showed that the centrifugal compressor efficiency was increased by 0.5%, indicating that the target efficiency is achievable.

4.3. Centrifugal Compressor Performance Substantiation

Following completion of the centrifugal compressor performance prediction by CFD analysis, aerodynamic performance tests were performed using a small-scale prototype to reduce engineering time of manufacturing and duration for substantiation testing in the same manner as the fan. Special consideration was also given to processing accuracy on prototype manufacturing and blade geometry was verified with a 3D coordinate measuring machine.

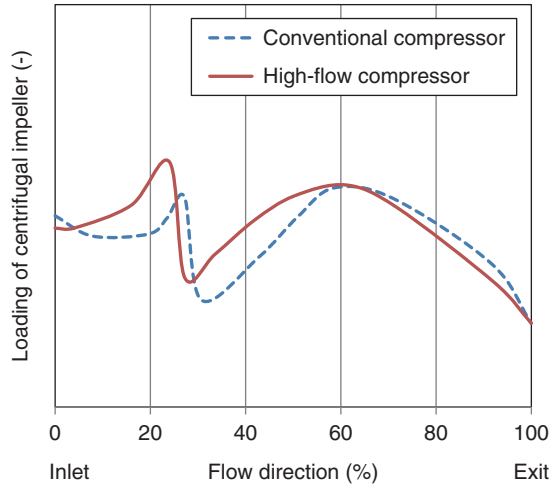


Fig. 10 Loading of centrifugal impeller

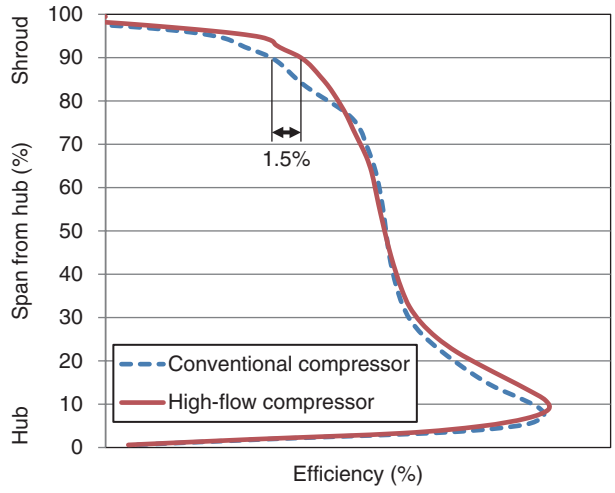


Fig. 11 Span-wise efficiency of centrifugal impeller exit

During the rig test operation, pressure and temperature measurement above and downstream of the centrifugal compressor where the air flow is stable was conducted to provide accuracy of test results.

The small-scale centrifugal impeller prototype is shown in Fig. 12, and the small-scale rig test facility is shown in Fig. 13.

Figure 14 shows the small-scale rig test efficiency map only in cruise condition considering little efficiency variation at various operating conditions. Peak efficiency is increased by 0.8%, indicating that the target efficiency increase is achieved. Exit specific flow rate of the high specific-flow-rate centrifugal compressor, which is compensated by the pressure ratio corresponding to that of conventional centrifugal compressor, is increased by 7%, achieving target flow rate. Small-scale rig tests in various engine-operating conditions were conducted and all results satisfied the requirements in each condition.

With these results, confidence in design and analysis were substantiated.



Fig. 12 High-flow centrifugal impeller of small-scale rig

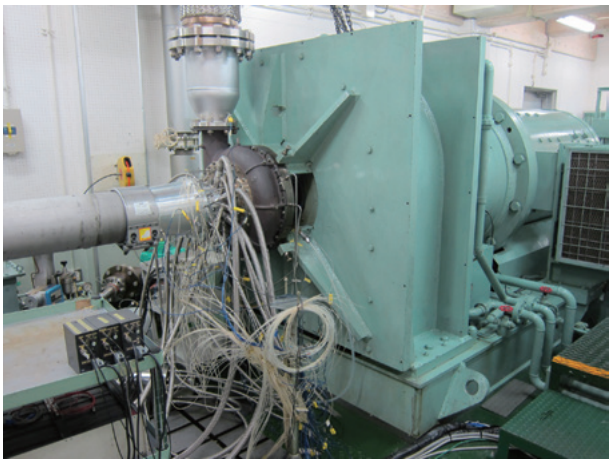


Fig. 13 Small-scale rig of centrifugal compressor

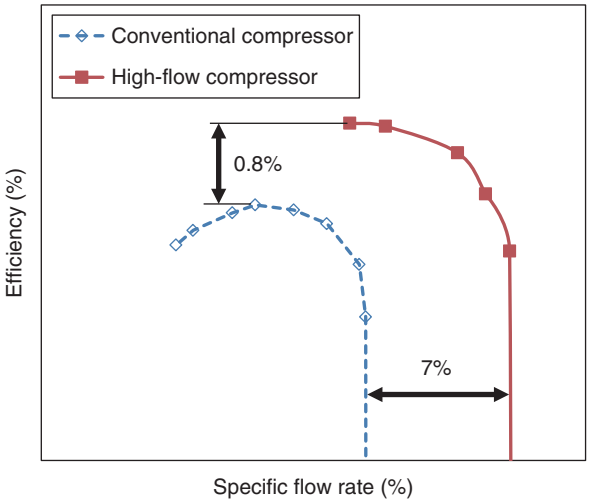


Fig. 14 Centrifugal compressor efficiency of small-scale rig

5. Conclusion

Prior to HF120 development, a study of aerodynamic technology that enables the design of a high-efficiency and high specific-flow-rate fan and centrifugal compressor was performed.

The fan design incorporated a swept fan configuration on fan rotor leading edge to weaken shock waves, and the centrifugal compressor design incorporated intentionally incremented aerodynamic load at the front portion of the blades where the boundary layer is thinner.

Performance prediction with CFD analysis verified reduced pressure loss from shock waves and enhanced efficiency of the entire span area of the fan, as well as enhanced efficiency of around at 90% span point on the centrifugal compressor.

Small-scale rig test substantiated enhanced fan efficiency by 1.5% or more and enhanced fan inlet specific flow rate by 2% in three typical operation conditions, plus enhanced centrifugal compressor efficiency by 0.8% and enhanced centrifugal compressor exit specific flow rate by 7% in cruise condition. Therefore, the test results of the fan and centrifugal compressor satisfied the numerical targets of the preceding research.

References

(1) Sonoda, T., Noda, E.: Kogata Bijinesu Jyetto yo HF118 Tabofan Enjin no Kaihatsu, Journal of Gas Turbine Society of Japan, Vol. 34, No. 3, p. 165-171 (2006) (in Japanese)
(2) Arima, T., Sonoda, T., Shirotori, M., Tamura, A., Kikuchi, K.: A Numerical Investigation of Transonic Axial Compressor Rotor Flow Using a Low Reynolds Number k-ε Turbulence Model, Journal of Turbomachinery, Vol. 121, No. 1, p. 44-58 (1999)
(3) Oana, M., Kawamoto, O., Otani, H., Yamamoto, Y.: Approach to High-Performance Transonic Compressor Design, Journal of Propulsion and Power, Vol. 20, No. 1, p.164-170 (2004)

Author


Hisato TANAKA


Mineyasu OANA

Structural Design and Verification of HF120 Turbofan Engine

Junichi IKEDA* Takafumi TANAKA* Ryuji SANO*

ABSTRACT

The HF120 turbofan engine had achieved top-class low fuel consumption and high thrust-weight ratio in the class of engine with comparable thrust, and at the same time, shown compliance with Federal Aviation Regulations. In order to accomplish these goals, characteristic structural design requirements as typified by life-limited parts design concept have been established. HF120 parts were confirmed to meet these design requirements in compliance with Federal Aviation Regulations by applying methods including CAE optimization and enhanced structural configuration. This paper uses the fan rotor as an example of how the rotating parts in the HF120 was verified to meet design requirements and Federal Aviation Regulations through computational fluid dynamics, numerical impact analysis, frequency analysis and substantiation test. The low-pressure turbine stage1 nozzle is used here as an example of how structural parts achieved lightweight, compact and low fuel consumption.

1. Introduction

The HF120 turbofan engine (HF120), developed by a joint venture of General Electric Company (GE) and Honda, not only achieved the target of competitive fuel consumption and thrust-weight ratio, but also acquired Type Certificate from the Federal Aviation Administration (FAA) by demonstrating compliance with Federal Aviation Regulations (FAR). Design requirements for the HF120 were defined to comply with the FAR while ensuring competitive engine performance. This paper describes structural design and verification methods applied to the HF120.

The HF120 engine comprises two shafts of low and high pressure, a cold section that includes the fan, the two-stage low-pressure compressor and a single-stage high-pressure compressor, and a hot section that includes a combustor, single-stage high-pressure turbine and the two-stage low-pressure turbine (LPT) as shown in Fig. 1. The fan, located at the inlet of the engine, sends inlet air into a bypass duct and a core passage. The compressor further raises the pressure of the passage air. Next, fuel is sprayed over the compressed air for combustion in the combustor. The turbine, located downstream, takes energy from the high-temperature gas that is used to rotate the compressor and fan via a rotating shaft.

This paper uses the fan rotor and the low-pressure turbine stage 1 nozzle (LPT1 nozzle) as examples of the structural design and verification. Specifically, the fan rotor highlights the adopted analysis method on computational fluid dynamics (CFD), numerical impact analyses and modal analysis, as well as the verification method combined with testing. The LPT1 nozzle highlights the structural characteristics. The latter part of this paper explains the life-limited parts design concept applied to the HF120 design.

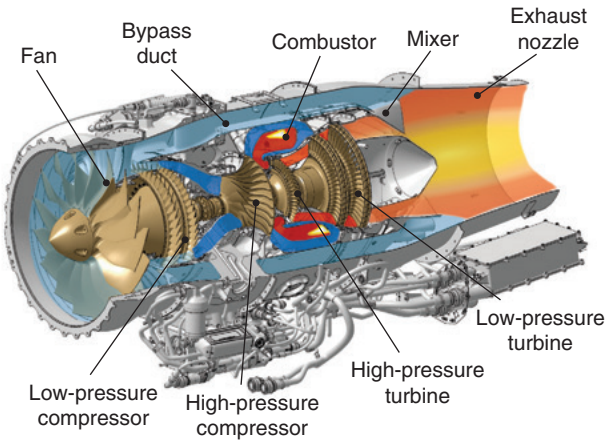


Fig. 1 Cutaway model of HF120 turbofan engine

* Aircraft Engine R&D Center

2. Fan Rotor Verification

2.1. Characteristics of Fan Rotor

Fan rotor design must take into account, among other things, damage that could be caused by foreign object ingestion as well as distortion of inlet air flow. The HF120 engine fan rotor is a light weight bladed disk configuration composed of 16 blades and a disk. Balancing of aerodynamics and structural strength, the design achieved both high efficiency and light weight. This chapter explains the verification methods used to assess Fan Blade Out (FBO), Foreign Object Damage (FOD), and High Cycle Fatigue (HCF), which are unique requirements of a fan rotor.

2.2. FBO Verification

FBO refers to separation of a fan rotor blade. The FAR[1] includes the following regulations for a FBO event. A failed blade must not cause damage to the aircraft, and under no-thrust-lever operation for at least 15 seconds after the blade is released, the engine must contain any damage without catching fire or failure of engine mounting attachments. To avoid damage by a failed blade, an HF120 design requirement was that the fan case must contain the failed blade. This section explains the containment verification method.

A detailed simulation using impact analysis software was performed. Figure 2 shows one of the analysis models. In this model, one blade of the rotating fan rotor is released around its root. This model is used to study the fan case configurations capable of containing the released blade (Fig. 3). GE and Honda had studied various configurations of the fan case and selected an appropriate one. An engine testing was then conducted to substantiate the configuration. The test result demonstrated that the fan case meets the containment requirement. The test also demonstrated compliance with FAR.

2.3. FOD Verification

A fan rotor is also required to conform to airworthiness when an engine has FOD, hail, slab of ice, or bird ingestion. This paper highlights medium-size bird ingestion verification. The design must ensure that sufficient engine thrust remains after the bird ingestion, even under conditions such as in take-off when the engine thrust reaches its maximum. The FAR[2] defines the size and quantity of the medium-size bird to be verified, as well as requiring engine thrust loss to be 25% or less. Thus, the design requirement also restricts thrust loss to 25% or less for a bird ingestion event in accordance with the FAR.

To verify whether the fan rotor meets this requirement, a detailed simulation was performed to predict damage to the fan rotor. The modeling method known as “Smoothed Particle Hydrodynamics (SPH)” was applied to bird modeling. An analysis model is shown in Fig. 4. The SPH analysis method is superior in predicting large distortions to a Lagrangian analysis and is thus appropriate for simulating bird impact on fan blades. Further work shortened the analysis run-time. To support this effort, studies were performed in advance to balance model size and analysis run-time. It was demonstrated that deformations of blades hit by the bird’s trunk have a dominant influence on thrust loss. Based on this finding, specific blades are hit by bird

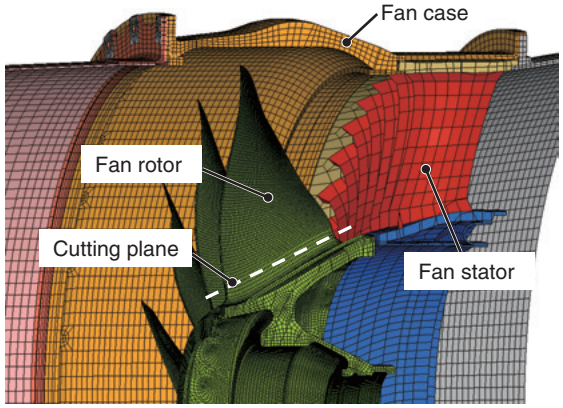
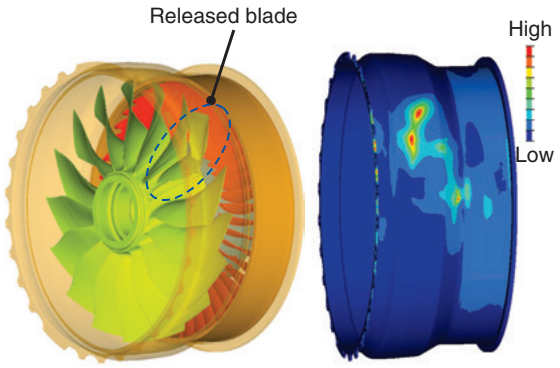


Fig. 2 Cutaway view of FBO analysis model



(a) Analysis model (b) Strain distribution

Fig. 3 Equivalent plastic strain of FBO damaged fan case

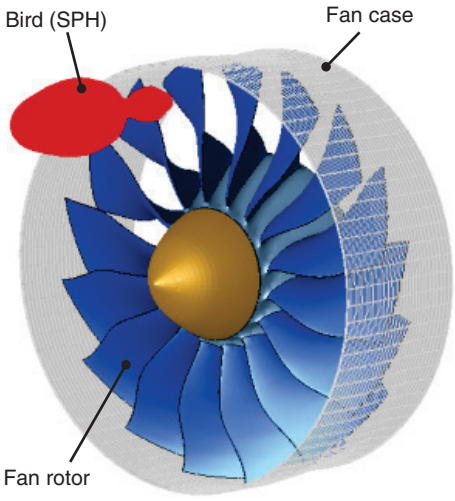


Fig. 4 Bird ingestion analysis model

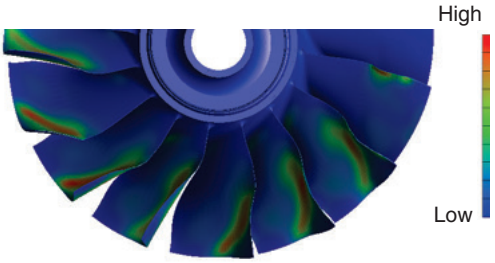
trunk are constructed of elastic-plastic elements, and the other blades are constructed of rigid elements in the model. Validation of this modeling method was performed using the existing engine, and the test result showed good correlation between analysis and testing (Fig. 5).

Using this analysis method, HF120 fan rotor configuration that satisfies the design requirement was identified. Then, a substantiation testing was conducted to demonstrate design compliance with FAR requirements. Figure 6 shows the rig test configuration of medium-size bird ingestion for the fan rotor. The damaged fan rotor blade was installed into an engine for thrust measurement. The result demonstrated less than 25% thrust loss, which meets both the design requirement and the FAR. Note that the test was conducted with the Honda Bioethics Committee's approval.

2.4. HCF Verification

Fan rotor blades can be excited by airflow distortion at engine inlet in integral multiples of engine speed. Another excitation source is non-uniform pressure distribution caused by the fan stator vanes located downstream (Fig. 7). FAR[3] limits stress induced from HCF that can be caused by these vibrations. Generally, stiffer blades lead to an increase in weight of the fan rotor and also other structural parts. Thus, in order to design a fan rotor with adequate blade strength, verification of HCF should be performed with appropriate accuracy.

The first step was to predict mode shapes and natural frequencies by simulation. Figure 8 shows a typical mode analysis result. The second step was to measure the response with strain gauges applied on subject blades during engine testing. Then maximum stress values were calculated by combining of measurement and analysis results. All plotted responses within the operation range are below the material fatigue limits. Thus, the evaluation demonstrated that the design complies with the FAR.



(a) Simulation result (Strain distribution)



(b) Test result

Fig. 5 Comparison between simulation and test

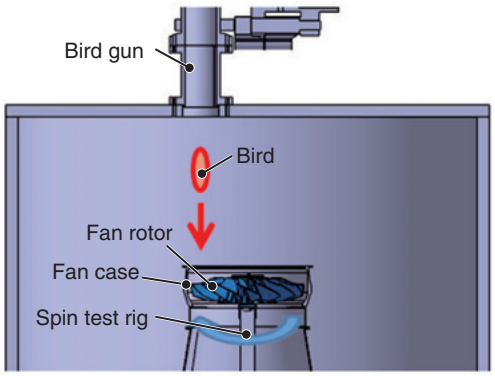


Fig. 6 Bird ingestion test layout

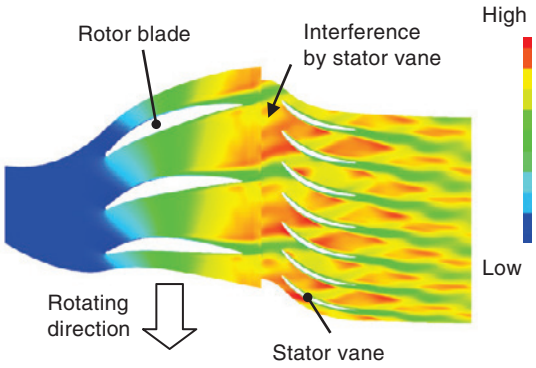
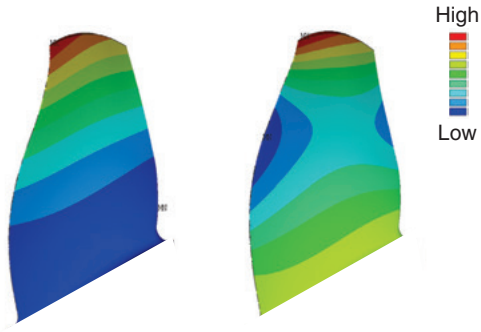


Fig. 7 Total pressure of fan flow



(a) First flex (b) Second flex

Fig. 8 Fan rotor displacement of typical modes

3. LPT1 Nozzle Structural Design

3.1. LPT1 Nozzle Configuration

The HF120 LPT is composed of two stages as illustrated in Fig. 9. The LPT1 nozzle design is a monoblock casting feature intended to be light-weight and compact, and to result in low-fuel consumption.

3.2. Vane Monoblock Casting Configuration

The turbine nozzle has high thermal load due to high

temperature conditions. In other designs, segmented vanes may be used to alleviate the thermal effect. This HF120 engine, however, adopted vane monoblock casting configuration. The advantages of monoblock casting include a light-weight, compact configuration and eliminating fuel gas leakage from the joints between separate pieces. As a result, the fuel consumption improves. At the same time, countermeasures against high thermal load were introduced.

The vanes are exposed to high-temperature and high-pressure gas after combustion in the combustor. The metal temperature of the vanes reaches the same level as the gas, while the metal temperature of the platform is kept relatively low by cooling air. Two countermeasures were adopted to address the high stress that could result from the temperature gradient. One was to adopt variable fillet curvature on span and chord directions (Fig. 10). The other countermeasure was to adopt a heat shield on inside of platform (Fig. 11). This heat shield helps form an intermediate temperature layer of which relieves the thermal temperature gradient from vane to platform (Fig. 12) and reduces the thermal stress.

The turbine layout is composed of the nozzle holder, outer and inner gas passages, seal holder, and heat shield.

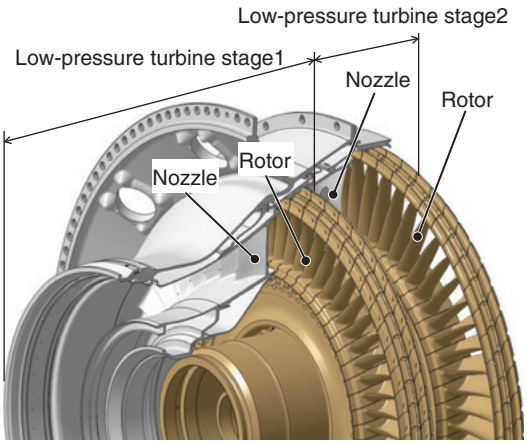


Fig. 9 Turbine module layout

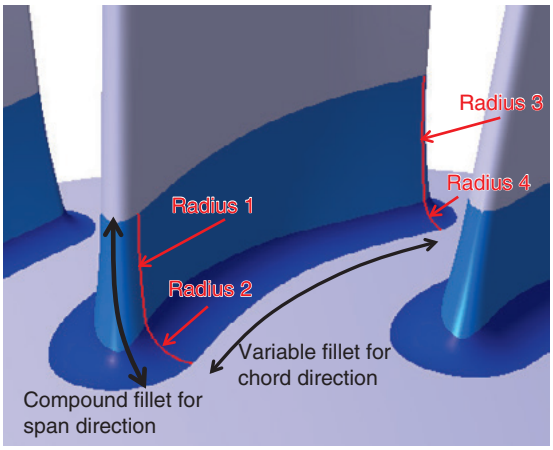


Fig. 10 Vane compound fillet

These features were integrated into the monoblock casting vane configuration. As a result, the gas leakage was avoided, and the design enabled a light-weight and compact LPT1 structure.

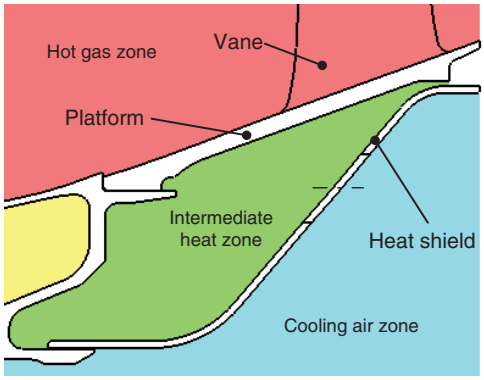
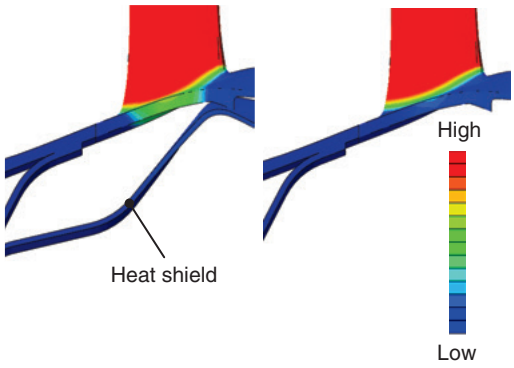


Fig. 11 Heat shield layout



(a) With heat shield (b) Without heat shield

Fig. 12 Metal temperature distribution

4. Parts Life Management

Chapters 2 and 3 described designs and verification methods for specific parts. This chapter explains the general design concept commonly applied to turbofan engine composition parts. A turbofan aircraft engine has the following characteristics: management of the engine operation envelope, management of the engine in-service time, definition of the Time Between Overhaul (TBO) and the repair or maintenance procedures on manual. These characteristics are incorporated into life-limited part design. In general, major parts comprising a turbofan aircraft engine are life-limited to make the engine more efficient and light in weight. These parts have life requirements that include crack initiation and propagation. Thus, the design must consider how the subject parts comply with these requirements based upon their features, material, interfaces, manufacturing process, and proper use of the engine. Parts life requirements vary depending on their criticality and environment. Figure 13 outlines the relationship between life-limited parts, non-life-limited parts, and TBO during

part in service. Most static parts are designed not to be life-limited, but instead to be continuously used until the engine is removed from service. On the other hand, some parts that operate under high temperature and high stress conditions are designed to satisfy a specified life. These parts' in-service histories are managed by the recorded flight operation log. An engine must undergo regular inspections and overhauls at designated times defined by the operation manual to determine if the subject parts maintain their integrity for continuous service. Any parts that reach their life limit must be replaced with new parts during the overhaul.

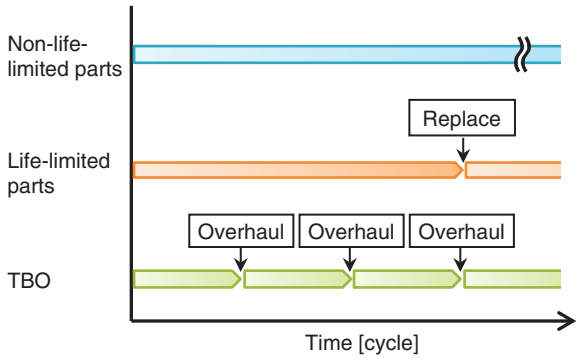


Fig. 13 HF120 life management

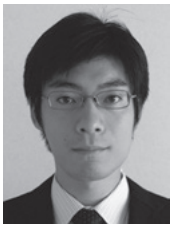
5. Conclusion

This paper describes HF120 turbofan engine design characteristics with a general perspective of engine structure, as well as two representative components, the fan rotor and the LPT1 nozzle. The fan rotor demonstrated compliance with internal design requirements and FAR for FBO, FOD, and HCF by a combination of CAE analysis and substantiation testing. The LPT1 nozzle configuration is light-weight, compact, and highly efficient nozzle with an optimized configuration feasible under high thermal load environments. In addition, the life-limiting concept was adopted on major engine parts design. The life requirement of each engine part was defined in accordance with criticality and characteristics, and parts are designed to meet these life requirements.

References

(1) Blade containment and rotor unbalance tests, 14 Code of Federal Regulations Part 33 Amendment 30 Section 33.94
(2) Bird ingestion, 14 Code of Federal Regulations Part 33 Amendment 30 Section 33.76
(3) Vibration test, 14 Code of Federal Regulations Part 33 Amendment 30 Section 33.83

■ Author ■


Junichi IKEDA


Takafumi TANAKA


Ryuji SANO

Application of CFRP Stator to HF120 Turbofan Engine

Michihide ANAKURA* Shuu TAGUCHI* Shuichiro YOSHIDA*

ABSTRACT

Materials such as aluminum alloys (A7075) are often mentioned as candidates for use in the manufacture of Fan Outlet Guide Vane components. As a part of weight-saving of the HF120 turbofan engine, an Fan Outlet Guide Vane made from CFRP was developed.

Sheet Molding Compound containing approximately 60% carbon fiber was used for the Fan Outlet Guide Vane. In order to apply the Sheet Molding Compound to the Outlet Guide Vane, material certification from the United States Federal Aviation Administration was acquired.

To utilize the light-weight characteristics of CFRP, the shroud and vane were integrally molded. The introduction of Sheet Molding Compound permitted the number of prepreg laminations reducing to six, even on the thick vane section, as well as achieving near-net-shape press molding within 20 minutes. As a result, weight was reduced by 40% in comparison with A7075, and press molding process time was reduced by 90% in comparison with the continuous fiber Carbon-Fiber-Reinforced Thermo-Plastic's molding process.

Outlet Guide Vane components underwent assessments such as impact and fatigue testing to ensure the successful completion of engine certification testing. Subsequently with the completion of certification testing, the application of CFRP Outlet Guide Vane in the HF120 has been achieved.

1. Introduction

The Fan Outlet Guide Vane (OGV), one of the stator vanes that constitutes the HF120 turbofan engine (HF120), is located behind the fan rotor in a relatively low-temperature environment. The OGV is generally larger and heavier than other stator vanes, and therefore provides a significant opportunity for a weight savings. Given this, research was pursued on the application of Carbon Fiber Reinforced Plastic (CFRP), one of light-weight materials, to the OGV. In the HF120's development, one of the established goals was integrally molding the vane and shroud to take an advantage of the light-weight characteristics of CFRP.

2. Part Configuration

The location of the OGV in the HF120 is shown in Fig. 1.

The OGV is a stationary part behind the fan rotor, and plays a role in the removal of residual swirl contained in the airflow from the fan rotor to increase static pressure. The air outflowed from the OGV is divided into the core side of the engine and the bypass duct.

To help utilize a design potentially using CFRP, the OGV was designed as an integral vane with shroud. The OGV is 125 mm high, 85 mm wide and 50 mm in length. The stainless-steel Leading Edge Protector (LEP) was bonded on the leading edge of the vane. This LEP protects a part of the leading edge of the CFRP from abrasion by the sand, and other contaminants that may be ingested by the engine inlet.

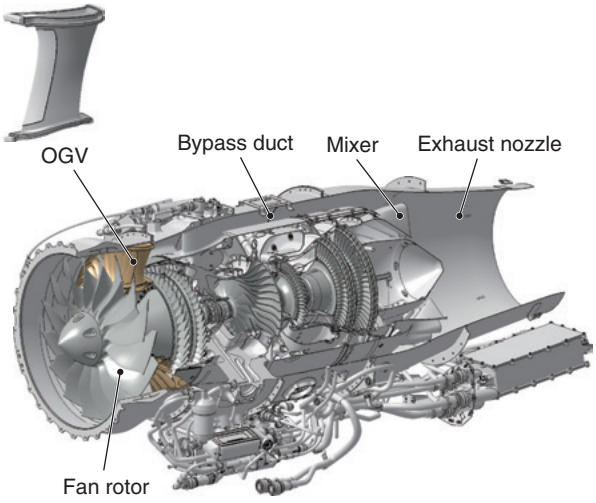


Fig. 1 HF120 OGV location

* Aircraft Engine R&D Center

The OGV assembly is configured by combining 42 separate OGVs, 42 sets of rubber boots made of silicone rubber and an inner ring made from aluminum alloy. Each OGV is joined to the adjacent OGV at the shroud by rubber boots, forming a circular ring, and this ring form is fixed by inner ring. The diameter of the OGV assembly is approximately 480 mm. Diagrams of the OGV assembly and the OGV are shown in Fig. 2.

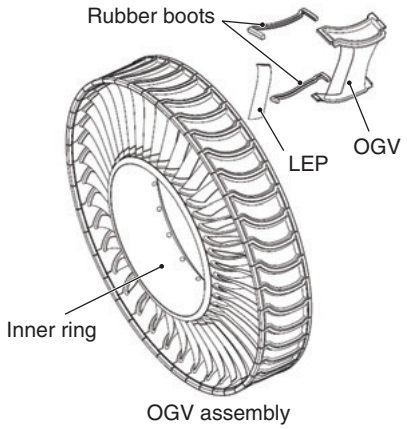


Fig. 2 Configuration of OGV and OGV assembly

3. Materials

3.1. Configuration of Materials

The main structural material for the OGV is an Sheet Molding Compound (SMC) composite material. Its matrix resin is epoxy and is reinforced by carbon fibers. A plain fabric material was applied to the airflow surface since the surface has an effect on aerodynamic character.

This SMC is a prepreg sheet approximately 2 mm in thickness, and is formed by randomly oriented and laminated carbon fiber bundles that were chopped off from unidirectional prepreg to be 50 mm in fiber direction and 8 mm in width. Photographs of the SMC are shown in Fig. 3. The volume fraction of carbon fiber after molding SMC is approximately 60%.

3.2. Mechanical and Light-weight Characteristics of Materials

The static specific tensile strengths of SMC and A7075 as a comparative material are shown in Fig. 4. The vertical scale indicates the rate of specific strength relative to the SMC specific strength at room temperature (R.T.) as 100%.

Judging from the finding that SMC specific tensile strength is higher than that of A7075, SMC was judged to be more suitable for weight saving than A7075. Utilizing the light-weight character of SMC and applying it to the OGV reduced the weight by 40%, as compared to A7075 applied to OGV.

The anisotropy of strength and stiffness per one ply of SMC is not more noticeable than unidirectional CFRP, because SMC form has randomly oriented carbon bundles. Also, the maximum tensile strength of SMC is lower than that of unidirectional CFRP. However, with respect to interlaminar fracture toughness which is typically believed to be the greatest weakness of CFRP, the toughness of SMC tends to be higher than that of unidirectional CFRP with a tough epoxy matrix. Since SMC's fiber bundles are mixed and laminated in the lamination direction by the effect of random orientation, when comparing Mode II interlaminar fracture toughness between SMC and unidirectional CFRP, the toughness of SMC is approximately twice as high as that of unidirectional CFRP. The comparison chart of unidirectional CFRP and SMC is shown in Fig. 5.

3.3. New Material Certification of SMC

As this SMC is a new material for aircraft engines, it is required to be certified by the Federal Aviation Administration (FAA) as a new material for application to aircraft engine parts.

Four years were required to complete the material certification process, starting from the selection of materials, followed by the material tests to investigate typical

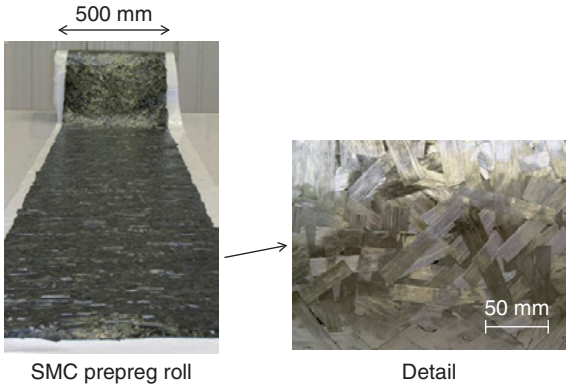


Fig. 3 Carbon-fiber-reinforced SMC

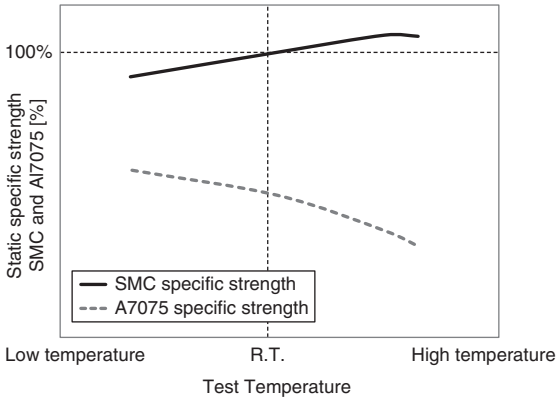


Fig. 4 Comparison of specific tensile strength

mechanical properties, examination of evaluation items, and finally the material certification test.

The evaluation tests were performed in the material certification test program regarding various items including mechanical properties, physical properties, and fatigue characteristics that were needed for OGV evaluation.

In the case of the composite material, even if test specimens are fabricated from the same prepreg, molding method and material anisotropy etc. has an effect on some test results. Thus, the material specification defines the methods for CFRP plate fabrication, cutting test specimen, and material tests. The specimens were manufactured and material tests were carried out based on the specifications. To calculate allowable design limits of aircraft engine parts from the test results, statistical processing was required based on military standards and other methods[1].

After completing above processes, a material specification was finalized reflecting the material test results of the SMC. Based on the material specification, the material certification report in compliance with the requirements of Federal Aviation Regulations (FAR)[2] was drawn up with General Electric Company (GE), Honda's joint venture partner on the HF120's development. The report was submitted to FAA and the SMC was certified.

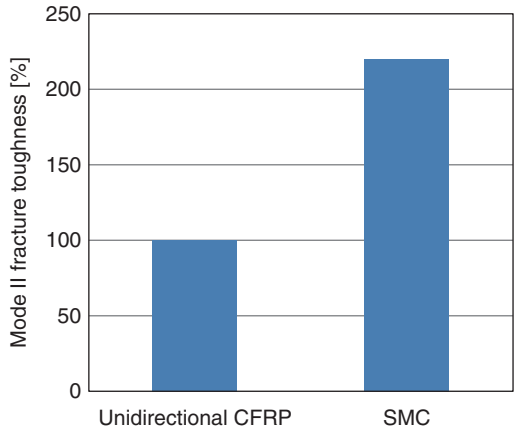


Fig. 5 Comparison of mode II fracture toughness

4. Manufacturing Process

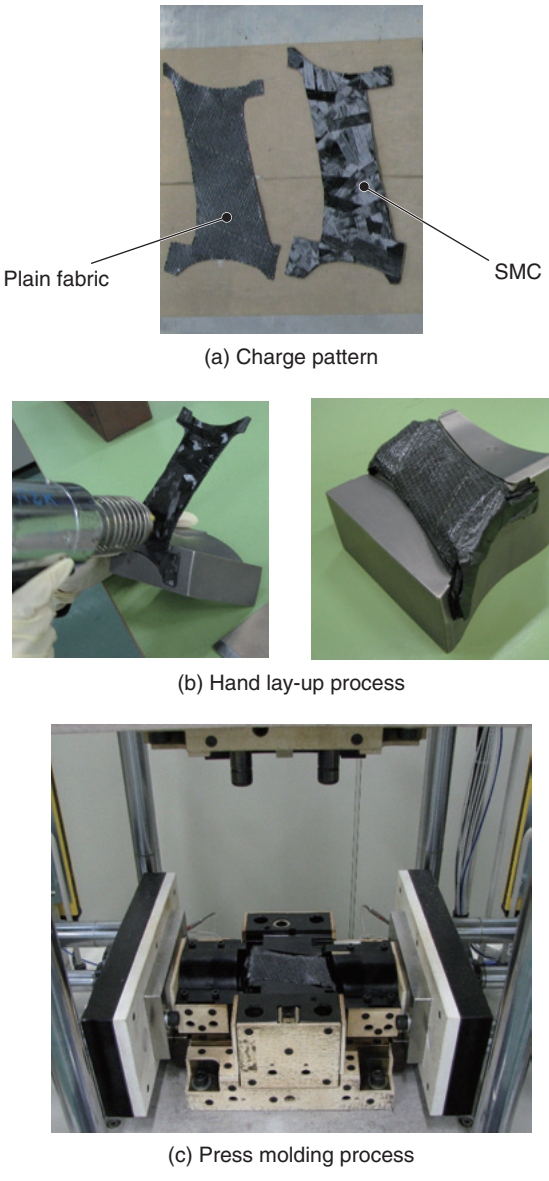
4.1. Press Molding CFRP Vane

Aircraft engine parts are sometimes produced in small lots and demand high precision. In addition, a high degree of freedom for molding is required, because an OGV is formed by varied thicknesses. As previously mentioned, high flexibility against complex shape forming was one of the reasons for selecting SMC for OGV.

The CFRP portion of the OGV was molded by an SMC method.

In the selected SMC method, a charge-pattern is cut to form as prescribed from SMC roll, multiple of those patterns are laminated in accordance with part thickness and weight, then hot pressed by mold die[3].

In past research, hot-press molding of continuous fiber Carbon Fiber Reinforced Thermo-Plastic (CFRTP) was carried out over 180 minutes, and the number of charge-patterns at a vane was 17. Use of SMC made it possible to reduce the charge-patterns to six sheets, and press time was reduced to 20 minutes, which is 90% shorter than that of the continuous fiber CFRTP. In addition, the cutout layout of the charge-patterns on the SMC roll became easier because it is no longer necessary to pay attention to precise details of fiber orientation angle. Shown below is the SMC method procedure applied to CFRP vane molding. Field pictures showing a part of the procedure are shown in Fig. 6.



(a) Charge pattern

(b) Hand lay-up process

(c) Press molding process

Fig. 6 SMC molding process of CFRP vane

(1) Material cutting [Fig. 6(a)]: cutting out charge-patterns from SMC and plain fabric material roll.
(2) Weight measurement and combination of charge-patterns: SMC charge-patterns have weight variation, therefore weight adjustment is performed in the combinations of SMC charge-patterns.
(3) Staging: the volatile components contained in resin are evaporated. In order to reduce excessive resin spill in the press molding process, curing of resin was started in advance.
(4) Lay-up [Fig. 6(b)]: lay-up charge-pattern of SMC and plain fabric material to the lay-up fixture.
(5) Press molding [Fig. 6(c)]: OGV is molded by a 2-axis press molding machine.
(6) Post-cure: in order to carry out complete curing of the epoxy resin, the molded part is held for a predetermined period at a constant temperature using a heating furnace.
(7) Trimming: trim resin burrs from molded CFRP vane.

4.2. Cold Press-Forming of LEP

LEP is formed by cold press using stainless steel sheet of 0.1 mm thickness. By rationalizing the press forming process condition of the thin sheet, the forming succeeded in cold press-forming of LEP, which has a complex shape and deep draw. After press forming, trimming is performed to attain the final shape. The image of LEP after press forming is shown in Fig. 7.

4.3. Bonding of LEP

The LEP is adhered to the CFRP vane of the OGV after post-curing. As pre-bonding surface treatment, surface roughening is applied to the LEP adhesion part of the CFRP vane with sandpaper, and LEP is etched. After pre-bonding treatment, an LEP and a CFRP vane are bonded by epoxy film adhesive, using an autoclave after bagging the parts under vacuum. After bonding, adhesive resin flash is trimmed as the finishing processing. The OGV after LEP bonding is shown in Fig. 8.



Fig. 7 LEP

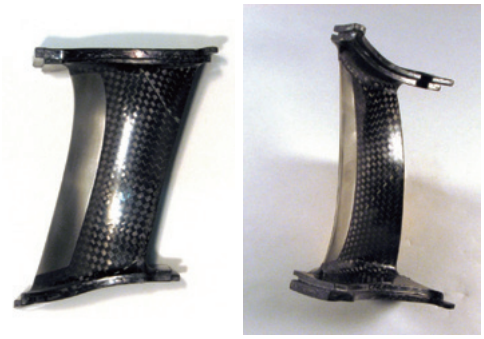


Fig. 8 OGV

5. Component Test

Prior to engine certification testing, component evaluation of the OGV was performed to ensure satisfactory completion of the engine certification test.

5.1. Evaluation Items

For application of the SMC material to an aircraft engine, evaluation of various items including environmental durability, impact resistance and fatigue properties is required. Impact resistance and high-cycle fatigue properties stand out among characteristic evaluation items. The former refers to the evaluation of impact load that can be caused by foreign objects ingested from the engine inlet, while the latter refers to the evaluation of high-cycle fatigue that can be caused by vibration excited from rotational parts.

5.2. Impact Resistance

It is possible that a foreign object such as bird or hail could strike the OGVs. One of the goals established was to preclude the separation of the part when it is struck by these foreign objects. This section describes the test result of OGV's resistance to impact by hailstorm. The pictures for the test are shown in Fig. 9.

After continuously impacting hail against the OGV at specified velocity and duration, the test results showed no cracking of the CFRP and no peeling of the LEP, thereby confirming OGV is resistant to impact caused by the assumed hail strikes in the test protocol.

5.3. High-Cycle Fatigue Property

Vibration modes found in parts during engine operation include bending modes and torsion modes. Fatigue test were performed for both vibration modes.

In order to make the impact of part fixation method on vibratory mode smaller, cantilever fixation holding the portion of shroud by resin was applied for part fixation method as shown in Fig. 10.

The natural frequencies of the parts in each vibration mode were checked by the holography. The photographs

of vibration mode form, which were obtained by the holography, are shown in Fig. 11. The striped pattern on the vane which can be found in Fig. 11 appears when the part is deformed by characteristic vibration. The deformation gradient of part is in a direction perpendicular to the stripe. From Fig. 11(a), vane is bending toward span (longitudinal), therefore, this is bending mode. Shown in Fig. 11(b) is torsion mode where vane is twisted.

Figure 12 shows fatigue test condition. Here the part was vibrated to the direction of arrow by adding natural frequency of each mode.



Fig. 9 Impact resistance test

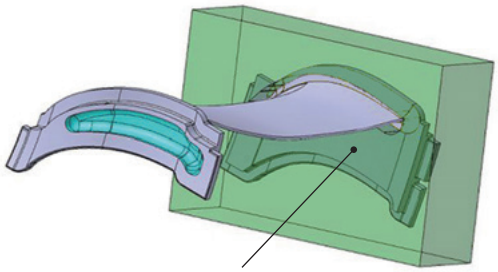
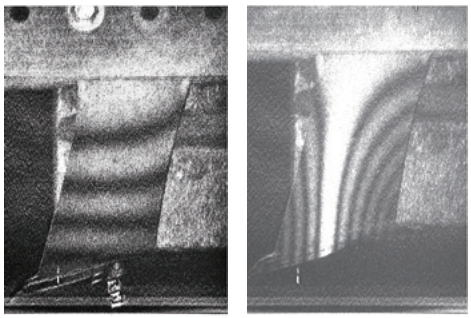


Fig. 10 Cantilever OGV for fatigue test



(a) Bend mode shape (b) Torsion mode shape

Fig. 11 Mode shape

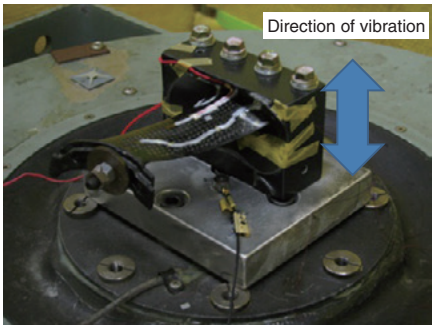


Fig. 12 Fatigue test

From the test result, it was confirmed that the OGV has enough fatigue property in bending mode and torsion mode for compliance with the engine certification test requirements.

6. Conclusion

Introduction of CFRP, which has both strong and light-weight characteristics, into the OGV design resulted in successful weight reduction and performance compared to A7075. Press molding process time was also reduced in comparison to that of continuous fiber CFRTP.

As a result of the component testing, it was confirmed that the OGV has sufficient impact resistance and fatigue properties for engine certification test requirements.

Reference

(1) Department of Defense: MIL-HDBK-17
(2) Federal Aviation Administration: Federal Aviation Regulations
(3) Hirano, Y.: Fukugo Zairyo Katsuyo Jiten, Vol.3, Chapter 2, Industrial Research Center of Japan, p. 497-501 (2001) (in Japanese)

■ Author ■


Michihide ANAKURA


Shuu TAGUCHI


Shuichiro YOSHIDA

Development of High Reliability Control Software for HF120 Turbofan Engine

Makoto TEZUKA* Shohei SUGIMOTO* Keisuke KAWAI*
Hideaki JINNO* Yuta AKAI*

ABSTRACT

When developing application software for an aircraft engine electronic control system, the development process is required to comply with DO-178B, one of the guidelines issued by the Radio Technical Commission for Aeronautics. All activities to be conducted during software development should be defined by each development organization, and Honda developed the software based on the process defined by Honda.

The application software was developed separately during the design phase consisting of requirement definition, software design and software implementation. The verification phase consisted of review, testing and analysis. In addition, Honda established the development system for the project tailored for the joint development between Japan, USA and Mexico with international time differences. Documents and design data could be shared and managed while maintaining the integrity within the development system for this project.

As a result, Honda established a highly reliable software development process for the HF120 turbofan engine control system in compliance with DO-178B. Jointly with General Electric Company, Honda obtained Type Certificate issued by the Federal Aviation Administration for the HF120 turbofan engine, including the engine control system software.

1. Introduction

At turbofan engine for an aircraft generally has a long service life, and durability is necessary for its control system components. The control system components control the engine appropriately based on the engine condition, even if a sensor fails. Therefore, a Full Authority Digital Engine Control System (FADEC) was applied as a control system for the HF120 turbofan engine (HF120). Honda co-developed the control system with General Electric Company (GE). The HF120 control system has engine control characteristics in its software so that change requests from an airframe manufacturer or the Federal Aviation Administration (FAA) can be accommodated during the service periods.

The Fuel Pump Metering Unit (FPMU), the Engine Control Unit (ECU) hardware and the Operating System Software (OS), the Application Software (AS) installed in the ECU are components for the overall control system. Honda was responsible for developing the AS, validating overall system integration, and confirming engine compliance.

The control system software development is used to satisfy DO-178B[(1)], the de-facto standard for software development process to assure airworthiness. DO-178B specifies certain activities to be performed during software development. Each development organization or team should define how to perform their tests, and the software development data generated by its process is used as objective evidence to demonstrate conformance of the overall software development using DO-178B.

This paper describes how Honda constructed its software development process to enhance reliability of the control system software.

2. Control System Overview

2.1. Aircraft Engine Control

Turbofan engines in modern jet aircraft need high precision thrust control. Engine controls also need to ensure thrust response capability for engine accelerations and decelerations with no compressor surge, stall and lean blowout.

The engine control system determines the necessary fuel

* Aircraft Engine R&D Center

flow rate as a function of thrust demand from aircraft and engine conditions, ambient conditions, aircraft operating conditions and other factors. Fuel flow rate is regulated by changing the fuel flow passage area determined by the position of the Fuel Metering Valve (FMV). Since turbofan aircraft engines are operated in high altitude with low air density, sufficient fuel control accuracy is needed for both low flow rate regions at high altitude and high flow rate regions closer to the ground.

2.2. Control System Architecture

Figure 1 shows the HF120 Control System Architecture. The system consists mainly of ECU, engine sensors, FPMU and the airframe interface.

Electronic components including the ECU and various sensors are designed to provide high reliability. Each channel of the ECU compares the health level of mutual electronic system via Cross Channel Data Link (CCDL) to control the engine. Even when the ECU has a malfunction in one of the two channels, usage of the faulty channel is immediately suspended and switched to the remaining healthy channel to continue proper engine control.

The FPMU is a key component to ensure the control function. The main functions of the FPMU are boosting of fuel pressure and supply of fuel to the engine combustor. The FPMU has an FMV to control fuel flow, a Bleed-Off Valve (BOV) Actuator to avoid surge and stall, and a Shut-Off Valve (SOV) to cut-off fuel in emergencies, all build in. Furthermore, the FADEC is operated by a dedicated power source of the Permanent Magnetic Alternator (PMA) built-in FPMU, and needs no external power source except for starting.

Airframe information for thrust control such as thrust lever position and cockpit switch signal is transmitted to the ECU through the airframe interface. Signals indicating engine running conditions are sent to the airframe through the airframe interface.

3. Overview of Developing Highly Reliable Software

3.1. Control System Requirements

The control system for an aircraft engine is required to meet the Federal Aviation Regulations of the Unites States, where airworthiness standards for engine control are described. Safe operation, fundamental control response of engine thrust, electromagnetic interference protection and reliability are specified.

Aircraft engine specifications are issued by an airframe manufacturer, and aircraft engine interface control documents are issued by the engine manufacturer. Based on these documentations, the engine requirements are prepared by the engine manufacturer. These engine requirements are flowed down to the control system requirements, then further down to software requirements and design detail specifications.

Development of all components including software is accomplished based on these requirements.

3.2. Software Development Method

Software development complied with the V model is shown in Fig. 2. Design flow is indicated on left side while verification flow on the right.

The result of an individual work project indicated by the V model is managed by a configuration management

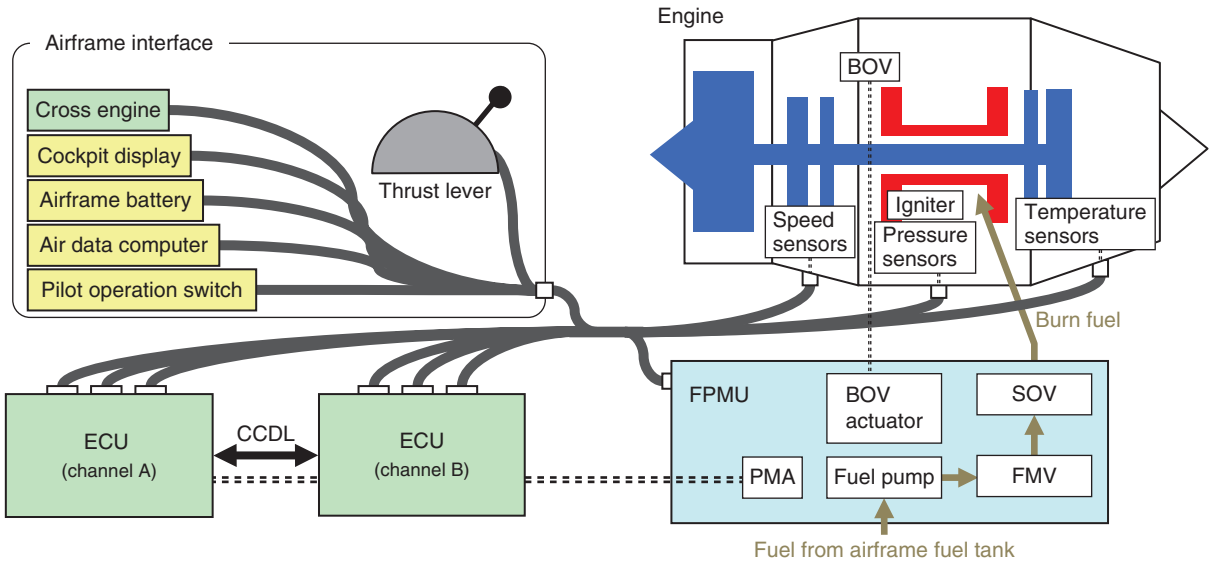


Fig. 1 FADEC system

database. The configuration management is composed of software release control, version control and change control for software elements. This is intended to record work traceability with respect to all work.

3.2.1. Software design technique

When receiving the defined engine level requirements, FADEC development starts by defining the control system requirements. Functional and non-functional requirements anticipated in FADEC need to be clearly stated and various types of interface specifications are set forth so as to define hardware and software requirements.

In the HF120 development, requests from customers were defined as part of the control system requirement. Then, a software requirement was flowed-down from the control system requirements.

Verification tasks in compliance with DO-178B are required to show 100% coverage of the software requirements by testing. Therefore, the software requirements were prescribed accurately following the method which is commonly accepted by the software engineering, so that all requirements are verifiable.

Afterwards, design and implementation were conducted based on the software requirements. In the HF120 development, Matlab/Simulink and Unified Modeling Language were used to design the software behavior, and those models were implemented in C language. Any model described by Simulink was implemented by using automatic code generation tool.

3.2.2. Software verification method

Verification activities occupy the majority of software development, and the verification method affects the reliability of control system software. The verification activities generally consist of review, testing and analysis. Main verification activities include code review, unit test, software integration test, system integration test and engine validation test as shown in Fig. 2. These activities help ensure the integrity of the verification process.

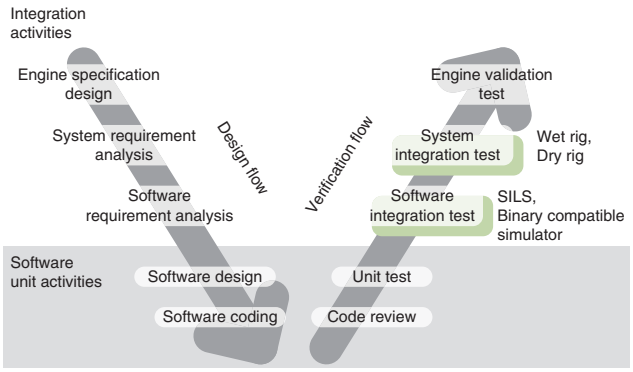


Fig. 2 Software development flow

4. Software Verification Method and Environment

Four types of environment for integration test were provided during the HF120 development, and each test had its optimum testing environment selected to conduct the verification.

Integration test environments can be classified into software integration test environment and system integration test environment. Modeling scope for each integration test environment is shown in Fig. 3. Software In the Loop Simulation (SILS) and binary compatible simulation can be classified as software integration test while dry rig and wet rig can be classified as system integration test environment.

SILS is a test environment modeling all elements of the FADEC system, making closed-loop simulation with the engine plant model possible. On the other hand, binary compatible simulator which incorporates no engine plant model is structured as an open-loop testing environment modeling only ECU hardware and OS.

The dry rig is a testing environment combining the ECU and a simulator, which can electrically drive the ECU on the basis of engine plant model computing result, and can simulate the ECU by closed loop. The wet rig is an environment where actual fuel can be flown through the FPMU, and can simulate a combined ECU and FPMU by closed loop.

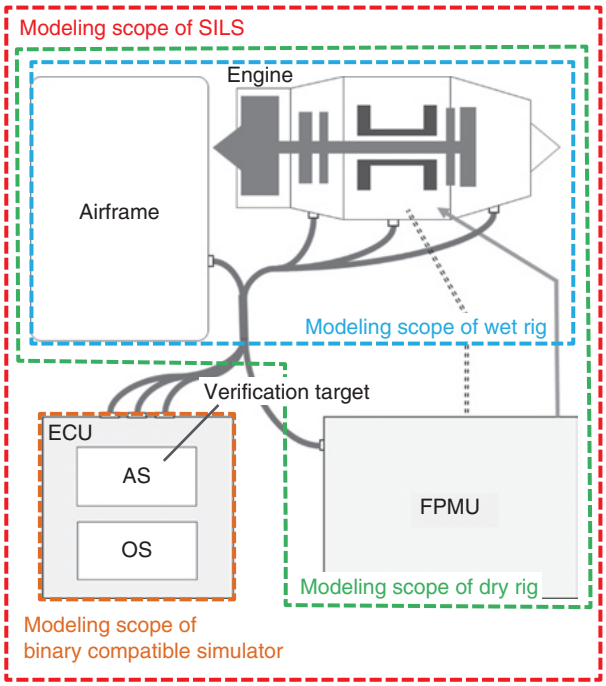


Fig. 3 Modeling scope

4.1. Software Integration Test

4.1.1. SILS test

In order to evaluate software accurately, specific environment was designed to simulate engine and software behaviors in nominal conditions by excluding the characteristics unique to hardware as well as noise characteristics of simulator equipment and the ECU. The noise injection test also needs a simulated environment that can precisely inject noise characteristics into the software. A verification method using SILS was introduced to meet these requirements for the simulation environment.

SILS was used for the verification related to thrust control and noise immunity during the verification process. For the thrust control related verification, SILS was constructed in parallel with the completion of software coding, and overall engine operating conditions including altitude and cabin bleed were simulated by SILS to confirm that every control response meets the design requirements. For the next step, the same conditions were tested in the dry rig including an actual ECU to evaluate if the difference between the test and the control response obtained from SILS was within the tolerance. It was demonstrated through these two steps that the software requirements are satisfied in nominal system conditions and, furthermore, the same software satisfies the requirements on the actual ECU.

For noise protection verification, SILS characteristics were utilized, making it possible for any reasonably conceivable noise pattern to be precisely injected into the software. Also, with test repeatability being available, software noise immunity properties were verified with accuracy and efficiency.

4.1.2. Binary compatible simulator test

Some software requirements describe details dependent on hardware characteristics, for example, access timing for communications and storage. Confirmation of such requirements by testing necessitates an environment to accurately simulate hardware behaviors. A binary Compatible Simulator was prepared to meet the following objectives in AS verification:

(1) Ability to generate ECU internal faults at any given point in time.
(2) Ability to send arbitrary patterns of communication data to ECU at any given point in time.
(3) Ability to virtually confirm the internal condition of the storage device at any given point in time.
(4) Ability to run an AS executable file to be loaded in an actual ECU with binary level compatibility, leading to an AS processing result in complete agreement with actual ECU.

This test environment was established on the CPU instruction set simulator by integrating actual AS and the other simulated component models. OS, ECU hardware, parts of the engine and engine diagnostic tools were subjected to modeling.

Under this environment, an ECU internal fault can be generated at arbitrary times, and test coverage can be obtained in response to the requirement for accommodation of the fault. The CCDL fault injection test is explained as a representative example. ECU hardware carries two sets of redundant boards inside of a single chassis to share control data between these boards by using CCDL communication. This environment modeled such dual redundant hardware and CCDL, simulating disconnection and data corruption for CCDL. Because of this, system robustness can be confirmed by encompassing fault occurrence patterns.

Other than the aforementioned advantages during the verification, usefulness of this environment in parallel development of AS and OS has also been recognized. In the HF120 development, the OS and AS interface was defined in advance. Then, AS development was executed by using an OS modeled by OS and AS interface specifications, and a simulative integration test was performed by the modeled OS prior to integrating AS and the formal release OS. Any interface inconsistency during the formal release OS acceptance test could smoothly be addressed by executing this advance integration test. Specifically, any difference in behavior between the formal release OS and the modeled OS can be tracked down by comparing the simulation results of these OSs, providing immediate determination of whether the difference comes from the unmet requirements or an interface definition issue.

4.2. System Integration Test

4.2.1. Dry rig test

The dry rig test uses the actual ECU hardware where OS and AS are loaded. In this test environment, software behavior can be verified on the hardware. For this reason, open and short-circuit test on the dry rig make the verification of the complex propagation of the faults in the ECU hardware and software possible.

Figure 4(a) shows the dry rig configuration. The simulator inputs an electrical signal to the ECU on the basis of engine model computing results. Output signal from the ECU becomes input to the engine model.

In order to increase reliability of the system integration test, approx. 90% of the test cases were automated in the dry rig test. Not only automated operation of the simulator but also version information such as ECU hardware and OS, data storage for statistical analysis and test report preparation using tables and charts were automated in the HF120 development. Establishment of such an automated technique helped achieve high software reliability from the following perspectives:

(1) Ability to perform the test repeatedly which is hard to do manually. This makes evaluation possible if the uncertainty of the hardware characteristics is within the acceptable range, and assures the robustness of the ECU given the test result.

(2) Ability to control multiple ECU inputs at short intervals, which is hard to set up manually. This makes full verification of complex and very rare timing possible.
(3) Ability to perform testing that assures repeatability. This makes the direct comparison of test results between different AS versions possible, and then identifies the functional area affected by software change in the development phase. The impact analysis from the test was also applied when there was a change in OS or ECU to diagnose and maintain the functionality of an integrated system.
(4) Achieved high quality of the test by standardization and automation. Specifically, the standardization was applied to the method to determine input conditions that can meet requirement-based test coverage, setting acceptable tolerances for pass or fail parameters, and furthermore, report format and how to display signals in charts. These standardized processes were then incorporated into the libraries so that many testers can import any standardized process.

4.2.2. Wet rig test

Verifications of FPMU-related FMV control and SOV control are conducted on SILS environment modeling FPMU or the dry rig. A wet rig was constructed to verify the combined actual FPMU and software as a final verification prior to full engine testing.

As shown in Fig. 4(b), the wet rig consists of an actual FPMU, actual ECU and fuel equipment supplying actual fuel to the FPMU, throttle valve simulating a fuel nozzle, test chamber, motor to drive the FPMU, and engine model simulator. In addition, the fuel equipment and test chamber simulate an aircraft environment so that low-to high-temperature control of the fuel can be made, and together with the engine model simulator, it can simulate various types of FPMU operating conditions.

The wet rig was used to conduct verification of the FPMU-related control functions prior to engine testing, providing accurate and efficient verification in a given operating condition.

4.3. Analyses

4.3.1. Analysis of requirement-based test coverage

In order to secure AS reliability, a test should demonstrate 100% coverage of the requirements. The coverage analysis was performed in two steps to show this completeness.

First, if the test was prepared to satisfy all requirements, then all requirements being testable were confirmed. Test completeness with respect to individual requirements was confirmed by focusing on the following three perspectives:
(1) Case Scenario – Find out if multiple likely cases have been tested. Engine start conditions, for example, takes into account of the case where initial condition is an inflight restart at high altitude.
(2) Boundary – When assuming two conditions, determine if static behavior at each condition (as well as dynamic behavior during the transition to another condition by crossing the boundary) have been tested. Parameters indicating flight condition, in particular, altitude, Mach number and ambient temperature were rigorously examined.
(3) Stress – In addition to normal conditions, failure condition must also be tested. By doing so, the equivalent behavior (as in normal condition) could be obtained or proper processing to address whether the failure condition would be activated was confirmed.

If any insufficient coverage was detected during the analysis process, appropriate test details were added. As an example, assume that an additional testing was deemed necessary for an ECU hardware internal fault after making a coverage analysis for the requirements on a dry rig test. In this instance, certain test items in the binary compatible simulator environment were added to secure the full coverage.

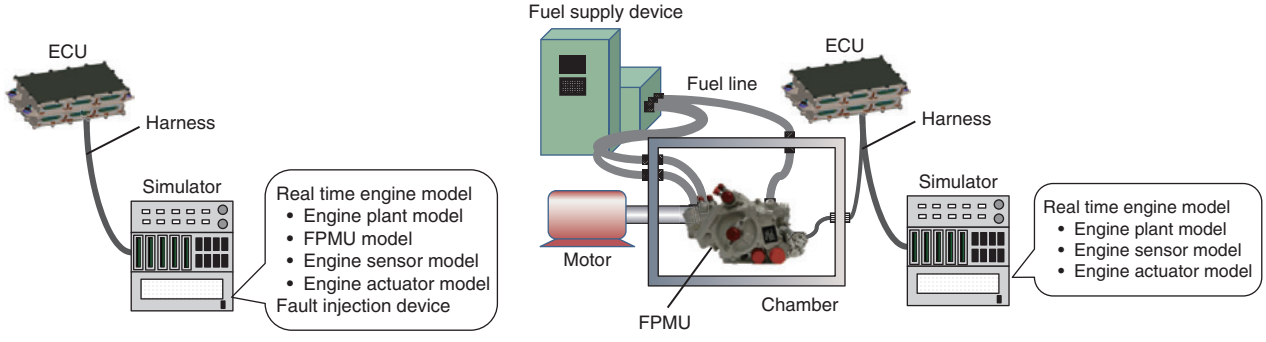


Fig. 4 Dry rig and wet rig

4.3.2. Execution time analysis

When a real-time control system fails to complete a task within the intended period of time, it may have an impact on its control target. System on Chip (SoC) used in recent embedded systems has high-speed processing functions such as multi-core, cache and various types of co-processors built-in as hardware. Use of these functions greatly improves calculation performance. In light of this, the following analysis was performed in order to derive the maximum execution time a task can take on an actual ECU.

First, an environment that can simulate SoC internal condition and its instruction set was prepared and used for the analysis of AS executable files. A software execution path that could cause maximum execution time was statically calculated by testing all branch points. Memory image causing the task to trace the execution path was also obtained by the analysis. This memory image was injected into an actual ECU to acquire actual task execution time and software execution path. After confirming the consistency between this software execution path and what was derived by the analysis, measured execution time was identified as the maximum execution time.

Implementation of engine maintenance functions was initiated in the HF120 during a stage where CPU throughput margin was small. In order to control the CPU throughput margin during development, this analysis was continuously conducted. This analysis also calculated CPU occupancy rate for individual software function by post-processing. When a heavily-loaded function is implemented beyond necessity, such information is visualized for our team to be able to share. In order to reduce CPU loading, the team discussed various countermeasures and dedicated design efforts. As a result, even at the occurrence of unexpected random events, this software completes the individual tasks within the intended period of time.

5. Software Configuration Management

A life cycle in the HF120 software development is triggered by the system requirement change representing a customer or other request.

This system change request is broken down into requirement change and software design change so as to manage progress at each stage.

Software release is recognized as an aggregate of system change requests so that any change incorporated into the release, software design constituting the release, and various types of deliverables during validation can be identified.

GE and Honda have established a Configuration Control Board and made acceptance or rejection decisions for the execution of the system level requirement changes by setting certain criteria.

The software configuration management scheme is shown in Fig. 5, and the description of individual elements supporting the scheme is provided below.

5.1. Requirements Configuration Management

All requirement-related documents used in AS development were prepared using a document management tool. Introduction of a document management tool was

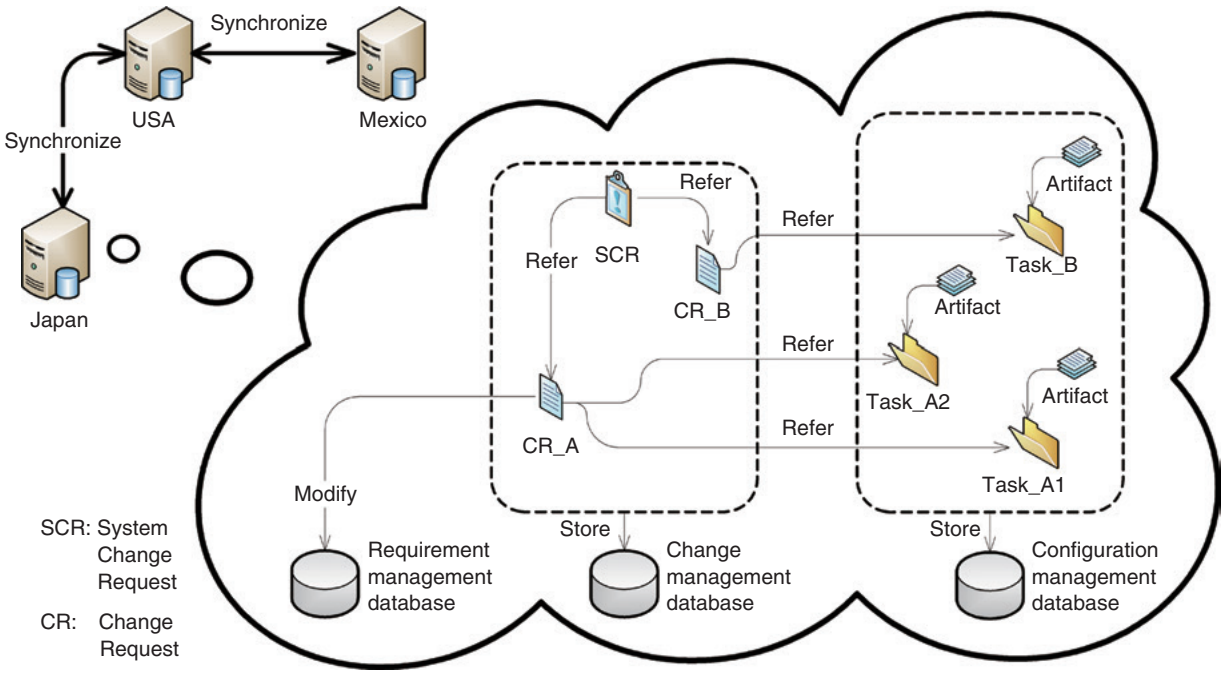


Fig. 5 Software development workflow

deemed important in order to cope with daily changes and keep the link between the affected documents updated. When a definition of a certain requirement is changed, this tool helps visualize the change impact across the related requirements. Other than identifying the statement of the requirement and the reason for its existence, how to verify the requirement was also defined within the database of the requirement specification. Because of this, a designer and verifier can reach agreement on verifiability at the preparation phase of requirement specification. Moreover, the document management tool is also used by the ECU supplier so that design activities interface specifications are objectively traced.

5.2. Software Life Cycle Data Configuration Management

Software is designed and updated using software design change requests, the design artifacts are registered with the revision history database. Change traceability information is prepared to show which software module was changed, how it was changed, and which change request prompted this change. This process shows where certain release is designated, for what purpose, and how it compares to the previous release. Configuration management information also manages system-level change descriptions, software change detail descriptions, and changes in software implementation level in coordination so that the desirable level of information can be extracted. Therefore, all software development members can utilize the configuration management information to better understand the related software's design history.

5.3. Sharing Configuration Management Database

The configuration management information indicates the latest status of development targets. Such information should be promptly shared between development organizations. For AS development, this has been achieved by scheduled database synchronization between companies in Japan, the U.S. and Mexico. As an example, code review and unit test of the software developed in Japan have been performed in Mexico. The synchronized configuration management database helped ensure the integrity of the software correction cycle performed in between Japan and Mexico.

This distributed database system is structured to recover the data from that at the other site even in the case of database deficiency at another site. Moreover, each site prepares a disaster recovery plan including off-site backup. Availability of respective sites and complementary backup between sites provide assurance of overall reliability.

6. Conclusion

This paper provided a general description of key processes to enhance the control system software reliability that constitutes the core of the HF120 Control System.

Honda flowed down the complete requirements during AS development, and achieved 100% coverage of established requirements by verification activities, resulting in the development of highly reliable software.

The software integration test focusing on the software and the system integration (including the hardware) were conducted in accordance with the intended use. These tests were complemented by analysis, verification, and coverage and reliability could be enhanced.

During the joint development across three countries, Honda established the software development system to rigorously manage software configuration and maintain high reliability of the control system software.

Honda added our own original ideas to the requirement creation, verification process and configuration management through the HF120 control system software development, resulting in a highly reliable software development process.

Reference

(1) DO-178B, Software Considerations in Airborne Systems and Equipment Certification, RTCA, Incorporated. (1992)

■ Author ■


Makoto TEZUKA


Shohei SUGIMOTO


Keisuke KAWAI


Hideaki JINNO


Yuta AKAI

Styling Design of 2014 Model Year ODYSSEY

Katsuaki HAYASHI* Ryusaku SENDA* Wataru MURAKAMI*

ABSTRACT

The grand concept for the 2014 model year ODYSSEY was set as creating the "Next Multi Seater Saloon," and the vehicle was developed as a minivan offering new value via an optimal balance between high levels of utility value and automotive value.

The realization of this concept involved the creation of a large and roomy cabin space based on an ultra-low floor platform and the realization of a high level of dynamic performance with a low center of gravity.

Advanced dynamic styling was realized for the exterior design based on the theme "Solid Streamline," while the three rows of seats in the interior each offer a sense of high quality based on the theme "Modern Suite Room."

1. Introduction

In 1994 Honda brought the first-generation ODYSSEY to the market, offering new value by enabling more passengers to experience comfortable mobility, and ushered in a minivan boom. Since then, the automotive value incorporated in the ODYSSEY has increased with each model change (Fig. 1).

During the development of the 2014 model year ODYSSEY, the 5th model, the results of a market survey revealed high expectations of the automotive values associated with the ODYSSEY brand: Style, dynamic performance, comfortable mobility, and fuel efficiency.

The survey also showed that in the current luxury minivan market, the popularity of vehicles with a high overall height that offer the large space associated with a box shape and that prioritize the value of user-friendly utility. The survey also considered the circumstances of customers changing over to luxury minivans, and indicated that while in the past the main trend was to change over from sedans to minivans, more recently changeover from one minivan to another has come to represent approximately 70% of the market, strongly demonstrating the importance of utility value.

Based on these survey results, the design team defined new value for the minivan as a sophisticated balancing of the utility value demanded by customers who have grown used to luxury minivans and the automotive value that is the particular asset of the ODYSSEY. It was also determined that sliding doors are strongly demanded by customers in this class, and it was therefore decided to use them for the first time in an ODYSSEY in the new model.

Seeking to bring together these elements, the design team strove to create the "Next Multi Seater Saloon," which in addition to a spacious cabin with three rows of seats and dynamic performance with a sense of stability, would offer premium quality through design (Figs. 2 and 3).

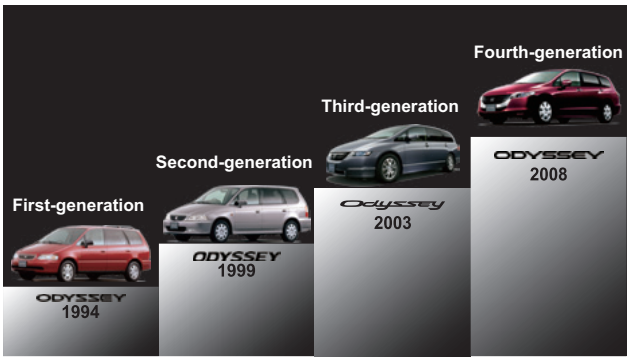


Fig. 1 History of ODYSSEY

* Automobile R&D Center



Fig. 2 Overview of ODYSSEY

2. Package Layout

The new value incorporated in the package design was the sophisticated fusion of two antagonistic values: The utility value that represents the strong point of a minivan, and the automotive value that represents the strong point of a sedan (Fig. 4).

This design realized the grand concept of a "Next Multi Seater Saloon" that would bring the experience of comfortable mobility to an even larger number of passengers.

To offer a clear overview of the details of the model change, Fig. 5 compares the 5th model and 2008 model-year ODYSSEY (the 4th model). The details of the package design are discussed below.

2.1. Evolving the Low-floor, Low-center-of-gravity Package

In the luxury minivan market, demand for greater space is increasing year by year. It would have been a simple matter to respond to this demand by increasing the total height of the vehicle, but this would have meant sacrificing the dynamic performance that had been a feature of the ODYSSEY since its first generation.

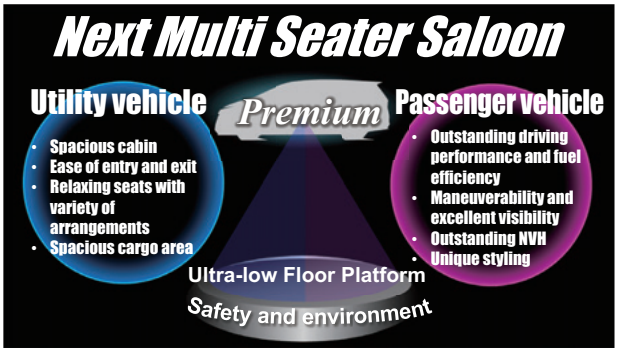


Fig. 3 Grand concept

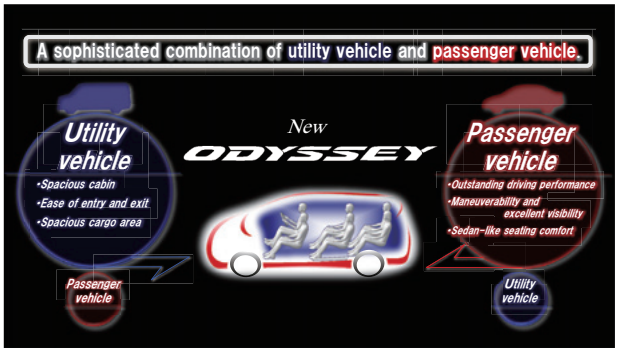


Fig. 4 Package design concept

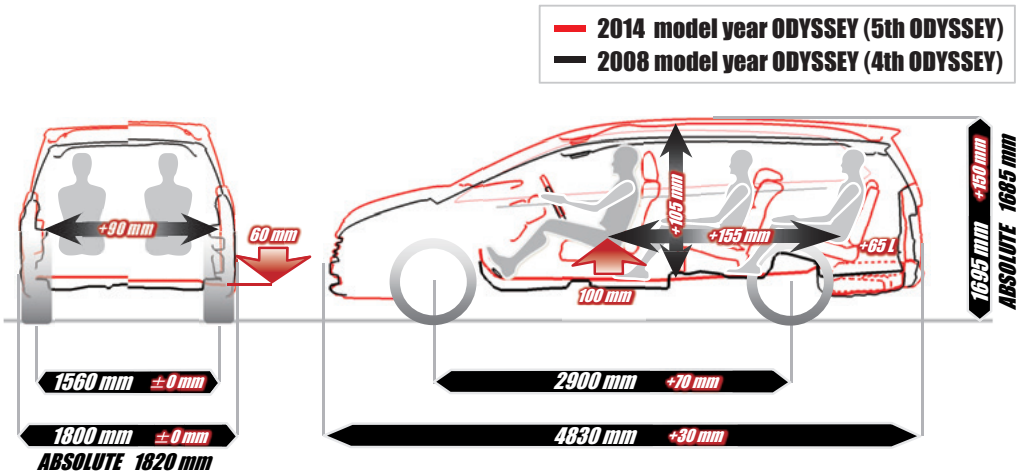


Fig. 5 Packaging

User comments were collected at the outset of the development process through surveys that focused on the family segment of the market. The surveys considered interior cabin height, head room, and maneuverability.

Based on these survey results, it was decided that it would be necessary to reconcile two conflicting targets: To maintain the interior cabin height that satisfied the market, while also taking vehicle motion into consideration, and setting a center-of-gravity height that would help to minimize roll and help prevent children from becoming carsick.

The survey also indicated that women had the impression that vehicles with a high total height were difficult for them to drive. It would therefore be necessary to attempt to realize satisfactory headroom while also controlling the overall vehicle height as much as possible (Fig. 6).

The design team therefore first attempted to evolve the low-floor package. The focus was a flat floor that would not merely be low, but would also give a visual impression of space and offer occupants freedom of movement within the large cabin space. The low floor also contributed to a low center of gravity realizing an exhilarating drive feel and a level of comfort that helps to prevent fatigue even on long-distance drives (Fig. 7).

Based on the concept of this low floor, the interior cabin height was increased by 105 mm against the 4th model to a spacious 1325 mm. The total height of the vehicle was restricted to 1695 mm to offer sedan-like handling. While realizing a total height in the upper medium-sized class, the vehicle's headroom corresponds to the large class, the next-highest class. Based on this, an unprecedentedly low step height of approximately 300 mm was realized for the sliding doors. This is similar to the step height of a low-floor bus, making it easy for children and elderly users to smoothly enter and exit (Fig. 8).

In order to lower the floor, it was necessary to redesign parts including the fuel tank, the exhaust system, and the suspension to make them smaller and thinner, in addition to rethinking their positioning.

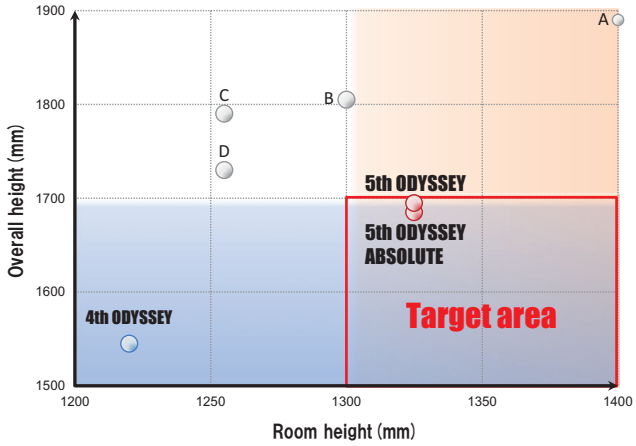


Fig. 6 Cabin height and overall height

2.2. Realizing Interior Space

Seeking to respond more comprehensively to the desire from the market for increased space, designers not only extended space in the direction of height, but also in the directions of length and width. To help ensure sufficient space for all occupants from the first to the third row of seats, the wheel base, which had remained unchanged since the first-generation ODYSSEY, was increased by 70 mm to 2900 mm. This increased the distance between passengers in the first and third rows of seats by 155 mm against the 4th model to 1850 mm.

In this seven-seater configuration, this makes it possible for occupants from the first to third rows of seats to be comfortably seated with space around them even when a 21-inch suitcase for each passenger is packed in the vehicle. This puts the ODYSSEY in the top class of spaciousness compared to other vehicles under the same conditions (Fig. 9). The luggage space has also been increased by 65 L against the 4th model to a high 330 L.

Taking ease of movement into consideration, the total width of the vehicle was maintained at the 1800 mm of the 4th model, and space was made for sunshades at the windows of the second row of seats in order to increase passenger comfort. Despite this, redesign of the shape of the cross-section made it possible to increase the interior width of the vehicle by 90 mm against the 4th model, to a

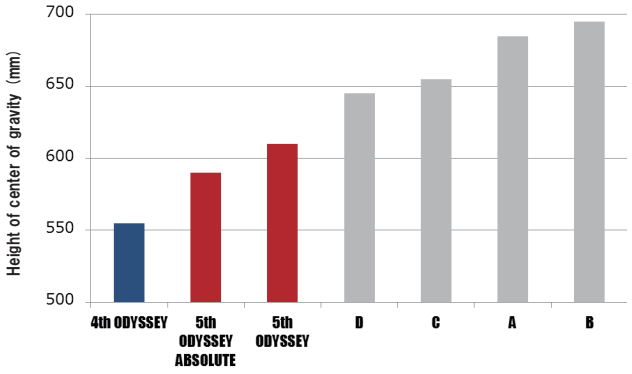


Fig. 7 Height of center of gravity

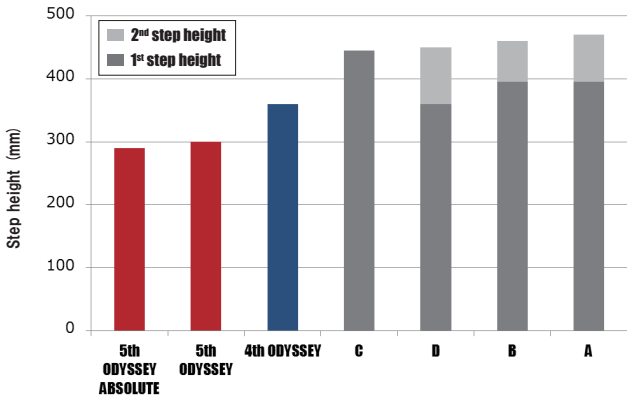


Fig. 8 Ultra-low-step specifications

roomy 1625 mm. At the same time, the distance between passengers in the horizontal direction was increased by 20 mm against the 4th model to 780 mm in the first row of seats, by 40 mm to 780 mm (with two passengers seated) in the second row of seats, and by 140 mm to 660 mm (with two passengers seated) in the third row of seats (Fig. 10).

The transition from the double-wishbone-type rear suspension used in the 4th model to a torsion beam-type controlled intrusion on the cabin space making it possible to realize seating room for three passengers in the third row of seats, an increase of one passenger over previous ODYSSEY models. As a result, the offering of a specification that includes a bench seat in the second row of seats makes this the first-ever eight-seater ODYSSEY.

The design team sought to offer a sense of space in addition to increasing interior dimensions, and realized a visual sense of space with good continuity by making the linings at the sides of the seats the same color as the seats (Fig. 11). For the roof lining, a smooth continuity in the plane connecting the upper surface and the side surface gives a visual sense of breadth (Fig. 12).

2.3. Cradle Seat

To help enable maximum use of the large, flat space realized by the low floor, in addition to the bench seat, premium cradle seats were newly employed in the second row of seats. In addition to the standard forward and rear movement, this makes it possible to move the seats horizontally, enabling a long slide of 740 mm when the third row of seats is stored away while still avoiding the rear wheel housing. This creates greater legroom offering a limousine-like level of comfort.

When the seatback is laid back in this position, the seat cushions are raised to the optimal angle, helping to prevent the occupant's body from becoming misaligned with the seat. The use of ottomans also disperses pressure on the body, helping to ensure a more relaxed posture.

The angle of the upper section of the seatback can also be independently adjusted, making it possible for the occupant to look forward with the seat laid back, offering a comfortable posture for watching the scenery or having a conversation (Fig. 13). Combined with the stable ride comfort offered by the low level of roll realized by the low floor, this comfortable posture gives a feeling of deluxe seating.

2.4. Visibility

The height of the seats in the first row is related to good visibility and ease of entry and exit.

When the height of the seats is raised, visibility improves, but raising the hips when entering and exiting the vehicle represents a burden. If the seat height is lowered, there is a loss of visibility, and if it is lowered too far, the hips sink deeply during entry to and exit from the vehicle, and this also increases the burden on the vehicle occupant. Given this, the sedan-like seating posture that had been well-received in previous models was maintained, while the

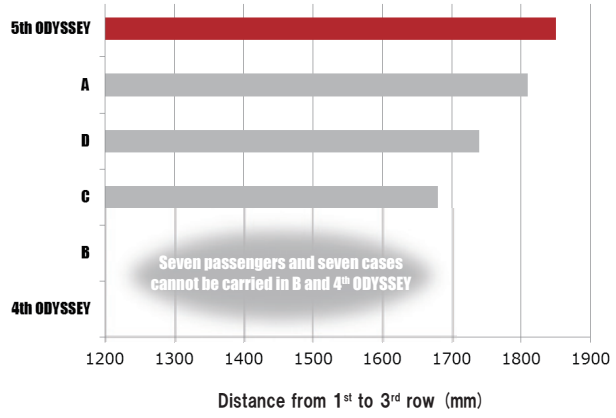


Fig. 9 Distance from 1st to 3rd row of seats when carrying seven passengers and seven suitcases



Fig. 11 3rd row seat



Fig. 10 Spacious cabin

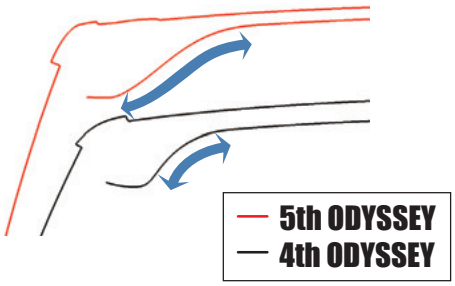


Fig. 12 Roof lining shape

height of the seats was increased by 100 mm against the 4th model to 685 mm, offering good visibility while driving.

This height makes it possible for the passenger to smoothly enter the vehicle without needing to significantly raise or lower their hips (Fig. 14).

With regard to visibility when cornering or changing lanes, in addition to the use of large triangular windows, the use of door mirrors attached to the door skin to minimize blind spots and positioned low in relation to the driver helps to promote improved recognition of pedestrians and other vehicles.

The fine tapering of the rear pillars towards the bottom has also made it possible to realize good rear visibility when parking.

2.5. Sliding Doors

Swing doors have been used for the rear doors since the first generation of the ODYSSEY based on the assumption that because the major share of the market previously transitioned from passenger vehicles to minivans customers would be familiar with them, and to increase the automotive value of the vehicle. However, user demand for sliding doors is strong in the domestic luxury minivan market, and sliding doors are now employed in the majority of vehicles.

Because of this, and with consideration of the compatibility of the low step, and given that families, who represent the main user segment would want to allow their children to enter and exit the vehicle in narrow parking spaces, sliding doors have been employed for the first time in an ODYSSEY.

However, if the width and height of the door openings were increased, body rigidity would be sacrificed. With regard to the width of the openings, the position of the center pillar was determined based on considerations of side impact and the positions of occupants, thus fixing the position of the anterior end. While the position of the posterior end was being determined based on the position of the rear wheels and the tire size, which are based in turn on the wheel base, the design team worked to increase body rigidity while reducing the size of the cross-sectional shape. Working within a variety of restrictions, lengthening the slide rail while attempting to ensure that there would be no effect on the shape of the rear combination lamps or the shape of the door break line, the design realized an opening width of 750 mm and an opening height of 1230 mm. This is in the top class of door opening dimensions compared to competitors while still maintaining a compact body size (Fig. 15). This not only makes for ease

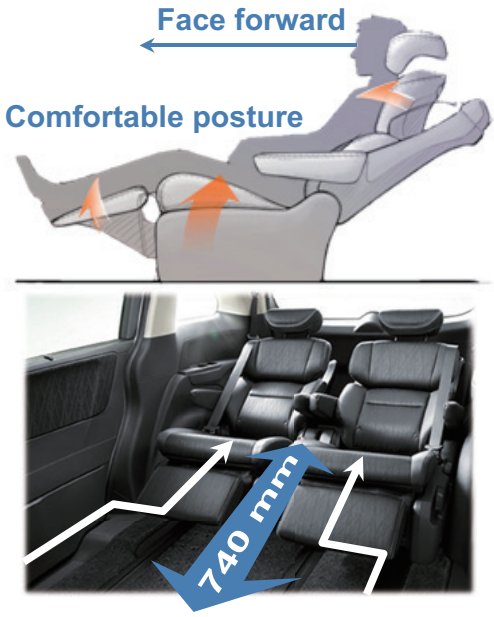


Fig. 13 Premium cradle seats

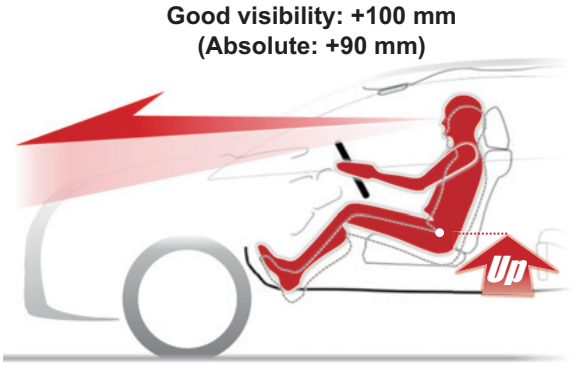


Fig. 14 Good visibility

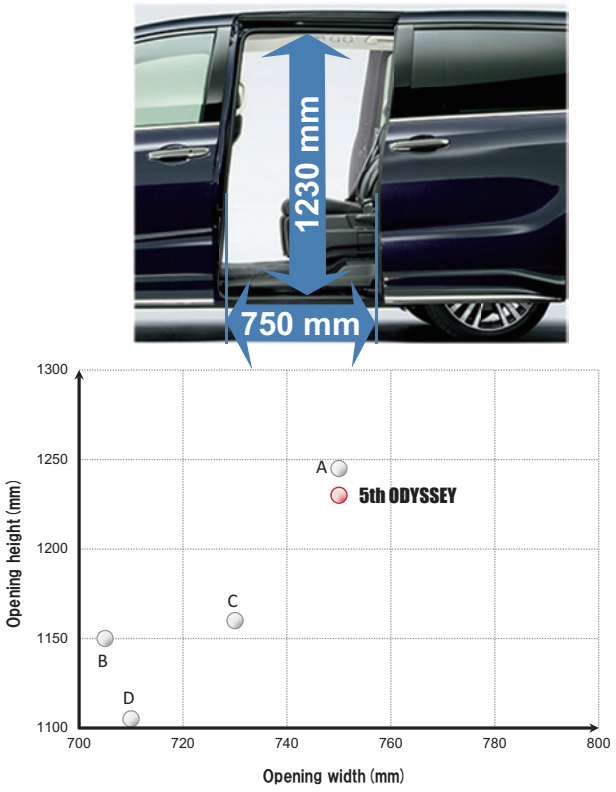


Fig. 15 Sliding doors

of entry and exit, but also allows for storage of large cases when the second row of seats is moved to the rear.

2.6. Convenience of Luggage Space

The height of the lower section of the tailgate opening has been lowered by 70 mm against the 4th model to 525 mm making it easy to load and unload heavy cases. The height of the opening has been increased by 205 mm against the 4th model to 1030 mm. The width of the lower section of the opening, which has a higher frequency of use, has been increased by 280 mm against the 4th model to a maximum of 1160 mm creating an opening that allows easy loading and unloading of large cases.

In addition, the use of a square shape creates an opening that also looks larger (Fig. 16).

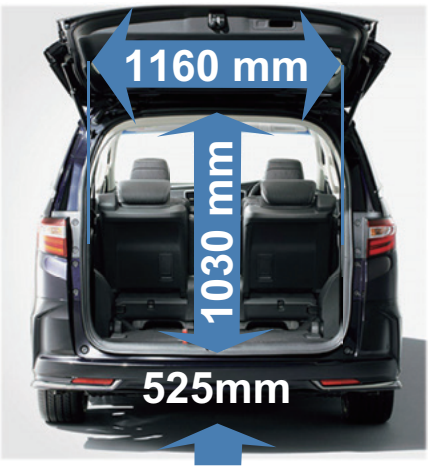


Fig. 16 Dimensions of tail gate opening

3. Exterior Design

The exterior design of the vehicle was based on the theme "Solid Streamline." Design efforts sought to achieve flowing and powerful proportions.

The silhouette employs a relaxed line that connects the slanted nose, created by the compact engine room, to the roof, the total height of which has been reduced. This creates a cabin with a sophisticated flow. At the same time, the protruding front and rear fenders and sculpturally folded midsection offer the appeal of dynamic power and stability (Fig. 17).

As a result of these basic shapes, despite the fact that in this model change the interior has become roomier and the total height has been increased against the 4th model, the exterior design sought to avoid producing a square box shape and aimed towards a design that would present an advanced and dynamic image that carried the ODYSSEY heritage on every level (Fig. 18).

For the front view, the "SOLID WING FACE," Honda's "new identity," has been applied. The employment of a design that establishes a continuous connection from the center of the front grille to the edges of the headlights offers a broad and technologically advanced image. The design team sought a sense of luxurious quality through the use of a grille that appears to have been carved from a block.

Three-dimensional shaping means that the thick nose, which is short but offers a sense of solid volume, and the lower grille, with its large open area, give a sense of power and unique presence (Fig. 19).

From the side view, a chrome beltline runs continuously from the front to the rear dividing the vehicle into upper and lower sections (upper cabin and lower body).

The aim was to create the visual effect of making the vehicle look lower than its actual total height. The beltline also contributes to creating a side view that gives a nimble and sporty impression (Fig. 20).

For the rear view, the aim was to create a three-dimensional form that would not look boxy and would



Fig. 17 Exterior design concept

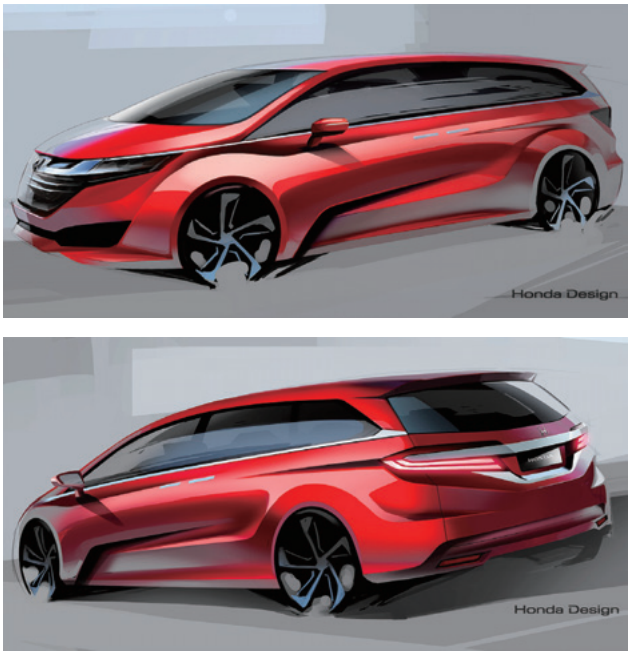


Fig. 18 Exterior rendering

not give a strong impression of corner ends by means of continuous rounding from the side surface to the rear surface. Fine tapering of the rear pillar towards the bottom creates a sharp and sporty design. This also contributes to ensuring a clear field of vision around the lower sections of the rear pillars, the most desirable area of visibility for the driver when reversing.

The rear combination lamps produce a line of light in the shape of wings, offering a broad and technologically advanced image (Fig. 21).

For the design of the roof, wind tunnel tests were employed to optimize the angle and length of the rear end of the roof. In terms of absolute specifications, the three-dimensional shaping of the front and rear bumper corners and the protrusion of the garnish of the lower edges of the doors creates the optimum shape for aerodynamic performance. These design features have generated a synergistic effect between sporty and impactful styling and increased aerodynamic performance (Fig. 22).



Fig. 19 Front view

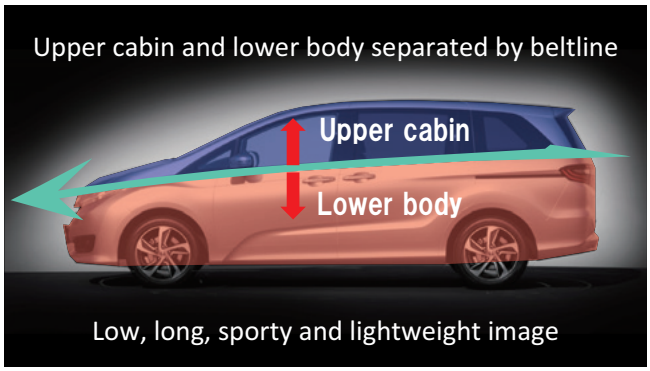


Fig. 20 Side view

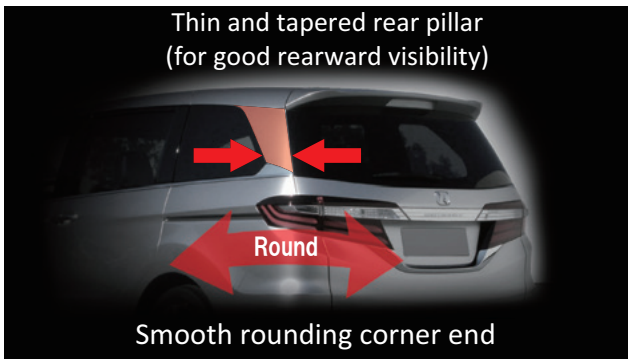


Fig. 21 Rear view



Fig. 22 Aerodynamic design

4. Interior Design

The concept for interior design was set as “Modern Suite Room,” with the image for the space as a whole being a suite in a modern luxury hotel.

A sense of high quality was realized in different ways for the three rows of seats: The first row of seats was imagined as a private desk for the owner, the space in the second row as a sofa for guests, and the third as a guest lounge. This made it possible to realize a high-quality mobile space with a modernity and universal appeal that will satisfy users for the life of the vehicle (Fig. 23).

For the instrument panel, a simple design with a powerful basic horizontal motif was employed in order to express high quality and the class of the vehicle. Positioning audio functions and meters in a central floating soft pad realized a fusion of modernity and luxury.

With regard to coloring, the basic tone is dark mocha, while the central soft pad is ivory with a deep-brown wood-grain panel positioned below it.

Silver decoration has been applied to the lower section of the wood-grain panel in order to provide a frame, offering a sense of modern luxury (Fig. 24).

A sunburst treatment has been applied to the deep wood-grain pattern on the decorative paneling giving a pure sense of the materials through three-dimensional shaping. A touch panel has been used for the heating control panel creating a smooth and refined visual impression.

Soft materials with a moist texture have been used in the central pad, and high-luster silver decoration has been applied to the edge of the outlet in order to add an accent.

A high-visibility large-diameter speedometer has been

employed, and a multi-information display positioned at its center. Forming these meters in three dimensions has realized a fusion of visibility and freshness. High quality and modernity have been expressed down to the finest details (Fig. 25).

Each of the seats has been generously shaped to give an impression of comfortable size. The seat covering is a lustrous suede-feel fabric with a moist texture. The same material has also been used in the door linings and the doors and armrests. This has given all the seats, including those in the second- and third-row, a richly relaxing and high-quality feel (Fig. 26).



Fig. 23 Interior design concept



Fig. 24 Instrument panel rendering



Fig. 25 Styling details

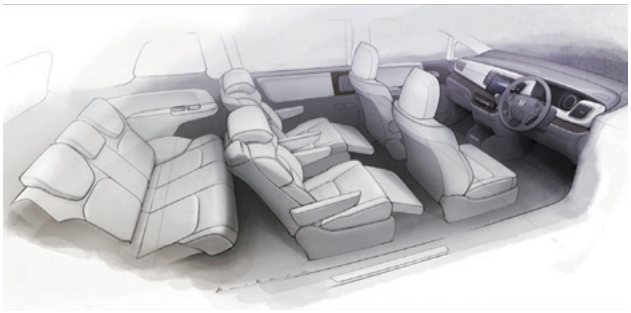


Fig. 26 Interior rendering

5. Conclusion

The name ODYSSEY means a long and adventurous voyage in ancient Greek. The first generation of the vehicle was true to this meaning in offering a greater number of passengers the new value of sporty mobility, and ushered in a minivan boom in Japan. Honda next turned the concept of the minivan on its head by offering the pleasure of driving at an exhilarating level.

The ODYSSEY is always ahead of its era, and in the latest development, designers reconsidered what a future mobile space should be, and created new value with a view towards the next revolution.

Born as the “Next Multi Seater Saloon” realizing an extremely high-level fusion between automotive value and utility value, the 5th model will fit the lifestyles of users in an even broader range of market segments, and will offer all users long-term pleasure and satisfaction through the experience of comfortable and luxurious hours in motion.

■ Author ■


Katsuaki HAYASHI


Ryusaku SENDA


Wataru MURAKAMI

Development of New 50 cc Scooter Dunk

Makoto MITSUKAWA* Shuji HIRAYAMA*
Mamoru OTSUBO* Yasushi TATEISHI*

ABSTRACT

Honda developed the new 50 cc scooter Dunk to revitalize the Japanese market for small (50 cc or below) motorcycles.

The Dunk, whose target users are male high school students, took "Premium Sneakers" as its development concept. The development theme was "A scooter that expands the fun of commuting of younger people and their daily lives as well." To realize that concept, the development team incorporated a design and a body packaging created under our new-concept. The 50 cm^3 engine eSP (enhanced Smart Power), which was dedicatedly developed for this application, was adopted as well to realize a superior economy and environmental performances. By implementing those factors, it was pursued to create a new scooter in superior quality that would be appreciated not just by high school students but also by a broader range of customers.

1. Introduction

The sales of small motorcycles (displacement of 50 cc or below) in Japanese market had peaked in 1982. Though it had experienced small scale sales increases several times, the market shrinkage has been continuing as an unchanged underlying trend. This tendency of shrinking market can be interpreted as the decline of the scooter market, which makes up more than 80% of small motorcycle market.

Two-stroke engines are commonly applied for scooters in small motorcycle class. However, with environmental awareness started to gain attention in the 1990s, Honda began developing scooters with four-stroke engines to enhance environmental performances, power and ease of handling. Then in 1999, the Giorno Crea Deluxe was developed as a scooter with a water-cooled four-stroke engine. It was also the world's first motorcycle with an idling stop system[(1)] for mass production. That model offered excellent environmental performances and a fashionable styling gaining considerable level of preferences from the customers.

To boost the market further, Honda released the Today, which was equipped with an air-cooled four-stroke engine, in 2002. It featured an affordable price with a simple vehicle configuration. Utilizing global resources within Honda, it was developed in Japan and manufactured in China. Through those efforts, the small motorcycle market was made stable at the level of annual sales about 500,000 units until 2007. However, the stricter emission regulation was issued in 2007 and the specification changes were made to comply with that change resulting in its price increase. Moreover, the Lehman Shock in 2008 imposed a significant impact on the market. With those influences on the market, the market stayed flat at about 240,000 units from 2009 through 2013[(2)] (Fig. 1).

Another serious issue is the aging of users[(3)]. Figure 2 shows the trends in motorcycle sales by customer age groups. As seen in this figure, younger people have been rapidly losing their interests in motorcycles. However, a small motorcycle is still a vital tool for the people who need short distance commuting and for the people who want to expand the range of everyday activities for fun. Honda made a firm decision for a commitment to ensure a

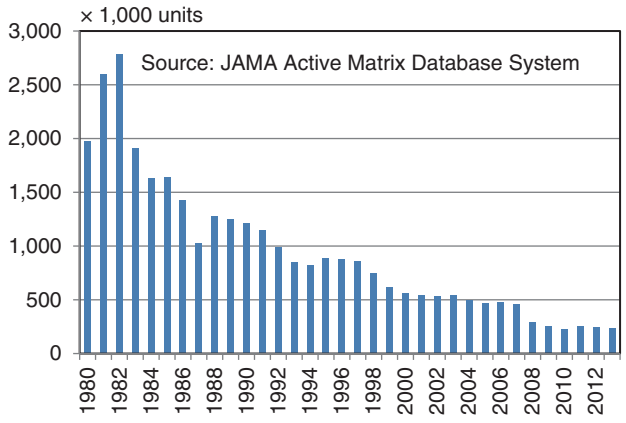


Fig. 1 Shipping volumes of 50 cm^3 class motorcycles in Japan

* Motorcycle R&D Center

vigorous motorcycle market in the future. Especially, it was considered to be the most important thing to get younger people to share the understanding on usefulness and attractiveness of motorcycles in this class.

In the scooter category of small motorcycle class, the DIO series used to be popular among a wide range of customers, especially among young male users. Since its market release in 1988, many customers showed their appreciation to it because of its practicality (e.g. a helmet can be stowed under the seat) and sporty styling (with a swift appearance). However, this continued customer appreciation created an unchanged stereotyped idea that younger people just like sporty design. With that established understanding, any in-depth study on changes in the tastes and values that younger people, particularly DIO users, have.

In this paper, the new scooter Dunk will be introduced (Fig. 3). Based on the aforementioned background, before starting its development, Honda conducted a research on the current situation of commuting for the students and what they expect to scooters. We also researched the values they recognize and the tastes in their life style. This research was conducted focusing on the targeted user group. Based on the research results, Honda proposed a new styling concept unlike that of any previous scooter. In addition, a new engine eSP (enhanced Smart Power) for a small scooter was dedicatedly developed and applied. The engine offers the sufficient acceleration performance required for a mixed traffic condition together with excellent environmental performances. Implementing those ideas and technologies, it was pursued to create a product in which younger people would naturally show their favor.

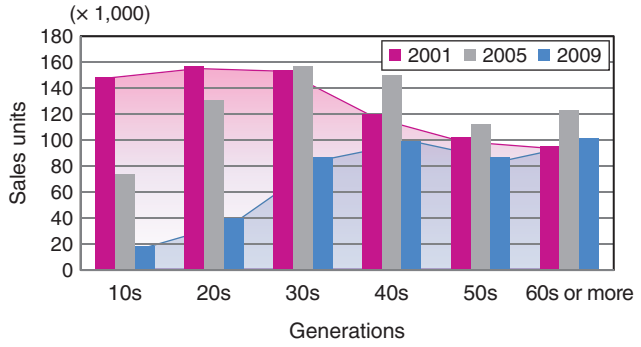


Fig. 2 Generation transitions of motorcycle buyers in Japan



Fig. 3 Exterior view of the Dunk

2. Concept

2.1. Defining the Target User

Under the objective of boosting small motorcycle market, the product concept was constructed focusing on users in younger age group. The core target customers were defined as male high school students using small motorcycles for their commuting.

To better know the surrounding situations of their motorcycle usage, various kinds of statistical data were analyzed as well.

First, the number of high school students who use small motorcycles for their commuting was investigated. It is conducted based on the data from the national census[4] and the driver's license statistics[5]. Figure 4 shows the population in age group of 16 to 18 years old, which corresponds to high school student ages, and the number of license holders of small motorcycles among the students in this age group. The data is shown for a sequence of years. Between 2001 and 2010, the population in this age group fell about 20%. Meanwhile, the number of license holders in this age group shows a steep decrease by about 60%. The study results show that the percentage of high school students having licenses decreased, roughly, from 10% to 5%.

However, breakdown of the data, into a specific age and gender, shows that there are about 50,000 potential users in 17 years old male group (i.e. in a sub-group of 16 to 18 years old, which is the age segment showing the largest

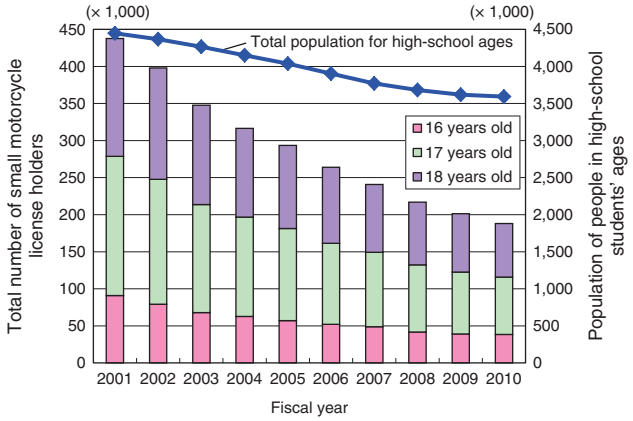


Fig. 4 Number of small motorcycle (under 50 cm^3) license holders in high-school students' ages

Table 1 Percentage of small motorcycle license holders of male in age of 17 years old in top 10 prefectures

Ranking	Prefecture	Number of holders	Prevalence of holders
1	Yamanashi	1,524	32.15%
2	Kagoshima	2,801	29.45%
3	Kumamoto	2,081	20.95%
4	Kochi	822	20.60%
5	Nara	1,387	18.80%
6	Ibaraki	2,836	18.58%
7	Osaka	7,289	18.51%
8	Tochigi	1,583	15.95%
9	Niigata	1,855	15.30%
10	Oita	802	13.26%

increase of license holders) (Fig. 5).

Research on various population statistics of each prefecture[4] and the statistics of driver's license[5] were also conducted. Through the research, it was tried to identify the regions where a large number of high school students are using small motorcycles for commuting. It was considered based on the number of 17 years old males with motorcycle licenses and its percentage to the whole population in that age group (Table 1).

The data indicates that cities in rural area have potential needs for high school students to use small motorcycles for commuting. Based on those research results and our considerations, the target user for the development was specifically defined as male freshmen of a high school living in a rural city.

2.2. Concept and Target of Development

In this development, the theme was set as "A scooter that expands the fun of commuting of younger people and their daily lives as well." Moreover, the conceptual vehicle identity for this development was defined as "Premium sneakers". Then it followed by the following development objectives.

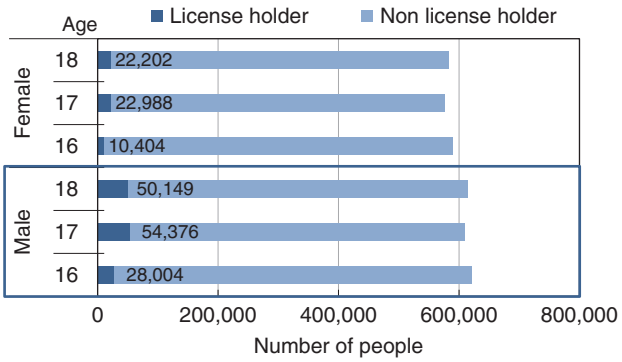


Fig. 5 Number of license holders of small motorcycles in high-school student age group

(1) Design: A simplified styling expressing a superior quality yet with casual feeling as well
- Showing an atmosphere of a natural behavior refraining an exaggerated appealing or showy ostentations
- Well-tended makeup that extends the intentions and devotions of the designers
- A rider and the scooter should be perceived not as separate substances but as a single whole mass united into one object

(2) Convenience: Equipment for enhancing the satisfactions of younger people in their "daily lives"
- A utility box with a large capacity that has enough room to hold a full-face helmet plus some additional space
- An accessory of an electrical socket, for charging smartphones, etc., a clock, and other conveniences that are easy to use in everyday life
- Good fuel economy contributing to less frequency of refueling

(3) Comfort: 30 minutes commuting without feeling tired
- A relaxing and comfortable ride in an upright seated posture
- Secured stability in riding posture even when the rider stretches the legs forward
- Performance with an ample of power for a comfortable cruising in a mixed traffic

3. Styling Design

3.1. "Daily Lives," the Sense of Value

For a creation of attractive exterior design fitting to the concept of a product, it is generally required to sort out in advance the conceptual approaches of the design with good understanding of feelings and perceptions of targeting users.

Accordingly, "the design that makes younger people to be stimulated for their ownership" was investigated to establish a design concept in line with the previously described product concept. The results pointed out the following trends in younger people's thinking and actions.

The image of the younger person who wears uniforms in a disheveled way and has a style that features their bangs is truer of the previous generation than of this one. The majority of younger people "daily lives" tend to prefer good-fitting clothes that they wear neatly, with hair that looks casual and natural. However, this does not mean that they do not care how their hair looks. They do not want to stand out, but younger people really think about how they can look natural.

They have decided that having a conspicuous hairstyle or wearing novel fashions is a way for performers or others to whom it might be appropriate to assert their individuality. Younger people want to know their place. Taking their peers as their standard, they figure out how to look natural and nonchalant among them. To this age group, this is what it means to look smart.

Following are some examples of products appealing inconspicuous smartness in the eyes of these younger people.

For example, fashionable road bikes and mountain bikes are not the bicycles they use to commute to school. Rather, they choose so-called "keikaisha" (light and comfortable bicycles) such as one can see anywhere. The most common color is inconspicuous silver. These bikes are meant to be practical, with a basket in front. However, this does not mean that just any inconspicuous, practical bicycle will do. Younger people choose manufacturers they trust, which is to say, it is the clever side of bicycles –practicality and durability– that younger people find smart. Something similar is happening with mobile phones, which are now indispensable to younger people. Smartphones are becoming more prevalent, and unlike in the past, they no longer choose according to color, form, and the like. Smartphones are all the same rectangular shape, and none of their external characteristics make them stand out. What satisfies younger people are the feel of well-built quality and functionality as a communication tool.

3.2. Styling Theme

When establishing the styling theme, the usual process was not chosen, which is to start from the styling of the scooter itself. Rather, we sounded out younger people's sense and took that as the starting point of our study. These users want to assimilate into their surroundings and choose possessions that assimilate into the owner. In other words, what we sought for was that neither of the vehicle or the rider solely stands out. The point is that those two objects are to be naturally balanced in total in its styling. That is to say, we pursued "the styling that incorporates the person who maneuvers the vehicle." This was chosen as the styling theme. Then, to ensure that the quality and function have a certain level of individual finishing, "high quality," "sturdiness," and "functionality" were chosen as important keywords embedded in this "styling."

To that end, the observations of younger people's postures were conducted when they are riding scooters. In 1990's, the popularity of high powered two stroke engine models was in its peak and the younger people were riding them in an untidy manner with a crab crotched posture. However, through the results of the research conducted this time, it was found out that they are no longer doing that way of riding in these days.

Younger people today sit towards the rear of the seat and stretch their legs so their feet are on the front end of the floor. Their backs are upright. Overall, their posture looks relaxed and quite natural. They adjust the length of the shoulder strap from which their rectangular sports bags hang, so that the bag rests lightly on the carrier and is less of a burden on the body. And in many cases they wear full-face helmets.

Based on the above, the "human form," was the first thing to be created, complete with full-face helmet and sports bag hanging from the shoulder while the rider is in the above riding posture. Once that was done, the "rider-incorporating styling" was designed.

To begin with, three points were determined indicating the height of the rider's head and the position of the front and rear tires, which are important for ensuring comfort. The line that encloses these three points was sketched out. Based on this form, a trapezoidal outline was defined so that the outline of the vehicle body and the rider fits to it without protrusions or indentations (Fig. 6).

Next, the form with an awareness of the angle of the rider's arms and legs were adjusted, creating "rider-incorporating styling."

Utilizing this base "form," it was made possible to create a compact and not unnecessarily oversized impression. On the other hand, it was also made possible to establish a balanced looking of stability in which the front and rear tires are showing the posture of firm standing on the ground.

3.3. Styling Expression

The essence of the design does not include an intention to create a strong characteristic, such as "sporty" or "pretty." Instead, the design focus remained squarely on integration with the owner's taste. With this direction of designing, the design features of "high quality finishing," "sturdiness," and "functionality" were expressed as seen in the things, such as smartphones or bags that younger people use in their lives (Fig. 7).



Fig. 6 Concept sketch showing styling theme



Fig. 7 Design sketches of front quarter view and rear quarter view

Specifically, the body achieves an elaborately designed finish quality that constructed of plain surfaces and multi-faceted elements with the integrated lamps (Fig. 8). In addition, the metallic mole line that wraps around the entire body from the upper side of the body below the handles puts the focus on the body's sense of unity. This helps eliminate the overly delicate impression that is peculiar to the scooter silhouette, which tends to look as if the portions in front of and behind the step floor are separate entities (Fig. 9).

The meter has a tough-looking exterior and a simple structure. The easy-to-read dial face and all the necessary information are positioned to be functional (Fig. 10).

3.4. Coloring

Keeping in mind the tastes of the target user, the body colors that would agree with the sensitivities of younger people today were chosen.

Six color coordination patterns were created considering the feature of tough outer appearance, with a simple shaped body design and a wide-strip mole line, and high quality atmosphere. This set of color patterns made it possible to satisfy large range of customers' preference (Fig. 11).

(1) Matte dark green with silver mole line: a condensed unified appearance



Fig. 8 Rear combination lamp assembly



Fig. 9 Metallic mole line



Fig. 10 Gauge unit



Fig. 11 Variations of color combinations

(2) Metallic black with silver mole line: the simplest, superior quality image
(3) Pearl white with smoke silver mole line: a natural, neutral image
(4) Metallic blue with turquoise mole line: a refreshing combination of blue denim color with a more vibrant shade of blue
(5) Candy red with smoke silver mole line: the combination of two low-chroma colors projects an aura of superior quality
(6) Matte black with pink mole line: a sophisticated combination with a striking plain and solid style

As the section on the styling theme mentioned, the coloring used on this model is more than simple decoration.

By emphasizing the sense of unity of the entire body, the coloring inspires confidence and expresses an understated look of superior quality. The metallic mole line that runs throughout the body is a particularly important part of this model. The mole line expresses not only the toughness and sense of unity of the whole body, but is also intended to protect the body exterior from minor scratches. Therefore the image expected of a mole line was explicitly stated.

In the early stage of the process of consideration, we fixed the ways to express the toughness with accompanying a high quality atmosphere. One of them is to have the stripe in metal tone and another is to make its width broad enough to some extent. Midway through the development process, after a three-dimensional mole line made of molded resin had been considered, it was decided to use film instead. Because young people were the target, keeping the price affordable was important. The above design elements were intended to help offer both a functional exterior and a reasonable price.

However, in order to express the concept illustrated in the drawing using this film material, there exist a various kinds of obstacles to be faced. It was necessary to use metal tone film capable of expressing superior quality, not the thin film that is ordinarily used and is so good at adhering closely to curving surfaces. Metal tone film draws the attention to the texture of the underlying paint and surface unevenness that results when foreign matter digs into the surface while applying the film. Therefore it was necessary to enhance the painting quality and consider the environment in which film is applied. It is also required to implement a technology to apply long film strips within a limited range of allowance. Furthermore, the relative positions of the films, which are separately affixed onto the individual parts, should create no discrepancies from mislocations when the assembly is completed into a whole vehicle.

It was required to solve all of those difficult issues at the same time while none of them had been experienced in the actual production site so far. When a metal film is applied, there is a tendency that dents and lumps on the surface significantly stand out if there is an irregularity on the paint surface of a part or there are some intrusions of dust particles. Therefore, it is strongly required to have a special effort for improving the paint finish quality and for maintaining the clean environment for film affixing process. Next, a technique capable of stable positioning of the film was established and verified. Furthermore, the other issues were addressed one by one, including enhancing assembly precision of each component. By applying the aforementioned elements for the structural shape in styling together with the optimized combination of body colors and metal tone mole colors, the message of the realization of both “sturdiness” and “high quality” was effectively expressed for easy understanding of the users.

4. Body Packaging

The “man maximum, mechanism minimum” (MM) concept was incorporated as a prerequisite to consideration of the body packaging. The MM idea of creating more space for people and requiring less space for the machinery underlies all of Honda’s craftsmanship.

Following this perspective, the comfort and convenience in everyday use was pursued, taking the following two key targets for the body of the Dunk.
(1) Lasting comfort for even long rides
(2) The most under-seat storage capacity in the small motorcycle class

One way to achieve these would be to simply make the motorcycle larger. However, for the sake of pull-up handling on a daily basis, a wheelbase was chosen equivalent to that of the Today, a previous scooter in the small motorcycle class. Therefore, for this development, the key targets above were achieved by selecting an appropriate placement and form for each component, starting with the orientation of the engine installation. Table 2 presents a comparison of the major specifications.

4.1. Comfort

The heights from the floor surface to the seat and to the handle bar were designed large enough while ensuring the minimum required body sizes considering a good pull-up handling of the vehicle. Figure 12 shows the riding position triangle, which connects the hip point, grip point, and foot point. The solid line shows the riding triangle of the Dunk, while the dotted line shows that of the Today, the formerly designed model. The riding triangle of the Dunk affords a more relaxed position.

The Dunk also has a longer seat and floor, which gives greater sitting and leg position freedom. The seat has a thick layer of urethane so users can make long rides in comfort. The under-floor fuel tank is directly mounted to the frame, using no stays or other devices in between. This keeps the floor from having to be raised too high and adds to comfort.

4.2. Under-seat Storage

In the new packaging design, a large capacity storage space was created under the seat. A several measures were adopted as described below.

Table 2 Comparison of major specifications

Model name	Dunk	Crea SCOOPY	Today
Curb mass (kg)	81	79	79
Dimensions (mm) (Length × Width × Height)	1,675 × 700 × 1,040	1,695 × 625 × 1,000	1,695 × 630 × 1,030
Wheelbase (mm)	1,180	1,190	1,180
Seat height (mm)	730	710	695
Ground clearance (mm)	110	115	110
Fuel tank capacity (L)	4.5	4.8	4.6
Brake system Front/Rear	Disk (CBS) /Drum	Drum (CBS) /Drum	Drum (CBS) /Drum
Tire size (Front/Rear)	90/90-10 50J	90/90-10 50J	80/100-10 46J

First, the fuel tank was placed under the floor, whereas many models put it behind the seat. A double under-bone type frame was chosen to do this, but this is basically heavier than the ordinarily used mono under-bone type frame. For this development, the diameter and thickness of the pipes were optimized, resulting in a frame of about the same weight as mono under-born type.

Next, The space for the compartment has been increased by shifting the lateral cross member tubing, which is supposed to be located behind the utility compartment, to the back end of the body. Figure 13 shows the configuration of frame, fuel tank, and utility box in the Dunk, while Fig. 14 shows the same for the Today.

The engine, which is located below the utility box and has a major impact on storage capacity, has an Alternative Current Generator (ACG) starter. As a result, the starter motor in the upper part of the crank case could be taken out. This helped to optimize the engine mounting angle and create space in the lower part of the utility box.

These innovations of the surrounding layout enlarged the utility-box storage capacity to 23 liters, big enough to hold both a full-face helmet and a raincoat. Because the opening of the utility box is so large, the box can hold an A4-size file folder, such as schools are increasingly distributing in recent years, without folding (Fig. 15).

In addition, the seat, which functions as the lid of the utility box as well, was designed to have enough length to

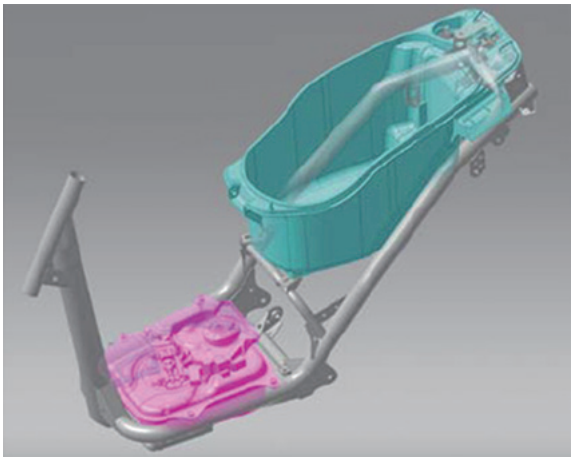


Fig. 13 Developed double under-bone type body frame

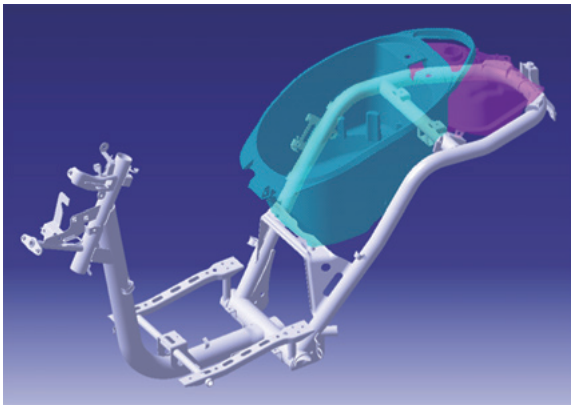


Fig. 14 Mono under-bone type body frame applied to Today

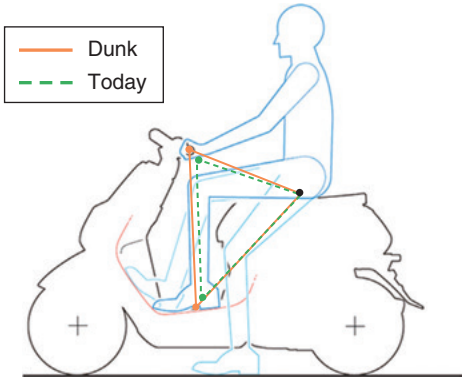


Fig. 12 Riding position



Fig. 15 Utility space

support a sports bag toted on the shoulder. This enhances both an undistorted styling and its practicality (Fig. 16).

4.3. Specifications and Equipment

For the convenience of senior high school students commuting to and from school, the Dunk comes with equipment not previously available on a small motorcycle class scooter. Smartphones have become a necessity for younger people, so an accessory socket that can recharge a smartphone is located in the glove box (Fig. 17). A digital liquid crystal clock was also added to the speedometer. The front inner bin is large enough to hold a 500 ml drink in a paper carton (Fig. 18).



Fig. 16 Seat length sufficient to support sports bag



Fig. 17 Charging socket for smartphones equipped in glove box



Fig. 18 A 500 ml drink packed in a regular paper carton can be stored in front inner bin

Other equipment provided for practicality and functions are a front disc brake with Combined Brake System (CBS), along with aluminum die-cast wheels (Fig. 19).



Fig. 19 Front disc brake with CBS and aluminum die-cast wheel

5. Development of 50 cc Scooter Engine eSP

Based on our development concept, the engine development target was defined as a lightweight and compact engine with a sufficient power compatible to a mixed traffic in urban areas with an excellent economy.

Honda developed the "eSP"[6] series of next-generation small scooter engines, which have previously been produced for 125 cc and 150 cc scooters like the PCX. For the Dunk, new 50 cm^3 engine was developed as a youngest brother of "eSP" series (Fig. 20). It was the first new development of a 50 cm^3 water-cooled engine for scooters since the 2001 Crea SCOOPY.

Because the currently mass-produced model Today has an air-cooled engine, this section will mainly discuss the developed engine in comparison to the engine for the Crea SCOOPY (2007 model), which has a water-cooled system like the Dunk. Table 3 shows the major specifications of these three engines.

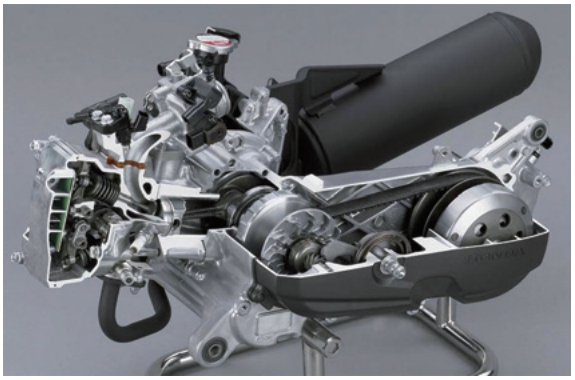


Fig. 20 Developed engine eSP

Table 3 Comparison of engine specifications

Model name	Dunk	Crea SCOOPY	Today
Displacement (cm^3)	49	49	49
Cooling system	Partial water cooled	Water cooled	Air cooled
Bore × stroke (mm)	39.5 × 40.2	37.8 × 44.0	37.8 × 44.0
Compression ratio	12.0	12.0	10.1
Cylinder offset (mm)	5.5	0	0
In. Valve diameter (mm)	21	20	20
Ex. Valve diameter (mm)	15.5	16.0	16.0
Rocker arm type	Roller	Slipper	Slipper
Decompression system	Equipped	Not equipped	Not equipped
PCV system	Not equipped	Equipped	Not equipped
Maximum power (kW/rpm)	3.3/8,000	3.2/8,000	2.8/8,250
Standing start acceleration performance : 0-200 m (sec)	16.0	16.7	17.3
Fuel consumption (class) : WMTC mode (km/L)	56.6 (class 1)	-	51.2 (class 1)
Engine mass (kg)	19.3	20.4	21.6

5.1. Enhancing Power Performance

In this engine, when Continuously Variable Transmission (CVT) ratio changes in the acceleration state with a full open throttle, the engine speed ranges from 7,000 to 7,500 rpm. The output on the crankshaft in this range was improved by 6 to 9% compared to the conventional water-cooled engines (Fig. 21).

The output on the axle of rear wheel was also enhanced over that of the former models by raising the engine speed of 500 rpm when changing speed ratio. The standing start acceleration performance from 0 to 200 meters has been enhanced by 0.7 seconds compared to the Crea SCOOPY and 1.3 seconds compared to the Today. The passing acceleration performance from 20 km/h has been enhanced by 0.5 seconds compared to the Crea SCOOPY and 1.3 seconds compared to the Today (Fig. 22). The techniques applied to enhance output are discussed as follows.

5.1.1. Enhancing charging efficiency

The bore and stroke of 37.8 mm × 44 mm of the existing engine was changed to 39.5 mm × 40.2 mm. The larger bore diameter enabled the enlargement of the intake valve diameter from 20 mm to 21 mm.

In addition, the angle between the inlet valve axis and the cylinder axis was made reduced by enlarging the inlet port curvature by about 15% (Fig. 23). These modifications expanded the effective intake valve opening area by 18% (Fig. 24) to enhance charging efficiency by as much as 20% (Fig. 25). Combining these modifications with a cylinder

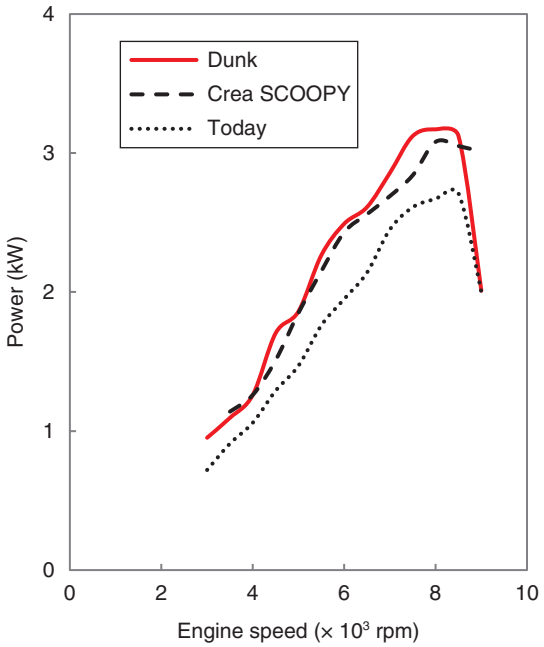


Fig. 21 Engine performance

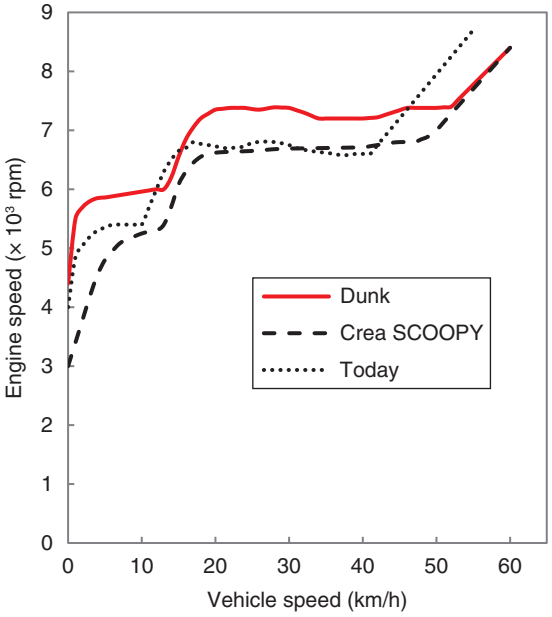


Fig. 22 Speed diagram

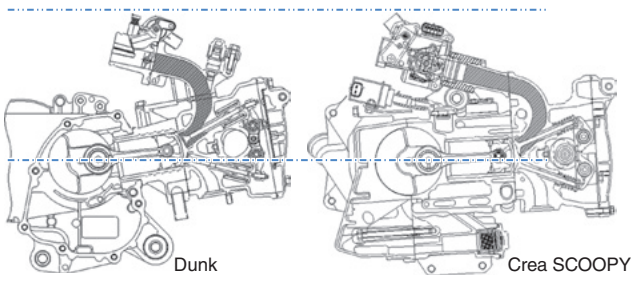


Fig. 23 Inlet port form

that is offset downwards by 5.5 mm (described later) enabled keeping the throttle body at about the same height as the former water-cooled engine.

5.1.2. Reducing friction loss

Typical examples to reduce friction loss were shown as follows. The percentages of friction loss reduction indicated hereafter are the values at 8000 rpm, which is the engine speed at the maximum output.

(1) The increase of intake valve diameter (from 20 mm to 21 mm) described above reduced pumping loss by 23%.
(2) The larger bore diameter made it easier to provide clearance between the connecting rod and cylinder skirt, so a cylinder offset of 5.5 mm was chosen (Fig. 26), reducing reciprocating motion loss by 10%.
(3) The rocker arm uses the small roller (exterior diameter ϕ13) used in the 2014 PCX, reducing cam drive loss by 54%.
(4) The engine uses a "partial-water-cooled configuration": only the cylinder head is water-cooled, while the cylinder itself is air-cooled. Compared to an ordinary water-cooled engine, this lowers the temperature of the cooling water at the radiator inlet and allows a smaller radiator cooling fan. With the fan now 4 mm lower, friction on the fan itself was reduced by 53% (Fig. 27).

5.2. Reducing Cost

Controlling manufacturing costs is also important to achieve outstanding economy. The adoption of partial-water-cooling helped control cost increases.

5.2.1. Eliminating the PCV system

Temperature goes up slower at the cylinder wall in a water-cooled engine after a cold start than that in an air-cooled engine. Therefore, if the motorcycle travels short distances repeatedly, water and some part of a constituent of gasoline may remain in liquid status and stay within

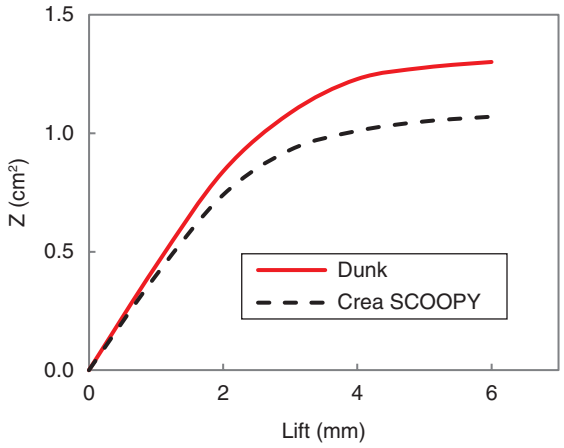


Fig. 24 Effective intake valve opening area

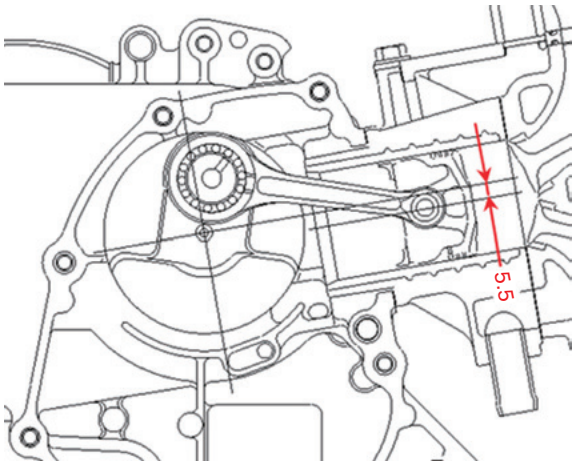


Fig. 26 Cylinder offset

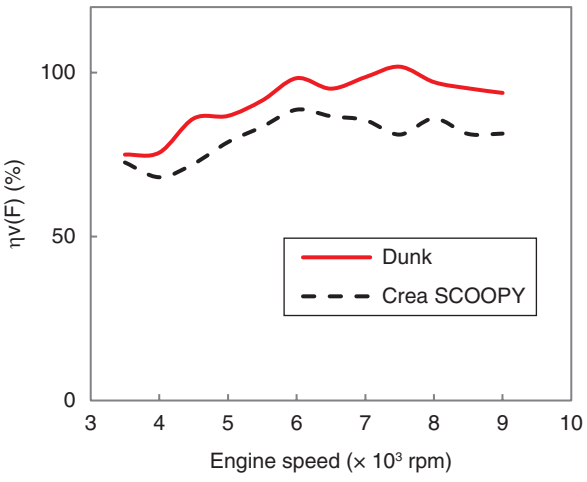


Fig. 25 Charging efficiency

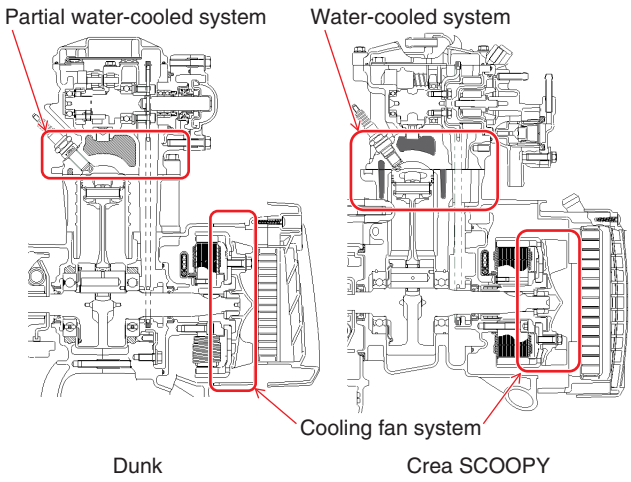


Fig. 27 Comparison of cooling system

the engine oil. Thus, former water-cooled engines for small scooter used a positive crankcase ventilation (PCV) system[7]. This helped decrease deterioration of the engine oil and thus the need to change it more frequently. In the case of the Dunk, a partial-water-cooled engine was chosen with the intent to ensure that the cylinder walls heated up as quickly as those in an air-cooled engine (Fig. 27). Figure 28 shows changes in cylinder wall surface temperature after the engine start. The developed partial-water-cooled engine achieved the warming-up characteristics compatible to air-cooled engines and made it possible to eliminate the PCV system.

5.2.2. A common cylinder clamping bolt pitch

In the partial-water-cooled engine, since the cylinder does not have a water jacket, the cylinder clamping bolt pitch was able to be reduced by about 6 mm as compared to a conventional water-cooled engine. This facilitated using the same dimensions as a 50 cm^3 and 110 cm^3 air-cooled engine, as Fig. 29 shows. This has enabled the usage of the same machining equipment that it already has in place for air-cooled engines at its production facilities outside Japan.

5.2.3. Vertical sprit of crankcases

Until now, 50 cm^3 scooter water-cooled engines manufactured in Japan have had a separate swing arm construction to facilitate modular assembly, and their crankcases have had a horizontal split. However, the crankcases of scooter engines currently manufactured outside Japan have a vertical split with a swing arm that is integrated into the left side. The developed engine also uses a crankcase with a vertical split so that it can be machined and assembled with equipment available at production bases outside Japan.

5.3. Lighter and More Compact

With the adoption of an ACG starter, a centrifugal clockwise decompression device was equipped for the first time in 50 cm^3 engine. This helped reduce cranking torque when starting the engine, lowering the ACG starter torque by 15% (Fig. 30). In addition, the increased external diameter of the ACG starter made it possible to reduce its width by 24% (Fig. 31) and thus 15% lighter. The width from the cylinder center to the exterior of the radiator

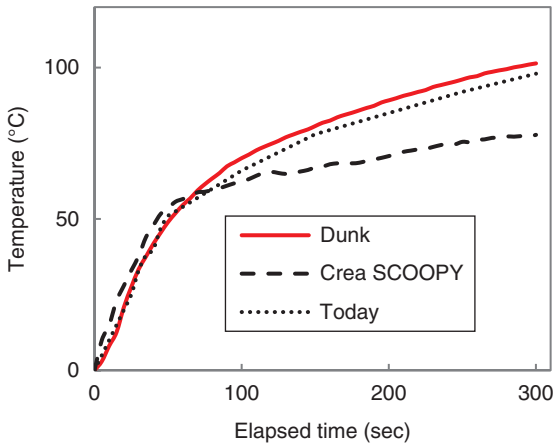


Fig. 28 Cylinder wall surface temperature

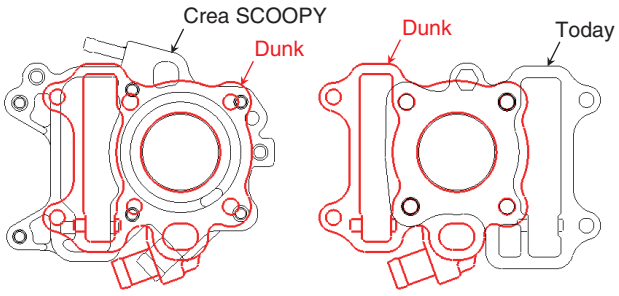


Fig. 29 Comparison of cylinder clamping bolt pitch

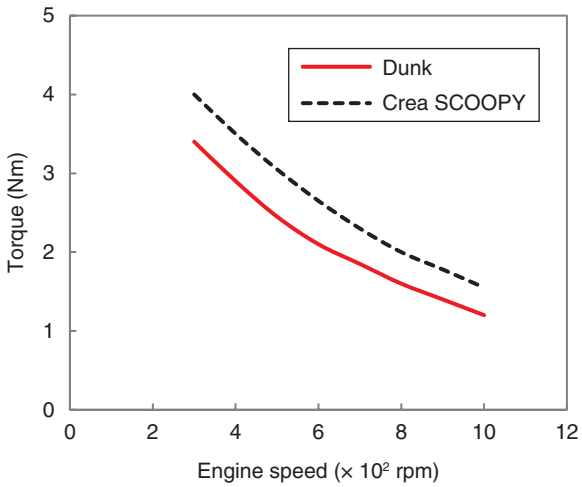


Fig. 30 ACG starter torque characteristics

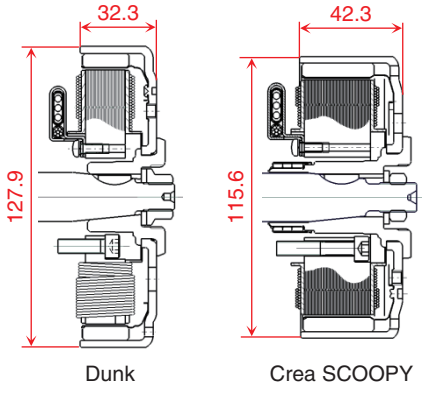


Fig. 31 ACG starter comparison of size

was shortened 14 mm with the lowering the height of the cooling fan as described previously.

Also, the adoption of vertical sprit of crankcases and the integration of swing arm to the left side of the crankcase enabled a weight savings of about 0.75 kg.

Consequently, these changes make it possible 1.1 kg in weight savings compared to the former water-cooled engine.

6. Conclusion

Honda developed the new 50 cc scooter Dunk targeting younger people in order to revitalize the market for small motorcycles.

It was built with styling integrated with the rider, the new engine eSP, and packaging based on the "MM concept." The result is a simple style with both a sense of easiness and superior quality, plenty of equipment for enriching the "daily lives" of younger people, and comfort that decreases fatigue even after 30 minutes of school commuting.

We hope that many younger people will use the model and that it will help revitalize the small motorcycle market when more people appreciate its styling and convenience.

References

(1) Sugioka, K., Sekiya, Y., Hayashi, H., Kasa, K., Nakajima, H., Toriyama, M.: Development of Scooter with 4-Stroke Engine - GIORNO Crea, HONDA R&D Technical Review, Vol.11, No.2, p. 9-14 (in Japanese)
(2) http://jamaserv.jama.or.jp/newdb/index.html
(3) http://www.jama-english.jp/release/release/2012/120404-4.html
(4) http://www.stat.go.jp/data/kokusei/2010/
(5) https://www.npa.go.jp/toukei/menkyo/index.htm
(6) http://world.honda.com/Global-125cc-engine/Tech-details/page05.html
(7) Moriyama, R., Muraoka, Y., Fujihara, K.: Development of Positive Crankcase Ventilation System for Four-stroke Engine Used in Small Motorcycles, Honda R&D Technical Review, Vol.16, No.2, p.165-170

■ Author ■


Makoto MITSUKAWA


Shuji HIRAYAMA


Mamoru OTSUBO


Yasushi TATEISHI

Development of HSL2511 Large-sized Snow Thrower

Kenta KOHIGASHI* Tsutomu MIZOROKE* Takashi HASHIZUME*
Shohei URANO* Jun SONG*

ABSTRACT

The HSL2511 residential-use large-sized snow thrower was developed on the concept of a flagship model that realizes ease of use and simple operation for tidy leveling of the snow-clearing surface.

An auger height motor and auger rolling motor move the snow-clearing system (auger) vertically and laterally using a control unit with built-in acceleration sensor to determine the inclination. This is also the first snow thrower in the world to be equipped with an auger assist function that remembers the vertical and lateral inclination of the snow-clearing system and keeps it steady while in operation. This reduces the need to expend care and attention on the inclination of the snow-clearing system during operation as well as the need to frequently manipulate the system controls. This model also has increased workability, so that even beginners can easily produce a smooth, orderly surface of cleared snow, or shape the cleared snow surface to the desired slope.

This model has a four-stroke V-twin engine with an electric governor and electronically controlled fuel injection system. It achieves increased workability and more efficient snow clearing by an operation mode change function, which switches to different engine power curves according to various operating conditions, as well as a speed guide function, which helps the operator find the optimal working speed.

The increased working efficiency achieved by the new model engine and the snow thrower's various functions has realized a 16% improvement in fuel efficiency.

1. Introduction

Honda developed its first residential-use small-sized HS35 snow thrower for the American market in 1980, when it entered the snow-thrower market. In Japan, Honda started selling the HS50 (5-PS class) residential-use small-sized snow thrower in 1982. Honda snow throwers are now being sold in 20 or more countries worldwide[(1)].

The line-up of snow throwers with gasoline engines on the Japanese market now includes models from 2 to 24 PS. Cumulative sales have reached 360,000 units.

The amount of snow coverage has been increasing in recent years, and areas experiencing heavy snow (snow with a high specific gravity) have been tending to expand. The labor of snow-clearing has been growing progressively heavier, and this in combination with the increasing age of the population in snow areas and the shortage of people to handle snow-clearing work has created demand for more efficient snow clearing.

In order to address these market needs, Honda has made a full model change of snow throwers in the large-model class (body mass of over 400 kg), and developed the HSL2511 residential-use large-sized snow thrower with increased work efficiency. This model is introduced here. Figure 1 shows an external view of the HSL2511.



Fig. 1 Overview of HSL2511

* Power Products R&D Center

Table 1 Major specifications of HSL2511

Items	Specifications
Overall length [mm]	2,425
Overall width [mm]	1,100
Overall height [mm]	2,060
Dry mass [kg]	595
Width of snow clearance [mm]	1,100
Height of snow clearance [mm]	715
Maximum snow-throwing distance [m]	26
Engine type	Forced air cooling, 4-stroke, 2-cylinder 90deg V-type, OHV
Displacement [cm^3]	688
Net power [kW/rpm]	16.5/3600
Fuel type	Unleaded gasoline
Fuel supply system	Electronically controlled fuel injection system
Auger height adjustment system	Electro-hydraulic cylinder
Auger rolling adjustment system	Electro-hydraulic cylinder
Main equipment	Auger assist
	Auger reset
	Auger lift
	Speed guide
	Operation mode switching system

2. HSL2511 Concept and Features

The development concept was formulated as a flagship model that realizes ease of use and simple operation for tidy leveling of the snow-clearing surface. It was developed with the aim of making this a product with the appeal to make it the model that is most frequently selected by customers from among snow throwers with gasoline engines in the large model class.

The specific features are as follows.

(1) The attitude control for the snow-clearing system (auger) has been computerized, and the snow thrower has been equipped with the world's first auger-assist function that maintains the auger at a constant inclination. This makes it relatively easy even for beginners to produce a smooth, level surface of cleared snow, or shape the cleared snow surface to the desired slope.

(2) The adoption of an electric governor[(2)] and inclusion of an operation mode-change function and speed-guide function enable the snow thrower to support a variety of different operating conditions and realize even more efficient snow clearing.

(3) The adoption of a four-stroke V-twin engine with an electronically controlled fuel injection system (FI system) realizes simplified starting (no fuel cock or choke operation required) and improved fuel efficiency.

Table 1 shows the major specifications of the product.

3. Main Equipment and Technology to Achieve Goals

3.1. Smart Auger

Smart Auger (trademark registration application filed) is the name of the auger attitude-control function in the HSL2511. It is equipped with the auger-assist function, auger-reset function, and auger-lift function described below.

Auger-assist function: This function controls the vertical and lateral inclination of the auger electrically, and maintains the auger at a fixed inclination as desired.

Auger-reset function: Simply pressing the reset button activates this function, returning the auger to the default position (a horizontal position when initiating the auger-assist function).

Auger-lift function: When the snow thrower moves in reverse during snow-clearing work, this function automatically raises the auger to prevent dragging in the snow. When moving forward again, the function automatically returns the auger to its previous position, switching quickly from travel to clearing.

3.1.1. Aims and effectiveness

(1) Reduce frequency of operations: Use of a large-sized snow thrower requires the operator to handle many operations and devices (engine speed, snow-throwing direction and distance, height and inclination of snow clearance, movement speed and direction, etc.) while performing snow-clearing work. This work can be challenging for an operator. Figure 2 shows the controls that must be operated using the right hand while engaged in snow-clearing work.

Of those operations, the one performed most frequently is adjustment of the height and inclination of snow clearance using the auger control lever. Due to inclusion of the auger-assist function, the system constantly operates automatically to maintain the auger at the fixed inclination that has been set by the operator. Thus, the number of operations involving the auger housing has been reduced, regardless of the proficiency of the operator, and the burden of snow-clearing work has been lessened (Figs. 3 and 4).

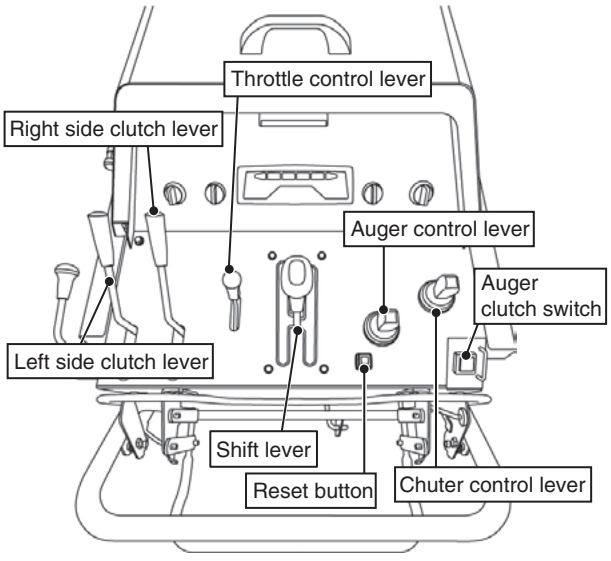


Fig. 2 Control panel view

(2) Simplify smoothing of surface of cleared snow: The main purpose of snow-clearing work is to relocate snow to create a clear passage for people and vehicles. In other words, it is necessary to form a surface of cleared snow that is as smooth and level as practicable. When operating the auger control lever in order to form a level surface of cleared snow, however, there is a time lag before the snow thrower moves onto irregularities in the snow-clearing surface so that the resulting tilt of the snow thrower itself becomes apparent, and that lag makes the timing of this operation challenging even for experienced operators.
The auger-assist function enables the auger to be maintained at a constant inclination to deal with unevenness in the traveling surface. This allows even beginners to achieve level surfaces of cleared snow on a par with experienced operators (Figs. 3 and 4).

(3) Simplify formation of cleared snow surfaces with the desired slope: Snow-clearing work is carried out in gardens, along the eaves of buildings, in parking areas, and numerous other kinds of locations. Parking areas in particular are commonly sloped for the purpose of drainage.
The auger-assist function enables the auger to be maintained at the desired inclination so that clearing can proceed at the desired inclination. This enables snow-clearing to be carried out cleanly even in parking areas and other such sloped locations.

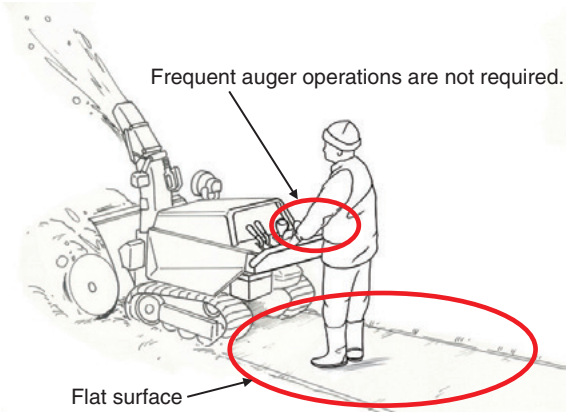


Fig. 3 Auger assist on

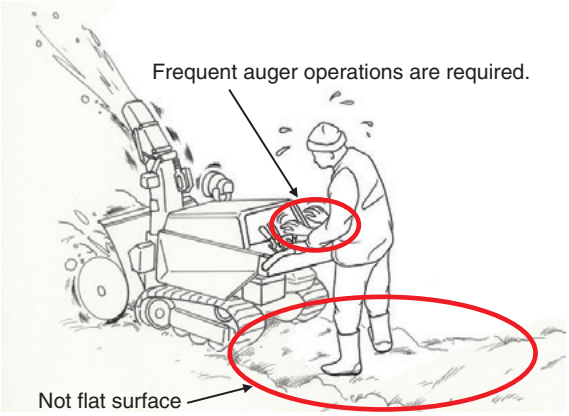


Fig. 4 Auger assist off

(4) Simplify even, horizontal snow-clearing: The auger control lever is used to adjust the height and inclination of snow clearance, but since there are few objects on the snow surface to serve as objectives, operators frequently lose track of the horizontal. Since the auger-assist function and auger-reset function work together, it has become a simple matter to set a horizontal surface as the control target value for the auger assist function, so that even if the operator loses track of the horizontal, the snow thrower can form a horizontal surface automatically.

(5) Effective overturning prevention: Since snow that has fallen and accumulated is not of consistent firmness, there may be soft patches and firm patches. When engaged in snow clearing on top of the snow, the snow thrower can sink into softer snow on one side, tilt, and tip over. With conventional snow throwers, the operator would cancel out the tilt of the machine by manually operating the auger control lever to make the auger operate toward the side away from where the snow thrower is sinking.
Adoption of the auger-assist function means that this operation can be performed automatically and with a fine degree of control. Since the snow thrower is leveled before it tilts too far, it is prevented from overturning before reaching that point.

(6) Reduction of lost time during snow clearing: Snow-clearing work very frequently involves moving in reverse, for example when the snow is firm and the auger is not biting into the snow properly, or when moving over to clear snow along a parallel path. At such times, if the snow thrower is backed up with the auger left at the height used for clearing, the auger housing can drag in the snow and interfere with backward movement. Therefore it was necessary to perform an operation to lift the auger before starting to move in reverse, and when the snow thrower was moved forward again, the auger had to be returned to the previous position.
Adoption of the auger-lift function means that operations to lift and lower the auger can be performed automatically. This eliminates forgetting to perform the operation, and enables efficient snow clearing (Fig. 5).

3.1.2. Explanation of snow thrower movements

The operator uses the auger control lever to adjust the vertical and lateral inclination of the auger, in accordance with conventional operation. That inclination of the auger then becomes the target value, and even if the surface on which the snow thrower is moving becomes uneven so that the snow thrower tilts, the snow thrower proceeds with the auger maintained at a constant inclination while clearing.

If the operator readjusts the vertical and lateral inclination of the auger, the system updates the target value

with the readjusted inclination.

So the inclination of the auger can be adjusted by the operator to the desired setting at any time according to the condition of the surface over which the snow thrower is moving. The system operates to maintain the auger automatically at a constant set inclination.

Figure 6 shows an example of lateral movement. (1) If the snow thrower starts tilting because the track on one side sinks into softer snow, (2) the system automatically moves the auger to the same angle by which it is tilting from the set target value on the tilting side, but in the opposite direction. (3) When the snow thrower proceeds to advance and perform snow clearing, the slope of the traveling surface comes to match the angle at which the auger has been set. (4) As the slope of the traveling surface returns toward the target value, the system returns the auger to its previous angle.

Figure 7 shows an example of movement in the vertical direction. The example shows the snow thrower forming a sloping surface as it climbs. (1) The vertical inclination of the auger is adjusted to the angle of the desired slope. The dotted line indicates the present snow surface, and the solid line is the desired slope that is to be formed. (2) As the snow thrower moves forward and begins clearing snow, the snow-clearing surface is formed at the target value angle. (3) As the snow thrower inclines to the slope of the snow-clearing surface, the vertical inclination of the auger is continuously lowered. (4) The snow thrower is thus able to climb while forming a slope at the desired angle. The movements in (2) and (3) are not easy to perform continuously in a smooth manner. When performed manually, the result will tend to be a wavy surface (the two-dot chain line in (4)), but since the auger-assist function adjusts the auger position quickly and smoothly, the snow thrower is able to form a tidy, evenly sloping surface.

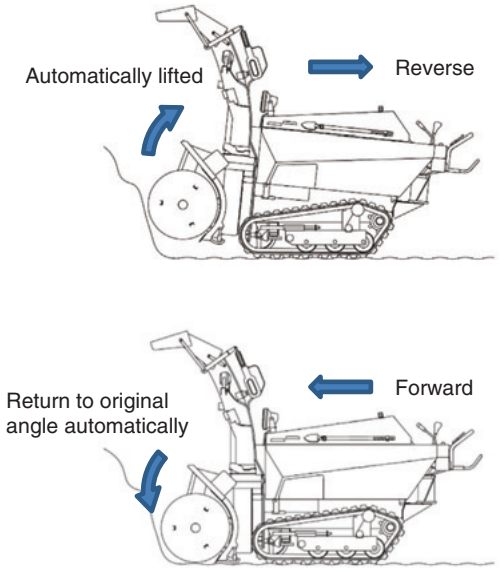


Fig. 5 Auger lift function

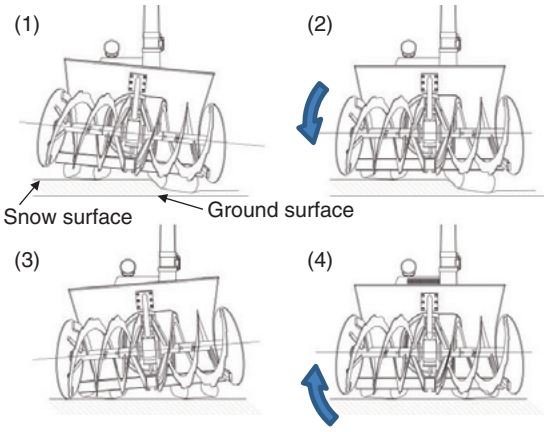


Fig. 6 Auger movement (rolling)

3.1.3. Structure and control system

A control unit with a built-in acceleration sensor is positioned on the snow thrower body in order to detect the vertical and lateral inclination of the auger in the direction of gravitational acceleration relative to the earth's axis.

Although the vertical inclination of the auger will be the same as that of the control unit mount, the lateral inclination of the auger will not be the same. An angle sensor has therefore been positioned on the connecting part that joins the auger to the snow thrower body to detect the lateral angle (Figs. 8 and 9).

The function of auger inclination adjustment was assigned to the auger control lever and auger reset button as before.

In order to allow the auger-assist action to function only during clearing, the travel motion clutch and snow-clearing clutch state is detected from the clutch switch and the auger clutch ON sensor and OFF sensor, while the forward and reverse travel state is detected by the travel speed sensor.

The functions of the actuators that change the inclination of the auger were assigned to the electro-hydraulic cylinder for height and to the rolling motor.

The vertical and lateral inclination of the snow thrower body is detected by a three-axis acceleration sensor. The acceleration sensor is influenced by vibrations from the auger, the driving system, and the engine, and its output is

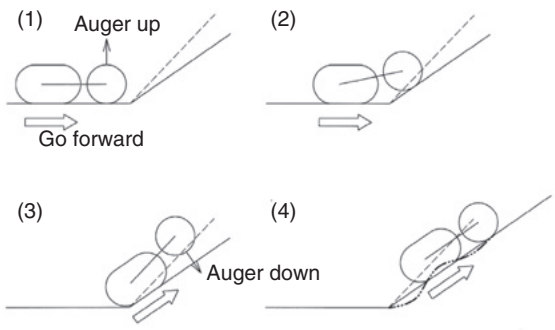


Fig. 7 Auger movement (height)

averaged. Steps are also taken to mitigate the influence of momentary acceleration due to standing starts, stopping, and height motor operation. The accuracy of auger and snow thrower inclination detection was heightened by detecting every state and filtering the sensor results.

Vertical inclination of the auger is calculated as the vertical inclination of the snow thrower body. Lateral inclination of the auger is calculated from the snow thrower body inclination and angle sensor values.

When the actual vertical and lateral inclination of the auger reach or exceed a certain deviation relative to the calculated targets for vertical and lateral auger inclination because of the state of the traveling surface, the auger starts operating.

The snow thrower can be made to operate at high speed when the deviation is a large value, and at a low speed when the deviation is a small value. This realizes speedy and finely controlled operation.

3.2. Operation Mode Change Function

3.2.1. Aims and effectiveness

A variety of conditions apply in snowfall areas, and there are some people who want to clear snow quickly while others want to throw the snow up higher. In order for a single snow thrower to meet these diverse operating conditions, however, extremely complex operations are required. These operations were found to involve considerable difficulty for beginners.

The HSL2511 is equipped with an operation mode-change function that can toggle between standard mode and throwing distance mode by means of a single switch. This enables even beginners to meet a variety of different operating conditions without performing complex operations (Fig. 10).

3.2.2. Explanation of function

The operation mode-change function changes the output power characteristics by changing the maximum engine throttle position and the engine speed-setting range in accordance with conditions. Figure 11 shows the torque characteristics in each mode.

In standard mode, the engine speed-setting range is 2000-3500 rpm, which can achieve work equal to a conventional snow thrower. This mode also regulates the maximum degree of governor open throttle for each engine speed, in this way changing the engine characteristics. On the low-engine-speed side, the snow thrower is operated with the degree of governor open throttle ranging from completely closed to wide open. As the engine speed increases, however, the maximum throttle position is stepped down in stages. This reduces the maximum output power on the high-engine-speed side. This allows a larger torque increase to accompany the reduction in engine speed.

When the snow thrower travel speed is set higher because the operator wishes to quickly clear large amounts of snow, the load from the snow is increased and the engine torque cannot keep up. Then, (1) the engine speed

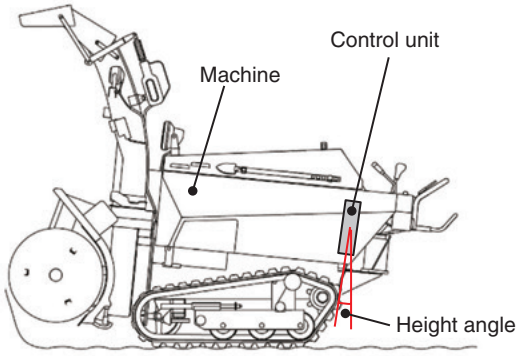


Fig. 8 Control unit location

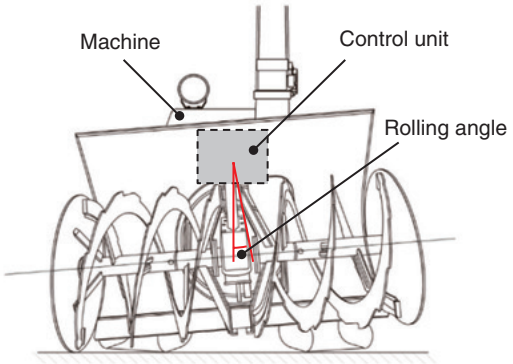


Fig. 9 Rolling angle

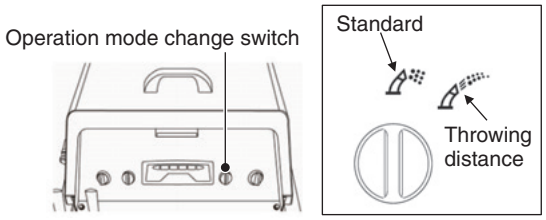


Fig. 10 Operation mode change switch

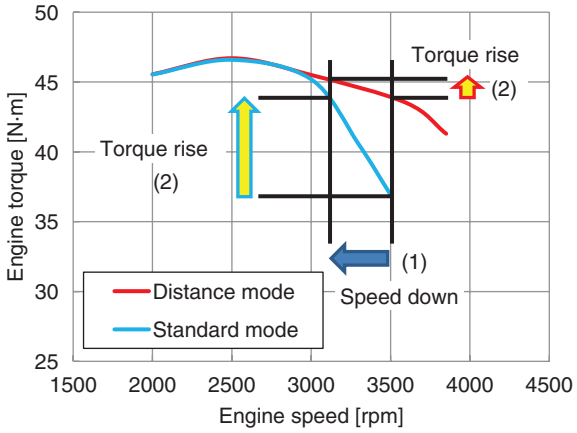


Fig. 11 Torque characteristics in each mode

decreases until the load and torque are balanced. When this happens, (2) in standard mode the torque rise is larger than in throwing distance mode, and the load from the snow and the engine torque quickly become balanced. This reduces the operator frequency of fine adjustments to travel speed, making the snow thrower easier to handle.

The operator can readily sense when the engine has reserves of power available because the rate of torque rise is large relative to the rate of engine speed decrease.

In throwing distance mode, the engine speed-setting range is 2000-3850 rpm, which is a wider range than in standard mode. A maximum throttle opening limit is not set, and the engine is operated throughout the entire range from completely closed to wide open. The engine characteristics here (the wide-open curve) are identical to those of the engine itself.

The maximum output power of the engine is greater than in standard mode, and the set engine speed is also higher. This means that the snow thrower can throw snow at higher engine speeds, and the operator can throw snow higher and farther.

3.2.3. Structure and control system

In order to change the maximum throttle opening in accordance with conditions, this model does not use a mechanical governor of the type widely employed in conventional snow throwers, but rather an electric governor as used in the HSM1590i[(3)] and other medium-sized hybrid snow throwers. An electric governor is a device that maintains the set engine speed regardless of changes in load by using a motor to drive the throttle to the target degree of governor open throttle calculated by the electronic control unit (ECU). For that purpose, the ECU is always capable of recognizing the degree of governor open throttle, and it has also gained the ability to change it freely. This snow thrower makes good use of that advantage by realizing the mode-switching function.

In specific terms, standard mode uses the following throttle opening limit (Fig. 12).

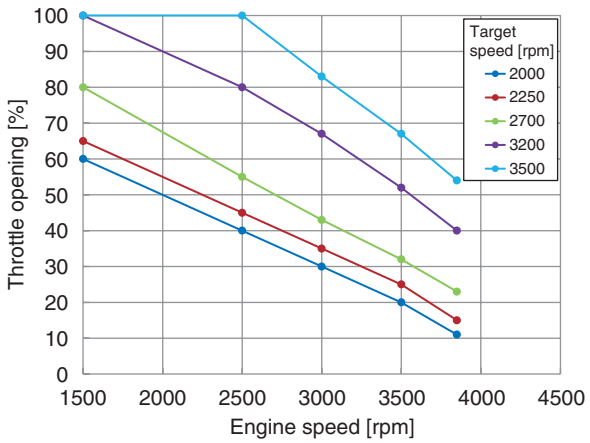


Fig. 12 Throttle opening limit

Table 2 Speed guide indicator lighting

Indication	Status	Operation
Light-off	Engine is not fully loaded	Can accelerate
Light-on	Optimal speed	Maintain speed
Blinking	Overloaded	Decelerate

3.3. Speed-Guide Function

3.3.1. Aims and effectiveness

Efficient snow clearing requires maintaining the engine at a constant speed. This is because operating efficiency and snow-throwing distance are in proportion to engine speed.

In order to maintain the engine at a constant speed, the load on the engine has to be maintained at a constant level. The load on the engine is determined by the operating volume, i.e., the snow-clearing volume (t/h). Since the snow-clearing volume is in proportion to the snow thrower travel speed, efficient snow clearing needs to make fine adjustments of the speed in accordance with the quality of the snow (snowdrift height, firmness, dampness, etc.).

However, the height, depth, and firmness of accumulated snow are not constant, and since the operator cannot readily grasp those variations in advance, it becomes challenging to maintain the optimal speed.

Adoption of the speed-guide function enables operators to easily determine whether they should accelerate or decelerate. They are able to operate the shift lever to perform snow clearing at the optimal speed, significantly reducing working hours.

3.3.2. Explanation of function

The speed-guide function guides the operator to the optimal travel speed by the status of the indicator light (Table 2).

The HSL2511 has two operation modes that change the optimal travel speed according to the respective operating conditions.

In standard mode, the function guides travel speed adjustment to the vicinity of the torque peak (2500 rpm), where operation is efficient and maximum snow-clearing volume can be obtained. In throwing distance mode, the function guides travel speed adjustment to the vicinity of the output power peak (3850 rpm), where snow can be thrown higher and farther and maximum snow-throwing distance can be obtained (Figs. 13 and 14).

3.3.3. Structure and control system

Even if snow clearing is being performed at the same travel speed, the condition of the snow will vary so that the load on the engine changes. It is necessary, therefore, to monitor the amount of load on the engine. One means of doing this is to use the degree of governor open throttle of the electric governor described in section 3.2.3. The engine speed and degree of governor open throttle at a particular

point are used to estimate the load, and the result is used to control the indicator lights. Specific details of indicator lighting are shown in Figs. 15 and 16.

When work is started in standard mode with the initial engine speed set at 3500 rpm (black arrows in Fig. 15), as the load increases the degree of governor open throttle increases as well. (1) When the degree of governor open throttle reaches 45%, the system determines that the load is optimal and turns on the indicator light. (2) When the load continues to increase and reaches 67%, the throttle-opening limit is activated so that the throttle does not open any farther and the engine speed starts to drop. (3) At the same time, the limit value for the degree of governor open throttle also rises and the torque increases. (4) When the engine speed drops below 3100 rpm, the system determines that overload is occurring and causes the indicator light to blink.

In throwing distance mode, when the engine speed is 3300 rpm or higher and the degree of governor open throttle is 70% or more, the system determines that the load is optimal and turns on the indicator light. When the engine speed is 3300 rpm or less and the degree of governor open throttle is 70% or more, the system determines that overload is occurring and causes the indicator light to blink. Otherwise, the indicator light is turned off.

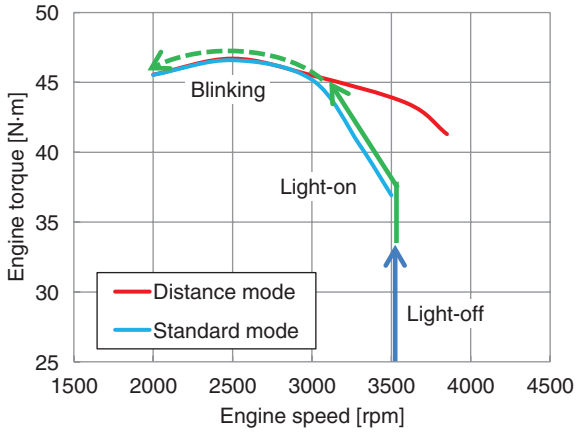


Fig. 13 Speed guide (standard mode)

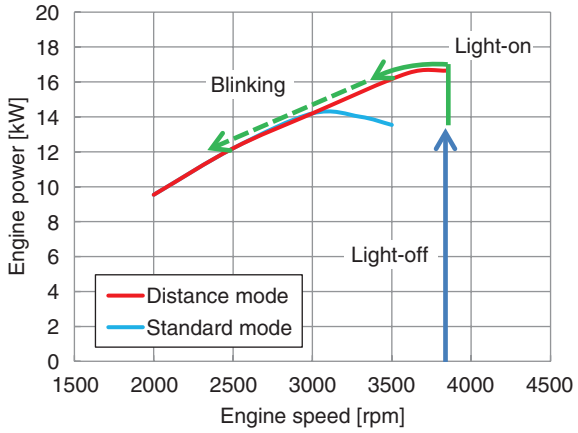


Fig. 14 Speed guide (distance mode)

3.4. New Model Engine with FI System

3.4.1. Aims and effectiveness

(1) Simplified starting and heightened workability: Adoption of a four-stroke V-twin engine equipped with an FI system enables simplified starting. Unlike an engine with a carburetor, the starting operations of opening the fuel cock, pulling out the choke lever, and setting the engine speed adjustment lever to the starting position are not required.

(2) Practical fuel efficiency improvement: Use of a four-stroke V-twin engine with an electric governor and FI system enables automatic and finely detailed adjustment of the fuel injection amount, heightens the working efficiency of each function, and, in combination with the adoption of a new model chuter, supports the EU Stage 2[4] emission regulations. The new model's fuel efficiency, however, is still improved relative to the conventional model HS2411Z that predates the model change.

Table 3 shows the results of a comparison under the same conditions of throwing distance and efficiency. The HSL2511 can perform the same work as the HS2411Z at lower engine speed and load factor, consequently achieving

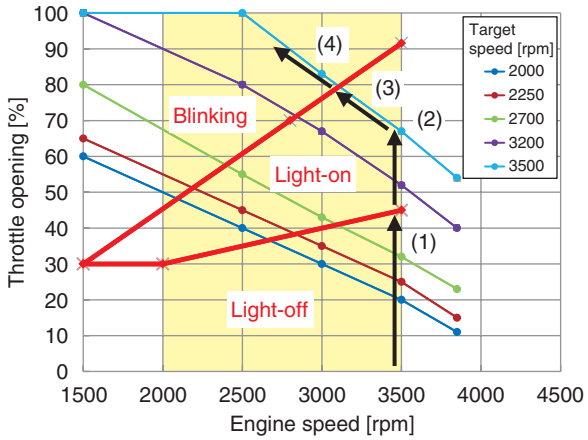


Fig. 15 Indicator lighting (standard mode)

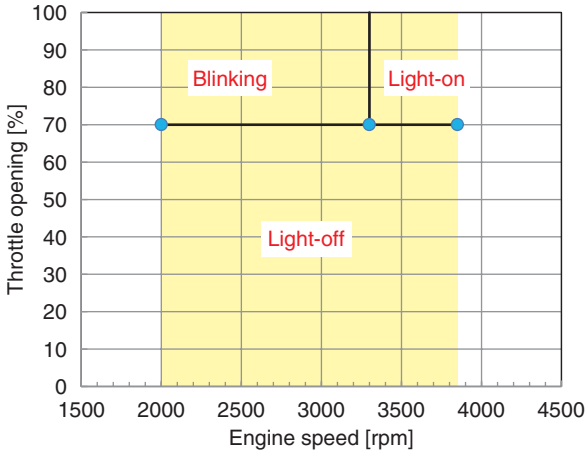


Fig. 16 Indicator lighting (distance mode)

Table 3 Fuel efficiency

	HSL2511	HS2411Z
Throwing distance [m]	18	
Clearing volume [t/h]	50	
Engine speed [rpm]	3100	3400
Engine load [%]	80	100
Fuel consumption [L/h]	6.9	8.3

a 16% improvement in fuel efficiency (using the HSL2511 in standard mode).

3.4.2. Structure and control system

Figure 17 shows the FI structure.

In this system, the intake manifold pressure sensor detects the atmospheric pressure. Unlike an engine with a carburetor, this means it is unnecessary to change settings for operation at higher elevations.

The starting operation involves turning the key switch over to the starting position. It then returns automatically to the ON position, and the starter motor operates continuously for a maximum of five seconds to start the engine. With a system able to start in this way, it is no longer necessary to turn the key switch and hold it in the starting position.

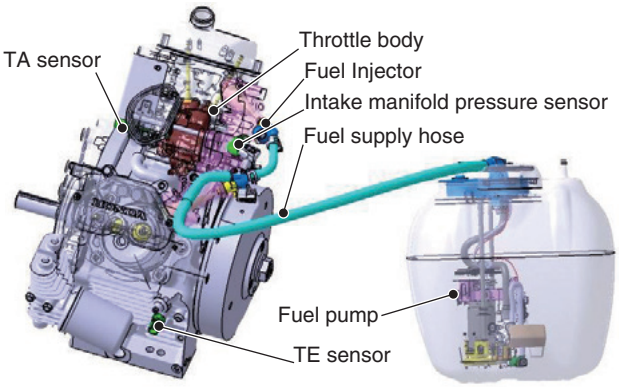


Fig. 17 FI system structure

4. Conclusion

Development of the HSL2511 large-sized snow thrower with a four-stroke V-twin engine and equipped with a smart auger, electric governor, and electronically controlled fuel injection system has achieved the following:

(1) An auger height and rolling motor moves the snow-clearing system vertically and laterally using a control unit with built-in acceleration sensor to compute the inclination. This is also the first snow thrower in the world to be equipped with an auger-assist function that maintains the snow-clearing system at a constant inclination while in operation. This makes it easier even for beginners to form a smooth, level surface of cleared snow or a cleared surface with the desired slope. This has also reduced the frequency with which the operator needs to operate the controls, and has improved workability.

(2) With the adoption of an electric governor and an operation mode-change function that switches to different engine power curves according to various operating conditions, complex operations have become unnecessary and workability has been increased. The system also includes a speed-guide function that guides the operator to the optimal working speed. The operator thus becomes able to use the optimal speed to realize efficient snow clearing.

(3) Installing a four-stroke V-twin engine equipped with an FI system has achieved a simplified starting procedure (fuel cock and choke operations are eliminated), reducing the burden on the operator. Furthermore, the increased working efficiency achieved by the various functions and the adoption of the new model chuter have together realized a 16% improvement in fuel efficiency.

References

(1) Hanafusa, J., Wakitani, T., Yamamoto, T., Inui, T. : Development of Hybrid HS1390i Snow Thrower, Honda R&D Technical Review, Vol. 14, No. 1, p. 31-38

(2) Fukushima, T., Matsuda, H., Shinogi, Y. Taniguchi, Y.: Governor System for General Purpose Engine Using Adaptive Control Theory, Honda R&D Technical Review, Vol. 17, No. 2, p. 58-64

(3) Wakitani, T., Kawakami, T., Shimizu, N., Yamazaki, N.: Development of Snow Thrower Control System with Engine Provided of Electronic Governor System, Honda R&D Technical Review, Vol. 18, No. 1, p. 51-56

(4) COMMISSION DIRECTIVE 2012/46/EU of 6 December 2012

■ Author ■


Kenta KOHIGASHI


Tsutomu MIZOROKE


Takashi HASHIZUME


Shohei URANO


Jun SONG

Development of High-Access Survey Robot for TEPCO's Fukushima Daiichi Nuclear Power Station

Hisashi SUGIURA* Takafumi FUKUSHIMA* Mitsuhide KURODA*
Ryusuke ISHIZAKI* Takashi MATSUMOTO*

ABSTRACT

A high-access survey robot system was developed to acquire images, doses of radiation, temperature, and humidity in locations high above the floor inside the reactor building at Tokyo Electric Power Company's Fukushima Daiichi Nuclear Power Station, where there is a high level of on-site demand for this capability.

This robot system has a crawler-type high-place work cart modified for remote operation and is equipped with an arm having 11 joints that can reach to a height of seven meters. It is also able to insert the arm tip deep into narrow spaces at locations high above the floor. The mechanical and electrical systems were developed according to requirements formulated using information brought from the site. An operating interface was also developed to reduce the burden of remote operation. Functionality assessments were carried out by endurance testing with a mock-up as well as by proving tests conducted in a reactor building at Hamaoka Nuclear Power Station, a physical environment that closely resembles the one in the Fukushima Daiichi Nuclear Power Station.

This robot performed missions twice in Unit 2 Reactor Building, on June 18 and July 23, 2013, and once in Unit 3 Reactor Building, on May 13, 2014, for a total of three missions. It acquired doses of radiation, which had not been available before then, from the upper areas inside the reactor building, as well as images from the vicinity of the primary containment vessel. It also acquired data on the geometry inside the reactor building that will contribute to various upcoming tasks involved in decommissioning of the reactor.

1. Introduction

The Great East Japan Earthquake of March 11, 2011 was accompanied by an accident at the Tokyo Electric Power Company's Fukushima Daiichi Nuclear Power Station (hereafter referred to as 1F). Since that time, there have been numerous hopeful calls for Honda to send in a robot on-site. There has also been a strong desire in-house to contribute somehow to improvement of the current state of affairs.

Given this background, Honda joined with the National Institute of Advanced Industrial Science and Technology (AIST) and Tokyo Electric Power Company (TEPCO) in June of the same year to start a three-party survey of on-site application of robot technology.

At that time, the situation inside the reactor building was still largely undetermined, so it was necessary first of all to carry out a survey of the interior circumstances. Initial surveys of the interior were, in fact, performed by compact robots about one meter in length. Packbot[(1)], for instance, made a survey of the ground floor of the reactor building, and led the way for other robots. Quince[(2)] climbed the stairs to the second and third floors and performed surveys there and of the operating floor above. Survey Runner[(3)] performed a survey of basement floors. As a result, the state of affairs and radiation doses in the reactor building up to 1-1.5 m high above the floor were determined.

With these compact robots, however, it was difficult to survey areas near the ceiling (locations high above the floor) on the first floor. These were areas inferred to be contributing a large proportion of the air dose in the reactor building. Locations high above the floor in the reactor building contain a complex maze of piping, ducts, cable racks, and other such potential obstacles that make surveys even more difficult to carry out.

The Honda team therefore developed a high-access survey robot capable of reaching to a height of seven meters as well as reaching deep inside narrow places to measure radiation, temperature, and humidity, and to acquire imagery. Figure 1 shows the high-access survey robot. On the left is the robot in driving posture and on the right its higher extended posture for surveying high locations.

This robot is made up of a high place work cart and a survey arm for which AIST and Honda were respectively in charge of development.

In following sections, this paper will relate the

* Fundamental Technology Research Center

development of the high-access survey robot, with a focus on the survey arm developed by Honda. It will describe how the requirements for the robot were determined, how the information for determining them was obtained under circumstances that did not allow direct entry to the 1F site, how a robot that would definitely be able to operate in the reactor building was developed, and how the robot was used in actual missions.

2. On-Site Circumstances

2.1. Survey Location

1F has nuclear reactor Units 1 to 6. Apart from Units 5 and 6, which avoided damage, surveys of reactor building interiors for the other reactors, Units 1 to 4, have been proceeding since the accident. These surveys are crucial for the planning and efficient implementation of future reactor decommissioning work. The first floor of these reactor buildings is where the robot is slated to perform surveys.

A cross-sectional view of a Boiling-Water Reactor (BWR) building of the same type as 1F is shown in Fig. 2, and a top view of it in Fig. 3. In the center of these is the Primary Containment Vessel (PCV), with various facilities and equipment installed around it. The developed robot is intended to perform surveys on the ground floor and in particular of the upper part of the Traversing Incore Probe (TIP) room, the upper part of the personnel access airlock room, and the catwalks in the vicinity of the PCV shown in Fig. 3. All of these locations are constricted spaces containing multiple pipes and are difficult to access.



Fig. 1 High-Aaccess Survey Robot
The driving posture (left) and higher posture (right)

2.2. On-Site Circumstances and Requests Regarding the Robot

2.2.1. Requests regarding the robot

Discussions with TEPCO showed the on-site need for a robot described as follows;

(1) Capable of acquiring radiation dose, temperature and humidity data, and imagery from narrow spaces at high locations;
(2) Be introduced on-site as quickly as possible;
(3) Able to perform as many surveys as possible during one mission;
(4) Possess a high level of operability;
(5) Able to be operated by personnel wearing layers of protective clothing and gloves;
(6) Able to perform its missions even during light rain;

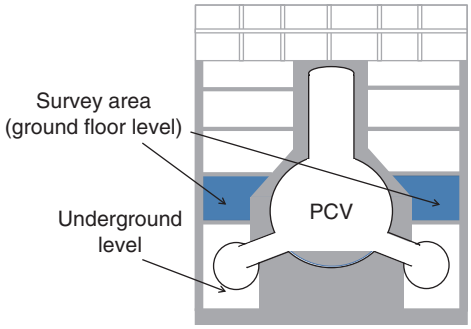


Fig. 2 Cross-section view of BWR reactor building

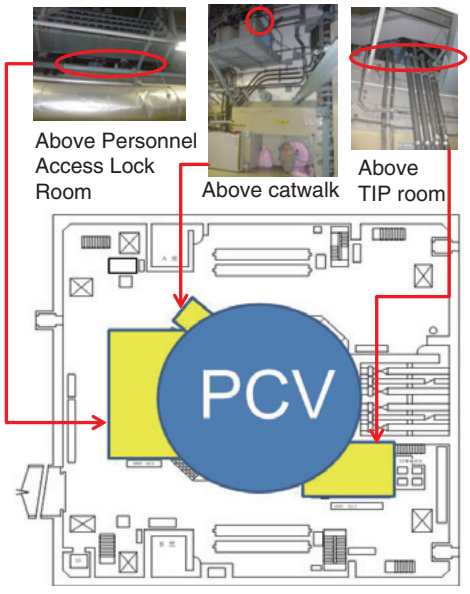


Fig. 3 Top view of BWR reactor building of ground floor
The survey target areas are filled with yellow. (Images provided by Chubu Electric Power Co., Inc.)

(7) Definitely able to make its way back out of the reactor building;
(8) Will not damage facilities inside the reactor building; and
(9) Able to repeat operation for at least 16 missions.

2.2.2. On-site circumstances

The circumstances in front of the reactor building, where the robot begins its movement, and inside the building, are as follows.

(1) There are locations with high-dose radiation in front of and inside the reactor building, and people cannot remain at those locations for extended periods of time.
(2) In front of the reactor building, there are differences in level where there are steel plates, uneven terrain where there is some gravel and so on.
(3) Inside the reactor building, facilities may have been damaged at some locations and there are no accurate pictures that show on-site conditions.
(4) Inside the reactor building, there are places where water drips down and there are puddles of water.
(5) In the upper part of passageways inside the reactor building there is temporary piping, work platforms and scaffolding, and ducts installed at a height of about two meters, as shown by the red arrow in Fig. 4. Work materials and equipment are also located on the floor along the sides of passageways.
(6) Survey locations are high above the floor, and survey work can be particularly difficult where such locations are constricted and convoluted due to piping and other obstructions.
(7) There is airborne radioactive material inside the reactor building.

These on-site conditions and requests were made into requirements in the various areas of mechanical systems, electrical systems, and operating interface. Design and development of the robot system were carried out accordingly.



Fig. 4 Inside reactor building (Image provided by TEPCO)

Table 1 Specification of high-access survey robot

Entire robot	Length	1.8 m
	Width	0.8 m
	Minimum height	1.8 m (when driving)
	Maximum height	7.0 m
	Weight	1.1 t
	Operating time	5 hours
High place work cart	Maximum velocity	2 km/h
	Maximum incline	15 degrees (back and forth) 20 degrees (right and left)
	Maximum bumping height	60 mm
Survey arm robot	Length	1.7 m
	DOF	11 (except parallel link)

3. High-Access Survey Robot

3.1. System Overview

The developed robot system is a high place work cart modified to enable remote operation and is equipped with a survey arm having 11 degrees of freedom. Table 1 shows the main specifications.

The length, width, and height in these specifications were decided according to the on-site passageway conditions described in section 2.2.2.

Figure 5 shows the sensors installed on the robot. For data acquisition purposes, the tip of the arm has a camera, dosimeter, thermo-hygrometer, and other such instruments. In order to enable passage through narrow spaces, the cart is equipped with cameras to show the area around the cart, cameras to check for obstacles to the upper part of the cart, Laser Range Finders (LRF) attached to the cart and to the tip of the arm, and other such equipment.

3.2. Operating Procedure

As shown in Fig. 6, the robot is operated over a wired LAN using a remote operation device (the operation PC) in the important anti-seismic building.

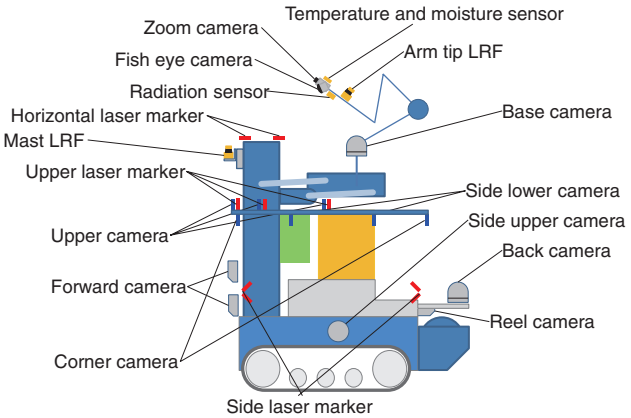


Fig. 5 Robot sensors

The LAN extends to the switching hub in front of the reactor building. The robot is transported by truck from the robot warehouse to the front of the reactor building, where the optical fiber cable installed on the robot is attached to the switching hub. Travel from there to the survey locations inside the reactor building and back, and the survey activity, are performed by means of the operation PC. When the surveys have ended and the robot exits the reactor building, it will be disconnected from the LAN and returned by truck to the robot warehouse. Communications will all be conducted through wired connections, except during emergencies. This is to avoid the risk that radio communication will be interrupted and to make certain that the robot will return.

At a survey location, the robot will be instructed to extend its mast and move its survey arm to acquire data on the survey location. The data is transmitted to the operation PC in real time.

Work sessions are anticipated to be completed within five hours.

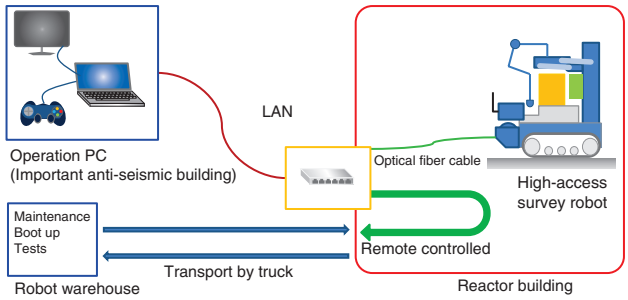


Fig. 6 Use case of robot

4. High Place Work Cart

A commercially available aerial work platform was used as a base for development in order to send in the robot as quickly as possible. The high place work cart has a low center of gravity in the first place, and the weight of the lower portion was further increased and the cart was given sufficient width, even where narrow, to assure stability. Its maximum travel speed is 2 km/h with a maximum bumping height of 60 mm. The cart was also equipped with cameras: two each were installed front and back, eight pointing downward around the periphery of the cart, and two on the sides pointing upward. The cart width is indicated using laser markers and LED lights to enable movement through narrow passageways in building areas where there is no illumination.

The optical fiber cable used for communication allowed for movement to a distance of 400 m when paid out from its reel. While the robot is moving, any excess length that occurs in the optical fiber cable could cause it to break if it becomes tangled with itself or caught on the body of the robot or on something in the environment. This is avoided by exercising control to maintain tension in the cable.

5. Survey Arm

A compact, highly reliable arm system was developed within a short time by maximizing the use of ASIMO[4] technology that had a record of results.

5.1. Mechanical System

The main requirements for the robot's mechanical system, based on sections 2.2.1 and 2.2.2, are as follows.

Requirement 1 That it not interact with upper obstacles while the robot is traveling

Requirement 2 That the mast not interact with obstacles at high locations when being raised and lowered, and that the arm can be brought close to survey objects

Requirement 3 That the tip of the arm can be inserted deep into narrow spaces

Requirement 4 That it not break down under rainfall when traveling outdoors or under dripping water when indoors

Requirement 5 That it allows decontamination of adhered radioactive substances

Requirement 6 That it be capable of operating for extended periods of time

Development was conducted on the basis of the above requirements.

Specifically, requirements 1 and 2 were satisfied by development of the arm transfer mechanism. Requirement 3 was satisfied by the articulated arm. Requirements 4 and 5 were addressed by development of dustproofing and drip-resistant functionality.

In order to satisfy requirement 6, reductions in electric power consumption were achieved by using the frame structure and configuration as well as technology for the motor and reduction gears that were cultivated during ASIMO development.

The arm transfer mechanism, articulated arm, and dustproofing and drip-resistant functionality will be explained in detail in the following sections.

5.1.1. Arm transfer mechanism

Given requirement 1, the developed robot needs to limit its total height while traveling. The aerial work platform used as a base, however, had a total height of 1.73 m, so that when the arm was mounted on top of it, the total height exceeded two meters, which would interact with upper obstacles. It would be desirable, therefore, to locate the arm on the periphery of the mast while the cart is traveling. On the other hand, it would be desirable to locate the arm on top of the mast while surveying due to requirement 2, so as to minimize the lift up area while the mast is being raised and lowered, and to meet the requirement that the arm be brought close to the survey object.

An arm transfer mechanism that uses a parallelogram link mechanism was therefore designed. As shown in Fig. 7, lowering the arm and folding it away while the cart is

traveling reduces the total height, and moving the arm onto the top of the mast while elevating it reduces the lift up area so that the arm can approach closely to the survey object.

These measures kept the robot compact while traveling, with a total height of 1.8 m. While surveying, it can rise through a high, narrow area of just 0.7 m square and reach a total height of 7.0 m.

5.1.2. Articulated arm

Given requirement 3, avoiding obstacles while approaching closely to the survey object necessitates an articulated arm. An articulated arm with normal redundancy typically has seven joints, which adds one axis as a redundant degree of freedom to the basic six axes that determine the position and attitude of the robot arm-end. Since the developed arm here will be inserted deep into a narrow spaces while avoiding obstacles, three more axes were added as redundant degrees of freedom, with another added to the arm-end to use in changing the attitude of sensors and cameras installed on the arm-end. This makes for an articulated arm with a total of 11 axes of motion.

The robot's axes were configured (Fig. 8) so as to shorten the computation time required for control of the arm. The base, shoulder, and wrist were therefore each given three orthogonal axes. A particular effort was made to allow a large angle of available motion on the Z-axis in the shoulder region as well as to take the feasibility of having three orthogonal axes into account. As a result, the axes were placed in the order Z, Y, and X from the base.

In order to avoid obstacles and to approach closely to the survey object for investigation, the arm tip is equipped with an LRF to observe conditions at the insertion point and around the arm tip and check for obstacles. There is a zoom-lens camera to look in the direction of the arm tip and a fisheye-lens camera to view the arm-tip periphery. There are also a dosimeter to measure radioactivity, a thermo-hygrometer, and a six-axis force sensor (6AF) for contact sensing mounted on the wrist and on the base. An inertial sensor to detect attitude is also mounted on the base, as are two dome cameras to observe the periphery when the arm is being raised and lowered and when it is being inserted.

As stated in item (8) of section 2.2.1, two base axes, one shoulder axis, one elbow axis, and the arm transfer mechanism are equipped with brakes so that the robot will not damage equipment or facilities if power to the drivetrain is interrupted. These brakes enable the robot to maintain its attitude. Details will be given in section 5.3.2.

5.1.3. Dustproofing and drip-resistant functionality

Requirement 4 necessitates drip-resistant functionality while requirement 5 necessitates shapes that can be easily decontaminated and/or dustproofing functionality.

As shown in Fig. 9, a cover that encompasses the entire arm was developed. The reason for this was that an articulated arm may be subjected to penetration by water from every direction. Also, since the arm has many component parts that have complex shapes, making it

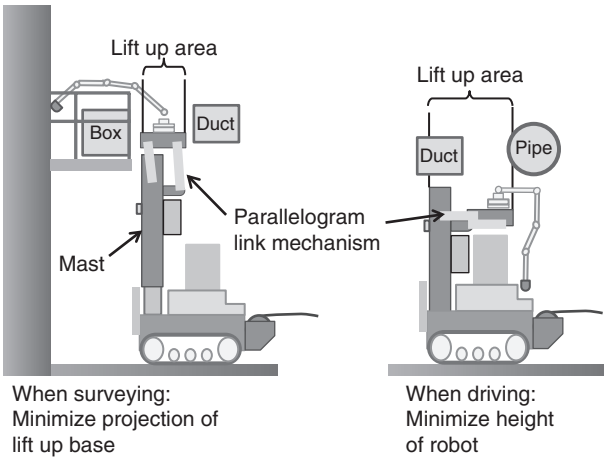


Fig. 7 Arm transfer mechanism

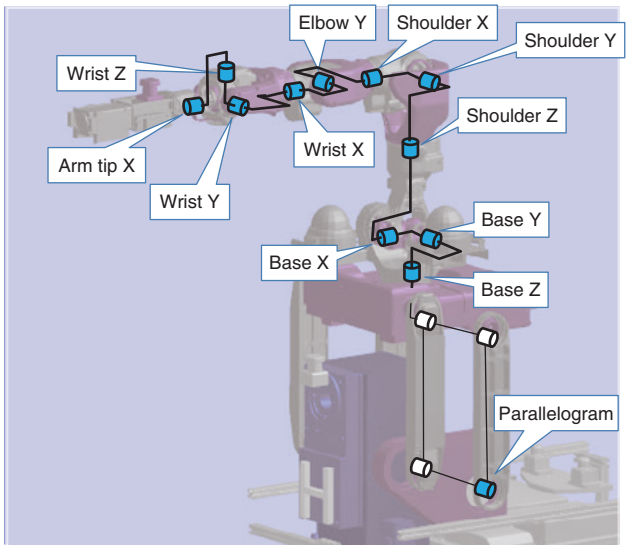


Fig. 8 Joint configuration of arm



Fig. 9 Cover for arm
Four arrows indicate holding points

drip-resistant and capable of decontamination by wiping is difficult. Development used cloth bonded to a water-resistant film with water pressure resistance to 20,000 mm H_2O and further took the following matters into consideration.

(1) It can readily be changed.

If large amounts of radioactive material adhere to the cover, the robot will be decontaminated by changing the cover. In order to reduce the amount of radiation exposure by workers when this is done, it is necessary for the cover to be changeable in a short time. In order to avoid catching or damaging the cover, corners in the robot arm are rounded or have resin covers attached to give it a smoother shape.

(2) It does not obstruct movements of the arm.

The developed arm has numerous joints and a wide range of movement. Therefore, a tight cover that closely follows the contours of the arm would subject the 6AF and drivetrain to the load generated by the stretching or twisting of the cover. On the other hand, a loose cover could become jammed in the joints or catch on objects in the environment. In either case, the arm movement would be affected and the cover itself could be damaged. Many prototypes were therefore created and repeatedly tested, and the outcome was a water-resistant cloth with 130% stretchability that is held in place at four locations, as shown by the red arrows in Fig. 9. This realized a cover that does not obstruct arm movement.

Item (1) above was confirmed by a worker who performed the operation in a short time during operational training. Results for item (2) above will be described in section 7, on reliability testing.

Drip-resistant construction will be discussed next. Drip-resistant functionality was realized for electrical equipment, such as sensors, batteries, switches, and charging connectors, and for the arm transfer mechanism by covering them in a shape that facilitates decontamination. The battery compartment, for example, is subject to penetration by water from above, and also must allow airflow and passage of wiring, so its drip-resistant functionality was achieved through a labyrinth structure and drainage structures.

A waterproof cover that covers the entire robot was also prepared to protect the robot from rainfall while being transported outdoors by truck.

5.2. Electrical Systems

In order to respond to demand for early on-site introduction of the robot, it was necessary to develop it within a short period of time. For this reason, highly reliable hardware and firmware that had a track record from use in ASIMO were also used in electrical systems as a base for development of control systems for the 11-axis articulated arm and arm transfer mechanism. In addition, new functionalities were developed such as external environment recognition, power source systems for the purpose of extended operation, dustproofing, and drip-resistance of printed circuit boards (PCB).

5.2.1. Control system

When the arm is being inserted into a narrow space, it is essential to have compliance control to allow contact with the environment so that operation errors or other such reasons do not result in damaging facilities or equipment caused by the arm interacting inside the reactor building. For that purpose, it was necessary to obtain data of forces applied to the arm and the angles of the joints in real time, and to drive the joints accordingly. The distributed control system developed for ASIMO was therefore applied to this robot. Data from the 6AF and inertial sensor located at the wrist and base of the arm, as well as from the joint encoders, are used to transmit control commands to the various motor drivers in real time.

5.2.2. Sensor systems

As shown in section 5.1.2, the developed robot possesses multiple external environment sensors for acquiring various data on the environment in narrow spaces at high locations. That sensor data must be transmitted to the operation PC in real time. It is also desirable to allow for the addition of new sensors as needed to meet further on-site needs. This led to the selection of sensors possessing USB or LAN interfaces that are scalable by means of hubs.

Selection of the dosimeter also involved the following special conditions:

(1) Should possess an on-site record of performance;
(2) Should be capable of acquiring data in real time; and
(3) Should be capable of directionality for the purpose of estimating radiation source locations.

The dosimeter satisfying given conditions (1) and (2) above transmits data using infrared communication. The infrared receptor located at the arm tip, however, was subject to being influenced by the LRF and other such optical equipment, and a shield was therefore installed.

Satisfying condition (3) above, however, would ordinarily involve not shielding the dosimeter so that it can measure air doses of radioactivity. The dosimeter was therefore given directionality by attaching a lead cover that can be used to shield the five faces other than the measurement face of the dosimeter when necessary for identifying a radiation source. Identification of radiation sources was further enabled by changing the attitude of the arm tip.

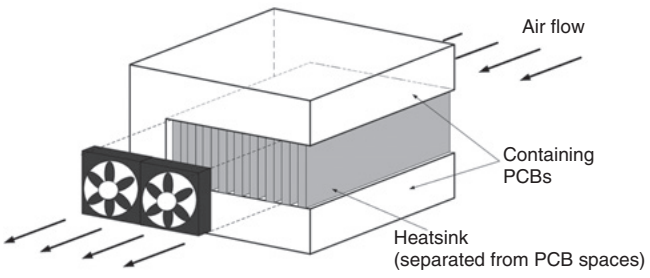


Fig. 10 Enclosure for electric devices

5.2.3. Power source systems

Based on section 3.2, since the developed robot must be able to operate for five hours, batteries developed for ASIMO were installed.

A new system was also developed for recharging batteries after a mission has ended. This allows multiple batteries to be recharged on-board, thereby reducing the amount of radiation to which workers are exposed.

This system uses a constant-voltage constant-current method in order to protect against over-charging. In the constant-voltage charging region close to a fully charged state, the amount of charge per unit time diminishes. However, if the interval to the next mission is not sufficient to fully recharge, more efficient recharging is required. Rather than fully recharging each individual battery, therefore, it was decided to switch batteries that need recharging at fixed time intervals so that all the batteries can be recharged rapidly in a constant-current region where charging is efficient.

5.2.4. Printed circuit board design for cooling, dustproofing, and drip resistance

It is necessary to assure the drip resistance of electrical components during operation outdoors and inside a building where water leakage may occur. Meanwhile, the system as a whole generates several hundred watts of heat, necessitating achievement of a balance between drip resistance and cooling performance, under the following constraints.

(1) Due to external heat discharge and cable layout, it is desirable to distribute electrical components to the various arm link locations. The drip-resistant cover described in section 5.1.3, however, makes it difficult to discharge heat from the arm into the air.
(2) The use of air-cooling is likely to draw radioactive substances into the robot interior, which would be difficult to decontaminate by wiping or other such methods. Therefore, the method of blowing air against the PCBs cannot be used.
(3) The cooling apparatus must not hinder movement of the arm and should be of a size that allows for a smaller lift up area when the mast is raised and lowered.

In order to satisfy above constraints (1) to (3), a compact enclosure was developed that could concentrate the PCBs in one location in a size (200×280×300 mm) that could be positioned on the rear surface of the mast. As shown in Fig. 10, the enclosure is hollow and has a heatsink located in the hollow portion, separated from the interior portion of the enclosure where the PCBs are housed. Heat simulation was used to arrange the PCBs in a layout that would transfer the quantity of heat in the enclosure to the heatsink and keep the device temperature of each PCB within the rated range. A fan attached to the exterior was then used to cool the heatsink.

5.3. High Reliability Design

Given the requests in section 2.2.1, the developed robot had the following specific requirements.

(1) It must not damage facilities or equipment inside the reactor building.
(2) It must definitely make its way back out without becoming stuck.

With regard to item (1) above, measures were taken to deal with the problem in the hardware that controls the survey arm at a point when the arm has been inserted into a narrow space. Fail-safes used in ASIMO were employed so that the arm would maintain its attitude without moving, depending on the problem, or a process would function to shut off the drive power, thereby preventing damage to equipment, facilities, or the robot itself.

With regard to item (2), in the unlikely event that the robot becomes stuck, the high levels of radioactivity inside the reactor building would make it difficult for workers to recover the robot. The developed robot is also relatively large and would interfere with future reactor decommissioning if unable to return. The reasons preventing its return were therefore analyzed and recovering procedures were prepared, together with multiple emergency detour procedures in the event that a system cannot be recovered. These procedures were built into the robot systems, increasing reliability. Some representative functions are described below.

5.3.1. Remote rebooting function

A rebooting device was developed to restore arm systems from the operation PC. This is intended to enable the robot to return even if control software deadlock occurs, or a CPU or other such component hangs, or another such system problem occurs.

As shown in Fig. 11, the connection between Hub1 and Hub2 passes inside the mast, so there is a possibility that the cable could be severed when the mast is raised or lowered. A separate communication line was therefore installed to transmit a reboot command by way of the cart controller. This establishes dual system redundancy for the reboot procedure and thus increases reliability.

5.3.2. Joint brake function

If the arm system experiences an abnormality while

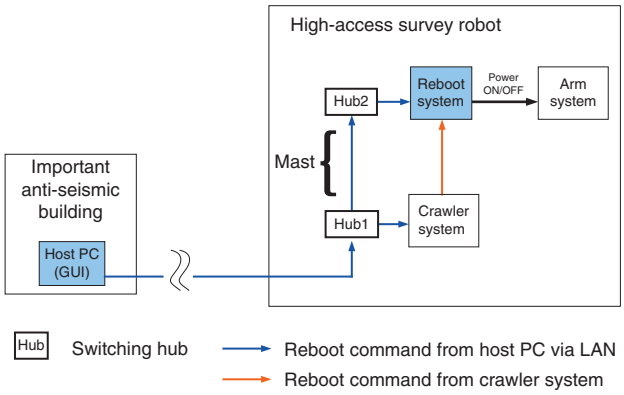


Fig. 11 Remote rebooting system

performing a survey at a location high above the floor, a reboot of the system as described in the preceding section could be considered. If this course is taken, the drive power source for the arm will also be cut off. Depending on the arm's posture, its own weight may cause the joint to move, interacting with equipment or facilities inside the reactor building. Consequently, non-excitation actuating brakes were installed on those joints that could experience a significant change of position due to the arm's own weight when drive power is not being supplied. This enables the arm to maintain its posture in those conditions.

In the unlikely event of a fatal abnormality that prevents recovery of the arm system even when the remote rebooting function is used, the cart will have to be operated to return with the arm held in position. It is conceivable, however, that with joints held in position by brakes, the arm might catch on equipment or facilities inside the reactor building. Taking this into consideration, dual systems were put in place so that the brakes on individual joints could be released not only by the arm system, but also remotely through the cart system.

5.3.3. Functionality for radio communication with rescue robot

The developed robot moves while paying out optical fiber cable. There is a possibility, therefore, that repeated bending at corners and other such actions may cause attenuation of the light intensity, or the cable may catch on some sharp object and be severed, terminating communication. Dual systems were therefore established so that both wired and wireless means of communication are available. Should communication by optical fiber cable fail, a rescue robot equipped with a radio is dispatched to the site to restore communication by radio.

Considering that the wired LAN connection between the arm system and cart system could also be broken, or that the radio equipment could malfunction, separate radio equipment was also installed in the arm and in the cart. The robot radio was configured with different Service Set Identifiers (SSID) on the arm and on the cart. The rescue robot can switch the SSID, thus realizing dual system redundancy.

6. Operating Interface

The developed robot is used in an environment where people cannot remain for extended periods. Consequently, sufficient training cannot be given in advance, and responses to unanticipated on-site circumstances may be required. The actions involved in inserting the arm into a narrow space that includes piping, ducts, and so on in a high place may also cause contact with the environment, resulting in damage. For these reasons, precise operation is required, and a Graphical User Interface (GUI) with a high level of operability was developed. Operation of the robot takes place remotely from an important anti-seismic building so as to minimize the operator's exposure to radiation. However, it may become necessary to operate the robot from a location near the reactor buildings if, for example, communication through the wired LAN between the important anti-seismic building and the switching hub in front of the reactor building, as shown in Fig. 6, is interrupted. At these times the robot will have to be operated by personnel wearing layers of protective clothing and gloves. In order to enable operation under these circumstances, it was decided against using a keyboard, opting for a mouse for arm operation and a gamepad for cart operation. This configuration allows operations to be separated into parts, thereby preventing operating errors by dividing up the objects of actions.

Feedback on the operating experience and other such factors was obtained from the actual operators during use so that the developed GUI could be given additional functionality and enhancements to make the interface intuitively understandable, less tiring, and less likely to produce errors. Figure 12 shows the arm operating screen in the developed GUI. The arm operating screen shows the arm position in animated form at the center of the screen. The camera displays are on the left side of the screen, and the controls for operating the arm are arranged on the right side of the screen.

The status of the arm and the cart are also displayed in icon form at the bottom of the screen where they can be instantly comprehended.

6.1. Methods for Representing the Environment to Operators

The goal of the developed robot is to perform surveys in narrow spaces through operation from a remote location. For that purpose, the surrounding environment is made known to the operator by presenting camera-acquired imagery. Camera imagery may omit depth information,

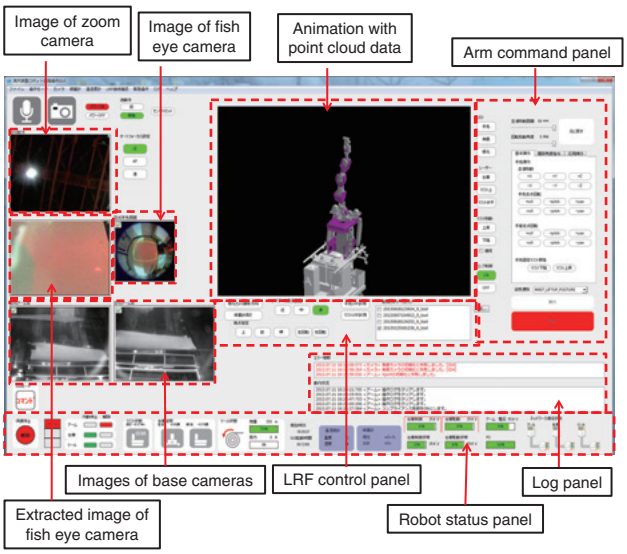


Fig. 12 GUI tab for survey arm

however, leaving the operator unable to judge the positional relationship between the arm and the environment. Then, when the arm is moved, it may come into contact with the environment.

On the arm operation screen, the camera imagery is presented only for the purpose of checking the presence and attributes of objects in the periphery. For ascertaining the positional relationship with the environment, the LRF installed on the arm tip is used. This LRF is a line-type two-dimensional scanner, and by rotating the arm tip, it can be used to acquire three-dimensional scanning data that is presented as point cloud data. A point cloud is a cluster of points that represents a three-dimensional position estimated from the data on position, attitude, and distance of an LRF when it is scanning an object. Presenting this information superimposed on the animated image in the center of the screen allows the positional relationship of the arm and an object to be checked from various points of view. Figure 13 (a)-(f) shows images of the environment presented to the operator following a scan.

Figure 13 (a) is a photograph taken of the robot exterior for reference. What the operator needs to check here is the positional relationship of the arm and the two bars shown inside red ovals. Imagery from the cameras installed on the robot, however, does not allow a grasp of positional relationships between the robot and the environment. As shown in Fig. 13 (b), (c), (d), and (e), therefore, the perspective of the animation depicting the point cloud and the robot is changed. The distances to the two bars can be determined from Fig. 13 (c) and (d). There can be cases, as shown in Fig. 13 (e), where the point cloud in the area being checked overlaps the depth dimension of the image that the operator wants to see, so that the area cannot be checked. When this happens, the press of a button in the GUI can erase the parts of the point cloud display that are distant from the robot. This eliminates the overlap on the depth dimension so that the system can display an image like that in Fig. 13 (f), from which the operator can easily check the distance.

6.2. Arm Movement Simulation Display

Arm operation involves checking the animation shown at the center of the screen in Fig. 12 while issuing commands for the arm tip position and amounts of positional movement. Ordinarily the arm will be displayed as on the left side of Fig. 14. When the desired amount of movement is entered by the GUI, however, the intermediate postures are superimposed onto the display shown on the right side. In this way, the kind of movement the arm will make is simulated internally by the GUI and displayed, together with transitional positions during the movement, before the movement command is issued. The operator can therefore check in advance whether there will be any contact with the environment represented by the point cloud, as described in section 6.1, and so even operations in narrow spaces can be carried out with a sense of security.

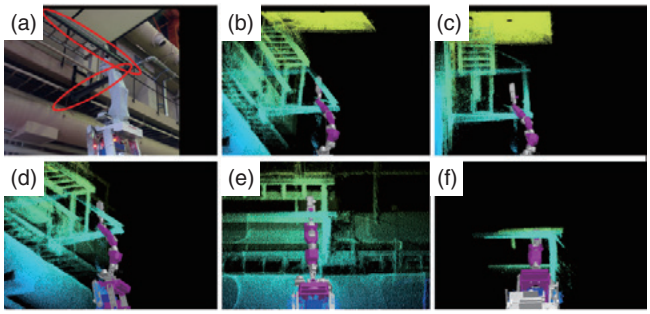


Fig. 13 Check minimal distances between robot and environment utilizing point cloud data

6.3. Synchronized Movement of the Arm and Mast

In order to keep the arm from coming into contact with the environment when being inserted into a narrow space, it is necessary to perform mast elevating operations linked to arm operations. For example, when entering a narrow space laterally as shown in Fig. 15 (a), raising the mast while moving the arm into the narrow space allows the arm access deep inside the space. As it happens, the mast elevating function of the developed robot is a repurposing of the hydraulic lift on the cart, which is not capable of accurate movement instructions or synchronized movement. What is done, therefore, is to raise the mast as shown in Fig. 15 (b) for a unit of time. The amount it was raised is then measured, and the arm is moved vertically by an amount that will cancel out the amount the arm was raised by the mast movement. After this operation has been repeated a number of times, the arm will be

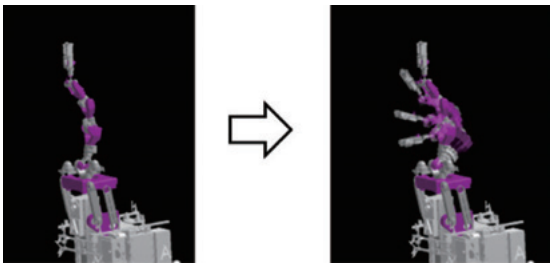


Fig. 14 Preview of arm movement

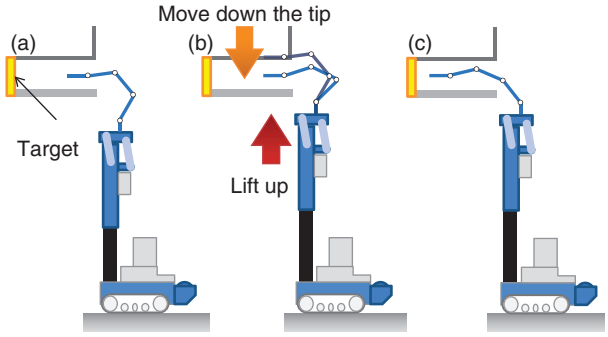


Fig. 15 Synchronization mast and arm movement

moved into the space as shown in Fig. 15 (c). As there is a possibility of contact with the environment when this is done, the amount the mast will be raised at one time is limited to about 10 mm. Since the amount the mast is raised is limited, this operation will have to be performed a number of times. However, the movement of raising the mast and then canceling out that amount by moving the arm can be configured as a single operation so that contact with the environment is avoided while mitigating the burden on the operator.

7. Reliability Testing

Reliability requirements were determined from the on-site environment and number of times of robot operation. The number of times of robot operation cited in section 2.2 was multiplied by a safety factor of 5 to arrive at 80 times of operation as the endurance requirement. The number of hours per mission is five hours. Reliability testing consists of endurance testing and environmental testing. The requirements are shown in Table 2.

As to radiation resistance, no actual testing was conducted because it was decided to suspend use of the robot when exposure exceeds a cumulative 20 Sv. This is following "the basic conceptual approach for assessment and management of radiation resistance in general-purpose heavy machinery and robots."[5]

7.1. Endurance Testing

7.1.1. Endurance testing of electrical functions

For the new functions developed for use with this robot, the number of times they would be used in each mission was estimated and endurance testing of each function was carried out. In the case of the brake function, for example, it was confirmed that the switching devices that control brake operation would not malfunction under the surge voltage generated when multiple brakes were controlled simultaneously.

7.1.2. Operating endurance testing

The arm joints were repeatedly made to move to the limit of their working range to confirm their endurance performance in mechanical terms. Confirmation was also made of matters such as that the cable would not be severed or broken by being dragged or bent, that the drip-resistant cover would not tear and that its elasticity presented no issues.

7.2. Environmental Testing

7.2.1. Heat cycle test

Electrical components were housed in the compact enclosure described in section 5.2.4 and a temperature sweep test was conducted at 0-40°C for 30 cycles of eight hours. During and after the test, it was confirmed that there were no problems with actuator driving or with any electrical functions.

Table 2 Test conditions

Test		Condition	
Endurance test	Electrical function	·Brake control, LED control and rebooting ·Charge and discharge of battery	
	Mechanical function	Repetitive movement to all working range ·Arm : 40 h ·Parallelogram link mechanism : 400 cycle	
Environmental test	Heat cycle test	·0 to 40°C ·30 cycle (8 h/cycle)	Transition (a) 0 to 40°C : 2 h (b) 40°C constant : 2 h (c) 40 to 0°C : 2 h (d) 0°C constant : 2 h
	Hygrothermal test	·Temperature: -10 to 40°C ·Humidity: Less than 90% ·1 cycle	Transition (a) 5°C, 80% (b) 20°C, 31% (c) 0°C (Humidity uncontrollable) (d) 30°C, 80% (e) -10°C (Humidity uncontrollable) - Waiting for heating up of arm system (40 min) - Reboot arm system (f) 40°C, 90%
	Vibration test	·Acceleration : Less than 5 G ·Vibration : 10 to 500 Hz ·11 min log sweeping ·30 h	
	Rainfall test	·10 mm/h, 25 min (without wind) ·10 mm/h, 10 min (with wind)	

7.2.2. Hygrothermal testing

Since the robot may be operated in winter, the system is required to start at -10°C. The robot was therefore placed inside the hygrothermal test apparatus and put through one cycle of the test pattern shown in Table 2. It was confirmed that acquisition of sensor data on the environment, control of the arm, and control of the cart does not have any problems.

7.2.3. Vibration testing

Conditions when the robot travels inside the reactor building and when it is transported by truck were envisioned and then vibration requirements were determined. Robot travel conditions inside the reactor building were determined from travel data acquired from another robot operating inside the reactor building and truck transport conditions were based on data acquired during actual transportation by truck. According to this data, the vibration condition was set at 5 G. With vibration testing of independent electrical systems and of the robot arm conducted under those conditions, it was confirmed that no screw loosening or other such mechanical defects occurred, and that there were no issues in operation of the system as a whole.

7.2.4. Rainfall testing

After workers unload the robot from a truck near the reactor building, the robot enters the reactor building under its own power, controlled by remote operation. It is conceivable that the robot could be affected by rain during that time. Taking the time required for the work and self-propelled travel into account, the rain exposure was set at 5 mm/h of rain for 20 minutes. Rainfall testing was conducted accordingly. Before testing, water submersion indicator

stickers were applied to locations where drip-resistance is necessary, and it was confirmed after testing that no water infiltration had occurred at any of those locations.

8. Field Testing

The robot systems were put through actions similar to those on an actual mission in a location resembling the actual use environment. System functions were assessed, and then functions for addition as well as points for improvement were identified.

The field testing was conducted at Unit 2 of Hamaoka Nuclear Power Station of Chubu Electric Power Co., Inc. This facility ceased commercial operation in 2009, it is approximately the same age as Units 1 to 4 at 1F, and it was constructed in a similar physical configuration.

Figure 16 shows scenes of the field testing. The photograph at the upper left shows the personnel access airlock room, the one on the upper right shows a penetration section on a catwalk, and the two on the bottom show the survey being conducted in the TIP room.

This field testing revealed the existence of a number of issues relating to the arm, as follows.

For example, there is limited space in front of the TIP room, and it was found that when the arm was moved from the driving posture shown in Fig. 7 to a higher extended posture, it would collide with facility features. The space required for this posture transition was therefore made smaller by breaking down the intermediate postures between driving posture and higher extended posture into smaller increments.

It was also found that operating the robot took more time than was initially anticipated. The overall mission time was therefore reduced by various means. When the arm is inserted into a narrow location, for example, the commands used to insert it are reversed in sequence by using the undo command to withdraw the arm. For another example, when scanning with the LRF, the rotation of the arm tip was made faster to reduce the time taken in scanning.

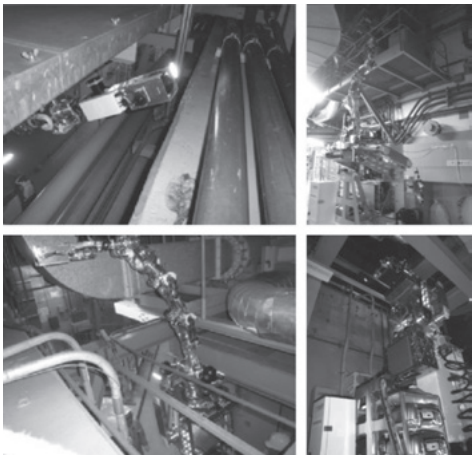


Fig. 16 Experiments in Hamaoka Nuclear Power Station (Images provided by Chubu Electric Power Co., Inc.)

9. Missions

Missions at 1F were conducted twice at Unit 2 and once at Unit 3.

9.1. Overview of Mission at Unit 2 Reactor

The mission at Unit 2 was made up of two steps. Figure 17 shows the areas where the robot conducted surveys for this mission and the postures taken by the robot while surveying for each step.

In the first step, the robot carried out an overall survey of the west side of the upper part of the ground floor of the reactor building. It made radiation dose and other measurements and acquired imagery.

In the second step, the robot arm was inserted into a narrow place for the purpose of acquiring imagery in the vicinity of a penetration on the southwest side of the PCV.

9.2. Results of Mission at Unit 2 Reactor

As a result, it was found that the radiation at locations high above the floor, where measurements previously could not be made, was 7-18 mSv/h and did not significantly differ from the radiation at lower locations. No damage to facilities or equipment was found near the ceiling in areas where the survey was conducted.

Some of the images acquired in the second step, which took place on July 23, 2013, are shown in Fig. 18[7] and Fig. 19[7].

The imagery resulting from the survey did not reveal any damage to facilities or equipment in the upper part of the personnel access airlock room. The surface of the PCV wall could not be examined in detail, but there are large numbers of pipes, ducts, and cables on the upper part of the PCV, and the existence of narrow spaces was confirmed.

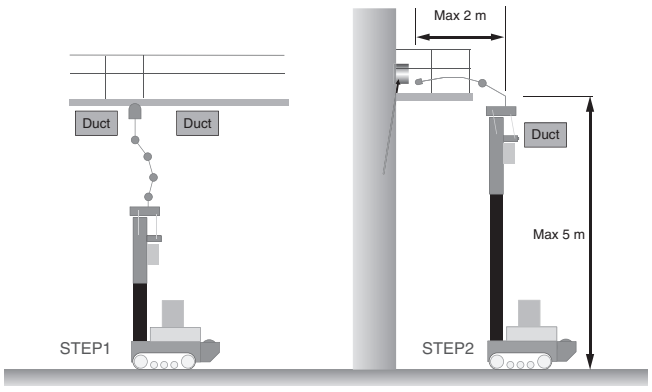


Fig. 17 Robot postures when robot surveying in missions
The left shows the step 1 and the right shows the step 2.

9.3. Mission at Unit 3 Reactor

The mission at Unit 3 Reactor took place on May 13, 2014. With a view to surveys inside the PCV, measurements were made of air dose, of the shapes of objects that would interfere with work, and of other such elements at a height of 2.4 m in the vicinity of the PCV penetration, which is to be used for the survey. The on-site radiation at the measurement points was a maximum of 98.3 mSv/h.

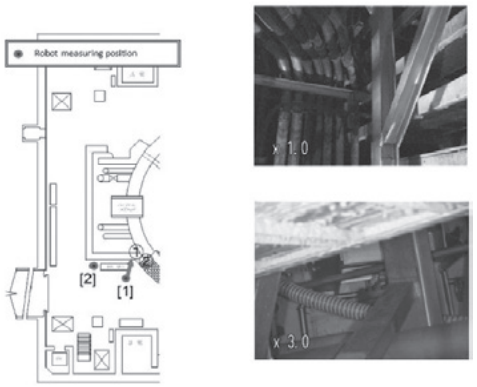


Fig. 18 Result of mission 2 (Provided by TEPCO) The pictures show the images of ① and ② from [1], respectively.

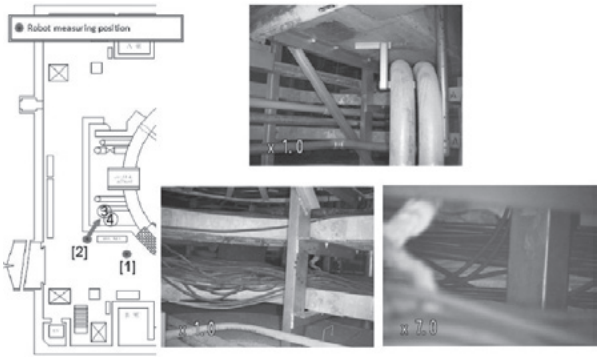


Fig. 19 Result of mission 2 (Provided by TEPCO) The top and bottom left pictures show the images of ③ and ④ from [2], respectively. The bottom right picture enlarges of the image of the bottom left.

10. Conclusion

A highly reliable high-access survey robot system was developed to carry out surveys in narrow spaces at high locations. Its purpose is to contribute to the work of dealing with the accident at TEPCO's Fukushima Daiichi Nuclear Power Station.

In the limited time available for development, a system capable of actual use was developed to carry out surveys of the Fukushima Daiichi Nuclear Power Station reactor building, where people are unable to enter and remain for extended periods of time. Use was made of existing systems in order to achieve the capability.

For that purpose, a detailed survey was made of on-site conditions and on-site needs regarding robots were ascertained. Development was carried out on the basis of requirements formulated accordingly. Reliability testing was then used to confirm the requirements, and tests were also carried out in an environment resembling that on-site. Problem areas in the system as a whole were revealed in this way and measures were taken to address them.

During the three missions that were conducted, imagery and radiation data were successfully obtained on locations high above the floor of the first story of the reactor building, where conditions had not been ascertained up to that point.

It was also confirmed that three-dimensional data inside the reactor building could be obtained from the point cloud used to operate the robot. This data is also slated to be employed in various upcoming tasks involved in reactor decommissioning.

The developed robot is slated for continuing use at TEPCO's Fukushima Daiichi Nuclear Power Station to conduct radiation surveys and to acquire three-dimensional data on the reactor building interior.

Acknowledgements

The assistance provided by the personnel of Hamaoka Nuclear Power Station of Chubu Electric Power Co., Inc., who generously provided a location for field testing during this research, is acknowledged with gratitude.

Reference

(1) http://www.irobot.com/en/us/robots/defense/packbot.aspx
(2) Nagatani, K., Kiribayashi, S., Okada, Y., Otake, K., Yoshida, K., Tadokoro, S., Nishimura, T., Yoshida, T., Koyanagi, E., Fukushima, M., Kawatsuma, S.: Emergency response to the nuclear accident at the Fukushima Daiichi nuclear power plants using mobile rescue robots, Journal of Field Robotics, Vol. 30, Issue 1 (2013)
(3) http://www.topy.co.jp/files/default/News_Release_survey_runner_F__1_.pdf, 2012/3/6
(4) Shigemi, S., Kawaguchi, Y., Yoshiike T., Kawabe, K., Ogawa, N.: Development of New ASIMO, Honda R&D Technical Review, Vol. 18, No. 1, p. 38-44
(5) http://roboticstaskforce.wordpress.com/2011/05/20110427-rcpt-radiation.pdf, (2011) (in Japanese)
(6) Yokoi, K., Kato, S., Yamanobe, N., Yoon, W-K., Morikawa, Y., Ogure, T., Shigemi, S., Matsumoto, T.: Koshochosayo Robottoshisutemuno Kaihatsu, THE 31st ANNUAL CONFERENCE OF THE ROBOTICS SOCIETY OF JAPAN (2013) (in Japanese)

(7) http://www.tepco.co.jp/nu/fukushima-np/handouts/2013/
images/handouts_130724_06-j.pdf

■ Author ■


Hisashi SUGIURA


Takafumi FUKUSHIMA


Mitsuhide KURODA


Ryusuke ISHIZAKI


Takashi MATSUMOTO

Study on Application of Engine Load Estimation Method Using Crank Angular Velocity Variation to Spark Advance Control

Hirotaka KAWATSU* Ryosuke IBATA*
Tetsuya KANEKO* Kenji NISHIDA*

ABSTRACT

The technology to estimate engine load using the amplitude of crankshaft angular velocity variation during a cycle, which is referred to as "$\Delta\omega$ (delta omega)", in a four-stroke single-cylinder gasoline engine has been established in our former studies. This study was aimed to apply this technology to the spark advance control system for small motorcycles. The cyclic variation of the $\Delta\omega$ signal, which affects engine load detection capability, was a crucial issue when developing the system. To solve this issue, filtering functions that can cope with various running conditions were incorporated into the computation process that estimates engine loads from $\Delta\omega$ signals. In addition, the system made it possible to classify engine load into two levels without a throttle sensor currently used. We have thus successfully developed the new spark advance system that is controlled in accordance with the engine speed and load.

1. Introduction

A large number of small motorcycles are used widely around the world, and the improvement of the fuel economy is one of the important issues to be solved from the global environmental viewpoint. One of the basic techniques for fuel economy improvement is the spark advance control that functions in accordance with the engine load. Generally, the engine load is detected by a throttle sensor. In small motorcycles, two types of throttle sensors are commonly used. One of the types is a potentiometer, which continuously detects throttle angle. Another is a throttle switch, which classifies throttle opening into two levels. The potentiometer is mainly applied to motorcycles equipped with a fuel injection system. In this type, the spark timing is controlled in accordance with the engine speed and throttle angle on the basis of three-dimensional control map stored in the ECU. The throttle switch is applied to some motorcycles equipped with a carburetor. In this type, the spark timing is controlled in accordance with the throttle opening by switching two kinds of two-dimensional control maps in which the relationship between the engine speed and the spark timing is stored. However, regarding small motorcycles with affordable prices using a carburetor, a large number of models are not equipped with a throttle sensor for spark advance control.

It has been known that the single-cylinder four-stroke engine has the typical pattern of variations in crankshaft angular velocity during a cycle consisting of intake, compression, expansion and exhaust strokes[(1)]. In our former studies, the technology estimating engine load with this amplitude of variation has been already established (we call it "$\Delta\omega$ method")[(2), (3)]. The amplitude ($\Delta\omega$) is calculated on the basis of signals from the crank position sensor which is commonly equipped in conventional engines.

In this project, we aimed to realize an alternative system to the conventional system using a throttle switch. In the alternative system, engine loads are classified into two levels using $\Delta\omega$ method. First of all, we worked out a basic logic using $\Delta\omega$ method. However, when the load-level classification using $\Delta\omega$ was tested on the marketed motorcycle, it was made clear as an issue that the spark timing was unstable due to hunting of engine load-level classification resulting from cyclic variations of $\Delta\omega$ signals. To cope with this issue, we theoretically studied the causes of cyclic variations of $\Delta\omega$ and clarified the conditions under which such variations occurred. Moreover, after conducting validation tests on the basis of the said presumption, new filtering processes were applied in the execution algorithm to classify the engine load-level, and the issue was resolve.

Consequently, the spark advance control system using $\Delta\omega$ method enabled to have the same level of load-level

* Motorcycle R&D Center

classification capability as the conventional system. We have thus successfully developed a simple spark advance control system without using a throttle switch.

2. Conventional Spark Advance Control

This section outlines a conventional spark advance control system. Such a system classifies engine load into two levels using output signals from the throttle switch, and controls the spark timing accordingly.

2.1. Experimental Motorcycle

Figure 1 shows the experimental motorcycle. Table 1 shows the major specifications of the experimental engine. The experimental motorcycle is a marketed small scooter equipped with a four-stroke, single-cylinder 110 cm^3 engine. The fuel is supplied by a carburetor.

2.2. Load-level Classification by Throttle Switch

Figure 2 shows the cross-sectional view of the piston-valve-type carburetor with the throttle switch. The throttle switch is attached to the side of the carburetor cylinder that retains the piston valve. The push rod is depressed at the specific piston position and the switching signal is transmitted. The switching signal turns off when the throttle opening exceeds the prescribed level at which a certain engine load is presumed. Accordingly, the engine load is classified in two levels using the throttle switch without dependence on the engine speed. Figure 3 shows a motion of the load-classification using the throttle switch.

2.3. Basic Logic of Spark Advance Control

Figure 4 shows a flowchart of a conventional spark advance control using a throttle switch. In the control flow, the engine speed is calculated, the engine load is classified by the throttle switch, the load-level signal is transmitted, and the spark timing map is selected according to the classified load. When the load is classified as "Low", the advancing map is selected correspondingly. On the other hand, when the load is classified as "High", the retarding map is selected. Finally, the spark timing matching the engine speed is picked up from the selected spark-timing map.

Table 1 Specifications of experimental motorcycle

Item	Specification
Engine type	Four-stroke single-cylinder
Cooling system	Air-cooled
Bore × Stroke	50.0 mm × 55.6 mm
Engine displacement	109.2 cm^3
Compression ratio	9.5
Spark supplying system	Full-transistor
Fuel supplying system	Carburetor
Transmission type	Continuously Variable Transmission (CVT)
Maximum brake power output	5.6 kW at 7500 rpm
Maximum brake torque	8.57 Nm at 5500 rpm
Curb weight	108 kg



Fig. 1 Experimental motorcycle

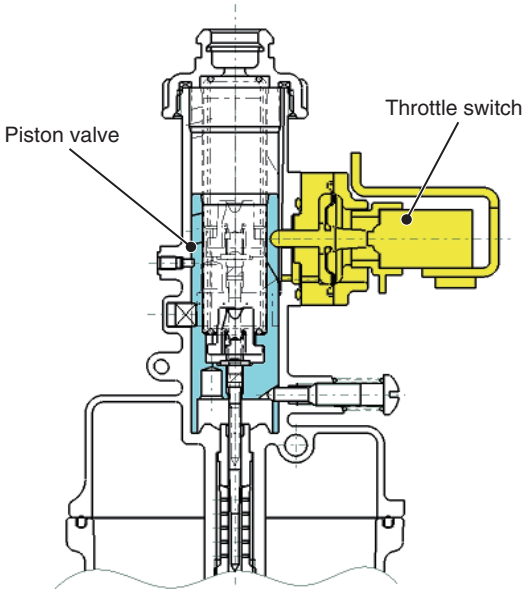


Fig. 2 Carburetor with throttle switch system

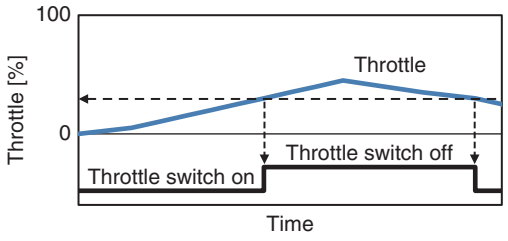


Fig. 3 Throttle switch motion

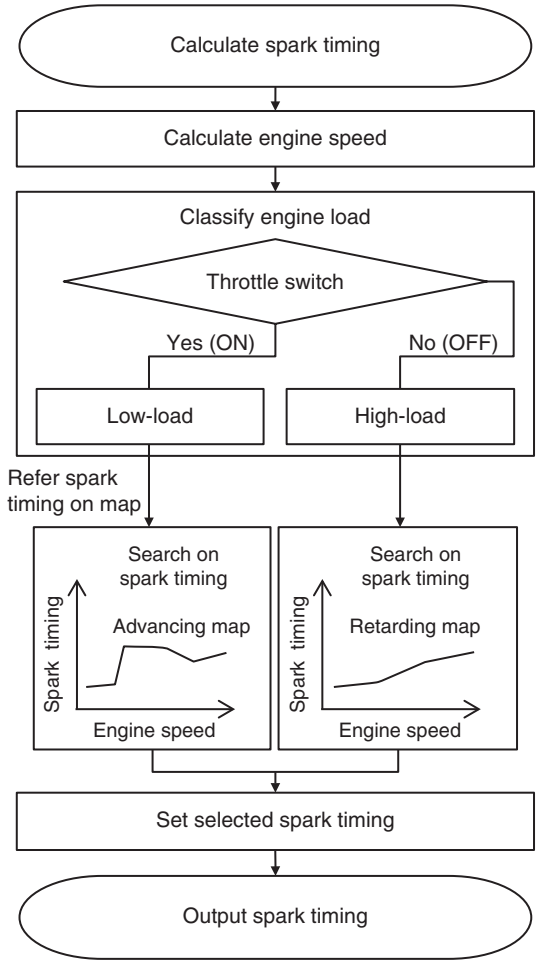


Fig. 4 Flowchart of conventional spark advance control

We investigated a new logic to replace the throttle switch method with $\Delta\omega$ method for the process of load-level classification.

3. Spark Advance Control Using $\Delta\omega$ Method

3.1. Basic Principles of Engine Load Estimation Using $\Delta\omega$

In this section, the system structure and the principles of $\Delta\omega$ method are explained, with reference to a previous papers[2), (3)].

3.1.1. Measurement of $\Delta\omega$

In the $\Delta\omega$ method, the crankshaft angular velocity ω_i (i = 1, 2) is used. Figure 5 shows the structure of the ω_i measurement system[(2)]. The crank position sensor detects the front end and the rear end of the reluctor on the alternator rotor. The ω_i is determined by Eq. (1) using the time τ_i between the detected signals P_1 and P_2, and the reluctor angle θ. Note that there are two suffixes (i) because P_1 and P_2 are detected two times during a cycle.

$$\omega_i = \frac{\theta}{\tau_i} \quad (1)$$

Figure 6 shows the waveform of crankshaft angular velocity (ω waveform), the measured ω_i, the reluctor pulse signals P_1, P_2, and the reluctor position[(2)]. These data were gotten under the constant load and engine speed (N_e) of approximately 3000 rpm. The continuous ω waveform is measured with the rotary encoder, which is integrated on an end of crankshaft and generates 360 pulses per revolution. When the ω_i in a cycle is defined as ω_1 in the compression stroke and ω_2 in the exhaust stroke, the $\Delta\omega$ is represented by Eq. (2).

$$\Delta\omega = \frac{\omega_2 - \omega_1}{2} \quad (2)$$

In this measurement method, $\Delta\omega$ is determined from the ω_i in the half of cycle, and a $\Delta\omega$ per cycles provided with a delay of a cycle (period: 4π).

3.1.2. Experimental studies on cyclic variations of $\Delta\omega$

The following two important features on $\Delta\omega$ under constant speed and load conditions have been proven by the previous papers[(2), (3)].

(a) $\Delta\omega$ is proportional to the indicated mean effective pressure.

(b) $\Delta\omega$ is counter-proportional to N_e.

The indicated mean effective pressure is represented by a value in that the cylinder work delivered to the piston over the entire four-stroke cycle is divided by the displacement, and denoted as $IMEP_{net}$ (Net Indicated Mean Effective Pressure). Figure 7 shows the relationship between the $\Delta\omega$ and the $IMEP_{net}/N_e$ at each engine speed, when operating with a wide open throttle. The plotted data are an average of approximately 500 cycles. From Fig. 7, it is proven that $\Delta\omega$ changes proportionally to $IMEP_{net}$ and counter-proportionally to N_e[(2)].

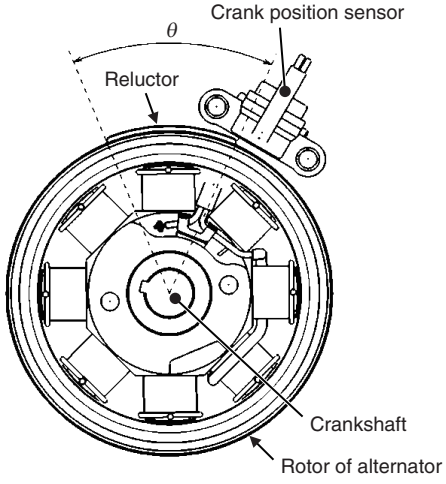


Fig. 5 Schematic of onboard system to detect $\Delta\omega$

Meanwhile, the relationship between $\Delta\omega$ and $IMEP_{net}$ at each cycle is also indicated in the previous papers[2), 3)]. Figure 8 shows the cycle-by-cycle data of N_e, $\Delta\omega$ and $IMEP_{net}$ at an idling. It has been confirmed from the figure that the cyclic variations of $\Delta\omega$ follow the variations of $IMEP_{net}$.

3.2. Basic Logic of Load-level Classification in $\Delta\omega$ Method

The following load-level classification logic was established to change the load-level classification process shown in the flowchart in Fig. 4 from a conventional system using the throttle switch to $\Delta\omega$ method.

3.2.1. Indexing of engine load conditions

$\Delta\omega$ proportionally changes to the engine load. However its proportionality constant changes inverse proportionally to the engine speed. We therefore defined the load ratio (hereafter referred to as *LR*), which is calculated from $\Delta\omega$, to standardize engine load conditions without dependence on N_e. *LR* is defined as the ratio of the value of $\Delta\omega$ when operating at a given throttle opening divided by the value of $\Delta\omega$ when operating at wide open throttle (defined as $\Delta\omega_{wot}$) as shown by Eq. (3). The relationship between $\Delta\omega_{wot}$ and engine speed is pre-written in the ECU in the form of two-dimensional data. The ratio of $\Delta\omega$ measured when operating, divided by the $\Delta\omega_{wot}$ at the same engine speed is calculated as the *LR* for each cycle.

$$LR = \frac{\Delta\omega}{\Delta\omega_{WOT}} \times 100\ [\%] \qquad (3)$$

3.2.2. *LR* characteristics in relation to engine speed

Figure 9 shows the relationship between the engine speed and $\Delta\omega$ together with the *LR*. The data shown in blue are for wide open throttle (WOT). The data in red are for partially open throttle (POT), where the throttle switch works. As the $\Delta\omega$ is counter-proportional to the engine speed, the higher the engine speed, the smaller the $\Delta\omega$ becomes. With *LR* introduced, $\Delta\omega$ at WOT is expressed as *LR* = 100%. Every load can be thus indicated between 0% and 100% at each engine speed. Using *LR*, the load level is classified by comparing it with the reference *LR*.

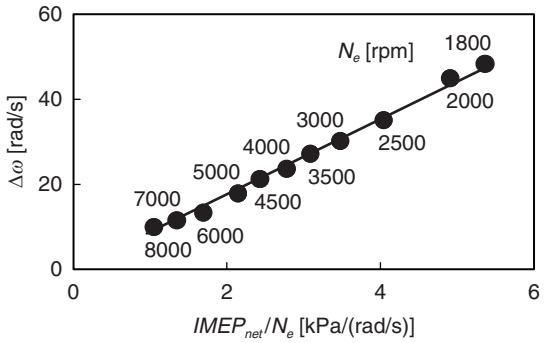


Fig. 7 Relationship between $\Delta\omega$ and $IMEP_{net}/N_e$

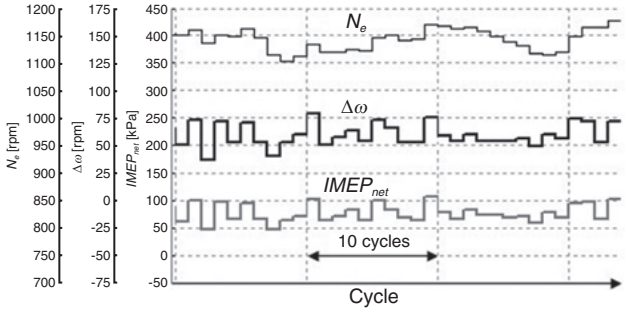


Fig. 8 Cyclic variation of $\Delta\omega$ and $IMEP_{net}$ at an idling

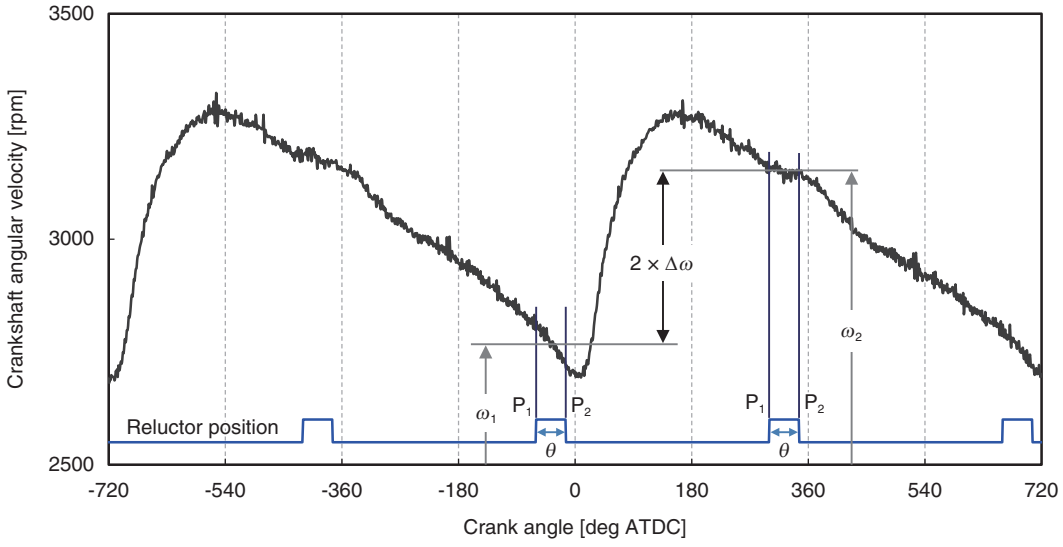


Fig. 6 Waveform of crankshaft angular velocity, reluctor position and definition of $\Delta\omega$

3.2.3. Load-level classification zone using *LR*

Figure 10 shows a schematic diagram of the load-level classification zone when the threshold level for load-level classification is set using *LR*. In this case, the threshold level was set referring to the *LR* at the throttle position where the throttle switch works. When the *LR* is larger than the threshold level, the load is classified as "High", and "Low" when smaller.

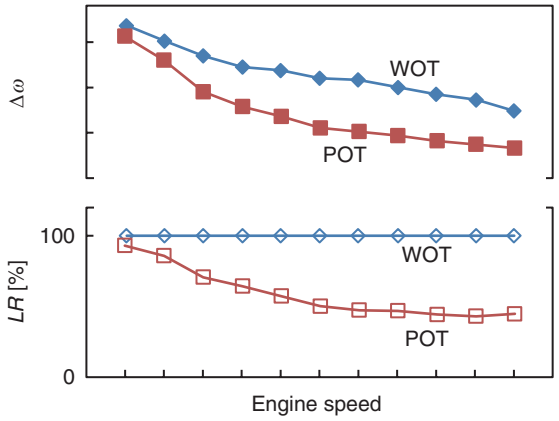


Fig. 9 $\Delta\omega$ and *LR* in relationship with engine speed

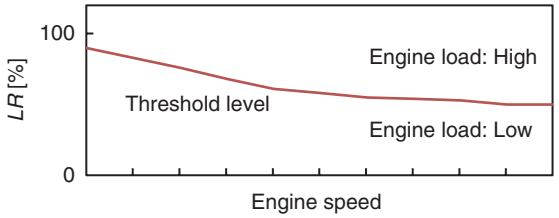


Fig. 10 Schematic diagram of load-level classification zone using *LR*

4. Theoretical Studies on How Cyclic Variations of $\Delta\omega$ Affect Load-level Classification

4.1. Issues in Load-level Classification

As mentioned in Chapter 2, the load-level classification using the throttle switch is performed referring to a specific throttle opening. Accordingly, when the throttle opening is fixed, the load-level classification and the spark timing map are fixed. Consequently, when the engine speed is constant, the spark timing becomes constant.

In the meantime, the load classification by the $\Delta\omega$ method is performed referring to a specific *LR*. In this method, when the $\Delta\omega$ cyclically varies even if the throttle opening is fixed, "hunting" of load-level classification occurs because the *LR* alternately moves across the threshold level. Consequently, it creates such a concern that the spark timing becomes unstable.

In order to obtain the same level of stability as the conventional spark advance control system using a throttle switch, the load-level classification and the spark timing should be constant when the engine speed and the throttle opening are constant. We call this requirement "spark timing stability".

Keeping the above in mind, we turned our attention to the cyclic variations of $\Delta\omega$ and clarified the conditions under which such variations occurred through the theoretical studies.

4.1.1. Governing equation of $\Delta\omega$

It is necessary to work out a governing equation of $\Delta\omega$ when studying cyclic variations of $\Delta\omega$. This chapter is therefore aimed at introduction of such a governing equation. The following preconditions are given to the motions of crankshaft system.

(1) Target is four-stroke, single cylinder engine
(2) The crankshaft system makes two-dimensional motions
(3) All components are assumed as a rigid body
(4) No change of conditions occurs in each contacting part
(5) Influence of gravity is ignored

The crankshaft system model is composed of the three modules, the assembly of crankshaft, the connecting rod and the assembly of piston as Fig. 11 shows. The geometric conditions of the crankshaft system are expressed by the general coordinate $\boldsymbol{q}$ and the geometric restriction function $\boldsymbol{h}(\boldsymbol{q})$ of the system. Vector $\boldsymbol{q}$ is defined by Eq. (4), and consisted of the coordinates (x_{ig}, y_{ig}) of each component's center of gravity and the rotational angle θ_i ($i = c$: crankshaft, l: connecting rod, p: piston) around that.

$$\boldsymbol{q} = \begin{pmatrix} x_{cg} \\ y_{cg} \\ \theta_c \\ x_{lg} \\ y_{lg} \\ \theta_l \\ x_{pg} \\ y_{pg} \\ \theta_p \end{pmatrix}, \boldsymbol{h}(\boldsymbol{q}) = \begin{pmatrix} x_{cg} - r_{cg}\cos(\theta_c + \varphi_{cg}) \\ y_{cg} - r_{cg}\sin(\theta_c + \varphi_{cg}) \\ x_{lg} - r_{cp}\cos\theta_c - r_{lg}\cos(\theta_l + \varphi_{lg}) \\ y_{lg} - r_{cp}\sin\theta_c - r_{lg}\sin(\theta_l + \varphi_{lg}) \\ x_{pg} - r_{cp}\cos\theta_c - r_{lp}\cos\theta_l - r_{pg}\cos\varphi_{pg} \\ y_{pg} - r_{cp}\sin\theta_c - r_{lp}\sin\theta_l - r_{pg}\sin\varphi_{pg} \\ y_{pg} - e_a - r_{pg}\sin\varphi_{pg} \\ \theta_p \end{pmatrix} = 0 \quad (4)$$

Next, think about the distribution of energy in the crankshaft system. The work W_{cyl} that the working fluid provides on the piston is redistributed in three ways, the kinetic energy K of the crankshaft system, the work W_{out} given out to the lower stream of crankshaft (hereafter referred to as resistance load) and the dissipation energy D. These energies satisfy Eq. (5).

$$W_{cyl} = K + D + W_{out} \quad (5)$$

Here, following the definition of $\Delta\omega$ seen in Section 3.1.1 and paying attention to the motions in a half cycle, the kinetic energy can be represented by Eq. (6) as a function of $\Delta\omega$. It should be noted that while I' is a function with a half cycle periodicity of the dimension, mass characteristics and θ_c of each component, it can be treated as a constant in this case.

$$K|_0^{2\pi} = I' \frac{\omega_2 + \omega_1}{2} (\omega_2 - \omega_1) = I' Ne' \Delta\omega \qquad (6)$$

Note that with respect to the N_e', which is an average of measured ω_1 and ω_2; there is an error δerr from the true N_e (one-cycle average of ω). Although the δerr can be made zero at an N_e depending on the position of reluctor seen in Section 3.1.1, as the ω waveform also changes in accordance with changes of N_e, it is impossible to make δerr zero at a given N_e. Accordingly, when the N_e and the N_e' are approximately equal, the $\Delta\omega$ is counter-proportional to the N_e.

Based on the aforementioned, Eq. (7) that governs $\Delta\omega$ is derived from Eq. (5) and Eq. (6).

$$\Delta\omega = \frac{1}{I' Ne'} \left\{ W_{cyl}|_0^{2\pi} - W_{out}|_0^{2\pi} - D|_0^{2\pi} \right\} \qquad (7)$$

Moreover, due to the facts that the Lagrangian in the crankshaft system depends only on K because the influence of gravity is ignored, and that the restricting conditions of each coordinate is acquired from $\boldsymbol{h}(\boldsymbol{q})$ of Eq. (4), the equation of motion around the crankshaft (8) is introduced from the Lagrange equation, thus determining ω_1 and ω_2.

$$(I_{cg} + \eta_2)\ddot{\theta}_c - \eta_1 \dot{\theta}_c^2 = T_{cyl} - T_f - T_{out} \qquad (8)$$

Note that the coefficients η_1, η_2 are a function composed of θ_c, geometric dimension, and mass characteristics, having a period of 2π.

The left side of Eq. (8) indicates the inertia. The right side is the torque around the crankshaft with the first term T_{cyl} representing the torque acquired from the working fluid, the second term T_f representing the friction torque, and the third term T_{out} representing the resistance load torque.

From the above findings, the parameters decisive for the crankshaft rotation characteristics and the $\Delta\omega$, and their features can be clarified from Eq. (7) and Eq. (8).

4.1.2. Cyclic variations of $\Delta\omega$

When ω_1 and ω_2, which are determined by Eq. (8), do not have a one-cycle periodicity, variations of $\Delta\omega$ occur. For this reason, cyclic variations of $\Delta\omega$ will occur if the vibrations without a one-cycle periodicity act on the crankshaft system. Figure 12 shows the characteristic diagram of parameters decisive for the $\Delta\omega$ based on Eq. (7) and Eq. (8).

In Fig. 12, geometrical and physical parameters decisive for (a) moment of inertia of the crankshaft system I' depend on the shape and density of each component. Unusual phenomena such as a large deformation, extensive wear, fracture, etc. are required to cause a change of shape or density during operation. Since such cases can be omitted as irregularities, the geometrical and physical parameters do not affect $\Delta\omega$ during operation.

In Fig. 12, a change of (b) engine speed N_e is counter-proportionally linked with $\Delta\omega$ by Eq. (7). Accordingly, $\Delta\omega$ also changes along with a change of N_e.

In Fig. 12, when a change occurs in (c) cylinder work W_{cyl} performed by the working fluid, the IMEP also changes. The cause is in the inconsistent combustion. The linked cyclic changes of IMEP and $\Delta\omega$ are evident in Fig. 8 in Section 3.1.2.

We consider the reason of such linked changes as follows.

The combustion characteristics depend on the characteristics of the working fluid. The air mass (O_2 quantity) in the cylinder depends on the volumetric efficiency (η_v), and the fuel mass depends on the air-to-fuel ratio (A/F). Moreover, the flow of working fluid creates mixture and determines concentration distribution. Such phenomena depend on the in-cylinder pressure (P_{cyl}) and the piston speed, in result of the ω. If a fixed ignition timing (θ_{ig}) and ignition energy (E_{ig}) are provided to the working fluid, the combustion corresponding to the given conditions should occur. Consequently, along with the heat generation pattern, the in-cylinder pressure P_{cyl} (θ_c) is determined uniquely. The P_{cyl} (θ_c) determines ω waveform ω (θ_c) through the equation

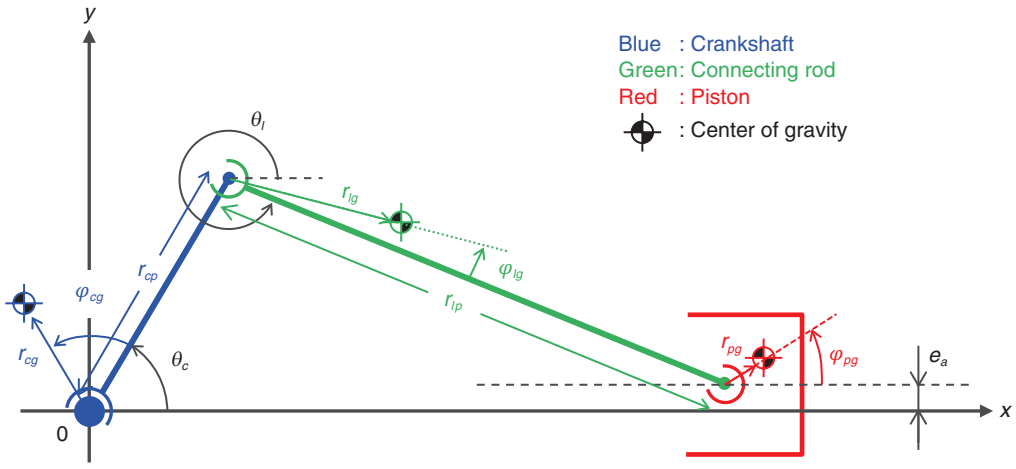


Fig. 11 Mathematical model of crank system

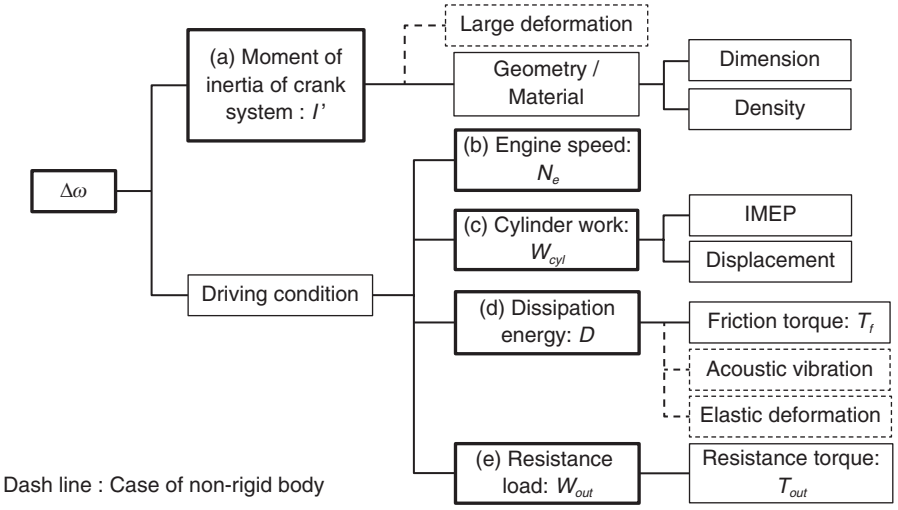


Fig. 12 Characteristic diagram of $\Delta\omega$

of motion (Eq. (8)) along with T_{out} and T_f.

In Fig. 12, (d) dissipation energy D depends only on the friction force under the presumption of a rigid body, which is a precondition. Among the friction forces, some shows self-exciting behavior such as the stick slip. In such a case, vibrations irrelevant to the one-cycle periodicity occur due to the friction force, causing cyclic variations of $\Delta\omega$. It should however be noted that such a phenomenon is deemed as occurring at the time of irregularity such as a piston seizure, and not subjected to the validation.

In Fig. 12, (e) resistance load W_{out} is applied freely regardless of the engine. Such a condition corresponds to the running resistance including the one from the road roughness and the air resistance depending on the randomly-changing wind direction, etc. The vibrations irrelevant to the engine and occurring in the subsequent system from the crankshaft system (e.g., influence of the damper in the drive train, etc.) also affect as an external force to the crankshaft system. As mentioned above, regarding the resistance load, a phenomenon containing vibrations without a one-cycle periodicity exists. Cyclic variations of $\Delta\omega$ therefore occur due to the resistance load without a one-cycle periodicity.

Finally, if the presumption that the component is a rigid body is freed, the vibration frequencies should occur due to the deformation as shown by the dotted lines in Fig. 12. In this case, as the natural frequency of each component is irrelevant to the one-cycle periodicity, the vibration frequencies provides cyclic variations to $\Delta\omega$.

From the above considerations, the cause of cyclic variations of $\Delta\omega$ is in the vibrations irrelevant to the one-cycle periodicity in addition to variations of IMEP. The specific example is shown in Table 2.

Table 2 Factors of cyclic variation of $\Delta\omega$

Classification	Factors	Parameters in Eq. (7) and (8)	Examples of specific phenomenon
Internal factors	(a) Change in moment of inertia of crank system	I'	Change deformation, Large ware, Breakage (Unusual phenomenon)
	(c) Variation of IMEP	T_{cyl}	Variation in combustion state, Occurrence of misfiring
	(d) Variation of friction	T_f	Repetition of sticking and slipping between piston skirt and cylinder sleeve (Unusual phenomenon)
	Vibration derived from deformation of components in crank system	Internal force	Torsional vibration, Out-of-plane vibration and In-plane vibration of components
External factors	(b) Variation of engine speed	N_e	Acceleration and deceleration by throttle control
	(e) Variation of load	T_{out}	Unevenness of the road surface, Changes of air resistance, Changes in posture of motorcycle and rider
	Vibration derived from deformation of components outside the crank system	T_{out}	Vibrations of drive system, vehicle body and crankcase, etc.

5. Examination and Considerations on $\Delta\omega$ Method

According to the studies in the chapter 4, the factors of cyclic variations of $\Delta\omega$ can be classified to two categories; (i) those affecting to the engine as internal factors, (ii) those affecting to the engine as external factors. To satisfy "spark timing stability" required for a spark advance control system using the $\Delta\omega$ method, we firstly analyzed how the internal factors affected cyclic variations of $\Delta\omega$ under the constant load and speed conditions. Then, we analyzed how the cyclic variations of $\Delta\omega$ from external factors affected "spark timing stability" under the non-constant load and speed conditions. On the basis of the findings from the analysis, we developed the system that ensures "spark timing stability".

5.1. Running with Constant Speed and Load

5.1.1. Test results

Keeping in mind the aforementioned requirements, tests were conducted on a chassis dynamometer under constant speed and load conditions to verify the spark timing control by the newly developed system.

Figure 13 shows cycle-based data for $\Delta\omega$ when the engine is running at 4500 rpm at 40% constant throttle opening. The load is classified as "High" by the throttle switch under this condition. It has been clarified that $\Delta\omega$ is not constant, but has variations up to approximately 50 rpm. It can be considered due to variations of $IMEP_{net}$.

Next, Fig. 14 shows the control operations based on basic logic corresponding to the $\Delta\omega$ variations shown in Fig. 13. The upper graph shows cyclic variations of *LR* and threshold level for load-level classification, the middle graph shows load-level classification signals based on *LR*, and the lower graph indicates the determined spark timing. The threshold level is set referring to the *LR* value at the throttle position where the throttle switch works.

Along with the fluctuations of $\Delta\omega$, the *LR* alternately moves across the threshold level, consequently causing hunting of the load-level classification signals and the spark timing. Accordingly, it was confirmed that the requirement of "spark timing stability" cannot be satisfied using this classification method.

We then analyzed how each engine speed affects the cyclic variations of $\Delta\omega$. Figure 15 shows the $\Delta\omega$ at each engine speed with WOT, its maximum variation $\Delta\omega_{p\text{-}p}$, and its variation ratio. The black dot in the upper graph shows $\Delta\omega_{ave}$, which is an average of $\Delta\omega$ over approximately 500 cycles, and the error bar indicates $\Delta\omega_{p\text{-}p}$. The lower graph shows the variation ratio ($\Delta\omega_{p\text{-}p}/\Delta\omega_{ave}$ ×100%). The $\Delta\omega_{p\text{-}p}$ stays almost a constant value irrespective of engine speed. However $\Delta\omega_{ave}$ decreases as engine speed increases. Accordingly, the variation ratio increases along with an increase of engine speed, and reaches the maximum of 20%. We consider that the variations are affected not only by the variations of $IMEP_{net}$, but also by the vibrations in the crankshaft system and the power train components including the reciprocating system listed in Table 2 in Section 4.1.2.

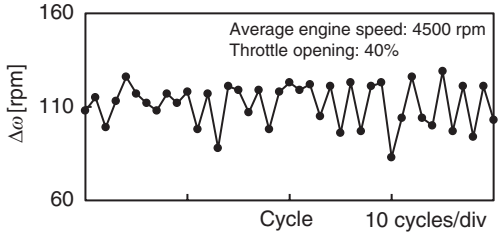


Fig. 13 Cyclic variations of $\Delta\omega$

5.1.2. Application of two thresholds

A hysteresis is applied to the threshold level shown in Fig. 10 to cope with the hunting of load-level classification caused by cyclic variations of $\Delta\omega$.

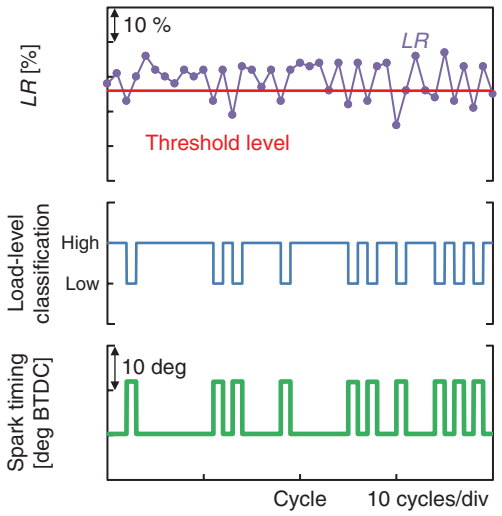


Fig. 14 Variations of *LR*, load-level classification signal and spark timing

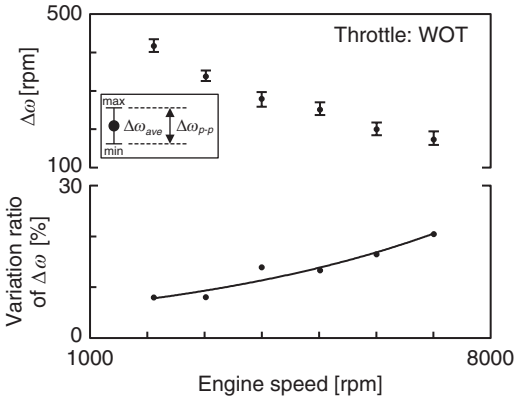


Fig. 15 Relationship between engine speeds and $\Delta\omega$, variation ratio of $\Delta\omega$

Figure 16 shows the schematic diagram of load-level classification having a hysteresis composed of two thresholds. The engine load-level classification turns from "Low" to "High" when the *LR* goes up above the high-threshold (red line), and turns from "High" to "Low" when the *LR* comes down under the low-threshold (black line). Here, the difference of *LR* between the two thresholds is defined as the hysteresis width. The yellow *LR* zone in the graph indicates the region with possibilities of knocking occurrence when the spark timing of the advancing map is applied (knock zone). The retarding map, therefore, must be selected. The green *LR* zone indicates the zone frequently used in city driving experienced in daily life. The blue line shows the load when cruising on a flat road. In these zones, it is required to apply the spark timing in the advancing map to improve fuel economy.

Each threshold, therefore, has been designated considering the following.

(1) High-threshold: To prevent knocking

The *LR* for the high-threshold is set at a level that corresponds to the throttle position where the throttle switch works. Thus, knocking can be prevented by selecting the retarding map when the load is above the high-threshold.

(2) Low-threshold: To stabilize spark timing and to improve fuel economy

To achieve spark timing stability, the hysteresis width must be larger than the cyclic variation width of $\Delta\omega$. At the same time, from the standpoint of fuel economy, a wide *LR* zone, in which spark timing is advanced, should be maintained. For that purpose, a small hysteresis width is preferable.

Taking the aforementioned into account, the hysteresis width was set at 25 points of *LR*. Consequently, this technique enabled the prevention of hunting of spark timing while suppressing knocking and, at the same time, improving the fuel economy when driving in city mode.

We have tested the above-mentioned load classification having hysteresis on the chassis dynamometer to clarify effectiveness in prevention of spark timing hunting. The operating conditions are the same as those in Section 5.1.1. The "High" threshold is set at the same level as in Fig. 12.

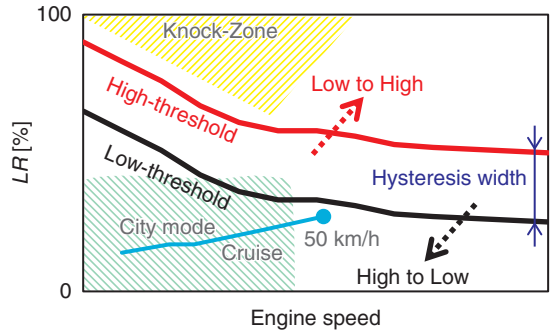


Fig. 16 Schematic diagram of load-level classification having hysteresis composed of two thresholds

Figure 17 shows the control operations when the load classification having hysteresis is applied. Although the *LR* alternately moves above and below the high-threshold, it never falls below the low-threshold, and the load-level classification remains continuously at "High". Thus, the requirement of "spark timing stability" has been satisfied.

5.2. Rough Road Running

5.2.1. Test results

As shown in Table 2, a rapid change of road load is a conceivable cause of cyclic variations of $\Delta\omega$. As the changes of resistance load corresponds to T_{out} in Eq. (8), if the variance between the T_{out} at the moment the ω_1 is measured and T_{out} at the moment the ω_2 is measured increases, the gap between ω_1 and ω_2 widens, causing the $\Delta\omega$ to increase. Conversely, if the gap narrows, the $\Delta\omega$ decreases. When such a variation does not have a one-cycle periodicity, cyclic variations occur in the $\Delta\omega$.

Based upon the above-mentioned considerations, it is required to satisfy "spark timing stability" under conditions where the resistant load changes most rapidly in order to make the system feasible. What is conceivable as such operating conditions is such a running in which the rear wheel repeats spinning and gripping from jumping and landing, i.e., running on off roads. We therefore measured cyclic variations of $\Delta\omega$ while running on a rough road in which the motorcycle was repeatedly jumping off and landing on the ground. The rough road consisted of trapezoid blocks, approximately 5 cm in height, laid on a flat surface at a constant interval.

Figure 18 shows $\Delta\omega$ and the control operations when running on a flat road with the throttle held at a constant opening. Figure 19 shows $\Delta\omega$ and the control operations when running on the rough road. Although no hunting

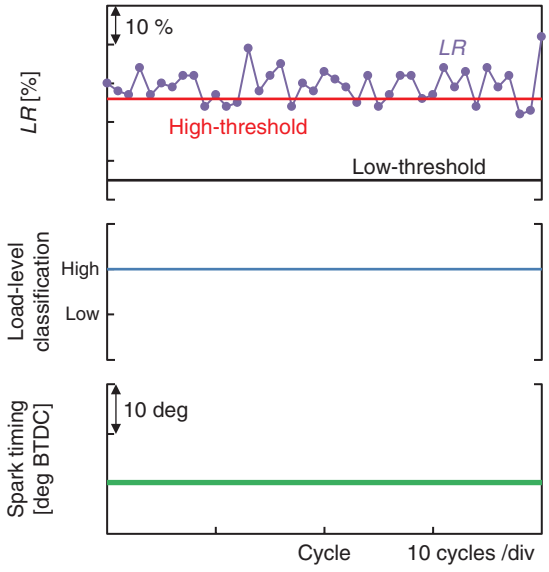


Fig. 17 Control operation of load-level classification having hysteresis

occurred in the load-level classification or in the spark timing when tested on the flat road, hunting occurred in the load-level classification and in the spark timing when tested on the rough road. It has been clarified from the comparison of Fig. 18 and Fig. 19 that an increase of cyclic variations of $\Delta\omega$ due to variations of N_e is a predominant cause of the hunting.

5.2.2. Application of wait counter for shifting classification

As mentioned before, the hunting can be avoided even when the cyclic variation amplitude of $\Delta\omega$ increases while running on a rough road if the hysteresis width is large enough. However, that enlargement of hysteresis makes it impossible to satisfy both requirements for knock suppression and for fuel economy improvement in driving under partial loads. For these reasons, we had to investigate different measures to prevent the hunting without changing the hysteresis width.

After this investigation, we decided to adopt a computation logic that shifts the classification of load levels only when detecting a sequence of *LR* signals crossing the threshold but does not shift for only a single signal. We call this "shift-wait counter", and we call the number of continuous signals crossing the threshold "triggering counts".

Figure 20 shows a schematic diagram of the shifting of load-level classification using a shift-wait counter. The upper graph indicates the variation of *LR*, the middle graph

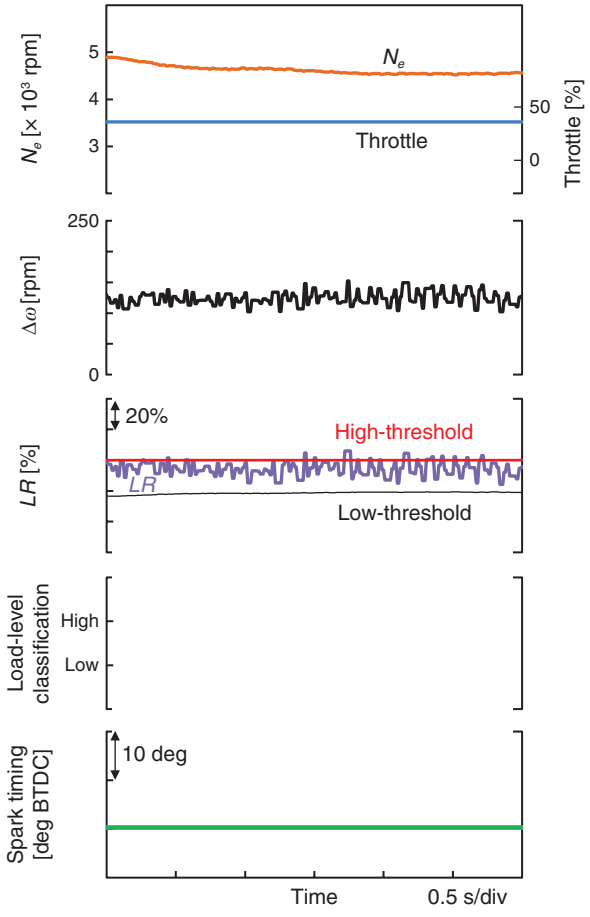


Fig. 18 $\Delta\omega$ variations and control on flat road

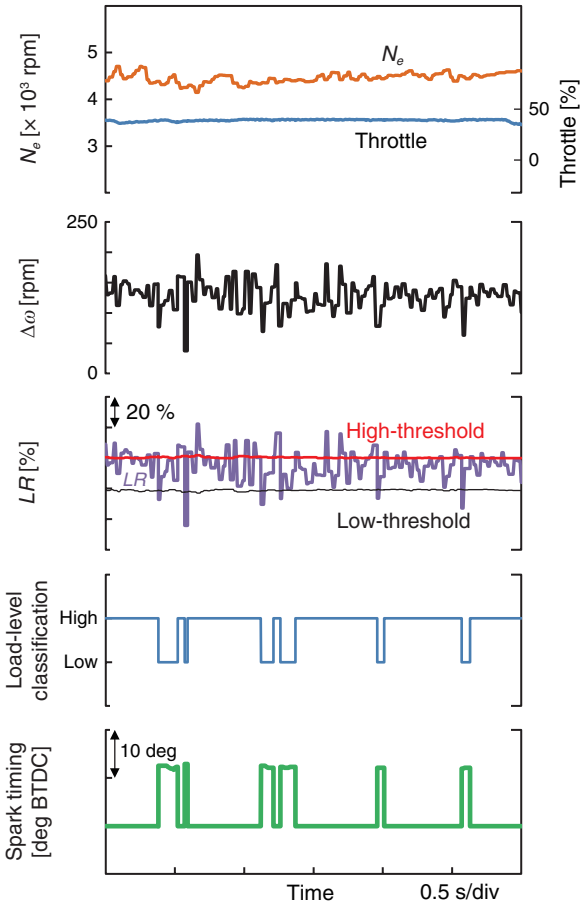


Fig. 19 $\Delta\omega$ variations and control on rough road

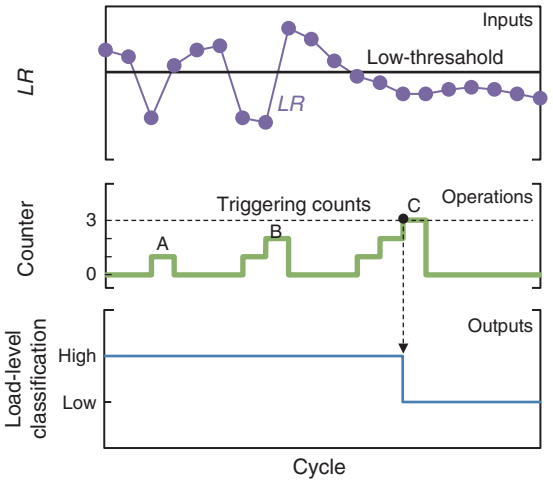


Fig. 20 Shifting of load-level classification by shift wait counter logic

shows the functional operations of the shift-wait counter, and the lower graph shows the load-level classification at that time. Here, the triggering count is set at three. As you see at Point A and Point B in the figure, the counts are not reaching the triggering counts. Consequently the load-level classification remains un-shifted. The load-level classification is first shifted at Point C where the requirement for shifting is satisfied. That is to say, the shifting occurs at the point where *LR* falls to the value under the low-threshold three times in a row. Although Fig. 20 shows only how the shift to the low load-level classification is determined, the same logic is applied to the shift to the high load-level classification.

We then verified the effectiveness of the shift-wait counter logic for the spark-timing hunting when running on rough roads. Figure 21 shows the control operation when the shift-wait counter is employed for the load-level classification. The operating conditions and the preset threshold are the same as those shown in Fig. 19. Although *LR* sometimes varies extensively along with the variations of N_e, and falls under the low-threshold, a shift to "Low level" is prevented by the application of the shift-wait counter. Thus, the "High level" classification is maintained, and the retarding map is continuously selected, satisfying the requirement of "spark timing stability".

5.3. Load-level Classification Logic Using $\Delta\omega$ Method

The load-level classification logic was created in which the previously mentioned filtering methods are applied. It is shown in Fig. 22. The flowchart is composed of the acquisition of the crank position signal, calculation of $\Delta\omega$, calculation of *LR*, load-level classification using the threshold-with-hysteresis and the shift-wait counter system, and transmission of the classification signal. This flowchart replaces the load-level classification using a throttle switch in the spark advance control flowchart shown in Fig. 4.

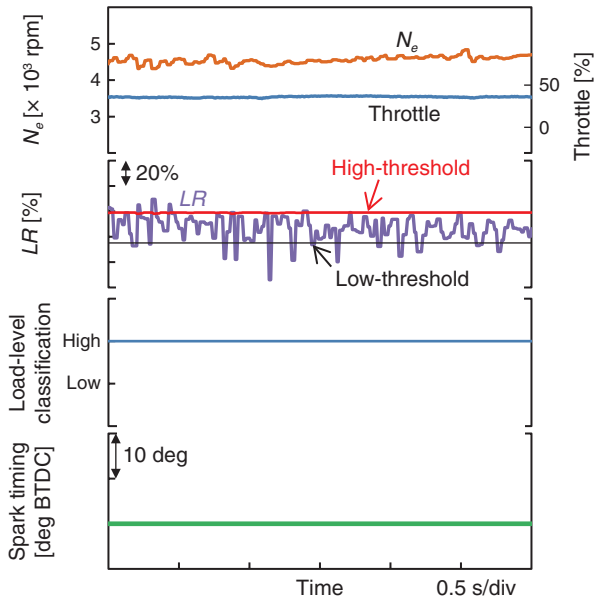


Fig. 21 Classification results of load-levels when shift wait counter was applied while running on rough roads

5.4. Validation of Modified System

The load-level classification logic using "thresholds with a hysteresis" and "shift-wait counter" was established to satisfy the requirement of "spark timing stability". To determine whether or not this logic can be applied as an alternative to load-level classification using the throttle switch, we ran validation tests to verify the operations of load-level classification. In addition, we check how they affect drivability. The tests were conducted to compare the current motorcycle using a throttle switch and the modified motorcycle using the $\Delta\omega$ method.

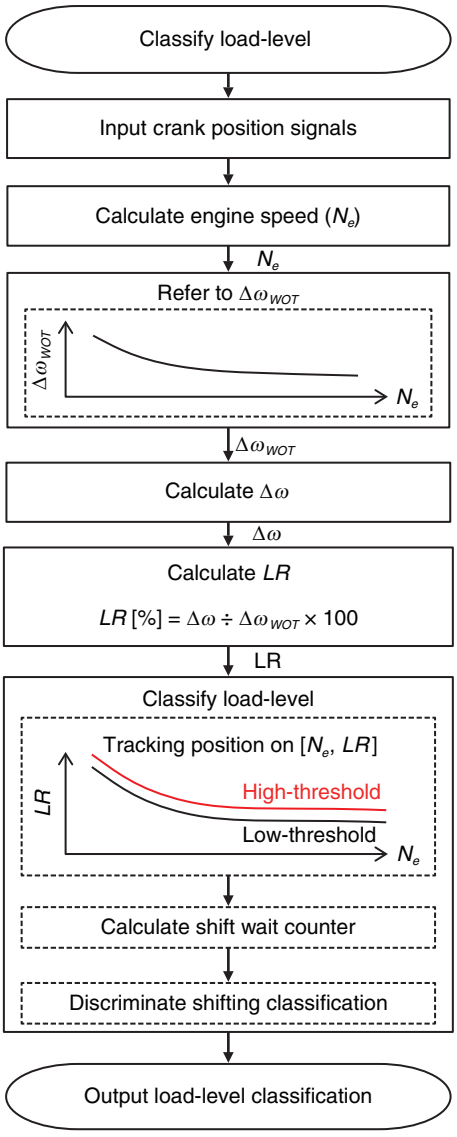


Fig. 22 Flowchart of load-level classification

Figure 23 shows the shifting of load-level classification when opening and closing the throttle. The driving condition of the motorcycle changes from acceleration to cruising. As the throttle is opened, N_e and *LR* increase, and a "High level" classification is determined when *LR* becomes higher than the high-threshold. The shift timing of classification is almost the same as for a throttle switch signal.

Then, as the throttle is closed, *LR* decreases and becomes lower than the low-threshold, and a "Low level" classification is determined before the change to cruising. Due to the application of "hysteresis" and "shift-wait counter", there is a slight delay in classification shift timing compared with a throttle switch signal. Nevertheless, the same level of drivability as the conventional system was verified through subjective evaluation by test riders.

Accordingly, the developed spark advance control system makes it possible to replace a conventional system using a throttle switch and to improve the fuel economy of the models with no throttle sensor.

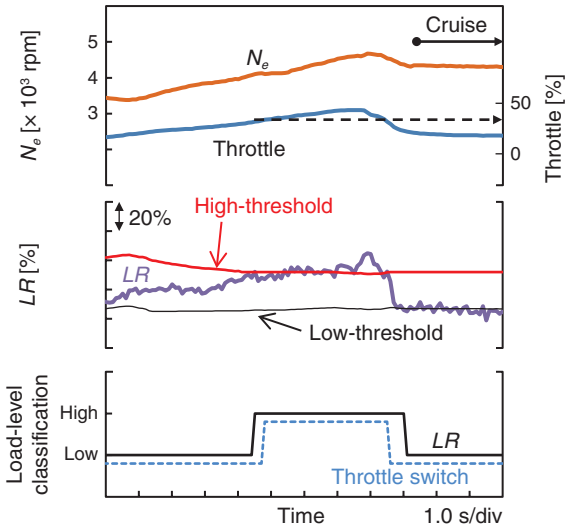


Fig. 23 Load-level classification when opening and closing throttle

6. Conclusions

We have established a logic that classifies engine load conditions into two levels using the amplitude of the crank angular velocity variation ($\Delta\omega$). Our conclusions follow:

(1) Theoretical studies were conducted in advance on how the cyclic variations of $\Delta\omega$ affected the spark advance control system which is applied the engine load estimation using $\Delta\omega$. Consequently, it has been clarified that the cyclic variations of $\Delta\omega$ is caused by the vibrations without one-cycle periodicity acting on the crankshaft system in addition to the variations of $IMEP_{net}$. Thus it is clarified that the cyclic variations of $\Delta\omega$ impairs "spark timing stability".

(2) Stable load-level classifications were made possible by applying a filtering procedure that adopts the two methods described below to cope with hunting of classification caused by cyclic variations of $\Delta\omega$.
- Hysteresis using two load-level classification thresholds
- "Shift-wait counter" to determine shifting after detecting a sequence of load signals that pass the load-level classification threshold

These methods enabled the same level of load-level classification functionality as the conventional system using a throttle switch and realized a simplified spark advance control system without a throttle switch.

The developed technology enables wider application of a spark advance control system that makes a significant contribution to the improvement of fuel economy.

References

(1) Marples, V.: Dynamics of Machines, McGraw-Hill Publishing Company Limited, p.149-151 (1969)

(2) Nishida, K., Kaneko, T., Takahashi, Y., Aoki, K.: Estimation of Indicated Mean Effective Pressure Using Crankshaft Angular Velocity Variation, JSAE 20119510/SAE 2011-32-0510 (2011)

(3) Nishida, K., Kaneko, T., Takahashi, Y., Aoki, K.: Development of System to Estimate Indicated Mean Effective Pressure Using Crankshaft Angular Velocity Variation, Transactions of Society of Automotive Engineers of Japan, Vol.43 No.5, p.1033-1038 (2012)

Author


Hirotaka KAWATSU


Ryosuke IBATA


Tetsuya KANEKO


Kenji NISHIDA

Simulation of Oil Separating Behavior for Engine Breather System

Makoto HAGA* Takumi KASAHARA**

ABSTRACT

The breather system of a reciprocating engine requires a function for separating the oil mist from the blow-by gas when ventilating the inside of the crankcase. Gas-liquid separation behavior inside the breather chamber is a complex phenomenon that involves liquid breakup and coalescence. Directly predicting this behavior by grid method, which is a typical numerical calculation method, is challenging, because the calculation grid deforms and moves excessively.

This study focused on a particle method suited to the analysis of complex fluid phenomena such as free surfaces and liquid breakup and coalescence, and attempted to predict the oil separating behavior of the breather chamber with the Moving Particle Semi-implicit method. An air resistance model was applied to accurately simulate particle motion based on the gas velocity field history that was calculated in advance by the grid method. In addition, a particle coarse-graining model was newly proposed to take into account the effect of air resistance on oil mist.

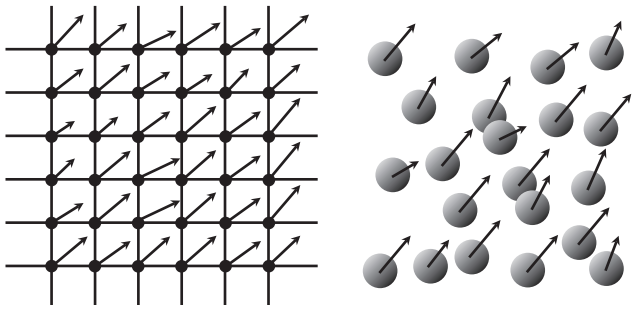
It was confirmed that the simulated oil scattering and separating behavior qualitatively agreed with the experimental results by high-speed camera, and that the oil separating behavior can be predicted by particle method.

1. Introduction

The inside of the crankcase of a reciprocating engine is filled with unburned gas and combustion gas (generally called “blow-by gas”) blown through from the combustion chamber. This produces issues such as increased pressure inside the crankcase that leads to oil leaks and the emission of atmospheric pollutants, dilution of the engine oil by the fuel and water vapor contained in the blow-by gas, and oil degradation by the NOx component in the gas. To address these issues, typical reciprocating engines are equipped with a breather system that ventilates the inside of the crankcase by discharging the blow-by gas to the intake manifold and taking fresh air into the crankcase. The blow-by gas contains large amounts of oil mist, and this mixing of oil to the intake manifold increases oil consumption, fouls the throttle valve and intake valve, and leads to a drop in emissions performance due to oil combustion. For these reasons, the breather chamber requires a function for separating the oil from the multiphase flow consisting of blow-by gas and oil mist.

Attempts have been made to predict and evaluate this oil separating function by the grid method, which is a typical numerical calculation method[(1), (2)]. However, dynamic behavior such as oil breakup and coalescence or oil adhered to the wall surfaces being carried away again by the gas flow is challenging to predict by calculation, because the calculation grid deforms and moves excessively. This means that there are still many unclear points regarding the oil separation behavior, and that all breather chamber specifications have not yet been determined by CFD.

This study focused on a particle method that calculates fluid motion using a Lagrangian approach by using particles to discretize the fluid without using a grid (Fig. 1). The



(a) Grid method (b) Particle method

Fig. 1 Concepts for grid and particle methods

* Automobile R&D Center

** Prometech Software, Inc.

particle method can directly extract the position of fluid using particles, so it is suited to analysis of complex fluids involving free surfaces, breakup and coalescence. This study used the fluid analysis software Particleworks[3] made by Prometech Software, Inc., which uses the Moving Particle Semi-implicit (MPS) method. In addition, an air resistance model, particle coarse graining model and surface tension model were introduced to create a method for analyzing the oil separating behavior inside the breather chamber.

2. Breather System

2.1. Overview of Breather System

Figure 2 shows an example of a breather system. Breather systems are also called Positive Crankcase Ventilation (PCV) systems, and ventilate the inside of the crankcase by using the negative pressure downstream from the throttle valve during partial load operation to discharge the blow-by gas to the intake manifold, and taking in fresh air from another passage upstream from the throttle. The blow-by gas flow rate is controlled by the PCV valve opening in accordance with the intake pressure. However, during idling or full-load operation the PCV valve is fully open, so the blow-by gas flows backward along the fresh air intake passage and is discharged to the intake manifold. In this case, the breather system has two blow-by gas discharge channels, and two breather chambers with oil separating functions are required.

2.2. Blow-by Gas and Oil Mist

The blow-by gas flow rate differs according to the engine displacement and the degree of piston ring and cylinder wear, and this flow rate can exceed 30 L/min for a 2 L inline 4-cylinder engine. The amount of oil mist contained in the blow-by gas differs greatly according to where the gas is taken from the engine, so the outlet port selection determines the amount of oil inflow to the chamber. The particle size of the oil mist in a gasoline engine has a distribution of approximately 1 μm to 10 μm.

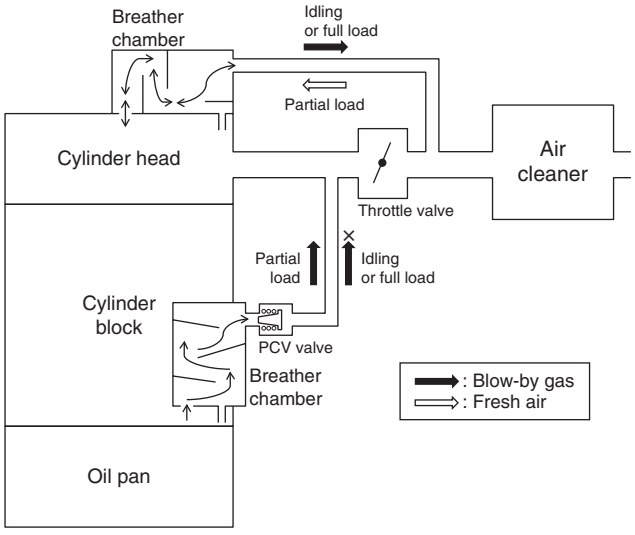


Fig. 2 Breather system

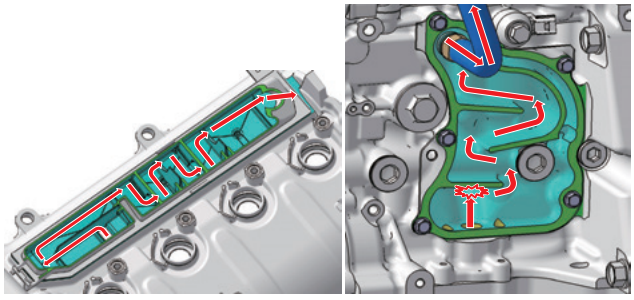
2.3. Oil Separation Methods

Oil separation methods are broadly divided into the labyrinth, impactor and cyclone types. Figure 3 shows examples of the labyrinth and impactor types. The labyrinth type has a long channel inside the chamber using partition plates and separates the oil mist by gravity as the gas flows along the channel. In contrast, the impactor type collides the gas with a collision plate and separates the oil mist using inertia. The cyclone type forms a swirling flow and separates the oil mist using centrifugal force.

3. Simulation Method

3.1. Overview of the MPS Method

The MPS method introduces semi-implicit algorithms for incompressible flows, and discretizes the governing equations by weighting the interactions between particles due to pressure and viscosity in accordance with the distance from particles existing within the effective radius r_e of the particle i shown in Fig. 4[4, 5]. The governing



(a) Labyrinth type (b) Impactor type

Fig. 3 Breather chambers

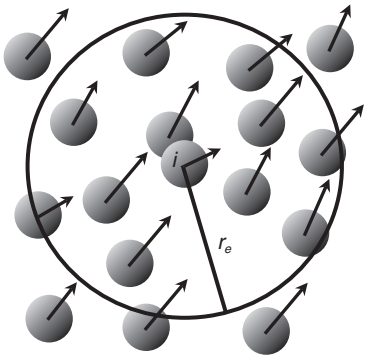


Fig. 4 Effective radius for MPS method

equations use the following equations described by the Lagrangian method. Equation (1) is an equation of continuity (Law of Conservation of Mass) and Eq. (2) is a Navier-Stokes equation (Law of Conservation of Motion).

$$\frac{D\rho}{Dt} = 0 \tag{1}$$

$$\frac{D\vec{u}}{Dt} = -\frac{\nabla P}{\rho} + \nu\nabla^2\vec{u} + \vec{g} \tag{2}$$

ρ: density, $\vec{u}$: velocity, P: pressure, ν: coefficient of kinematic viscosity
$\vec{g}$: gravitational acceleration, $\frac{D}{Dt}$: Lagrangian derivative

3.2. Application to Simulation of Oil Separating Behavior

The fluid inside the breather chamber is a gas-liquid multiphase flow consisting of blow-by gas and oil. In the particle method, when the behavior of fluids with greatly differing densities such as gas and liquid is calculated with particles, the pressure calculation becomes unstable[5]. Therefore, this study applied an air-resistance model to accurately simulate particle motion based on the gas velocity field history that was calculated in advance by the grid method. Figure 5 shows the simulation procedure. In addition, a particle coarse graining model and surface tension model were also introduced to enhance the particle behavior calculation accuracy. The contents of each model are described below.

3.2.1. Air-resistance model

In the air-resistance model, the particles move while satisfying the following Navier-Stokes equation Eq. (3), which adds a drag term to Eq. (2).

$$\frac{D\vec{u}}{Dt} = -\frac{\nabla P}{\rho} + \nu\nabla^2\vec{u} + \vec{g} - \frac{1}{m}\vec{D} \tag{3}$$

m: liquid mass, $\vec{D}$: drag

$\vec{D}$ is defined as shown by Eq. (4) below.

$$\vec{D} = \frac{C_D}{2}\rho_{air}\left|\vec{u}_l - \vec{u}_g\right|(\vec{u}_l - \vec{u}_g)\,S \tag{4}$$

C_D: coefficient of drag, ρ_{air}: mass density of air, $\vec{u}_l$: liquid velocity
$\vec{u}_g$: gas velocity, S: Liquid body surface area

3.2.2. Particle coarse graining model

In order to accurately calculate the motion of the oil mist, the size of the calculation particles (hereafter, "MPS particles") used by the MPS method should be the same as the particle size of the oil mist (1 μm to 10 μm). However, this would require a vast number of particles relative to the inflow oil volume, making it unlikely that results could be obtained within a practical period of time. In consideration of practicality, the particle size of MPS should be set to approximately 250 μm to 500 μm. Therefore, this study coarse grained the MPS particles as grouped droplets so that the effect of air resistance on the MPS particles is the same as that on the oil mist. Figure 6 shows a concept drawing of coarse graining. The relationship between the sizes of the coarse-grained MPS particles and the oil mist particles is as follows.

$$R_{cg} = \frac{D_l}{d_l} \tag{5}$$

$$N = R_{cg}{}^3 \tag{6}$$

R_{cg}: coarse graining ratio, D_l: particle size of MPS, d_l: particle size of oil mist
N: number of grouped droplets

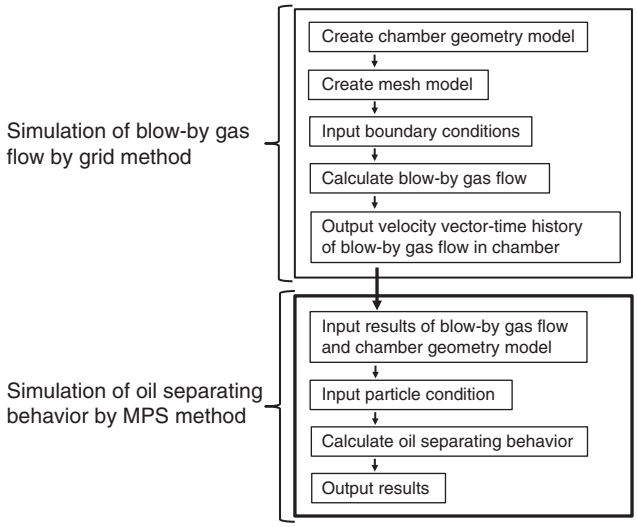


Fig. 5 Flowchart of simulation

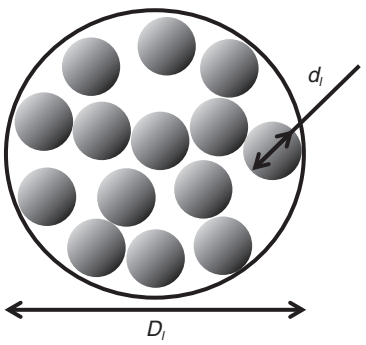


Fig. 6 Coarse graining model

In addition, the coefficient of drag C_D in Eq. (4) is given by Eq. (7) and Eq. (8) below[6].

$$Re = \frac{d_l \left| \vec{u}_l - \vec{u}_g \right|}{\nu_g} \tag{7}$$

$$C_D = \begin{cases} \dfrac{24}{Re}\left(1 + \dfrac{Re^{2/3}}{6}\right) & Re \le 1000 \\ 0.424 & Re > 1000 \end{cases} \tag{8}$$

Re: Reynolds number, ν_g: coefficient of kinematic viscosity of the gas

The air-resistance force applied to the coarse-grained MPS particles is the resultant force of the forces applied to N number of grouped oil mist particles, and the MPS particles move while satisfying Eq. (9) below.

$$\frac{D\vec{u}}{Dt} = -\frac{\nabla P}{\rho} + \nu \nabla^2 \vec{u} + \vec{g} - \frac{R_{cg}{}^3}{m_l} \vec{D} \tag{9}$$

m_l: oil mist mass

3.2.3. Surface tension model

A surface tension potential model was introduced to take into account the influence of the surface tension of the liquid in the gas-liquid separation process. Particles influenced by surface tension move while satisfying the following Navier-Stokes equation Eq. (10).

$$\frac{D\vec{u}}{Dt} = -\frac{1}{\rho} \nabla P + \nu \nabla^2 \vec{u} + \vec{g} + \nabla \Phi \tag{10}$$

The fourth term in Eq. (10) is the surface tension term of the potential model, and is calculated as shown by Eq. (11) and Eq. (12) below.

$$\nabla \Phi = \sum_{j \neq i} \frac{d\varphi}{dr_{ij}} \cdot \frac{\vec{r}_{ij}}{\left| \vec{r}_{ij} \right|} \tag{11}$$

$$\Phi = C\varphi \tag{12}$$

i, j: particle numbers, $\vec{r}_{ij}$: position vector from particle i to particle j

φ expresses the potential energy, and uses an original Prometech Software equation.

C is the potential coefficient that determines the size of the potential force, and the value is proportional to the coefficient of surface tension of the liquid.

In addition, the wettability between the particles and the wall surfaces was taken into account by using the potential coefficient C_{fs} in Eq. (13) below.

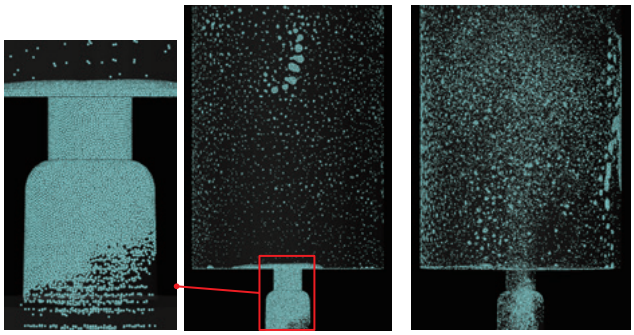
$$C_{fs} = \frac{1}{2}(1 + \cos\theta)\, C \tag{13}$$

θ: contact angle

3.3. Necessity of the Coarse-Graining Model

In order to verify the coarse-graining model, MPS particles with coarse graining not performed ($R_{cg} = 1$) and with the coarse graining ratio R_{cg} set to 100 were flowed into a simple shape chamber for which the gas flow was calculated in advance, and the particle behavior was compared. The initial interparticle distance (particle size of MPS) was 500 μm. Figure 7 shows the simulation results. When coarse graining is not performed ($R_{cg} = 1$), the MPS particles are equivalent to a 500 μm oil mist, which is larger than the particle size of the actual oil mist (1 μm to 10 μm). As a result, changes of the particle velocity due to air resistance were small, and the particles gradually cohered due to the surface tension and completely obstructed the inlet hole at the 0.5 s mark. In contrast, when the coarse graining ratio R_{cg} is 100, the effect of air resistance on the MPS particles is the same as that for a 5-μm equivalent oil mist, so the particles scattered inside the chamber without obstructing the inlet hole.

Based on the above results, the coarse-graining model was determined to be necessary in order to calculate the behavior of the oil mist in the blow-by gas. Therefore, subsequent calculations presuming a breather chamber were performed with the coarse-graining ratio set to $R_{cg} = 50$ and $R_{cg} = 100$, which are equivalent to oil mist particle sizes of 10 μm and 5 μm, respectively.



(a) $R_{cg} = 1$ [at 0.5 s] (b) $R_{cg} = 100$ [at 0.5 s]

Fig. 7 Comparison of particle movement between $R_{cg} = 1$ and $R_{cg} = 100$

4. Simulation of Oil Separating Behavior

4.1. Simulation Conditions

4.1.1. Simulation subject

In this study, the impactor-type separator of the breather chamber built into the cylinder block was selected as the simulation subject. Evaluation testing of the oil separation performance of the breather chamber was performed using the size of the blow-by gas inlet hole and distance to the first collision plate of an actual chamber as parameters,

Table 1 Specifications of breather chambers

Breather chamber	TYPE 1	TYPE2
Oil separation performance	Good	Poor
Volume [cm^3]	215	
Distance to first collision plate from inlet hole [mm]	30	15
(1) Blow-by gas inlet hole		
Diameter [mm]	15	6
(2) Blow-by gas outlet hole		
Diameter [mm]	7	
(3) Connecting channel to cylinder head		
Diameter [mm]	7	
(4) Oil drainage holes		
Diameter [mm]	8	

and two specifications with markedly different separation performance were compared. Figure 8 and Table 1 show the appearance and specifications of the compared chambers. TYPE1 has an inlet hole size of ϕ15 mm and a distance of 30 mm from the inlet hole to the first collision plate. TYPE2 has an inlet hole size of ϕ6 mm and a distance of 15 mm from the inlet hole to the first collision plate.

4.1.2. Calculation of the blow-by gas flow by the grid method

The gas flow inside the chamber was calculated by the grid method in order to calculate particle motion based on the gas velocity field history in the air-resistance model. The calculations applied the same conditions as the operating condition of an engine speed of 6000 rpm at which the maximum blow-by gas flow rate of 40 L/min was measured in the oil separation performance verification tests. The pressure pulsation inside the crankcase was set as the boundary condition for the gas inlet hole (1), atmospheric pressure was set as the boundary condition for the gas outlet hole (2) that was left open to the atmosphere during the tests, and the pressure pulsation inside the cylinder head was set as the boundary condition for the connecting channel (3). The oil drainage holes (4) connect into the oil in the oil pan, so a boundary condition was not set. Figure 9 shows the simulation results by the grid method. The gas periodically flowed into the chamber due to pressure pulsation, and the maximum collision velocity to the collision plate was 30 m/s for TYPE1 and 40 m/s for TYPE2. These results were input to Particleworks as the boundary conditions for the air-resistance model.

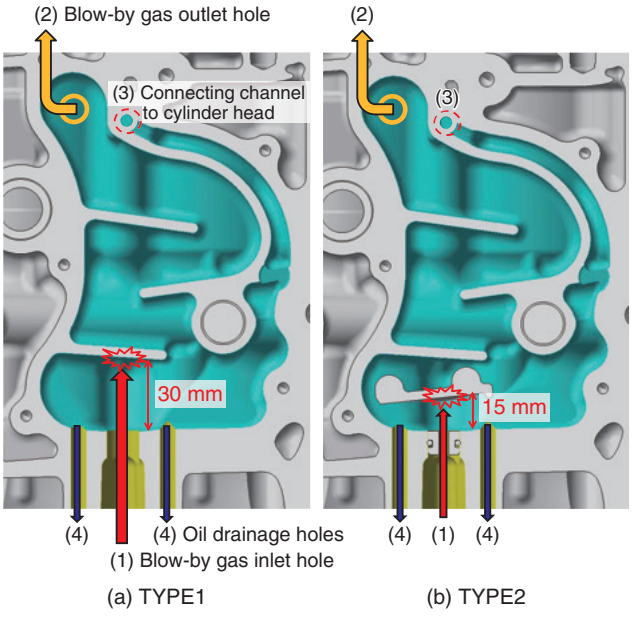


Fig. 8 Schematic of measured breather types

4.1.3. Simulation conditions for the particle method

The oil mist flow rate was assumed to be 1% of the volumetric flow rate of the blow-by gas, and the conditions were set so that MPS particles equivalent to that flow rate flowed into the chamber from the inlet hole (1) synchronized with the gas inflow speed. In addition, the coefficient of kinematic viscosity, coefficient of surface tension and contact angle of the oil at 80°C were input as the physical property values of the MPS particles. The particle size of MPS was 500 μm, and calculations were performed using the two conditions of a coarse graining ratio R_{cg} of 50 (equivalent to an oil mist particle size of 10 μm) and 100 (equivalent to 5 μm).

4.2. Simulation Results

4.2.1. Particle behavior

Figure 10 shows the behavior of the MPS particles in TYPE1 with a coarse graining ratio R_{cg} of 100. The MPS particles are indicated by velocity vectors, and the numbers in the figures correspond to the pressure pulsation phases in the graph above. The particles periodically flowed into the chamber and collided with the collision plate due to the effects of the gas flow that fluctuates in accordance with the pressure pulsation inside the crankcase.

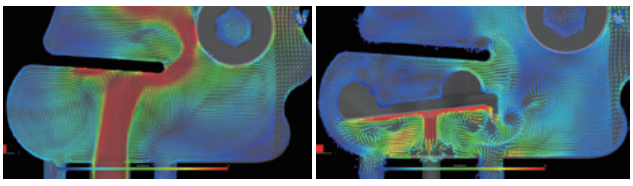


Fig. 9 Simulation results of flow in breather chamber by grid method

Figure 11 shows the behavior of the particles near the collision plate in TYPE1 and TYPE2. The arrows in the figures show the flow of the particles adhered to the wall surfaces. In TYPE1, the particles that collided with the collision plate were separated from the main gas flow and adhered to the right and left wall surfaces of the chamber. In particular, direction of movement of the particles from the right end of the collision plate was periodically changed by the influence of the pressure pulsation. In addition, the particles adhered to the right and left wall surfaces flowed along the wall surfaces toward the bottom of the chamber, forming a flow toward the oil drainage holes. In contrast, in TYPE2 it was confirmed that particles near the oil drainage holes were blown about by the gas flow, and in particular the particles adhered on the right wall surface did not flow toward the bottom of the chamber due to the effect of the gas flow deflected by the collision plate. Instead, the particles were blown upward again by the gas flow and flowed toward the downstream of the chamber. That is to say, TYPE2 can be judged to have a structure that makes it easy for separated oil to again become caught up in the airflow.

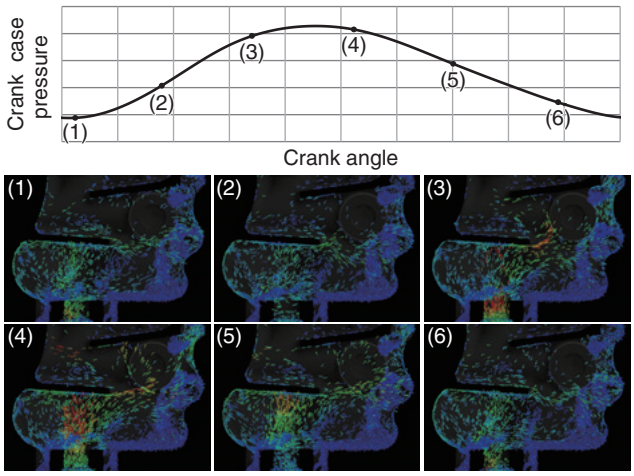
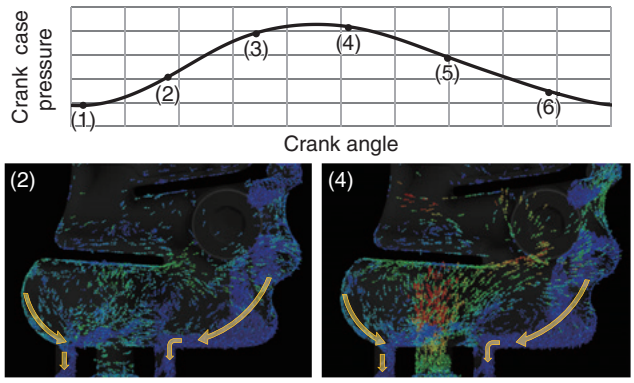


Fig. 10 Simulation results by MPS method [TYPE1, $R_{cg} = 100$]



(a) TYPE1

(b) TYPE2

Fig. 11 Velocity vectors of MPS particles [$R_{cg} = 100$]

4.2.2. Differences in particle behavior by coarse graining ratio

Figure 12 shows the simulation results for a coarse graining ratio R_{cg} of 50 and 100 in TYPE1. Comparison of the particle behavior due to the difference in the coarse graining ratio showed that the particles scattered farther downstream when $R_{cg} = 100$, which corresponds to a 5-μm oil mist, and differing tendencies were also seen in the proportion of particles flowing to the right and left oil drainage holes.

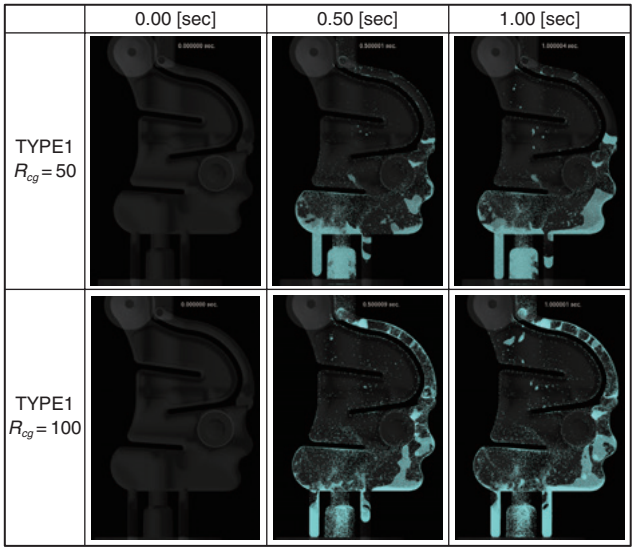


Fig. 12 Comparison of particle movement between $R_{cg} = 50$ and $R_{cg} = 100$

5. Verification and Examination of Simulation Results

5.1. Verification of Simulation Results by Actual Breather Chamber Visualization Tests

Actual breather chamber visualization tests were performed to verify the simulation results. The insides of the chambers were imaged for visualization by a high-speed camera while operating at an engine speed of 6000 rpm,

which is the same as the analysis condition at which a blow-by gas flow rate of 40 L/min was measured. The frame rate was 15000 fps and the shutter speed was 1/30000 s.

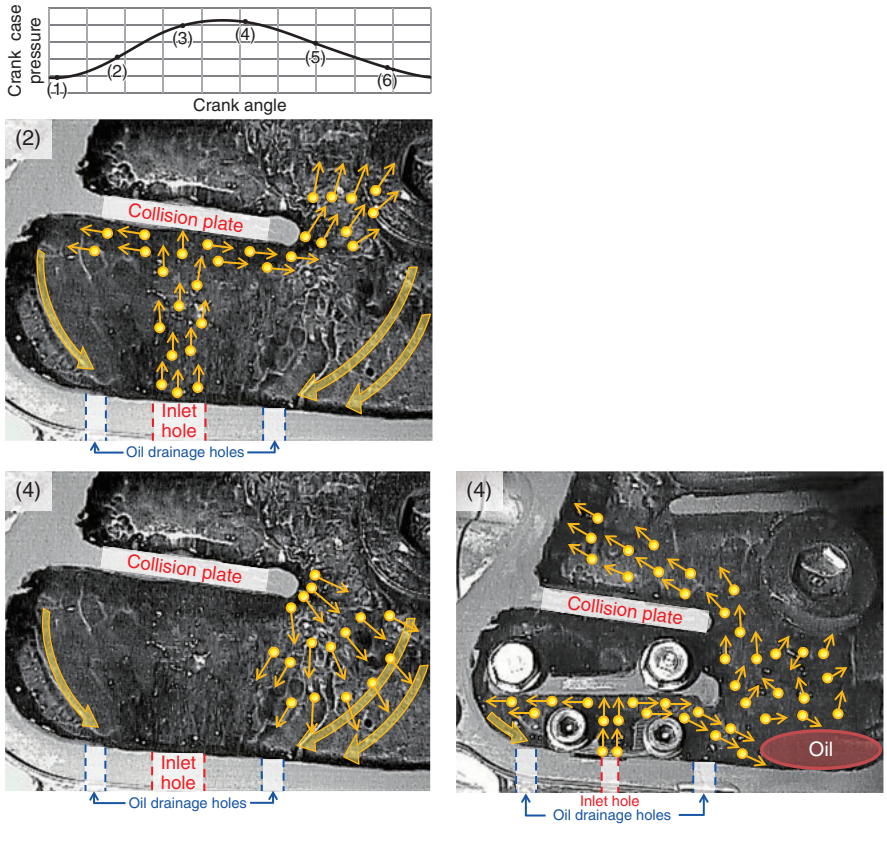
Figure 13 shows images of the visualization results with schematics representing the characteristic oil behavior. The numbers in the figures correspond to the pressure pulsation phases in the graph above. The oil mist was observed to periodically flow into the TYPE1 chamber, collide with the collision plate and scatter due to the pressure pulsation produced by volumetric changes inside the crankcase. In particular, due to the influence of changing direction of the gas flow by pressure pulsation, oil scattering direction at the right end of the collision plate was observed to change periodically. In addition, the oil adhered to the right and left wall surfaces of the chamber was observed to gradually fall toward the bottom of the chamber due to gravity. These tendencies agreed with the simulation results for both coarse graining ratios of 50 and 100.

On the other hand, although the oil mist was also observed to periodically flow into the TYPE2 chamber in the same manner as TYPE1, the oil was confirmed to accumulate and form a liquid lump at the bottom right of the chamber. This liquid lump did not flow toward the oil drainage holes due to the gas flow deflected by the collision plate, and was instead observed to be blown upward by the airflow, with part flowing toward the downstream of the chamber. Liquid lump formation was not observed in the simulation results for TYPE2, but a similar tendency was confirmed where the particles adhering to the right wall surface of the chamber accumulated without flowing toward the oil drainage holes, and the accumulated particles were blown upward again by the airflow and flowed to the downstream of the chamber. Therefore, the simulation results are thought to simulate the initial stage of liquid lump formation.

The above results showed that the simulated macroscopic oil behavior inside the breather chamber qualitatively agrees with experimental results. This confirmed that the macroscopic oil separating behavior inside a breather chamber can be predicted by introducing an air-resistance model, coarse-graining model and surface tension model to the MPS method.

5.2. Prediction of Oil Mist Behavior for Different Particle Sizes

The oil separation performance is thought to be affected by the particle size of the oil mist. Therefore, the total number of inflow particles and separated particles were



(a) TYPE1 (b) TYPE2

Fig. 13 Results of visualized measurement

counted for a coarse graining ratio R_{cg} of 50 (equivalent to an oil mist particle size of 10 μm) and 100 (equivalent to 5 μm), and the behavior of oil mists with different particle sizes was analyzed based on the results of calculations up to 1.0 s performed in this simulation. Figure 14 shows the inlet flow rate and separation flow rate time histories calculated from the number of inflow particles and the number of particles falling toward the right and left oil drainage holes for a coarse graining ratio R_{cg} of 50 and 100. Comparison of the inlet flow rate histories shows that a greater number of particles flow into the chamber when R_{cg} = 100, which corresponds to a 5-μm oil mist. This indicates that oil mist with a small particle size tends to easily flow into the chamber, and oil mist with a large particle size tends to be easily separated in the upstream region of the chamber (red frames in the figures). In addition, comparison of the flow-rate histories of the right and left oil drainage holes shows that more particles are separated from the left oil drainage hole when R_{cg} = 50, which corresponds to a 10-μm oil mist. This indicates that oil mist with a large particle size tends to collide with the collision plate, scatter toward the left side of the chamber and become separated from the main gas flow.

It is thought that the behavior of oil mists with different particle sizes can be analyzed by using the coarse graining ratio as a parameter as shown above. Thus, use of the developed method enables investigation of chamber structures in accordance with the particle size of the target oil mist.

6. Conclusion

A method based on the particle method was created for predicting the oil separating behavior of a breather system that was a challenge to analyze using the grid method, which is a typical numerical calculation method. The following results were obtained.

(1) A calculation method was created by introducing an air-resistance model, particle coarse-graining model and surface tension model to the MPS method as a means for predicting the oil separating behavior of a breather system.

(2) The simulated oil scattering and separating behavior inside the breather chamber qualitatively agreed with the experimental results by high-speed camera.

(3) The behavior of oil mists with different particle sizes can be analyzed by using the coarse graining ratio as a parameter. This enables investigation of chamber structures in accordance with the particle size of the target oil mist.

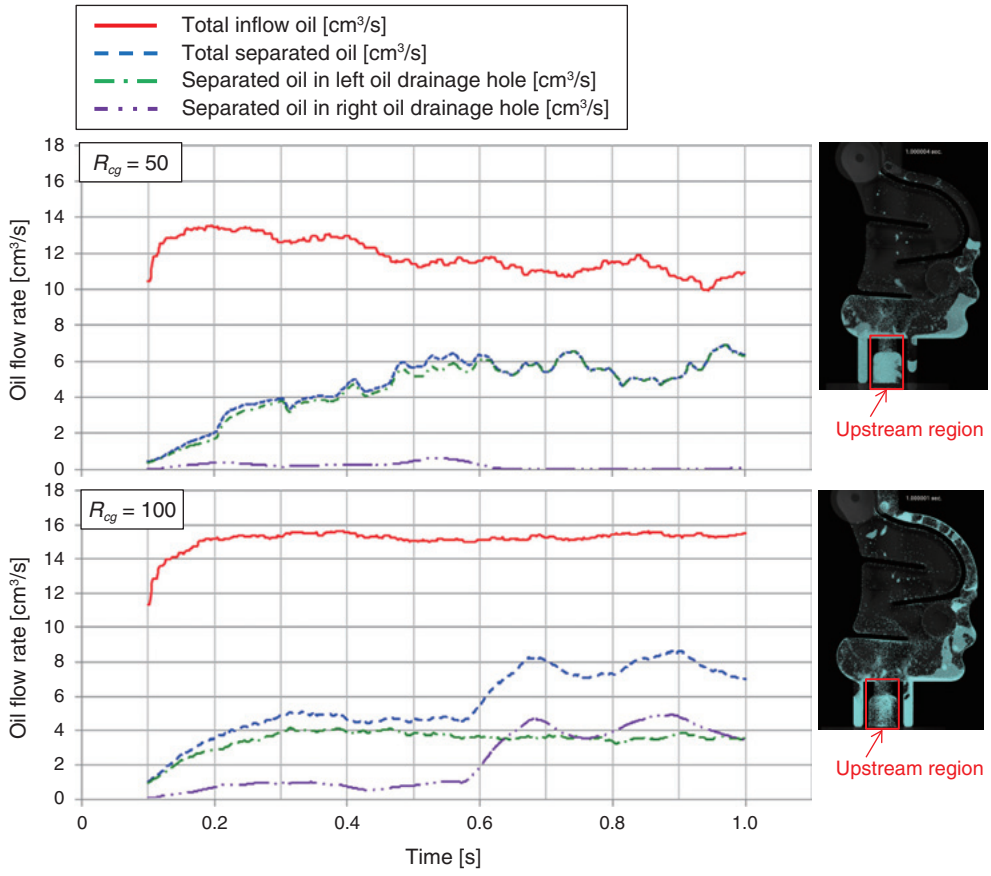


Fig. 14 Comparison of oil flow rate between R_{cg} = 50 and R_{cg} = 100

7. Afterword

Future plans include modeling the wall impact behavior of micro-droplets and the creation of analysis techniques that reflect the particle size distribution of the oil mist in order to quantitatively predict the oil separation capability.

Reference

(1) Satoh, K., Ishikawa, M., Matsuoka, T.: Development of Method of Predicting Efficiency of Oilmist Separator, Transactions of Society of Automotive Engineers of Japan, Vol. 30, No. 2, p. 75-80 (1999) (in Japanese)
(2) Endo, K., Kobayashi, A., Sudo, M.: The Development and Realization of Compact Oil Mist Separator with High Performance, JSAE Annual Congress Proceedings, No. 62-07, p. 13-16 (2007) (in Japanese)
(3) http://www.prometech.co.jp/particleworks.html
(4) Koshizuka, S.: Numetrical Analysis of Flow using Particle Method, Nagare 21, p. 230-239 (2002) (in Japanese)
(5) Koshizuka, S.: Particle Methods (Computational dynamics lecture series), The Japan Society for Computational Engineering and Science, Maruzen Publishing Co., Ltd, 156p. (2005) (in Japanese)
(6) Takagi, M.: The Present Situation and Issue on Fuel Spray Simulation, Papers of National Maritime Research Institute, Vol. 8, No. 2, p. 209-214 (2008) (in Japanese)

■ Author ■



Makoto HAGA



Takumi KASAHARA

Model-Based Development Technologies to Support Increasingly Complex Power Train Systems

Hidekazu ARAKI* Kanako SAITO* Ryosuke OHGUCHI*
Masayuki FUNAKOSHI* Kensuke YAMAMOTO*

ABSTRACT

In order to support power train systems as they become increasingly complex, as well as to raise the efficiency and quality of development, it is useful to (1) clearly define requirements and verification items, (2) structure requirements and clearly define interfaces, and (3) assure the traceability of requirements.

The present research project used Systems Modeling Language, which is a semi-formal notation. By formulating the project's own original guidelines, the above three items were achieved.

Requirement models written in Systems Modeling Language are also published to suppliers as requirement specifications for the platform area of the power train electronic control unit. Therefore the tasks involved in efficiently and accurately verifying not only the validity of the requirements, but also whether or not problems exist in how they are written as requirement specifications, were defined and applied in parts to the development of 2015 model year mass-production models.

1. Introduction

Automobile power train control systems have tended to increase in scale and complexity in recent years. The following initiatives are being pursued in the automobile industry as a whole, as manufacturers approach a balance between increased development efficiency and quality.

The first, as shown in Fig. 1, is an initiative to achieve control development that results in less reworking. This approach here is to confirm the validity of control specifications at the specification design stage of the power train electronic control unit (PT-ECU) development process. After that, the work moves on to the implementation process, thus achieving control development that results in fewer returns. In order to confirm the validity of control specifications at the specification design stage, the control requirements must be formed into a hierarchy, as in Fig. 2, and the validity of the control requirements must be verified at each level.

The second is the initiative to make use of simulations to confirm the validity of the control specifications at the specification design stage. In order to implement simulations at the specification design stage before software is created, it is necessary to model the controlled objects and control algorithms. It is also essential to assure traceability among requirements, verification items, and control algorithms, which involves ascertaining what requirements a control algorithm is tied to, and determining which verification items need to be satisfied in order to judge it valid.

The third is the initiative to design control software in a form that is in conformity with the Automotive Open System Architecture (AUTOSAR)[(1)] standard specification for automotive software. Together with the software architecture shown in Fig. 3, the interface between architectures is also specified in AUTOSAR. By designing software architectures and interfaces

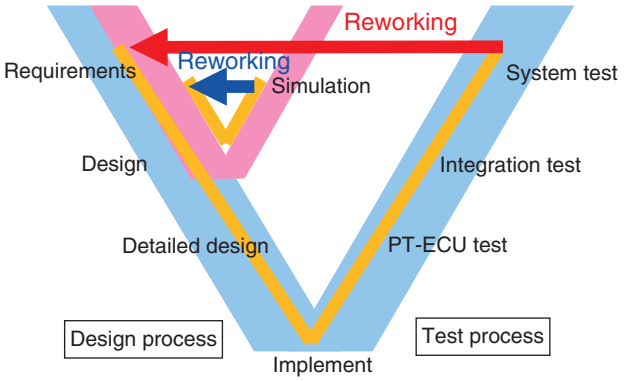


Fig. 1 V-model

* Automobile R&D Center

between architectures in forms that are in conformity with the standard, the control software can be made more reusable. However, there are differences between Honda's existing software architecture and AUTOSAR software architecture. As a result of this, when PT-ECU suppliers implement software in conformity with AUTOSAR, the large amount of time taken to bring the Honda software architecture and AUTOSAR standards into compatibility became an issue. It was reasoned that this issue could be effectively addressed by structuring requirements in light of the AUTOSAR standards and deciding on an interface between architectures.

The present research project took the initiatives described above into consideration and examined the creation of the methods described below as a means of heightening the reusability of control software in development of mass-production models from the 2016 model year on, and achieving control development with less reworking.

(1) Methods for placing control requirements in a hierarchy and validating them using Systems Modeling Language (SysML)
(2) Method for confirming the validity of requirements by Model in the Loop Simulation (MILS)
(3) Method for structuring software that takes AUTOSAR standards into account

2. Construction of a Method for Placing Control Requirements into a Hierarchy and a Method for Confirming Validity of Control Requirements Using SysML

SysML is a modeling language that demonstrates its effectiveness when bringing a system to realization. Since it can be applied to the development of system specifications, for analysis and design, and to the validation and verification of a system, it is widely used today in the automotive, aerospace, telecommunications, and other such fields[2].

In the present research, methods using SysML to place control requirements into a hierarchy and to confirm the validity of control requirements were created for use with the control requirements included in the platform area in Fig. 4.

2.1. Method for Placing Control Requirements into a Hierarchy Using SysML

In forming the hierarchy in Fig. 2, the levels were defined as follows.

Level 1 is the level where the primary control requirements of the functions that are to be achieved become clearly defined, together with the interfaces between those functions and other functions. Even if such

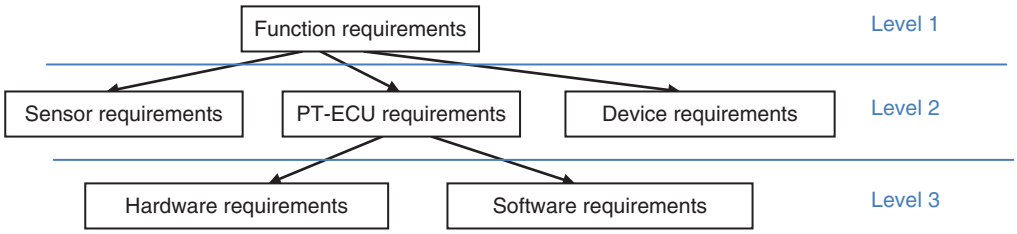
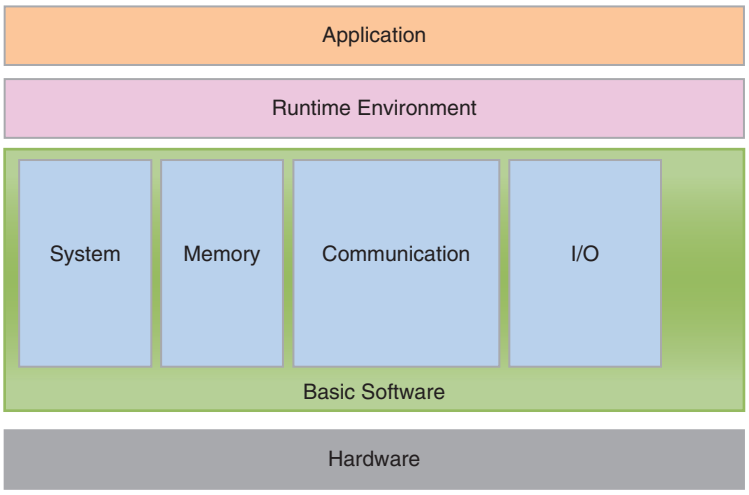


Fig. 2 Hierarchy of control requirements



I/O: Input Output

Fig. 3 AUTOSAR software architecture

component elements as the PT-ECU, sensors, and devices are reconsidered, the control requirements and interfaces at this level do not change.

Level 2 is the level where it is clearly defined what PT-ECU, sensors, and devices are to be used and how they are to detect and operate. At this level, the control requirements to be achieved by the PT-ECU, the control requirements to be achieved by the sensors, and the control requirements to be achieved by the devices are clearly defined. The interface between the PT-ECU and the sensors and devices is also clearly defined at this level.

Level 3 is the level where the control requirements to be achieved in software and the control requirements to be achieved in hardware, as well as the data that is handled in software and hardware transactions, are all finally determined.

Taking the ease of verification of each level into consideration, the structure of each level is determined so as to have the minimum number of output signals. In Fig. 5, for example, Structure A has four inputs. When each input is expressed as ON or OFF, the test pattern exists in 2^4=16 varieties. If Structure A can be divided into Structure A-1 and Structure A-2, then the test pattern can be reduced to $2^2 \times 2$=8 varieties, making verification easier.

The control requirements that are assigned to each structure have the operation requirements for the structure stated in natural language. The seven category types shown in Table 1 were defined so that the control requirements can be isolated exhaustively.

Table 1 Category types

No.	Category type
1	Operation
2	Safety
3	Market value
4	Regulation
5	Design policy
6	Diagnosis
7	Quality

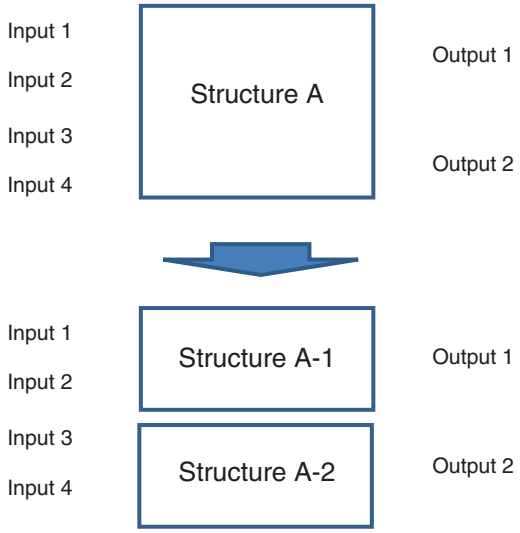


Fig. 5 Division of structure

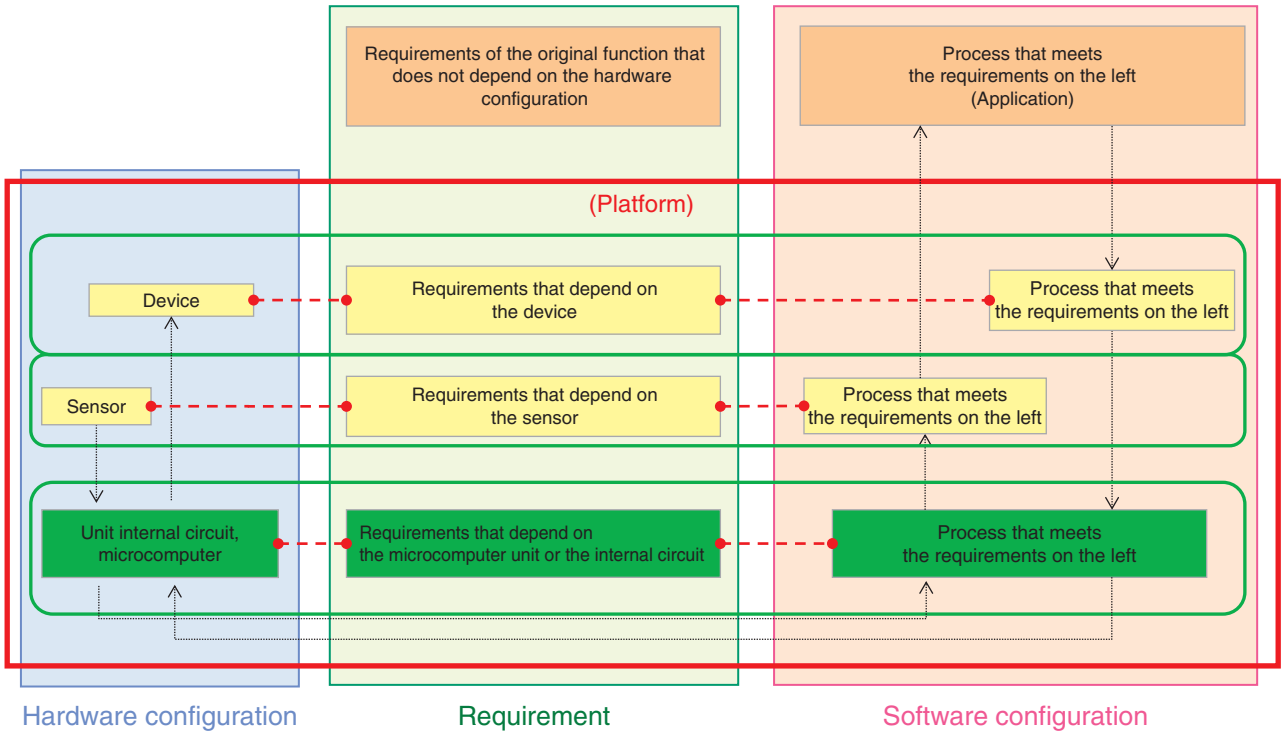


Fig. 4 Platform area

Table 2 Listed items of verification items

No.	Item	Provisions
1	Preconditions of tests	Required test conditions for verification
2	Parameters for test condition	Parameters and their values that correspond to the required test conditions for verification
3	Pre-state	State of the function before testing
4	Operating parameters and volume	Parameters that trigger transition to post-state, and the volume to operate
5	Post-state	State of function after testing
6	Measurement parameters	Measurement parameters that are subject to verification
7	Judgment criteria	Expected value of measurement parameters

2.2. Method for Confirming the Validity of Control Requirements

In order to clarify the criteria for judging whether or not control requirements are being met, one or more verification items are created for each control requirement. The verification items are used as judgment criteria for confirming the validity of the control specifications by means of the MILS or prototype at the specification design stage. In addition to that, they are used as judgment criteria for conformity verification at the ECU testing stage. Anticipating that verification will be automated in the future, the seven items shown in Table 2 were specified to be listed when creating verification items.

Given the above, the diagrams shown in sections 2.2.1 to 2.2.4 are created for each level.

2.2.1. Creation of criterional requirement diagrams

As shown in Fig. 6, the criterional requirement diagram (CRD) records the structure, control requirements, and verification items together with their respective traceability information.

2.2.2. Creation of block diagram

As shown in Fig. 7, the block diagram (BD) records the structures included in that level together with traceability information in relation to upper-level structures. Consequently, a BD is not created for Level 1, which is the uppermost level.

2.2.3. Creation of internal block diagram

As shown in Fig. 8, the internal block diagram (IBD) records the flow of data between lower-level structures.

This approach facilitates the distinction between a variable that concludes within a function and an interface with another function during the influence analysis and safety analysis that are conducted when specifications are changed.

2.2.4. Creation of requirement diagram

As shown in Fig. 9, the requirement diagram (RD) records the traceability information in relation to control requirements included in that level and upper-level control requirements. Consequently, an RD is not created for Level 1, which is the uppermost level.

The definitions for placement into a hierarchy, category types for extraction of requirements, items listed when creating verification items, and method of writing the diagram are determined. The traceability of requirements

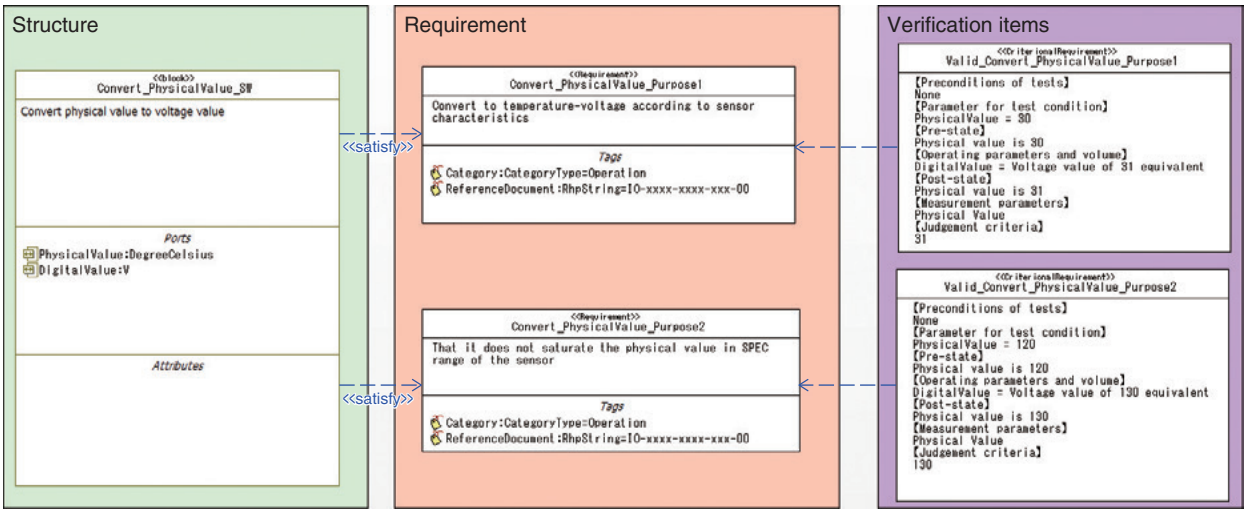


Fig. 6 Criterional requirement diagram

between levels, traceability of structures between levels, and the traceability information for structures, requirements, and verification items at each level are clearly defined. This enables validation of the control requirements.

The present research aimed to enable application of control requirement placement in a hierarchy and confirmation of control requirement validity to 2016 model year mass-production models by using content written in SysML as system design requirement specifications. To that end, it carried out anticipatory application to 2015 model year mass-production models, identified issues, and implemented measures to address them.

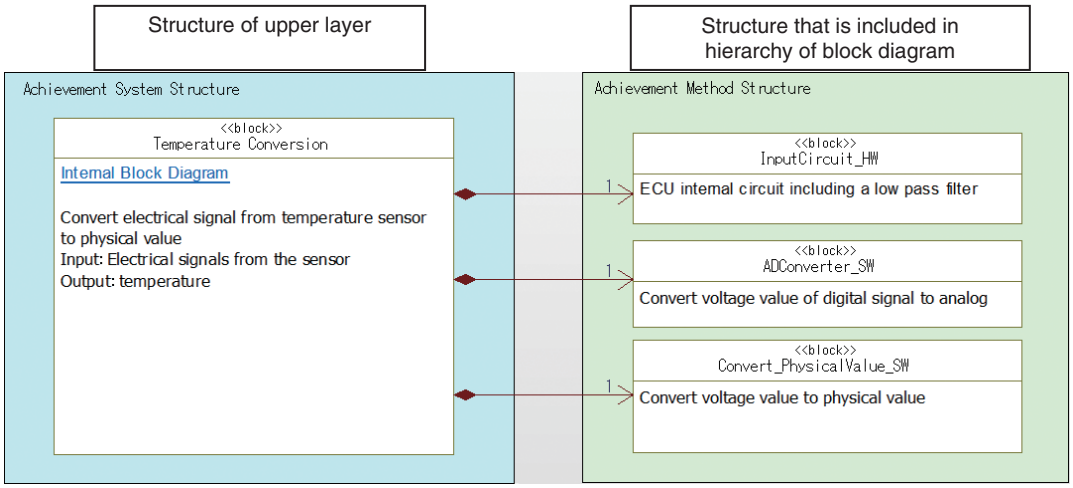


Fig. 7 Block diagram

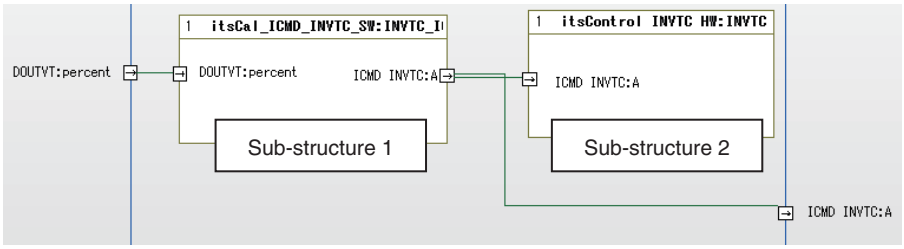


Fig. 8 Internal block diagram

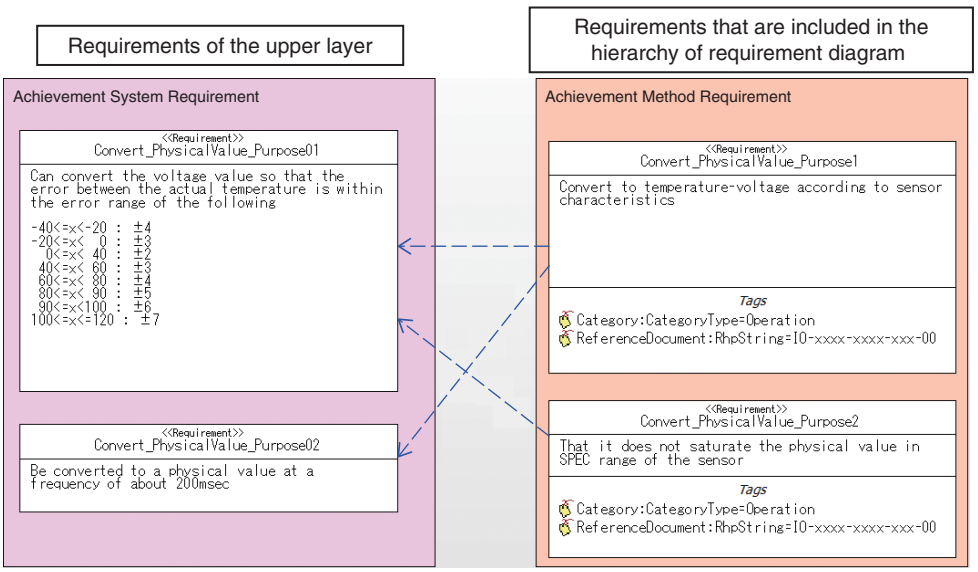


Fig. 9 Requirement diagram

3. Method for Confirming the Validity of Requirements Using MILS

In order to reduce reworking from development and to increase development efficiency, it is necessary to verify the validity of control requirements and increase the accuracy of requirements before conducting PT-ECU hardware development or software development. The method chosen for this is to implement operation verification by MILS with a Simulink model.

3.1. Creation of Simulink Model for Platform Verification

The ECU operation verification of the platform is implemented with the configuration shown in Fig. 10 in order to verify PT-ECU operation using input from sensors and output to devices.

MILS is a method of verification that models actual sensors and devices and performs desktop simulation of electronic control unit software operation.

The Simulink model shown in Fig. 11 was created for the implementation of MILS on the platform in the present research.

The plant model in the figure corresponds to sensors, devices, and so on. The controller model corresponds to control requirements. The test model corresponds to input from other systems. The input-output (I/O) model corresponds to the input-output circuits of the ECU.

3.2. Test Pattern Creation and Verification

The controller model, which is the test object, is made up of a sensor malfunction detector, a device malfunction detector, a sensor controller, and a device controller. Each part has to be verified. Platform verification is conducted in two sections: the basic operation verification and the malfunction detection verification.

(1) In basic operation verification, input values (target values) received from other systems are dynamically changed as shown in Fig. 12. The values output by the PT-ECU output unit relative to the input values go through verification to make certain they are valid values that match with the listed verification items.

(2) In malfunction detection verification, malfunctions due to sensor and device open circuits, ground faults, short circuits, etc. are simulated in the model. The value of the platform malfunction detection status is then verified to make certain it is a valid value that matches with the listed verification item.

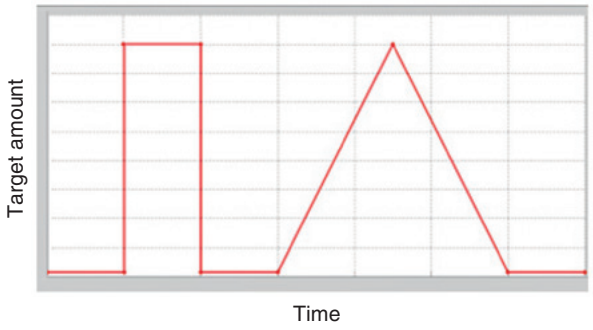


Fig. 12 Simulation test pattern

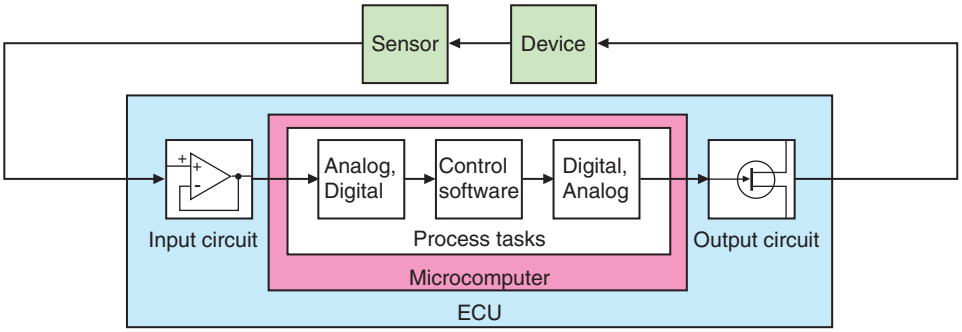


Fig. 10 Real-world environment

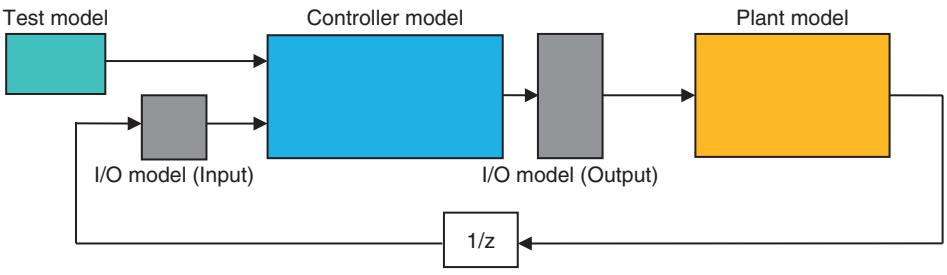


Fig. 11 Virtual environment

The validity of requirement specifications can be confirmed by unit of system function of the platform through MILS using the Simulink model.

The present research confirmed the usefulness of MILS and the issues involved by applying it to new device development in the 2015 model year. This was anticipatory application performed so that validation by MILS can be applied to the development of new devices from the 2016 model year on.

4. Method for Structuring Software with Consideration for AUTOSAR Standards

Overviews of the various parts of the AUTOSAR architecture shown in Fig. 3 are given below.

The application is PT-ECU hardware-independent software. It is positioned as an area of competition among automotive manufacturers.

The runtime environment is software that abstracts connections among sensors, devices, PT-ECU internal circuits, and microcontrollers, so that even if this hardware configuration changes, the interface between applications as well as the interface between applications and the basic software (BSW) will not change.

The BSW is software that changes the program due to changes in the microcontroller or the PT-ECU internal circuits. It is configured as internal functional modules that can be plugged in and unplugged to match the hardware configuration, so that it can be more reusable.

4.1. Platform Function Categories

In order to overcome the issue of the large amounts of time taken to bring Honda's existing software architecture and AUTOSAR standards into compatibility, the platform functions were divided into the six groups shown in Fig. 13.

Overviews of the various groups are given below.

The scheduler in the figure performs PT-ECU task control.

The on-board diagnosis and regulation executes self-diagnosis of the on-board computer and generates data for legal compliance.

The memory performs management of non-volatile data.

The controller area network implements communication to and from other units.

The off-board tester implements communication to and from external diagnostic equipment.

The I/O implements electronic control unit input and output.

4.2. Interface that Takes AUTOSAR Standards into Account

In creating software specifications for the platform functions included in each group, the meaning of the interface published to an application is made to conform to the interface provided to applications by the functional module in AUTOSAR that is matched to each group. The interface name is generated as a combination of standard abbreviations used in the automotive industry.

The measures in section 4.1 and section 4.2 not only facilitate the plugging in and unplugging of software matched to the hardware configuration; they can also make software more reusable, for example by mitigating the burden of work on interface compatibility with applications when PT-ECU suppliers implement platform software in conformity with AUTOSAR.

In the present research, software specifications that support new architecture were created and partially

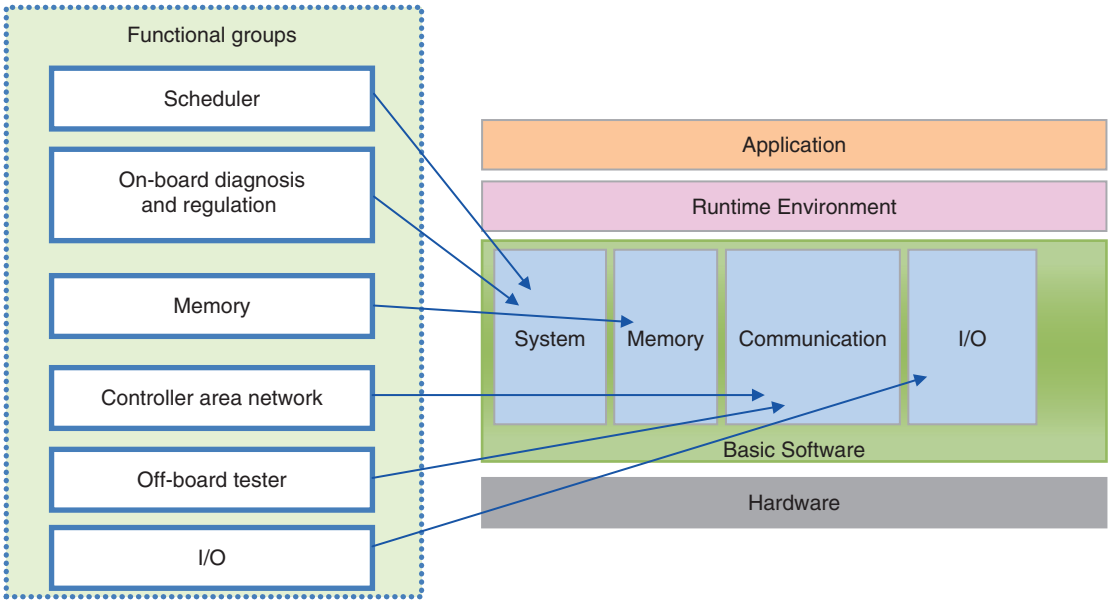


Fig. 13 Linkage of functional groups and AUTOSAR structure

applied to 2015 model year mass-production models. The objective is to make all software architecture for platform functionality transposable into new architecture in the 2016 model year mass-production models.

5. Application to Development of 2015 Model Year Mass-Production Models

5.1. Placement into a Hierarchy and Confirmation of the Validity of Control Requirements Using SysML

SysML is used to place control requirements into a hierarchy and confirm their validity, and the objective here is to apply this to the development of mass-production models. To that end, guidelines were created for the definitions of the levels described in section 2.1 and for the method of creating the diagram described in section 2.2.

At the system design level, SysML demonstrates advantages for the purpose of assuring traceability, which establishes relationships among items of information. Items of information that are similar end up being dispersed, however, and it is a characteristic of SysML that isolating just a specific type of information may not be readily achieved. This has been found to result in the issue of inability to efficiently check into information excesses and deficiencies during verification. As a result, the necessary tasks were defined before verifying system design requirement specifications as a measure to increase the efficiency of verification.

5.1.1. Information materials presented for verification

In order to efficiently display the information that is subject to verification, the creator of the specifications will create an HTML report in advance. The HTML report will extract and record items necessary for verification, such as diagrams, requirement items, component elements, and verification items.

The HTML report can have a template created in advance to specify the items of information that are necessary for verification, as well as how to display them. Doing this will allow automatic creation of reports with the same format by anyone. HTML reports can also connect related items of information using hyperlinks, which can allow verification to proceed more efficiently.

The interface report shown in Fig. 14 is one example of application to an HTML report. The report shows the input and output ports for each design block by level and in table format. Using these tables, input and output for multiple blocks that cannot be displayed simultaneously in the SysML format can be put through comprehensive verification.

The use of these HTML reports for verification of requirement specifications can reduce the amount of time spent in presenting requirement specifications to the verifier, thereby enabling more efficient verification.

5.1.2. Style check of requirement specifications

In order to raise the quality of requirement specifications,

Interface of Platform_IAT11

This table is generated from L3 flowports

Name	In/Out	Description	Unit	OwnerBlock
IntkAirT1B1_st	In	IAT11 status information	Integer	FI-control
IntkAir_t1B1	In	Engine intake air temperature (IAT11)	DegreeCelsius	FI-control
IAT11AD	Out	IAT11 sensor input voltage value after the AD conversion	V	IAT11_calc
IntkAirT1B1_st	Out	IAT11 status information	Integer	IAT11_calc
IntkAir_t1B1	Out	Engine intake air temperature (IAT11)	DegreeCelsius	IAT11_calc

This table is generated from L4-1 flowports

Name	In/Out	Description	Unit	OwnerBlock
IntkAir_t1B1	In	Engine intake air temperature (IAT11)	DegreeCelsius	IAT11_DetectRangeFail
IAT11AD	Out	IAT11 sensor input voltage value after the AD conversion	V	IAT11_Conversion
IntkAir_t1B1	Out	Engine intake air temperature (IAT11)	DegreeCelsius	IAT11_Conversion
Obd10D_st	Out	IAT11 OutOfRange status information	Integer	IAT11_OBD_Common
Obd10_st	Out	IAT11 status information	Integer	IAT11_OBD_Common

This table is generated from L4-2 flowports

Name	In/Out	Description	Unit	OwnerBlock
IntkAir_t1B1	In	Engine intake air temperature (IAT11)	DegreeCelsius	OutOfRange_Lo_Detection_SW
IntkAir_t1B1	In	Engine intake air temperature (IAT11)	DegreeCelsius	OutOfRange_Hi_Detection_SW
IAT11AD	Out	IAT11 sensor input voltage value after the AD conversion	V	IAT11_ADC_SW
IntkAir_t1B1	Out	Engine intake air temperature (IAT11)	DegreeCelsius	IAT11_PhyConv_SW
Obd10DH_st	Out	IAT11 OutOfRange High status information	Integer	OBD_Common_SW
Obd10DL_st	Out	IAT11 OutOfRange Low status information	Integer	OBD_Common_SW
Obd10H_st	Out	IAT11 Limit High status information	Integer	OBD_Common_SW
Obd10L_st	Out	IAT11 Limit Low status information	Integer	OBD_Common_SW

Fig. 14 Interface (I/F) report

it is necessary to verify that the requirement specifications have been created using documentary forms and formats that conform to the requirement analysis guidelines that have been formulated. Human visual inspection, however, may result in omissions and oversights, and so requires enormous amounts of time for verification. It was decided, therefore, to proceed using tools developed in-house, so that the person creating specifications could perform simple advance checks of the documentary forms and formats of requirement specifications and present those results (Figs. 15 and 16). Performing style checks before verification enables the written requirement specifications to be verified with contradictions and connections not envisioned in the design removed. This allows the emphasis to be placed on checking the validity of the content of requirement specifications.

With the identification of issues and the measures to address them described above, there is now a prospect that placing control requirements into a hierarchy and confirming their validity using SysML can be applied to mass-production models in the 2016 model year.

5.2. Confirming the Validity of Requirements using MILS

In order to implement the method of confirming the validity of requirements by means of MILS, guidelines were formulated for creation of the Simulink model for platform verification described in section 3.1 and for creation and verification of the test pattern described in section 3.2.

In connection with the development of new devices scheduled for application to 2015 model year mass-production vehicles, the validity of requirements was verified by means of MILS. The following findings were obtained.

(1) In the opening phases of development, when there is no PT-ECU hardware, software, or actual devices, MILS demonstrates its effectiveness in such applications as provisionally deciding on the control cycle, and

ProjectFileLocation **D:¥Platform¥Platform_Brake.rpy**

Result	No	Check point	Result details
OK	1-8	Does the model have a comment named “Diagram” in the package “Index”.	
Failure	1-8-1	Does the model have hyperlinks to all diagrams except internal block diagram in the description of the comment named “Diagram”.	Hyperlink to diagram does not exist L4-1::L4-1_CRD_BrakeNoSwDet_ECU L4-1::L4-1_BD L4-1::L4-1_RD_Diagnosis L4-1::L4-1_RD_Operation L4-1::L4-1_CRD_BrakeNcSwDet_ECU L4-1::L4-1_CRD_BrakeNcSwErrorDet_ECU L4-1::L4-1_CRD_BrakeNoSwErrorDet_ECU L3::L3_CRD_BrakeStDet
CHK	2	Does the model have a block.	block exist.
OK	2-1	Are the names of blocks in the model all different.	
OK	2-2	Do the names of blocks in the model all start with capital letters. Also, does the model use only alphanumeric text and the underscore character.	

Fig. 15 Style check sheet

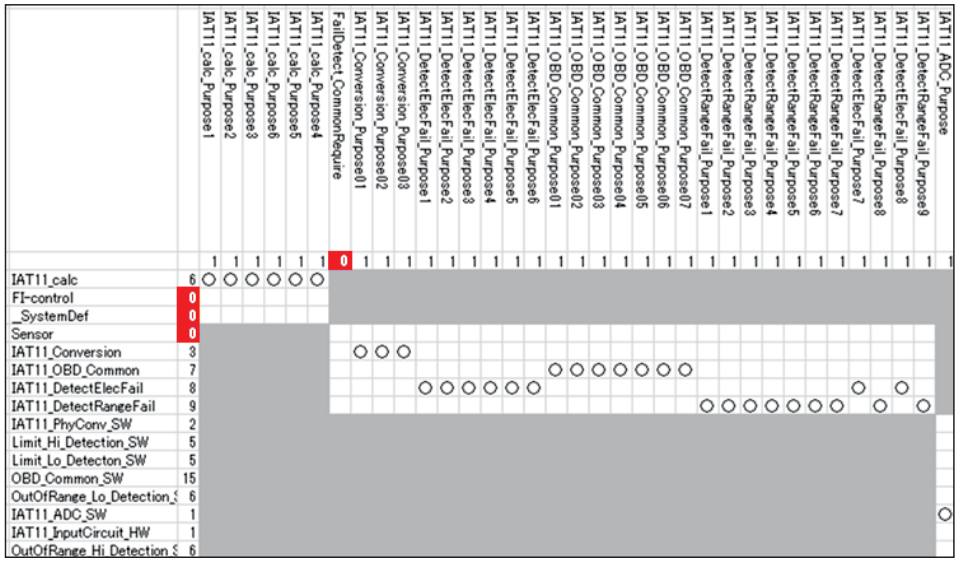


Fig. 16 Requirement-block connection check

ascertaining what kinds of abnormal operations could occur.

(2) The feasibility of verification is dependent on the craftsmanship of the plant model used by MILS. Consequently, under present conditions, verification using actual hardware is essential for this decision on the control cycle, and decisions on threshold values for determining abnormalities and other such purposes. The questions of what kind of verification should be conducted with MILS and on actual hardware, respectively, will require further continued study.

These measures have made clear that MILS is useful and that there are issues involved. There are now prospects for the application of validation using MILS to the development of new devices in the 2016 model year and beyond.

5.3. Structuring Software in Consideration of AUTOSAR Standards

The policy for dividing up functions and the policy for deciding on the interface described in section 4 were followed in creating software specifications to support a new architecture for the four groups of on-board diagnosis and regulation, memory, controller area network, and off-board tester.

Software specifications were also created to support new architecture for those portions of the two groups of scheduler and input/output that had changing function requirements from before.

The above software specifications supporting new architecture were applied to mass-production models for the 2015 model year. This yielded the prospect of replacement with the new architecture in all the platform function groups in mass-production models for the 2016 model year.

6. Conclusion

The methods below were devised, and they were applied to the development of mass-production models for the 2015 model year. This enabled the preparation of arrangements to achieve control development that results in fewer returns.

(1) A method for placing control requirements into a hierarchy using the SysML format, and a method for confirming the validity of control requirements

(2) A method of validation by means of MILS that uses the Simulink model at the specification design stage

(3) A method for structuring software architecture for the platform that takes AUTOSAR into consideration

Reference

(1) http://www.autosar.org/

(2) Information-technology Promotion Agency, Japan: jobun, shisutemu enjiniaringu ni tsuite, moderu besu shisutemuzu enjiniaringu donyu no tebiki, p. 13-36 (2013) (in Japanese)

■ Author ■


Hidekazu ARAKI


Kanako SAITO


Ryosuke OHGUCHI


Masayuki FUNAKOSHI


Kensuke YAMAMOTO

Driving Simulator for Power Plant Controller Development

Satoshi KODO* Shigeki FUJIMOTO*
Takashi ONO** Tetsuya SUZUKI***

ABSTRACT

A driving simulator environment with the minimum configuration considered necessary for power plant controller development was added to a Hardware in the Loop Simulation environment that mounts the plant model created in the previous report (Development of High-performance Engine Plant Model and Sequential System Identification Environment for Realization of Model-based Development). This created a development environment that makes it possible to incorporate situational maneuvers performed by humans, which were previously acquired through actual vehicle tests in the final process of model-based development, into the virtual vehicle tests in the upstream processes. Driving maneuvers performed by humans were measured using the created driving simulator, and it was confirmed that maneuvers performed by humans in response to various surrounding situations can be acquired, which was not possible with a driver model. In addition, the created driving simulator was applied to actual controller development, and was verified to be useful in discovering control issues that occur in everyday driving situations, and to increase the accuracy of model-based development.

1. Introduction

In model-based development (MBD), the actual vehicle tests that are performed in the final process of development are performed virtually in each upstream process by reproducing non-existent components as plant models in the upstream processes. This made it possible to increase the accuracy of the output in each process, reduce development reworking requiring to return from downstream to upstream processes, reduce development costs, and increase the speed and quality of development by front-loading development.

Figure 1 shows the relationship between the controller, plant model and driver. The High Performance Engine plant Model (HPEM) created in the previous report[(1)] was used to create an environment in which controller design can be performed using the response from a plant model that exhibits real behavior relative to the control command values of the controller. This enabled more accurate controller design in the upstream processes of development compared to the previous method. Among the inputs to the power plant controller, the new environment increased the accuracy of the response from the plant model, which is the controlled object. However, the driving maneuvers input from a separate route to the controller continue to use the previous method, with the result that reworking process time still occurs.

The virtual vehicle tests performed in the upstream processes of MBD use the evaluation drive-patterns used by

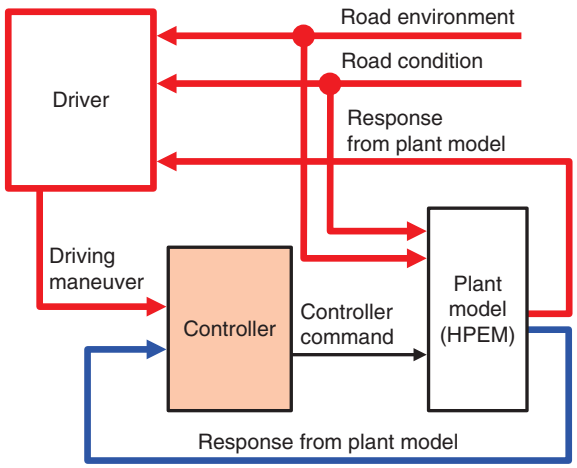


Fig. 1 Input and output of controller

* Automobile R&D Center
** P's Staff Co,. Ltd.
*** RYOMO SYSTEMS CO., LTD.

each country to measure exhaust emissions and evaluation drive-patterns that reproduce specific conditions extracted by requirements analysis and Fault Tree Analysis (FTA). Driving maneuvers are generated as before from a simple driver model that performs accelerator pedal operations so that the vehicle speed-tracks the target vehicle speeds of the drive-patterns. In the actual vehicle tests performed in the final process, evaluation is performed using the above-noted evaluation drive-patterns, under special conditions on test courses, and in various road environments under road conditions that take into account constantly changing weather and road surface conditions and the effects of traffic flow such as surrounding vehicles and pedestrians. In this case, the driving maneuvers are generated by humans actually driving vehicles under these conditions. As a result, the maneuvers include situational maneuvers performed by humans in response to various surrounding circumstances and that reflect the driver's personality, mental state and driving skills, so control issues may also be discovered through these situational maneuvers. In this manner, the evaluation conditions used for virtual vehicle tests in the upstream processes of current MBD differ from the evaluation conditions used for actual vehicle tests in the final process. This difference in evaluation conditions is a factor resulting in development reworking and an issue for front-loading of development.

Issues rooted in differences in evaluation conditions are not unique to MBD of power plant control. For this reason, approaches are recently being made in the automotive industry to increase the accuracy of MBD by reproducing the driver maneuvers obtained through actual vehicle tests in the final process of MBD in the virtual vehicle tests performed in the upstream processes[2]. In order to satisfy the evaluation conditions, it is necessary to reproduce various road environments and road conditions, including weather, road surface, surrounding vehicles and pedestrians, and to prepare a lineup of drivers to operate the vehicles. Ideally, to efficiently perform MBD, all of these elements should be modeled and multiple driver models with diverse characteristics should be used to perform evaluation on roads around the world under various conditions. Like understanding the operating range of each component comprising a vehicle, it is not so challenging to apply a driver model to evaluation that requires typical maneuvers in response to various road environments and road conditions. In contrast, power plant control that performs calculations at high frequency based on driving maneuvers should function adequately for all conceivable driving maneuvers. For this reason, there are demands that the driver maneuvers used for this evaluation include all situational maneuvers that humans might perform in response to various surrounding situations. However, a driver model capable of performing these maneuvers requires the creation of auto-driving control that performs ideal driving[3] and control that takes into account human personalities, experience and emotions, presenting quite a challenge. Furthermore, the accuracy of the driver model behavior in various situations would be constantly questioned when analyzing the various evaluation results.

Therefore, this study virtually reproduced road environments and road conditions using a model. However, the driver lineup was not modeled, and instead a driving simulator environment was created where humans drive on virtually reproduced roads.

2. Development Goals

Examples of applying driving simulators for R&D purposes include the following. Driving simulators are used to analyze driver behavior under conditions that cannot be reproduced using an actual vehicle, such as when a person suddenly runs into the road[4]. In the development of Human Machine Interfaces (HMI) such as the switches and meters inside a vehicle, driving simulators are used to investigate operability and visibility. In addition, driving simulators are used in controller development to investigate autopilot and active safety functions such as autonomous emergency braking and Electronic Stability Control of vehicles. Recently, use is also increasing for vehicle dynamics that require simulator environments that can reproduce real vehicle body behavior such as vehicle handling stability and ride comfort.

The emphasized driving simulator functions differ according to the application. In analysis of driver behavior and HMI development, visual information and the tactile sensation of the equipment surrounding the driver are emphasized. In vehicle dynamics, calculation of real vehicle body behavior and the ability to have drivers experience real bodily sensations such as acceleration and vibration are emphasized. Therefore, actual vehicles or driver's seats reproduced by cutting out a part of an actual vehicle are used for the former, and a plant model that accurately calculates the body behavior of an actual vehicle and a motion device that lets humans experience the results of those calculations as bodily sensations are used for the latter.

The ideal case is a driving simulator that reproduces the entire vehicle in a realistic manner and can be used regardless of the application. However, using a driver's seat equivalent to an actual vehicle increases the weight, thereby increasing the load capability required of the actuators in the motion device. Thus, accurate reproduction of acceleration involves tradeoffs such as the need for more powerful actuators, so large and expensive facilities would be needed to satisfy all requirements. Furthermore, accurately reproducing an entire vehicle with a plant model requires vast amounts of creation and identification time and also increases the calculation load. This means that expensive arithmetic units are needed to perform calculations in real time.

As described above, pursuit of the ideal driving simulator environment increases both the process time and cost. The goals of MBD are to reduce development costs by

reducing development reworking and to increase the speed and quality of development by front-loading development. This means that these goals cannot be achieved if the cost required to create a driving simulator exceeds the cost reduction effects of MBD or if creation requires so much process time that it adversely affects the front-loading of development. Therefore, it is necessary to create a driving simulator environment that is appropriate for the purpose in order to achieve the maximum MBD effects with a low cost and a short process time.

3. Creation of a Driving Simulator for Controller Development

3.1. Functions Required for Controller Development

Controller development can be broadly divided into the steps of understanding the dynamic characteristics of the controlled object, creation of the control logic, and calibration of the setting values. Therefore, the plant model used in the driving simulator must support these steps.

With regards to understanding the dynamic characteristics of the controlled object and creation of control logic, the plant model is used to confirm the dynamic characteristics extracted from the overall vehicle that are related to the control being developed, and to confirm the validity of the created control logic. Therefore, the plant model should be able to express unexpected dynamic characteristics in addition to the dynamic characteristics understood by the controller developers. In order to express unexpected dynamic characteristics, the plant model should be able to output responses to inputs in accordance with rules and principles. This demands configurations that are based on physical rules and empirical formulas rather than map combinations of characteristics understood by the controller developers.

When calibrating setting values, accuracy of the absolute values of responses is also demanded in addition to responses that follow rules and principles. However, while there are differences due to the degree of detail of the model, plant models are merely simplified representations of the dynamic characteristics of actual objects. This means that it is not possible to calibrate setting values at an accuracy equal to that for an actual vehicle, and the calibration value accuracy that can be set is proportional to the accuracy of the plant model. There are also cases where a developed power plant is applied to multiple vehicle body types and the number of body variations increases after the completion of development. Therefore, even if setting values are calibrated exactly for a specific vehicle body type in the upstream development processes, this does not lead to reduced development reworking or to front-loading of development. For this reason, when calibrating the setting values in the upstream development processes, it is considered sufficient if tentative calibration can be performed to limit the setting value ranges. Thus, accuracy is not necessarily required for the absolute values of the responses from the plant model used in the driving simulator.

Figure 2 shows the relationship between the plant model, controller, external information, and the driver. The plant model behavior is conveyed to drivers using the broad categories of visual information, auditory information and bodily sensations, and is a source of information for situational maneuvers by humans.

Visual information is conveyed as the vehicle traveling speed, cornering and inclination states, and auditory information is conveyed as changes in the engine noise relative to the engine speed and changes in the road noise relative to the vehicle speed. Differences between this virtual information and reality are interpreted by humans as a feeling of unnaturalness, so the highest accuracy that can be obtained at present is demanded.

In contrast, bodily sensations are affected by differences in the vehicle body, and humans misinterpret differences from reality as being due to differences in the vehicle body, so it is thought that accuracy of bodily sensations is not as important in power plant controller development. This means that it is sufficient if humans can physically sense changes in vehicle body behavior relative to changes in the power plant output and vibrations or other phenomena rooted in power plant issues.

In addition to the plant model response, drivers also determine maneuvers in accordance with the external visual information, that is to say the road environment and road conditions. In most cases this visual information is provided regardless of the driver's wishes. Furthermore, the more unexpected the provided visual information, the more noticeable the influence of the driver's personality, mental state and driving skills, and the greater the difference from normal driving. This increases the likelihood of driving maneuvers that cannot be acquired by having the simple

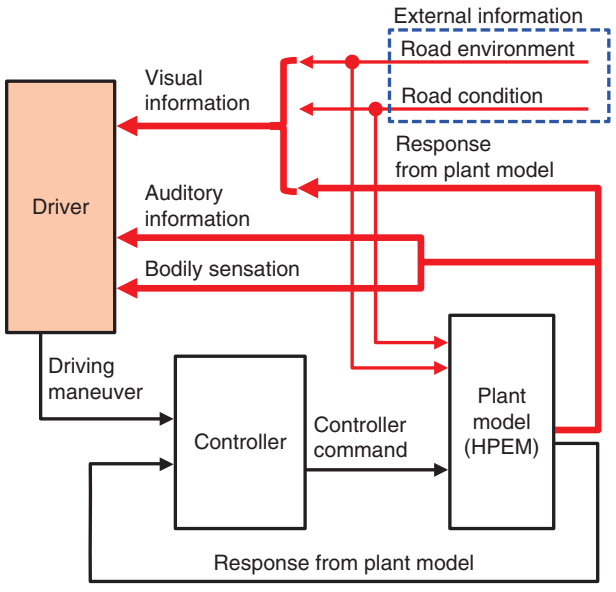


Fig. 2 Input and output of driver

driver model described previously travel in accordance with evaluation drive-patterns, and is useful for discovering control issues. This means that a video library and driving scenarios that can reproduce uncommon driving situations in addition to everyday driving situations are also necessary.

3.2. Driving Simulator Configuration

Figure 3 shows an overview and Fig. 4 shows the configuration of the driving simulator created for power plant controller development. The driving simulator consists of a commercially available visual simulator for R&D purposes, a Hardware in the Loop Simulation (HILS) that performs the calculations for the plant model that is the virtual vehicle, a driver's seat used by a human driver to perform driving maneuvers, and an ECU that mounts power plant controller.



Fig. 3 Overview of driving simulator

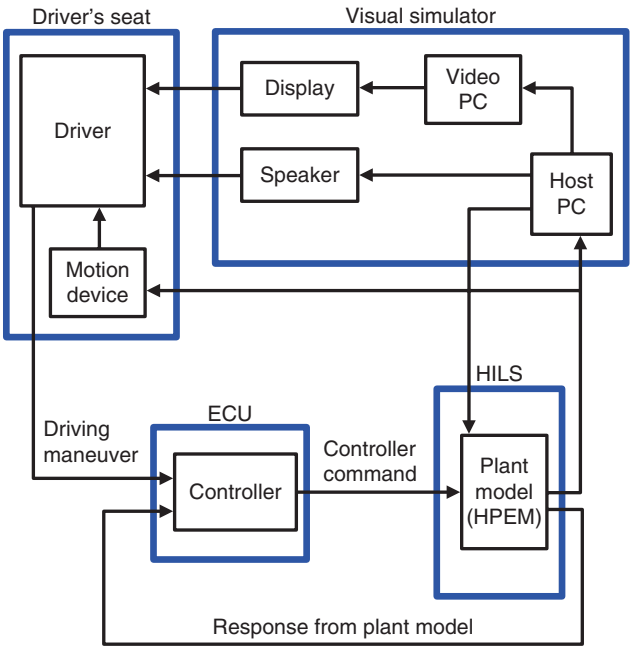


Fig. 4 Configuration of driving simulator

The visual simulator consists of a host PC that calculates the driving conditions and sound effects of the driver's vehicle and the surrounding traffic flow status, a video PC that calculates the surrounding scenery, a video display unit that displays the various calculation results, and a speaker.

The host PC calculates the driving conditions such as the gradient and coefficient of friction of the road to be traveled, the wind velocity, the position of the driver's vehicle, and the arbitrarily set surrounding traffic flow. Specifically, the host PC can reproduce elements such as vehicles that drive in accordance with traffic rules, vehicles that perform special behaviors such as sudden braking or weaving, maneuvers in accordance with arbitrarily set signal timings, and pedestrians. Diverse scenarios from everyday driving situations to uncommon driving situations can be set by combining these elements. In addition, sound effects are calculated and output in accordance with the plant model behavior.

The video PC is equipped with a video library that includes video of actual urban districts, expressways and mountain roads, and also virtual urban districts and virtual expressways that can be arbitrarily created, making it possible to reproduce various road environments. In addition, light and shade conditions can be changed according to the time period, weather conditions such as rain or snow can be selected, and various car and motorcycle models and pedestrians can also be displayed.

The video display unit used five 55-inch LCD displays to secure a viewing angle of approximately 210 degrees in consideration of the viewing angle when checking the blind spots when making a turn or lane change.

The HILS calculates the behavior of the virtual vehicle using the ECU controller command values and the driving conditions calculated by the host PC. The plant model mounted in the HILS uses the HPEM created in the previous report for the power plant, and a commercially available full-vehicle dynamics model for the vehicle body. The plant model for the power plant is required to produce responses to controller command values in accordance with rules and principles, and to perform accurate real-time calculations in order to match the human sense of time. The HPEM is described using physical rules and empirical formulas, and its behavior satisfies the requirements for use in the MBD controller hierarchy test. The HPEM can also stably perform real-time calculations on the HILS, so it can be applied without special modification. As described in the previous report, the plant model output values have an error accuracy of 3% or less compared to actual power plant measurements, which is sufficiently accurate for tentative calibration of the control setting values.

The plant model for the vehicle body is a kinetic model consisting of 10 rigid bodies such as the sprung mass, unsprung mass and wheels, and has a total of 27 degrees of freedom for the movement and axis of rotation of these rigid bodies. The dynamic behavior of the vehicle can be simulated by setting parameters such as the aerodynamic

characteristics of the body, the kinematic and dynamic characteristics of the suspension and steering, and the longitudinal and lateral force characteristics, rolling resistance and relaxation length of the tires.

In addition, use of the HILS realized connection between an actual ECU and the plant model, and enabled smooth transfer of power plant controller developed using the driving simulator to the actual vehicle phase.

The driver's seat did not use expensive items sold for R&D purposes, and was instead created by combining commercially available products marketed to hard-core players of PC-platform racing games. These products provided a sufficiently realistic operation feeling and enabled acquisition of bodily sensations such as changes in vehicle body behavior and vibration. In addition, the steering wheel, pedal and shift lever feelings and the vehicle behavior differ according to the model genre and vehicle size class, so the created driver's seat is thought to possess the necessary functions for power plant controller development applications.

4. Effects of the Driving Simulator

An example of situational maneuvers by humans that were acquired using the created driving simulator is described below.

Figure 5 shows the vehicle speed, accelerator pedal position, and transmission gear (shift) position measured using the condition when following a vehicle in front that is traveling at the prescribed vehicle speed pattern. The human measurements were obtained by the development team members using the driving simulator. The test condition was for each subject to drive normally as in everyday life.

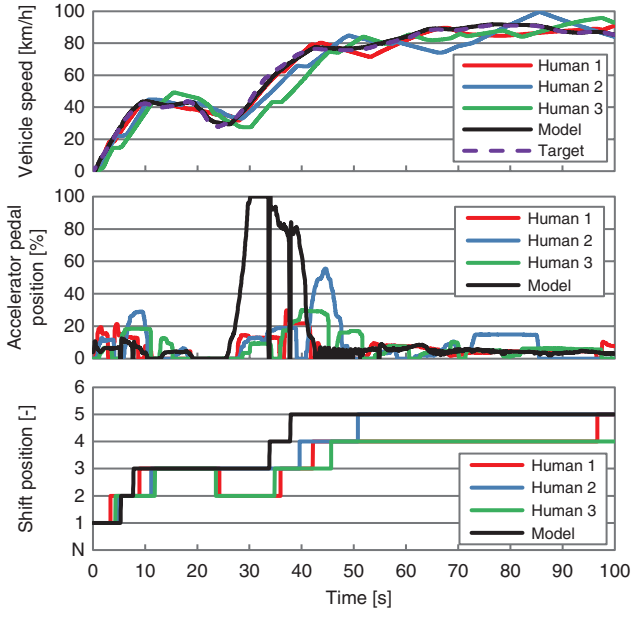


Fig. 5 Following traveling test results

The driver model assumed traveling at a constant distance following the vehicle in front, and shows the results when the accelerator pedal was operated by Proportional Integral Derivative (PID) control using the vehicle speed pattern of the vehicle in front as the target value.

The human results for vehicle speed obtained by this test exhibit differences with a long variation cycle from the vehicle speed pattern during gradual acceleration and deceleration from the 40 s mark onward. These differences differ for each test subject, which is thought to be because the situational maneuvers performed by humans in response to changes in the distance between the vehicles obtained from the visual information differ for each person. In contrast, the driver model performed driving that accurately traced the drive-pattern, so there was no difference in vehicle speed from the drive-pattern.

Comparison of the accelerator pedal position also showed differences so large between drivers that it did not appear as if they traveled using the same drive-patterns. These differences are thought to have occurred because the gear selection and the method of adjusting the distance from the vehicle in front differ according to driving characteristics based on the personality and experience of each driver.

In addition, the driver model differs from humans in that the amount of change in the accelerator pedal position per unit time is more prominent as shown in Fig. 6. No major difference was observed between 0 s and 30 s during which there was clear acceleration and deceleration. However, during gradual acceleration and deceleration after the 40 s indicated by the dashed line, the human subjects determined the distance from the vehicle in front as the situation

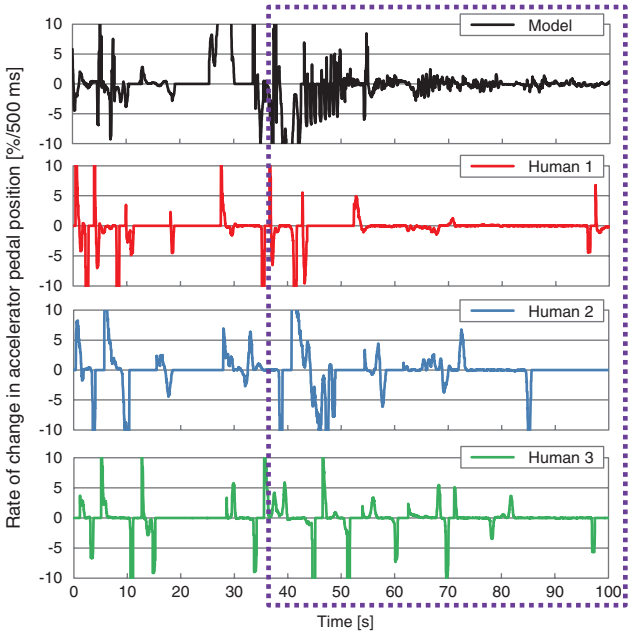


Fig. 6 Comparison of rate of change in accelerator pedal position between human and model

developed, so they held the accelerator pedal position for a longer time, resulting in operation with greater speed variation. In contrast, the driver model constantly performs minute accelerator pedal operations in order to more accurately trace the vehicle speed pattern.

As described above, the maneuvers performed by the driver model were mechanical maneuvers that perfectly followed the vehicle traveling in front. In contrast, the maneuvers performed by humans differ each time, even when driving under identical test conditions. This confirmed that the created driving simulator can be used to acquire situational maneuvers that humans perform in response to various surrounding situations and that are influenced by the driver's personality, mental state and driving skills.

5. Example of Application to Controller Development

An example of a control issue identified by applying the created driving simulator to controller development is described below.

Figure 7 shows a block diagram of a simple engine torque controller in which issues were identified.

This controller uses the feedback engine torque to control the throttle angle to achieve the target torque value. In addition, the throttle angle and the engine torque have a nonlinear relationship, so a response surface model[5] that outputs the throttle angle relative to the intake airflow and the engine speed is used to enhance the control characteristics. This enables the PID controller to treat the intake airflow, which has a strong linear relationship with the engine torque, as the controlled object.

The driving simulator was used to drive a manual transmission virtual test vehicle in an urban district, and a control issue was discovered in the following type of driving situation. Figure 8 shows a driving situation in which the vehicle traveling in front decelerated and made a right turn to enter the parking lot of a shop on the opposite side of the road. In this case, the vehicle in front decelerated to wait for an oncoming vehicle to pass in the condition without the turn signal activated. As a result, the driver performed unexpected strong deceleration, and then gradually accelerated.

As shown in Fig. 9, the engine speed dropped due to the deceleration, so under normal conditions the driver would shift down and then accelerate. However, due to the influence of the unexpected strong deceleration on the driver's mental state, the driver pressed the accelerator pedal without shifting down, which produced fluctuation in the engine output torque. When driving was performed again thereafter under the same conditions to confirm the issue, the output torque fluctuation did not occur. Comparison of the data for the cases with and without output torque fluctuation showed that in the latter case, the acceleration started from a state with less deceleration and a smaller drop in the engine speed compared to the initial case. This is thought to be because the driver knew in advance that the vehicle in front would decelerate strongly, so the driver unconsciously increased the distance between the vehicles.

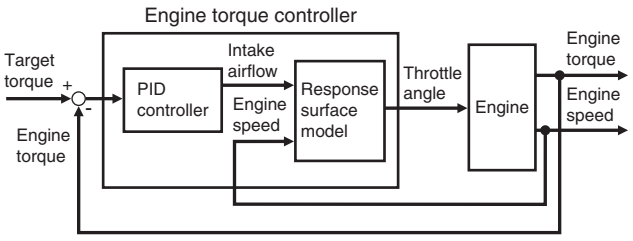


Fig. 7 Engine torque controller block diagram



Fig. 8 Test situation reproduced by driving simulator

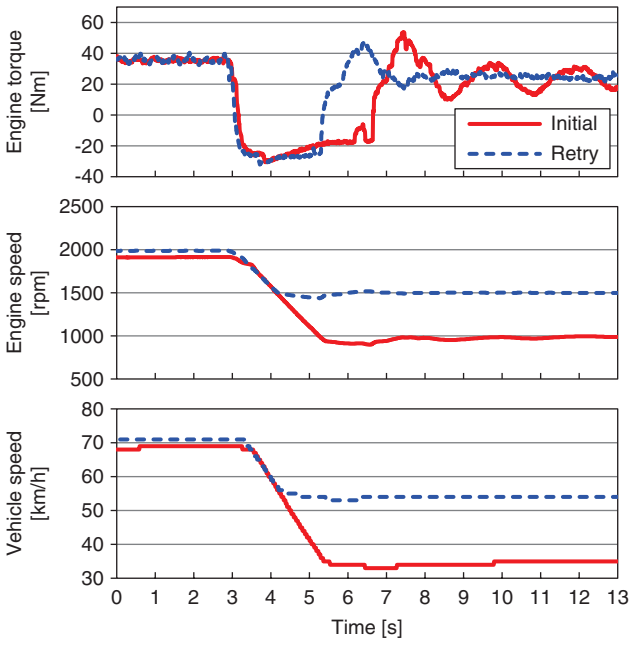


Fig. 9 Original controller behavior

The reason for this result was investigated, and an issue was found in the settings of the response surface model shown in Fig. 10. The throttle angle was large relative to the intake airflow and there was an area with insufficient linearity at the operating point where the issue occurred. As a result, the controller operated the throttle by more than the amount of change in the throttle angle that was physically necessary relative to the intake airflow, and the engine output torque also changed greatly. This triggered hunting in the feedback control, which produced fluctuation in the engine output torque.

Previously, the validity of the response surface was confirmed in the initial stages of controller development. However, one reason for this was that numerical judgment using a coefficient of multiple determination[5] that expresses the approximate accuracy of the response surface was emphasized in order to clarify the basis for judgment. Therefore, the control specification requirements table was revised so that judgment is performed by both confirming the detailed response surface shape from a physical perspective and according to the value of the coefficient of multiple determination.

In addition, the overall controller was also evaluated using the evaluation drive-patterns used by each country to measure exhaust emissions and evaluation drive-patterns when starting acceleration that were created based on conditions extracted by requirements analysis and FTA. However, some evaluation conditions were not covered by the evaluation drive-patterns of each country, and even in the evaluation drive-patterns when starting acceleration, the ranges where issues occurred were narrower than the evaluation point interval (10-Nm increments) for the target torque, so issues could not be discovered.

However, the engine output torque fluctuation could be eliminated as shown in Fig. 12 by using the modified response surface shown in Fig. 11.

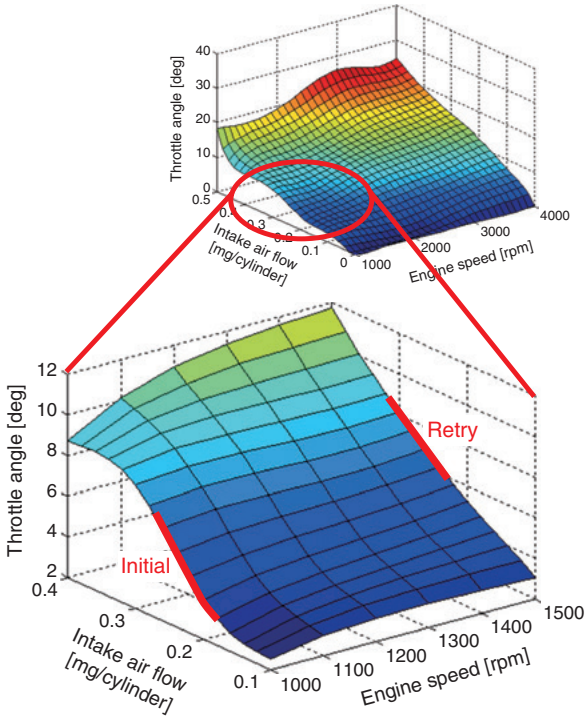


Fig. 10 Original response surface model

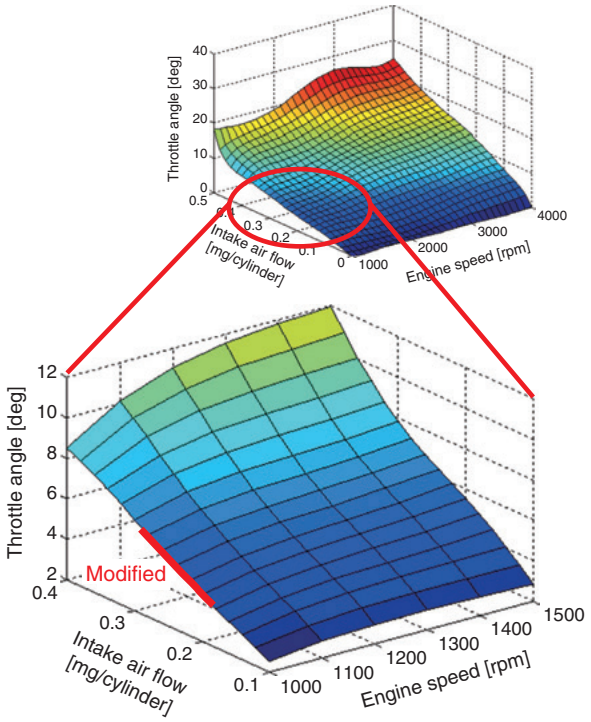


Fig. 11 Modified response surface model

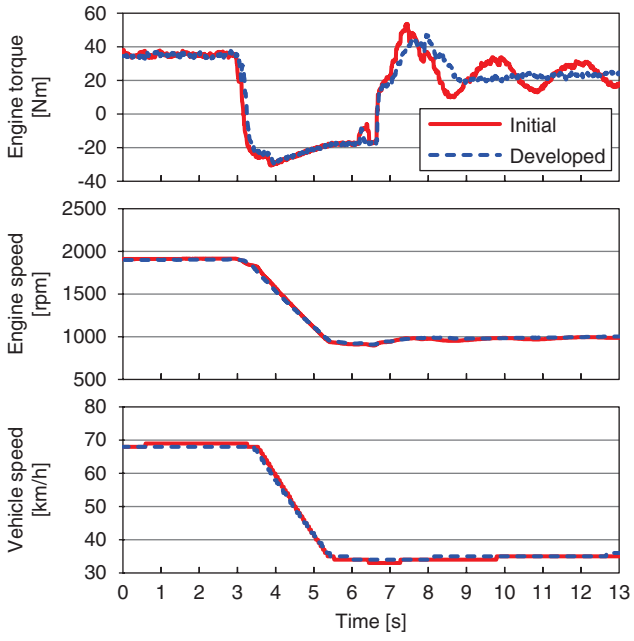


Fig. 12 Behavior of developed controller

As described above, the control issue in this study occurred as a result of a situational maneuver performed by humans in response to a driving situation present in the everyday driving of automobile users. However, this driving situation could not be reproduced in evaluation that was previously performed using virtual vehicles and driver models in evaluation drive-patterns in the upstream processes of MBD. In addition, it is thought that the issue would not have been easily discovered even in evaluation performed using actual vehicles on a test course that does not assume actual traffic flows.

As shown by this example, when developing new controllers, omissions may occur in the control specification requirements tables created based on the results of requirement analysis and FTA. The use of a driving simulator to evaluate the controller makes it possible to discover control issues in the upstream processes of MBD that would be a challenge to discover prior to evaluation using actual vehicles that assumes traffic flows on ordinary roads, which is the final stage of the conventional development method.

6. Conclusion

In power plant controller development, the following items were performed to reduce development reworking and issues with front-loading of development that occur due to differences between the evaluation conditions of virtual vehicle tests in the upstream processes of MBD and the evaluation conditions of actual vehicle tests in the final process of MDB.

(1) Evaluation using situational maneuvers performed by drivers in various driving situations was incorporated into the upstream processes of MBD.
(2) A driving simulator environment with the main objective of power plant control development was created as a means of acquiring situational maneuvers performed by drivers.
(3) The created driving simulator environment was confirmed to help increase the MBD accuracy.

References

(1) Fujimoto, S., Ohtaka, Y., Kodo, S.: Development of High-performance Engine Plant Model and Sequential System Identification Environment for Realization of Model-based Development, Honda R&D Technical Review, Vol. 24, No. 2, p. 126-133
(2) Dagci, O., Pereira, N., Cherry, J.: Maneuver-Based Battery-in-the-Loop Testing - Bringing Reality to Lab, SAE Int. J. Alt. Power, No. 2013-01-0157 (2013)
(3) Nakagawa, M., Yasunobu, S.: Intellectual Auto-Driving System of Electric Four-Wheeled Vehicle that Pays Attention to Dynamic Obstacle Evasion, Fuzzy System Symposium Paper (CD-ROM), Vol. 21, p. 9D4-3 (2005) (in Japanese)
(4) Horii, Y., Doi, S.: Effective Assessment of Night time Visibility of Pedestrians Using a Driving Simulator, DENSO Technical Review, Vol. 17, p. 103-108 (2012) (in Japanese)
(5) Todoroki, A.: Outoukyokumenhou niyoru hisenkeimondai no saitekisekkei nyumon, The Japan Society of Mechanical Engineers workshop (No. 99-73), p. 11-24 (1999) (in Japanese)

■ Author ■


Satoshi KODO


Shigeki FUJIMOTO


Takashi ONO


Tetsuya SUZUKI

Development of 8-Speed DCT with Torque Converter for Midsize Vehicles

Shoji MACHIDA* Noriyuki YAGI* Kazunori MIYATA*
Masayuki SADAKIYO* Tomoya OKAJI* Tomonori YAMANE**

ABSTRACT

Honda has developed the world's first 8-speed dual-clutch transmission equipped with a torque converter that achieves greater fuel economy performance while highlighting the pleasure of driving. The torque converter was adopted to provide smooth, powerful initial acceleration, together with quick shifting enabled by reduced inertia in the driveline; rhythmical, seamless acceleration by multi-staging with close ratios; and other such elements that create a sporty driving feel. Wider range, lower friction, and other such measures have achieved a 15% increase in power performance and an 8% increase in fuel economy performance relative to a conventional 5-speed automatic transmission. The use of common gears across the entire gear train, a unique dual shaft structure, an ultra-flat torque converter, and other such techniques enabled the size and weight to be kept down to the level of a conventional 5-speed automatic transmission for the same vehicle class while simultaneously increasing the number of gear stages.

1. Introduction

The transmission plays an important role in the high level of environmental performance that is being required of motor vehicles today. There is growing adoption worldwide of a wider range of ratios in transmissions, multi-staging, and the use of continuously variable transmissions (CVT). The dual-clutch transmission (DCT) is one multi-stage transmission that achieves a balance of environmental performance with the elements that make driving fun and yield a direct, linear gearshift feeling in response to throttle operation. On the other hand, transmissions that use clutch operation to make a standing start have issues affecting product appeal, such as a jerky feeling[(1)].

Given this background, Honda has developed the first 8-speed DCT with torque converter in the world to achieve a balance between product appeal for standing starts and a sporty gearshift feeling in a midsize vehicle. This paper will describe the development goals for this DCT, its basic construction, and the principal technologies involved.

2. Development Goals

The following items were defined as goals for the development of this DCT.

(1) Creation of a sporty driving feel
(2) Achievement of fuel economy performance at the top level in its class
(3) Assuring installation on a par with conventional 5-speed automatic transmissions (AT)

3. Basic Structure and Main Specifications

Figure 1 shows a main sectional view of the DCT, while Fig. 2 shows the vehicle speed map and Table 1 the main specifications.

The gear train was structured with driven gears shared by 1st, 2nd, and reverse, by 3rd and 4th, by 5th and 6th, and by 7th and 8th gears. The transmission also incorporates a dual shaft structure, with an inner shaft that directly links to the clutch and an outer shaft that is combined with a shift mechanism for gear selection. An ultra-flat torque converter with a high-attenuation damper was also adopted. These three features were steps taken to achieve eight speeds while also keeping the overall length of the transmission down to that of a 5-speed AT.

The adoption of a torque converter achieved powerful, smooth standing-start performance. The diameter of rotating parts was also reduced, and instead of the tandem clutch[(2)] ordinarily found with a conventional DCT, a small-diameter

* Automobile R&D Center
** Honda Motor Co., Ltd.

single clutch was arranged on each shaft in order to reduce inertia. These measures enabled quick gear shifting.

With expansion of the gear range to eight gears, the gear ratios could be lowered and set closer. Compared to the 2008 model-year TSX, the 1st gear ratio was lowered 20% and the top gear (8th gear) ratio was raised 12%. This achieved a balance between sporty driving and fuel economy performance. The wider ratio range enabled raising the ratio range to 7.0.

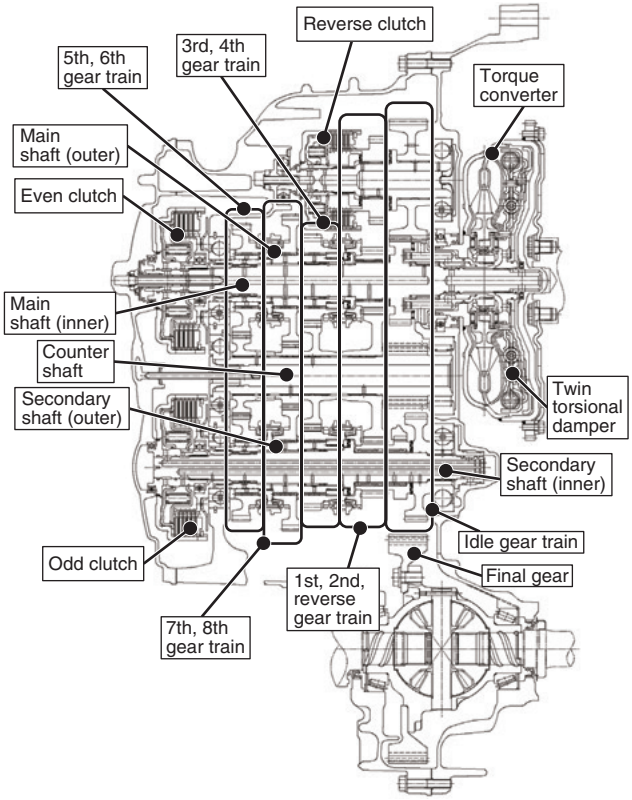


Fig. 1 Main section of 8-speed DCT

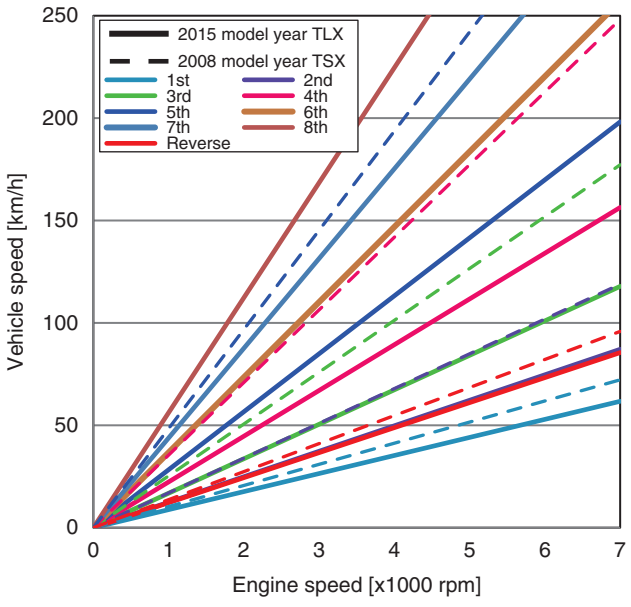


Fig. 2 Vehicle speed map

Table 1 Transmission specifications

Model		2015 model year TLX 2.4 L	2008 model year TSX 2.4 L
Torque capacity [Nm]		270	230
Overall gear ratio	1st	14.084	11.768
	2nd	9.974	7.160
	3rd	7.379	4.801
	4th	5.560	3.429
	5th	4.389	2.512
	6th	3.383	-
	7th	2.835	-
	8th	2.212	-
	Reverse	10.169	8.875
Ratio range		6.367	4.687
Overall length [mm]		388	379
Weight [kg]		95.0	92.6

4. Main Technologies

4.1. Torque Converter with High-Attenuation Damper

The effect that adopting a torque converter has on vehicle body acceleration in a standing start at full throttle is compared with competitors' vehicles in Fig. 3. The time taken to reach peak vehicle acceleration was reduced by

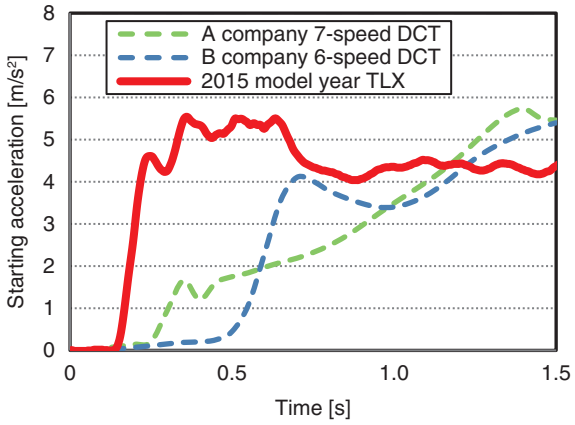


Fig. 3 Comparison of starting acceleration

approximately one second compared to other companies' DCTs.

Measures taken to reduce inertia and reduce friction in this DCT raised the issue of a rattling noise in the gears due to the engine speed fluctuation while the lockup clutch (LC) was engaged. In order to limit those engine speed fluctuations, a twin torsional damper (Fig. 4) was developed. This involved adding intermediate inertia and a secondary damper to a conventional single torsional damper, as well as optimizing the inertia arrangement, the spring layout, and the load distribution. These measures achieved a 40% reduction in the damper spring rate and a 30% reduction in the friction generated during damper operation. The result was a 58% reduction in rotational fluctuations in the main shaft, which were the origin of the vibration underlying the rattling noise. This achieved a balance between realizing the feeling of direct response from expansion of LC direct drive range and resolution of the rattling noise (Fig. 5).

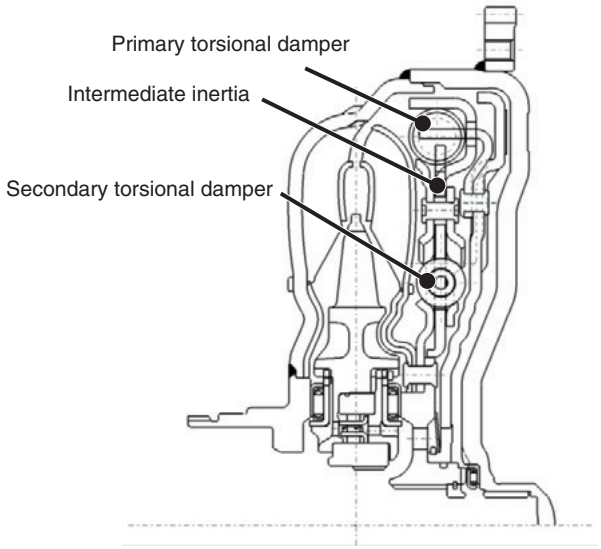


Fig. 4 Structure of twin torsional damper

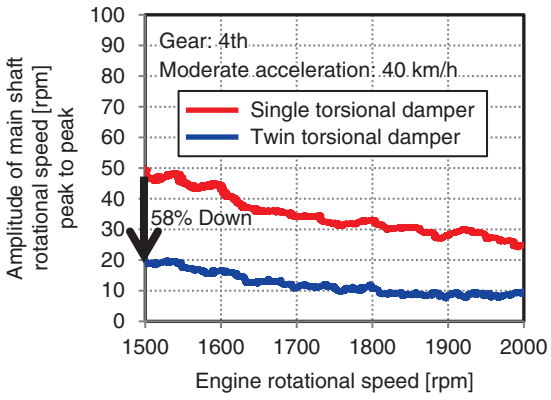


Fig. 5 Comparison of damping effect

Another measure was taken with regard to the increase in total torque converter length due to adoption of the twin torsional damper. By making the torque converter flow path ultra-flat, that length was kept equal to or shorter than the dimension of conventional torque converters. New blades were designed by analysis using computational fluid dynamics (CFD), and this successfully maintained the torque converter characteristics on a par with those of a conventional 5-speed AT while also reducing flow path width by 33%.

4.2. Dual Clutch

All the gear changes in a DCT are performed using two clutches. Consequently, the stored heat and increased number of operations during consecutive gearshifts made clutch durability an issue.

Adopting a single structure for the clutches has enabled appropriate distribution of lubricant to each clutch. The development of new facing materials and the use of a new fluid has reduced the coefficient of static friction by approximately 30% relative to a conventional AT and enabled reduction in the number of disks. As a result of measures to optimize heat capacity, the durability of the clutch could be assured while also keeping the unit to the same size as a conventional AT clutch.

4.3. Shift Mechanism

The shift mechanism is based on the manual transmission (MT) structure with a hydraulic servo piston used to operate the shiftfork (Fig. 6). The structure of this DCT was devised to reduce inertia in the synchronization parts when selecting a gearshift stage. Since the load required for synchronization is small, the diameter of the

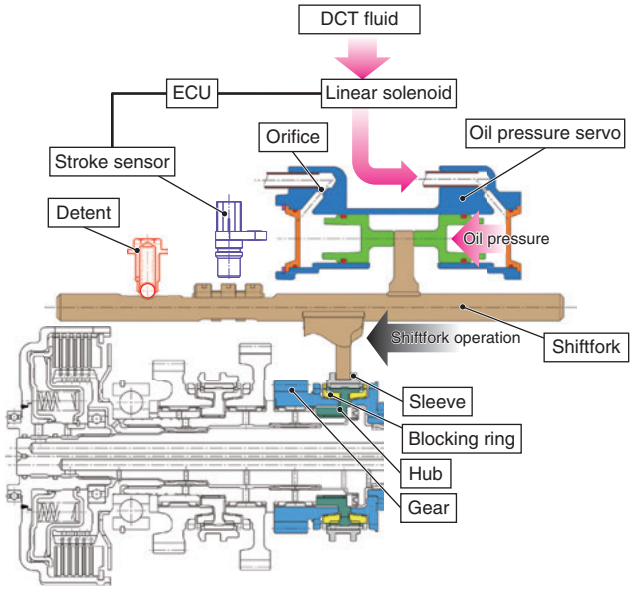


Fig. 6 Gear shift system

hydraulic servo piston could be made smaller. As a result, the responsiveness was increased and the gearshift stage could be selected more rapidly.

However, one distinctive DCT issue is the noise from operation of the shift mechanism. The gearshift noise in an MT occurs simultaneously with the shifting operation by the driver, and so does not become an issue. In a DCT, however, the gearshift noise occurs at a different time from the change in gear. The cause of this is the gear rattling noise that occurs while the gearshift is taking place. It occurs at three points during the gearshift operation process: at the start of balk, at the point when the sleeve comes in contact with the gear dog, and when the sleeve engages the gear dog teeth (Fig. 7).

During the shift operation process, there is a correlation between the sleeve stroke speed and the gearshift noise (Fig. 8). Given this result, the issue of gearshift noise was resolved by reducing the stroke speed.

The method used to reduce the stroke speed involved hydraulic control matched to the stroke, change of the detent shape, and addition of an orifice in the hydraulic servo piston chamber. However, reducing the stroke speed sometimes results in breakdown of synchronization in the process from balk to dog contact, and this was addressed by adjusting the detent profile to provide the proper brake load for the torque that causes the breakdown of synchronization.

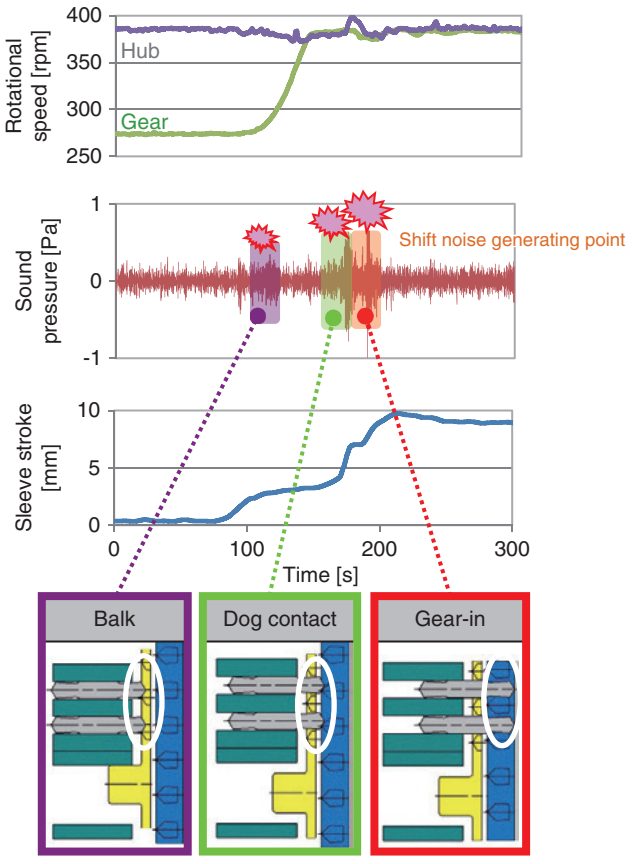


Fig. 7 Shift noise generating point

4.4. Hydraulic Control System

In a conventional AT, a gearshift is completed when the clutch reengages the gear. In the DCT, however, the next gear must first be selected by the shift mechanism before the clutch reengages the gear, which means that gearshift responsiveness becomes an issue. This issue was addressed by enabling simultaneous control of the shift mechanism and the clutch. For that purpose, a hydraulic circuit structure was adopted that augments the linear solenoids used to control the clutch on each shaft by placing linear solenoids to operate the shift mechanism, which consists of two sets on each shaft, together with ON/OFF solenoids.

The volume of the clutch accumulator was also reduced in order to shorten clutch control time when shifting gears. The shift shock caused by variations in clutch control pressure then becomes an issue. Hydraulic sensors were therefore applied, and the linear solenoids were trained to make corrections to the hydraulic pressure. This reduced the difference between the target hydraulic command value and the actual hydraulic pressure, and it achieved a balance between gearshift responsiveness and product appeal.

4.5. DCT Control

In order to obtain the exhilarating gearshift feeling that is intended for the DCT, a balance between resolution of the “shift-busy” feeling and gearshift responsiveness was achieved using the following methods.

In order to resolve the “shift-busy” feeling, the gear stage regions on the shift map were configured so that 10% or more of each region could be secured by means of the accelerator pedal (AP) opening (i.e., throttle opening). This configuration allows drivers to select gear stages more

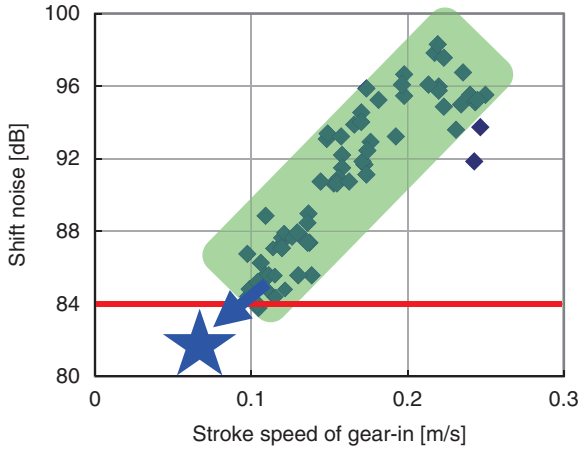


Fig. 8 Relationship between shift noise and stroke speed

easily (Fig. 9).

Gearshift responsiveness was addressed by adopting fast shift control (Fig. 10). This uses the driver's accelerator pedal operating speed to predict the drive force that will be demanded by the driver, and implements control that initiates kick-down (KD). When the accelerator pedal operating speed and the throttle opening exceed the judged value (fast shift judgment), the gear stage is selected according to the predicted AP opening. This enables the drive force demanded by the driver to be produced quickly.

4.6. DCT Fluid

The DCT structure includes the wet-type clutch and other such constituent elements of an AT together with a shift mechanism and other such constituent elements of an MT. A new fluid was therefore developed to satisfy the characteristic requirements that arise from both those constituent elements.

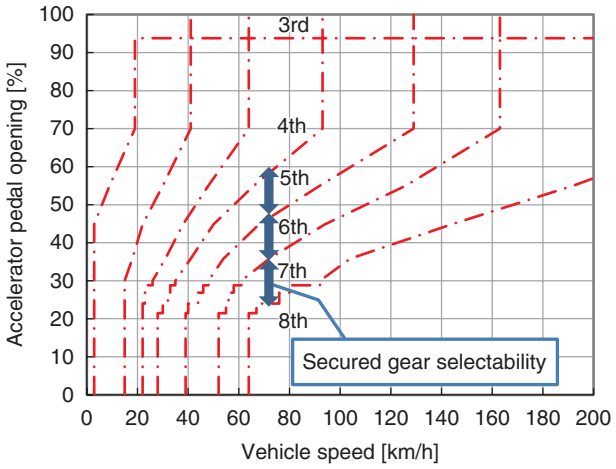


Fig. 9 Shift map (only KD line)

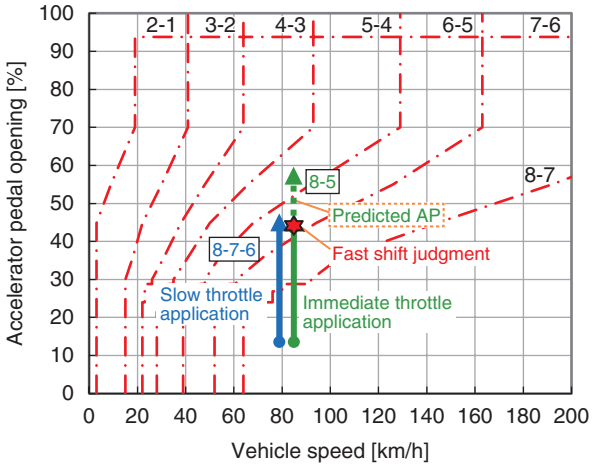


Fig. 10 Fast shift

The types and compounded amounts of friction modifiers, which are performance additives, were adjusted to optimize the wet-type clutch frictional characteristics. The amount of sulfur type extreme-pressure additive was also increased in order to assure the necessary reliability of the gears and shift mechanism.

Steps were also taken to lower viscosity in the normal temperature region with the aim of reducing agitation resistance in order to increase fuel economy. A low molecular weight-type viscosity index improver was adopted, and with a base oil optimally suited to it due to its viscosity, achieved a kinematic viscosity of 5.5 mm^2/s at 100°C (Fig. 11). This places the fluid at the top level for such fluids that are compatible with DCT construction.

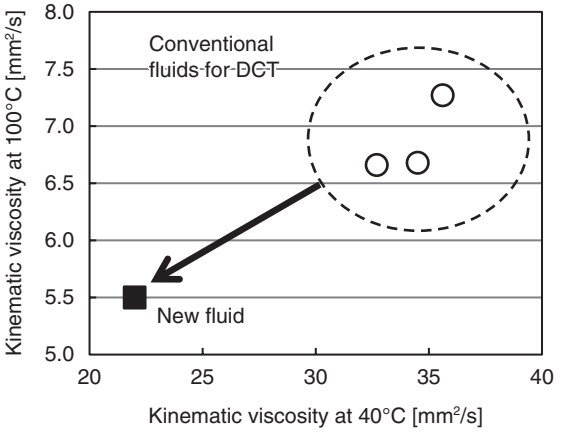


Fig. 11 Viscosity characteristics of new fluid

5. Driving Performance and Fuel Economy

5.1. Driving Feel

In order to produce a sporty driving feel, rhythmical gear shifting and a direct feeling of power were achieved at levels exceeding the 2008 model-year TSX and DCTs from other manufacturers.

The rhythmical quality of gear shifting was evaluated under the two headings of rate of change in engine speed when changing gears and gear change interval. In this DCT, the ratio of an adjacent gear ratio (hereafter, the common ratio) is set to be linear so that from 1st through 5th gear the common ratio is low by comparison with the 2008 model-year TSX and DCTs from other manufacturers (Fig. 12). This brought the rate of change in engine speed when gears are shifted at wide-open throttle to an average 7.2% lower than in the 2008 model-year TSX (Fig. 13). Similarly, the gear change interval was also shortened (Fig. 14) and rhythmical gear shifting was realized.

The feeling of direct response was evaluated under the two headings of gear change time and LC direct drive

range. In addition to superiority in hardware terms, such as its low inertia construction, this transmission has shortened gear change time 37% in average shifting up from 1st to 2nd, 2nd to 3rd, and 3rd to 4th gears relative to the 2008 model-year TSX (Fig. 15) by increasing the estimated torque accuracy of torque-on-demand control of the engine and by adopting predictive pre-shifting.

About LC control, a superior feeling of direct response was achieved by lowering the slip ratio and expanding the direct drive range. Figure 16 shows a comparison of LC slip ratios.

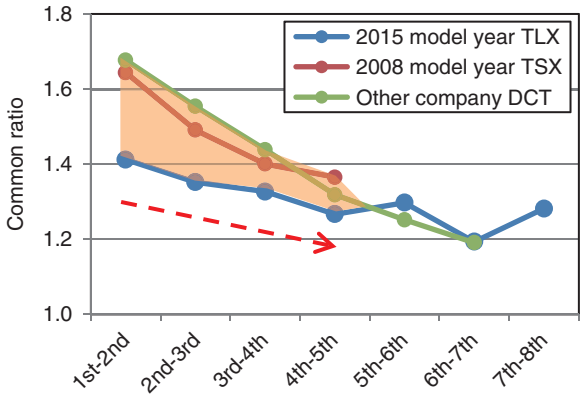


Fig. 12 Common ratio

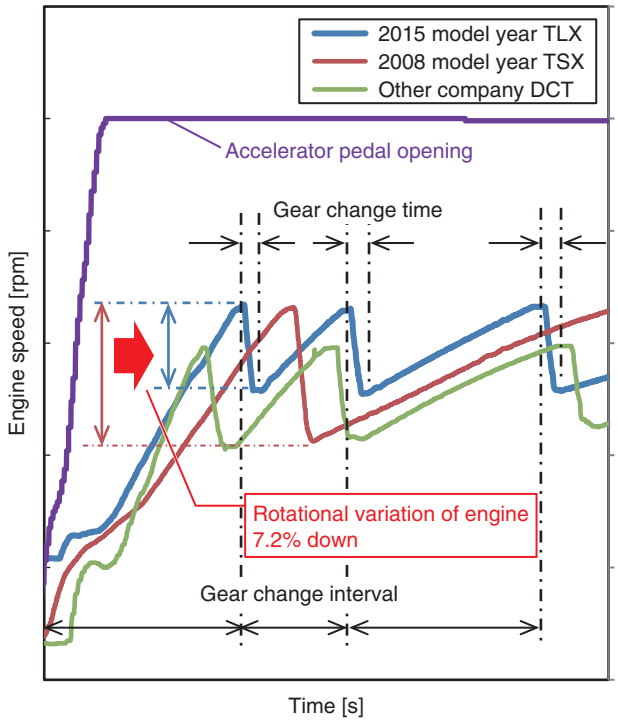


Fig. 13 Engine rotational variation

5.2. Driving Performance

The gear ratios in the low-speed gear train were lowered to enhance drive force and shorten gear change time. With this, the 2015 model-year TLX achieved a 1.3-second reduction relative to the 2008 model-year TSX in the time taken to accelerate at wide-open

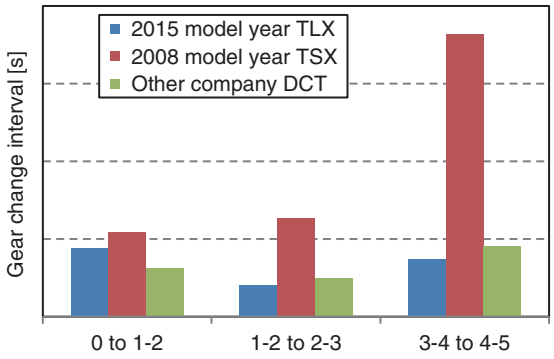


Fig. 14 Gear change interval

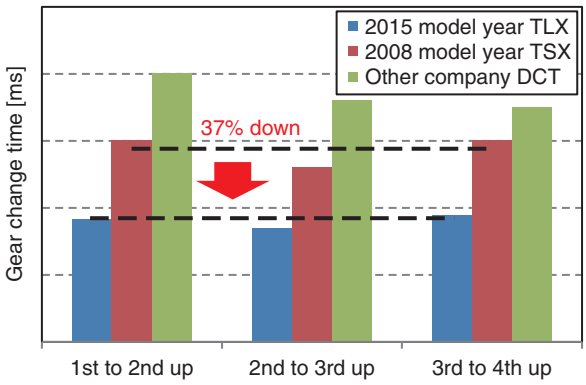


Fig. 15 Gear change time

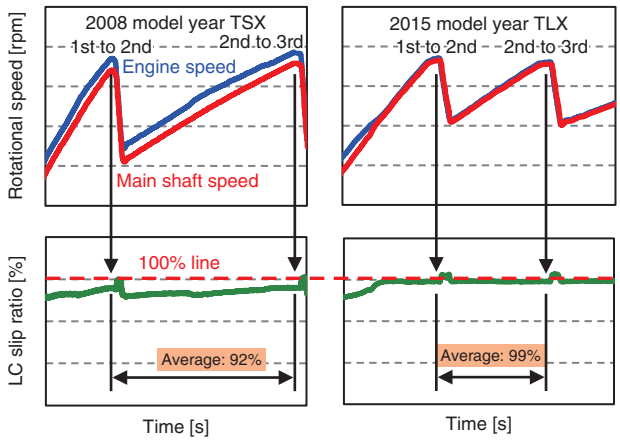


Fig. 16 LC slip ratio

throttle from 0 to 60 mph. This realized a 15% rise in driving performance. Figure 17 shows a comparison of longitudinal acceleration when accelerating at wide-open throttle.

5.3. Friction Torque

The adoption of line pressure control in response to the torque that needs to be transmitted by each clutch, reduction in agitation resistance by construction with separate clutch chambers, and control that keeps all the gears but the gear being driven on standby in neutral, together achieved a 28% reduction in friction torque relative to a conventional 5-speed AT (Fig. 18).

5.4. Fuel Economy

Multi-staging, wider range, expansion of LC direct drive range, reduction in friction torque, and heightened torque transmission efficiency achieved an 8% increase in fuel economy in US combined mode relative to a conventional 5-speed AT.

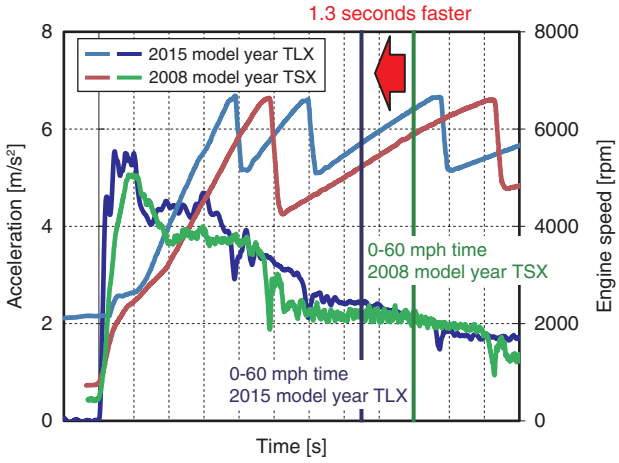


Fig. 17 Wide open throttle acceleration

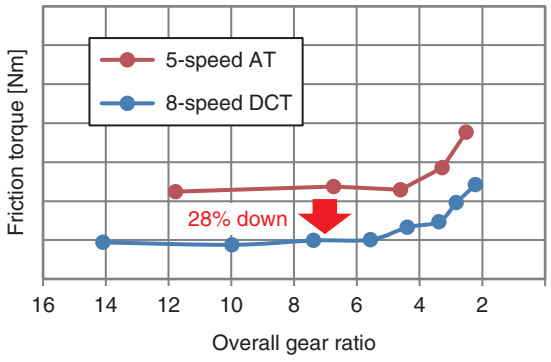


Fig. 18 Friction torque

6. Conclusion

An 8-speed DCT with torque converter was developed with the aims of a sporty driving feel, greater fuel economy, and compactness. The following results were obtained.

(1) The adoption of a torque converter realized sporty driving characterized by powerful, smooth initial acceleration together with rhythmical gear shifting and a feeling of direct power. Compared to the 2008 model-year TSX, this model shortened the time taken to go from 0 to 60 mph by 1.3 seconds, achieving a 15% rise in driving performance.

(2) An 8% increase in fuel economy in US combined mode was achieved relative to a conventional 5-speed AT.

(3) The adoption of a structure with common gears in shifting across the entire gear train, a dual shaft structure, and an ultra-flat torque converter achieved an 8-speed transmission while also keeping the overall length of the transmission down to that of a 5-speed AT.

References

(1) Okamoto, M., Terayama, S., Morimoto, S.: Hydraulic Control Technologies with Robust Stability and Performance for CVT Start Clutch, Honda R&D Technical Review, Vol. 19, No. 1, p. 82-88

(2) Kawai, N., Ohta, K., Masaoka, Y., Konishi, H., Kobayashi, H.: Development of 7-speed Dual Clutch Transmission for SPORT HYBRID i-DCD, Honda R&D Technical Review, Vo. 26, No. 1, p. 28-33

■ Author ■


Shoji MACHIDA


Noriyuki YAGI


Kazunori MIYATA


Masayuki SADAKIYO


Tomoya OKAJI


Tomonori YAMANE

Technology to Predict Input Force to Engine Mount at Rapid Start of MT Vehicle

Yasufumi JO* Takahiko MURATA*
Masaki OKUMOTO* Satoshi YAMASHITA*

ABSTRACT

Technology was created that gives the capability to predict engine mount input force during rapid starts. This input force is used for the strength design of the engine mounts for cars with a manual transmission (MT). Clutch engagement during a rapid start was modeled from time series characteristics of the clutch clamping force derived from actual measurements of clutch pedal delay and engagement time. The engine mount was modeled by applying force-displacement curves that had been tested up to high load. Wheel torque and engine mount input force were successfully predicted by means of full vehicle simulation using multi-body analysis. The parameters of that model were then changed to the upper limit and lower limit values within their obtainable range to confirm the rate of change in wheel torque and engine mount input force.

1. Introduction

There is demand for further shortened development times in order to respond to customer needs. In order to meet this demand, design accuracy will have to be increased in the initial stages of development. In strength areas, strength is evaluated on the basis of input force to the vehicle that occurs while actually driving. Therefore, the input force to each region has to be predicted accurately. There have been reports of techniques for accomplishing this by input force prediction technology with full-vehicle simulation using multi-body analysis[(1)-(5)]. These are being used as replacement techniques for measurement of inputs on actual vehicles and for simple input prediction based on vehicle specifications. Many of these cases, however, focus on suspension input force and body input force from uneven road surfaces such as when driving on a rough road or running over a curb. None of them appear to have focused on engine mount input force from driving reaction force, which is needed for reinforced engine mount design.

The full-vehicle model used for strength areas was, therefore, augmented with a drivetrain model that includes a clutch and an engine-mount model that takes account of non-linear high loads. The addition of these models created a technology that would be able to predict engine mount input force during rapid starts in an MT vehicle. That model was used to study the influence of vehicle parameters on engine mount input force, and those results will also be reported.

* Automobile R&D Center

2. Rapid Starts in MT Vehicles

In an MT vehicle, a standing start involves half-clutch operation, but the rapid start addressed in this paper involves keeping the engine at a higher speed than usual and, while in that state, releasing the clutch pedal and simultaneously pressing down on the accelerator. This causes the clutch to engage suddenly so that input force exceeding that from engine torque occurs in the drivetrain and the engine mount. The vehicle's rapid start is accompanied by wheel spinning. This scenario assumes misuse in the actual use environment.

Figure 1 shows the main input force and the behavior that occurs. The arrows indicate the direction of the force from the road surface side received on the body side. The

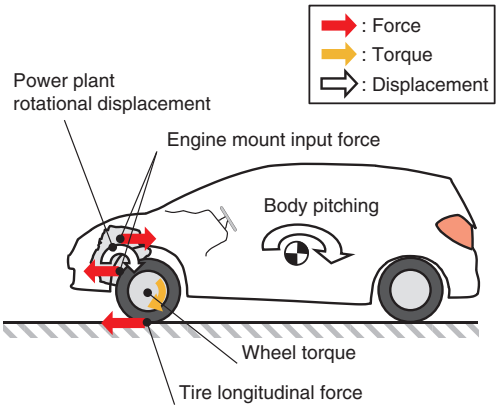


Fig. 1 Rapid start of MT vehicle

drive torque transmitted from the engine and clutch to the wheels causes a longitudinal force to be exerted at the tire contact patch, and the vehicle body exhibits pitching behavior while the rapid start occurs. At the same time, the power plant displays a rotational behavior caused by the driving reaction force, and the engine mount, which supports the power plant, receives an input force.

Engine mount strength is evaluated with bench tests using the peak value for input force during rapid starts. Therefore, input force peak values have to be predicted accurately.

3. Overview of the Models

The engine mount input force that occurs during rapid start in an MT vehicle is influenced by numerous physical elements of the vehicle. Multi-body analysis was, therefore, used to create a full-vehicle model (Fig. 2).

3.1. Engine Model and Clutch Model

The engine was modeled with the engine torque map for each throttle position, as shown in Fig. 3. The time series data for throttle position corresponding to accelerator pedal operation during rapid start is input, the engine torque is calculated, and that load is applied to the flywheel.

Figure 4 shows the clutch on an MT vehicle. The clutch model uses the clutch coefficient of friction μ, clamping force F, and effective radius R in Eq. (1) to calculate the transmission torque T.

$$T = 2\mu FR \tag{1}$$

It was decided to use the time series characteristics of the clamping force to model the clutch engagement resulting from clutch pedal operation during rapid start. In order to examine the time series characteristics, therefore, actual measurements were made of the clutch pedal stroke and mainshaft torque during rapid starts. One example of this is shown in Fig. 5(a). When the driver's foot is taken off the clutch pedal, the pedal stroke begins. It was found, however, that mainshaft torque does not rise at the same time. There is a delay of approximately 0.04 sec before it rises. It was also found that clutch engagement takes the relatively short time of approximately 0.05 sec. The time series characteristics obtained from these results, shown in Fig. 5(b), were input to the model. The delay and the time taken to engage the clutch may vary with the model of vehicle, but the time series characteristics can be changed in

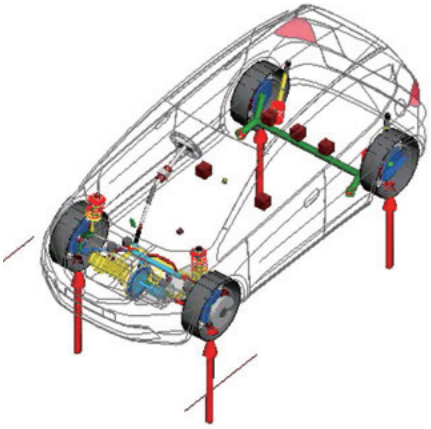


Fig. 2 Full vehicle model

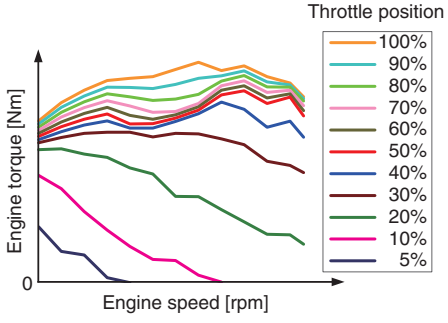


Fig. 3 Engine torque map

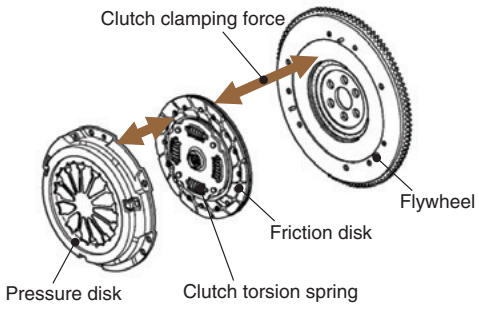


Fig. 4 Main structure of MT clutch

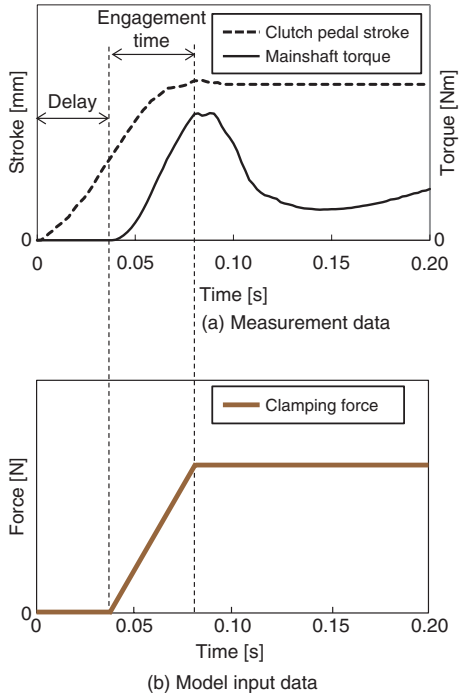


Fig. 5 Identification of clutch clamping force characteristic

order to model such vehicles.

The clutch torsion spring and the driveshaft were modeled by their respective torsional characteristics.

3.2. Other Models

The engine mount was modeled using force-displacement curves tested up to high load, as shown in Fig. 6, to account for the magnitude of the loads that occur with a rapid start. This took account of the influence from the bush spring rise characteristics.

The suspension was modeled as a multi-body model with rigid-body links (Fig. 7).

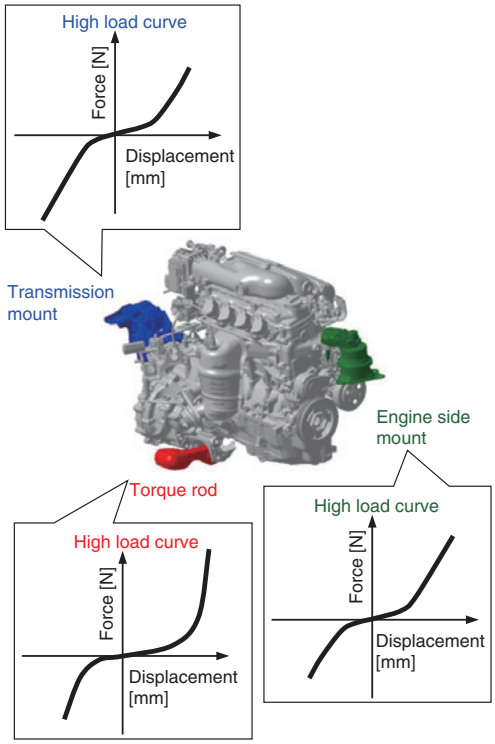


Fig. 6 Engine mount model

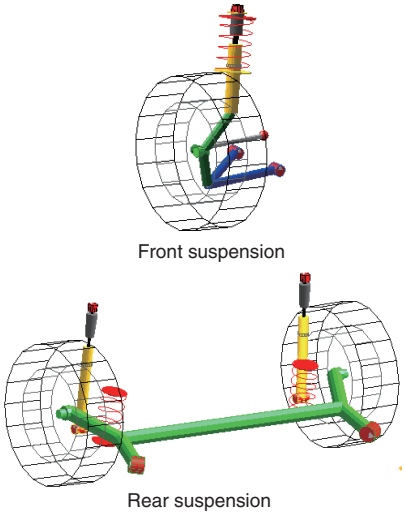


Fig. 7 Suspension model

The tire model uses the Magic formula capable of calculating the longitudinal force of the tire from the wheel load, the slip ratio, and so on.

4. Simulation Verification Results

A comparison was made of the simulation and actual measurement values for wheel torque and engine mount input force, which are driving reaction forces.

4.1. Small Vehicle Comparison Results

Figure 8 shows the results of wheel torque comparison for a small vehicle with a 1.5 L-displacement gasoline engine. Wheel torque rises due to the rapid start, and the first peak on the waveform is the maximum peak. It was confirmed that the peak value differential is slight and the time-series waveforms also matched closely.

Figure 9 shows the results of engine mount input force comparison. With the engine mount input force, as with wheel torque, the first peak on the waveform was the maximum peak. The peak value differential, which is needed for strength evaluation, was slight, and this model was confirmed to have adequate predictive accuracy.

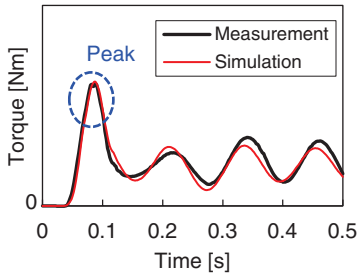


Fig. 8 Wheel torque comparison for small vehicle

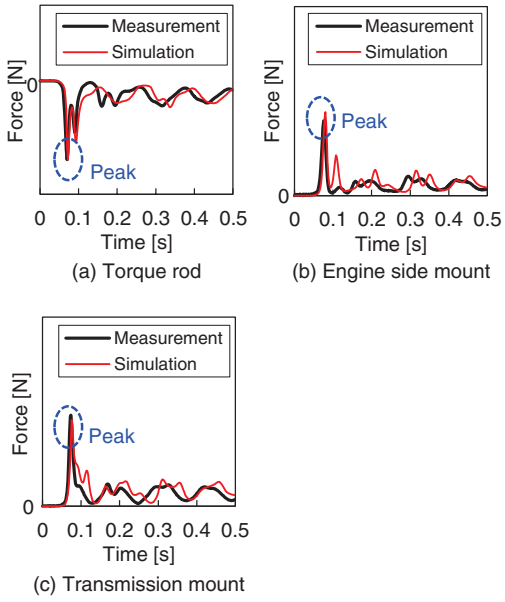


Fig. 9 Engine mount input force comparison for small vehicle

4.2. Large Vehicle Comparison Results

The simulation and actual measurement values were also compared on a large vehicle with a 2.2 L-displacement diesel engine, which has greater torque. Wheel torque comparison results are shown in Fig. 10 and the engine mount input force comparison results in Fig. 11. The peak value differentials for both wheel torque and engine mount input force can be seen to be slight. This confirmed predictive capability with large vehicles as well as with small vehicles.

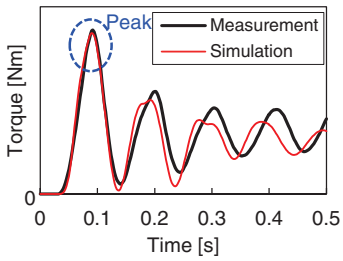


Fig. 10 Wheel torque comparison for large vehicle

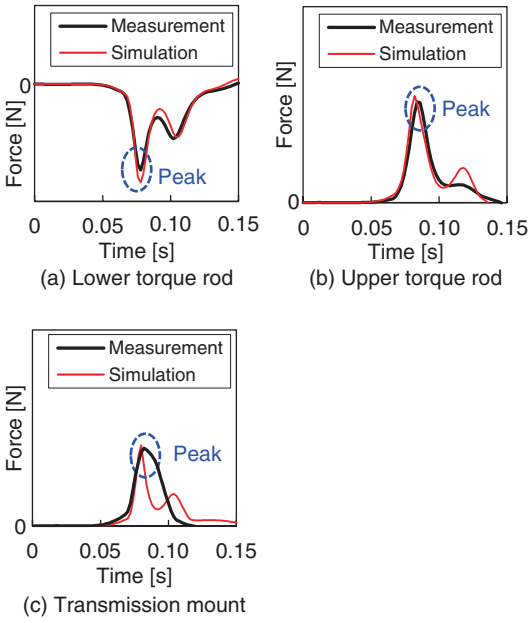


Fig. 11 Engine mount input force comparison for large vehicle

5. Influence of Parameters on Input Force

5.1. Input Force Reduction Parameters

It would be useful for design work in the initial stages of development to start with a grasp of the vehicle parameters that have greater influence on input force and of the tendencies for changes to these parameters to increase or reduce input force. The vehicle parameters shown in Table 1 were, therefore, changed to their upper-limit and lower-limit values within their respective obtainable ranges. The rates of change of the wheel torque peak value and engine mount input force peak value were confirmed. The focus in this paper is on the reduction rates.

Table 1 Vehicle parameter

Power plant	Power plant center of gravity coordinate
	Power plant mass
	Power plant inertia moment
	Flywheel inertia moment
Drivetrain	Clutch clamping force
	Clutch engagement time
	Mainshaft inertia moment
	Driveshaft torsional stiffness
Engine mount	Engine mount coordinate
	Engine mount bush spring
	Engine mount stopper clearance
Suspension	Suspension coil spring constant
	Suspension buffer clearance
Tire	Wheel inertia moment
	Tire friction
	Tire radius
	Tire inertia moment
Vehicle body	Body inertia moment

Figure 12 shows the parameters that had a higher wheel torque reduction rate, together with their reduction rates. It can be seen that the clutch engagement time, clutch clamping force, and driveshaft torsional stiffness have higher reduction rates.

Figure 13 shows the parameters that had a higher torque rod input force reduction rate, together with their reduction rates. It is apparent that parameters with higher wheel torque reduction rates generally also have higher torque rod input force reduction rates. Others are the torque

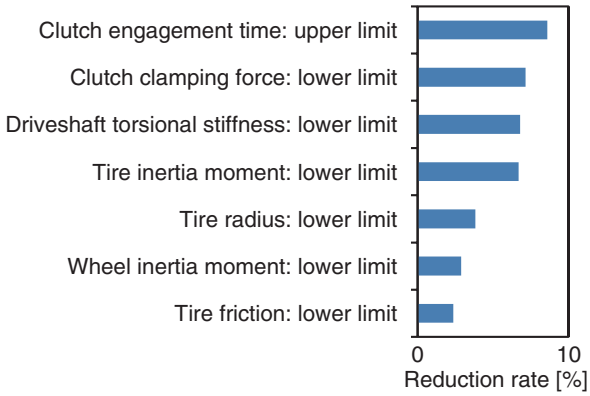


Fig. 12 Wheel torque reduction rate

rod stopper clearance, vertical coordinate, bush spring, and power plant inertia moment. This suggests that engine mount input force can be reduced by drivetrain parameters and engine mount parameters.

5.2. Influence of Torque Rod Stopper Clearance

As described above, the stopper clearance has a relatively large influence on torque rod input force. When the clearance is smaller, the input force is reduced. In order to verify this simulation result, different torque rods with stopper clearance of 2 mm, 6 mm, and 11 mm were fabricated and measurements were made of the input force on an actual vehicle.

Figure 14 shows the results for comparison of the simulation and actual measurements. The vertical axis shows the rate of input force change with respect to torque rod input force with a stopper clearance of 6 mm. The horizontal axis shows the stopper clearance. This confirmed that the actual measurements showed the same tendencies as in the simulation to increase or reduce the input force.

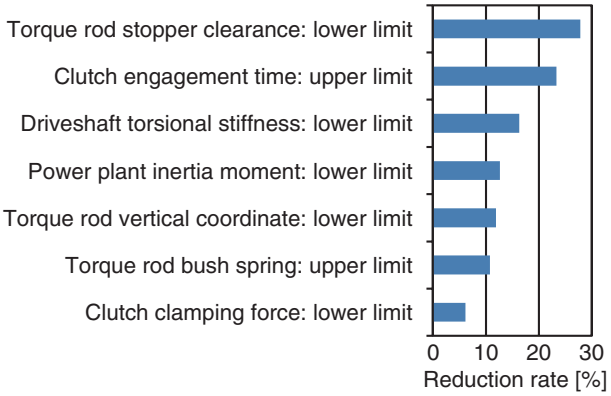


Fig. 13 Torque rod input force reduction rate

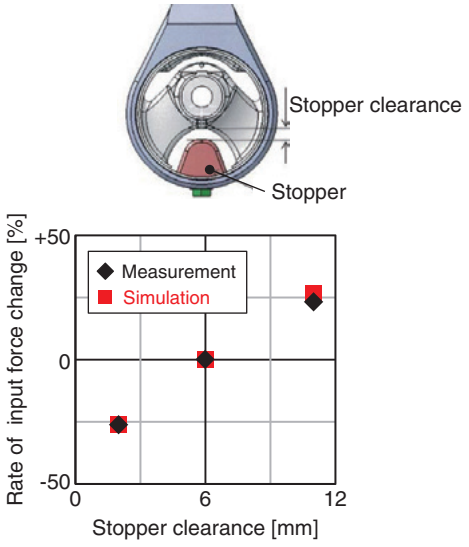


Fig. 14 Rate of input force change to stopper clearance

This also confirmed that the rate of change was predicted with adequate accuracy.

The inertial force of power plant dynamic rotational behavior during rapid starts has a relatively large influence on torque rod input force. Consequently, the input force is thought to be smaller when the stopper clearance is smaller, because the stopper then takes effect before the angular velocity of the power plant has increased. The way in which a smaller power plant inertia moment results in a reduced torque rod input force can also be considered to be due to the influence of the inertia force.

5.3. Influence of Suspension System Parameters

When suspension system parameters are changed, change also takes place in the wheel load movement that results from vehicle body pitching behavior during rapid starts. This is accompanied by change in the longitudinal force of the tire, which is thought to cause increase or decrease in the wheel torque and engine mount input force. The influence of suspension system parameters, however, was slight.

Measurements were therefore made of vertical force at the front wheel center during rapid starts and the wheel load movement was confirmed. Figure 15 shows the actual measurement results together with the simulation results. It is apparent, first of all, that the simulation corresponds closely with the actual measurements, and that the model successfully predicts wheel load movement. The focus was next placed on wheel load from before rapid start to the time when wheel torque peaks, and it was found to remain virtually unchanged. Thus, the occurrence of an input force peak, as indicated in chapter 4, is a briefer phenomenon when wheel load movement does not take place. This is thought to be the reason that suspension system parameters have such little influence.

The fact that engine mount input force can be predicted regardless of the suspension indicates that input force can be predicted at an early stage of vehicle development, for example, even if the suspension characteristics have not been decided.

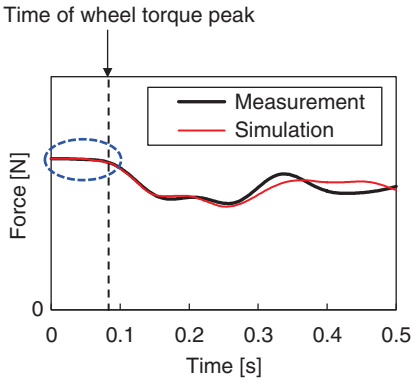


Fig. 15 Vertical force at front wheel center

6. Conclusion

A full-vehicle model of an MT vehicle was created, rapid start simulation was conducted, and the following results were obtained.

(1) Wheel torque peak values and engine mount input force peak values on a small vehicle and a large vehicle were compared with actual measurements, and this model was confirmed to have adequate predictive accuracy.
(2) Clutch engagement time, clutch clamping force, and driveshaft torsional stiffness were found to have relatively large influence on wheel torque peak values.
(3) Other than wheel torque, the engine mount stopper clearance, vertical coordinate, bush spring, and power plant inertia moment were found to have relatively large influence on engine mount input force peak values.

References

(1) Haga, H.: Evaluation of Road Load Prediction by Multi-body Simulation Including Flex-Body -Load Prediction for Durability Using a Tire Model-, JSAE Annual Congress Proceedings, No. 21-06, p. 9-12 (2006) (in Japanese)
(2) Haga, H.: Evaluation of Road Load Prediction by Multi-body Simulation Including Flex-Body (Second Report) -Load Prediction for Durability Using a Tire Model-, JSAE Annual Congress Proceedings, No. 136-06, p. 11-14 (2006) (in Japanese)
(3) Haga, H.: Evaluation of Road Load Simulation on Rough Road Using a Full Vehicle Model (The Second Report) -Load Prediction for Durability Using a Tire Model-, JSAE Annual Congress Proceedings, No. 123-08, p. 23-26 (2008) (in Japanese)
(4) Shimodaira, T., Kataoka, S., Mori, M., Yokoyama, S.: Development of Road Input Prediction Technology for Setting of Suspension Durability Conditions, Honda R&D Technical Review, Vol. 25, No. 1, p. 79-85
(5) Sakai, E., Tominaga, H., Kato, Y., Yamamoto, N., Matsuki, H.: Development of Technique for Estimating Suspension Input Force During Endurance Run on Rough Road, Mitsubishi Motors Technical Review, No. 17, p. 45-48 (2005) (in Japanese)

■ Author ■


Yasufumi JO


Takahiko MURATA


Masaki OKUMOTO


Satoshi YAMASHITA

Development of Active Control Engine Mount System for Reduction of Resonance Vibration at Engine Restart

Tatsuhiro YONE* Hideyuki OKAMOTO* Takashi YAMAGUCHI*
Shintaro FURUI* Hirotomi NEMOTO*

ABSTRACT

Active Control Engine Mounts are in mass production as a technology for the reduction of noise and vibration in complete vehicles associated with the use of V6 variable-cylinder engines. The research discussed in this paper developed a next-generation active control engine mount system that reduces vibration in complete vehicles occurring when the engine is restarted following idle stop or EV operation in a hybrid system. The fact that the timing of the powerplant resonance vibration that occurs at engine restart correlates strongly with the angle of rotation of the crankshaft was focused on, and a new control method was developed that predicts the timing and magnitude of resonance vibration and cancels it. In addition, the development of a system able to respond to high-amplitude engine resonance vibration has increased noise and vibration performance at engine restart following idle stop or EV operation in a hybrid system.

1. Introduction

Active Control Engine Mount (ACM) technologies actively operate the engine mounts using a pulse synchronized with engine speed as a reference signal in order to reduce the vibration transmitted to the body from the engine[(1), (2)]. These ACM technologies are mainly employed in V6 variable-cylinder engines. Variable cylinder systems are technologies that reduce pumping loss and increase fuel efficiency by closing the valves in one bank of three cylinders during low-load operation, such as when the vehicle is traveling at a constant speed or decelerating. The amplitude of vibration increases in comparison to six-cylinder operation during three-cylinder operation due to the halving of the fundamental order frequency of the engine (from 3rd-order to 1.5th-order) as a result of the reduction in the number of firing cylinders and increased combustion pressure resulting from the increased work performed by each cylinder. ACM technologies realize the same level of noise and vibration (NV) performance during cylinder idling (three-cylinder operation) as during full-cylinder operation (six-cylinder operation), and thus contribute to the achievement of a balance between fuel efficiency and NV performance.

At present, the potential for introducing technologies such as idle-stop systems and hybrid systems to V6 variable-cylinder engines as a means of further increasing fuel efficiency is being investigated. Idle-stop systems control fuel consumption by shutting off the engine when the vehicle is stationary; hybrid systems perform the same function by shutting off the engine when the vehicle can be operated by the motor. These systems turn the engine off and restart it repeatedly during vehicle operation. Vibration occurs when the engine is restarted, and while it is of the same magnitude as the vibration that occurs when the driver intentionally starts the engine using an ignition switch or start button, it is more prone to be noticed because it suddenly occurs with no intention on the driver's part. In addition, a high frequency of stopping and restarting the engine while the vehicle is in operation makes the vibration even more noticeable, affecting the commercial appeal of the vehicle. Using a mass-production ACM system as a base, the research discussed in this paper advanced its functions to develop the first-ever ACM system that boosts NV performance at engine restart.

2. Development Goals

Goals for the development of a next-generation ACM system that would control the transmission of engine vibration to the vehicle at restart and realize NV

* Automobile R&D Center

performance targets were set as follows:

(1) Study of the timing of vibration at engine restart, and development of a new ACM control method that operates the ACM at an amplitude that cancels the vibration; and

(2) Development of an ACM system able to respond to high-amplitude resonance vibration at engine restart.

3. Configuration of ACM System

Figure 1 shows the ACM system fitted in a vehicle. The ACM are positioned at the front and rear of the V6 variable-cylinder engine, and an electronic control unit for control of the ACM (ACM-ECU) is positioned in the cabin. The data necessary for estimation of engine resonance vibration is received from an engine control unit (FI-ECU) positioned in the engine room. Figure 2 shows the communications configuration of the ACM system. The ACM-ECU receives an engine crank-angle signal, a top-dead-center signal, and engine information (information on the state of cylinder idling and information for judgment of the commencement of engine restart) from the FI-ECU, and operates the two ACM to reduce the transmission of engine vibration to the body.

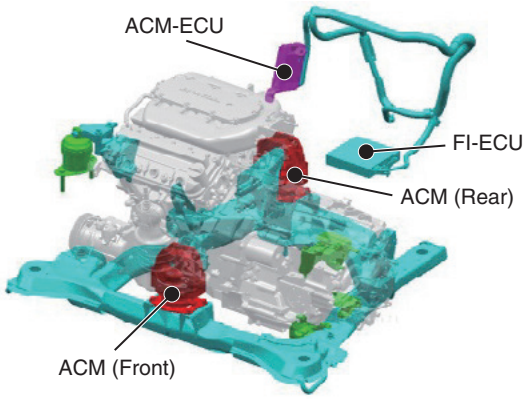


Fig. 1 ACM system layout

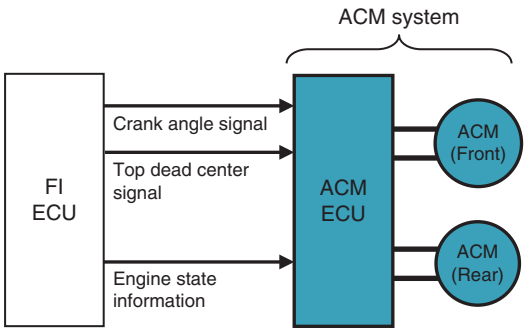


Fig. 2 ACM system communications configuration

Figure 3 shows the basic principle of reduction of vibration by the ACM. Vibration in the direction of rotation of the crank (roll), originating in torque fluctuations, is input to the front and rear engine mounts. In the case of conventional mounts, loads input from the engine are transmitted to the body via the mount rubber. By contrast, ACM systems reduce the transmission of vibration to the body by cancelling the engine vibration by means of the displacement of actuators positioned in the mounts.

Figure 4 shows the internal configuration of an ACM that cancels engine vibration. The ACM consists of a liquid-sealed mount and a linear solenoid. The impression of a current causes a plunger in the linear solenoid to oscillate vertically, vibrating an exciter plate that is connected to the plunger. This action causes the liquid pressure inside the liquid-sealed mount to fluctuate, displacing the rubber in the mount. The resulting vibration of the upper section of the mount, which is connected to the engine mount bracket, makes it possible to cancel engine vibration.

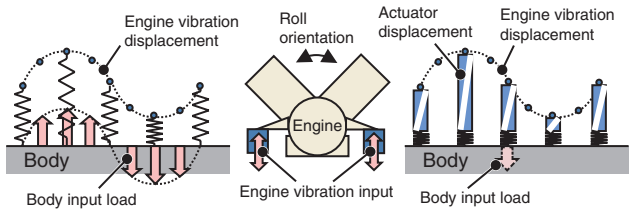


Fig. 3 Principle of vibration reduction

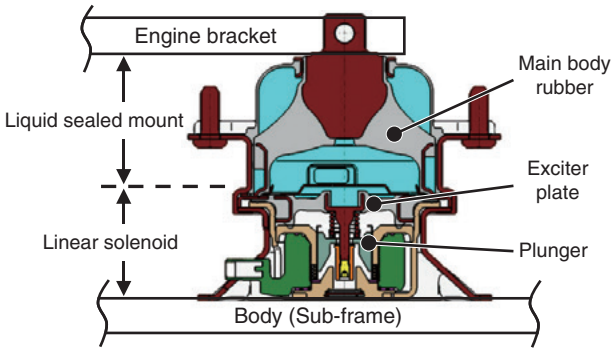


Fig. 4 Configuration of ACM

4. Reduction of Transmission of Resonance Vibration at Engine Restart to Body

4.1. Mechanism of Occurrence of Resonance Vibration at Engine Restart

As an example of the phenomenon of resonance vibration at engine restart, Fig. 5 shows vibration occurring when the engine is restarted following EV operation in a

hybrid system. This section will discuss the mechanism of occurrence of resonance vibration at engine restart.

When the engine is started, torque provided by the hybrid system motor rotates the engine crankshaft, and the pistons in the cylinders move up and down. At this time, the rotation of the crankshaft fluctuates, due mainly to in-cylinder pressure. The vibration resulting from this fluctuation is amplified as resonance vibration when engine speed increases and reaches the area of resonance, as determined by the spring characteristic of the engine mounts and the mass of the powerplant. This resonance vibration occurring at engine start is transmitted to the body via the engine mounts that support the powerplant. The difference between this phenomenon and the resonance vibration that occurs at engine restart in an idle-stop system is that the source of start-up torque is a starter motor rather than a hybrid system motor, and the starter motor torque does not reach the area of resonance of the powerplant, passing it due to the first firing of the engine. However, the basic principle of both types of resonance vibration is identical.

4.2. Development of ACM Control at Engine Restart

Resonance vibration at engine restart is a transient phenomenon, making the use of feedback control employing vibration data detected by sensors a challenge. In addition, the timing and magnitude of resonance vibration of the engine also change with the rapidity of the increase in engine speed when it passes the area of resonance of the powerplant. It was therefore necessary to develop a feed-forward control that would identify the timing and magnitude of resonance vibration in advance and control the ACM at the optimal timing and amplitude.

As indicated above, the vibration originating in fluctuation of the rotation of the crankshaft at engine restart is amplified and becomes resonance vibration when it reaches the area of resonance of the powerplant. This fluctuation in the rotation of the crankshaft is linked to the position of the pistons, in other words to the angle of crankshaft rotation, and the occurrence of resonance vibration at engine restart also has a correlation with the angle of rotation of the crankshaft. Figure 6 shows engine speed and resonance vibration at engine start-up in relation to the angle of rotation of the crankshaft. When the engine speed passes the area of resonance of the powerplant, the first resonance vibration occurs, with its point of origin at the angle of rotation that represents top dead center. It is possible to estimate the timing of resonance vibration using the angle of rotation (crank angle) that becomes this point of origin.

To make it possible to estimate the magnitude of resonance vibration, it is necessary to stabilize that magnitude. Engine and motor control therefore attempts to prevent fluctuations in the magnitude of resonance vibration by controlling the speed of increase in engine speed at restart to a constant level.

Based on the above, using the crank angle and applying control to the speed of increase in engine speed at restart, a method of control was developed making it possible to estimate the timing (the crank angle at which vibration occurs) and magnitude of resonance vibration by means of the ACM-ECU.

Control of the ACM drive in response to transient high-amplitude resonance vibration will next be discussed. In order to respond to continuously occurring vibration in a variable-cylinder engine during full-cylinder and cylinder-idling operation, conventional ACM systems are able to rely on the continuous operation of the actuator to make it possible to change the amplitude of the ACM and cancel vibration. By contrast, in this case the actuator would not be in operation when resonance vibration occurred at engine restart, making it necessary to realize high-amplitude ACM operation by means of initial current control.

Figure 7 shows the control method employed in order to achieve the necessary amplitude of ACM vibration using initial current control. Vibration is generated in the ACM by repeated suction on the plunger in the ACM actuator due to the impression of a current in the coils and opening of the plunger due to the spring force of the exciter plate. At this time, the exciter plate position that represents the point of

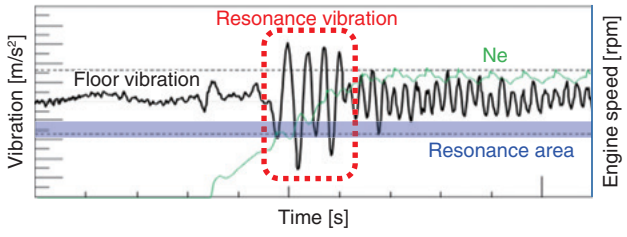


Fig. 5 Engine restart vibration (V6 engine hybrid vehicle)

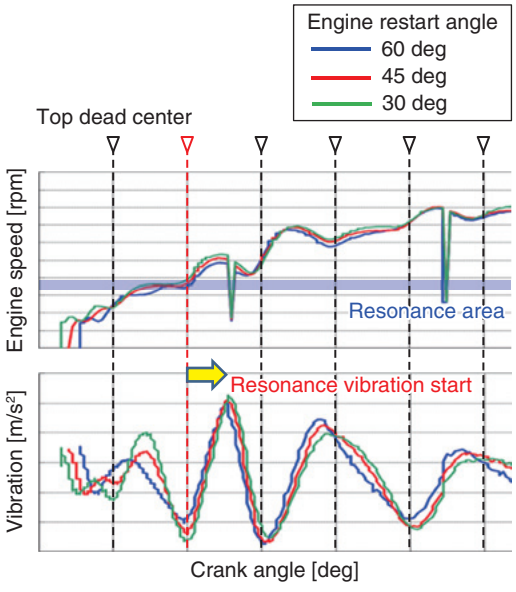


Fig. 6 Vibration at engine restart

balance between suction and opening of the plunger shifts further to the suction side the greater the magnitude of the vibration. The method adopted in order to cancel engine resonance vibration was therefore to impress a DC current in the coils and shift the position of the exciter plate to the suction side in advance, following which initial ACM current control is applied. Figure 8 shows the effects of this control method. The impression of an initial DC current makes it possible to drive the ACM to produce an amplitude of vibration that cancels resonance vibration at engine restart.

This method has made it possible to realize a feed-forward ACM control that accurately identifies the timing and magnitude of resonance vibration at engine start and drives the ACM to produce the necessary amplitude of vibration to cancel the resonance vibration.

4.3. Development of a High-amplitude ACM System

The maximum amplitude of vibration demanded from the ACM system in order to respond to resonance vibration at engine restart represented more than 1.5 times the force produced by a conventional ACM system. In addition, the greater amplitude of vibration also necessitated the realization of increased current responsiveness in the actuators. In this development, it was therefore necessary to develop an ACM system that balanced high amplitude and high responsiveness.

To generate a high amplitude of vibration, it was necessary to increase the magnetomotive force that provides the source for ACM actuator thrust. Because magnetomotive force is the product of the number of coils in the actuator and the impressed current, this could be achieved by increasing the number of coils. However, if the number of coils was to be increased while retaining a conventional configuration, the exterior dimensions of the actuator would increase, thus increasing the size of the ACM, a factor that would affect their ease of vehicle fitting. In order to realize high amplitude without increasing the size of the ACM, a bobbinless configuration that did away with the bobbin that provided the support structure for the coils was adopted (Fig. 9). This helped to ensure coil winding space on the inner diameter of the coils, contributing to the prevention of an increase in the external dimensions of the ACM and making it possible to maintain the dimensions of a mass-production ACM while realizing high-amplitude operation.

The realization of the necessary increase in current responsiveness by increasing the number of coil windings will be discussed below. Current response, $I(t)$, is expressed by Eq. (1), and inductance, L, used in Eq. (1), is expressed by Eq. (2).

$$I(t) = \frac{V}{R}\left[1 - \exp\left(-\frac{R}{L}t\right)\right] \quad (1)$$

V: Voltage impressed in coil
R: Coil resistance
L: Inductance

$$L = \frac{\mu N^2 \pi r^2}{l} \quad (2)$$

μ: Magnetic permeability
N: Number of coil windings
r: Radius of coil
l: Length of coil

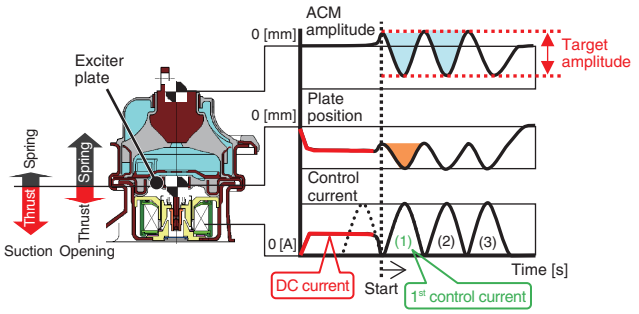


Fig. 7 ACM control method of using initial DC current

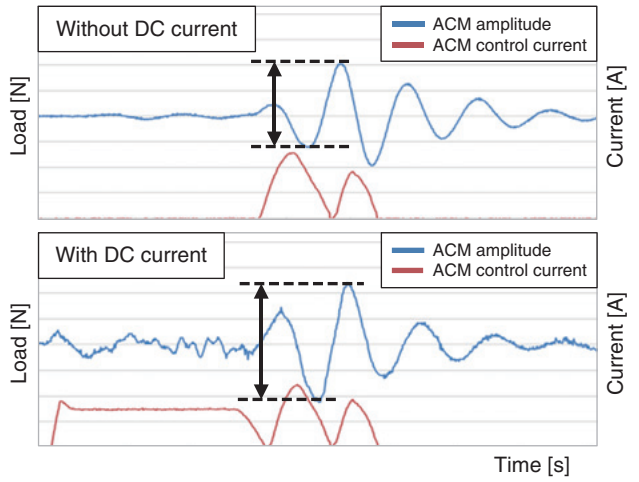


Fig. 8 Effect of developed ACM control method



Fig. 9 Bobbinless ACM actuator

Equations (1) and (2) indicate that increasing the number of coil windings, N, in order to realize high amplitude will increase coil resistance, R, and inductance, L, resulting in a decline in current responsiveness. This research therefore employed a booster ACM ECU provided with a voltage booster circuit in order to increase current responsiveness by increasing the voltage impressed in the coil, term V in Eq. (1).

The use of a bobbinless actuator and a booster ACM ECU (Fig. 10) balanced high amplitude with high response, helping to enable the development of an ACM system able to respond to high-amplitude resonance vibration at engine start.

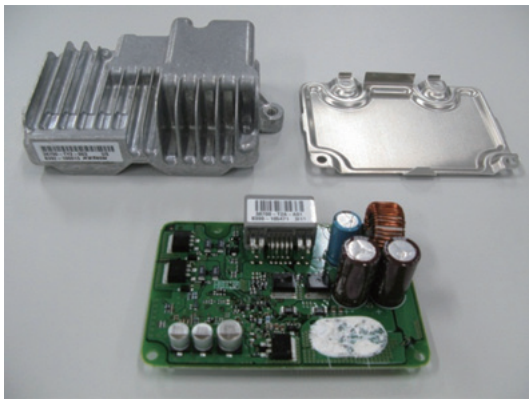


Fig. 10 Booster ACM ECU

5. Effect of System in Complete Vehicle

The effect of reduction in the transfer of resonance vibration to the body at engine restart realized by ACM control and the high-amplitude ACM system was verified. Figure 11 shows vibration measurement points in a complete vehicle. The load under the rear ACM (Point A in Fig. 11) and floor vibration under the driver's seat (Point B in Fig. 11) were selected for measurement, and the effect of the system on NV performance in a complete vehicle was studied.

Figure 12 shows the load under the rear ACM at engine restart with the ACM in operation and not in operation. The use of ACM control makes it possible to reduce the transmission of resonance vibration to the body at engine restart by 60% or more. Figure 13 shows vibration of the floor in the cabin at engine start. The target for NV performance in the complete vehicle is shown by the arrow. The use of ACM control reduced floor vibration, making it possible to realize the targets for NV performance.

The results discussed above verify the effect of application of ACM control at engine restart on NV performance in a complete vehicle.

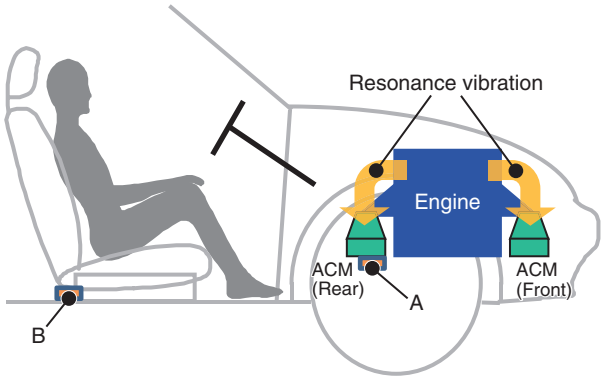


Fig. 11 Measurement points

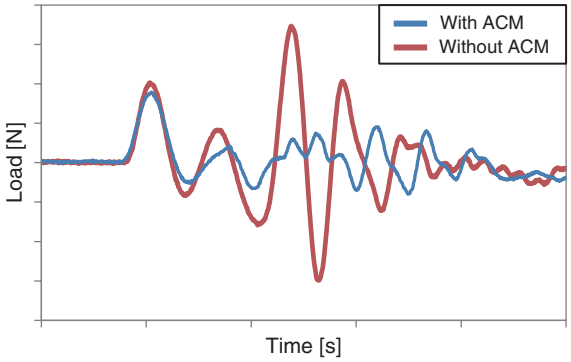


Fig. 12 Input load for rear ACM

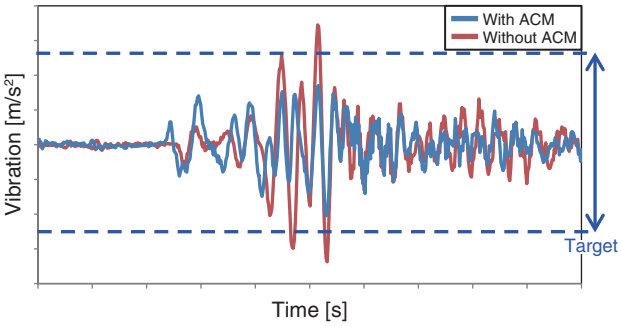


Fig. 13 Floor vibration

6. Conclusion

The development of a next-generation ACM to respond to the issue of resonance vibration produced at engine restart without the intention of the driver made it possible to realize NV performance targets in a complete vehicle.

(1) A new ACM control method was developed that identifies the timing of resonance vibration at engine restart and impresses a DC current in advance, making it possible to realize the high-amplitude ACM drive

necessary to cancel the resonance vibration of the engine using initial current control, thus reducing the transmission of vibration to the body.

(2) The use of a bobbinless actuator and a booster ACM ECU made it possible to develop an ACM system realizing high-amplitude vibration and high current responsiveness when resonance vibration occurs at engine restart.

References

(1) Matsuoka, T., Mikasa, T., Nemoto, H.: Development of Active Control Engine Mount, Honda R&D Technical Review, Vol. 15, No. 2, p. 209-214

(2) Ishiguro, T., Yone, T., Nemoto, H.: Development of Active Control Engine Mount System which Reduces Higher Harmonic Vibration, Honda R&D Technical Review, Vol. 22, No. 1, p. 185-191

■ Author ■


Tatsuhiro YONE


Hideyuki OKAMOTO


Takashi YAMAGUCHI


Shintaro FURUI


Hirotomi NEMOTO

Control Parameter Optimization for Reduction of 2nd Order Vibration in Hybrid Drive Mode of SPORT HYBRID i-MMD

Tatsunori TSURUTA*

ABSTRACT

During development of the 2014 model-year Accord Hybrid, for which the SPORT HYBRID i-MMD new model hybrid system was adopted, 2nd-order vibration transmitted to the steering became an issue. This occurred because the vehicle has higher engine net torque than a gasoline engine vehicle, so that there is larger crankshaft revolution 2nd-order fluctuation, which is the source of the vibration. There is concern that using only reduction of engine net torque as the means to lessen crankshaft revolution 2nd-order fluctuation could cause an increase in the brake-specific fuel consumption. Therefore the combustion control parameters, such as ignition timing and valve operation timing, were changed as a way of optimizing crankshaft revolution 2nd-order fluctuation, engine net torque, and brake-specific fuel consumption. These measures achieved the steering vibration target while also determining the optimal point where the amount of engine net torque reduction could be lessened by 5 Nm and 1% of the increase in brake-specific fuel consumption could be recovered.

1. Introduction

As hybrid electric vehicles (HEV) are now being sold by automobile manufacturers, it has become important to enhance the appeal of HEV qualities other than fuel economy performance. In this context, noise and vibration (NV) performance has become an issue because the cabin noise level in a moving HEV differs greatly between when the engine is running and when it is not, and this difference is easy to recognize[1].

In 2012, Honda announced the SPORT HYBRID Intelligent Multi-Mode Drive (SPORT HYBRID i-MMD) as a new HEV system comprising a 2.0-L gasoline engine and two motors in combination[2), 3)]. Integrated Motor Assist (IMA)[4], which is a conventional one motor-type HEV system, is a parallel hybrid mechanism, but the SPORT HYBRID i-MMD is a series hybrid system, and has achieved the low fuel consumption of 30.0 km/L in JC08 mode.

In hybrid drive mode, which involves series hybrid operation, the engine power is used only to generate power from a generator. The actual driving of the vehicle is performed only by the motors. Since the engine power is not directly linked to the drivetrain when this happens, the engine operating conditions are not dependent on the vehicle acceleration or the vehicle speed demanded. Consequently, engine control can set operating conditions that minimize brake-specific fuel consumption (BSFC).

In gasoline engine vehicles, the engine and the drivetrain are directly linked. When driving under moderate acceleration, the required engine net torque is 30 Nm lower than when operating at minimum BSFC, so these vehicles cannot operate in the minimum BSFC region. In the hybrid drive mode of the SPORT HYBRID i-MMD, however, the engine can be operated at high engine net torque in which BSFC is always at a minimum. As a result, the increase in crankshaft revolution 2nd-order fluctuation causes increased engine 2nd-order vibration that is transmitted to the vehicle body. It is the resulting steering wheel 2nd-order vibration that has become an issue.

When using reduction of engine net torque alone to lessen crankshaft revolution 2nd-order fluctuation, increased BSFC becomes a concern. A method was therefore employed to limit engine net torque by means of control that changes the ignition timing, valve operation timing, and other such combustion control parameters so as to optimize the crankshaft revolution 2nd-order fluctuation, engine net torque, and BSFC. This paper reports on the content of this series of control events.

* Automobile R&D Center

2. SPORT HYBRID i-MMD Characteristics

Figure 1 shows the SPORT HYBRID i-MMD system configuration[5]. The engine is the source of power, and the generator uses that power to produce electricity. The generated electricity is stored in batteries and used as the power to drive the motors. The solid lines in the diagram show the route of mechanical transmission of power, and the dotted lines show the route by which electricity is transmitted.

The SPORT HYBRID i-MMD switches the driving mode according to the vehicle speed and the battery level at the time. Figure 2 shows the route by which power is transmitted in each mode. The heavy solid lines in the figure indicate the routes by which power and electricity are actually transmitted in each mode.

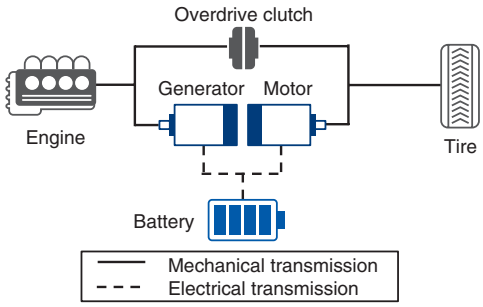


Fig. 1 SPORT HYBRID i-MMD system configuration

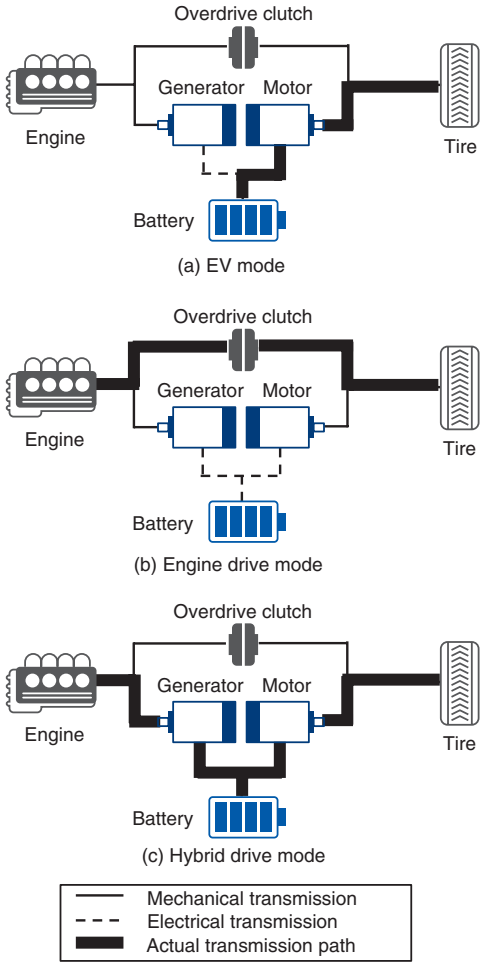


Fig. 2 Three drive modes in SPORT HYBRID i-MMD

In the electric vehicle (EV) mode shown in Fig. 2(a), the engine is stopped and the motors drive the tires using electricity stored in a battery.

In the engine drive mode shown in Fig. 2(b), the overdrive clutch is engaged and engine power goes directly to the tires via mechanical transmission. This is used when cruising at a vehicle speed of 70 km/h or more, where the engine is more efficient than the motors.

In the hybrid drive mode shown in Fig. 2(c), engine power does not go directly to the tires via mechanical transmission, but instead is used only to generate electric power with the generator. Power transmission to the tires occurs entirely from the motors. This is used when cruising at a vehicle speed of 70 km/h or less, where the motors are more efficient than the engine. This hybrid drive mode is not found in the conventional IMA, which is a parallel hybrid mechanism, and this is the greatest distinguishing characteristic of the SPORT HYBRID i-MMD.

3. Steering Vibration Issue and Reason for Overrunning Vibration Target

3.1. Steering Vibration Level in the Prototype

Figure 3 shows the level of steering wheel 2nd-order vibration occurring in the prototype 2014 model year Accord Hybrid (new model Accord Hybrid) when driving under moderate acceleration. The prototype overran the target line by 4 dB at approximately 1800 rpm to 2000 rpm, and this overrun had to be reduced.

3.2. Reason for Overrunning Steering Wheel 2nd-order Vibration Target

The mechanism by which the steering wheel 2nd-order vibration overran the target was analyzed in terms of the vibration exciting force.

The steering wheel 2nd-order vibration in a gasoline engine vehicle occurs via two routes. In one, crankshaft revolution 2nd-order fluctuation is transmitted from

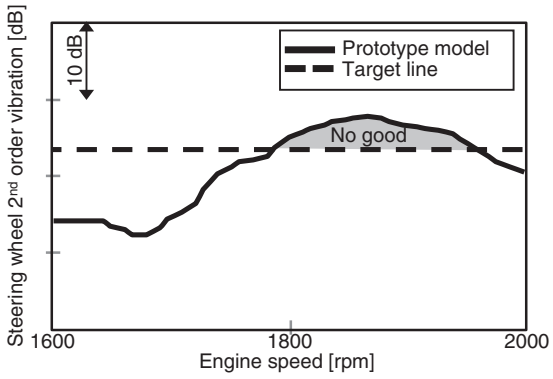


Fig. 3 Prototype model steering wheel 2nd order vibration and target line

drivetrain parts through suspension parts to the steering wheel. In the other, engine 2nd-order vibration that originates in crankshaft revolution 2nd-order fluctuation is transmitted through the engine mounts to the steering wheel.

When the new model Accord Hybrid is in hybrid drive mode, the engine power is used only to generate electricity with the generator, and there is no transmission route from the engine to the drivetrain. Therefore, the steering wheel 2nd-order vibration occurs through the transmission route by means of the engine mounts.

Figure 4 is a BSFC contour diagram that shows control configurations minimizing BSFC for each engine net torque in the 2.0-L engine used with the SPORT HYBRID i-MMD. It indicates that areas in the diagram where BSFC values are smaller have better fuel economy.

The outlined area marked with diagonal lines shows a gasoline engine vehicle traveling under moderate acceleration. The engine net torque varies greatly according to how the driver utilizes the accelerator, even at the same engine speed. Since the engine and the drivetrain are directly linked together, if the driver attempts to drive in the area of minimum BSFC, the resulting high engine net torque ends up causing the vehicle to accelerate suddenly. When driving under moderate acceleration, therefore, the high torque area where BSFC is minimal cannot be used readily.

When the new model Accord Hybrid is in hybrid drive mode, however, the engine power is not directly linked to the drivetrain. Consequently, the engine is not dependent on how the driver utilizes the accelerator, or on the vehicle acceleration or the vehicle speed demanded, and control can be implemented to keep the engine tracing the solid line in the diagram where the BSFC is always at a minimum. As a result, the engine net torque generated under moderate acceleration is greater than in a gasoline engine vehicle.

Figure 5 shows the relationship between engine net torque and steering wheel 2nd-order vibration, engine 2nd-order vibration, and crankshaft revolution 2nd-order fluctuation at 2000 rpm. The round symbols (◯) in the figure mark the positions where engine net torque changed when the new model Accord Hybrid was operating in hybrid drive mode under moderate acceleration. The square symbols (□) mark the positions where a gasoline engine vehicle was operated under moderate acceleration. These correlations exist because when the engine net torque increases, the engine 2nd-order vibration and crankshaft revolution 2nd-order fluctuation increase, and there is also a tendency for the steering wheel 2nd-order vibration to increase.

The prototype of the new model Accord Hybrid has engine net torque that has increased by approximately 30 Nm relative to gasoline engine vehicles. The engine 2nd-order vibration shows an increase of 5 dB and the crankshaft revolution 2nd-order fluctuation an increase of 6 rpm.

This suggests that the main reason for overrunning the steering wheel 2nd-order vibration target in hybrid drive

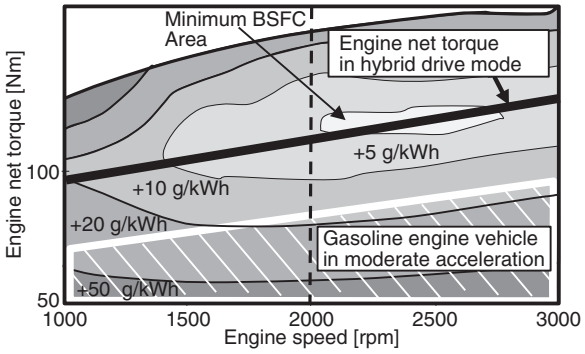


Fig. 4 BSFC and engine net torque under moderate acceleration in Accord Hybrid

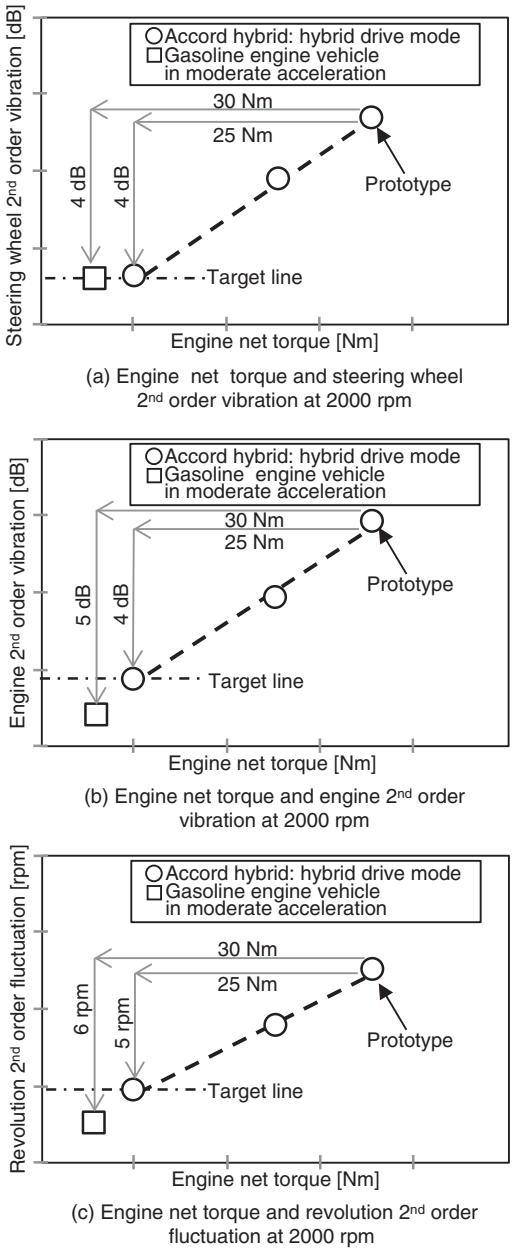


Fig. 5 Engine net torque and each 2nd order parameter at 2000 rpm

mode is the increase in engine net torque.

It is also apparent that the engine 2nd-order vibration must be lowered by 4 dB and the crankshaft revolution 2nd-order fluctuation must be reduced by 5 rpm in order to meet the steering wheel 2nd-order vibration target.

4. Reduction of Crankshaft Revolution 2nd-order Fluctuation and Reduction of BSFC as Mutually Exclusive Aims

The extent of change in the BSFC due to steps to reduce crankshaft revolution 2nd-order fluctuation by limiting engine net torque was checked.

Figure 6 is a graph showing the relationship between engine net torque and BSFC. The tendency here is the reverse of what was seen in Fig. 5. When the engine net torque is reduced, the BSFC increases, and it is apparent that crankshaft revolution 2nd-order fluctuation and BSFC are mutually exclusive aims. This is because when engine net torque is reduced, it becomes more distant from the solid line marking minimum BSFC in Fig. 4. When engine net torque is reduced to a level that meets the crankshaft revolution 2nd-order fluctuation target, the BSFC increases by 6% relative to the prototype. It was decided, therefore, to investigate methods for obtaining a better BSFC level.

5. Mitigating the BSFC Increase by Combustion Control Parameter Optimization

The ideal in terms of NV and fuel economy is control that will meet the crankshaft revolution 2nd-order fluctuation target while reducing the amount by which engine net torque is limited so as to mitigate the BSFC increase. When the amount of electricity generated by the generator is also taken into account, it is desirable to have a higher engine net torque.

An investigation was made of a procedure to achieve this in which combustion control was configured by standards that would yield the BSFC values in Fig. 4

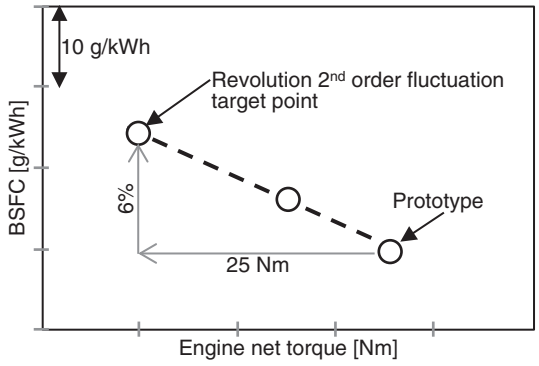


Fig. 6 Engine net torque and BSFC in hybrid drive mode at 2000 rpm

for every engine net torque. Then, from that, the ignition timing, valve operation timing, and other such combustion control parameters were altered to limit the engine net torque. In this way, the crankshaft revolution 2nd-order fluctuation, engine net torque, and BSFC were optimized.

5.1. Altering Combustion Control Parameters to Change Crankshaft Revolution 2nd-order Fluctuation and BSFC

A parametric study test was conducted of combustion control parameters as represented by throttle position (TH), ignition timing (IG), EGR volume, and valve operation timing (VTC) in the variable intake valve system. The test was used to search for a control point at which the 2nd-order fluctuation target is achieved while BSFC is kept to a minimum. This engine speed was set at 2000 rpm.

Figure 7 shows a 3D contour diagram that compares all the data from the test. The VTC 75 deg in the upper row and the VTC 50 deg in the lower row are the results of changes to TH, IG, and EGR volume. Larger VTC angles indicate timing that is farther on the advanced side. The left column shows contour diagrams of crankshaft revolution 2nd-order fluctuation, with darker red colors indicating larger values. Dotted lines demarcate the area in which the crankshaft revolution 2nd-order fluctuation target is achieved. The right column shows contour diagrams indicating BSFC, with darker red colors indicating larger BSFC.

Altering the combustion control parameters was found to significantly change the crankshaft revolution 2nd-order fluctuation and BSFC values.

5.2. Extracting the BSFC Minimum Point from the Crankshaft Revolution 2nd-order Fluctuation Target Achievement Area

Figure 8 shows an organized view of the parametric study test results from Fig. 7 with engine net torque on the horizontal axis and BSFC on the vertical axis. The contour diagram that is completely colored in shades of gray shows the magnitude of the crankshaft revolution 2nd-order fluctuation, with darker gray indicating a larger value. The target value for crankshaft revolution 2nd-order fluctuation was 8 rpm.

The solid line in the figure represents the line of change that occurs when engine net torque in the base settings for combustion control is reduced from the level marked with the round (◯) symbol with regard to the prototype. The dotted lines in the figure link together the points marked with the X (×) symbol where BSFC is at a minimum under control conditions with crankshaft revolution 2nd-order fluctuation at 6, 7, 8, 9, and 10 rpm.

Comparison of these two lines shows that engine net torque is larger and BSFC is smaller on the dotted lines than on the solid lines. This is the case even when the crankshaft revolution 2nd-order fluctuation is the same.

The point on the solid line where the crankshaft revolution 2nd-order fluctuation target is achieved is marked

with a blank triangle (△) symbol, and the point on the dotted lines where the target is achieved is marked with a black triangle (▲) symbol. These two points are the same as the control points marked with a blank triangle (△) symbol and a black triangle (▲) symbol plotted on the 3D diagram in Fig. 7. On the black triangle (▲) symbol, the crankshaft revolution 2nd-order fluctuation is equal to that on the blank triangle (△) symbol, but the engine net torque is 5 Nm higher on the former. This is therefore the optimal combustion control point where 1% of the BSFC increase relative to the prototype is also recovered.

In this way, the optimal point for reducing the amount by which engine net torque is limited and mitigating the BSFC increase while achieving the crankshaft revolution 2nd-order fluctuation target was found.

5.3. Characteristics of the Cylinder Pressure Waveform When Optimizing Combustion Control Parameters

Figure 8 made clear that optimization could be sought by means of combustion control parameter conditions. An examination was made of the characteristics of the cylinder pressure waveform when that is done, as well as of the parameter changes that are necessary when seeking optimization by means of combustion parameters.

Table 1 presents a comparison of combustion parameters for Control A and Control B where engine net torque and BSFC are the same, but the crankshaft revolution 2nd-order fluctuation is different. Figure 9 shows the combustion pressure waveform for one cylinder at every crank angle for Control A and Control B in the upper half of the graph, and the total value of engine net torque for

Table 1 Comparison of engine control parameters for Control A and Control B

	TH [deg]	IG [deg]	EGR [%]	VTC [deg]	Revolution 2nd order fluctuation [rpm]	Engine net torque [Nm]	BSFC
Control A	15	15	20	75	11	100	Same
Control B	17	28	10	50	9.2		

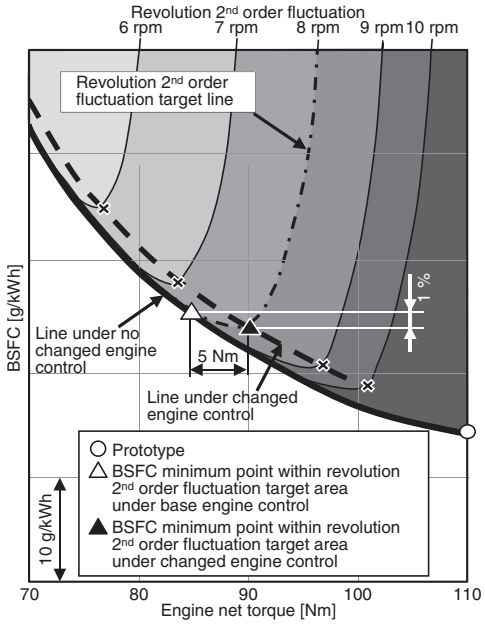


Fig. 8 Comparison of engine net torque, BSFC, and revolution 2nd order fluctuation under different engine combustion controls at 2000 rpm

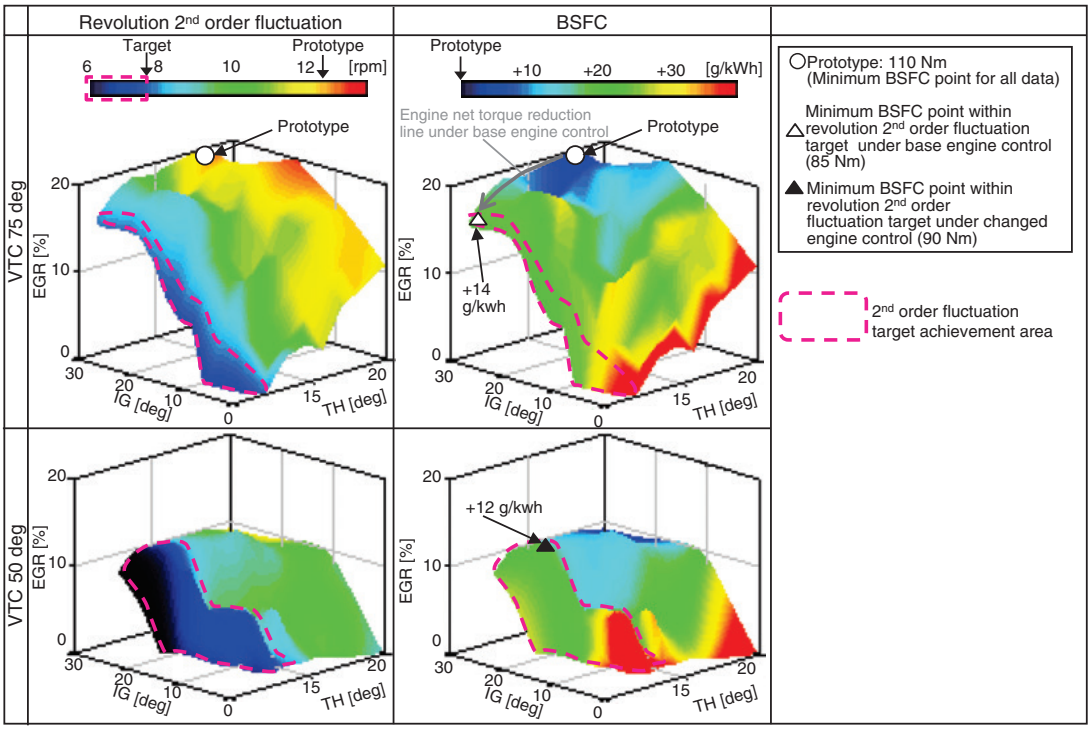


Fig. 7 Relationship of revolution 2nd order fluctuation and BSFC under various TH, IG, EGR, and VTC at 2000 rpm

all cylinders in the lower half of the graph. The crankshaft revolution 2nd-order fluctuation is smaller in Control B than in Control A, so Control B can be considered advantageous in this comparison of the two.

Focusing on the combustion pressure waveform, it is apparent that the Control B compression pressure near crank angle 340 deg, just before compression top dead center, is smaller than in Control A. On the other hand, the cylinder pressure peak that occurs after compression top dead center, near crank angle 375 deg, is higher than the peak in Control A and the position of the occurrence is also further on the advanced side of the ignition timing than in Control A. This indicates that the amount of air inflow in Control B is smaller than in Control A and that the ignition timing is further advanced. The influence of the amount of air inflow results in a smaller absolute value for the torque just before compression top dead center in Control B.

On the other hand, the torque after compression top dead center is the same in Control A and B. This is because, although the Control B cylinder pressure peak is higher because of the advanced ignition, the position where the peak occurs is near compression top dead center, and as a result, the component of cylinder pressure force that is converted into crankshaft torque is smaller.

Figure 10 shows a graph that compares each order of engine net torque fluctuation components for Control A and B. The 2nd-order component that is at issue in this paper is smaller in Control B.

This suggests that the compression pressure before compression top dead center has a significant influence on torque 2nd-order fluctuation. If the position where cylinder pressure immediately after compression top dead center reaches a peak is on the advanced side, at around crank angle 375 deg, it is likely to have little influence on torque 2nd-order fluctuation.

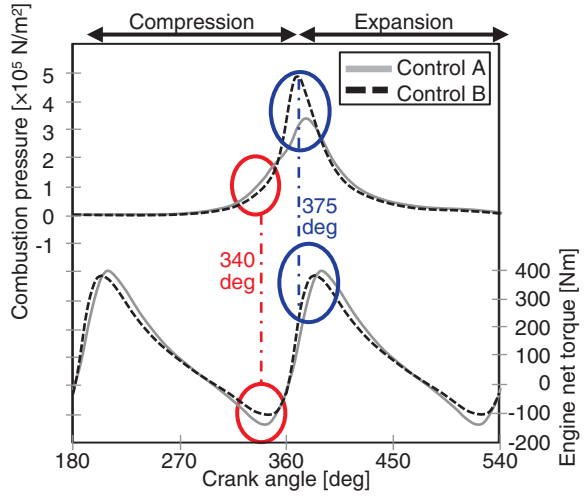


Fig. 9 Crank angle data of combustion pressure and engine net torque for Control A and B at 2000 rpm

These results indicate that combustion control that is desirable from the perspective of reducing crankshaft revolution 2nd-order fluctuation will close down the throttle and reduce the amount of air inflow into the cylinder while advancing the ignition timing to a point just before knocking begins in order to address the engine net torque deficit.

From the perspective of engine net torque and BSFC, on the other hand, it is desirable for combustion control that opens the throttle wide and advances the ignition timing in order to increase the amount of air inflow and reduce pumping loss. This increase in the amount of air inflow, however, results in increased crankshaft revolution 2nd-order fluctuation. Therefore, although advancing the ignition timing is effective in addressing both matters, the two are mutually exclusive aims where the throttle is concerned.

In order to achieve a balance of the two, it is effective to retard the VTC, which means adopting the Atkinson cycle so as to return the air that has flowed into the cylinder back into the intake during the compression cycle. That, together with the combination of a wider open throttle and advanced ignition timing, can be used to bring about optimization.

When the matter of reducing steering wheel 2nd-order vibration in the new model Accord Hybrid first came under investigation, it was thought that crankshaft revolution 2nd-order fluctuation was governed by the influence of combustion pressure after compression top dead center. The focus therefore was on reducing combustion pressure in order to limit engine net torque. At that time, no consideration was yet being given to compression pressure before compression top dead center. However, parametric study test results revealed that it was not only a matter of combustion pressure after compression top dead center; compression pressure before compression top dead center also exerted an influence that could not be ignored. It was found that extending consideration to reducing compression pressure, therefore, could realize more efficient combustion control.

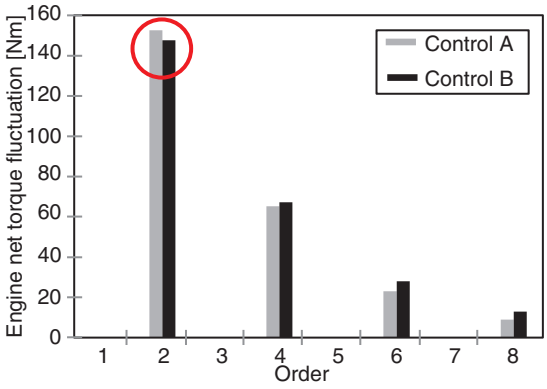


Fig. 10 Orders of engine net torque fluctuation for Control A and B at 2000 rpm

6. Results from Verification of Steering Wheel Vibration Reduction in the Actual Vehicle

Investigation of combustion control parameter optimization was also conducted by the same method for engine speeds other than 2000 rpm. This yielded the prospect of achieving objectives for 2nd-order vibration and fuel economy, and the approach was applied to a mass-production model.

Figure 11 shows the steering wheel 2nd-order vibration reduction effect. The steering wheel 2nd-order vibration in the mass-production vehicle was reduced a maximum of 4 dB relative to the prototype, enabling achievement of the target.

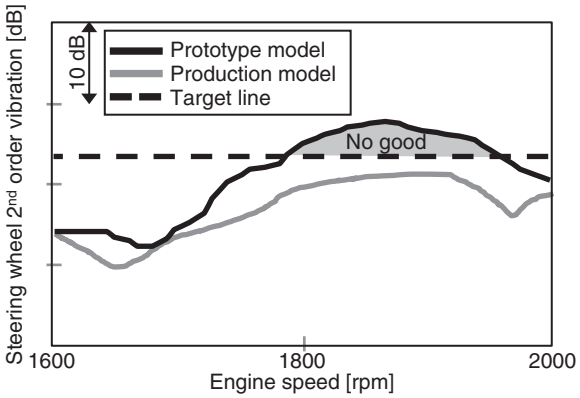


Fig. 11 Steering wheel 2nd order vibration

7. Conclusion

Analysis of the cause of steering wheel 2nd-order vibration and establishment of methods for reducing such vibration are described below. These enabled achievement of the steering wheel 2nd-order vibration target in an actual vehicle.

(1) When the new model Accord Hybrid is in hybrid drive mode, implementing operation control that holds BSFC to a minimum at each engine speed raises the engine net torque by approximately 30 Nm relative to a conventional gasoline engine vehicle driving under moderate acceleration. That influence causes engine 2nd-order vibration to increase a maximum of 5 dB and crankshaft revolution fluctuation to increase by 6 rpm. This is the main reason that steering wheel 2nd-order vibration overran the target figure in the prototype.

(2) A parameter study was conducted of combustion control that optimizes crankshaft revolution 2nd-order fluctuation, engine net torque, and BSFC for the purpose of reducing steering wheel 2nd-order vibration. The result was discovery of the optimal point at which combustion control aimed at adopting the Atkinson cycle limited engine net torque and achieved the crankshaft revolution 2nd-order fluctuation reduction target while also recovering 1% of the BSFC increase relative to combustion control before changes were made.

References

(1) Matsumoto, S., Ishikura, M.: The Latest Hybrid Passenger Cars, Journal of Society of Automotive Engineers of Japan, Vol. 61, No. 9, p. 49-54 (2007) (in Japanese)

(2) Yonekawa, A., Watanabe, O., Sekiya, N., Ishikawa, N.: Development of New 2.0 L Gasoline Engine for Accord Hybrid, Honda R&D Technical Review, Vol. 25, No. 2, p. 27-32

(3) Ide, H., Sunaga, Y., Higuchi, N.: Development of SPORT HYBRID i-MMD Control System for 2014 Model Year Accord, Honda R&D Technical Review, Vol. 25, No. 2, p. 33-41

(4) Ochiai, S., Uchibori, K., Hara, K., Ttsurumi, T., Suzuki, M.: Development of a Motor Assist System for a Hybrid Car - INSIGHT, Honda R&D Technical Review, Vol. 12, No. 1, p. 7-14

(5) http://www.honda.co.jp/ACCORD/webcatalog/performance/details01/

■ Author ■



Tatsunori TSURUTA

Design of Floating Seat for Control of Seat Resonance Frequencies

Kengo YABE* Toru INAGAKI* Takashi KONDO*

ABSTRACT

A method of seat design that makes it possible to control resonance frequencies of the seat in order to reduce seat vibration when the vehicle is idling and when it is in motion has been proposed. The research discussed in this paper made it possible to reduce vibration by controlling the resonance frequencies by replacing the structures of the seat-mounting unit with floating structures using rubber bushings. It was also shown that partly replacing the mounting unit with floating structures makes it possible to control the resonance frequencies of the entire seat. Compared to a design that replaces the entire seat-mounting unit with floating structures, this design makes it possible to optimally position floating structures for each type of seat. The issue of balancing vibration reduction with strength and durability and crash safety performance due to fitting the floating structures to the seat-mounting unit was addressed using stopper structures optimized for each type of input. The use of the floating structures in an actual vehicle realized a lighter-weight seat configuration than the use of conventional vibration countermeasures.

1. Introduction

Automotive seats are a part with which a vehicle occupant's body is constantly in contact, from entering to exiting the vehicle, making them an important part that affects the commercial appeal of the vehicle. From the perspective of vibration performance, identifying how to reduce the vibration felt by vehicle occupants through the seat when the vehicle is idling and when it is in motion is an important issue in the development process. Measures that reduce the vibration input from the mounting points of the seat[(1)] and measures that reduce the vibration response of the seat itself by adding inertia masses or adopting dynamic dampers are employed to address this issue. Measures against vibration by the use of dynamic dampers are widely used, however this increases the weight of the entire seats. Currently, the automotive industry is seeking to reduce the weight of all the parts that compose vehicles in order to increase fuel efficiency and reduce CO_2 emissions. For seats as for other parts, it is necessary to restrain increasing mass even if this enhances vibration performance. Against this background, the research set out to balance the reduction of the weight of the seat with vibration performance.

In order to reduce vibration of the seat, an effective method is to attempt to ensure that the resonance frequencies of the seat do not coincide with the frequencies of the input vibration, thus reducing the vibration response of the seat to the target frequencies. However, in order to control the seat's resonance frequencies without increasing weight, it is necessary to reduce the stiffness of the seat bottom, and this has made the achievement of a balance with strength and durability performance and crash safety performance an issue. The present research added rubber bushings provided with stopper structures to sections of the seat-mounting unit structure, making it possible to realize a balance between control of the seat's resonance frequencies and strength and durability performance and crash safety performance.

2. Development Goals

The phenomena that represent issues in the area of seat vibration are vibration while the vehicle is idling and vibration while the vehicle is in motion. As Fig. 1 shows, vibration while idling is a phenomenon that occurs because the resonance frequencies in the longitudinal and lateral directions of the seat are close to the frequencies of vibration input from the engine.

As Fig. 2 shows, vibration while the vehicle is in motion occurs because the torsion mode frequencies of the body and the lateral resonance frequencies of the seat are close to each other when random frequency input is imparted from the suspension to the body. Because the body mode that excites the longitudinal vibration of the seat is rarely close to the range of the resonance frequencies of the seat, longitudinal vibration of the seat is seldom an issue.

* Automobile R&D Center

In order to respond to these issues, it is necessary to conduct design keeping the longitudinal and lateral resonance frequencies of the seat away from the vibration frequencies of the input and body modes that are factors in the occurrence of the issues. Conventionally, the method adopted has been to reduce the seat's resonance frequencies by adding inertia masses[2]. In many cases the control of the seat's resonance frequency using inertia masses is inadequate, and dynamic dampers are also widely used. Both of these methods increase the weight of the seat. Figure 3 shows the results of an analysis of the optimization of the thickness of sections of the seat in order to obtain the necessary resonance frequencies without increasing the weight of the seat. In this analysis, the longitudinal resonance frequency was varied from 19 Hz to 15 Hz, and the lateral resonance frequency was varied from 18 Hz to 16 Hz. As the figure indicates, using a conventional seat structure, it would be necessary to reduce the thickness of the base of the seat by half in order to obtain the necessary resonance frequencies. This would represent an issue in terms of achieving a balance with strength and durability performance and crash safety performance.

This research therefore sought to develop a method of seat design that would realize the following three goals:

(1) Make it possible to control the seat's resonance frequencies;
(2) Realize a balance with strength and durability performance and crash safety performance; and
(3) Realize a reduction in weight against a seat using inertial mass or dynamic dampers.

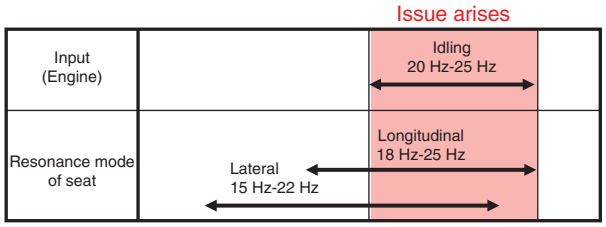


Fig. 1 Frequency of vibration when vehicle is idling

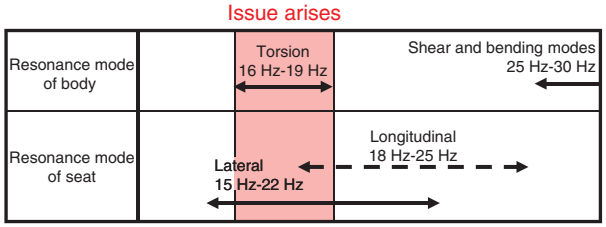


Fig. 2 Frequency of vibration when vehicle is in motion

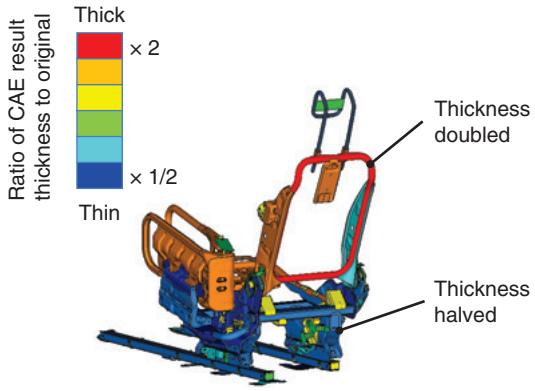


Fig. 3 CAE result for reducing resonance frequency of seat

3. Floating Seat Design Method

In this research, the target seat design method was realized by replacing the mounting structure of the seat with rubber bushings provided with stopper structures. These rubber bushings will be termed "floating structures," and seats to which they have been applied will be termed "floating seats" below.

3.1. Concept of Positioning of Floating Structures

The resonance frequencies demanded from the seat differ depending on the resonance frequencies of the body modes of the specific vehicle and the engine speed set for idling. The basic structure of the seat also differs depending on the seat of the specific vehicle, and the resonance frequencies of the longitudinal and lateral eigenmodes change respectively. As a result, there are vehicles in which the resonance frequency in the longitudinal direction represents an issue, and vehicles in which the resonance frequency in the lateral direction represents an issue. The verification regarding the number of floating structures employed and the positions in which they are employed was performed to realize the control method for optimal resonance frequencies in response to the specific vehicle body and seat. Figure 4 shows changes in resonance frequencies when all of the mounting points of the seat are replaced with floating structures, when only the rear mounting points are replaced with floating structures, and when only the mounting points on the outer sides of the seat are replaced with floating structures. The seat using the



	Conventional	Floating structure		
		All	Rear	Outer side
Longitudinal resonance mode	23 Hz	16 Hz (-7 Hz)	17 Hz (-6 Hz)	18 Hz (-5 Hz)
Lateral resonance mode	19 Hz	13 Hz (-6 Hz)	17 Hz (-2 Hz)	16 Hz (-3 Hz)

Fig. 4 Differences in resonance for different floating structure positions

floating structures for all the points reduce the resonance frequencies the most in both longitudinal and lateral directions. Comparison of a seat using floating structures for the two mounting points at the rear of the seat and a seat using floating structures for the two mounting points at the outer sides of the seat showed that the former had a greater resonance frequency reduction effect in the longitudinal direction and the latter had a greater effect in the lateral direction.

Figure 4 indicates that even when only some floating structures are employed, it is possible to reduce its resonance frequencies. It also indicates that it is possible to realize optimal designs in relation to the necessary characteristics by changing the positioning and number of the floating structures in accordance with the longitudinal or lateral directions in which the reduction of the resonance frequency is desired.

3.2. Specific Structure

Three characteristics are demanded of the floating structures: To possess a spring constant making it possible to realize the desired seat resonance frequencies in the small amplitude area required for vibration performance; To continue to satisfy the spring constant following strength and durability tests; and To avoid the seat from being displaced during crash safety tests. Figure 5 shows the actual structure of the floating seat. Figure 5(a) shows the rubber bushing that helps to realize the desired seat resonance frequencies. The seat resonance frequencies are controlled by adjusting the spring constant. Figure 5(b) shows a stopper structure that helps to prevent the rubber bushing from breaking under the input experienced during strength and durability tests. This helps to retain the desired seat resonance frequencies even after strength and durability tests. Figure 5(c) shows a stopper that helps to ensure that the floating structure itself will not break even in the event that rubber parts (a) and (b) break in response to the large input associated with a crash. It was verified that the structures displayed no issues even as a result of the input associated with crash safety performance tests.

In addition, the example of the specific layout for the floating structures is shown in Fig. 6. The floating structures can also be fitted in the seat-body assembly area as shown in (a), or fitted inside the mounting structure of the seat as shown in (b). It is possible to realize the optimum positioning for the specific seat structure to achieve a balance with other mechanisms.

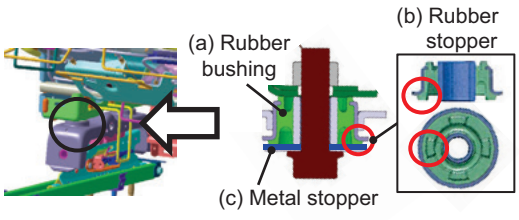
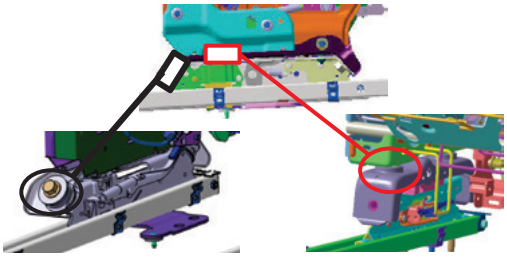


Fig. 5 Parts of floating structure

3.3. Method of Setting Spring Constant

The floating structure spring constant necessary for the realization of the seat resonance frequencies demanded by seat vibration performance was set after conducting frequency analysis by means of CAE using FEM. The seat resonance frequencies are affected by the stiffness of the seat frame and mounting section. CAE is therefore used in modeling the structure of the seat unit and the mounting section as shown in Fig. 7 by considering the body as a rigid body. With regard to the coupling of the seat to the vehicle body, constraint conditions were applied in the actual bolt-coupling sections. In addition, the rubber bushing was analyzed by setting the spring constant to six-degree-of-freedom. The spring constant of the rubber bushing was varied and a parameter study conducted, making it possible to determine the characteristics that would produce the optimum resonance frequencies.

A variety of methods have previously been employed in predicting resonance frequencies when a seat is occupied[3]. The method adopted in this research was to estimate the change in the resonance frequencies between unoccupied and occupied seats in advance, following which an analysis was conducted for an unoccupied seat.



(a) Positioned between seat and body (b) Positioned in seat

Fig. 6 Layout of floating structure

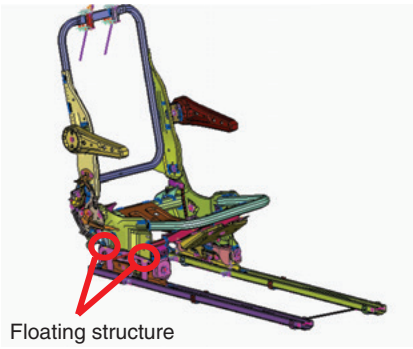


Fig. 7 Model for calculation of seat resonance frequencies

4. Results of Actual Vehicle Tests

This chapter will discuss the results of verification that used an actual SUV mounted with a 4-cylinder engine.

4.1. Setting of Resonance Frequency Target

The resonance frequency target was a frequency that would make it possible to achieve a 5-dB reduction in vibration, equivalent to the reduction achieved by conventional measures. Considering a damping ratio of 1.4 using a one-degree-of-freedom model of displacement excitation, it would be necessary to realize a resonance frequency 0.91 times the input frequency in order to obtain a 5-dB vibration reduction. The engine speed during idling was set at 720 rpm and the frequency of the main vibration input from the engine was 24 Hz. The resonance frequency of the body torsion mode was 18 Hz. During the vehicle development process, the resonance frequency target with the seat occupied was set at 16 Hz or less for the lateral direction and 21.5 Hz or less for the longitudinal direction, and the seat was designed on this basis.

4.2. Applied Structure

CAE prediction of resonance frequencies using a seat model with a conventional configuration showed that no reduction of the resonance frequency in the longitudinal direction was necessary, but a reduction of 4 Hz was required in the lateral direction. The configuration shown in Fig. 8, in which two floating structures are employed at the mounting points on the outer sides of the seat, was therefore employed due to its effectiveness in reducing resonance frequency in the lateral direction. As Table 1 shows, the mass increase against a conventional structure has been limited to approximately 0.07 kg.

4.3. Setting of Spring Constant of Floating Structure

The spring constant was set based on frequency analysis results obtained using CAE. The actual use environment in which seat vibration becomes an issue is when the seats are occupied, and the effect of the occupant on the resonance frequencies of the seat therefore cannot be ignored. Based on the change in resonance frequencies of a similarly shaped seat, in this research the change in resonance frequencies when the seat was occupied against resonance frequencies when it was unoccupied was estimated at plus 4.0 Hz in the longitudinal direction and plus 0.5 Hz in the lateral direction. This meant that the resonance frequency targets for CAE were 17.5 Hz in the longitudinal direction and 15.5 Hz in the lateral direction. Figure 9 shows changes in the resonance frequencies of the seat when the spring constant of the floating structures is changed using the CAE analysis. In the figure, the value in the horizontal axis is the spring constant for the vertical direction of the vehicle, however spring constants of other degrees of freedom were also changed in the same ratios. The results show that for the longitudinal mode, even when the spring constant is high, the resonance frequency is sufficiently low in relation to the target. A spring constant of 420 N/mm was therefore set in order to realize the target for the lateral mode. The shapes of the actual rubber bushing and rubber stopper were designed based on this spring constant and strength and durability

Table 1 Comparison of mass between conventional and floating seat

Part name	Conventional seat [kg]	Floating seat [kg]
Cushion side frame	0.70	0.80
Foot member	1.14	0.60
Foot bracket (Include floating structure)	0.62	1.02
Bracket	-	0.11
Total	2.46	2.53

performance and crash safety performance. These were employed in the actual vehicle under development, and tests of strength and durability performance and crash safety performance showed that a similar level of performance as the conventional structure was maintained.

4.4. Effect of Floating Structures

This section will discuss results for resonance frequencies and vibration performance in actual vehicle tests. Figure 10 shows the results for resonance frequencies. All the measurements were made under the condition that a seat is occupied. The broken lines in the figure show the resonance frequencies for seats in which a rigid body had been used for the seat-mounting unit. These results make it possible to verify the effect of the floating structures in controlling resonance frequencies. The resonance frequency of the longitudinal mode has been reduced by 2 Hz, and that of the lateral mode by 3 Hz. The effect of reduction in the lateral direction is greater than in the longitudinal direction, verifying the effect of employing floating structures for the

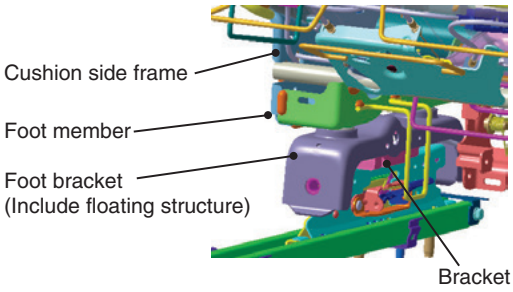


Fig. 8 Structure of floating seat

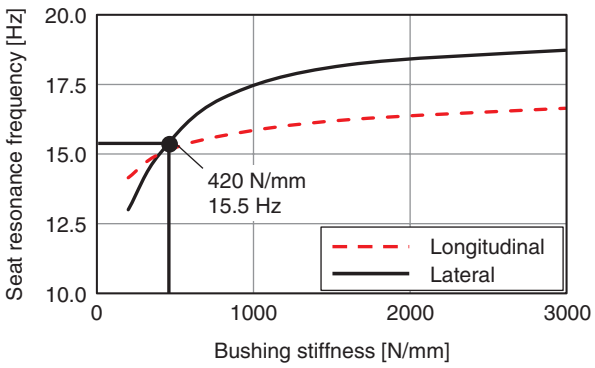
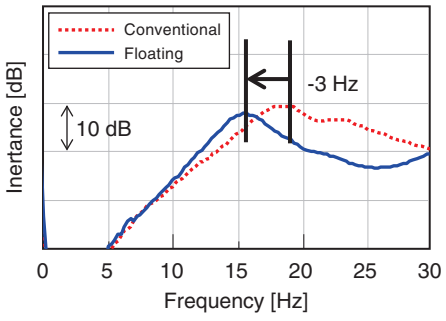


Fig. 9 Relationship between seat resonance frequencies and bushing stiffness

two mounting points on the outer sides. In addition, the targets for a lateral direction resonance frequency of 16 Hz or less and a longitudinal direction resonance frequency of 21.5 Hz or less when the seat is occupied were realized.

Vibration performance will be discussed next. Figure 11 shows results for seat vibration in the lateral direction while the vehicle is in motion. The effect of the body torsion mode is significant and lateral vibration of the seat is an issue, but the floating structures achieve a 5-dB reduction in vibration against a seat using rigid supports, realizing the targets set for the method.

Figure 12 shows results for seat vibration in the longitudinal direction while the vehicle is idling. Regarding vibration while idling, the resonance frequencies of the seat do not coincide with vibration frequencies input from the engine, even when the floating structures are not used, however their use results in a further reduction of 3 dB for vibration.



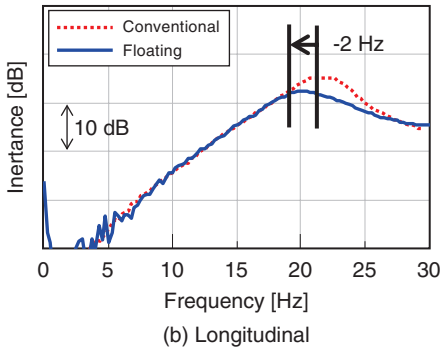


Fig. 10 Resonance frequencies of floating and rigid seat

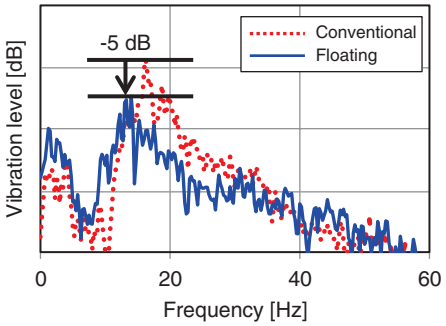


Fig. 11 Results for vibration when vehicle is in motion

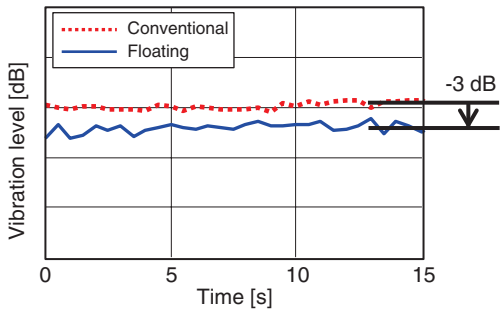


Fig. 12 Results for vibration when vehicle is idling

5. Conclusion

The following outcomes were obtained in relation to the three goals of the research discussed in this paper.

(1) Seat resonance frequencies were controlled by fitting floating structures to sections of the seat-mounting unit.

(2) In order to achieve a balance between vibration reduction and crush durability performance and crash safety performance, the use of stoppers in the floating structures made it possible to maintain a similar level of performance to a conventional support structure.

(3) The use of the method made it possible to reduce the weight of the seat by 0.88 kg per foot against the conventional similarly shaped seat employing dynamic dampers.

Target vibration performance was realized through the application of this method to a seat fitted in an actual vehicle. The developed floating seat will be used in vehicles to be developed in the future.

References

(1) Matsuoka, H., Mikasa, T., Nemoto, H.: Development of Active Control Engine Mount, JSAE Annual Congress Proceedings, No. 84-03, p. 5-8 (2003)

(2) Tamaki, R., Konishi, K., Murata, M.: A study of harshness improvement by seat based on human sensitivity, JSAE Annual Congress Proceedings, No. 138-13, p. 1-5 (2013) (in Japanese)

(3) Kato, K., Kitazaki, S., Tobata, H.: Prediction of Seat Vibration with a Seated Human Subject Using a Substructure Synthesis Method, SAE Technical Paper, 2004-01-0371 (2004)

■ Author ■


Kengo YABE


Toru INAGAKI


Takashi KONDO

Predictive Simulation of Flow-induced Noise using CFD

Katsutomo KANAI* Hideki KATSUYAMA**
Yuichi FUSHIMI* Norikazu YAMAMOTO*

ABSTRACT

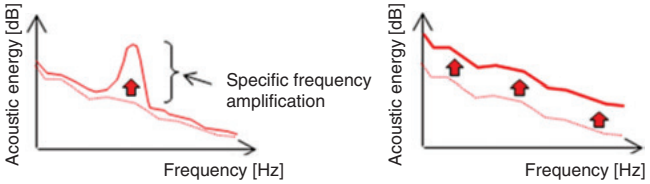
A method of predictive simulation of flow-induced noise using computational fluid dynamics has been developed. In order to simulate flow-induced noise, it is necessary to compute detailed vortex flows and density change of air. This paper introduces the existence of flow-induced noise predicted by unsteady compressible flow calculations using large vortex simulation, a type of turbulence model. The target flow-induced noise for prediction was narrow-band noise, also known as whistling noise, a type of noise in which sound increases at specific frequencies. With the exhaust pipe, including the complex shape of the silencer, as the subject of predictive simulation of flow-induced noise, predictive accuracy was verified by simulating the measurement conditions of steady-state flow. The developed method makes it possible to judge whether narrow-band noise will be generated or not, and to identify the position of the sound source.

1. Introduction

Today, demand is increasing for the reduction of the burden placed on the environment by cars and trucks and for the realization of increased fuel efficiency. As part of this trend, in the area of powerplants the use of hybrid vehicles is becoming more widespread and vehicle chassis are being reduced in weight. At the same time, from the perspective of commercial appeal, it is desirable to reduce noise occurring in the vehicle cabin in order to increase passenger comfort. Carmakers are working to develop noise abatement technologies targeting the various sources of cabin noise, including engine noise, road noise, and flow-induced noise. Hybrid cars are that the vehicle interior of a room became calm, flow-induced noise becomes conspicuous as cabin noise. Flow-induced noise is produced when a flow of air strikes an object. In the case of a car, flow-induced noise occurs in a variety of areas where airflows exist, for example around the exterior fittings, in the air conditioner, and in the exhaust pipe.

Flow-induced noise can be divided into two types: broad-band noise and narrow-band noise (Fig. 1). In the case of broad-band noise, sound pressure increases across a broad frequency range, as shown in Fig. 1 (b). Wind roar corresponds to this type of noise. In the case of narrow-band noise, sound pressure increases only at specific frequencies, as shown in Fig. 1 (a). Narrow-band noise produces a sound like whistling. Because of this, vehicle occupants are prone to become aware of narrow-band noise, and it represents an issue from the perspective of commercial appeal.

The development of a method of predictive simulation of flow-induced noise would be desirable from the perspectives of the achievement of increased efficiency in the development process and the realization of increased quality. Because flow-induced noise is sensitive to small changes in the shape of elements including small steps and crevices and the curvature of flow paths, prediction at the blueprint stage would be desirable. Conventionally, it has not been possible to conduct evaluations of whether noise that represents an issue will be generated until the measurements are made using prototypes. If it is judged based on measurements that correction is necessary, it is



(a) Narrow-band noise (b) Broad-band noise

Fig. 1 Classification of flow noise

* Automobile R&D Center
** HONDA R&D AMERICAS, INC.

then necessary to identify factors and modify the shape, and therefore change the design. Commercial computational fluid dynamics (CFD) software offers computation models[1] based on steady-state calculation as a method of simulating broad-band noise. However, because narrow-band noise necessitates fluid computations that take time history changes into consideration, resulting in a high computation load, the method is challenging to apply.

Sound is propagated by cyclical changes in the density of the air forming a wave motion. In order to simulate sound, it is essential to perform fluid computations of sufficient resolution to achieve an understanding of flow fields that include minute vortex flows that produce infinitesimal pressure fluctuations. In addition, by contrast with noise generated by the vibration of structures, high-frequency components are dominant in flow-induced noise, and the target frequency band is 1000 Hz and above. Because it is necessary to finely discretize computation space and time in order to compute high-frequency components with short wavelengths, the computation burden is further increased. However, recent advances in computer performance have made it possible to compute detailed vortex flows. Simulation methods using the computation methods Direct Numerical Simulation (DNS) and Large Eddy Simulation (LES) have been reported as methods of computing flow-induced noise[2, 3]. With regard to efforts to reduce flow-induced noise, the application of measures to the areas around the door mirrors has been reported[4], but few reports have thus far been produced.

The research discussed in this paper developed a technology for the prediction of flow-induced noise, with narrow-band noise as the specific target. Comparison of simulation and measurement results indicated that the method was a predictive method able to reproduce measured phenomena. Because the aim for the developed prediction method was application in the vehicle development process, the research sought to produce a method with an appropriate level of accuracy and an appropriate computation burden for application in development.

2. Target for Computation

2.1. Selection of Target for Computation

The target for computation for the development of a narrow-band noise simulation was a steady-state flow test in a silencer and exhaust pipe combination (the combination is simply termed “exhaust pipe” here). The internal structure of the exhaust pipe was made up of complex shapes, encompassing areas in which small holes are formed in the pipe and separators, thin pipe walls, curvature and branching of pipes, and connections between parts (Fig. 2). Because of this, there were numerous areas that represented factors in producing noise, and this made identifying the noise sources an issue. In order to reproduce the phenomenon of noise production, the actual shape rather than a simplified shape was used in measurements and simulations.

2.2. Narrow-band Noise

Figure 3 shows the method used to measure noise in the exhaust pipe. Figure 4 shows the measurement results. The results show that from 5000 rpm to 6000 rpm, sound pressure is higher close to 3800 Hz than in other frequency domains. This is narrow-band noise.

Exhaust noise is made up of a variety of types of noise, including noise produced by flows, noise produced by sudden temperature differentials, and noise produced by the vibration of structures. Flow-induced noise in the exhaust system is generated when the exhaust pulse from the engine changes as a result of engine speed, changing the flow in the exhaust pipe. It is thought that when narrow-band noise is being generated, cyclical fluctuations in volume are occurring due to typical structures in the interior of the exhaust pipe. Under certain flow-speed conditions, there is mutual interference between cyclically generated vortices, producing cyclical fluctuations in pressure, resulting in

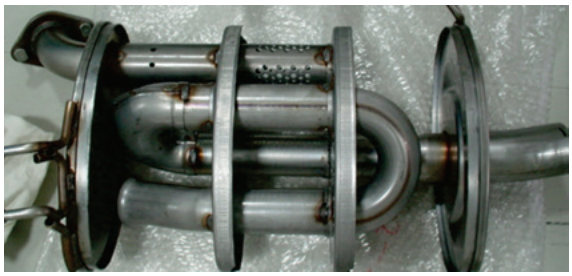


Fig. 2 Silencer internal structure

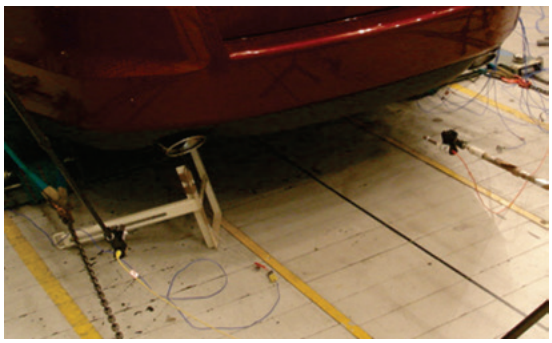


Fig. 3 Noise measurement landscape

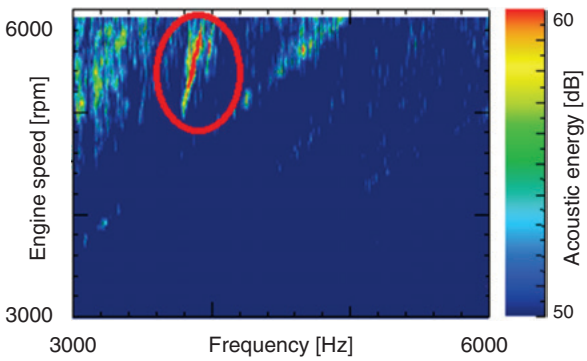


Fig. 4 Noise measurement result

the generation of noise due to phenomena such as the generation of edge tones or cavity tone at the various structures inside the exhaust pipe[5].

2.3. Development Goals

The aim of prediction of narrow-band noise was to make it possible to study items at the blueprint stage that it was previously not possible to judge without measurement. The following three development goals were set for the predictive simulation:

(1) Ability to judge, during the vehicle development process, whether an unacceptable level of narrow-band noise will be generated;
(2) Prediction of the peak frequency of generated noise to an accuracy of ±200 Hz; and
(3) Ability to identify the position of the sound source.

3. Development of Analytic Methods

Narrow-band noise occurs because there is a mechanism in the exhaust pipe that amplifies sound in specific frequency domains. The computation of this amplification mechanism necessitates the use of a method that enables the unsteadiness of the flow field and the propagation of pressure to be understood at a high level of spatial resolution, rather than the conventional method, in which a time-averaged flow field is solved for use when determining the flow rate, pressure loss, and coefficient of resistance. The computation burden produced by the extremely high mesh number needed for the use of the method represented an issue, but large-scale parallel computation dispersed the burden, making it possible to obtain a solution within a practical time frame.

3.1. Application of Turbulence Model LES

In order to calculate flow, a model for carrying out the numerical computation of the turbulent flow is used. Reynolds-Averaged Navier-Stokes equations (RANS) and LES are the two representative turbulence models. Figure 5 shows a comparison of LES and RANS. RANS models and computes the entirety of turbulent motion, and is mainly suited to the solution of steady-state averaged flows. LES directly computes comparatively large vortices using the Navier-Stokes equation, and models and computes fine flows. LES is able to simulate more detailed flows than RANS, and is also superior in simulating highly unsteady phenomena such as vortex shedding.

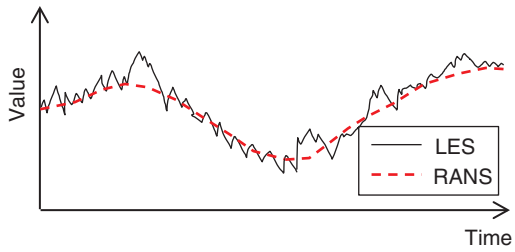


Fig. 5 Comparison of LES and RANS

3.2. Consideration of Compressibility

In order to simulate the minute changes in pressure occurring as a result of the formation and dispersion of turbulent vortices, in calculating the density of the air, it is necessary to calculate pressure-dependence using the equation of state of an ideal gas. Figure 6 shows the results of a simulation of cavity tone, a noise-producing phenomenon that occurs due to the curvature or the rapid expansion and contraction of a flow channel. The impact of the vortex formed at the edge upstream in the cavity against the edge downstream in the cavity produces a sound wave. The propagated sound wave promotes the generation of a still stronger vortex at the upstream edge. The repetition of this phenomenon in a fixed cycle produces a cavity tone. The use of computations that take compressibility into consideration makes it possible to express the propagation of sound waves and resonance within the cavity, therefore making it possible to simulate the existence of sound pressure peaks in specific frequency domains.

3.3. Application of Non-iterative Time Advancement

In order to understand the periodicity of flow fields by computation, it is necessary to conduct unsteady-state calculations for fixed time intervals. This increases computation costs in comparison to analyses in which time-averaged flow fields are determined. When the Non-Iterative Time Advancement (NITA)[3] algorithm is applied, the outer iteration for each time step is performed only once. This makes it possible to reduce computation cost in comparison to the conventional complete Iterative Time Advancement (ITA) algorithm (Fig. 7). Figure 8 shows that the overall trends reproduced by ITA and NITA correspond, but that the detailed pressure fluctuations are not reproduced in the NITA simulation. Because of this, it was necessary

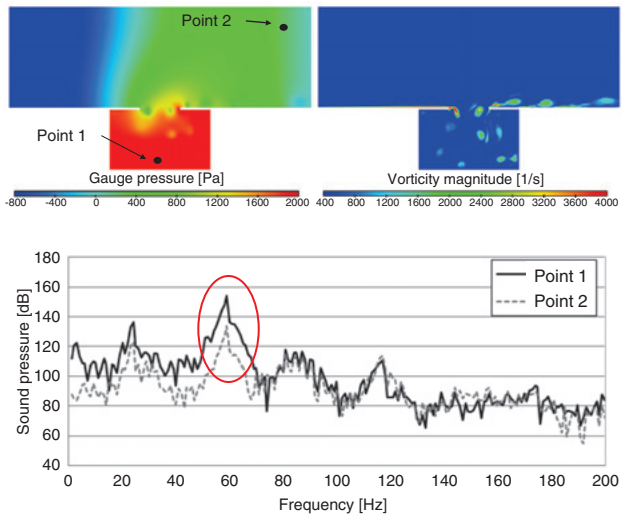


Fig. 6 Cavity tone calculation results

to use NITA only during the process until a convergence solution was obtained, switching to conventional ITA when periodicity was observed in the pressure fluctuations.

3.4. Setting Conditions

In addition to a high level of spatial resolution, a high level of time resolution is necessary in order to understand the flow motion that produces narrow-band noise. As will be discussed below, because the subject of the analysis in the present research was the several-kHz frequency domain, flow motion with a periodicity of the 0.1 ms-order could be considered to occur. To compute this flow motion, it would be necessary to divide this cycle into several tens of 0.001 ms-order time-step lengths. In addition, in order to obtain computational stability using computational fluid dynamics, it is necessary to set mesh size to produce Courant numbers of the 1 to 10^1 orders. Time-step length and mesh size were determined on this basis. The flow rate ratio during flow test measurements was set as the inlet boundary condition. Atmospheric discharge was set as the outflow boundary condition. The temperature of the fluid was ambient temperature.

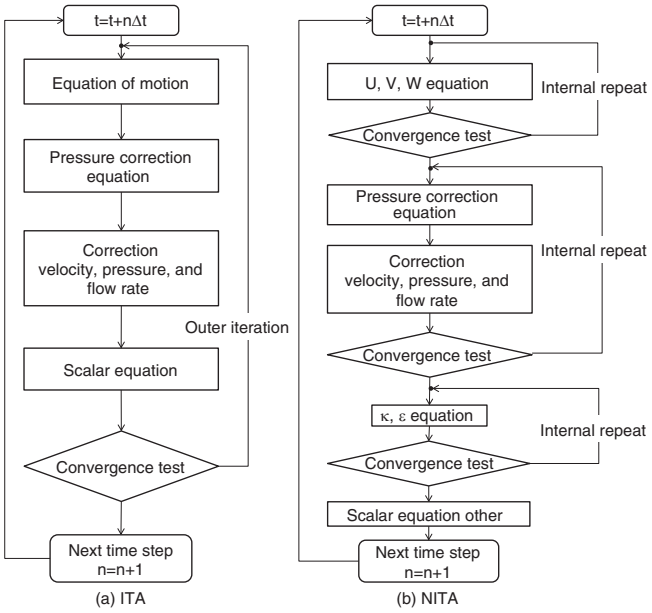


Fig. 7 Convergence process

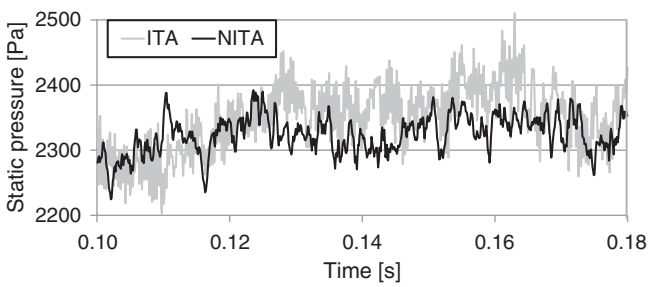


Fig. 8 Pressure fluctuation comparison

In order to reduce computation time, the solution of a steady-state fluid analysis was set as the initial flow field. Unsteady-state computation was commenced, and a pressure monitoring point positioned in the analytic domain was monitored. When the simulation results were stable and periodicity was observed in the pressure fluctuations, data for evaluation was sampled.

3.5. Form of Analysis

Figure 9 shows the shape of the entire exhaust pipe used in this research. Flow visualization measurements were able to verify that sound-absorbing materials in the chambers inside the exhaust pipe would have minimal effect on the downstream section of the pipe. The shape of the chambers upstream of the branch was excluded from the fluid analysis. Figure 10 shows an interior view of the silencer. Inside the silencer, there are numerous small holes, in a pipe and in the separators. Tests conducted prior to this study indicated that the effect of vortices generated close to these holes would have a strong effect in producing noise, and the holes in their entirety were therefore modeled using mesh for this computation.

Excluding sound propagation from consideration made it possible to restrict the computation space to the shape of the interior of the exhaust pipe. In sound simulations, it is usual to make both the formation of the sound source and the propagation of sound to the measurement position subjects of computation. It was possible to compute the formation of the sound source by means of unsteady compressible flow calculation using LES, as discussed above. Sound propagation can be computed by fluid

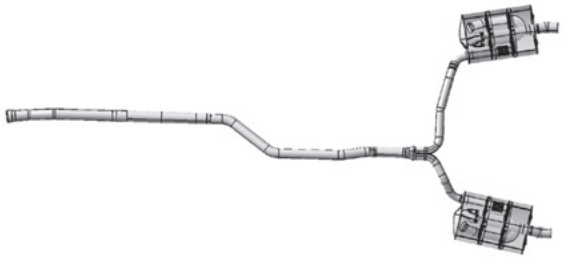


Fig. 9 Entire exhaust pipe

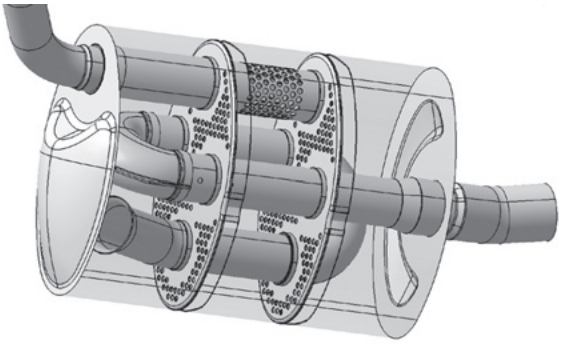


Fig. 10 Inner view of silencer

computation or acoustic computation. Because sound attenuation does not have an effect when propagation is not considered, the absolute value of sound pressure cannot be compared. However, it is considered possible to judge whether or not narrow-band noise will be generated from the surrounding sound and the difference between the outstanding peaks. To compute propagation using fluid computation, it is necessary to take reflection and other factors into consideration and utilize a large computation space of several meters. The solution of propagation necessitates the use of mesh that divides the wavelength of the sound wave into between 15 and 20 subdivisions. Assuming that the subject of a simulation was a maximum frequency of 5000 Hz, the wavelength would be 68 mm, and the minimum necessary mesh size would be no more than 4.5 mm. The discretization of a space of several meters using mesh of 4.5 mm or less would dramatically increase the mesh number, thus also increasing the computation burden. For this reason, in the present study narrow-band noise was determined without consideration of propagation in order to reduce the computation burden.

3.6. Computation Space

The flow field computed by LES is dependent on the resolution of the mesh. Prediction of whether or not narrow-band noise will be generated necessitates a mesh size that makes it possible to understand the behavior of the turbulent vortices that induce it. Figure 11 shows the results of LES computation of the formation of Karman vortex streets following the passage of a uniform flow through a cylinder. Because the simulation possessed sufficient spatial resolution with regard to the diameter of the cylinder and the velocity of the flow, it was possible to compute the formation of alternate vortex streets, and to verify that areas of low pressure are generated cyclically. As a result of the fact that the necessary spatial resolution is dependent on the flow velocity and characteristic length of the flow field (in this case, the diameter of the cylinder), it is necessary to select the appropriate spatial resolution for each subject of analysis.

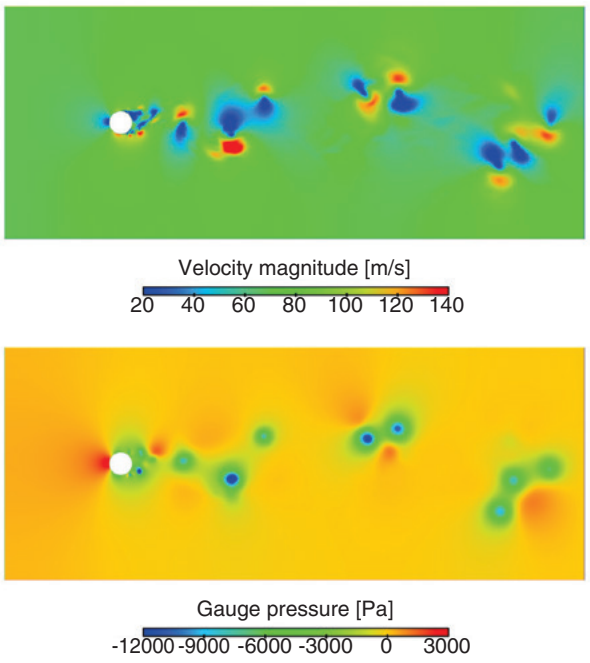


Fig. 11 Cylinder flow calculation results

3.7. Application of Cartesian Grid Cut-cell Method

In order to accurately compute the flow inside the exhaust pipe, it is essential to express the holes in the pipe and separators and the thickness of the pipes in mesh shapes. For shapes of this type, the cut-cell method not only offers ease of mesh generation and mesh size control, but also presents advantages in terms of the reproducibility of shapes at boundaries (Fig. 12).

Because local mesh size control made it possible to refine mesh size exclusively in areas in which the flow is complex, computation time could be reduced by reducing the mesh number. Hexagonal mesh formed using Cartesian grids makes it possible to use higher-order space finite differences rather than tetrahedral mesh of equivalent size. This helps to enable control of numerical diffusion, and is effective in making possible accurate computation of local pressure fluctuations.

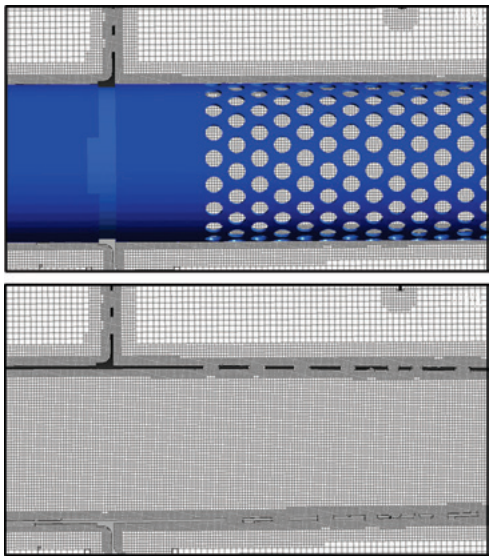


Fig. 12 Cut-cell mesh

4. Study

4.1. Evaluation Method

4.1.1. Comparison with measurements

Measurement data for sound pressure around the outlet of the exhaust pipe for inlet conditions producing narrow-band noise was compared with measurement data for pressure inside the pipe. Figures 13 and 14 show the results of frequency analyses of each set of measurement

data. While figures differ because both sets of data were separately measured, they both display peaks at close to 2800 Hz. This indicates that there is a strong correlation between sound pressure at the exhaust pipe outlet and pressure fluctuations inside the pipe. With this as a precondition, in the present simulation observation points were situated inside the exhaust pipe, and the existence of narrow-band noise was predicted with pressure fluctuation as a criterion for judgment. Situating the observation points inside the exhaust pipe restricted the computation space for the simulation to the interior of the pipe. This made it possible to reduce the computation load.

4.1.2. Evaluation of sound

Figure 15 shows the observation points used in the simulation. Because it was not possible to output sound data for each observation point from fluid calculations, time history data for static pressure was used. Fast Fourier Transform (FFT) was applied to the static pressure data to convert it into frequency components, and sound was evaluated. The data-sampling period was set as 0.15 s, and

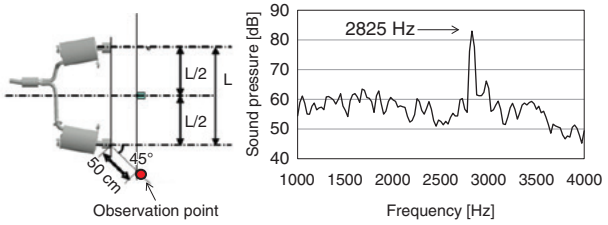


Fig. 13 Sound pressure measurement

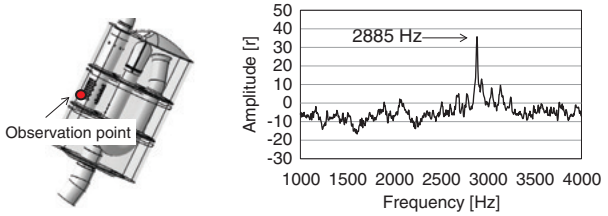


Fig. 14 Pressure measurement

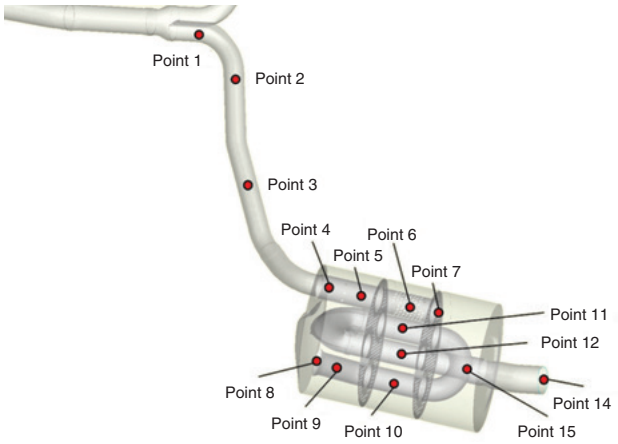


Fig. 15 Simulation observation points

Table 1 Implementation condition

Shape	Pressure [Pa]	Measuring peak frequency [Hz]
A	4000	2600
A	5500	2825
B	5500	No Peak

data was output at $1x10^{-4}$ s intervals. Sets of 0.15-s data were subdivided into 0.04-s units, and FFT was applied with an overlap of 50%. Frequency resolution was 25 Hz.

4.1.3. Method of judgment of occurrence of narrow-band noise

Judgment during the development process of whether or not unacceptable narrow-band noise would occur was based on the degree of prominence of the peak frequencies. The level of background noise other than the target noise was estimated from the results of frequency analysis at each observation point, and its difference with peak values was calculated. The existence of narrow-band noise was judged by comparison of these differential values with values determined by measurement.

4.2. Implementation Conditions

An overview of the measurements that represented the implementation conditions for the simulation is shown in Table 1. Table 1 shows the shape, the back pressure conditions, and the frequency of narrow-band noise occurring at the time of measurement. The subjects of comparison in this case were differences in back pressure and differences in shape. A comparison was conducted for Shape A in Fig.16 at back pressures of 4000 and 5500

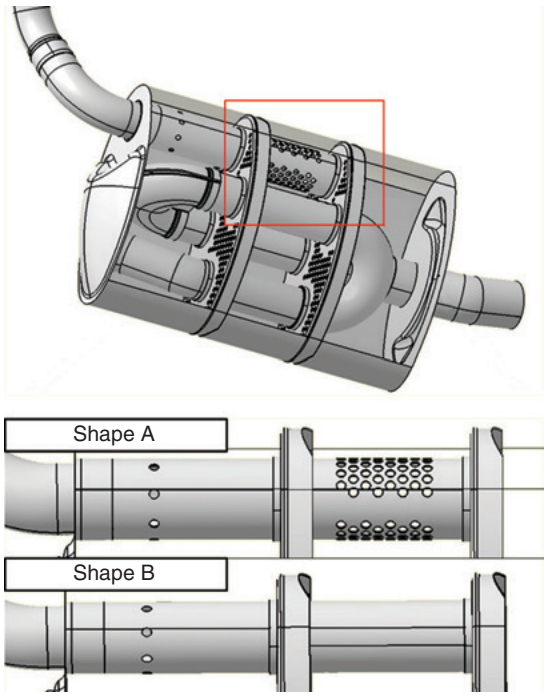


Fig. 16 Shape difference specification

Pa. The measurements show that the peak frequencies for narrow-band noise shifted in response to back pressure conditions. In terms of shape difference, Shape A and Shape B, in which the holes in the pipe were filled in (Fig. 16), were compared. For Shape B, no narrow-band noise was generated, and no frequency peaks were observed. Simulation results for the two conditions discussed above were compared, and the accuracy of the simulation was verified.

4.3. Results of Analysis

This section will discuss the results of comparison of the simulation and measurements. The values from the simulation were computation results for pressure at each observation point within the exhaust pipe. This discussion will focus on Point 7 in Fig. 15.

4.3.1. Results for different back pressure conditions

Figure 17 shows the results of a comparison of the simulation and measurements. Because the observation points differed between the measurements and the simulation, absolute values for sound pressure do not correspond, but the results match in terms of the general tendency of existence of peaks. In both simulation and measurement results, clear peaks occur at approximately the same frequencies. The frequency shift and increase in sound pressure when the back pressure condition is increased from 4000 to 5500 Pa was also reproduced by the simulation. In addition, because criterion values were exceeded under back pressure conditions of both 4000 and 5500 Pa, it was assumed that narrow-band noise was generated. Given the above, it can be concluded that narrow-band noise can be predicted by simulation.

4.3.2. Results for different shapes

Figure 18 shows a comparison of measurement and simulation results for Shape B, in which the holes in the pipe inside the silencer had been filled in, under a back pressure condition of 5500 Pa. Across the entire frequency range, no conspicuous peaks exist in either the measurement or simulation results. In addition, the peaks occurring at a back pressure of 5500 Pa for Shape A in Fig. 17 are significantly reduced in the case of Shape B. With regard to the occurrence of narrow-band noise, the difference between the peak close to 2800 Hz and background noise was minimal, and it was therefore judged that narrow-band noise was not generated. CAE and measurement results for the non-occurrence of narrow-band noise under differing shape conditions also corresponded. Based on the above, it can be concluded that it is possible to predict the non-occurrence of narrow-band noise by simulation.

Table 2 Peak frequency comparison

Pressure [Pa]	Measurement [Hz]	CFD [Hz]	Difference [Hz]
4000	2600	2550	50
5500	2825	2775	50

4.3.3. Verification of accuracy

Because target values for the determination of CAE accuracy in the present research were evaluated in the 1/3rd-octave band when measurements were evaluated, the deviation between frequencies in the measurement and CAE results was set at ±200 Hz, falling within this range.

Table 2 shows the deviation between frequencies occurring in measurement and CAE results for Shape A. The deviation is 50 Hz for a back pressure condition of 4000 Pa and 50 Hz for 5500 Pa. Target values were realized under both back pressure conditions, indicating that the developed method displays sufficient accuracy for prediction.

4.4. Identification of Sound Source

The ability to predict narrow-band noise also makes it possible to identify sound sources from calculation results. Sound sources were identified by means of comparison of power spectrum density (PSD) values at each observation point.

Figure 19 plots PSD values at 2775 Hz for each observation point. This graph shows the magnitude of sound at 2775 Hz at each observation point. The maximum PSD value at Point 7 can be considered to be the sound source. Figure 20 shows contour diagrams of differences in static pressure over time in a cross-section

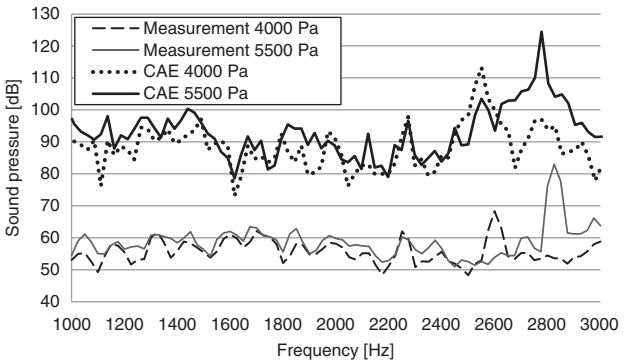


Fig. 17 Comparison results of pressure conditions

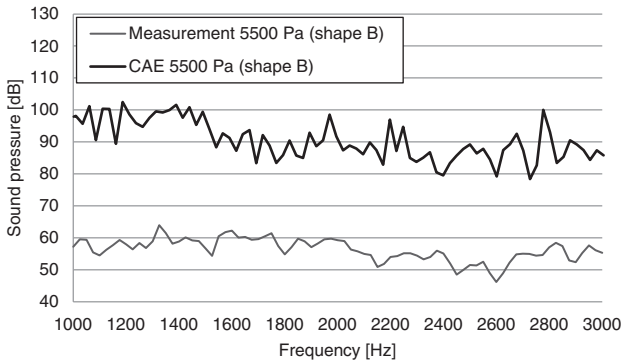


Fig. 18 Results with different shapes

of the silencer. Figure 20 (a) and (b) show results for different computation times. The circled areas are believed to be the sound sources. It is clear that changes in static pressure over time in the circled areas are greater than in other areas. The phenomena shown in Figure 20 (a) and (b) are repeated cyclically. This indicates that it is also possible to predict that noise will be generated from a contour diagram based on cyclical fluctuations in static pressure in one position.

The results of sound source identification measurements showed that the same position was the sound source for each shape. The fact that the sound source was located in the same position despite the differences in Shape A and B indicates that correction of the shape of the sound source would have an effect on the existence of narrow-band noise. The results discussed above verified that sound sources could be identified from CAE results.

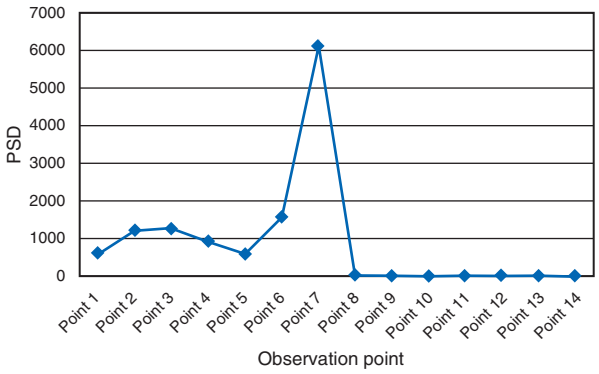
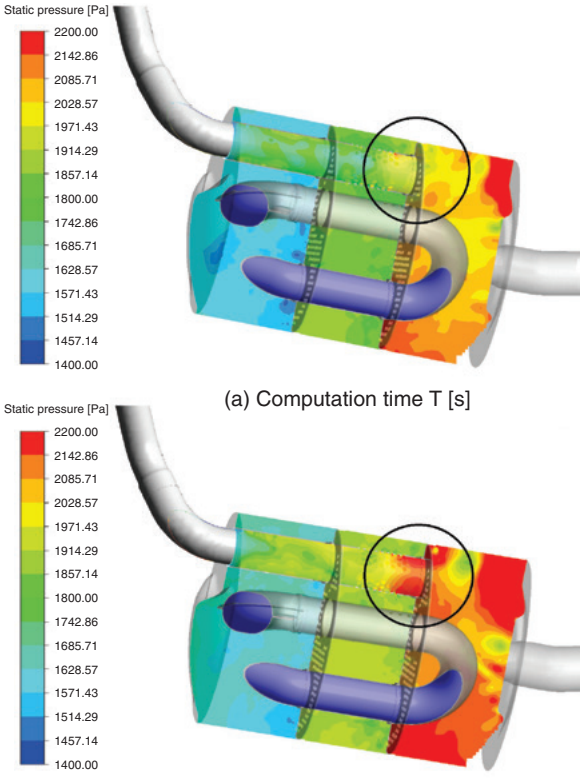


Fig. 19 2775 Hz-PSD



(a) Computation time T [s]

(b) Computation time T+⊿t [s]

Fig. 20 Static pressure of silencer section

5. Conclusion

A method of predictive simulation of narrow-band flow-induced noise using CFD has been developed. Because the target for prediction in this method was narrow-band noise, fluctuations in fluid pressure in the analytic domain were focused on. The three goals set for the development of the simulation method were realized as follows.

(1) Simulations of the generation of narrow-band noise from pressure fluctuations were conducted based on fluid computation using LES. Criterion values were set, making it possible to predict the existence of noise that would represent an issue.

(2) For the subject of the analysis, predictive accuracy for peak frequencies was a deviation of 50 Hz. It was verified that the target accuracy of within ±200 Hz was realized.

(3) It was verified that the position of the sound source could be identified by comparing the magnitude of peak frequencies at each observation point based on fluid computation results.

The developed method has made it possible to judge whether narrow-band noise will occur and to identify the position of the sound source prior to the manufacture of prototypes using three-dimensional shape data. It is thus possible to predict the existence of noise and correct the relevant shapes at an early stage of the development process. In the future, in order to quantitatively evaluate the generated sound pressure, it will be necessary to separate sound pressure fluctuations from fluid pressure fluctuation calculations, and conduct simulations that consider the propagation path from the sound source to the reception position outside the exhaust pipe.

References

(1) Perot, B. J.: An Analysis of the Fractional-Step Method, Journal of Computational Physics, Vol. 108, p. 51-58 (1993)

(2) Takahashi, K., Miyamoto, M., Ito, Y., Iwasaki, T., Takami, T., Kobayashi, T., Nishida, A., Aoyagi, M.: 3jigen Earidogakki no Ryutaiongen to Hasshintokusei, RIMS Kokyuroku, Vol. 1776, p. 100–114 (2012) (in Japanese)

(3) Yokoyama, H., Kato, C.: Fluid-Acoustic Interactions in Acoustic Radiation in Turbulent Cavity Flows, Transactions of the Japan Society of Mechanical Engineers, Series B, Vol. 75, No. 760, p. 2369–2378 (2009)

(4) Iida, A.: Study on Aerodynamic Noise of Automobiles,

Journal of Wind Engineering, Vol. 36, No. 3, p. 250-257 (2011) (in Japanese)
(5) Mochizuki, O., Maruta, T.: Nagare no Oto ha Dokokarakurunoka, Ryutaion Kogaku Nyumon, Asakura Publishing Co., Ltd., p. 74 – 97 (1996) (in Japanese)

■ Author ■


Katsutomo KANAI


Hideki KATSUYAMA


Yuichi FUSHIMI


Norikazu YAMAMOTO

Development of Component Based Middleware for Intelligent Robot Software

Makoto SEKIYA* Norio NEKI*
Zenta MIYASHITA* Nobuyuki ONO*

ABSTRACT

As robots become more intelligent, the software systems for realizing functions are becoming larger and more complex. This makes the use of component based middleware an effective means of design by dividing the overall system into function units (components) and then joining these components with the appropriate interfaces.

Intelligent robot software systems require composite components and finite-state machine components. The issues when developing middleware are the ability to synchronize these components to specific timings, and guaranteeing hard real time performance of minimum and predictable processing times including communication so that processing can finish in a certain sequence within a certain time.

This paper introduces Honda Robotic Technology Middleware, which is original component based middleware developed to address the above issues.

In consideration of use by outside organizations, the middleware specifications comply with the Robotic Technology Component specification formulated by the Object Management Group, which is an international standards organization. In addition, work is underway within the Object Management Group to standardize the original expanded specification.

1. Introduction

The ASIMO software system (hereafter, "system") started from bipedal walking control[1] and has evolved to include abilities for working and human-robot interaction[2), (3)]. Recently, the system scale and complexity are expanding at a rapid pace, and the use of component based middleware is an effective means of design by dividing the overall system into function units (components) and then joining these components with the appropriate interfaces. This is because it allows understanding and verification of the system in smaller, simpler function units.

When developing component based middleware that can be applied to intelligent robot systems such as ASIMO, functions for designing and executing composite and finite-state machine (FSM) components are needed in order to componentize existing systems. The issues in this case are the ability to synchronize these components to specific timings, and guaranteeing the hard real time performance of minimum and predictable processing times including communication so that processing can finish in a certain sequence within a certain time.

This paper introduces Honda Robotic Technology Middleware (HRTM), which is component based middleware developed to address the above issues.

2. Component Based Middleware

Component based middleware (hereafter, "middleware") is a development environment for realizing component based development, and has a hierarchical architecture consisting of the three elements of a design tool, component specifications, and a framework as shown in Fig. 1.

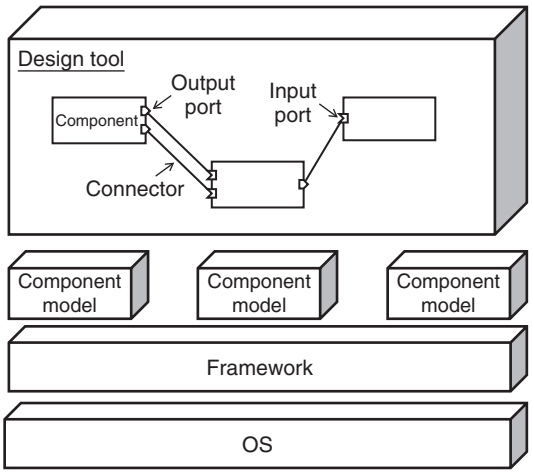


Fig. 1 Architecture of a component based middleware

* Fundamental Technology Research Center

The design tool is used to define components and design connection relationships using visual methods, and to generate the component source code. In some cases the design tool also has features such as debugging support functions.

The component specifications define the common interfaces used to invoke common function units (components) on the middleware. The defined elements typically include ports for sending and receiving data, and interfaces for getting and setting parameters.

The framework is a special program that executes the actual processing via the common interface defined in the component specifications, such as component startup and communication processing.

The framework should provide the functions required by the components in the Software In the Loop Simulation (SILS), Hardware In the Loop Simulation (HILS) and target environments in order to realize the reuse of components in each environment.

3. Requirements of Middleware for Intelligent Robots

The roles of middleware for intelligent robot systems are as follows.

1. Componentization of intelligent robot systems
2. Realization of component reuse between the SILS, HILS and target environments

This section describes the specific requirements for each element of component based middleware derived from the above roles. The distinct requirements in this development were to support composite components, FSM components and multiple communication protocols.

3.1. Design Tool Requirements

3.1.1. Ability to design systems using a standard modeling language

The use of an original modeling language for system design increases the time and effort required to master the tool operation methods and understand the design contents, and also means that existing design tools cannot be reused. Furthermore, a widely known standard modeling language should be used for the design tool in consideration of use by outside organizations.

3.2. Middleware Requirements related to Components

3.2.1. Ability to design hierarchically nested components

Large-scale and increasingly complex intelligent robot systems realize single functions using multiple hierarchically nested sub functions. Therefore, in order to componentize these systems, component design should be possible using hierarchically nested sub components.

3.2.2. Ability to design FSM components

Complex state transitions are used to implement the abilities for working and human-robot interaction of intelligent robot systems, and enhancing the maintainability of these state transitions is an issue. To address this issue, it should be possible to design FSM components by modeling the internal state transitions.

3.2.3. Compliance with standard component specifications

Widely adopted standard component specifications should be used to enable easy creation of systems by reusing the many components developed by outside organizations.

3.3. Framework Requirements

3.3.1. Ability to execute components on various OS

The hardware systems of intelligent robots consist of multiple sensors with different roles. These sensors operate on various OS due to restrictions such as the provided drivers, and the programs used to process the data from the sensors at high speed are executed on the same OS as the corresponding sensors.

In order to componentize these types of systems, the framework should support multiple platforms to provide an environment for executing components on various OS.

3.3.2. Ability to reuse source code between different OS

The framework should enable the component source code to be compatible with different OS in order to realize component reuse between the SILS, HILS and target environments.

3.3.3. Ability to use multiple protocols for communication between components

Communication between programs within an intelligent robot system normally uses TCP/IP, UDP, shared memory, bus communication or other protocols in accordance with the application.

The reason for using different communication protocols according to the application is that using the fastest communication method that can be used in the program-running environment leads to shorter processing times.

In addition, components may also use different communication protocols between the SILS, HILS and target environments. In these cases, the framework should support multiple protocols for communication between components and it should be possible to select the protocol when compiling and executing components in order to realize both component reuse and high-speed processing.

3.3.4. Minimal framework processing time

If componentization notably increases the processing time, it may be a challenge to transfer from the SILS environment to the target environment in which the system runs on a real-time OS with limited processing capability. The framework should enable execution of processing including communication in a minimum and stable time in order to increase the ability to reuse components.

Table 1 Comparison of robotic middleware

Name	HRTM	OpenRTM-aist	ROS	OROCOS
Composite component	Yes	Up to sub-component	No	No
FSM component	Yes	No	Yes (Python)	No
Supported OS	Linux Windows Mac OSX	Linux Windows Mac OSX	Linux	Linux Windows Mac OSX
Supported protocol	CORBA shmem bus	CORBA	TCP/IP UDP	TCP/IP UDP
Supported RTOS	Proprietary RTOS	ART-Linux	No	No
System modeling language	UML	Original block diagram	No	No
Component model	RTC	RTC	Original	Original

4. Development of HRTM

When developing HRTM, the major implementations of robotic middleware were investigated. The investigated middleware are described briefly below.

OpenRTM-aist[4] is robotic middleware developed by the National Institute of Advanced Industrial Science and Technology (AIST) in Japan. It complies with the Robotic Technology Component (RTC) specification[6] issued by the international standards organization Object Management Group (OMG)[5], supports a wide range of OS, and uses the international standard OMG CORBA[7] as the communication protocol. OpenRTM-aist also has proven results supporting hard real time performance on ART-Linux[8].

ROS[9] is robotic middleware developed by Willow Garage Inc. (U.S.), and development is currently being continued by the Open Source Robotics Foundation. ROS is an open system and there is a wide range of products by numerous developers, but the officially supported OS is limited to Ubuntu[10].

OROCOS[11] is a robotic software development project started under the sponsorship of the European Union. It supports the major OS and has proven operating results in real-time environments, but it does not have a component model, and has thus far been positioned as a software library for developing robotic control functions. Development is currently continuing with the support of PAL ROBOTICS SL (Spain), and steady advances are being made including the addition of original component models.

As a result of the investigation, it was found that there is currently no middleware that satisfies all the requirements described in Chapter 3, and that OMG RTC can be used as an international standard component specification. Therefore, development of the original middleware HRTM was started with the goal of realizing component specifications that satisfy the requirements while also complying with the international standard OMG RTC.

Table 1 compares the functions of HRTM and major middleware.

5. Achieved Functions

The features and functions achieved by HRTM are described below.

5.1. System Design Tool

HRTM enabled system design by a visual design tool that uses Unified Modeling Language (UML)[12], which is an international standard modeling language.

The design tool enables defining of parameters such as component input/output port types, connection relationships and execution sequences using UML composite structure diagrams expanded in accordance with the RTC specification. The design tool also issues warnings when detectable errors such as input and output data type mismatch occur.

In addition, state transition diagrams are designed using UML statecharts, enabling the internal design of FSM components described hereafter. A statechart is a state transition diagram with a hierarchical structure, and enables creation of an easy to understand design when designing complex state transition rules for working and human-robot interaction.

Skeleton code generated automatically from the completed UML diagram is used when creating a new component. Common functions such as data communication based on the component specifications are processed by the framework, so component developers need only implement the internal processing to the skeleton code.

5.2. Component Specifications

5.2.1. Compliance with international standards and specifications

HRTM complies with the RTC specification that is defined as a component specification for robotic applications. However, the RTC specification is highly expandable and there are also examples of application to fields other than robotics[13]. RTC-compliant middleware has multiple implementations such as the previously described OpenRTM-aist[14, 15], and is used by research centers and universities both domestically and overseas.

HRTM and OpenRTM-aist components can be interconnected based on the RTC specification, so the ASIMO software system and existing components can be easily connected when performing joint research with an outside research organization.

5.2.2. Composite components

As described above, when componentizing large-scale systems, compositing is a key function for enhancing system visibility and maintainability. Therefore, HRTM implements a multi-tiered composite component function that expands the RTC specification.

The composite component based on the RTC specification consists of the following elements (Fig. 2).

1. Super component
2. Sub component

3. Public port
4. Execution thread

A super component includes one or more internal sub components. A public port is a super component port used by a sub component to communicate with external components. An execution thread executes one or more assigned sub components.

The RTC specification does not clearly state the means for specifying the execution sequence of the sub components contained in a composite component. Therefore, a sequential execution thread was developed as an original HRTM function that can specify the sub component execution sequence to the execution thread using parameters.

5.2.3. FSM components

The abilities for working and human-robot interaction of intelligent robot systems are implemented using complex state transitions, and enhancing maintainability has been an issue. HRTM realizes visual design of FSM models using UML statecharts, making it possible to express complex state transitions in a concise manner.

Figure 3 shows an example of a simple FSM model. The black circle in the figure represents the initial state, the rectangles with rounded corners represent states, and the arrows represent transitions. The labels indicate the names of the corresponding elements. The FSM model shown in Fig. 3 first automatically transitions from the initial state to State A. Thereafter, the state transitions according to the transition rules. For example, when Event A, Event B and then Event C are input from the initial state, the state transitions to State B, State C and then State A.

Figure 4 shows a model with a transition rule added to the model in Fig. 3. Here, State A and State B both transition to State C when Event B occurs. This type of shared transition rule between states is often used for reset and other processing even in actual models. However, as the number of states and transition rules increase, it becomes easier to forget to assign transition rules.

Shared transition rules for sub states can be integrated by designing the states in a UML statechart in a hierarchical manner. Figure 5 shows the same model as that in Fig. 4 converted to a hierarchically nested model. In this figure, State A and State B are designed as a Super State sub component. In the UML statechart specification, sub components follow the state transition rules of the parent Super State, so the transitions to State C due to Event B are integrated into a single Super State transition rule. Comparison of Fig. 4 and Fig. 5 shows that composite design enables concise description using a model.

Implementation of the designed FSM model is included in the FSM component skeleton code, so there is no need for developers to implement the FSM. In addition, errors in the FSM model are detected on the design tool, so illegal FSM models cannot be output as skeleton code.

These functions facilitate maintenance of complex state transitions and enable elimination of bugs and other issues during implementation.

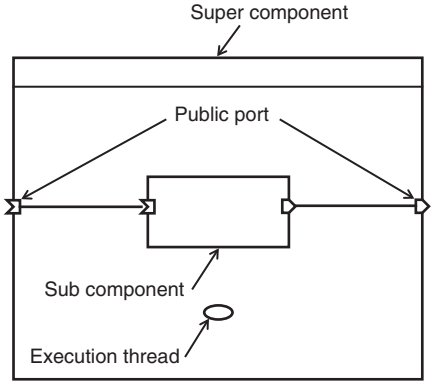


Fig. 2 Overview of a composite component

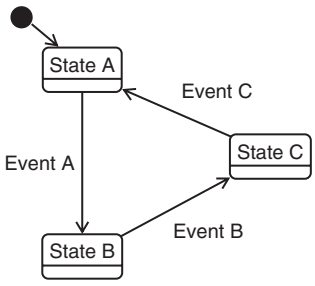


Fig. 3 UML statechart of simple finite state machine

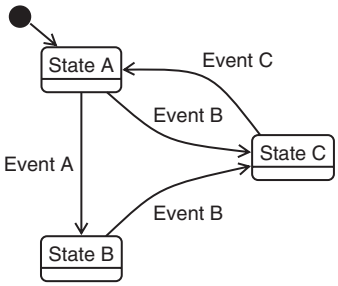


Fig. 4 UML statechart of finite-state machine in which different states have share transition rule

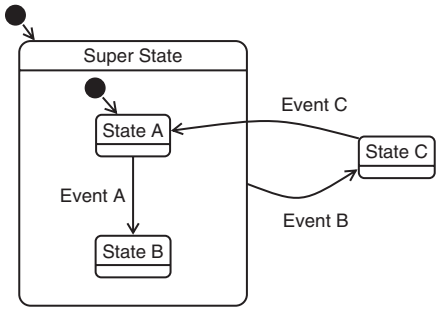


Fig. 5 UML statechart of the finite state machine in Fig. 4 with hierarchically nested states

5.3. Framework

5.3.1. Support of multiple platforms

Execution of components on various OS is a requirement of the framework, so an OS abstraction layer that hides multiple OS including real-time OS was created between the OS and the framework (Fig. 6).

Programs created using this abstraction layer can be compiled and executed on multiple OS without changing the source code. This made it possible to realize a highly portable framework that supports multiple platforms.

5.3.2. Support of multiple communication protocols

A function was implemented in HRTM that stores the parameters for specifying the communication protocol between components in the database of each component and selects the appropriate protocol when executing the components.

Communication processing using the selected protocol is executed by the framework, and component implementation does not depend on the communication protocol. Therefore, the unmodified component source code can be reused and executed even when the communication protocols that can be used differ between the SILS, HILS and target environments.

5.3.3. Hard real time performance

The control system of a bipedal walking robot needs to guarantee hard real time performance that completes calculation of command values in a certain sequence within a certain time while synchronizing with specific timings such as hardware interrupt signals. In order to guarantee the hard real time performance of components, efforts were made with HRTM to develop a synchronized sequential execution thread that executes components based on priorities and to reduce the framework execution processing time.

In addition to the sequential execution thread functions, the synchronized sequential execution thread can specify the synchronization source, such as hardware interrupts or an internal clock, using a parameter. This enables specifying of the execution sequence with the minimum component processing time within a specific cycle, thereby allowing guarantee of hard real-time performance.

Reduction of the framework processing time was the most challenging technical issue in HRTM development, so this is described in detail as follows. The framework processing time when executing components was analyzed in the initial development stage. The results showed that the communication time accounted for a large percentage of the processing time, so the main issue was to reduce the communication time. Table 2 shows the results of measuring the processing time required to send and receive 1000 bytes of data via TCP/IP before measures to reduce the communication time.

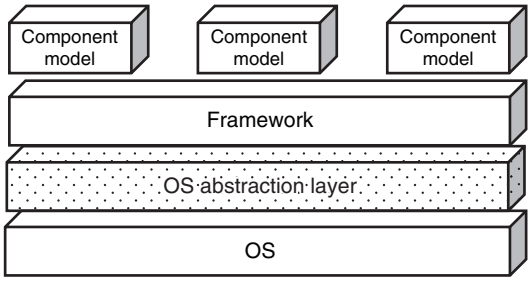


Fig. 6 OS abstraction layer of HRTM

Table 2 Processing time to send/receive 1000 bytes data [us]

	Data conversion	Data copy	Data receive	Data send	Total
Send	100	13	-	75	188
Receive	100	13	10	-	123

Table 3 Required processes and types of communication

	Send or receive	Data conversion	Data copy	Data receive	Data send
Network	Send	Yes	Yes	-	Yes
	Receive	Yes	Yes	Yes	-
Inter-process	Send	No	Yes	-	Yes
	Receive	No	Yes	Yes	-
Inner-process	Send	No	Yes (address)	-	Yes
	Receive	No	Yes (address)	Yes	-

The measurement results show that the receive processing time is 123 μs and the send processing time is 188 μs. These values account for a large percentage of the average processing time of programs running in hard real time in the ASIMO system. Therefore, the componentization of existing programs that involve data input and output leads to a notable increase in the processing time.

The main factors increasing the processing time are the processing time of 100 μs for converting the data to the network format and back again, which is included in the communication time based on the RTC specification, and the data send time of 75 μs required to send data via TCP/IP. The data send time can be shortened by replacing the communication protocol with a protocol faster than TCP/IP, but eliminating the data conversion processing would result in non-compliance with the RTC specification.

Therefore, HRTM expanded the RTC specification to enable selection of three types of connection formats (network, inter-process, intra-process) in addition to the communication protocol. When connecting with RTC specification components, this expansion enabled use of RTC-compliant communication methods for inter-process communication that omits the data conversion processing and for intra-process communication that replaces the data copy processing with address reference processing. This realized high-speed communication between HRTM components, which shortened the communication time (Table 3).

Table 4 Processing time of intra-process communication [us]

	Data conversion	Data copy	Data receive	Data send	Total
Send	-	7	-	-	7
Receive	-	13	3	-	16

When using the fastest available intra-process communication between components, the above measures reduced the communication processing time from 123 μs to 16 μs when receiving data and from 188 μs to 7 μs when sending data (Table 4). Intra-process communication is performed by referencing the address in the process memory space, so the communication time is definite, making it possible to guarantee hard real time performance.

6. Application to ASIMO

The results of application to the path tracking walk module of the ASIMO system are described here as verification of practical use of HRTM functions. The path tracking walk module is a program that performs walking along a tracking line by repeatedly calculating the next footstep landing position (hereafter, "step") along a given path relative to the current position as shown in Fig. 7.

6.1. Overview of Path Tracking Walk Module

Figure 8 shows an overview of the path tracking walk module. The path tracking walk module repeatedly receives a timer interrupt, checks the walk state, and calculates the next step at a 5 ms cycle, so it is a suitable subject for verifying hard real time performance including communication performance.

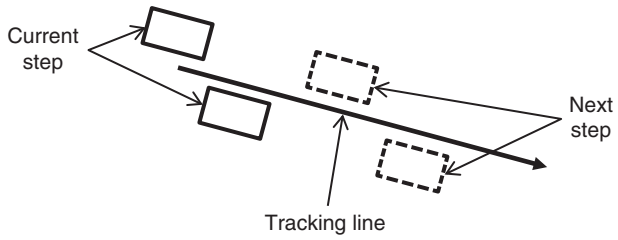


Fig. 7 Overview of path tracking walk

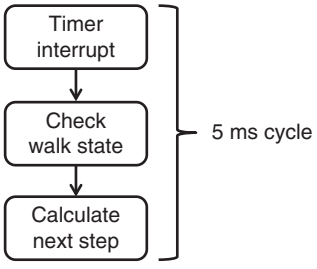


Fig. 8 Processing steps of path tracking walk

6.2. Application Procedure

The procedure for applying middleware to the path tracking walk module was as follows.

1. Component design
2. Confirmation of execution in SILS
3. Confirmation of execution in the target environment

6.3. Component Design

Figure 9 shows the architecture of the path tracking walk module before componentization. The foot step planner processing for path tracking receives an interrupt signal at a 5 ms cycle, executes the series of steps shown in Fig. 8, and then transfers the calculation results to the leg controller block via the shared memory.

The leg controller is also executed at the same 5 ms cycle, and realizes path tracking walk by calculating the track for placing the footstep in the given step position and then moving the leg accordingly.

The approach for componentization was to model the state transitions in the footstep planner as an FSM component. Therefore, the footstep planner processing was stratified and divided internally into an FSM and a robot status notifier (blue line part in Fig. 10). The divided FSM and status notifier are both executed at a 5 ms cycle, but execution needs to be performed in order of status notification and then state transition, so the sub component execution sequence was set

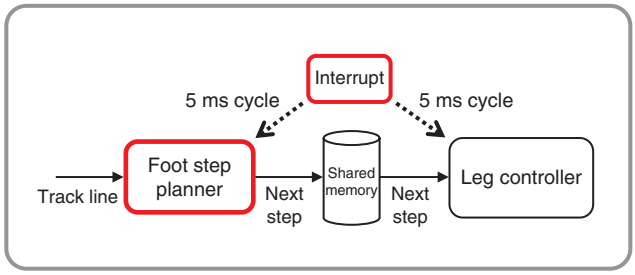


Fig. 9 Original architecture of path tracking walk (red line part)

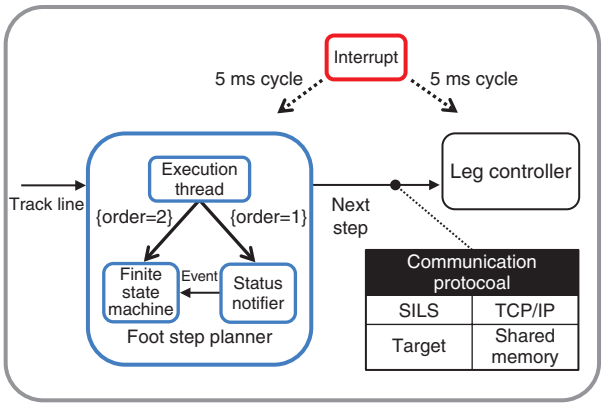


Fig. 10 Componentization of path tracking walk (blue line part)

using parameters. Figure 11 shows the model of the footstep planner actually created by the design tool, and Fig. 12 shows the model of the FSM component.

6.4. Confirmation of Execution in SILS

The component skeleton was automatically generated from the designed model, and the functions were ported from the program before componentization to the SILS environment.

The completed component was used to compare execution in the SILS environment before and after componentization, and it was confirmed that the results matched completely.

6.5. Confirmation of Execution in the Target Environment

When confirming execution in ASIMO, the component source code used for SILS could be executed without modification simply by recompiling it in the target environment.

All the parameters that change according to the environment were stored in a file or the component internal database, making it possible to check the component reusability.

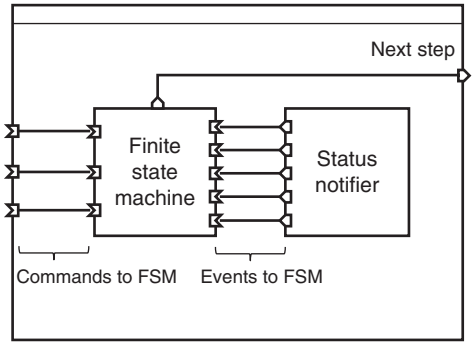


Fig. 11 UML diagram of foot step planner

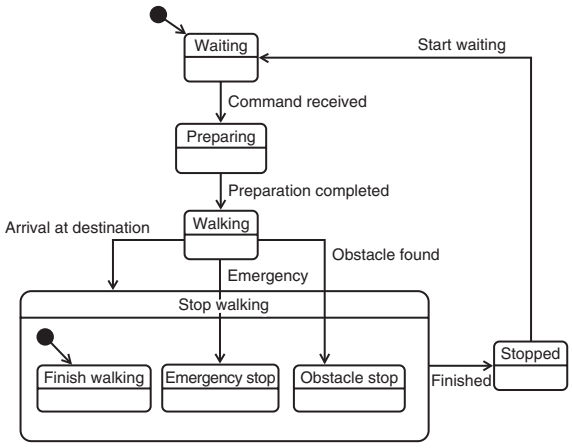


Fig. 12 UML statechart diagram of FSM component

Table 5 Comparison of processing time [us]

	Interruption processing	Input port processing	Walk status checking	Next position calculation	Total
Original	42	-	309		351
Component	22	80	50	280	432

6.5.1. Comparison of execution results

The results of walking tests using ASIMO confirmed that the componentized path tracking walk module executed at a 5 ms cycle and that the FSM component performs the designed state transitions.

In addition, comparison of the leg trajectory before and after componentization confirmed that both matched completely.

6.5.2. Processing time measurement results

The path tracking walk processing time was measured before and after componentization to verify whether hard real time performance is satisfied (Table 5). When componentizing path tracking walk, the implementation of the timer interrupt process was changed from the original program and the status notification and next position calculation were separated. This made it difficult to directly compare the processing time of each component, but the overall processing time after componentization increased by 81 μs (23%).

6.6. Observations

Componentization of ASIMO path tracking walk module made it possible to confirm that the source code of components generated automatically from the designed model is available in both the SILS and target environments without modification.

In addition, componentization increased the processing time by 23%. This is within the allowable range for the ASIMO operation in this study, but methods of reducing the increase in the processing time should be examined in consideration of use under stricter conditions.

One item that can be reduced by modifying the component design is the number of input ports. There are a total of eight input ports to the FSM component of the footstep planner as shown in Fig. 11, and the receive data size ranges from 10 to 20 bytes. Each input port performs receive processing in sequence, so the total processing time is the product of the number of ports and the receive time. The measurement results show that the data receive time for intra-process communication is 9.4 μs when receiving 20 bytes, so the estimated processing time when receiving data with all eight ports is $9.4 \times 8 = 75.2$ μs. Compared to this value, the input port processing time of 80 μs obtained from Table 5 is thought to be a valid value.

In the component design for this study, a port was created for each command and status notification type as shown in Fig. 11. However, design can also combine commands and status notifications into a single port. In this

case, Table 4 shows that the time required to receive 1000 bytes is 16 μs, so the increase in the processing time could be kept to 16 × 2 = 32 μs (10%) or less.

7. Standardization Activities

Lastly, the standardization activities related to HRTM are described below. HRTM also implements the following extended specifications with respect to the RTC specification.

- A data porting specification that can handle multiple protocols
- An interface specification for notifying and obtaining the current FSM component status

Efforts to standardize these extended specifications are being promoted by the Infrastructure Working Group under the Robotics Domain Task Force, which is the committee in charge of formulating OMG specifications in the robotics sector, with the goal of release as publicly available FSM4RTC specifications in 2015.

Standardization of these extended specifications will enable the reuse of compatible high-speed inter-component communication and FSM components between RTC-compliant middleware.

8. Conclusion

The component based middleware HRTM was developed that includes original extensions and complies with the international standard RTC specification.

In addition, ASIMO path tracking walk module was modeled and existing programs were ported to the generated skeleton code to verify the performance of the HRTM framework. The verification results proved that the components can be reused between the SILS environment and the ASIMO target environment, and that hard real time performance is also satisfied.

Componentization can be realized by adding part of the source code omitting the communication and other processing from existing programs to the skeleton code generated from the system model defined by the design tool. This can be expected to reduce the amount of source code handled by developers and to enhance both maintainability and quality.

In the future, efforts will be made to expand the effects of component based development by using HRTM in ASIMO development, to standardize the extended specification as FSM4RTC, and to expand the range of HRTM application to external research organizations and fields other than robotics.

References

(1) Hirose, M., Takenaka, T.: Development of the Humanoid Robot ASIMO, Honda R&D Technical Review, Vol. 13, No. 1, p. 1-6
(2) Shigemi, S., Kawaguchi, Y., Yoshiike, T., Kawabe, K., Ogawa, N.: Development of New ASIMO, Honda R&D Technical Review, Vol. 18, No. 1, p. 38-44
(3) Shigemi, S., Kawabe, K., Nakamura, T.: Development of New ASIMO - Realization of Autonomous Machine -, Honda R&D Technical Review, Vol. 24, No. 1, p. 37-45
(4) Ando, N., Sehiro, T., Kotoku, T.: A Software Platform for Component Based RT-System Development: OpenRTM-aist, International Conference on SIMULATION, MODELING and PROGRAMMING for AUTONOMOUS ROBOTS (SIMPAR 2008), p. 87-98 (2008)
(5) http://www.omg.org/
(6) http://www.omg.org/spec/RTC
(7) http://www.omg.org/spec/CORBA
(8) http://www.ros.org/
(9) http://www.dh.aist.go.jp/jp/research/assist/ART-Linux//
(10) http://www.ros.org/reps/rep-0003.html
(11) Bruyninckx, H.: Open Robot Control Software: the OROCOS project, Proceedings of the 2001 IEEE International Conference on Robotics and Automation, Vol. 3, p. 2523–2528 (2001)
(12) http://www.omg.rg/spec/UML
(13) http://daqmw.kek.jp/
(14) http://www.sec.co.jp/robot/openrtmnet/introduction.html
(15) http://www.gostai.com/products/rtc/

Author


Makoto SEKIYA


Norio NEKI


Zenta MIYASHITA


Nobuyuki ONO

System Design Process in Compliance with ISO26262 Using Model-Based Design

Hiroki SAGAMI* Shinji HIRONAKA*
Ryoji MORI* Takuyuki MUKAI*

ABSTRACT

It is necessary for automotive electrical and/or electronic systems to conform to the functional safety standard ISO 26262. ISO 26262 stipulates the implementation of Processes and the creation of Work Products in order to prove safety. However, ISO 26262 is based on a V-model development process, and the definition of structures and requirements at the design stage affects whether or not there is an increase in person-hours across the course of the development as a whole. The research discussed in this paper therefore focused on the system design stage, an upstream process, and formulated a system design process that conforms to ISO 26262 using model-based design as a means of controlling increases in person-hours. As a result, a process was formulated that makes it possible to implement processes conforming to ISO 26262 and create Work Products as a series of procedures, in addition to accurately defining structures and requirements by means of models.

1. Introduction

The functional safety standard ISO 26262 (Fig. 1) officially came into effect in November 2011[(1)]. This standard seeks to ensure safety through the reduction of potential risks associated with automotive electrical and/or electronic systems to allowable levels. In order to conform to this functional safety standard, it is necessary to implement a development process and create Work Product (WP)s that provide theoretical proof of safety as specified in the standard.

However, because there are numerous requirements to be met in order to conform to the standard, there are concerns that the person-hours involved in development will increase in comparison to developments conducted prior to its issuance. In addition, the basis of ISO 26262 is a V-model development process, and waterfall development featuring stage-by-stage design and verification is fundamental to the process[(2)]. As Fig. 2 shows, in a V-model development process, the further upstream the design stage is, the further downstream verification becomes. Given this, the accuracy of design more strongly affects the amount of

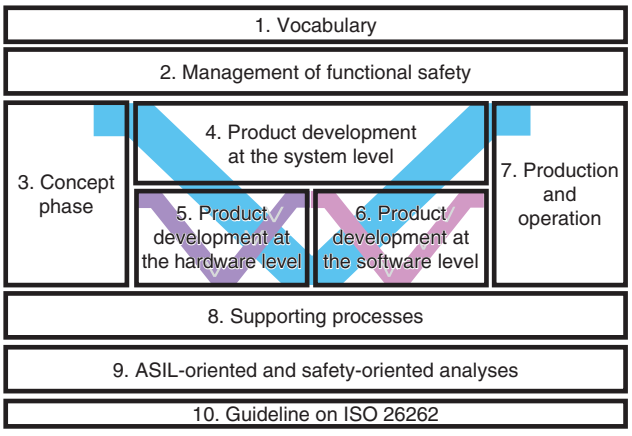


Fig. 1 Overview of ISO 26262

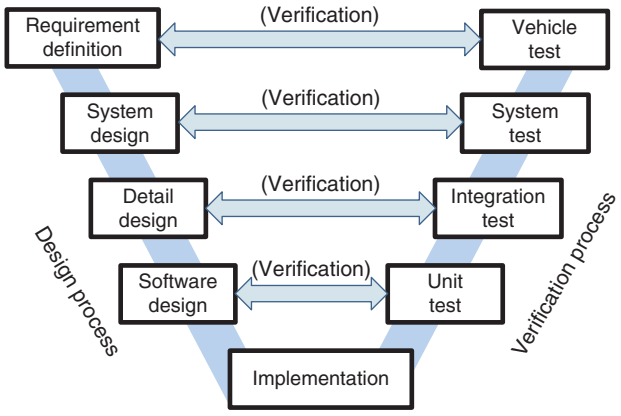


Fig. 2 General V-model development process

* Automobile R&D Center

rework that will be required the more upstream the design process is, and this is ultimately linked to increased person-hours. Against this background, determining how to control the increases in person-hours that are predicted to result from conforming to the standard is an issue for the future development of electrical and/or electronic systems.

The research discussed in this paper therefore focused on the system design stage, an upstream process of the V-model development process (corresponding to ISO 26262 Part 4), and developed an ISO 26262-compliant system design process using model-based design as a means of addressing the issue.

2. Goals of Development of Process

Figure 3 shows an overview of ISO 26262 Part 4. Part 4 of the standard stipulates the implementation of a V-model development process at the system level. The clauses that relate specifically to the design stage are Clauses 6 and 7. The focus of Clause 6 is the specification of the technical safety requirements, and it stipulates the definition of concrete methods of reducing potential risks in systems to help to ensure safety based on system characteristics. The focus of Clause 7 is system design, and it stipulates the definition of the system structures necessary for the realization of the technical safety requirements defined in Clause 6.

As indicated in Chapter 1 above, in order to conform to ISO 26262, it is necessary to implement the development process and create the WPs stipulated by the standard. Determining how to link the implementation of the development process and the creation of the WPs is an important factor in attempting to conform to ISO 26262 while at the same time controlling increases in person-hours.

In addition, because the system-level design process is an upstream process in terms of the development as a whole, it is essential to identify and express a certain amount of necessary information. Test verification will be conducted at the system level in the processes downstream from system design following the development of hardware (HW) and software (SW) in order to realize the design. As a result, identifying information with a high degree of precision and making accurate determinations with regard to requirements and structures are also important in limiting the amount of rework in later stages.

Based on the above considerations, the following goals were set for process development:

(1) The development of a mechanism making it possible to directly reflect the information obtained as a result of the design process in the WP.

(2) The development of a mechanism making it possible to accurately define requirements and structures related to functional safety at the system level.

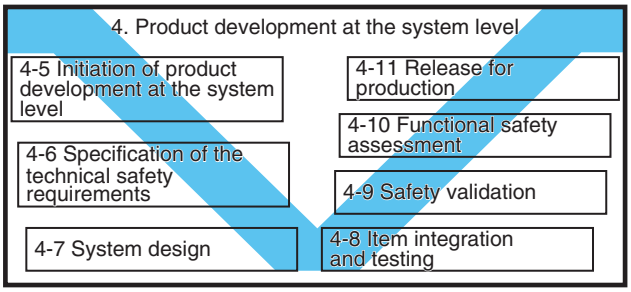


Fig. 3 ISO26262 Part 4

3. System Design Process conforming to ISO 26262

3.1. Overview of Process

Model-based design (Fig. 4) was employed in order to implement the V-model development process stipulated by ISO 26262. Model-based design is an effective method for the efficient implementation of a V-model development process. Here, a model is defined as expressing the results of identification and organization of system information. The model expressing the system includes the system structures, the requirements demanded of the system, and the behavior of the system. System modeling languages (SysML) are among the methods available for the notation of the model[3]. In addition to making it possible to eliminate ambiguity and define the system at an early stage of the design process, the use of model-based design in which a model is employed in design also makes it possible to conduct verifications at an early stage through the use of the model in simulations. Hierarchization of the model also makes it possible to increase the detail of requirements and specifications in stages, helping to enable clear expression of the connections with upstream and downstream processes. Based on the above, the use of the method can be expected to control increases in person-hours by helping to eliminate ambiguities and oversights from system definitions, thus doing away with factors requiring rework.

During this development of an ISO 26262-compatible system design process, the hierarchy of system structures

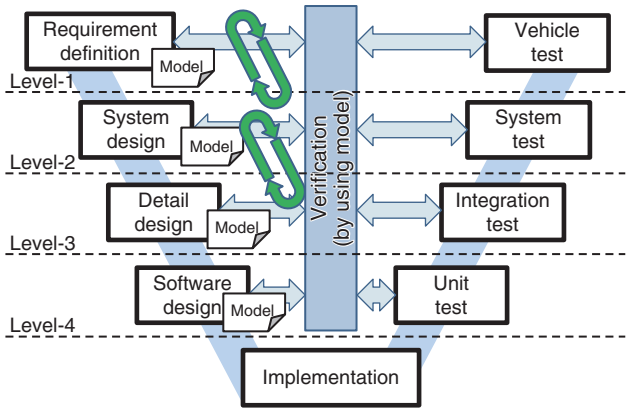


Fig. 4 V-model development process using model-based design

and requirements shown in Fig. 5 was defined in order to make it possible to express systems by means of models. SG are the safety goals necessary at the top level for the avoidance of hazardous events, and FSR are the functional safety requirements necessary at the concept level in order to realize the SG. TSR1 are the technical safety requirements defined as the methods of realizing the FSR, and TSR2 are further elaborations of these methods of realization of the FSR (this includes discrimination of HW and SW, allocation to elements, etc.). Figure 6 shows an example of the expression of a hierarchy using SysML.

The design process for structures and requirements at the system design level to help ensure conformity to ISO 26262 will be discussed below.

3.2. Process of Specification of Technical Safety Requirements

Technical safety requirements are defined as the concrete methods of realization of the functional safety requirements, the safety requirements at the concept level. Failsafe technologies and other concrete specifications are defined by further elaboration of the technical safety requirements. ISO 26262 stipulates that technical safety requirements should be defined with no oversights in order to help ensure that no hazardous events occur as a result of system failures.

Figure 7 shows the process of specifying technical safety requirements accurately and without oversights. In the explanation of the process that follows, it is assumed that the concept-level structures and the allocated FSR have already been defined as prerequisites, as shown in Fig. 7(a).

3.2.1. Definition of preliminary architectural assumption

The upper-level requirements (the concept-level requirements) are analyzed, and the methods of realizing the concept and the preliminary architectural assumption of the structures at the system level are defined [Fig. 7(b)].

3.2.2. Implementation of safety analysis

A safety analysis (e.g., FTA[4], FMEA[5], or HAZOP[6]) is conducted in relation to the preliminary architectural assumption, and any elements that might lead to violate safety goals, and the failure modes of those elements, are identified [Fig. 7(c)].

3.2.3. Definition of TSR1

TSR1 are defined as methods of helping to prevent the occurrence of hazardous events as a result of the failure modes of the elements identified in Section 3.2.2 and of realizing FSR, the upper-level requirements [Fig. 7(d)].

3.3. System Design Process

The purpose of system design is to determine the structures that will realize the technical safety requirements. In ISO 26262, in order to fulfill this purpose, it is necessary

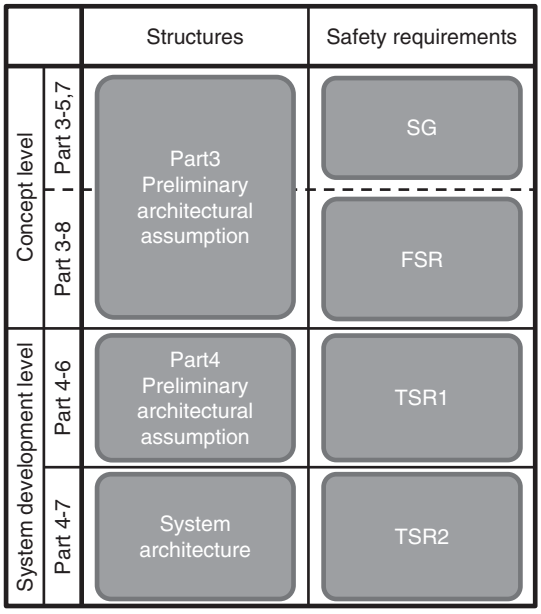


Fig. 5 Hierarchical definition of structures and requirements

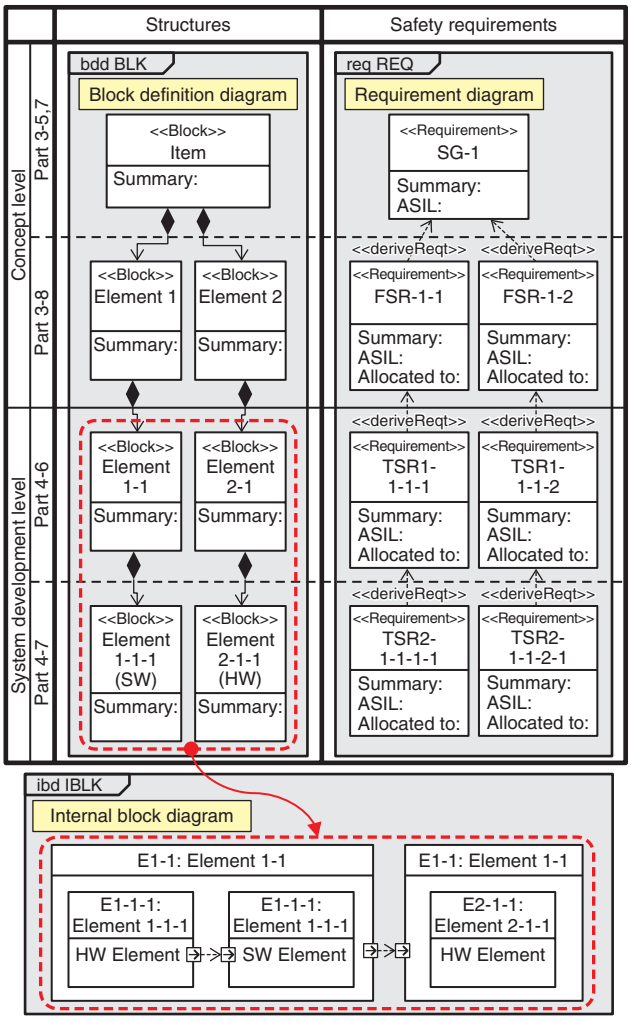


Fig. 6 Structure and requirement definition using SysML

to specify the elements that will realize the technical safety requirements, clarify the roles of HW and SW in realizing the technical safety requirements, and specify the interfaces between HW and SW elements.

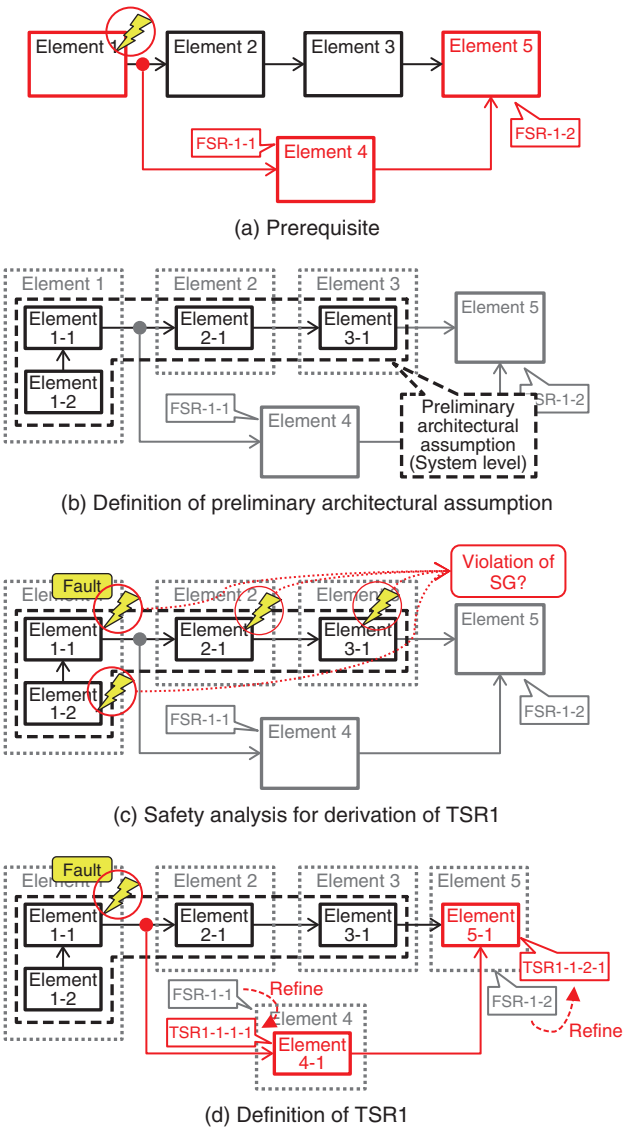
A process of determination of structures, incorporating the above items, relating to the TSR1 defined in Section 3.2 will be discussed in this section (Fig. 8).

3.3.1. Definition of system architecture

An architecture that has been further elaborated in relation to the system requirements and preliminary architectural assumption defined in Section 3.2.1. up to the stage at which the roles of HW and SW are able to be specified is defined as the system architecture [Fig. 8(a)].

3.3.2. Implementation of safety analysis

A safety analysis of the system architecture defined in Section 3.3.1. is conducted, and elements of the system



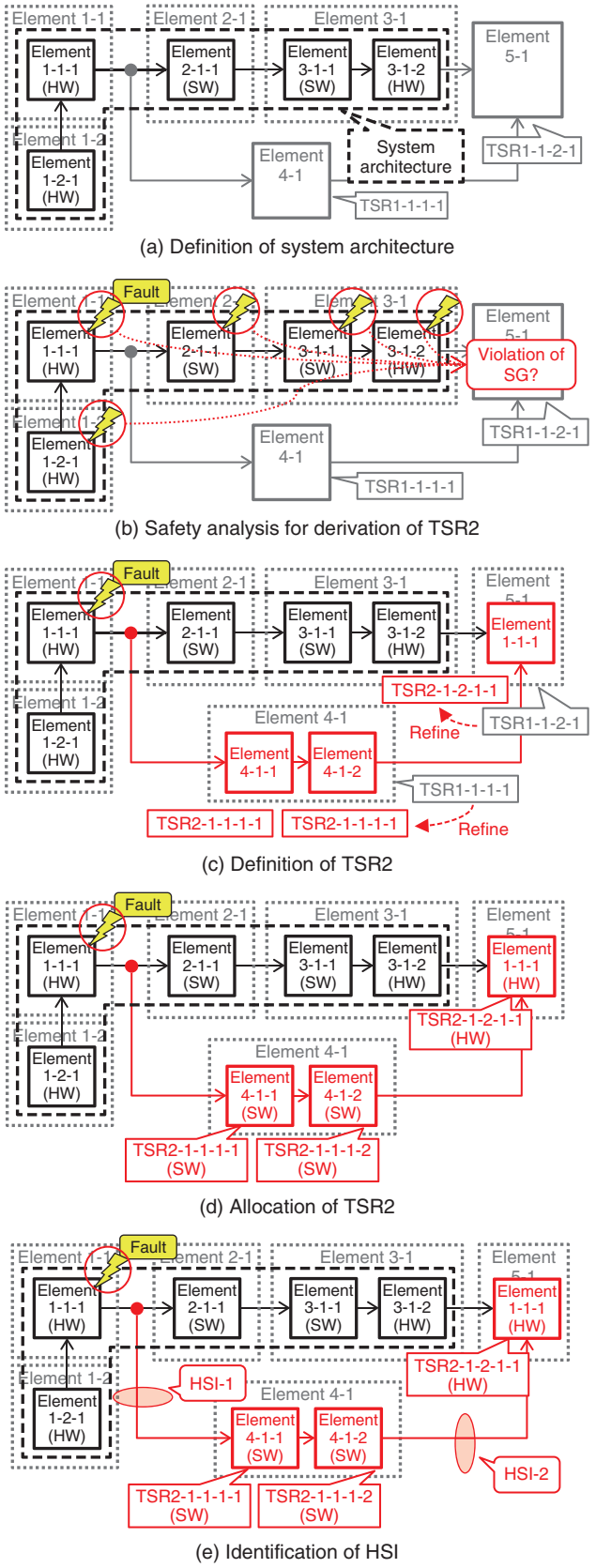
(a) Prerequisite

(b) Definition of preliminary architectural assumption

(c) Safety analysis for derivation of TSR1

(d) Definition of TSR1

Fig. 7 Procedure for derivation of TSR1



(a) Definition of system architecture

(b) Safety analysis for derivation of TSR2

(c) Definition of TSR2

(d) Allocation of TSR2

(e) Identification of HSI

Fig. 8 Procedure for system design (Including derivation of TSR2)

architecture that might lead to violate safety goals, and the failure modes of these elements, are identified. However, where elements that will not lead to violate safety goals have been identified in the safety analysis conducted in Section 3.2.2., it is not necessary to conduct a safety analysis when these elements are updated later in the process [Fig. 8(b)].

3.3.3. Definition of TSR2

The TSR1 defined in Section 3.2.3 are further elaborated to the stage at which the roles of HW and SW can be specified in relation to the failure modes of the elements of system architecture identified in Section 3.3.2. The results of this process are defined as TSR2 [Fig. 8(c)].

3.3.4. Allocation of TSR2 and determination of roles of HW and SW

The TSR2 defined in Section 3.3.3 are allocated to the elements of the system architecture. If necessary in order to realize the TSR2, new elements are added to the system architecture at this time. The respective roles of HW and SW are also defined [Fig. 8(d)].

3.3.5. Definition of hardware-software interfaces

HW and SW elements related to the TSR2 are specified in the updated system architecture formulated in Section 3.3.4. Interface specifications in areas in which HW elements and SW elements are directly connected are defined as hardware-software interfaces (HSI) [Fig. 8(e)].

4. Creation of WPs

4.1. Overview of WPs

ISO 26262 stipulates the formulation of technical safety requirements as WPs for Part 4-Clause 6, and of technical safety concepts, system design specifications, and HSI specifications as WPs for Part 4-Clause 7. All of these are essential documents proving theoretical compliance with functional safety standard ISO 26262, and it is necessary to formulate them having implemented the process demanded by the standard.

The development of a process to help ensure conformity to ISO 26262 was discussed in Chapter 3. Given this, it would be sufficiently possible to prove theoretical compliance with the functional safety standard via the WPs if the information obtained in the implementation of this process was reflected in them.

This section will therefore discuss a procedure for the creation of WPs based on the process discussed in Chapter 3.

4.1.1. Specified technical safety requirements

The TSR1 and TSR2 respectively formulated in Sections 3.2.3. and 3.3.3. are organized to become WPs for technical safety requirements. It is possible, by reflecting the information obtained as a result of the hierarchical design process (including traceability information) in the WPs, to formulate documents able to prove compliance with the functional safety standard without any additional work. For example, if TSR1 and TSR2 are formulated using SysML requirement diagrams, it is possible to use the requirement diagrams themselves as WPs. As another example, the process from FSR to TSR2 can be organized and expressed as a table, as shown in Table 1.

Table 1 Example of work product of TSR

SG	FSR	TSR1	TSR2
SG-1	FSR-1-1	TSR1-1-1-1	TSR2-1-1-1-1
			TSR2-1-1-1-2
		TSR1-1-1-2	TSR2-1-1-2-1
			TSR2-1-1-2-2
	FSR-1-2	TSR1-1-2-1	TSR2-1-2-1-1
			…
…	…	…	…

Table 2 Example of work product of technical safety concept

TSR2	Allocated system element	HW or SW
TSR2-1-1-1-1	Element A	HW
TSR2-1-1-1-2	Element B	SW
TSR2-1-1-2-1	Element C	HW
...	...	...

Table 3 Example of work products of HSI

Description	HW			SW			Interface type	Related TSR2
	Symbol	Range	Unit	Symbol	Range	Type		
XXX1	xxx1h	0 to 5	V	xxx1s	0 to 255	Byte	A/D	TSR2 –...
...								

4.1.2. Technical safety concept and system design specifications

The results of allocation of TSR2 to the elements of the system and of the selection of the roles of HW and SW are organized as WPs for the technical safety concept. It is sufficient to clearly express the subjects of allocation of TSR2 and the roles of HW and SW, as shown in Table 2.

4.1.3. HSI specifications

The interfaces between the HW and SW elements specified in Section 3.3.5 are organized as WPs for HSI specifications. Documents of the type shown in Table 3 can be used as HSI specifications documents.

5. Case Study of Application to Electric Power Steering Control System

Electric power steering (EPS) systems are systems designed to reduce the steering load for the driver. These systems determine the amount of assistance to output based on the driver's steering torque.

Using a representative example of EPS, this chapter will present a case study of the application of the process developed in Chapters 3 and 4 to an actual development.

5.1. SG and FSR

For this discussion of an example of system design in relation to functional safety in EPS systems, a representative example of an EPS system, with a concept definition including the SG and FSR necessary as preconditions, has been defined. SG is defined as prevention of output that would turn the vehicle against the driver's intentions. FSR is defined as isolation of output when a failure in the steering torque detection function is detected. The concept architecture based on the above was defined as shown in Fig. 9.

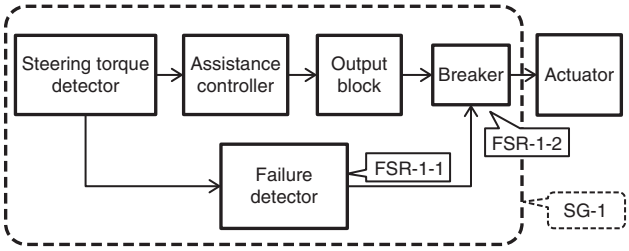
5.2. Formulation of TSR1

Figure 10 shows the preliminary architectural assumption for the EPS system at the system level. Steering torque is detected by a torque sensor, and the amount of assist provided is determined based on the figure output by the sensor. Motor control is applied in order to output the amount of assist, and the actual amount of assist is output by the motor.

Based on this preliminary architectural assumption, the factors of failure which might lead to violate the SG set in Section 5.1. were analyzed. The results showed that if a failure in torque sensor output resulted in the output of a figure that deviated from the specified range, and an inappropriate amount of assist was calculated and output, there is a possibility that SG is violated and a hazardous event might occur. Based on these results, TSR1 was defined as the cutting off of motor drive by means of a relay function if torque sensor output deviated from the specified range for a specific period or longer (Fig. 11).

5.3. Formulation of TSR2

Figure 12 shows the system architecture of the EPS system. This is the result of further elaboration until the roles of HW and SW in relation to each element of the preliminary architectural assumption formulated in Section 5.2. can be discriminated. Here, another analysis



SG	FSR
EPS shall avoid output which turns vehicle freely. (SG-1)	Failure of steering torque detector shall be detected. (FSR-1-1)
	Output shall be blocked. (FSR-1-2)

Fig. 9 Example of SG, FSR, and architecture at concept level

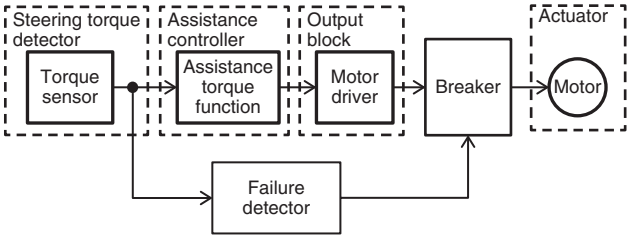
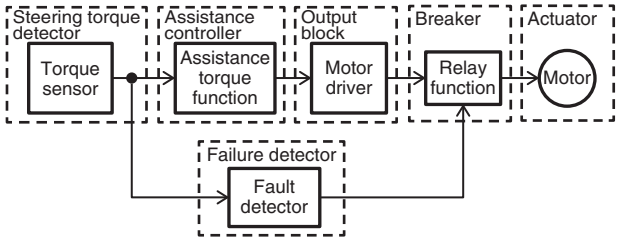


Fig. 10 Example of preliminary architectural assumption at system level



FSR	TSR1
Failure of steering torque detector shall be detected. (FSR-1-1)	If torque sensor output deviates from specified range for xx msec, torque sensor shall be judged as having failed. (TSR1-1-1-1)
Output shall be blocked. (FSR-1-2)	Motor driver output shall be blocked by relay function. (TSR1-1-2-1)

Fig. 11 Example of TSR1 and refined preliminary architectural assumption at system level

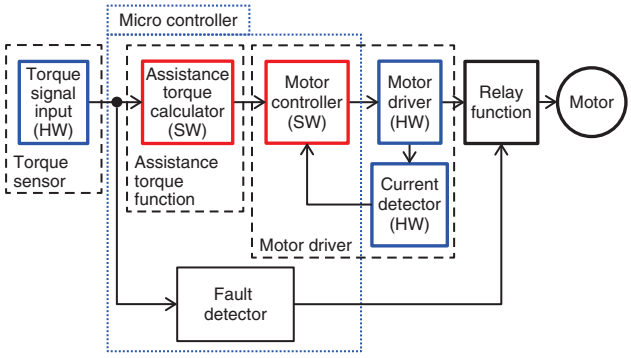


Fig. 12 Example of system architecture

of elements at the system architecture level was conducted. The results showed that if a failure occurred in the torque signal input, an HW element, the phenomenon identified in Section 5.2. would occur. Based on these results, TSR2 was defined as the cutting off of motor drive by means of a relay if the output of the torque signal input deviated from the specified range for a specific period or longer.

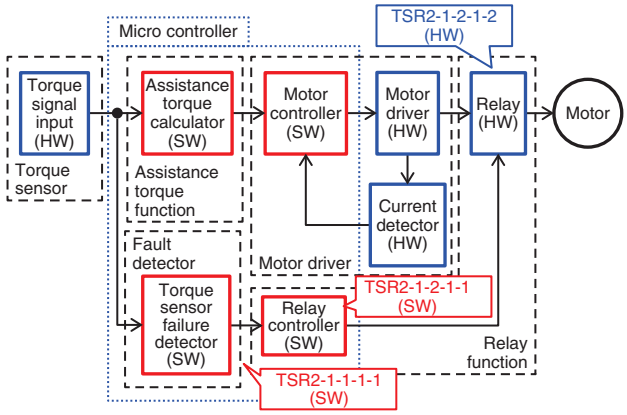
In addition, TSR2 was compartmentalized and allocated to elements of the system architecture. The TSR2 allocated to the torque sensor failure detector, an SW element, was defined as monitoring the deviation of the output of the torque signal input from the specified range for a specific period. The TSR2 allocated to the relay controller, an SW element, was defined as outputting instructions to switch the relay off. The TSR2 allocated to the relay, an HW element, was to cut off the output of the motor drive by switching the relay off. Based on these results, the system architecture was updated as shown in Fig. 13.

5.4. Formulation of HSI

In the updated system architecture formulated in Section 5.3., the interfaces between the torque signal input and the torque sensor failure detector, and between the relay controller and the relay, were related to TSR2, and were therefore identified as elements subject to definition as HSI (Fig. 14).

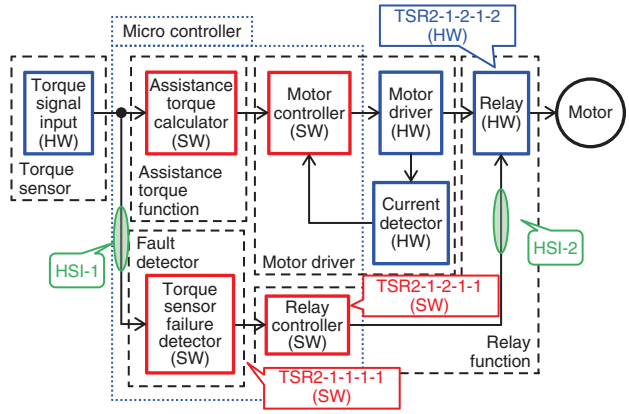
5.5. Effect of Application of Development Process

As a result of application of the newly formulated development process in the design of an EPS system, it was possible to eliminate potential factors that could lead to violate safety goals and result in rework in downstream processes. As one example, the verification accuracy of the reviews, simulations, and other procedures conducted at the design stage to identify and eliminate elements has been increased, thanks to system structures and requirements being clearly and hierarchically defined. In addition, because the system architecture made clear the subjects of HW and SW development in downstream processes, it was possible to eliminate factors originating in oversights when communicating information.



TSR1	TSR2
If torque sensor output deviates from specified range for xx msec, torque sensor shall be judged as having failed. (TSR1-1-1-1)	If output of torque signal input deviates from specified range for xx msec, torque signal input shall be judged as having failed. (TSR2-1-1-1-1)
Motor output shall be blocked by relay function. (TSR1-1-2-1)	Instruction of turning relay off shall be output. (TSR2-1-2-1-1)
	Relay shall block motor driver output by giving an instruction to turn relay off. (TSR2-1-2-1-2)

Fig. 13 Example of TSR2 and refined system architecture



Description	Hardware			Software			Interface type	Related TSR2
	Symbol	Range	Unit	Symbol	Range	Type		
HSI-1	Trq1h	0 to 5	V	Trq1s	0 to 255	Word	A/D	TSR2-1-1-1-1
HSI-2	Rly1h	0 to 5	V	Rly1s	0 to 1	Byte	A/D	TSR2-1-2-1-1 TSR2-1-2-1-2

Fig. 14 Example of HSI

6. Conclusion

A new development process has been formulated with the following results:

(1) It was possible to control increases in the person-hours associated with the creation of WPs by directly reflecting information obtained in the design process in the WPs.

(2) It was possible to control increases in person-hours by hierarchically defining system structures and safety requirements in order to reduce the number of factors that might lead to violate safety goals and result in rework.

References

(1) ISO26262: Road Vehicles – Functional Safety (2011)

(2) Murakami, M., Nomura, K., Hisaki, T., Kasahara, Y.: System Modeling Technology for Powerplant Control

Systems, Honda R&D Technical Review, Vol. 22, No. 2, p. 101-108
(3) http://www.omgsysml.org/
(4) IEC61025: Fault tree analysis (FTA) (2006)
(5) IEC60812: Analysis techniques for system reliability – Procedure for failure mode and effects analysis (FMEA) (2006)
(6) IEC61882: Hazard and operability studies (HAZOP studies) – Application guide (2001)

■ Author ■


Hiroki SAGAMI


Shinji HIRONAKA


Ryoji MORI


Takuyuki MUKAI

Development of Configuration Management System for ISO26262

Hitoshi TAKUMI* Yasuo KUROSAKI* Hiroshi ISHIDA*

ABSTRACT

The functional safety standard ISO 26262 was published in November 2011. It is a functional safety standard for electrical and/or electronic systems within road vehicles. Compliance with this standard requires that the development process be defined and that numerous documents be created as proof that the development process has been implemented. The documents to be created in accordance with the development process were defined in advance and a configuration management system was developed to be capable of storing them together with the review results for each event during development. In order to realize traceability, a proprietary function was developed that automatically extracts items that are considered to require management for the purpose of functional safety from documents that are entered in predefined formats. This function is capable of displaying a list of the items, as well as a list of the definitions of the relations between items.

This system contributes to compliance with ISO 26262 and contains the increasing operational and administrative load.

1. Introduction

Recently there has been rising demand for increasingly advanced safety, environmental, comfort, and other such performance features in road vehicles. In order to satisfy this kind of demand, numerous electrical and/or electronic systems within road vehicles (in-vehicle E/E systems) are being installed. Assuring the safety of road vehicles will call for quality control of parts to prevent the outflow of faulty parts that may contribute to hazards and so that hazards themselves will not occur. In addition to this conceptual approach of intrinsic safety, it will also be necessary to conduct development by applying the conceptual approach of functional safety, whereby hazardous events that could occur are envisioned and reduced to acceptable risks by the function of safety devices and other systems that are designed to be fail-safe and fault-tolerant, thus assuring safety. The international standard that prescribes development procedures and requirement management during development for the purpose of applying this functional safety to products is the ISO 26262[(1)] functional safety standard.

ISO 26262 is based on international standard IEC 61508[(2)] by the International Electrotechnical Commission (IEC), relating to the functional safety of electrical, electronic, and programmable electronic systems in processing and plant industry. Work on ISO 26262 standardization began in November 2005, and the standard was officially published on November 15, 2011.

In order to comply with ISO 26262, it will be necessary to perform the following kinds of operations for the configuration management for development of in-vehicle E/E system safety mechanisms.

First of all, development is initiated in accordance with the in-vehicle E/E system development process, and the configurations of documents (Work Product: WP) that are created by that activity are defined and managed. Second, the Automotive Safety Integrity Level (ASIL) that indicates the risk level of hazardous events is configured as a system for development. The WP is subjected to audit and assessment in accordance with the ASIL, and those results and the WP are stored together. Third, in preparation for an impact analysis when changes are made, relations with design and test results related to functional safety requirements are defined and traceability is enabled. Finally, the created WP is subjected to revision management, and when a change is made to the WP, the range of impact due to the change is specified and the approval of an appropriate manager is sought for the substance of the change and the reason(s) for it.

Honda began supporting ISO 26262 in 2008, and conventional in-vehicle E/E system development already took functional safety into account. Concepts are brought to maturity, however, by repeated meetings between the people in charge when development concepts are being considered. Consequently, estimations of the range of impact of changes and the number of iterations of audit and assessment of the content of changes are increasing. Furthermore, ISO

* Automobile R&D Center

26262 requires WP configured with traceability, and there is concern that this will further increase the operational and administrative load.

A system that would be capable of readily implementing configuration management and traceability therefore became necessary as a means of complying with ISO 26262 while also holding down the increase in development man-hours to a minimum.

2. Support for ISO 26262

2.1. Overview of ISO 26262

ISO 26262 is made up of 10 parts, from Part 1 to Part 10. It is configured as a standard for the entire lifecycle, from development and production of road vehicle in-vehicle E/E system to service (Fig. 1).

The content of these parts is as shown below.

Part 1 contains definitions of vocabulary and Part 2 contains requirements for corporate culture (safety culture) and company organization for the purpose of implementing functional safety activities as part of functional safety management.

Part 3 to Part 7 contain a systematic presentation of requirements for the corporate divisions that implement functional safety activities.

Development divisions of vehicle manufacturers have charge of the concept design specified in Part 3. Part 3 establishes Safety Goals for reducing risk to the level of what is acceptable as functional safety or lower. In terms of development results, it specifies that the appropriateness of safety goals be validated. It also defines the Functional Safety Requirements (FSR) that are required in order to achieve the safety goals, and it also provides that development results be verified.

Working from that content, the development divisions or suppliers are in charge of the system development specified in Part 4. Part 4 specifies that the FSR presented in Part 3 are to be elaborated in greater detail, Technical Safety Requirements (TSR) are to be designed, and development results are to be verified.

Similarly, more detailed requirements are elaborated for hardware design in Part 5 and software design in Part 6. They also specify that development results are to be verified.

For production and operations, Part 7 specifies content that the production division and service division are to be in charge of.

Part 8 specifies supporting processes relating to functional safety development as a whole. These include management of requirements for functional safety as well as management of traceability, configuration management of documents, software libraries to be reused, and qualification of tools.

Part 9 defines the methods for implementing ASIL decomposition and the requirements involved in its implementation as ASIL-oriented and safety-oriented analysis.

Part 10 presents guidelines for the application of ISO 26262.

2.2. Definition of ASIL

Functional safety necessitates the assumption of hazardous events. In order to define the level of risk of a hazardous event, the frequency of occurrence of the

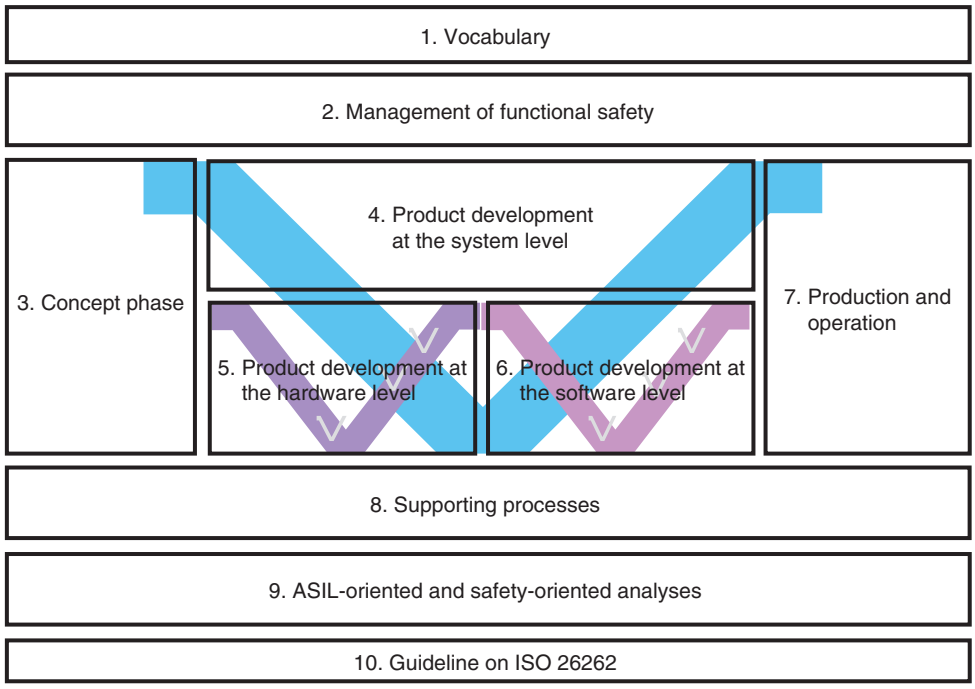


Fig. 1 Overview of functional safety standard

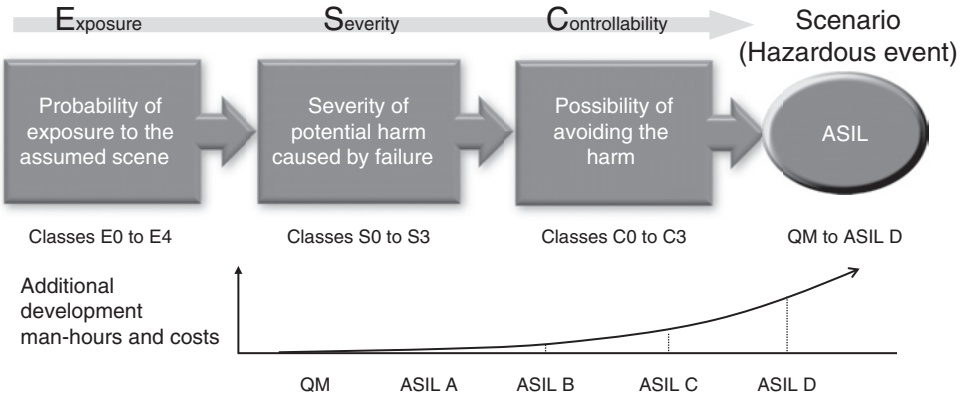


Fig. 2 Definition of ASIL and development cost

hazardous event (Exposure), the severity of harm to human beings caused if the hazardous event occurs (Severity), and the probability of whether human beings can take evasive action if the hazardous event occurs (Controllability) are used.

The three parameters (exposure, severity, and controllability) shown in Fig. 2 are estimated. They are then checked against a table defined in ISO 26262 to determine the ASIL for each assumed scenario. The ASIL is expressed by the letters A to D, where D is defined as the highest risk level.

The number of iterations of audit and assessment of the WP created, and the conditions regarding the approver, are set forth in accordance with the ASIL.

3. System Development Policy

Data management applications for the purpose of complying with ISO 26262 are already available on the market from software development companies.

The applications from the various companies were evaluated in terms of the reduction of man-hours.

No applications that satisfy Honda's requirements for configuring traceability and operability were found. The decision was therefore made to develop a proprietary system.

Analysis of ISO 26262 was carried out during development, and the following items for achievement were formulated.

(Item 1) The system is to be capable of defining the development process, revision management of the created WP is to be possible, and the WP is to be shareable between projects.

(Item 2) It is to be capable of extracting requirements and related items from within Microsoft Office documents, setting up the relations between the extracted items, and displaying those relations in list form.

(Item 3) It is to be capable of operations to upload the WP in a simple manner, of assisting with audits and assessments in the system, and of managing the results.

(Item 4) Requirements and WP are to be easily exchanged with suppliers.

The technical issues involved in incorporating these four items into a system were defined and system development was carried out.

4. System Development Headings

4.1. Configuration Management

Achieving the configuration management specified in Part 8 of ISO 26262 requires that management of the development process, configuration management of the WP, Change Management, and traceability be configured.

Conceptual database design was conducted of a database to implement the above content during in-vehicle E/E system development work and to record the management content.

Configuration management first involved definition of the function under development (Project), the development process (Process), and the scheduled product (Work Product Box: WPBox) to be created as the result from implementation of that development process. These were configured so that they could be recorded in the database.

Traceability was defined as management of the relationship (Relation) with the item subject to management (Object) that was extracted from the WP (Fig. 3).

The next phase was Process Management. This involved enabling the establishment of status, which indicates the state of progress, and of schedule, which includes the date of work commencement, the date of completion, and other such attributes individually for the Project, the Process, and the WPBox.

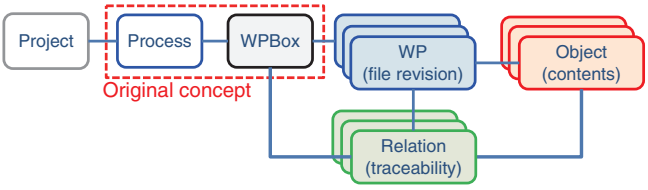


Fig. 3 Concept of configuration management

The final phase was Change Management. In order to preserve the results from verification of the development results, this involved defining the scheduled audits and assessments in the system as verification meetings (Events), so that the WPBox could be configured as an object of verification. When an Event was implemented, the revision number of the WP that was to be subject to audit and assessment was registered for the WPBox. The system was configured to enable implementation of an approval process (Approval Flow) that was in accordance with the ASIL of the function under development.

The WP that was finalized in accordance with the Approval Flow was used as a Baseline for when changes would be implemented. When development was completed and the transition to mass production was to be made, this could be treated as a Safety Case (Fig. 4).

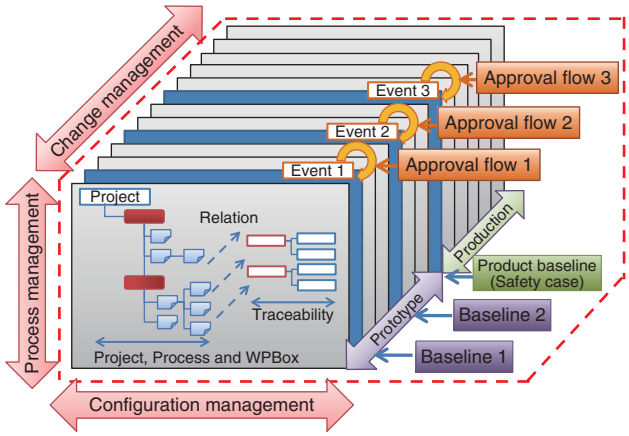


Fig. 4 Concept of data management

4.1.1. Tree structure and revision management

Under ISO 26262, it is necessary to simultaneously manage the development process and the WP created as a result.

This content was represented by a tree structure. A node on the tree was defined as a Process, and a leaf that is created under a node was defined as a WPBox.

The tree structure with the Process and WPBox created for each Project on the system was configured so that additions, changes, and deletions could be made. The tree structure was also configured so that its history could be managed (Fig. 5).

The WP uploaded in a WPBox is automatically assigned a control number in the order of uploading. The WP is identified by this number.

In this way, even if the same WP is uploaded multiple times, it will not be overwritten within the system. The control number can be used to conduct revision management. When designers want to refer to a past WP, they can specify its control number to view it.

4.1.2. Set carry-over

A function called set carry-over was developed for when the parts of an already developed E/E system are to be changed and used for the development of a similar E/E system. Set carry-over is a function that refers to the WPBox of the source project from the project that is to be partially changed.

When the WP in the already developed WPBox (the carry-over source) is changed using this function, the most up-to-date WP is also automatically made available

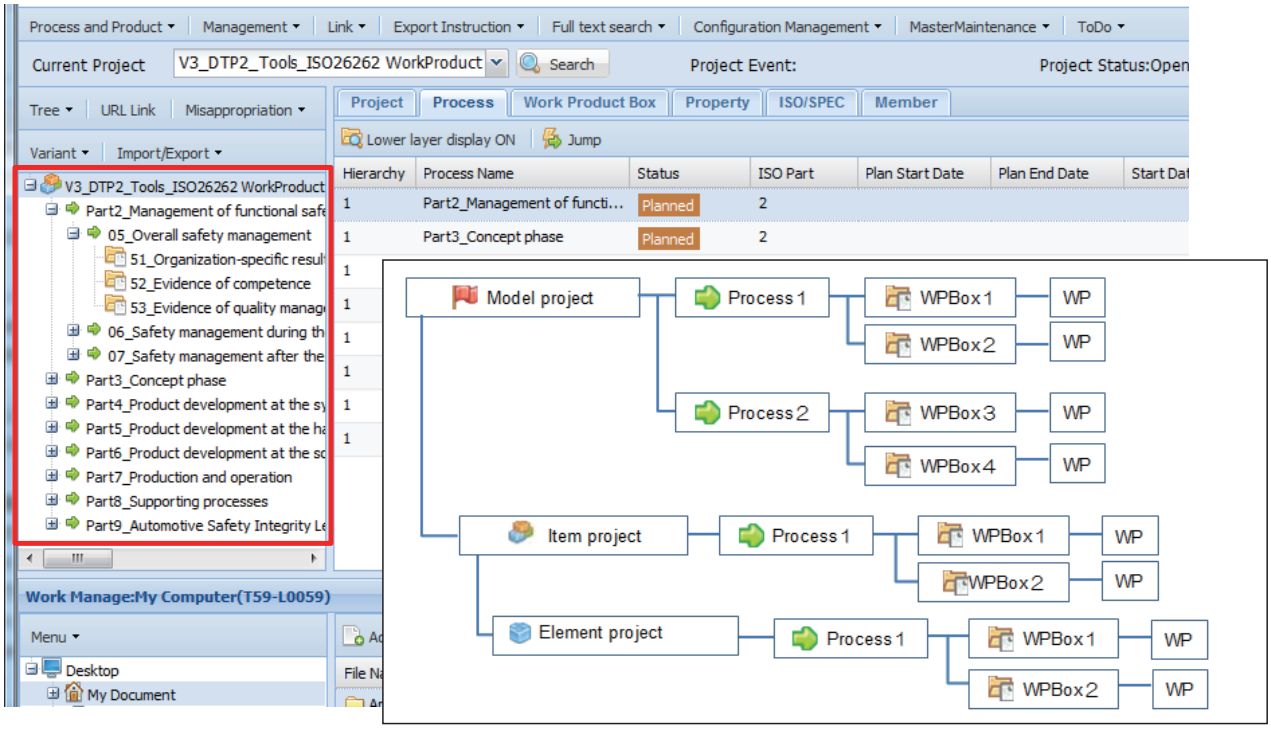


Fig. 5 Project tree, process and WPBox

for reference in the WPBox (the carry-over target) of the project that is to be partially changed.

When there is no desire to adopt the content of the most up-to-date changes or when there is a desire to add unique changes with no reference, a new WP can be uploaded in the carry-over target WPBox. This will automatically cancel the relationship with the WPBox in the carry-over source, allowing the development to proceed.

When set carry-over is executed, a Relation is set up between the WPBoxes in the carry-over target and the carry-over source. This enables traceability. They can therefore be handled as objects for calculation of impact, to be discussed later, and the man-hours involved in design changes can be reduced.

4.2. Traceability

Achieving the traceability sought in ISO 26262 requires more than establishing Relations with WPs. It also necessitates establishing the relations with requirements and test results themselves that are contained within a WP so that they can be tracked.

Relations of requirements can be set up by hierarchization of the control number assigned to the requirement when elaborating the detail of the requirement in accordance with the development process.

Items to be tested to verify the design content can be subjected to stand-alone testing, unit testing, inter-function linked testing, and so on. Since the testing is conducted in phases and the test items are aggregated, a control number is assigned for each phase of the testing and the relations between numbers are set up according to aggregation.

In order to verify whether the requirements for functional safety have been achieved, it is necessary to configure traceability between requirements and test items (Fig. 6).

A function was developed that can extract the requirements and test items from the WP uploaded in the system, set up the relations, and display the content in list form.

4.2.1. Extraction of items from within documents

The WP containing notations of safety goals and FSR to be achieved is published as a specification form and the information is transmitted to related Honda divisions and suppliers.

Templates for specification forms containing notations of items involved in complying with ISO 26262 are created as Microsoft Office documents. The system was configured so that those templates can be analyzed using Office Open XML, which is published by Microsoft, and the Objects can be extracted from XML tag names and recorded content (Fig. 7).

The hierarchical structure of Objects expressed in templates can also be extracted. The system is configured so they can be registered and stored in the database.

4.2.2. Conceptual approach of the Relation

In this system, configuration management involves defining the Process and WPBox. Revision management is carried out on the WP that is uploaded in the WPBox [Fig. 8(1)].

When the WP has been uploaded, the system automatically adds a Relation between the WPs according to the Relation between WPBoxes [Fig. 8(2)].

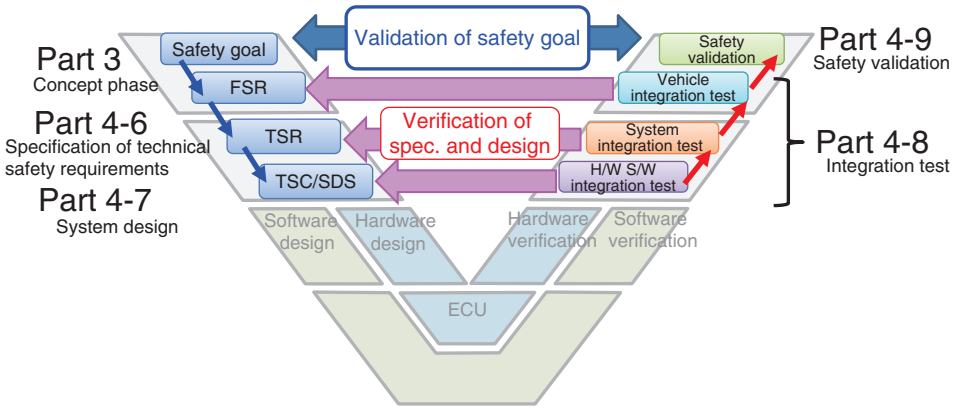


Fig. 6 Verification and validation in ISO 26262

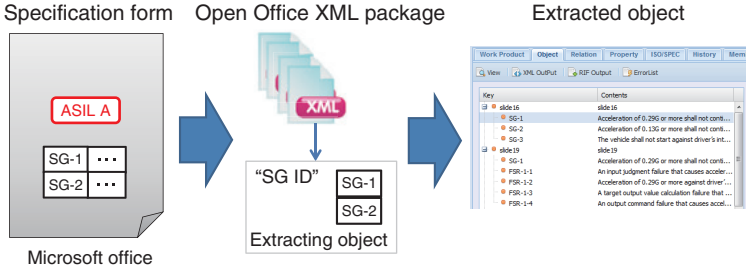


Fig. 7 Extracting object from Microsoft office

When a WP that has been changed is uploaded in a WPBox by means of revision management within WPBoxes, this allows a Relation between WPs that was set up before the change to continue with the same setting after the change [Fig. 8(3)].

It is also a distinctive feature of this function that when setting up a Relation, the kind and direction can also be set up.

Depending upon the direction set up in the Relation, it can represent the relationship of referencing between Objects or the relationship of being referenced. By setting the kind of Relation, the meaning of the relationship can be represented (Fig. 9).

4.2.3. Calculation of the range of impact

When requirements are changed, it is necessary to search the related design content and test results and to specify the range of impact of the change.

In this system, the set up Relations are traced in order and the related items are displayed in a hierarchical structure. This allow the range of the impact to be clearly indicated (Fig. 10).

The kind and direction of the Relation and the depth of the hierarchical structure can be set up as search conditions. When the range of impact is specified, the search results can be further focused. The search conditions can be reset for items displayed as search results so that a series of calculations of the range of impact can be performed consecutively. This can be used as a measure to increase the efficiency of search operations during development.

As shown in Fig. 11, a form can also be created to

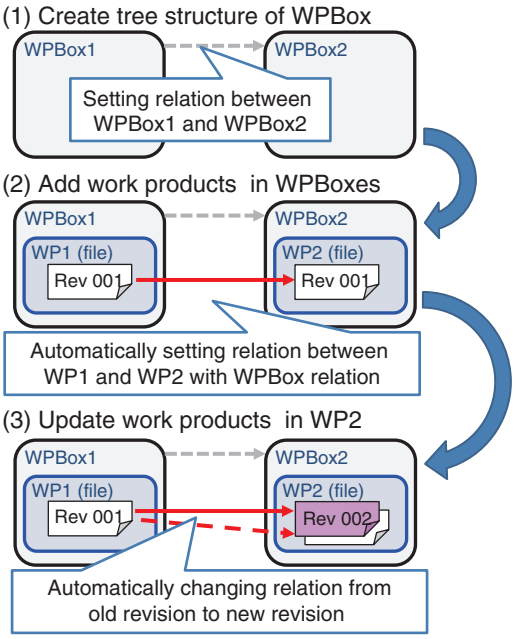


Fig. 8 Automatically setting a Relation

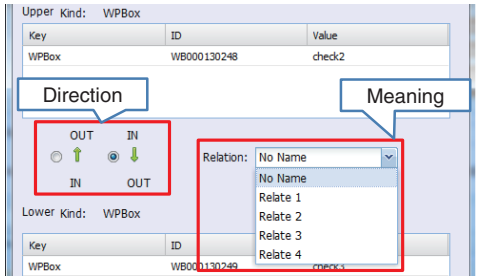


Fig. 9 Setting direction and meaning of a Relation

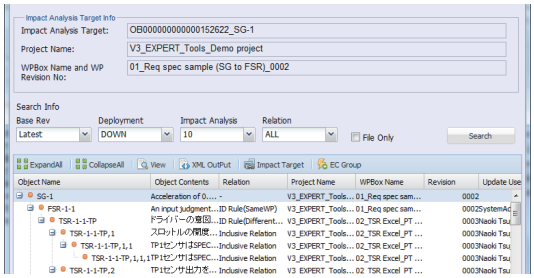


Fig. 10 Results of impact analysis

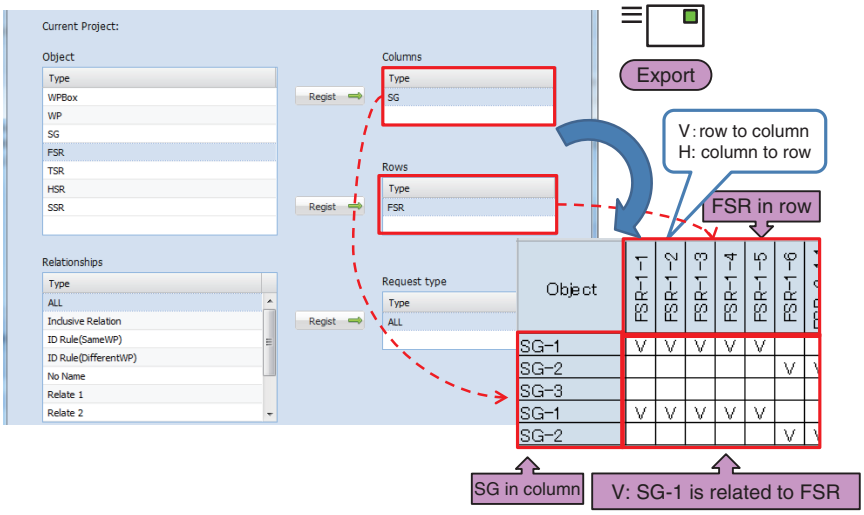


Fig. 11 Matrix of objects and Relations

specify items selected from among the extracted items to be displayed along vertical and horizontal axes, and to specify the kind of Relation set up among those items and cross-tabulate them. This form can be used to check whether any relationships have been omitted from set up.

4.3. Usability

It is necessary to be able to reference and upload documents without installing any special applications. The ability to run on a web browser was therefore made a system requirement.

Rich Internet Application (RIA) technology and the Extjs Javascript library were adopted in order to enhance usability on web browsers. This has enabled the use of drag-and-drop in web browsers, and achieved more intuitive operation when uploading documents and setting up relations (Fig. 12).

4.4. Supplier Coordination and Collaboration

In order to comply with ISO 26262, a vehicle manufacturer needs to transmit its requirements accurately to the parts suppliers. The suppliers to which requirements have been transmitted must design functions to achieve the requirements and present the design results to the vehicle manufacturer as a WP. Since these operations of requirements, design content, and test results have to be configured for traceability, a function for data exchange between the vehicle manufacturer and suppliers was developed (Fig. 13).

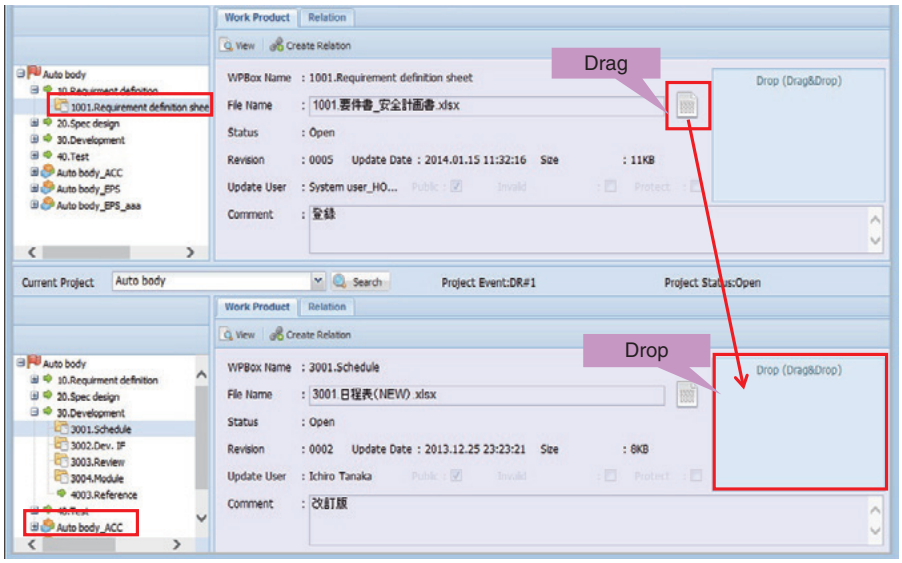


Fig. 12 Setting relations with drag and drop operation

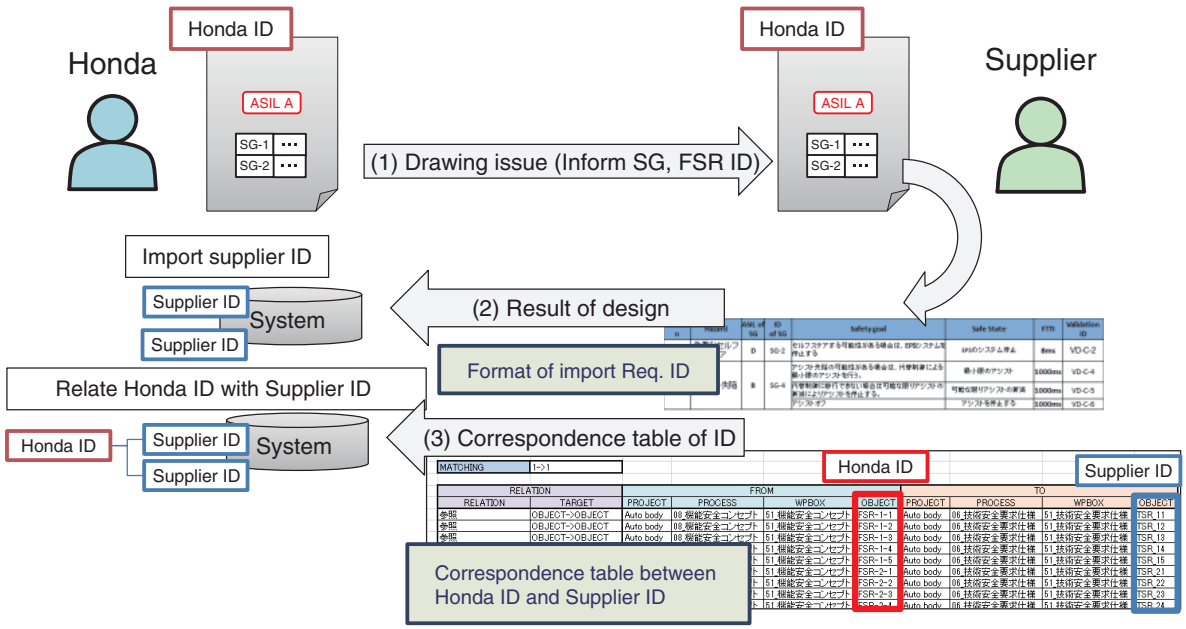


Fig. 13 Data exchange between Honda and suppliers

4.4.1. RIF output of requirements

The Requirements Interchange Format (RIF) is a format devised for the exchange of requirements between enterprises. It was created by an organization called the Hersteller Initiative Software (HIS)[3], which is made up of five companies: Audi, BMW, Daimler, Porsche, and Volkswagen.

The RIF format has been adopted by commercially available applications for managing requirements. In order to convey requirements to suppliers, this format must be supported.

The system was therefore configured so that the requirements contained in specification forms could be extracted and the content stored in the database could be output in a format (XML file) that complies with RIF.

However, the commercially available applications that support RIF differ in the content they include in their RIF format. This makes a conversion operation necessary when exchanging data (Fig. 14).

4.4.2. Importing and exporting of configuration management content

Under ISO 26262, a WP that complies with the standard has to be put together and stored when the development has been completed. Since the stored WP is used as the Baseline when design changes are made, it needs to be capable of restoration at any time.

It is considered desirable to exchange not just functional safety information with suppliers, but also information required for development of functions, so as to heighten the efficiency of development operations.

In order to achieve these objectives, a function was developed to enable import and export both of tree structures created in configuration management and of WP with specified revision numbers.

This function was configured to confirm whether any items transmitted to suppliers or confidential items are included by providing the output for export in accordance with the Approval Flow set up in the system (Fig. 15).

The function was configured to reflect WP import after confirming the impact on configuration information in the system (Fig. 16). Data that can be imported is basically assumed to be XML data output from the system. However,

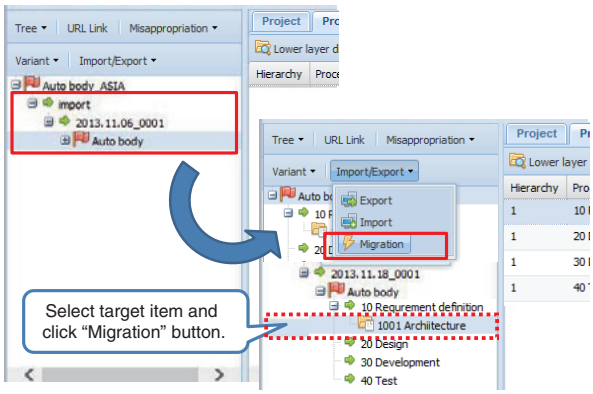


Fig. 16 Import operation

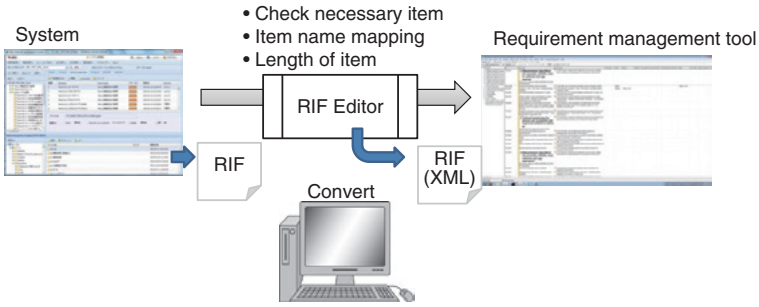


Fig. 14 Convert RIF format for exchange

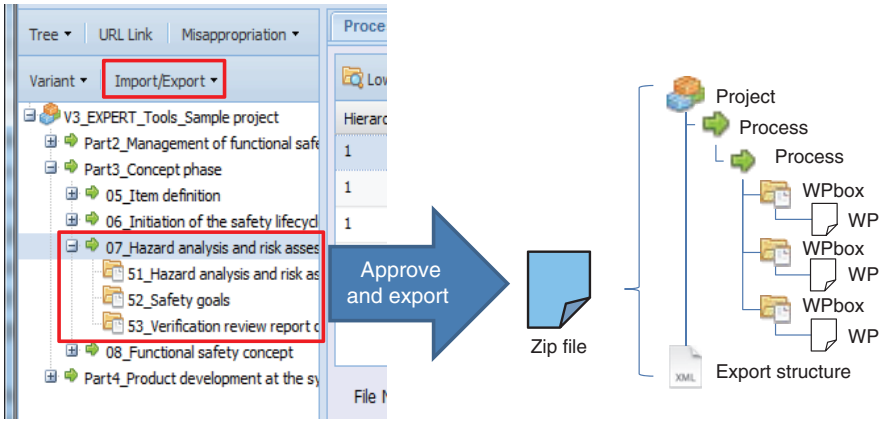


Fig. 15 Export operation

XML data output from other tools can be converted for use by this system so that import is possible.

5. Conclusion

Development of the system described above yielded the following:

(1) Development processes and WP that are compliant with ISO 26262 can be defined in the system.
(2) Traceability was achieved by automatically extracting requirements from registered WP and defining Relations between requirements.
(3) Verification meetings in the course of development can be defined in the system as Events, and product and verification results can be retained in storage.
(4) By displaying the Relations between configured items in list form, the system became capable of identifying the range of impact and reducing man-hours spent on search.

References

(1) ISO 26262 : Road Vehicles – Functional Safety (2011)
(2) IEC 61508: Functional Safety of Electrical/Electronic/ Programmable Electronic Safety-related Systems (2000)
(3) http://www.automotive-his.de/rif/ 2014/4/14

■ Author ■


Hitoshi TAKUMI


Yasuo KUROSAKI


Hiroshi ISHIDA

Development of MEA with Built-in Oxygen Sensor for Measurement of Oxygen Concentration around Fuel Cell Cathode Electrode Layer

Masahiro MOURI*

ABSTRACT

A membrane electrode assembly with a built-in fiber-optic oxygen sensor able to measure the oxygen concentration around fuel cell cathode electrode has been developed to clarify the effect of a variety of generating conditions on the transport of oxygen to the area around cathode electrode. Changes in the phosphorescence lifetime of an oxygen-sensitive dye coated on the tip of the optic fiber are used to measure oxygen concentration. This paper presents an example of the first-ever simultaneous measurement of the oxygen concentration distribution around cathode electrode and the current density distribution, which expresses the distribution of generation in the active area, in a vehicle-onboard cell during generation. Specifically, it was found that obstruction of transport of oxygen gas to the cathode electrode affects generation output under conditions of high current density operation and generation stability under conditions of low current density operation.

These results, together with the results of neutron radiography observation, indicate that condensed water formed in the gas channels of the cell impede the supply of gases, and can result in a decline in generation performance.

1. Introduction

Against the background of environmental issues including global warming and air pollution, in addition to the instability of the supply of gasoline and other fossil fuels, the development of fuel cell vehicles, which do not emit CO_2 or other pollutants and are considered the ultimate environmentally friendly vehicles, is picking up pace. The ZEV Regulation introduced by the California Air Resources Board (CARB) stipulates that a specific percentage of all the vehicles sold in California by manufacturers that sell more than a specified number of vehicles in the state must be zero emission vehicles (ZEV). From 2018, the state will make the transition to ZEV2.0, which will restrict the ZEV appellation to electric vehicles and fuel cell vehicles. This move increases the importance of development of fuel cell electric vehicles. Honda is proceeding with the development of fuel cell vehicles using polymer electrolyte fuel cells (PEFC), which are able to start at low temperatures and have the potential to be reduced in size. For generation by PEFC, it is necessary to utilize the appropriate amount of water for proton conductivity of polymer electrolyte membrane (PEM). However, excess water formed in the gas channels and the gas diffusion layers (GDL) is a factor in impeding the supply of gas to the electrode catalysts, the site of the generation reaction. Under conditions of high current density operation, this can reduce output, and under conditions of low current density operation, it can reduce the stability of generation. This makes it necessary to appropriately control the water inside the fuel cell during power generation. The use of a special visualization cell provided with a visualization window, in which the walls of the cathode gas channels have been coated with an oxygen-sensitive dye, and a laser spectrum is available as a method of directly evaluating impediments to gas supply that may cause a decline in generation output or generation stability[(1)]. However, this method of evaluation is restricted to the special visualization cell, and in addition does not enable the oxygen concentration close to the cathode electrode, the reaction site, to be directly measured. In order to address this issue, the research discussed in this paper sought to develop a membrane electrode assembly (MEA) provided with a built-in oxygen sensor.

* Automobile R&D Center

2. Necessity for Measurement of Oxygen Concentration

2.1. Fuel Cell

A fuel cell is a power-generating device that produces electricity by means of electrochemical reactions between hydrogen and oxygen. The reactions are a hydrogen oxidation reaction at the anode electrode, shown by Eq. (1), and an oxygen reduction reaction at the cathode electrode, shown by Eq. (2). Water is produced at the cathode as a by-product of the reaction.

$$\text{Anode: } H_2 \rightarrow 2H^+ + 2e^- \quad (1)$$

$$\text{Cathode: } 1/2O_2 + 2H^+ + 2e^- \rightarrow H_2O \quad (2)$$

Figure 1 shows a schematic image of a PEFC. The PEFC is made up of a MEA, a catalyst layer (CAT) and a GDL on each side of the PEM, and separators provided with gas and coolant channels. This minimum configuration is termed a single cell. A stack is formed by layering multiple single cells. The PEM conducts protons (H^+) formed by the hydrogen oxidation reaction shown in Eq. (1). The CAT positioned on either side of the PEM respectively catalyze the reactions shown by Eqs. (1) and (2). The GDL diffuse reactant gases to areas not exposed to the gas channels, in addition to conducting electricity. The separators supply reactant gas to the anode and cathode electrodes, isolate the reactant gases from the reactant gases of neighboring cells, cool the cell by supplying coolant, and conduct electricity from the CAT. The cell is also provided with micro-porous layers (MPL) between the CAT and the GDL that further promote the exchange of wastewater and gas from the CAT.

2.2. The Importance of Water Management in Fuel Cells

It is necessary to appropriately control the water in the fuel cell during generation in order to help ensure output and generation stability. The realization of increases in the rate of oxygen use is demanded for fuel cells for automotive use in order to help achieve size reductions, including reduction of the size of the fuel cell system overall, and to limit the power necessary for air pumps and other equipment. Technologies capable of high current density operation, which produces a higher volume of water, are necessary in order to move towards realizing further reductions in the size of the fuel cell stack.

The fuel cell stacks used in the 2009 model FCX Clarity realized a volumetric power density 50% higher than the stacks used in the 2005 model. In addition, the mass power density of the 2009 stacks was 67% higher than that of the 2005 stacks[(2)].

2.3. Necessity for Measurement of Oxygen Concentration around Cathode Electrode

As discussed above, humidified water supplied to help ensure proton conduction and water produced by power generation condenses and impedes the transportation of reactant gases during power generation. This is referred to as flooding. During power generation, energy loss occurs as a result of the three types of polarization losses shown in Fig. 2. These are activation polarization losses, originating in activation of the catalyst, ohmic polarization losses, originating in proton conduction and electron conduction, and concentration polarization losses, originating in transport resistance of the reactant gases.

The cell voltage is each of the polarization losses divided by the theoretical electromotive force resulting from the difference in electrical potential between hydrogen and oxygen. Theoretical electromotive force corresponds to open circuit voltage (OCV). Flooding accelerates concentration polarization losses, which expresses the transport resistance of the reactant gases, and can reduce cell voltage. Water is produced at the cathode electrode, and water is also transferred to the cathode electrode from the anode electrode as accompaniment water by electro-osmosis, promoting the accumulation of water at the electrode and in the GDL. Because of this, the cathode electrode is more prone to concentration polarization than the anode electrode. The tendency towards flooding is also affected by differences in the wettability of the GDL and electrode materials by water. In addition, as Fig. 3 shows, flooding is more prone to occur in the downstream rather than upstream sections of the gas channels for cathode

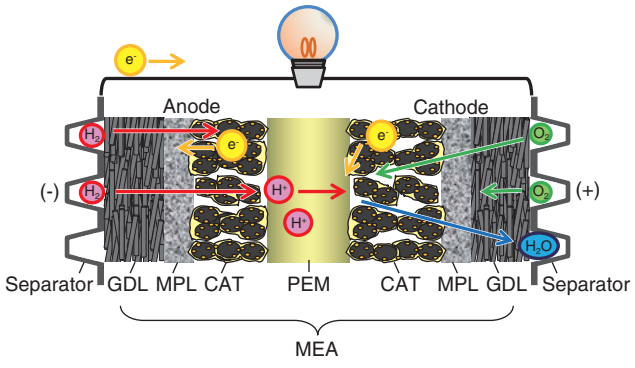


Fig. 1 Schematic image of PEFC

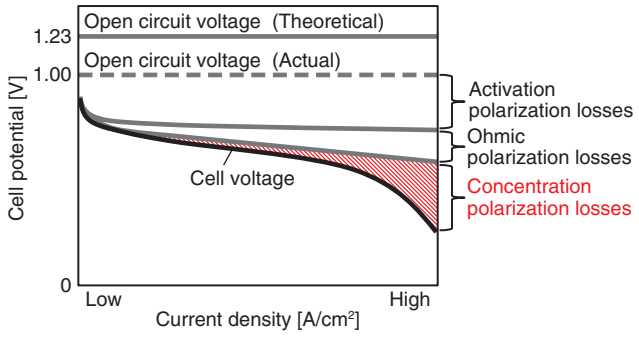


Fig. 2 IV curve and various polarization losses of operating fuel cell

reactant gases located in the active area. This is due to the fact that some of the water produced in the upstream sections of the gas channels by the cathode reactant gases evaporates and becomes water vapor, and the further this vapor travels downstream in the gas channels the more it accumulates and approaches the saturation vapor pressure.

In addition, oxygen present in the air is used as the reactant gas at the cathode electrode; its partial pressure is lower and its molecular weight is higher than the hydrogen employed as the reactant gas at the anode electrode, meaning that it is more easily affected by the diameter of the pores used for gas passage. Concentration polarization at the cathode electrode is therefore more marked under conditions of high current density operation. Transport of oxygen, the cathode electrode reactant gas, within the cell can be broadly divided into:

(1) Vapor-phase diffusion within the pores of the cathode GDL and MPL;
(2) Vapor-phase diffusion within the pores of the cathode CAT; and
(3) Vapor-phase and dissolution diffusion into the cathode CAT electrolyte.

The mode of oxygen diffusion differs depending on the diameter of the pores. The pore diameter of the carbon paper generally used in the GDL mentioned in (1) is around 50-100 μm. The diameter of the pores in the CAT mentioned in (2) and (3) is around 0.01-0.1 μm[3]. If the diameter of the pores is sufficiently greater than the mean free path of the gas molecules, molecular diffusion can be regarded as dependent upon collisions between the gas molecules themselves. However, when the pore diameter is low, collisions between the gas molecules and the walls of the pores cannot be ignored, and Knudsen diffusion is dominant[4)-6]. The GDL is dependent on molecular diffusion and the CAT, which has a low pore diameter, is dependent on Knudsen diffusion. Knudsen diffusion is lower the larger the molecular weight of the molecules. Therefore, given that the molecular weight of oxygen is 32 and the molecular weight of hydrogen is 2, the diffusion constant of oxygen in the pores is around one-quarter that of hydrogen. In addition, because the consumption of reactant gases increases under conditions of high current density operation, the cathode electrode is more prone than the anode electrode to be affected by Knudsen diffusion. In order to verify the effect of Knudsen diffusion, a technology able to measure the oxygen concentration around cathode electrode under a variety of generation conditions is required.

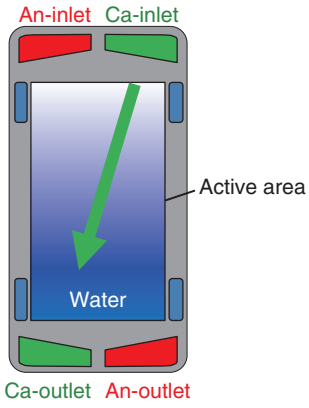


Fig. 3 Water distribution in active area

3. Development of MEA with Built-in Fiber-optic Oxygen Sensor

3.1. Selection of Oxygen Concentration Measurement Method

Among standard methods of measuring oxygen concentration are the zirconia sensor type, which uses the electromotive force of concentration cells, the magnetic oxygen meter type, which uses the paramagnetism of oxygen, and the mass spectrometry type, which uses differences in mass number. Based on six considerations, the present research employed a fiber-optic oxygen sensor using an oxygen-sensitive reagent. The six considerations were ability to be built into an MEA, no consumption of gas for sampling, ability to conduct measurements in a gas and liquid two-phase state, electrical insulation performance and explosion-proof performance, rapid transient responsiveness, and ability to conduct multiple-point simultaneous measurement.

It was necessary that the external diameter of the sensor probe should be less than the combined thickness of the CAT and GDL, making a diameter of 250 μm or less desirable. Based on this figure, fiber-optic sensors with external diameters of 90 μm (a core diameter of 50 μm and a cladding layer of 40 μm) and 220 μm (a core diameter of 200 μm and a cladding layer of 20 μm) were manufactured.

3.2. Fiber-optic Oxygen Sensor Probe and Configuration of Measurement Equipment

An oxygen-sensitive dye was employed in measurements of oxygen concentration. A Ru-porphyrin complex was used as the dye. Ru-porphyrin complexes become excited and emit phosphorescence when they absorb light corresponding to the band gap energy[7]. When oxygen molecules exist around the Ru-porphyrin complex, part of the phosphorescent energy emitted is used as excitation energy for the oxygen molecules. Therefore, the higher the oxygen partial pressure, the more the strength of the phosphorescence is reduced, and the shorter the phosphorescence lifetime. Figure 4 shows the relationship between excitation light and the phosphorescence lifetime of the Ru-porphyrin complex.

Given this, measurements of the phosphorescence lifetime of the dye can be converted into oxygen partial pressure and oxygen concentration. Phosphorescence lifetime is converted into oxygen concentration using the Stern-Volmer equation [Eq. (3)].

$$I_0/I = 1 + Ksv \cdot [Q] \quad (3)$$

I_0: Phosphorescent strength in an oxygenless state
I: Phosphorescent strength when oxygen exists
Ksv: Stern-Volmer constant (Quenching constant x Phosphorescence lifetime)
$[Q]$: Oxygen partial pressure [Pa] or oxygen concentration [%]

Figure 5 shows a photograph and a schematic of the fiber-optic oxygen sensor manufactured for this research. A multi-mode type with low wavelength selectivity and a large light-transmitting core diameter was selected as the optic fiber. A window was formed in one side of the fiber-optic sensor probe corresponding to the sensing section, and an SMA905 connector was formed on the opposite side for connection to a relay cable. Giving consideration to increasing the light-receiving area and reducing the reflected component of the excitation light, the sensing section window was formed such that its surface displayed a taper angle of approximately 30°. The surface of the window was mirror polished. A polyimide resin coating that had been applied to the fiber-optic cable in order to protect its outer circumference remained in place other than in the window section. The Ru-porphyrin complex was dispersed and fixed in a silica glass membrane using the sol-gel coating technique and used to coat the surface of the window. This coating membrane was a porous membrane with a gas dispersion function[8), (9)].

Figure 6 shows the configuration of the fiber-optic oxygen concentration measurement system. The measurement system consists of an excitation light source, a detector with a built-in lock-in amp synchronized with the light pulse of the excitation light source, a fiber-optic oxygen sensor probe and a fiber-optic relay cable. An LED light source with a wavelength of 470 nm, corresponding to the excitation wavelength of the Ru-porphyrin complex, was used as the excitation light source. An optical fiber splitter was used to introduce the excitation light signal to the sensor probe. The two-branched fiber-optic relay cable also fulfilled the function of sending the reflected light signal, which included the phosphorescent component from the sensor probe window, to the detector. The detector was provided with a band pass filter with a wavelength of 610±15 nm, corresponding to the peak wavelength of the phosphorescence. The band pass filter fulfilled the functions of isolating the benchmark phosphorescence signal wavelength and removing the excitation light component. A photo diode was used to detect the phosphorescence signal.

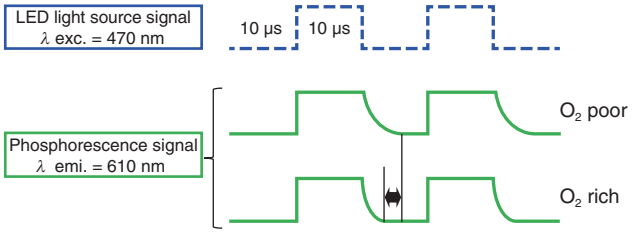


Fig. 4 Relationship between excitation light signal and phosphorescence signal

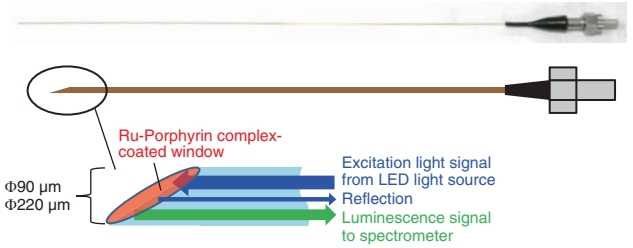


Fig. 5 Schematic image of fiber-optic oxygen sensor probe

3.3. Characteristics of Oxygen Sensor Operation

As shown in Fig. 4, the excitation light signal was operated at approximately 50 kHz with a pulse width of 10 μs for both on and off. The Ru-porphyrin complex phosphorescence signal, the indicator for measurement of oxygen concentration, was defined as the lifetime from the cessation of the excitation light pulse to the attenuation of the phosphorescence. Figure 7 shows the calibration curve expressing the relationship between oxygen concentration as determined by an actual oxygen

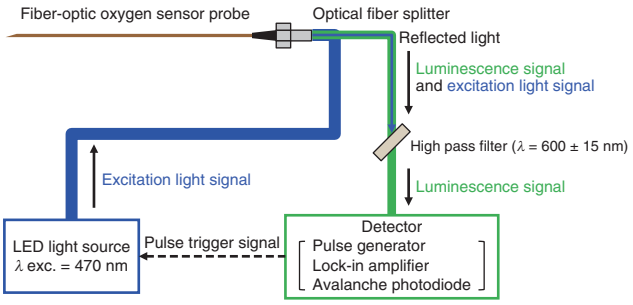


Fig. 6 Block diagram of fiber-optic oxygen sensor system

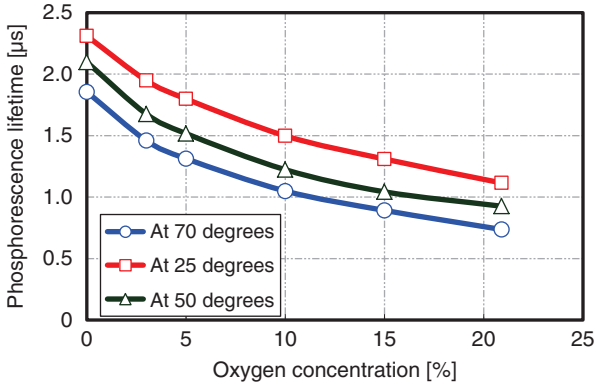


Fig. 7 Relationship between oxygen concentration and phosphorescence lifetime

sensor and the Ru-porphyrin complex phosphorescence lifetime. The phosphorescence lifetime decreases as the partial pressure increases. The phosphorescence lifetime is also dependent on the temperature around the sensor. The temperature-dependent quenching rate of phosphorescence follows Arrhenius' equation[6]. The phosphorescence quenching rate of the Ru-porphyrin complex becomes more rapid as temperature increases, and its phosphorescence lifetime is reduced. When using the Ru-porphyrin complex phosphorescence lifetime in order to measure oxygen concentration, it is therefore necessary to take temperature measurements close to the measurement points and apply temperature correction.

The measured phosphorescence lifetime differed for each sensor. These differences originated in variations in the concentration of the Ru-porphyrin complex and the pore size distribution of the coating membrane that functioned to disperse gas. Because of this it was necessary to obtain calibration curves for all of the oxygen sensors used in measurements.

4. Tests

4.1. Operating Conditions

The developed MEA with built-in fiber-optic oxygen sensor was used in measurements of the oxygen concentration around the cathode electrode during power generation. Specifically, the effects of oxygen transport resistance under conditions of high current density operation and the effect on generation stability of the condensed water produced in the gas channels under conditions of low current density operation, which is frequent, were studied.

4.2. Evaluation Cells

Cells of the type employed in the FCX Clarity were used as the evaluation cells. Figures 8 and 9 show schematics of the evaluation cells. The cells shown in Fig. 9(b) were used in the evaluation.

The flow of reactant gases in the cells for both the anode and cathode electrodes is a V-flow that follows the direction of gravity. In addition, in order to reduce size and weight, one cooling structure is employed for each two cells. Because of this there are two types of cell: A Cell, in which the cathode electrode surface is cooled; and B Cell, in which the anode surface is cooled. The smallest unit formed by the combination of A Cell and B Cell was defined as the cell unit complex.

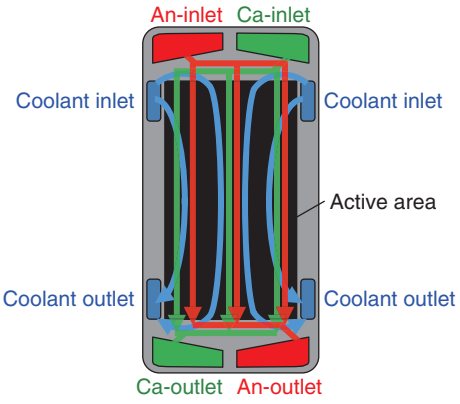
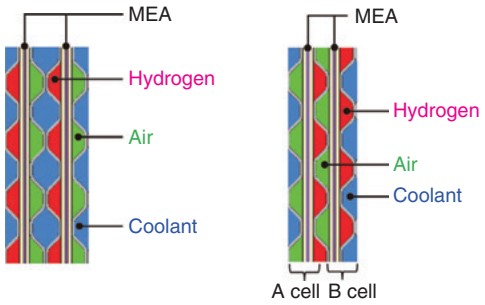


Fig. 8 Schematic image of cell structure

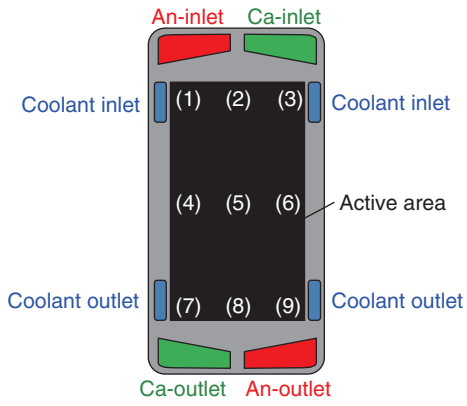
4.3. Oxygen Sensor Measurement Position

Figure 10 shows the load points of the oxygen sensors built into the MEA. The oxygen sensor with an external diameter of 220 μm was employed. Oxygen sensors were positioned at nine points in order to make it possible to

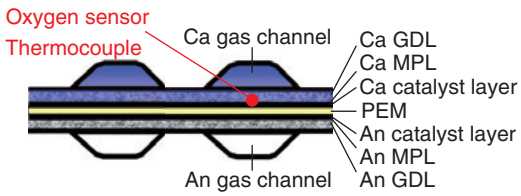


(a) Two cooling layers per two cells (b) One cooling layer per two cells

Fig. 9 Schematic images of two modes of stacking



(a) Plane view



(b) Cross-sectional view

Fig. 10 Schematic image of oxygen measurement positions

measure the trend of distribution of concentration for the entire electrode area (the active area). Thermocouples were also positioned next to the oxygen sensors at these points in order to take temperature measurements for temperature correction. K-type thermocouples with an extra-fine cable coated in Teflon to help ensure electrical insulation were employed as the thermocouples. The oxygen sensor and the thermocouple were separated by a gap of around 5 mm, and positioned directly below the cathode electrode gas channels, as shown in Fig. 10(b). The respective sensors were sandwiched between the cathode electrode MPL and the cathode electrode, and were fixed in place by hot pressing during the bonding of the membrane and the electrode. The foundation layer, which functions to promote exchange of wastewater and gas, also acts as the adhesive that bonds the membrane and the electrode. The formed MEA was fastened between separators to form a cell unit complex. The sections of the sensor that straddled the seal lines formed on the separators to isolate them from gases were coated in a silicon-based liquid seal in order to fasten and cure it and help to prevent gas leaks. One cell unit complex consisting of A Cell and B Cell, each incorporating an MEA with a built-in oxygen sensor and thermocouple, was positioned at the center of a stack for evaluation. Figure 11 shows the position of the cell unit complex with built-in oxygen sensors and thermocouples. Prior to the evaluation of the cell unit complex, the relationship between oxygen concentration and phosphorescence lifetime was studied for single cell units and calibration curves were formulated. In order to calibrate oxygen concentration, calibration curves were obtained by rendering the amount of cathode gas constant under a variety of generation conditions without generating electricity, and mixing oxygen and nitrogen to vary the gas composition.

4.4. Simultaneous Measurement of Oxygen Concentration and Current Density Distribution

A sensor plate for the measurement of current density distribution, which would assist in understanding the distribution of generation in the active areas, was positioned in the stack adjacent to the rear of A Cell in the cell unit complex with built-in oxygen sensor. Figure 11 shows the position of the sensor plate in the stack. Figure 12 shows an enlarged view of the positioning of the equipment after installation in the actual stack. The sensor plate was able to divide the active area evenly into a large number of segments and measure the current flowing in each segment with a high degree of accuracy. The greater the amount of current flowing in a segment, the greater the amount of electricity generated. This made it possible to conduct the first-ever simultaneous measurements of oxygen concentration, temperature distribution, and generation distribution around the cathode in the cell active area in the generating environment of an actual stack using a cell for automotive use.

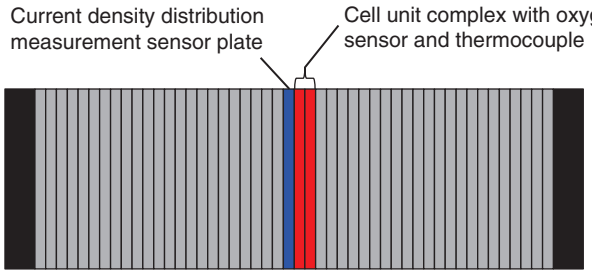


Fig. 11 Schematic image of sensor position in stack

4.5. Condition for Evaluation of Generation

The stoichiometry-dependence of the cathode reactant gases was studied in order to determine the effect of transport resistance of oxygen to the cathode electrode and condensed water produced during generation. In this paper, the gas flow rate will be expressed as stoichiometry. Stoichiometry is determined using Eq. (4), and is a relative value expressed as 1 when the gases necessary for the reactions in the fuel cells are supplied without excess or deficiency.

$$\text{Stoichiometry} = \text{Amount of gas supplied}/\text{Gas quantity required for reaction} \quad (4)$$

The evaluation was conducted with the gas supplied to the anode at a relative humidity (RH) of 60%, and the gas supplied to the cathode at an RH of 95%, which is the level directly before condensed water is formed.

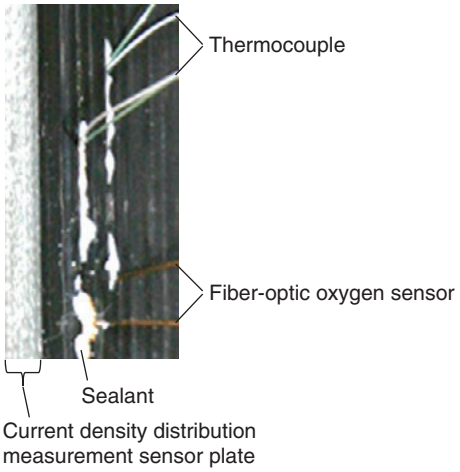


Fig. 12 Enlarged view of sensor position in stack

5. Results

5.1. Verification of Operation of Oxygen Sensor

In order to verify the operation of the oxygen sensor, generation conditions were held constant at 1.0 A/cm^2, and the sensor's ability to track fluctuations in load was studied.

Figure 13 shows the results of a load fluctuation cycle test in which the load was applied at a rate of 0.1 A/cm^2/s. Figure 14 shows the results of using current densities from OCV to 1.0 A/cm^2 in multiple steps for fixed time periods. The measured oxygen concentration is from position (5) in Fig. 10(a).

The oxygen concentration measurements taken in the load fluctuation cycle test were able to track the rapid changes in concentration at the cathode electrode due to oxygen consumption during generation. The oxygen concentration measurements taken when holding current density steady for fixed time periods also expressed the differences in oxygen consumption with changes in load. Based on the results discussed above, it was judged that oxygen concentration measurements taken using the developed method made it possible to understand the oxygen concentration environment around the cathode electrode during power generation.

5.2. Evaluation of High Current Density Operation

In order to determine the effect of oxygen transport resistance under conditions of high current density operation, the oxygen concentration distribution and the current density distribution in the cathode area were compared at 1.0 A/cm^2 and 1.5 A/cm^2. The results are shown in Fig. 15. The results of comparison of the standard deviation of current density distribution in the cathode area at 1.0 A/cm^2 and 1.5 A/cm^2 are shown in Fig. 16. The decline in oxygen concentration in the midstream and downstream sections of the cathode gas channels is greater at 1.5 A/cm^2. This is considered to be due to the progression of flooding as a result of the increase in water production and the progression of gas diffusion limitation due to the increase in the consumption of reactant gases for power generation. This is also verified by the expansion of the current density distribution in the active area and the tendency towards a decline in current density in the downstream sections of the cathode gas channels under 1.5 A/cm^2 conditions.

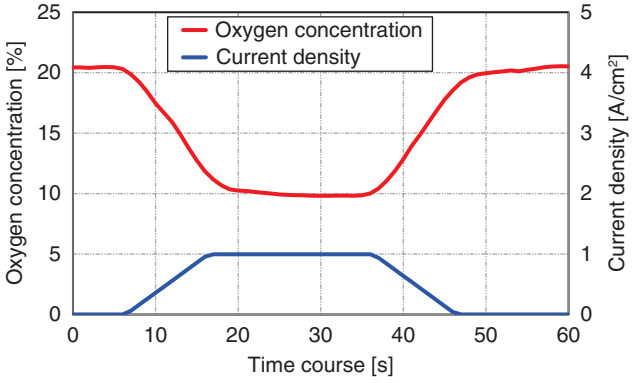


Fig. 13 Change in measured oxygen concentration over time with current density fluctuation

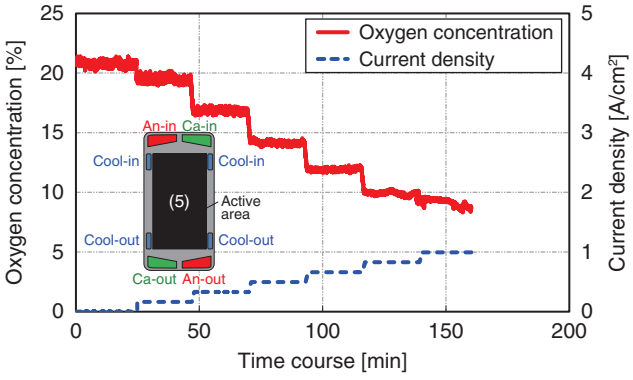


Fig. 14 Measured oxygen concentration at various current density

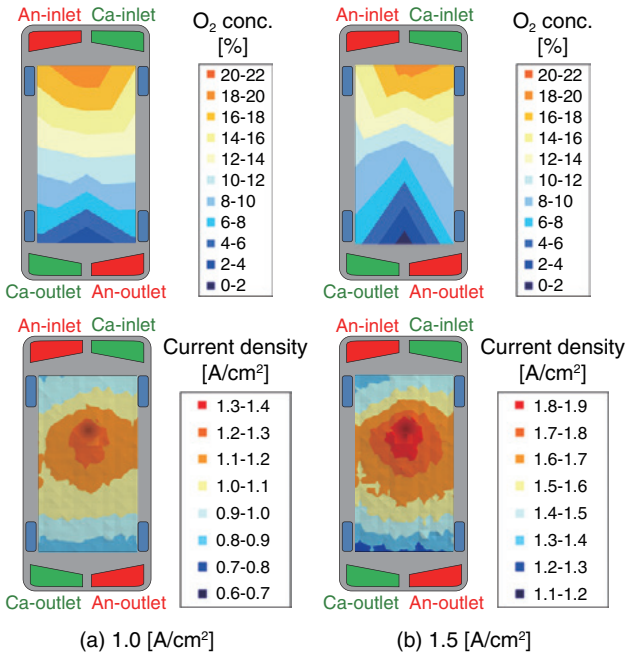


Fig. 15 Oxygen concentration distribution and current density distribution under conditions of high current density

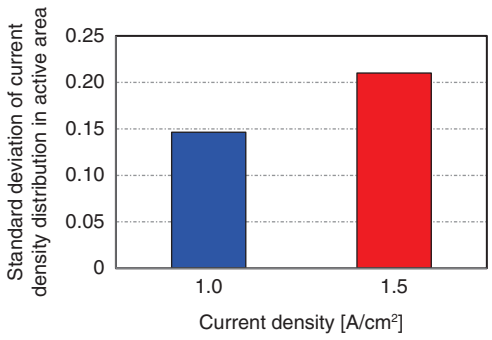


Fig. 16 Comparison of current density distribution at 1.0 A/cm^2 and 1.5 A/cm^2

Local declines in the oxygen concentration in the center of the downstream sections of the cathode gas channels displayed a correlation with the stoichiometry distribution of the cathode reactant gases. Figure 17 shows a comparison of the oxygen concentration distribution in the cathode area and the stoichiometry distribution of cathode reactant gases at the upper extremity of the active area, the point of introduction of cathode reactant gases, under 1.0 A/cm^2 conditions. The stoichiometry distribution for the cathode reactant gases was converted from the flow velocity distribution for each gas channel by means of Particle Image Velocimetry (PIV) using a model of the cathode gas channels in the cell. In concrete terms, in areas in which the stoichiometry of the reactant gases is low when they are supplied, the decline in oxygen concentration due to oxygen consumption is higher.

5.3. Evaluation of Low Current Density Operation

The stoichiometry-dependence of the cathode reactant gases was tested under 0.1 A/cm^2 current density conditions in order to study the effect of oxygen transport resistance under low current density conditions. Figure 18 shows the results of a comparison of oxygen concentration distribution and current density distribution in the cathode area.

The results make it possible to verify that when the stoichiometry of the reactant gases is insufficient when they are introduced, the oxygen concentration of the cathode area positioned in the midstream and downstream sections of the cathode gas channels declines. This tendency is most conspicuous in B Cell. The results also show a decline in current density, indicating a decline in the amount of generation, in the same sections. The areas in which the decline in oxygen concentration occurred correspond to areas in which condensed water formed in the gas channels. Figure 19 shows the results of a study, using neutron radiography[10], of areas of the cell in which condensed water forms when the stoichiometry of the cathode reactant gases upon supply is insufficient. More condensed water forms in the areas of the gas channels positioned in the active area for both the anode and the cathode in the case of B Cell. This is related to the fact that the B Cell coolant channel is positioned at the rear side of the anode gas channel.

Because polarization losses are lower in the case of the anode reaction, expressed by Eq. (1), than the cathode reaction, expressed by Eq. (2), it generates less heat. In

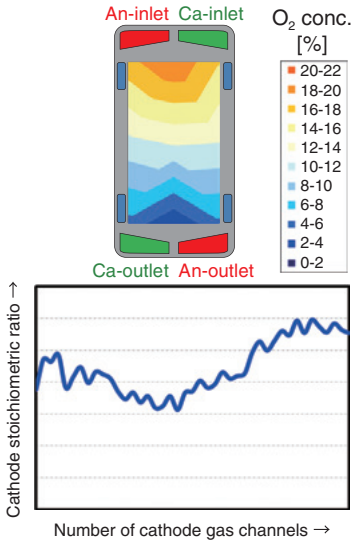


Fig. 17 Comparison of oxygen concentration distribution and cathode stoichiometric ratio distribution in cathode gas channel at 1.0 A/cm^2

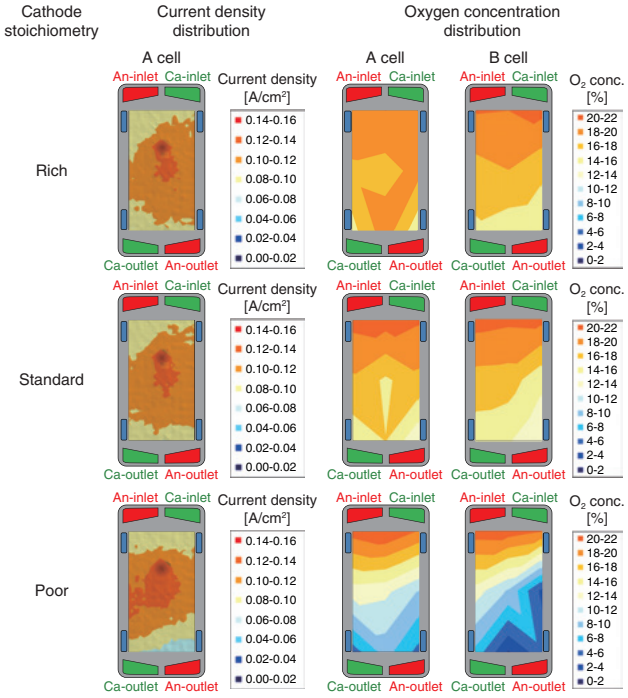


Fig. 18 Cathode stoichiometry-dependence at 0.1 A/cm^2

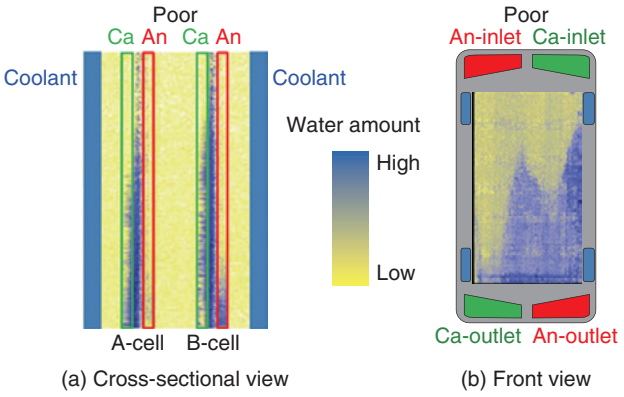


Fig. 19 Neutron radiography images of fuel cell at 0.1 A/cm^2

addition, because the surface of the coolant for B Cell is positioned at the rear of the anode gas channel, in which less heat is produced, its temperature environment is cooler than the surface of the A Cell coolant, which is positioned at the rear of the cathode gas channel. Because of this, B Cell is more prone than A Cell to produce condensed water in both the anode and cathode gas channels[10]. There is therefore a difference in the stability of generation in A Cell and B Cell. Figure 20 shows the results of a comparison of the stability of generation as determined from cell voltage. The cell voltage is an enlarged display from a specified potential window. When the stoichiometry of the cathode reactant gases upon supply is insufficient, the stability of generation in B Cell declines, and the decline in the cell's performance also increases.

In addition, the decline is also affected by the fact that, because the flow rate of the introduced reactant gases is lower under conditions of low current density than conditions of high current density, the drainage capacity of the condensed water forming in the gas channels is lower. Figure 21 shows a model of water drainage in a gas flow channel. Two forces tend to promote retention of the condensed water forming in the gas channels. These are the force of adhesion to the walls of the gas channel and the gas pressure acting on the condensed water in the opposite direction to the gas flow. For drainage, it is necessary to overcome these forces promoting the retention of condensed water. As Eq. (5) shows, one method of doing so is by means of the weight of the condensed water itself, and another is to increase the gas pressure produced by the gas flow on the condensed water in the same direction as the gas flow to a level higher than the gas pressure on the condensed water in the opposite direction to the gas flow, which acts to push the condensed water back. The force that pushes the condensed water out increases in proportion to the flow rate of the gas. Given this, in order to discharge the condensed water in the gas channels that produces instability in power generation, it is necessary to increase the stoichiometry of the reactant gases to help ensure a gas flow rate of a specific level or higher.

$$\text{Water drainage capacity} \propto \text{Pressure 1} - \text{Pressure 2} + \text{Gravity} \quad (5)$$

Figure 22 shows the results of a comparison of the standard deviation of the distribution of oxygen concentration, the voltage difference, and the standard deviation of the current density distribution for Cells A and B.

The results show that when the stoichiometry of the cathode reactant gases falls below the benchmark level, the current density distribution, which expresses the voltage difference and distribution of generation between Cells A and B, becomes broader. This tendency is also true of the

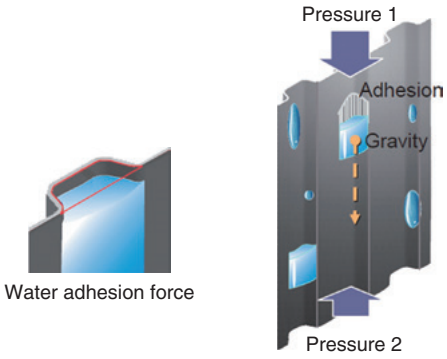


Fig. 21 Water drainage model of gas flow channel

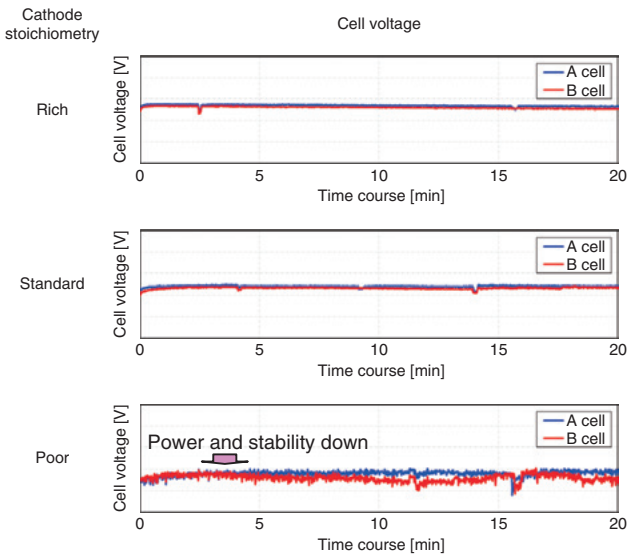


Fig. 20 Cell voltage trend data for A cell and B cell at 0.1 A/cm^2

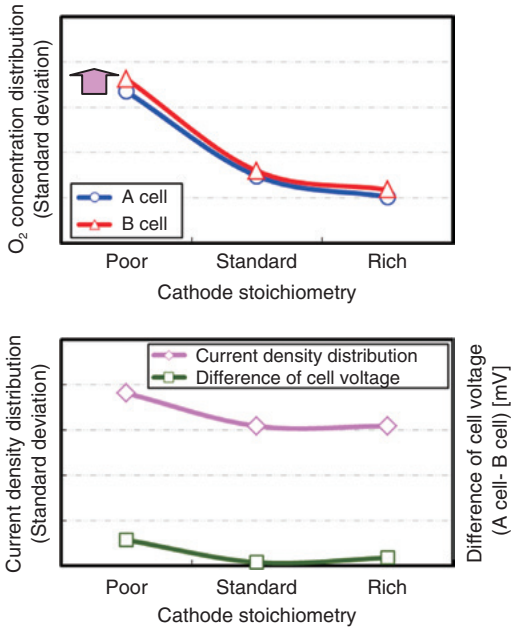


Fig. 22 Cathode stoichiometry-dependence of various parameters at 0.1 A/cm^2

oxygen concentration distribution in the cathode area, and is more conspicuous in B Cell. Based on this, it is considered that the condensed water formed in the gas channel of B Cell produces a resistance, and impedes the supply of cathode reactant gases.

6. Conclusion

A technology for the simultaneous measurement of the oxygen concentration around the cathode electrode during generation and the distribution of generation in the active area in a fuel cell fitted in a vehicle has been developed. The MEA with built-in oxygen sensor developed in the research discussed here can be considered to display merit as an evaluation tool to assist in the determination of fuel cell design guidelines and guidelines for operating conditions to help enable the realization of uniformity in generating environments.

References

(1) Inukai, J., Miyatake, K., Takada, K., Watanabe, M., Hyakutake, T., Nishide, H., Nagumo, Y., Watanabe, M., Aoki, M., Takano, H.: Direct Visualization of Oxygen distribution in Operating Fuel cells, Angewandte Chemie International Edition, Vol. 47, Issue 15, p. 2792-2795 (2008)
(2) Saito, N., Kikuchi, H., Nakao, Y.: New Fuel Cell Stack for FCX Clarity, Honda R&D Technical Review, Vol. 21, No. 1, p. 16-23
(3) Xie, Z., Navessin, T., Shi, K., Chow, R., Wang, Q., Song, D., Andreaus, B., Eikerling, M., Liu, Z., Holdcroft, S.: Functionally Graded Cathode Catalyst Layers for Polymer Electrolyte Fuel cells - II Experimental Study of the Effect of Nafion Distribution -, Journal of the Electrochemical Society, Vol. 152, No. 6, p. A1171-A1179 (2005)
(4) The Japan Society of Fluid Mechanics: Section 5 Saikoukouzounai no Kitainagare to Yusougensyo, Chapter 25 Takouseikotaichuu no Nagare, Ryutairikigaku handbook 2nd edit., p. 1173 (1998) (in Japanese)
(5) Takagi, T., Matsumoto, Y., Nanbu, K., Kamiyama, S.: Section1 Kihakuryuu towa Nanika, Chapter 2 Kihakuryuu no Kaiseki, Nennryou, Kihakuryuu, Konseiryuu, Denjibuttai no Kaiseki, University of Tokyo Press, p. 37 (1995) (in Japanese)
(6) Kubo, N.: A Study on Performance Improvement of Polymer Electrolyte Fuel Cell for Automotive Applications, Doctoral dissertation, Waseda university, p. 87-108 (2006) (in Japanese)
(7) Kameda, M., Egami, Y., Asai, K.: Pressure sensitive paints in wind tunnel testing, Reito, Vol. 77, No. 901, p. 991-996 (2002) (in Japanese)
(8) Krihak, M., Shahriari, M. R.: A Highly Sensitive All Solid State Fiber Optic Oxygen Sensor Based on the Sol-gel Coating Technique, Electronic Letters, Vol. 32, No. 3, p. 240-242 (1996)
(9) Klimant, I., Wolfbeis, O. S.: Oxygen-Sensitive Luminescent Materials Based on Silicone-Soluble Ruthenium Diimine Complexes, Analytical Chemistry, Vol. 67, No. 18, p. 3160-3166 (1995)
(10) Chiba, H., Iwasawa, C.: Optimization of Fuel Cell Generation Environment by Water Observation using Neutron Radiography, Honda R&D Technical Review, Vol. 25, No. 1, p. 122-131

■ Author ■



Masahiro MOURI

Verification Test Results for Solar Hydrogen Station in Japan

Nobuyoshi YOSHIDA* Aoi MIYAKE*

ABSTRACT

A high differential pressure water electrolysis-type solar hydrogen station was installed on the grounds of the Saitama Prefectural Offices and a two-year verification test was carried out. This was the first time for Honda to hand over a high differential pressure water electrolysis-type solar hydrogen station to a public institution such as the Saitama Prefectural Offices for verification testing in this way. The verification test involved using hydrogen produced by a high-pressure water electrolysis system to supply as fuel for an FCX Clarity fuel cell electric vehicle used as an official vehicle by Saitama Prefecture, collecting data, and conducting analysis. During the two years of the verification test, the outdoor environmental suitability of the system and the changes in performance of the high differential pressure water electrolysis stack were confirmed. This also demonstrated the ability to maintain hydrogen quality and provide a constantly stable supply of hydrogen. All of the hydrogen supplied to the FCX Clarity automobile was provided entirely with the electric power from photovoltaic cells. Since the Saitama Prefectural Offices operated one FCX Clarity automobile, this had the reduction effect of approximately 16% on the CO_2 emitted by all the official Saitama Prefectural vehicles operated by the particular office that operated the FCX Clarity. There is a likelihood that a CO_2 reduction of approximately 41% can be further achieved by maximizing the use of electric power from photovoltaic cells.

1. Introduction

Honda has long been engaged with countermeasures under the three headings of atmospheric pollution, global warming, and the energy problem. The company has been developing fuel cell electric vehicles as a next-generation powerplant that is capable of simultaneously addressing those three headings.

At the same time, Honda has also been pursuing the parallel development of hydrogen generation technology. The company has been conducting verification tests of solar hydrogen stations that use high pressure water electrolysis technology with photovoltaic cells as the power source.

The first step was taken at Honda R&D Americas, Inc. Los Angeles Center in Torrance, California, where a solar hydrogen station that combined commercially available equipment was tested starting in July 2001. A normal pressure water electrolysis-type solar hydrogen station (SHS1)[(1)] with a water electrolyzer using unique Honda technology was added in October 2003. In January 2010, the SHS1 was replaced with a high differential pressure water electrolysis-type solar hydrogen station (SHS2)[(2), (3)] and verification tests have been carried out.

This paper will introduce the results of verification tests conducted of the domestic SHS2, which has been operated since its installation on the grounds of the Saitama Prefectural Offices in March 2012. The verification test period for this paper is the two years from March 2012 to March 2014.

The purpose of this verification test was mainly to confirm the matters under the following three headings.

(1) Environmental suitability (waterproofing, low temperature)
(2) Changes in high differential pressure water electrolysis stack performance
(3) Hydrogen quality in the high pressure water electrolysis system

This system was installed by four parties: the Saitama Prefectural Offices; Iwatani Corporation; Honda Motor Co., Ltd.; and Honda R&D Co., Ltd. It was part of the CO_2 Emission Reduction System that Combined Small Scale Solar Hydrogen Station and Fuel Cell Electric Vehicles, which was one of the fiscal year 2011 Low Carbon Technology Research and Development Programs of the Ministry of the Environment.

2. System Overview

2.1. Principle of High Differential Pressure Water Electrolysis

Figure 1 shows a schematic view of the high differential pressure water electrolysis cell. When a water electrolysis

* Automobile R&D Center

cell using a solid polymer proton exchange membrane (PEM) is supplied with purified water and a voltage is continuously applied to the PEM, the cell continues to generate oxygen and hydrogen. When a high-pressure storage tank is installed at the hydrogen outlet, therefore, the pressure in the tank continues to rise gradually, ultimately yielding high-pressure hydrogen gas. The oxygen, on the other hand, is left at atmospheric pressure, so that interposing a PEM in the high differential pressure water electrolysis cell causes a pressure differential to form.

When a voltage is applied to both ends of a PEM in high differential pressure water electrolysis, purified water on the anode side becomes oxygen and protons (H^+). The protons migrate to the opposite electrode and form hydrogen. This phenomenon is ordinarily the same as normal pressure water electrolysis, but an electromotive force generated by the difference of partial pressure in the hydrogen has to be applied when the protons migrate to the opposite electrode.

Equation (1) is the equation for the electrolysis voltage E_{WE} that is required for high differential pressure water electrolysis. The electrolysis voltage E_{WE} is reached by applying the theoretical electrolysis voltage E_1 and the cell resistance Ir of normal pressure water electrolysis and, in addition, the potential difference in hydrogen concentration required by a gas concentration cell[4]. The second term of Eq. (1) yields the electromotive force from the difference of hydrogen concentration in the Nernst Equation.

$$E_{WE} = E_1 + \frac{RT}{2F} \ln \frac{P_1}{P_2} + Ir \qquad (1)$$

R : Gas constant
T : Absolute temperature
F : Faraday constant
P_1 : Hydrogen partial pressure of high pressure side
P_2 : Hydrogen partial pressure of low pressure side

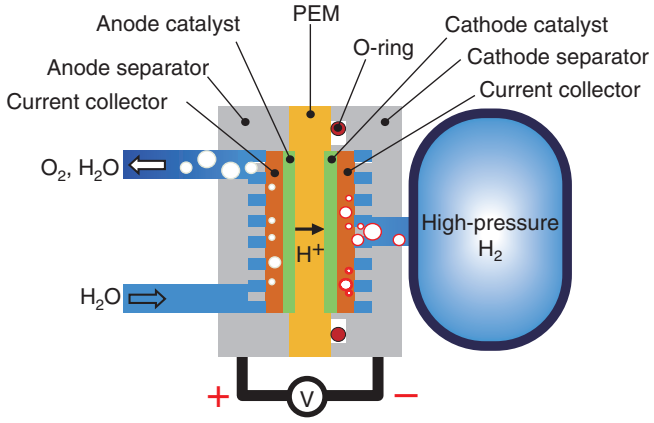


Fig. 1 Schematic of high-differential-pressure water electrolysis cell

2.2. System Configuration

Figure 2 shows a system configuration diagram of the domestic SHS2. This system is configured from a high-pressure water electrolysis system and photovoltaic cell in combination, and a distinctive feature is that it does not emit CO_2 in the course of producing hydrogen. The photovoltaic cell has a CIGS (copper, indium, gallium, and selenium compounds) thin-film solar cell[5] with 10.5 kW output that is manufactured by Honda Soltec Co., Ltd. On the assumption that the FCX Clarity official vehicle would be driven an annual maximum distance of 20,000 km, the photovoltaic cell was designed with the capacity to produce the required amount of hydrogen using electric power obtained entirely from the photovoltaic cell.

The system also allows for use of the electrical grid so that hydrogen can be generated even in rainy weather and at night. Also, where the FCX Clarity hydrogen tank has a capacity of 4 kg, the system hydrogen tank has a storage capacity of approximately 20 kg (35 MPa, 828 L).

2.3. Exterior Appearance

The exterior appearance of the domestic SHS2 described in this paper is shown in Fig. 3.

The system with these specifications consists of an electrolysis unit that produces high pressure hydrogen gas by means of photovoltaic cell modules and a high differential pressure water electrolysis device, a dispenser

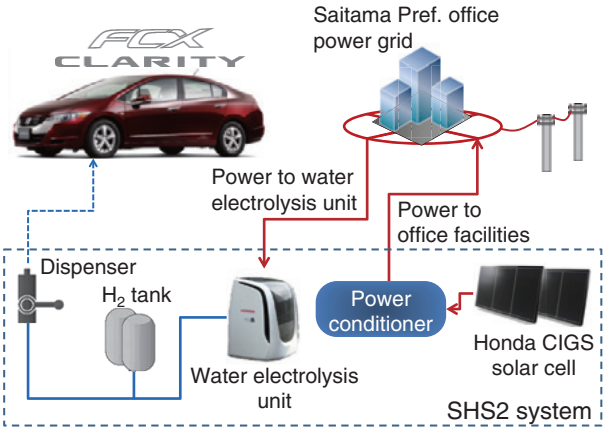


Fig. 2 System layout of SHS2

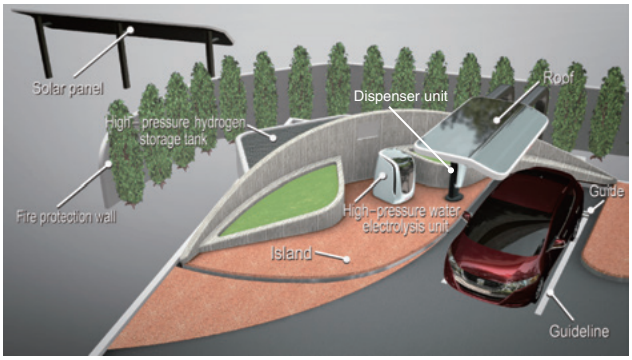


Fig. 3 External view of SHS2

Table 1 Specifications of SHS2

Hydrogen production	Flow rate	0.7 Nm^3/h
	Filling pressure	35 MPa
	Purity	>99.99%
	Storage	20 kg
Component	Photovoltaic module	CIGS 10.5 kW
	Electrolysis unit	High-differential-pressure electrolyzer
Utility	Electricity	200 VAC /50 Hz
	Water	Tap water
Unit volume		Approx. 0.33 m^3

unit that fills the FCX Clarity with hydrogen, and a hydrogen storage tank.

The installation area was finished and system colors were selected so that the component units would merge harmoniously into the surrounding environment within the Saitama Prefectural Offices campus. The exterior was designed with simple curves to convey a sense of affinity, safety, and ease of use.

2.4. Specifications

Table 1 shows the specifications for the domestic SHS2.

Given a supply of tap water and electricity, the SHS2 can produce and store high-pressure hydrogen gas at a maximum pressure of 35 MPa, and when required can fill the FCX Clarity. The hydrogen generation volume is 0.7 Nm^3 per hour, so if it is operated for 24 hours, it will produce enough hydrogen for the FCX Clarity to drive approximately 150 km.

The domestic SHS2 differs from the equipment installed at the Honda R&D Los Angeles Center. Projecting that operation at temperatures below freezing would take place, freeze-proofing measures were put in place within the electrolysis unit of the domestic SHS2.

Figure 4 shows an overview of the freeze-proofing measures. Parts that should be kept warm are not only inside the electrolysis unit, but also include the water supply pipe, the vent pipes for releasing generated oxygen, and other areas that are exterior to the electrolysis unit. Different heat retention methods that would be effective in the various parts were therefore adopted. The interior of the electrolysis unit was heated as a whole by coupling an air heater to the air intake duct that brings in outside air. For the water supply pipe and oxygen vent pipes, which are directly exposed to the outside air, an explosion-proof piping heater and insulation material were used as freeze-proofing measures.

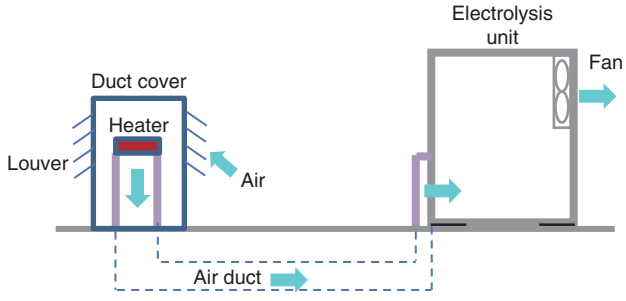


Fig. 4 Ventilation and heating system

3. Verification Test Results

3.1. Environmental Suitability

During the initial installation period, a sheet of sprayed rainwater could be sucked into the interior of the electrolysis unit from the ventilation fan during heavy rains, and especially during rainstorms, causing the interior water leakage sensor to mistakenly report leaks. This had not been experienced by the equipment installed at the Honda R&D Los Angeles Center. Weather conditions in Japan are rainier and more humid than in Los Angeles, and Japanese and US ventilation flow rate regulations are different[6], so that the domestic equipment had been given a higher ventilation flow rate than the US equipment. These are thought likely to be the main causes of rainwater being sucked in. Measures to counter infiltration by rainwater were taken by adding a waterproof cover, as shown in Fig. 5, to the ventilator intake.

Figure 6 shows the changes in temperature in the



Fig. 5 Duct cover

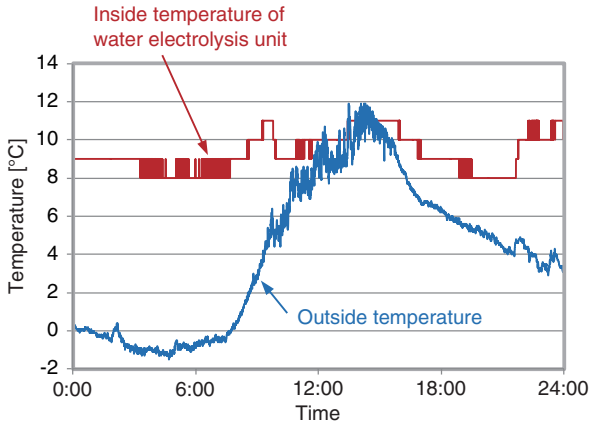


Fig. 6 Temperature change in a winter day (Jan. 16, 2014)

interior of the electrolysis unit and in the outside air in the course of one day during the winter. As anticipated in section 2.4, there actually were some times when the outside air temperature dropped below freezing. It was found, however, that the interior temperature of the electrolysis unit rose higher than the outside air temperature. This was found to be because part of the piping that drew outside air into the electrolysis unit was buried, and the heat retention effect of being underground warmed the piping. Therefore, the interior temperature of the electrolysis unit never actually fell below freezing. Piping exposed to the outside was also kept from freezing by the effects of piping heater and insulation material.

The equipment was operated at temperatures below freezing during the winter, but equipment trouble due to freezing was successfully avoided.

3.2. Changes in Performance of High Differential Pressure Water Electrolysis Stack

Figure 7 is a graph showing the rate of change in the efficiency of the high differential pressure water electrolysis stack with operation over time, where initial performance is taken as 100. Figure 8 similarly shows the rate of change in efficiency with respect to the number of times the electrolysis unit is started. The electrolysis unit was subjected to confirmation of endurance by bench testing at Honda using the same system prior to the verification test at the Saitama Prefectural Offices. (The equipment evaluated internally at Honda is referred to as a prototype.) As shown in Figs. 7 and 8, changes in the performance of the high differential pressure water electrolysis stack operated at the Saitama Prefectural Offices and of the prototype stack are generally the same. The prototype was subjected to endurance operation of repeated starting and stopping under the constant condition of an ambient temperature of 25°C, and starting and stopping by a fixed schedule one time during each nine-hour period. In the verification test at the Saitama Prefectural Offices, however, the ambient temperature changed according to the season and the time of day. Furthermore, the operating times were changed randomly according to the FCX Clarity filling quantity, and the operating cycles were also irregular. As indicated in Figs. 7 and 8, there was no divergence in performance due to operating time or frequency. This demonstrated that there was no performance differential resulting from differences in the environment of installation, whether in-house with the prototype or in the real world at the Saitama Prefectural Offices. At the same time, therefore, this has also confirmed the validity of the operating mode used in endurance testing of the prototype performed in-house at Honda.

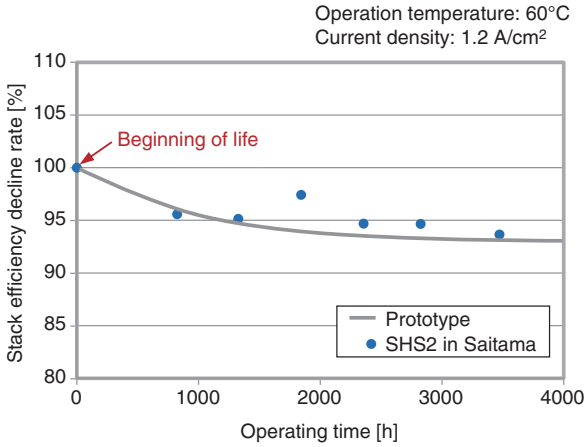


Fig. 7 Decline rate accompanied by operating time

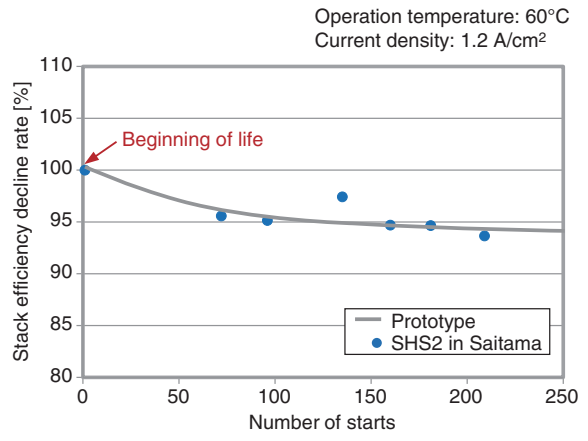


Fig. 8 Decline rate accompanied by number of starts

Table 2 Hydrogen quality of SHS2

	Sampling date		ISO 14687-2
	Feb. 16, 2012	Mar. 14, 2014	
H_2O (ppm)	< 5	< 5	< 5
O_2 (ppm)	< 1	< 1	< 5
N_2 (ppm)	4.7	< 1	< 100
CO (ppm)	< 0.1	< 0.1	< 0.2
CO_2 (ppm)	< 0.1	< 0.1	< 2
HC (ppm)	< 0.1	< 0.1	< 2

3.3. Hydrogen Quality

Table 2 shows the results from analysis of the main impurity elements found in the hydrogen produced by the electrolysis unit. There is no change in the hydrogen quality between the time of initial installation in February 2012 and two years later in March 2014. Furthermore, the values in either case meet the standard for Grade D[(7)] purity specified in ISO 14687-2. This demonstrates that hydrogen of stable quality was successfully supplied over a two-year period. Consequently, the verification test at the Saitama Prefectural Offices was implemented without delays and without any malfunction due to fuel or other such issues occurring in the FCX Clarity. Since the electrolysis unit electrolyzes purified water to obtain

hydrogen, the only major impurities contained in that hydrogen gas are oxygen and moisture. Since an oxygen pressure differential of 35 MPa occurs between one side of the membrane and the other, only an extremely small amount of oxygen gas diffuses through the membrane to the cathode side. As to the moisture, it is removed by an adsorbent, which will be discussed later. Figure 9 shows the water concentration in the 35-MPa hydrogen manufactured by the electrolysis unit, converted into dew point temperature. The ISO reference value of 5 ppm when converted into dew point temperature at 35 MPa is approximately -16°C. As shown in Fig. 9, the water concentration was found to stay lower than the reference level, maintaining levels of 5 ppm or below throughout the entire two-year period of operation. The volume of adsorbent was set at a level to allow approximately three-month intervals between replacement when the electrolysis unit was operated continuously for 24 hours.

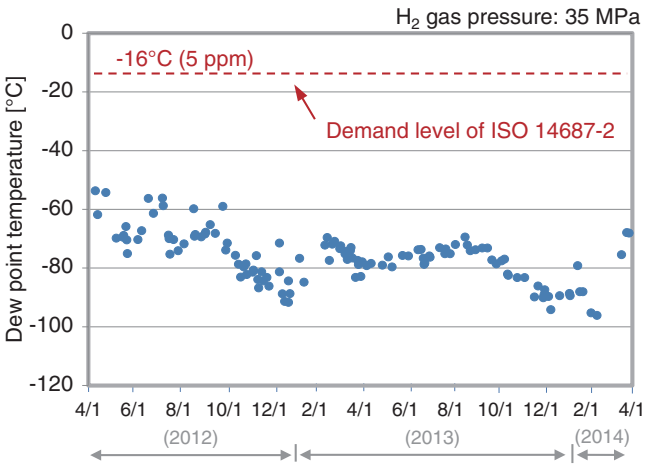


Fig. 9 Dew point temperature of hydrogen

4. Operational Results and CO_2 Reduction

4.1. Amount of Hydrogen Produced and Photovoltaic Power Generated

Figure 10 shows the amount of electric power generated by the photovoltaic cell during the two-year period of operation. The cumulative amount of electric power generated comes to approximately 28 MWh. The solid line in Fig. 11 likewise shows the cumulative amount of hydrogen produced by the electrolysis unit during the two-year period of operation. The hydrogen produced by the electrolysis unit was stored in the tank, and when the tank became full, the electrolysis unit would go into standby. When hydrogen from the tank was subsequently used to fill the FCX Clarity so that the pressure in the tank dropped, the electrolysis unit would resume operation. Since this operational cycle is repeated, the amount of hydrogen generated by the electrolysis unit has a strong correlation with the amount of hydrogen consumed by the FCX Clarity. The cumulative amount of hydrogen shown by the solid line in Fig. 11, therefore, changes with the frequency of use of the FCX Clarity at the Saitama Prefectural Offices. The dotted line in Fig. 11, on the other hand, shows the amount of hydrogen production if it is assumed that the total amount of electric power generated by the photovoltaic cell is converted into hydrogen produced. This dotted line shows the amount of hydrogen production calculated from the amount of electric power generated by the photovoltaic cell, and this amount of hydrogen production is greater than the actual amount of hydrogen production by the electrolysis unit. This indicates that all of the hydrogen produced by the electrolysis unit was produced using electric power from the photovoltaic cell. Using only the electric power supplied from the photovoltaic cell, the amount of hydrogen that could be produced in the two-year period was 486 kg, whereas the actual hydrogen generation amount was 190 kg.

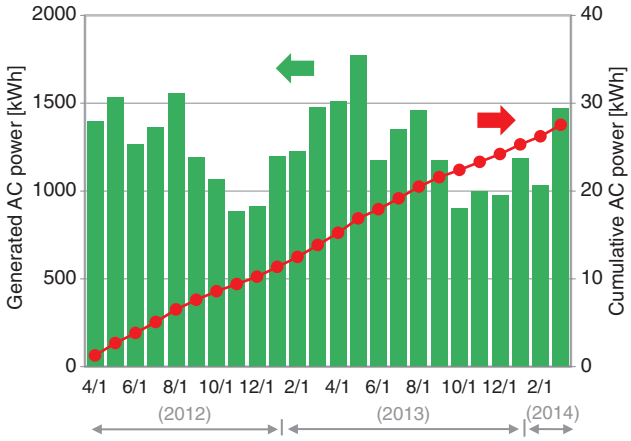


Fig. 10 Amount of AC power generated by photovoltaics

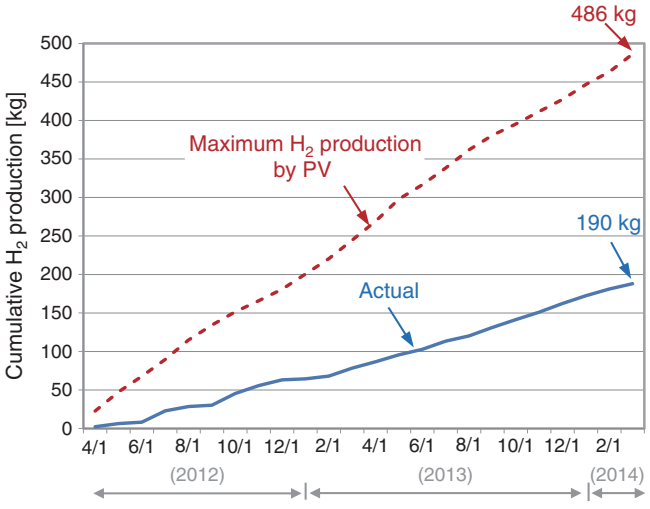


Fig. 11 Amount of H_2 production

4.2. FCX Clarity Filling Frequency

During operation over a two-year period, the SHS2 filled the FCX Clarity165 times. Figure 12 is a histogram showing the amounts of hydrogen that were used to fill the FCX Clarity each time. When empty, the tank in the FCX Clarity can be filled with approximately 4.0 kg of hydrogen. As the figure indicates, the hydrogen filling quantities for one filling during this verification test centered on the average filling quantity of 1.0 kg, with 90% or more concentrated in a range of 2.0 kg or less. The fuel tank was therefore being filled when the amount remaining in the tank was 50% or more. Gasoline cars, by contrast, are generally said to be refilled on average when the amount remaining in the tank goes down to approximately 20%.

This is thought likely to be the result of psychological uneasiness about running out of fuel because there are no hydrogen stations at the destination or on the way to or from it when operating the FCX Clarity as an official vehicle of the Saitama Prefectural Government Office.

4.3. CO_2 Reduction Effect at the Saitama Prefectural Offices

One FCX Clarity was operated at the Saitama Prefectural Offices, resulting in the production of 190 kg of hydrogen over a two-year period. At the same time, the amount of electric power generated by the photovoltaic cell over the same two-year period was approximately 28 MWh. The amount of hydrogen that can be produced from those 28 MWh of electric power without emitting any CO_2, as shown in Fig. 11, is 486 kg. If the present utilization rate is taken as a reference, this amount of hydrogen production is sufficient to operate approximately three FCX Clarity automobiles. Figure 13 shows the CO_2 reduction effect from use of the FCX Clarity, based on the CO_2 emitted by all official vehicles used by the Saitama Prefectural Office that operated the FCX Clarity. As a result of using the 190 kg of hydrogen produced as fuel to operate the FCX Clarity, there was a reduction effect of approximately 16% on the CO_2 emitted by all the official vehicles operated by that Saitama Prefectural Office. In addition, if it is supposed that all of the electric power from the photovoltaic cell is converted into hydrogen and used as fuel in the FCX Clarity, then it appears likely that CO_2 can be reduced approximately 41%. The above CO_2 reduction is the result of operating one FCX Clarity, and increasing the number of FCX Clarity automobiles operated could further increase the CO_2 reduction effect.

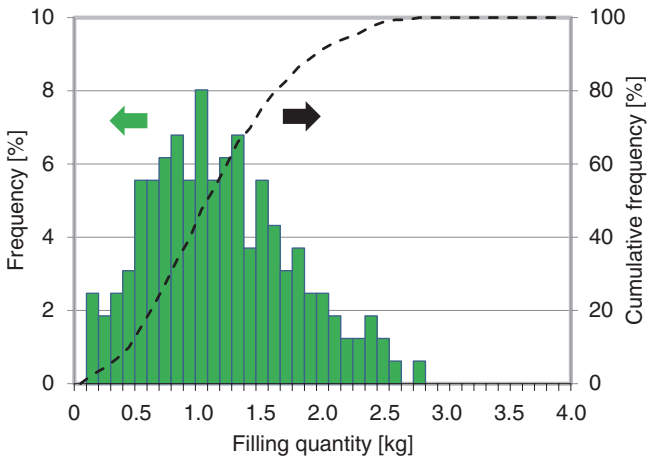


Fig. 12 Histogram of filling quantity

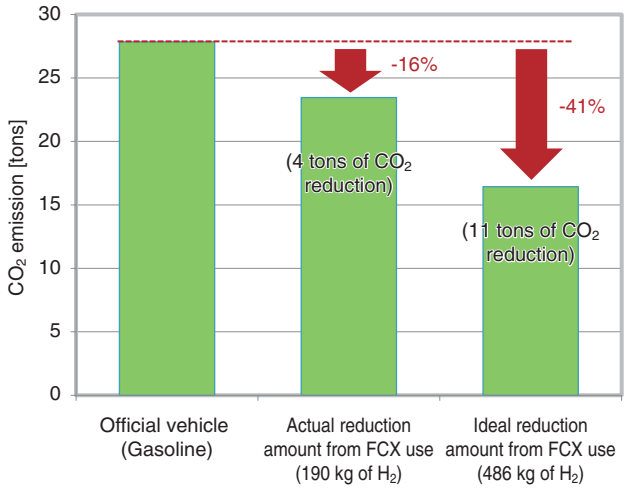


Fig. 13 CO_2 reduction effect by SHS2

5. Conclusion

Carrying out the verification test of the domestic SHS2 yielded the following results.

(1) Findings regarding domestic specifications for environmental suitability (waterproofing, low temperature) were obtained.

(2) The performance of the high differential pressure water electrolysis stack showed generally the same changes as the in-house Honda prototype, demonstrating that the difference between real world and test bench results is slight. At the same time, this also confirmed the validity of the operating modes used in endurance testing of the in-house Honda prototype.

(3) The quality of the hydrogen produced by the electrolysis unit remained unchanged from when testing began, demonstrating the ability to supply hydrogen of consistently stable quality for the FCX Clarity. Consequently, the verification test at the Saitama Prefectural Offices was implemented without delays and without any malfunction due to fuel or other such issues occurring in the FCX Clarity.

(4) Operation of one FCX Clarity automobile at the Saitama Prefectural Offices resulted in reduction of approximately 16% of the CO_2 emitted by all the official Saitama Prefectural vehicles operated by the particular office that operated the FCX Clarity. Furthermore, if it is assumed that all of the electric power from the

photovoltaic cell could be converted into hydrogen, it appears probable that CO_2 can be reduced approximately 41%.

References

(1) Okabe, M., Nakazawa, K., Taruya, K., Handa, K.: Verification Test of Solar-powered Hydrogen Station (SHS) with Photovoltaic Modules, Honda R&D Technical Review, Vol. 20, No. 1, p. 72-79
(2) Nakazawa, K., Nagaoka, H., Takeuchi, J., Moburg, F., Yamashita, I., Okabe, M.: Introduction of High Differential Pressure Water Electrolysis-type Solar Hydrogen Station (SHS2), Honda R&D Technical Review, Vol.22, No.2, p.28-35
(3) Nagaoka, H., Yoshida, N., Cun, D., Yamashita, I., Okabe, M.: Verification Test of High Differential Pressure Water Electrolysis-type Solar Hydrogen Station (SHS2), Honda R&D Technical Review, Vol. 24, No. 2, p. 74-81
(4) The Electrochemical Society of Japan: Electrochemical handbook, Vol. 5, p. 155 (2000)
(5) http://www.honda.co.jp/soltec/cigs/index.html, 2012/8/24
(6) Takeuchi, J., Nakazawa, K., Yoshida, N., Ito, J., Okabe, M., Yamashita, I.: Introduction of Solar Hydrogen Station Installed in Japan, Honda R&D Technical Review, Vol. 25, No. 1, p. 86-92
(7) ISO14687-2: Hydrogen fuel – Product specification – Part 2, Type 1, Grade D

■ Author ■



Nobuyoshi YOSHIDA



Aoi MIYAKE

Project for Locally Rooted Design Development in Field Tests of Next-Generation Personal Mobility

Tadahiro YAGUCHI*　　Kazunori HARADA**

ABSTRACT

Honda Motor Co., Ltd. concluded a “Comprehensive Agreement Regarding the Electric Vehicle Testing Program for Next-Generation Personal Mobility Products” with Kumamoto Prefecture in August 2010, directed toward realizing the joy of free mobility and a prosperous sustainable society. On that basis, Honda has been conducting field tests on a variety of different themes. As soon as field testing began, it became apparent that design needs existed in the area of communication to bring together EV field testing with local communities. Therefore, Honda joined with Kumamoto Prefecture and Sojo University in a cooperative development project on the subject of “interface design linking people, EVs, and the community.” Various topics were formulated from the perspective of university students (consumers) who were local residents, such as “field test messages,” “EV charger sign design,” and “design promoting shared use of Monpal four-wheel electric scooters.” A number of items were created and their effectiveness was confirmed during the field test.

One major result of this field test is that concrete form was given to the process of linking the creation of products to activities of this kind to originate new designs in the local community. In other words, local residents engaged in thinking about things they would themselves be using in their own neighborhoods, as well as looking for solutions to issues in their own local community.

1. Introduction

With a view to realizing the joy and freedom of mobility as well as a sustainable society where people can enjoy life, Honda concluded the “Comprehensive Agreement Regarding the Electric Vehicle Testing Program for Next-Generation Personal Mobility Products” with Kumamoto Prefecture in August 2010. Honda conducted field tests from then until March 2014. The purpose of the field tests was to verify the effectiveness of using solar power and other such sustainable electrical energy for personal mobility in terms of achieving a low-carbon society, and to investigate the concept of a future personal mobility capable of contributing to an enhanced quality of life (QOL) for residents (Fig. 1).

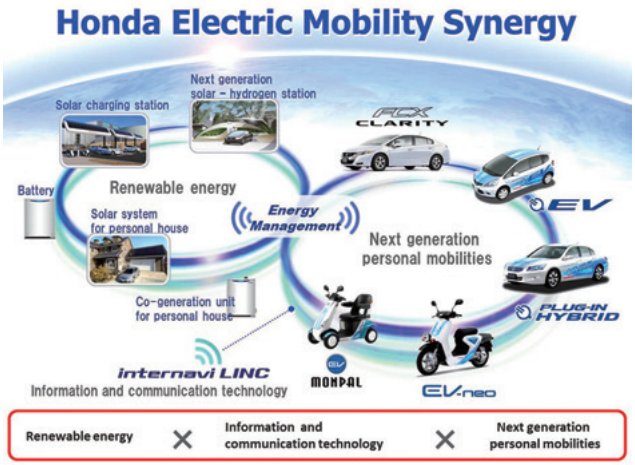


Fig. 1　Honda electric mobility synergy

* Automobile R&D Center

** Sojo University

2. Design Needs for Field Test Promotion

When testing first began, it was thought that the field test would proceed smoothly if Honda deployed the EVs provided for the testing and the prefectural government completed installing the charging facilities.

As it turned out, however, as soon as the field tests began, many inquiries starting coming in: Where are the prefectural charge port facilities located, and how should the vehicle be charged? They want to borrow a Monpal electric cart, but can they stop and park it anywhere?

Even in the campaign to recruit a wide range of people to act as EV trial riders and test monitors, it was found that understanding of the EV itself as well as awareness of the field test were in short supply. There were various concerns, including the question of obtaining participants, and it became clear that promotion of the testing involved issues and design needs.

Initially, Honda styling design departments were tasked to identify the needs and investigate designs to address them. Then, the idea came up that investigating, developing, and verifying designs within the local community, based on distinctive local concerns and preferences, would not only contribute to the output of effective results, but would also provide opportunities to return some of the experience and expertise obtained in real-world design development to the community. It was therefore decided to propose a joint research project to a design school in the prefecture, the Department of Design of the Faculty of Art at Sojo University.

Approval was also obtained from Professor Urushihara, Dean of the Faculty of Art, who said that “the EV is in a transitional period on the way to widespread acceptance, and it would be good to interest our students in participating in the field test.” He also remarked that “the designs that are proposed will be modified out in the world, so this is a fine opportunity for a designer to get that feedback.” Thus, Honda engaged in design development on such themes as “interface design linking people, EVs, and the community” with design students at a local university who are the local leaders of the future.

3. Design Project

3.1. Field Test Message Logo

The first task taken on was message logo design. The idea was simply for a graphic motif for a wrap design on the body of the transporter, which would transport electric carts and electric motorcycles. The aim was to soften the impact of the term “field test” for what the prefecture was engaging in and to foster a sense of closeness to EVs in people. A rather long and explanatory but nevertheless readily understandable and simply phrased slogan was created: “Let’s build it together, an exciting EV community.” This was incorporated into the logo together with the shape of an electric plug that plugs into a power socket.

The field test covered a wide range of objects, extending from electric carts and electric motorcycles to four-wheeled EVs, and beyond that to the infrastructure of those vehicles and their surrounding environment. These were assigned to various working groups that engaged as teams in a full range of activities, but this sometimes had the effect of making them lose track of the full picture. The unified message logo that was produced appears to have had the effect of making those various field tests and projects feel like collaborative parts of one large undertaking.

The promotional figure of the “Kumamon” (a mascot character used in Kumamoto Prefecture promotion) employed in the transporter message logo visually emphasized that this was a Kumamoto Prefecture project. The message logo was, thereafter, applied in a variety of media, including charger guidance signs, banners for special events, leaflets about the field tests, and the design of the luggage box on the EV-Neo (an EV motorcycle manufactured by Honda) bikes loaned out at tourist sites. This became an effective case of increasing the breadth of field test promotion by means of graphic design (Figs. 2 and 3).



Fig. 2 Wrap design for transpoter



Fig. 3 Logoed items

3.2. Design of EV Charger Installation Signs

The field test involved numerous different measures, including a system of subsidies, for expanding and upgrading the charging infrastructure. This was considered essential to the popularization of the EV. As a result, charging facilities were installed in numerous locations. The chargers used were themselves of many different forms, and the installation locations were also varied, ranging from Michi-no-Eki (roadside rest areas) to areas within city hall parking lots. Initially, this was left to be handled subjectively by the people in charge of individual installations; consequently, the signs lacked unity, and the necessity for standard signs was keenly felt. What was done, therefore, was to select a number of locations where new charging stations were scheduled to be installed, to consider designs with a new unified look, and to put signs in place accordingly.

People generally were not even initially aware of the difference between quick chargers and normal chargers, and the signs were therefore considered to be very important in terms of enhancing their distinguishability, as well.

In installing the signs, deployment suited to the particular sites was considered (Fig. 4). Some signs, for example, were banners and other temporary items created to promote the field tests; at locations with walls, only panel signs were put up.

3.2.1. Pictograms

There are many places that use the pictogram recommended by Tokyo Electric Power Company for EV chargers. Their use is not uniform, however, and as things currently stand, there are multiple types of pictogram in use. There are even cases where the same charging facility uses different signs on the road than it does on walls. The situation invites confusion.

In order to address these circumstances, pictograms were created to clearly indicate the type of charger (quick charger or normal charger). The pictogram designs were created based on the JIS-approved pictograms of the Foundation for Promoting Personal Mobility and Ecological Transportation. This was done with consideration for ease of use when the pictograms are used side by side with the existing pictograms that are already displayed on signboards at Michi-no-Eki rest areas and other such locations (Fig. 5).

Where there are charging stations that have dedicated areas for charging, pictograms were also created to match the EV types that are supported (Fig. 6), and consideration was given to making them readily understandable. Honda has registered these pictograms as trademarks, but this is not with the aim of obtaining their exclusive use. The purpose is rather to prevent others from easily altering the original designs and making use of them.

The pictogram coloring was initially made a light green to match the message logo. Considering the poor contrast with the white base and other such factors, however, dark green was instead chosen as the standard color for the Kumamoto specification (Fig. 7).



Fig. 5 New pictogram matching JIS pictograms

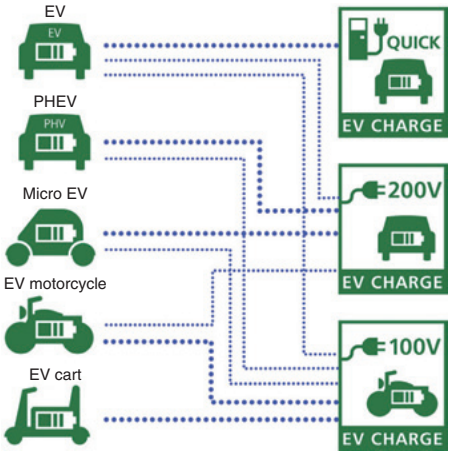


Fig. 6 Guidance signs for charger types available for specific EVs

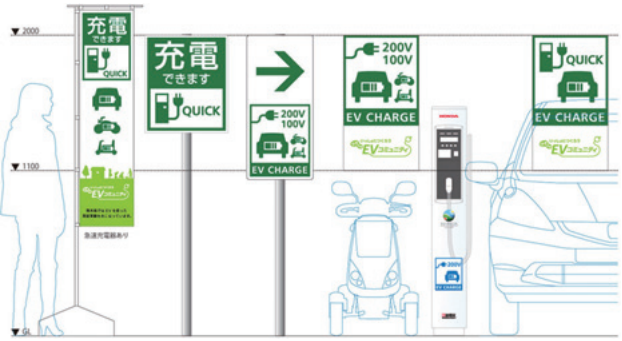


Fig. 4 Guidance signs for charging stations



Fig. 7 Guidance signs for municipal parking lot No. 2 at Kumamoto Castle

When chargers were installed at Honda dealers, the markings themselves were kept the same but the coloring was changed to blue. Figure 8 shows pictograms that are being used at a number of Honda dealers.

In Kumamoto Prefecture, maps were also made on paper media to provide guidance to charging facilities within the prefecture. It is extremely useful to have pictograms on such maps to indicate the locations with their types of charger. Since it appears likely that charging facilities will also come to be indicated on car navigation systems, it will become important to employ readily understandable pictograms in a unified manner.

3.2.2. Guide to sign design

Display using pictograms basically conveys meaning without depending on written characters or words. Since chargers were at a transitional state of promoting popularization, however, it was thought important to express content in readily understandable form, so some signs were made with the text string "charge available here" prominently displayed. This was also effective for guiding users in from the roadway entrance, for example when chargers are located deeper inside the facility. Information material that explains the sequential arrangement of guide signs was made publicly available on the Kumamoto Prefecture website. Kumamoto Prefecture is endorsing the use of the pictograms and related material outside the prefecture, and they can be freely downloaded in data form and used (Fig. 9).

3.2.3. Application Graphics

Although not a direct development of sign design proper, a smartphone app for monitoring electric carts was created during the field tests, and pictograms are used as graphics in that app interface, as well. This did not advance as far as modifications to the interface reflecting people's comments that using smartphones is difficult for elderly people in itself, but interfaces for this kind of mobile equipment will be important for the future (Fig. 10).

3.3. Promoting Shared Use of Monpal Electric Carts

Field tests of shared use of Monpal electric carts in town were conducted four times in Kumamoto City. In the initial field test, many people showed interest in taking part, but hesitated to take actual test rides. The questionnaires that were handed out also involved a considerable burden on responders. On further thought and reflection, it was decided to first create public information leaflets to make the testing more widely known. The leaflets were distributed to local organizations, and enhancements were made, for instance so that people would relate more easily to the loan-out stations (Fig. 11).

3.3.1. Monpal electric cart wrap design

For the final field test, the six Monpal electric carts used for loaning out were given wrap designs, each with a different motif. The purpose was to make people want to talk about them. Votes were held during the testing



Fig. 8 Guidance sign at Uto Honda Cars dealership

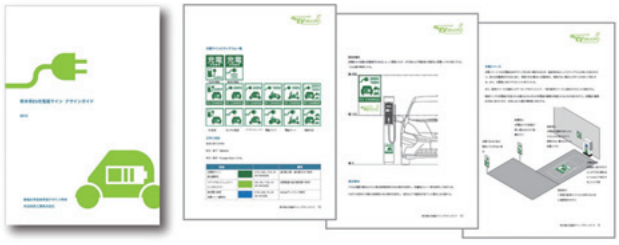


Fig. 9 Design guide pamphlet available on Kumamoto Prefecture website



Fig. 10 Application interfaces



Fig. 11 Leaflets for experimental project event and area map

period to decide which design was most popular, and an effort was made to heighten the special event qualities of the project. The wrapping designs were given motifs from specialty products and famous places of Kumamoto such as mustard-pickled lotus root and Kumamoto Castle. In the popularity voting, the "Kumamon" mascot design took first place. This project was planned to appeal to the mass media, but it seems also to have contributed to overturning the impression that Monpal electric carts are just rides for elderly people (Fig. 12).

The Monpal electric cart bearing this "Kumamon" mascot design was taken over (with the design) by a contractor loaning out electric carts for tourists around Suizenji Park in Kumamoto City, and is still in active use there.

3.3.2. Parking spot signs

In the final test, three loan-out stations were used in an arrangement that allowed the electric carts to be returned to any of them. Therefore, it was thought necessary to have a map showing all the station locations. Together with recommended routes for driving, the map also presented information to induce enjoyable activities such as shopping by showing locations in shopping streets where the electric carts could be safely left. On shopping streets that are no-parking zones throughout, people could park such carts in front of shops and enjoy their shopping without worries. In front of shops at eight locations, parking spots were marked on the road surface with mat-type signs. The information was arranged so that plotting those locations on the map would unerringly lead to a place where a cart could be parked (Fig. 13).

These markings on the road surface to show parking spots had been slated for installation only during the testing. However, the shops that had generously loaned their space expressed requests to make further use of those spaces. Signs were then created to indicate that parking was available not just for Monpal electric carts, but for general-purpose electric carts as well, and these continue to be used even after the field tests. In shopping streets where it is difficult to ride electric carts into a shop, assuring space for parking is crucial. The lack of development of this kind of environment is one of the hurdles that users face.



Fig. 12 Wrap design options for "Monpal"

3.4. New Electric Cart Design

Various needs for the Monpal electric cart were identified by providing these carts on long-term loan to elder care and other such facilities, as well as through short-term loans for field testing in the city center. Some students started addressing those needs with simple modifications, and by the third year they had also created the prototype of a concept model for their graduation research project in product design.

3.4.1. Enhanced parts design

Paper poster stickers were commonly observed affixed to seatback surfaces, and this method was adopted to display a variety of messages on the carts in shared use. Commercially available clear plastic folders were used in the design of a message board that could easily be affixed to a cart. This was simple to make and was used in a variety of scenarios (Fig. 14).

Work was done next to modify baskets on the carts. Baskets that were made slim to match the cart body were particularly unpopular with users who wanted to use them for shopping. Net baskets from bicycles were adapted and made wider. Fittings were added to cloth shopping baskets so they could be attached to and detached from a cart. A number of different designs were made and the prototypes were fabricated.



Fig. 13 Parking spot designation



Fig. 14 Multi-purpose message board

Users had also requested an extension cord for use in recharging the cart, which occasionally became necessary while out riding. Cords were therefore attached together with the baskets, leading to the perception that people actually wanted even more luggage space (Fig. 15).

3.4.2. Electric cart with expanded luggage space

The shopping basket idea described above was further developed, and a design was proposed for a prototype electric cart with expanded luggage space. Taken on as a graduation research project for university students, this design proposal was more for a cart specialized in transporting cargo than for styling. Since it was especially important to confirm the design on a full-size cart, the outer decorative parts were removed from an existing Monpal electric cart, and with just the frame as a base, the modifications were made and a prototype was built.

The prototype was built using simple methods, such as by repurposing motorcycle parts. The parts were combined in a deliberate effort to distance the impression given by the prototype from the styling of the current model (Fig. 16).

The main points in the proposed design are as follows.

- A rough design of a space frame like that of industrial equipment, so receiving some scratches is not worrisome.
- Simplify the seat, change the battery for one more compact, and use the space below the seat for luggage.
- Make the charge cord reel larger and stronger, and the cord longer.
- Allow for the seatback to be removed and a folding hand cart (for use inside shops) to be carried there.

A model created to satisfy the above demands was shown to users, who were then asked their impressions and opinions. The results are as follows. (Fig. 17)

- Youthful, fashionable impression. Stylish.
- Being able to carry luggage down low makes for a lower center of gravity, which is good.
- It's not certain whether the carriers on either side of the seat can be used or not, but they serve as handholds when getting on and off.
- Some simpler way of loading the hand-cart should be considered.
- The seat surface is somewhat high, but it gives better visibility so that is good.

People showed little resistance to the concept of specialization in carrying capacity and having a shape like a construction vehicle. It seemed likely to be acceptable to elderly people.

There were many instances of the resin portions of cart bodies breaking or being marred during the field tests, so the design deliberately exposed the frame. Consequently, the safety aspects of use in urban spaces shared with pedestrians will require adequate verification.

The field tests of Monpal electric carts in Kumamoto Prefecture also included some loaned out to elderly people living in mountainous areas. Some expressed concern about safety on steep slopes and bad roads, however, and some said they could never forgive themselves if they damaged something they had borrowed. This kind of humble user consciousness made them feel hesitant about using electric carts, and it was found that different surrounding environments and methods of use resulted in differing needs and opinions. Given the limits to how many demands can be met by a single model, it appears likely that providing optional parts that allow for multiple alternatives could be a direct and effective shortcut to addressing users' needs.

A variety of methods of shared use were also surveyed during the field tests. The kind of cart body style that is in demand is different for shared use and for private ownership. The suitability of the design will therefore need to be considered.



Fig. 15 Removable shopping baskets



Fig. 16 Modified prototype model



Fig. 17 New models in use on the street

4. Conclusion

The urban setting of the future, endowed with next-generation personal mobility, should be a comfortable space for both resident consumers and visitors. In order to accomplish this, design solutions are sought not just in the design of personal mobility as a single separate component, but also in the interface that effectively links consumers, the community, and personal mobility.

One major outcome of these field tests was the activity of creating new designs locally, expressed as "local residents engaged in thinking about things they would be using in their own neighborhoods" and "local people looking for solutions to issues in their own local community," leading in a connected fashion to product creation and then to implementation in society.

Reference

(1) http://www.pref.kumamoto.jp/site/evtaunkousou/ev-sign.html, 2013/9/25
(2) http://www.honda.co.jp/demo-program/report04/

■ Author ■



Tadahiro YAGUCHI



Kazunori HARADA

Study of Optimization of Reciprocating Parts for General-purpose Engine with Aluminum-alloy Connecting Rods

Masami OKUBO* Masato SUZUKI*

ABSTRACT

The connecting rods employed in the reciprocating parts of general-purpose engines are manufactured from aluminum alloy, and therefore display lower material strength than steel connecting rods. In terms of operating conditions, general-purpose engines are frequently operated under high load while being held at a comparatively low engine speed, necessitating strength and durability in relation to combustion pressure. Realizing a balance between the rigidity of each part is an important factor in reconciling the achievement of weight reduction in the reciprocating parts while also maintaining strength. The research discussed in this paper developed a structure optimization system to examine shape parameters for reciprocating parts, and studied shapes that would balance the reduction of weight with the maintaining of strength. It was shown from calculation results that the annular stress of a connecting rod originates in piston pin displacement, and in order to achieve both weight reduction and strength retention, results confirmed that reducing the diameter of the piston pin and the formation of thick walls of connecting rod small-end annular sections are effective. This realizes a combination of shapes in which the stress generated on each part is equivalent to or lower than the stress generated on the mass-production shape, while reducing the mass of the piston pins by 20%. Tests were conducted on the reduced-weight shapes, and the effectiveness of this optimization system was verified.

1. Introduction

Low weight and compactness are important factors for small general-purpose engines. Portability and freedom of fitting are demanded of the engines for use in applications such as construction equipment, agricultural equipment, and industrial equipment. In addition, the engines are frequently used under high loads while being held at comparatively low engine speed, demanding strength and durability in relation to combustion pressure more than inertia force.

A variety of methods have been used in the past to realize lightness and compactness in general-purpose engines[(1)-(3)].

Of the reciprocating parts of general-purpose engines in most standard spark-ignition gasoline engines, the pistons and connecting rods are manufactured from aluminum alloy, and the piston pins are manufactured from steel. The engines use a fully floating configuration for the piston pins.

Aluminum alloy is employed for the connecting rods in order to reduce weight. It also makes bearings unnecessary, reducing the number of parts and increasing productivity, which represents a significant advantage in terms of reducing costs.

The big ends of aluminum-alloy connecting rods also employ a separate cap structure, which makes the replacement of parts an easy matter and offers excellent maintenance performance.

It is often the case that users in emerging nations replace parts themselves, and ease of maintenance therefore contributes significantly to increasing commercial appeal.

Because they satisfy the needs of general-purpose engines so effectively for all of these reasons, aluminum-alloy connecting rods are used in the main moving sections of the majority of general-purpose engines.

The aluminum alloys used in connecting rods are lower in strength than steel materials, making detailed consideration of strength essential in the design of weight reduction around the piston pins.

For example, reducing the weight of piston pins with high specific gravity would be effective in achieving weight reduction, but reducing the thickness of the pins would increase annular crushing deformation of the pins due to combustion pressure. As a result, stress around the piston pins and stress on the connecting rod small ends would

* Power Products R&D Center

increase in tandem with the deformation of the piston pins.

As phenomena of this type indicate, the realization of weight reduction and the maintaining of strength in the reciprocating parts are in a tradeoff relationship.

Because of this, structural analysis using FEM is employed during the design of the connecting rod small ends and the area around the piston bosses in order to judge strength and increase the accuracy of the blueprints prior to the prototype stage.

The conventional method of review is to create a 3D model and determine strength following a structural analysis.

However, this presents the issue of requiring an enormous amount of time for the calculation of large numbers of models of shape differences while studying the optimum shapes.

The linkage of CAE analysis and optimization tools is today attracting attention as an approach to analyses of this type, and has been employed in a variety of development processes[4), (5)]. The research discussed here set out to determine by calculation the respective part shapes of the reciprocating parts of a general-purpose engine that would maintain strength while also reducing weight, and to verify the effectiveness of these shapes in tests.

2. Overview of Shape Optimization System

2.1. Conditions for Structural Analysis of Reciprocating Parts

Generally, evaluation of the strength of connecting rods as reciprocating parts includes the buckling and bending strength of the rod sections in areas other than the vicinity of the piston pin holes. When aluminum alloy is employed in the connecting rods, the cross-sectional area of the rod section is increased in order to reduce stress, compensating for the low strength of the alloy. Because of this, the rod sections of connecting rods manufactured from aluminum alloy tend to display adequate stiffness, and buckling and bending strength rarely represent issues. Taking this into consideration, the present study focused on the strength of the connecting rod small end in the vicinity of the piston pin holes, and set conditions for the analysis on this basis. Figure 1 shows the analysis conditions in detail.

Because the strength of the connecting rod was focused on only in relation to the small end around the piston pin holes, the center of the rod section between the big and small ends was cut out. The cut section was constrained only in the z direction; deformation was allowable in the directions of the x and y planes. One-half-cut models were used for each part in order to allow a greater focus on deformation and reduce calculation time. Gap elements were used to reproduce load conditions and the distances between parts, based on consideration of an analysis discussed in a previously published report[6]. Table 1 shows the material specifications used in the structural analysis. Figure 2 shows the areas for evaluation of stress. Areas

Table 1 Material specifications

Part	Piston	Piston pin	Connecting rod
Material Heat treatment	JIS AC8B equivalent T7	SCM420 Carburizing	JIS ADC12 equivalent T6
Specific gravity	2.76	7.83	2.70
Young's modulus	75 GPa	204 GPa	72 GPa
Fatigue strength at room temperature	120 MPa	600 MPa	100 MPa
Fatigue strength at 150°C	115 MPa	600 MPa	95 MPa

in which high levels of stress are generated were selected based on the results of previously conducted structural analyses and tests. Two areas were selected in the piston and two in the connecting rod small end, for a total of four areas. Piston pin deformation was also evaluated in order to study the relationship between stress in each of the parts and piston pin stiffness. Despite the fact that high levels of stress are generated in the piston pins, because the material fatigue strength of the pistons and the connecting rods is lower than that of the piston pins, the pins were not part of the focus for stress evaluation in this research.

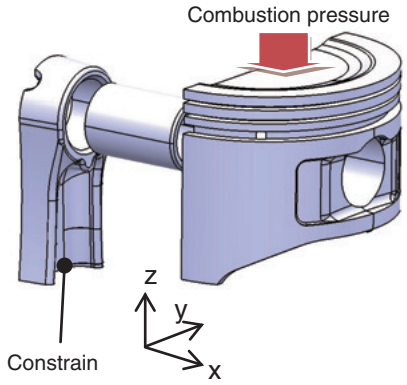


Fig. 1 Conditions for analysis

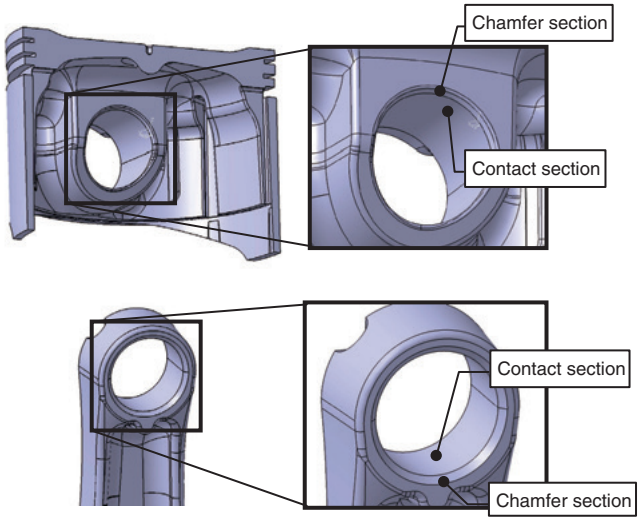


Fig. 2 Stress evaluation points

Figure 3 shows nine dimension parameters that have an effect on the four areas for stress evaluation. A parametric model was formulated, in which the three-dimensional shape was automatically updated to reflect changes in these dimensions. Dimensions were variable within appropriate limits, taking into consideration shape constraint conditions and mass producibility. In addition, of the nine dimension parameters, (e) was fixed at the initial stage of the study as a shape that reduced length by 8%. It was known from previous studies that the reduction of the length of (e) has the effect of reducing mass without reducing strength. Given this, calculation cost was reduced by reducing the degree of freedom of change in dimensions. This change reduced mass by 1.3% against the mass-production specification.

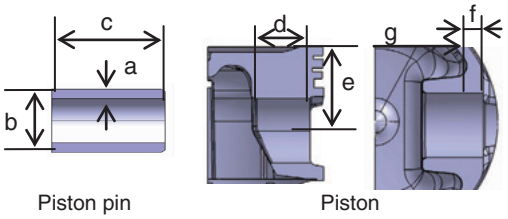
2.2. Optimization Algorithm

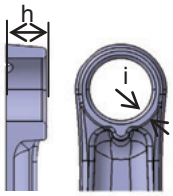
The aim of the present study was to minimize weight while attempting to help ensure that the stress generated in the four evaluation areas was equivalent to or less than figures for the mass-production shapes. The details of the optimization algorithm and the calculation conditions were as follows:

Test planning method: Uniform random number method
Number of initial generations: 36
Response curves: Kliging
Optimization algorithm: MOGA-II
Number of iterations: 30

Optimal solutions that produced the lightest models while also realizing levels of stress at the four evaluation points equivalent to or lower than the target values were selected from candidate solutions obtained from the calculations. Concrete details will be discussed in the following chapter.

With regard to software, CATIA V5 was used for structural analysis and for the formulation of the parametric model. The general-purpose optimization tool





a. Piston pin thickness
b. Piston pin diameter
c. Piston pin length
d. Piston boss length
e. Piston compression height
f. Piston lib thickness
g. Piston lib position
h. Connecting rod small end length
i. Connecting rod small end thickness

Fig. 3 Model parameters

Table 2 Engine specifications

TYPE	4-stroke air-cooled single-cylinder gasoline engine (OHV)
Number of cylinder	1
Bore × Stroke	68 × 54
Engine displacement (cm^3)	196
Compression ratio	8.5 : 1
Maximum power (kW/rpm)	4.1 / 3,600
Maximum torque (N·m/rpm)	12.4 / 2,500
Rated power (kW/rpm)	3.7 / 3,600
Fuel category	Unleaded gasoline for cars
Dry mass (kg)	17.1
Dimension: Length × Width × Height (mm)	352 × 376 × 346

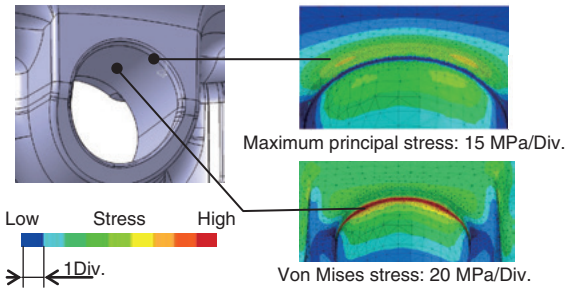
modeFRONTIER was employed for all processes from the implementation of the optimization algorithm to data processing.

3. Results of Analysis

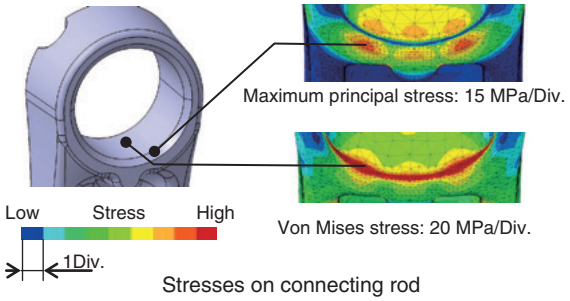
Using the analytic method discussed in Chapter 2, shape optimization was conducted for the reciprocating parts of a general-purpose engine with a displacement of 200 cm^3. Table 2 shows the specifications of the test engine.

3.1. Mechanism of Generation of Stress

Figure 4 shows the stress on each part when a combustion pressure load is acting on them. These results demonstrate that a high level of stress is generated on



Stresses on piston

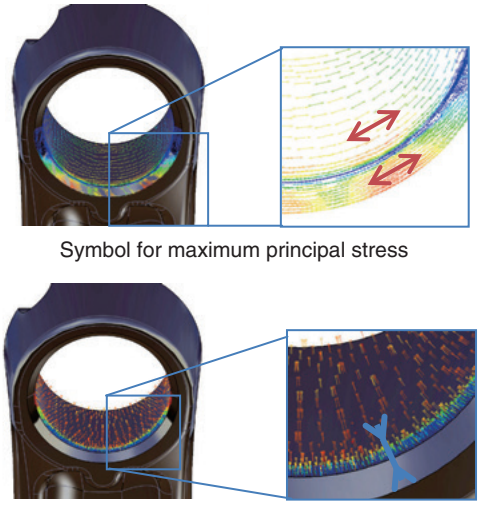


Stresses on connecting rod

Fig. 4 Stress contour

the chamfer sections and the contact sections of both the pistons and the connecting rods, as discussed above. The method used to evaluate these two stress states was as follows. In the chamfer sections of both the pistons and the connecting rods, tensile stress in the circumferential direction is dominant, as shown in Fig. 5. Given this, maximum principal stress was used for the evaluation of these sections. The contact sections present biaxial stress fields in which compressive stress and tensile stress are respectively generated in the radial and the circumferential directions. Here, Von Mises stress was used as the indicator to make it possible to evaluate these two stress states based on a single value.

Using these stress indicators, stress on the pistons and the connecting rod small ends was compared. The connecting rods displayed 1.4x the stress on the pistons in the chamfer section, and 1.2x in the contact section. Because the level of material fatigue strength of the connecting rods is also somewhat lower than that of the pistons, the result is that the connecting rod small ends are the weakest of the reciprocating parts. This made it necessary to study specifications that would reduce weight while maintaining the strength of the connecting rod small ends. Next, the mechanism of generation of stress in the connecting rods was studied based on the state of deformation of the piston pins. The piston pins display two main deformation modes when a combustion pressure load is applied. The first of these shows bending deformation, as shown in Fig. 6(a). The second shows crushing deformation, in which the annulus is flattened, as shown in Fig. 6(b). Figure 7 shows the results of an analysis of the relationship of correlation between these two states of deformation and stress on the connecting rod small ends. The coefficients of correlation between each type of deformation and each type of stress were as follows: For the chamfer sections, 0.8 (a) for bending deformation and 0.5 (b) for crushing deformation; and for stress in the contact sections, 0.9 (c) for bending deformation and 0.7 (d) for crushing deformation. Each type of stress therefore displayed a correlation with piston pin deformation. This indicated that the reduction of deformation in the piston pins would be effective in reducing stress on the four areas under study.



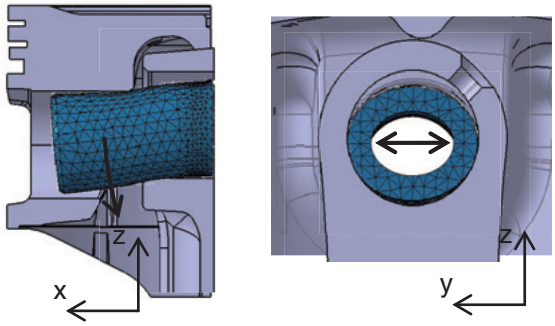
Symbol for maximum principal stress

Symbol for minimum principal stress

Fig. 5 Symbols for stress

3.2. Identification of Optimum Shapes

Figure 8 shows the relationship between stress in each of the four areas for evaluation of stress and total mass. The solutions on the curved boundary line are Pareto solutions, and represent candidates for optimal solutions. The red lines show the mass of the reciprocating parts for the mass-production shapes, and the blue lines show stress on each part for the mass-production shapes. In the graphs, only solutions that satisfy the constraint conditions for mass and stress are plotted as black; solutions that do not satisfy the conditions are plotted as gray. The shapes that realized the



(a) Bending deformation (b) Crushing deformation

Fig. 6 Piston pin deformation

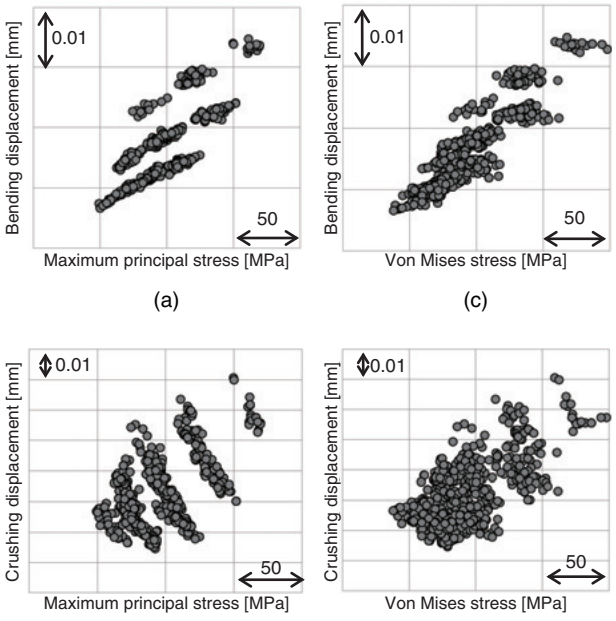


Fig. 7 Correlation matrix charts

lightest weight were selected from among the solutions satisfying stress conditions in each of the four evaluation areas as the optimal solutions. The shapes judged as optimal are shown as orange in the graphs. The results show that it is possible to reduce the weight of the optimal shapes by 10% against the mass-production shapes.

3.3. Characteristics of Optimal Shapes

Analysis of optimal shapes demonstrated the following characteristics. For the piston pins, diameter was reduced by 11% and length by 3%, while thickness remained the same as the conventional shape, for an overall reduction in mass of 20%. In the case of the connecting rod small ends, while a reduction in diameter increased the annular thickness of the pin holes by 25% against the mass-production shape, because the annular length of the boss was reduced by 8%, the mass of the part only increased by 2%.

These results show that despite the fact that there will be an increase in the mass of the connecting rod unit, it is possible to reduce the size of the piston pins.

3.4. Verification in Actual Engine

The optimal reciprocating part shapes selected in Section 3.3 were manufactured as prototypes, and their strength was tested in an actual engine. The prototype parts were fitted in a test engine, a static load corresponding to combustion pressure was applied to the combustion chamber, and stress was measured using a strain gauge. Figure 9 shows the conditions for measurement in the actual engine. Figure 10 shows the results of a comparison between stress measured in the chamfer sections of the piston pins and connecting rods and stress values predicted in the structural analysis. The measured stress values are within ±5% of the predicted values. It is conjectured that this represents error due to intersection of the clearance between the fully floating sections.

When using the developed system in product development and similar processes, it will be necessary to set a safety factor that considers factors such as dimensional variations of this type.

3.5. Analysis of Optimal Results

The orientation for weight reduction via the shapes discussed in the previous section was reduction of piston pin diameter and length and increase in the thickness of the connecting rods. The combination of these shapes can be considered an important element in reconciling strength and the reduction of weight in the reciprocating parts. Combination of three dimensions was studied. Using the results of optimization calculations, shapes that resembled each other were clustered in order to form groups for this study.

By means of grouping of shapes, the candidate optimal shapes were divided into three groups. The characteristics of each group were as follows.

Group A: Weight was reduced by reducing the diameter of the piston pins and stiffness was increased by increasing the annular thickness of the connecting rod small end.

Group B: Weight was reduced by reducing the diameter of the piston pins, and stiffness was increased by increasing the thickness of the piston pins.

Group C: Stiffness was increased by enlarging the diameter of the piston pins, and weight was reduced by reducing the thickness of the piston pins and reducing the annular thickness of the connecting rod small ends.

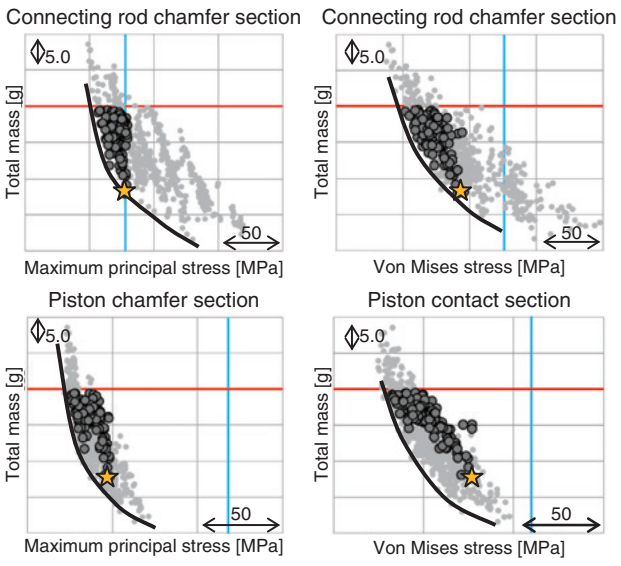


Fig. 8 Scatter diagrams

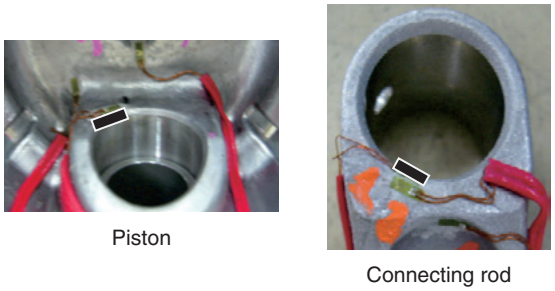


Fig. 9 Measurement of gauge stress

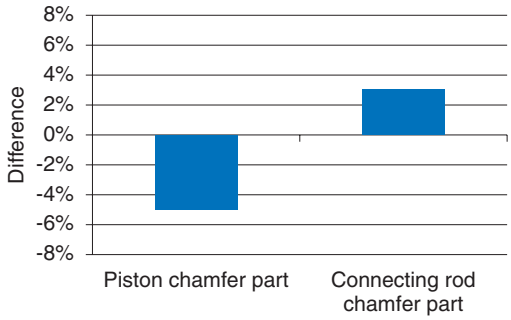


Fig. 10 Difference between measurement and calculation

Figure 11 shows a pattern diagram of the three relationships between dimensions and mass in these groups. In this research, the shapes in Group A were selected as offering the greatest reduction in weight.

The results discussed above indicate that in order to maintain strength and reduce weight in engine reciprocating parts using aluminum-alloy connecting rods, the appropriate design orientation is to reduce weight by reducing the diameter and length of the piston pins, while supplementing the reduced stiffness by increasing the annular thickness of the connecting rod small end.

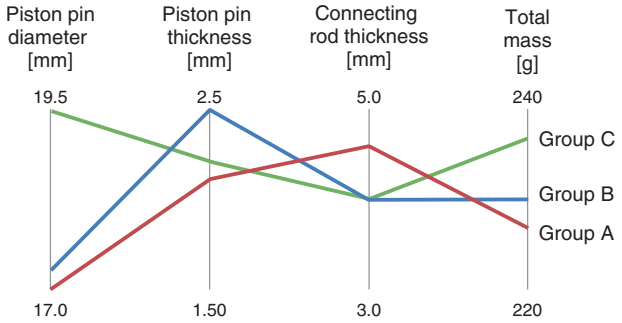


Fig. 11 Groups of optimal solutions

4. Conclusion

The effectiveness of a structural optimization system for the optimization of the shape of reciprocating parts for general-purpose engines using aluminum-alloy connecting rods has been verified. The system has made it possible to introduce specifications that reduce the weight of the piston pins by 20%, maintaining strength while reducing the weight of the reciprocating parts. The lighter specifications reduce the diameter of the piston pins while maintaining the same thickness as the mass-production specifications, and increase the annular thickness of the connecting rod small end. The new specifications were tested in an actual vehicle, and satisfied strength criteria. This verified the effectiveness of the structural optimization system. The results of the research discussed in this paper were as follows:

(1) The weakest section of the reciprocating parts is the chamfer section of the connecting rod small end, due to stress originating in bending and crushing deformation of the piston pins.

(2) Three dimensions are related to stress on the connecting rod small end. By reducing the diameter of the piston pins, employing equivalent piston pin thickness to the mass-production specifications, and increasing the annular thickness of the connecting rod small end, it was possible to reduce the unit mass of the piston pins by 20% while maintaining the strength of the reciprocating parts.

(3) When the strength of the weight-reducing specifications was tested in an actual engine, the results displayed an error of around ±5% with predicted values. Because of this, the application of the method to actual engine developments will necessitate the setting of safety factors that take into consideration the range of error.

(4) The three dimensions discussed above were classified into three groups that would reduce weight while maintaining strength. The weight-reducing shapes selected in the present research belonged to the group that realized the greatest weight savings.

References

(1) Suzuki, T., Hojo, H., Inoue, S., Moriyama, H., Fujinaga, Y.: Development of General Purpose OHC Engine with Built-in Timing Belt, HONDA R&D Technical Review, Vol.10, p.122-127 (in Japanese)

(2) Kawase, S., Urata, H., Ishijima, Z., Shikata, H.: Development of Powder Metallurgy Forged Ai-Si Alloy for Connecting rod, Honda R&D Technical Review, Vol.9, p.197-205 (in Japanese)

(3) Takasaki, M., Yoshimura, Y., Sato, K., Sugimoto, Y., Sato, T.: Development of Alloy for the High Pressure Die Casting Piston, HONDA R&D Technical Review, Vol.13, No.1, p.175-184

(4) Goto, T., Endo, H. : CAE Models and Optimization Technology in the Engine Development Process, Journal of Society of Automotive Engineers of Japan, Vol.67, No.5, p.56-61 (2013) (in Japanese)

(5) Obayashi, S., D. Sasaki, D.: Visualization and data mining of Pareto solutions using self-organizing map, Proceedings of the 2nd International Conference on Evolutionary Multi-Criterion Optimization, Springer-Verlag Heidelberg, p. 796–809 (2003)

(6) Koya, E., Handa, M., Yoshimoto, A., Nakagawa, M., Seto, T., Okutomi, N.: Prediction of Piston Strength by CAE, HONDA R&D Technical Review, Vol.5, p.43-50 (in Japanese)

■ Author ■


Masami OKUBO


Masato SUZUKI

Advanced Ignition Control Technology for HCCI Combustion

Kiminori KOMURA* Masanobu TAKAZAWA* Teruyoshi MORITA*

ABSTRACT

Spark-Assisted HCCI combustion, which assists ignition by igniting direct injection spray with a spark, has been proposed to help enable the practical realization of homogeneous charge compression ignition combustion, thereby achieving high thermal efficiency. This method increases the controllability of ignition, an issue of homogeneous charge compression ignition, and expands the range of ignition combustion by a maximum of three times compared to the conventional method.

The fuel efficiency of Spark-Assisted HCCI was verified, with results indicating a decrease of 16% in steady-state fuel consumption against cooled EGR combustion technology and a JC08 mode fuel efficiency simulation showing an increase of 4.5% in fuel efficiency.

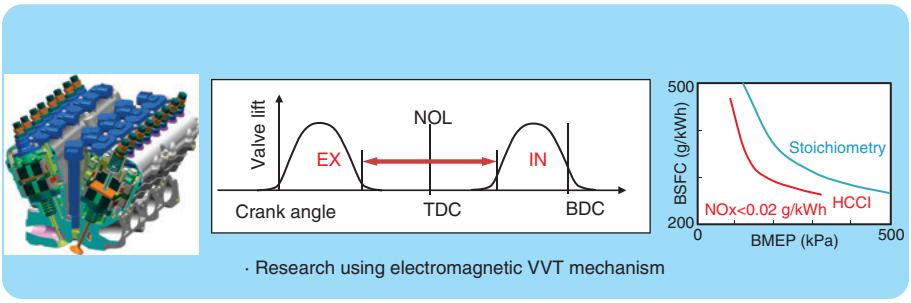
1. Introduction

Given today's high level of concern towards global environmental issues, the automotive industry is being called on to develop technologies that will further reduce CO_2 emissions in order to help to mitigate climate change and address the issue of depletion of fossil fuels. Because the realization of increased thermal efficiency can contribute to reducing CO_2 emissions, research towards this end is being continuously conducted in a wide variety of fields by companies and university and other research institutes[1), 2)]. Homogeneous-Charge Compression Ignition (HCCI) technology makes it possible to stably combust lean air-fuel mixtures through auto-ignition of a homogeneous mixture. This reconciles a high theoretical thermal efficiency with low NOx emissions, and HCCI thus presents good prospects as a mode of combustion in future engines[3)-6)].

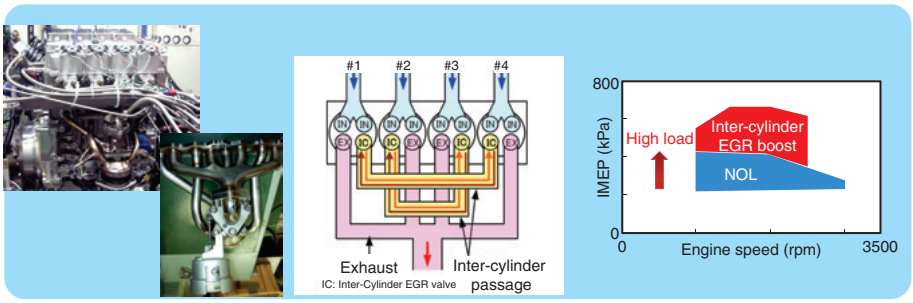
Figure 1 shows details of Honda's main HCCI initiatives up to the present. In 1999, Honda commenced fundamental research towards the realization of HCCI by increasing the compression temperature via Exhaust Gas Recirculation (EGR) realized by means of Negative valve Overlap (NOL) in an engine with an electromagnetic variable valve timing system. This research increased efficiency and realized low NOx emissions in the low-load range. Using this technology in combination with inter-cylinder EGR boost, which introduces EGR using exhaust blowdown pressure from other cylinders, made it possible to extend the operating range into the medium-load range. Figure 2 shows examples of the operating range for HCCI when using NOL EGR and the expansion in the operating range realized by inter-cylinder EGR boost. Honda has proceeded with numerous other initiatives in this area of research, for example increasing the controllability of combustion through the use of dual fuels (introducing the use of alcohol fuels)[7)-9)].

However, this research is still at the concept engine level, and has not yet been practically realized. One of the main factors standing in the way of the practical realization of HCCI is the challenge represented by control of ignition timing to help enable continuous stable combustion. The authors therefore proposed Spark-Assisted HCCI (SA-HCCI) as a method of accurate ignition timing control, verified the combustion concept in the NOL range, and developed the necessary hardware.

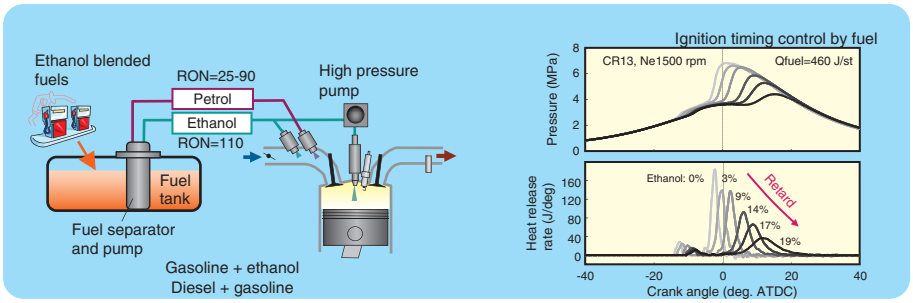
* Automobile R&D Center



(a) NOL (1999-2004)



(b) Inter-cylinder EGR boost (2004-2012)



(c) HCCI combustion control using dual fuel (2003-2007)

Fig. 1 Research on HCCI at Honda

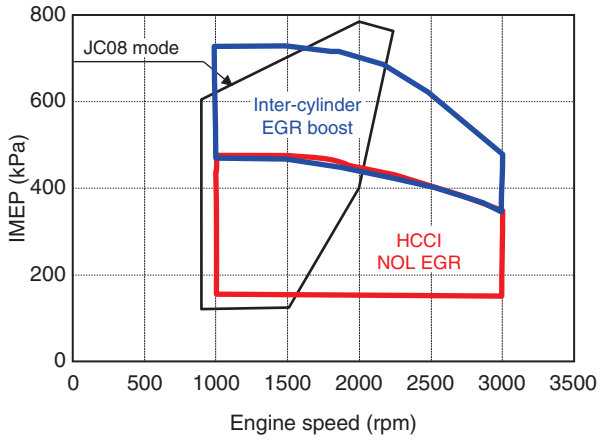


Fig. 2 HCCI operating range

2. SA-HCCI Combustion Concept

2.1. Merits of HCCI

HCCI is a type of homogeneous premixed combustion in which high compression ratios and internal EGR realized using the methods shown in Fig. 1 increase the temperature of the mixture in the cylinders to approximately 1000 K at close to compression top dead center, causing a reaction in the entire mixture in the combustion chamber resulting in auto-ignition. By initiating combustion through auto-ignition, it becomes possible to employ lean combustion at the air-fuel ratio range of A/F25 and above, which represents a challenge in terms of the realization of combustion stability when spark ignition (SI) combustion, in which combustion is initiated by spark ignition, is used.

Making possible leaner combustion than SI by means of auto-ignition, HCCI displays high theoretical thermal efficiency and low pumping loss and time loss. In addition, because the combustion temperature is low, heat loss is low and NOx emissions are minimal. Given these merits, this combustion method can be expected to increase fuel efficiency by around 20% against stoichiometric SI, and at the same time will also be able to realize low emissions (EM).

Figure 3 shows P-V diagrams for SI and HCCI with internal EGR realized by NOL in the same engine. HCCI is clearly able to minimize pumping loss and time loss.

However, HCCI also presents a number of issues that are barriers to its practical realization.

2.2. Issues of HCCI

Three major issues of HCCI can be recognized. These are:

(1) The operating range is narrow;
(2) Combustion ignition control represents a challenge; and
(3) Exhaust gas purification performance is poor in the lean environment.

With regard to Issue (1), the HCCI operating range, despite the fact that the expansion of the range via inter-cylinder HCCI, as shown in Fig. 2, is able to extend it to largely cover JC08 mode, HCCI operation is not possible in the high-load, high-engine-speed range outside the mode. At present, therefore, it is not possible to cover the entire necessary engine operating range using HCCI alone.

Issue (2), ignition control, is an important issue for vehicles used in a wide range of environments.

Figure 4 shows a diagrammatic representation of the heat generation history for HCCI from the compression stroke to auto-ignition, including the mixture oxidation reaction process.

In HCCI combustion, a low-temperature oxidation reaction that produces a cool flame commences from a mixture temperature of around 600 K. The accumulation of formaldehyde and the proliferation of CO and OH radicals generates a blue flame, until finally a hot flame that generates CO_2 from CO is produced. When employing SI combustion, in which the spark plugs advance the reaction rapidly and a hot flame is produced, ignition timing can be easily controlled by control of the spark timing of the plugs. In the case of HCCI, because changes in temperature and pressure during the compression stroke change the oxidation reaction process, control of ignition timing represents a challenge. To help ensure stable combustion in a variety of environments, it will be necessary to accurately control ignition timing, and attempt to reliably prevent misfires, torque fluctuations, and increases in emissions.

With regard to after-treatment, Issue (3), the temperature of exhaust gas generated by HCCI is lower at the exhaust manifold outlet than stoichiometric SI exhaust gas. At an indicated mean effective pressure (IMEP) of 400 kPa, HCCI exhaust gas is around 320˚C, compared to 500˚C for SI. In addition, because combustion is lean, clearing EM regulations via the conventional method of employing a three-way catalyst (TWC) also represents a challenge. This makes a new after-treatment system essential.

Of these issues, it is the controllability of ignition, Issue (2), that it is particularly necessary to address, or it will not be possible to employ HCCI in automotive engines. The research discussed in this paper focused on this issue of controllability of ignition.

2.3. Concept of SA-HCCI Combustion

As discussed above, in order to realize stable ignition timing, which represents one of the issues of HCCI, a method has been tested in which auto-ignition is assisted by a miniscule combustion event (trigger flame) generated by igniting a miniscule amount of directly injected fuel via the spark plug. Figure 5 shows the differences in the method of increasing temperature in the cylinders and the heat release history for conventional HCCI and SA-HCCI. In the majority of cases, standard HCCI increases temperature by means of internal EGR and pressure in order to induce auto-ignition of the lean, homogeneous mixture. By contrast, in SA-HCCI, a small amount of fuel is directly injected towards the spark plug during the compression stroke, and the propagation of a flame by the spark plug increases temperature, inducing auto-ignition. The heat release history for SA-HCCI shows that by contrast with conventional HCCI, a trigger flame releases heat prior to auto-ignition. Because the position of the combustion center of gravity for the realization of increased thermal efficiency is close to 10 deg ATDC, as in the case of SI and conventional HCCI, the aim was to realize combustion with a heat release history in

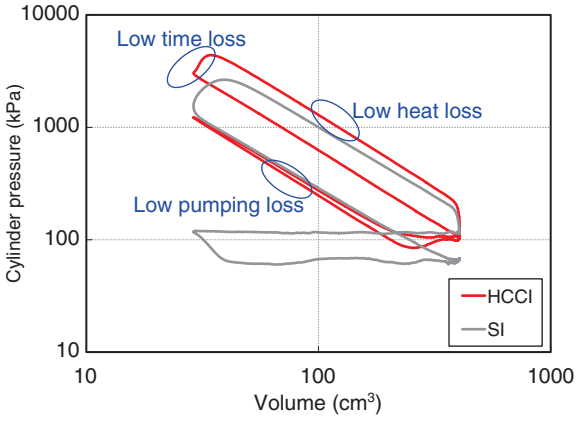


Fig. 3 Comparison of cylinder pressure

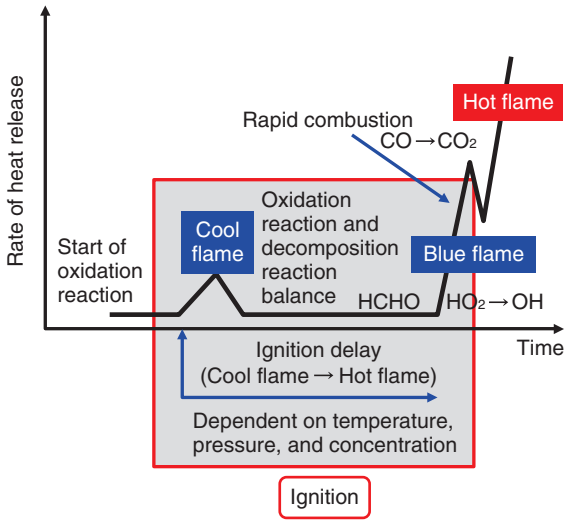


Fig. 4 Oxidation reaction process for HCCI

which auto-ignition occurred at close to 2 deg ATDC.

At the same time, because the trigger flame is propagated by spark ignition, it is necessary to set the conditions for the trigger flame fuel injection at close to stoichiometric conditions. Therefore, the trigger flame combustion temperature is high, and NOx is locally produced. Figure 6 shows the results of shadowgraph visualization of the ignition process for HCCI and SA-HCCI. This shows the process of induction of auto-ignition by flame propagation via direct injection in SA-HCCI.

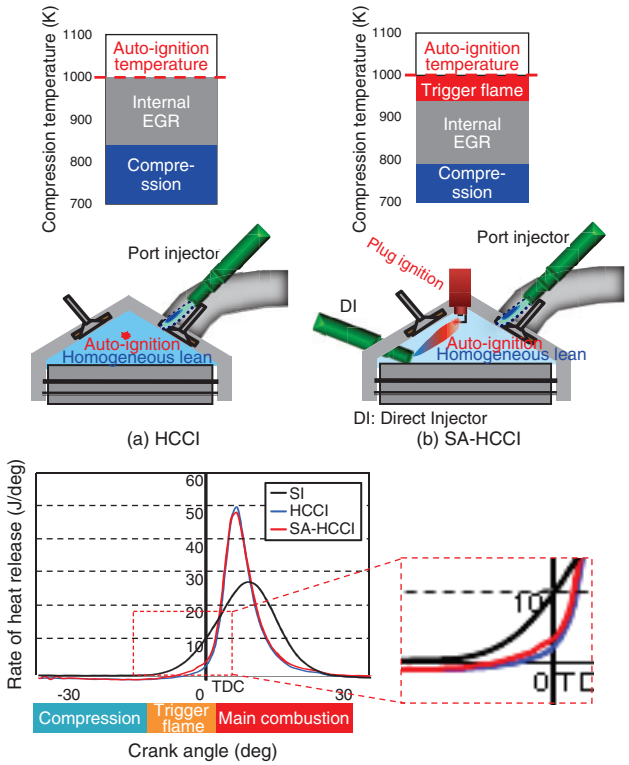


Fig. 5 SA-HCCI

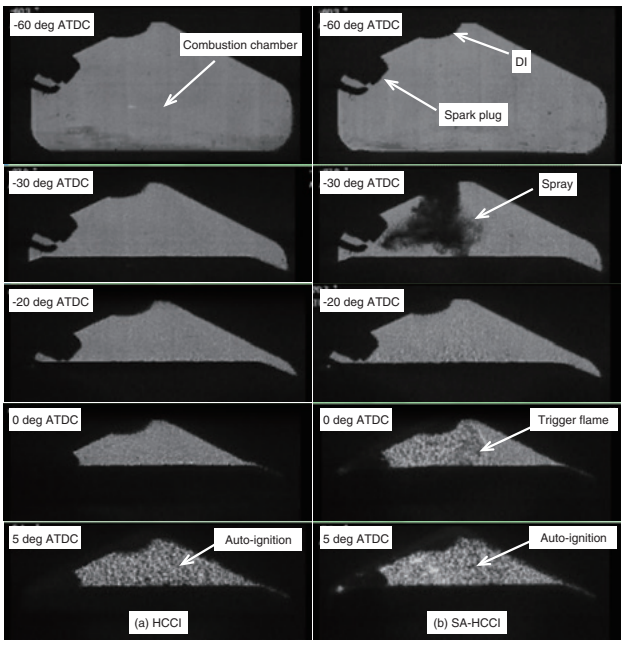


Fig. 6 Visualization of combustion chamber by shadowgraph method

3. Technologies Required for Realization of SA-HCCI

3.1. Setting of Trigger Flame

The setting of the trigger flame is an important factor for SA-HCCI. It was necessary to set the trigger flame with consideration of the following:

(1) Required calorific value for trigger flame;
(2) Spray distance for arrival at plug (penetration); and
(3) Restriction of NOx emissions.

These factors will each be discussed in detail below.

3.1.1. Required calorific value for trigger flame

It is necessary to realize a calorific value for the trigger flame that will cause the mixture to burst into a hot flame.

The necessary calorific value was back-calculated from the target heat release history, and was set with consideration of realization of a flame propagation speed that made it possible to achieve the temperature for auto-ignition at close to 2 deg ATDC. Figure 7 shows an in-cylinder temperature history at an engine speed (Ne) of 1500 rpm and an IMEP of 350 kPa. The necessary gas temperature for ignition of the mixture was approximately 1070 K, and it was not possible to realize this temperature via the temperature rise due to internal EGR and piston compression. Because of this it would be necessary to realize the target temperature following a temperature increase of approximately 50 K, realized by combustion of a directly injected mixture. With 375 cm^3 as the precondition for each cylinder, the necessary level of trigger flame heat for a temperature increase of 50 K would be approximately 10 J per cylinder.

3.1.2. Penetration to reach plug

Because the stratified mixture that would generate the trigger flame would be ignited by the spark plug, it was essential for the DI spray to arrive at the plug. If the fuel flow rate for the trigger flame was insufficient, the spray

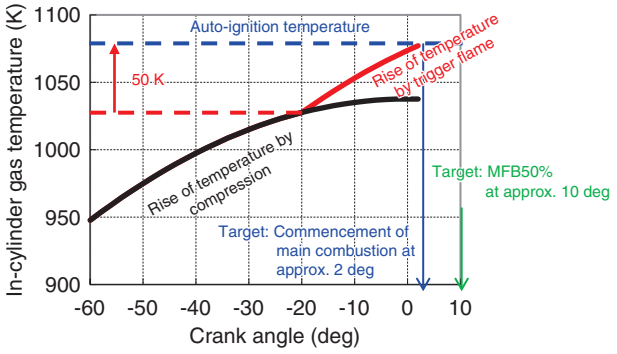


Fig. 7 Temperature rise process for SA-HCCI

would possess inadequate penetration, and depending on the distance between the plug and the direct injector, the spray would not arrive at the plug.

Figure 8 shows results for the relationship between the distance between the direct injector and the plug and DI fuel energy enabling ignition.

The calorific value of the trigger flame to help ensure ignition (the flow rate of the DI spray) is determined by the distance between the direct injector and the spark plug. However, when the calorific value of the trigger flame increases, NOx emissions also increase. When the distance between the direct injector and the spark plug is set at 30 mm, the level of heat generation by the trigger flame to help ensure penetration is 20 J per cylinder.

3.1.3. Restriction of NOx emissions

Increasing the calorific value of the trigger flame would increase the controllability of ignition, but NOx emissions would also increase, and the benefit of lean burn would be lost. Figure 9 shows the relationship between the calorific value of the trigger flame and NOx emissions.

The allowable level of NOx emissions varies based on the engine type and EM regulations. Assuming an engine displacement of 1.5 L, in order to realize a reduction in NOx emissions of 75%, as specified by Japan's Post New Long-Term Regulation, it would be necessary to control

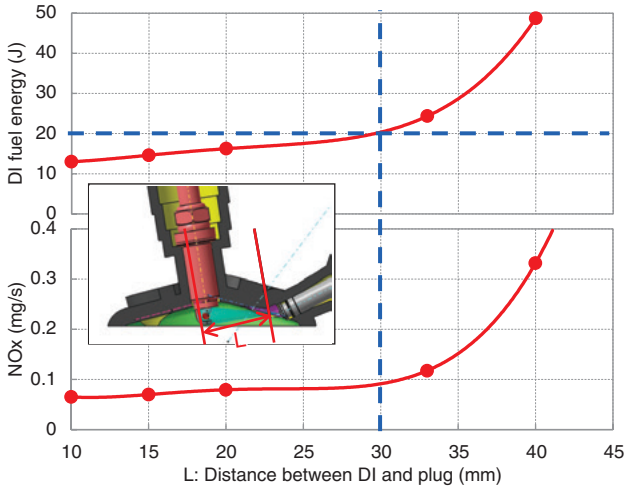


Fig. 8 Relationship between DI flow and DI penetration

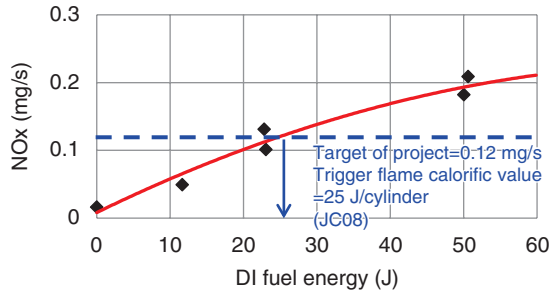


Fig. 9 Relationship between DI fuel energy and NOx

emissions to an upper limit of approximately 0.12 mg/s. At an Ne of 1500 rpm and an IMEP of 350 kPa, the upper limit for the calorific value of the trigger flame would therefore be 25 J per cylinder.

3.1.4. Summary of setting of trigger flame

Figure 10 shows the method of setting the trigger flame, with the temperature of the gas in the cylinders as the benchmark.

10 J was set as the minimum calorific value necessary for the supplied homogeneous lean air-fuel mixture to auto-ignite and produce a hot flame. A further 20 J was added as corresponding to the flow rate necessary to help ensure that the DI spray would arrive at the spark plug. The range from 20 J to 25 J, the upper limit value for NOx emissions, was therefore established as the range of setting values for the trigger flame. The calorific value above the 10 J necessary for the trigger flame represents a temperature margin, and is available to make it possible to absorb variations in environmental conditions and amount of control.

3.2. SA-HCCI System Configuration

Figure 11 shows the necessary system configuration for the practical realization of the SA-HCCI concept.

For (1) in the figure, internal EGR control, a variable

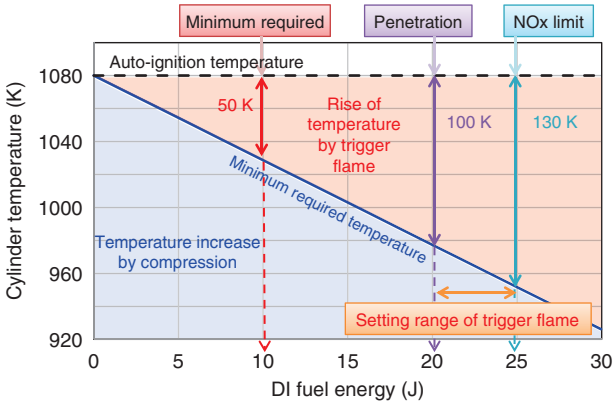


Fig. 10 Method of setting trigger flame

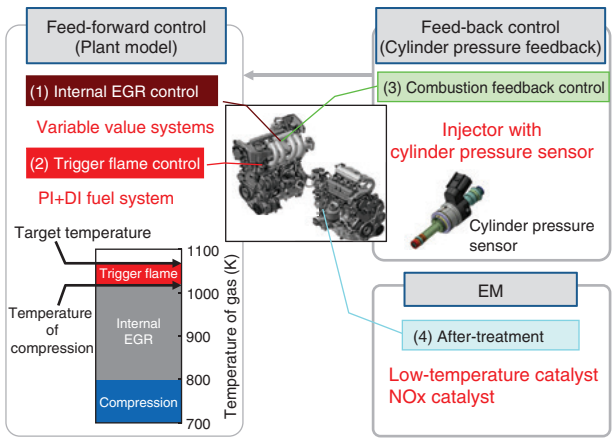


Fig. 11 SA-HCCI system configuration

valve system making it possible to change the intake (IN) and exhaust (EX) valve timing is necessary. As Fig. 12 shows, the amount of internal EGR can be appropriately controlled in response to load by varying NOL via Valve Timing Control (VTC) employing IN and EX cams.

For (2) in the figure, trigger flame control, two injection systems are necessary: A low flow-rate direct injector to produce the trigger flame, and a port injector for control of load. Precise specification of the flow rate at a low level is necessary for the direct injector for the trigger flame. The reason for this is that because the injector cannot provide the dynamic range necessary to cover fuel injection amounts across the entire load range, and injection is highly oriented towards the direction of the spark plug, there are concerns that injection of too much fuel would cause combustion to become unstable.

In-cylinder pressure sensors are necessary for feedback combustion control, (3) in the figure. The state of the mixture is estimated based on the values measured by the in-cylinder pressure sensors, and ignition timing control is precisely applied with the amount of internal EGR calculated from operating conditions and the calorific value and injection timing necessary for the trigger flame as parameters. The use of in-cylinder pressure sensors built into the direct injectors[10] was made a prerequisite.

For (4) in the figure, after-treatment, an HC purification catalyst to respond to the low exhaust temperatures of lean combustion and an NOx purification catalyst to make it possible to broaden the HCCI combustion range are necessary.

This paper will not discuss details of after-treatment and combustion control.

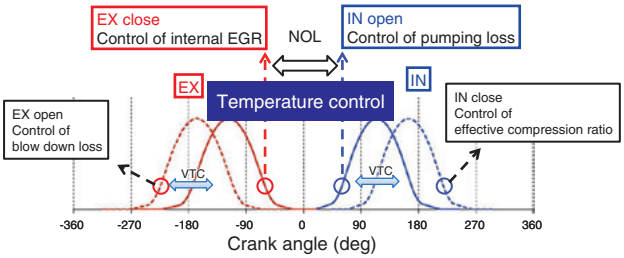


Fig. 12 Variable valve systems

4. Results of Verification of Concept

The SA-HCCI system discussed above was tested in a 4-cylinder engine. Table 1 shows the specifications of the engine used in verification.

4.1. Verification of Controllability of Ignition Timing

Figure 13 shows the results of comparison of the controllability of ignition in HCCI and SA-HCCI at an Ne of 1500 rpm and an IMEP of 420 kPa. The verification compared the combustion range when the in-cylinder temperature was varied by varying the amount of internal EGR. The combustion range was defined as a combustion fluctuation rate of 4% or less and a pressure rise rate ($dP/d\theta$) (an index of combustion noise) of 400 kPa and below. The combustion range within which standard HCCI satisfied the conditions above was a narrow range between EGR rates of 50% and around 53% (the difference in in-cylinder gas temperature at this time was around 6 K). In the case of SA-HCCI, despite the fact that the EGR rate was lowered and the in-cylinder temperature was reduced, the advancement of the trigger flame ignition timing and the increase in the combustion amount for the trigger flame made it possible to realize continuous combustion in the range above an EGR rate of 10% (in-cylinder temperatures of 20 K and above).

Table 1 Engine specifications

Number of cylinders	4
Displacement [cm^3]	1500
Bore × Stroke [mm]	ϕ 73 × 89.4
Compression ratio	14
Valve train	IN EX VTEC and VTC
Gasoline	91RON

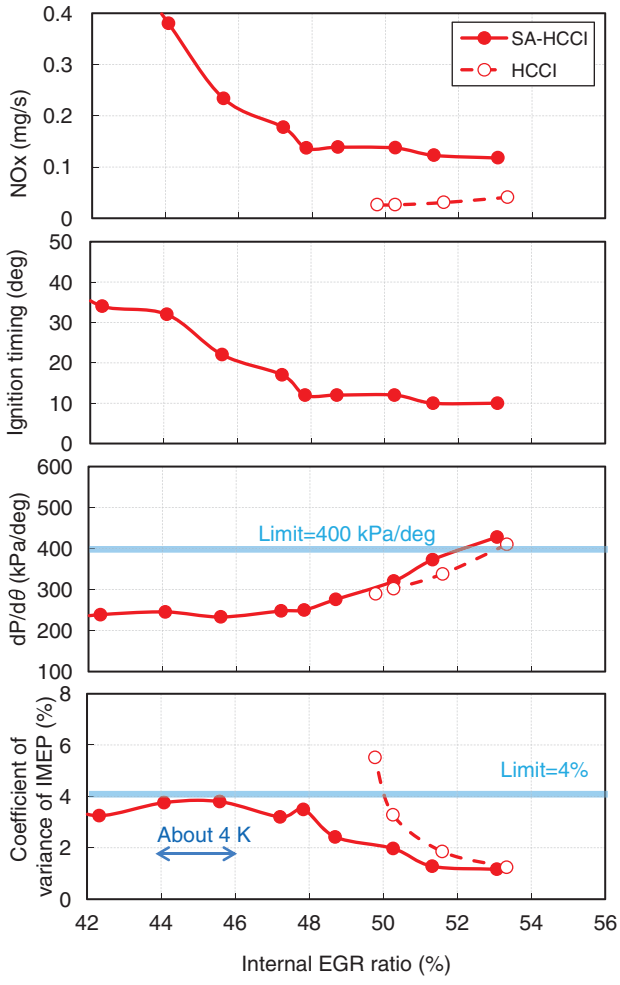


Fig. 13 Concept verification

At the same time, an increase in NOx emissions was also observed as a result of the increase in the combustion amount for the trigger flame. The status of SA-HCCI can also be expressed by the waveforms of the heat release rate, dQ, as shown in Fig. 14. The results show that a trigger flame combusts prior to auto-ignition and that the advancement of ignition timing has expanded combustion of the trigger flame in comparison to HCCI.

Figure 15 shows the results of verification of the combustion range under various load conditions. The results show that SA-HCCI has a greater effect than HCCI at all loads.

As the results discussed above indicate, by increasing the controllability of ignition, SA-HCCI has increased the combustion range in relation to the amount of EGR by two to three times against HCCI.

4.2. Verification of Steady-state Fuel Consumption

Figure 16 shows a comparison of the results of fuel consumption and NOx measurements at an Ne of 1500 rpm for SA-HCCI and stoichiometric SI combustion. Table 2 shows the main specifications of the technologies under comparison. Based on indexes for commercial appeal, the upper limit for the operating range of SA-HCCI was a brake mean effective pressure (BMEP) of 400 kPa, and brake specific fuel consumption (BSFC) was lowest at this figure. Figure 17 shows a comparison of the difference in fuel consumption at the BMEP 400 kPa point between SA-HCCI and SI combustion using cooled EGR, the condition under which fuel efficiency is best, in addition to a breakdown of a thermal analysis. SA-HCCI reduces fuel consumption by approximately 16% against cooled EGR combustion.

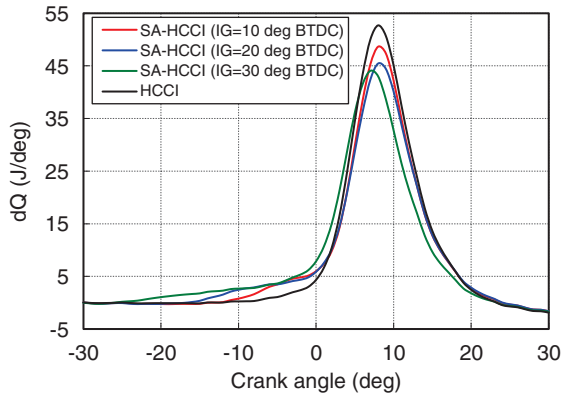


Fig. 14 Comparison of heat release rates

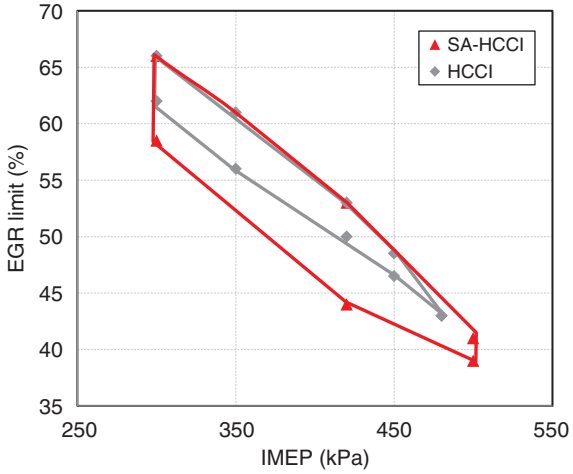


Fig. 15 Comparison of combustion range

Table 2 Engine specifications

	Stoichiom -etry	Atkinson cycle	Cooled EGR	SA-HCCI
Number of cylinders	4	4	4	4
Displacement [cm^3]	1.8	1.8	1.5	1.5
Compression ratio	11	13	13	14
EGR	None	Hot 15%	Cooled 25%	Internal 30-60%
Gasoline	91RON	91RON	91RON	91RON

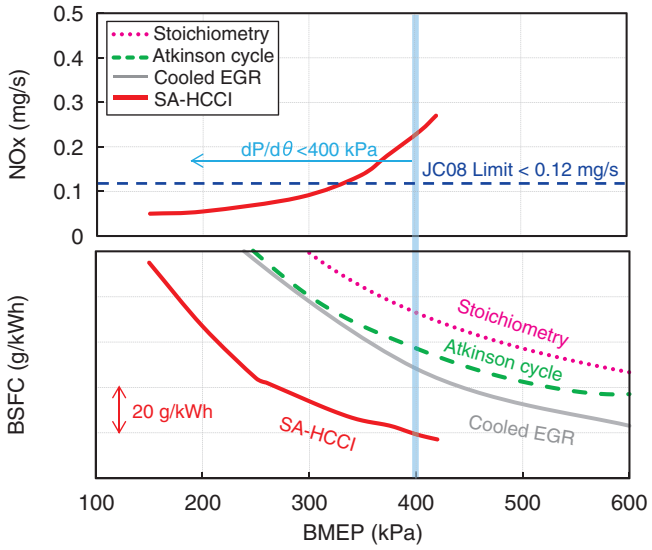


Fig. 16 Results for 4-cylinder engine

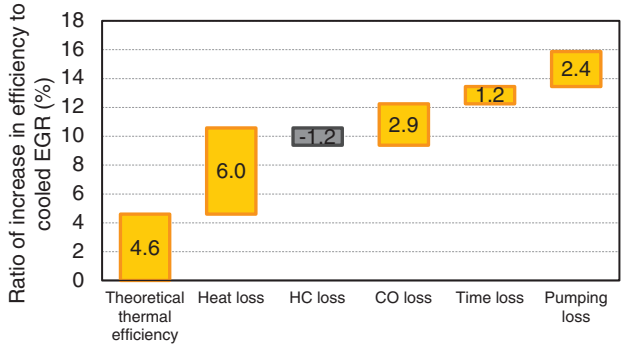


Fig. 17 Ratio of increase in efficiency to cooled EGR

Table 3 Specifications of simulated car

Car	FIT
Weight [kg]	968
Displacement [cm^3]	1500
Transmission	CVT

Among the main factors in this are an increase in theoretical thermal efficiency (as a result of an increase in the ratio of specific heat due to increased leanness and the dilution of EGR, and the expansion of the compression ratio) and a reduction in heat loss. In the future, further increases in fuel efficiency can be expected as a result of efforts to reduce the pressure rise rate and expand the range of operating loads.

With regard to NOx emissions, figures are low in the area below 300 kPa, but as load increases emissions increase rapidly. In the low-load area, because the gas temperature of the main combustion area is low, NOx is only produced by the trigger flame; however, as the gas temperature of the main combustion area increases with increasing load, it also produces NOx. At present, emissions exceed the level that would clear the established target of a 75% reduction in NOx emissions, as specified by Japan's Post New Long-Term Regulation, with operation up to a maximum load point of BMEP 400 kPa as a prerequisite. The use of lean NOx catalysts in order to maximize the increase in fuel efficiency offered by SA-HCCI will be considered, and operation up to a BMEP of 400 kPa is projected.

4.3. Results of Verification using JC08 Mode Fuel Efficiency Simulation

A verification of the system was conducted using a JC08 mode fuel efficiency simulation, based on the current SA-HCCI operating range and results for steady-state fuel consumption performance. Table 3 shows the main specifications of the vehicle used in the simulation. The mode fuel efficiency of cooled EGR combustion and cooled EGR combustion with SA-HCCI combustion were compared.

Figure 18 shows the simulation results. The results show that the addition of SA-HCCI to the cooled EGR technology increases fuel efficiency by approximately 4.5%.

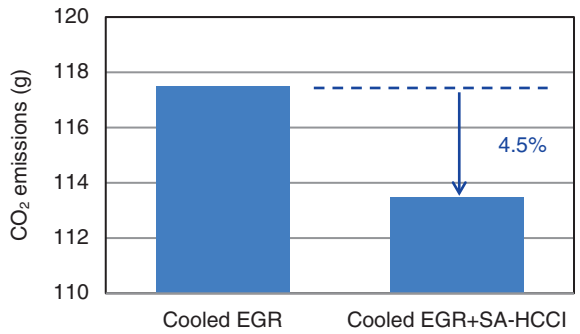


Fig. 18 Simulation results

5. Conclusion

A development with a focus on the controllability of ignition was conducted towards the practical realization of HCCI, with the following results.

(1) SA-HCCI was developed to assist HCCI ignition using direct injection in an attempt to increase the controllability of ignition. Verification of the concept showed that it expanded the combustion range by two to three times against conventional HCCI.

(2) The fuel efficiency of SA-HCCI was verified, demonstrating that the system reduced steady-state fuel consumption by approximately 16% against cooled EGR. Simulation verification of JC08 mode fuel efficiency indicated that an increase of approximately 4.5% in fuel efficiency could be expected.

References

(1) Wang, C., Daniel, R., Xu, H.: Research of the Atkinson Cycle in the Spark Ignition Engine, SAE Technical Paper, 2012-01-0390 (2012)

(2) Lecointe, B., Monnier, G.: Downsizing a Gasoline Engine Using Turbocharging with Direct Injection, SAE Technical Paper, 2003-01-0542 (2003)

(3) Aoyama, T., Hattori, Y., Mizuta, J., Sato, Y.: An Experimental Study on Premixed-Charge Compression Ignition Gasoline Engine, SAE Technical Paper, 960081 (1996)

(4) Hiraya, K., Hasegawa, K., Urushihara, T., Iiyama, A., Itoh, T.: A Study on Gasoline-Fueled Compression Ignition Engine – A Trial of Operation Region Expansion, SAE Technical Paper, 2002-01-0416 (2002)

(5) Fuerhapter, A., Piock, W. F., Fraidl, G. K.: CSI-Controlled Auto Ignition – the Best Solution for the Fuel Consumption – Versus Emission Trade-Off?, SAE Technical Paper, 2003-01-0754 (2003)

(6) Koopmans, L., Strom, H., Lundgren, S., Backlund, O., Denbratt, I.: Demonstrating a SI-HCCI-SI Mode Change on a Volvo 5-Cylinder Electronic Valve Control Engine, SAE Technical Paper, 2003-01-0753 (2003)

(7) Urata, Y., Awasaka, M., Takanashi, J., Kimura, N.: Study on Gasoline HCCI Engine Equipped with Electromagnetic Variable Valve Timing System, Aachener Kolloquium Fahrzeug- und Motorentechnik (2004)

(8) Kuboyama, T., Moriyoshi, Y., Hatamura, K., Yamada, T., Takanashi, J., Fujii, N., Urata, Y.: A Study of HCCI (Homogeneous Charge Compression Ignition) Gasoline Engine Supercharged by Exhaust Blow-Down Pressure, JSAE Annual Congress Proceedings, No. 124-08, p. 7-10 (2008) (in Japanese)

(9) Kamio, J., Kurotani, T., Sato, T., Kiyohiro, Y., Hashimoto, K., Gunji, T.: A Study on Combustion Control by Dual-Fuel Strategies, JSAE Annual Congress Proceedings, No. 55-07, p. 19-22 (2007) (in Japanese)

(10) Yamamoto, Y., Sato, G., Hayashi, T.: Development of Cylinder Pressure Sensor Integrated with Direct Injector, Honda R&D Technical Review, Vol. 24, No. 1, p. 55-59

■ Author ■



Kiminori KOMURA



Masanobu TAKAZAWA



Teruyoshi MORITA

Identification of Brake-drag Mechanism in Coasting-down Mode and Proposal of Brake-drag Stabilization and Reduction Methods

Yasushi KOBAYASHI* Yuta HIGUCHI* Naoki NAKAMURA**

ABSTRACT

The displacement of brake parts and values for brake drag were monitored during bench testing in coasting-down mode. In this mode, the brake-drag measurement process is preceded by a brake operation process while the vehicle is running warm, and at this time the brake disks undergo heat deformation as their temperatures rise. The subsequent brake-drag measurement process involves a reduction in disk temperature. This is accompanied by a return of the disk from its heat-deformed state so that the disk approaches more closely to the inner pad, and when it impinges on the pad, drag occurs. Also, when the inclination of the inner brake pad to the brake disk at that time is such that there is less clearance between the disk and the pad on the rotation input side (leading side) and there is more clearance on the rotation output side (trailing side), the pad is drawn toward the disk so that the drag suddenly increases. This force that draws the pad and disk together is the force of the vacuum pressure generated between them. This force was successfully used to both stabilize and reduce brake drag by establishing a setting that balances the load from the pad return spring, which is a structure for the purpose of reducing drag, between the leading side and trailing side, and by establishing guidelines for the amounts of caliper piston rollback and caliper body deformation.

1. Introduction

Growing demands for increasing fuel economy with a view to global environmental protection are being accompanied by proposals for various drag reduction methods for disk brakes. The mode used to measure running resistance, which is necessary for projecting fuel economy, is the coasting-down (C/D) mode[(1), (2)]. Since this was measured using actual vehicles that were being driven, measurement was influenced by various factors such as road surface and air resistance, resulting in the measured brake drag being unstable. Here, the mode was transposed to a bench test and analyzed. This reduced the variations that result from test conditions, but variations were still found in the measurement results. In other words, even though attempts were made to ascertain the actual value of brake drag for each specification, valid figures could not readily be determined. Furthermore, even when new methods for reducing drag were proposed, their effectiveness could not readily be evaluated in a quantitative manner. Stabilization of drag was therefore sought by bench testing to clarify the mechanism of brake drag during mode testing and identify the main factors that influence the resulting drag values. On that basis, specifications for further reduced drag could then be created. This development project is intended to yield a clearer understanding of front brakes of the single-piston pin-slide caliper type, which are the main type used on mass-production vehicles.

2. Development Goals

The following three points are the main objectives of this development project.

(1) Clarification of the drag mechanism
(2) Identification of the main factors in drag
(3) Proposal of methods for stabilizing and reducing drag

The stable reduction of brake drag is crucial for increasing fuel economy. Figure 1 shows the basic brake caliper structure, and Fig. 2 shows an overview of the general mechanism of brake drag as it has been understood to date. When the brake is released from its operational state, the caliper piston rolls back because of the elastic deformation of the piston seal (piston R/B) and returns to its position that is removed from the disk. At this point, the

* Automobile R&D Center
** Nissin Kogyo Co., Ltd.

pad remains in contact with the disk, and this resistance that is generated when the brake is not operating is brake drag[3), (4)]. There are also calipers now that reduce drag by a mechanism that uses a spring to move the pad away from the disk together with the piston (Figs. 3 and 4), but the measured drag was not stable.

Figure 5 shows the results for vehicle speed and brake pad temperature measurements when the C/D mode was transposed onto a bench test. It is characteristic of this approach that the brake drag measurement process is preceded by vehicle operation to warm up the engine, and this process involves repeated operation of the brakes. After that, the vehicle was allowed to decelerate naturally from 140 km/h to 0 km/h. This natural deceleration process was repeated five times and the resistance was measured with and without brake pads each time, the difference being taken as the drag value. It is apparent from this figure that the brake pad temperature rises in the process of repeated brake operation.

Figure 6 shows data on brake drag derived from measurement of a single front wheel during bench testing in C/D mode (the figure shows the data for the wheel on one side multiplied by two). During the first brake drag

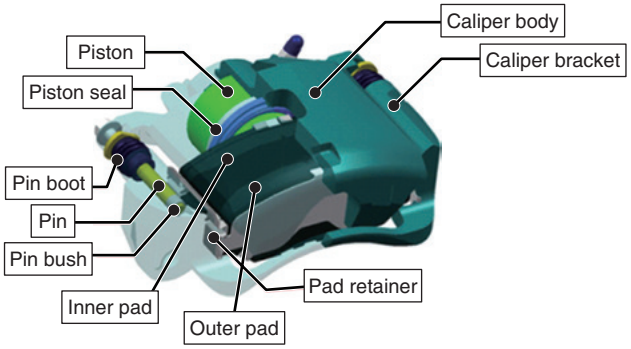


Fig. 1 Basic caliper structure

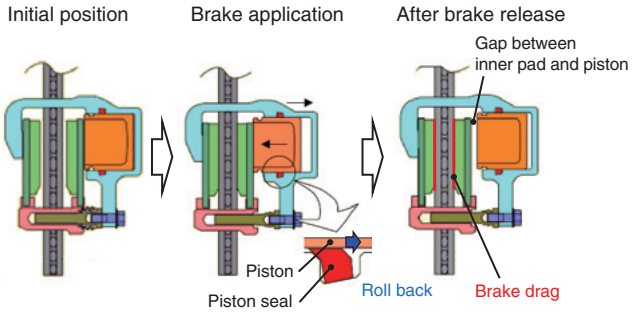


Fig. 2 Conventional brake drag theory

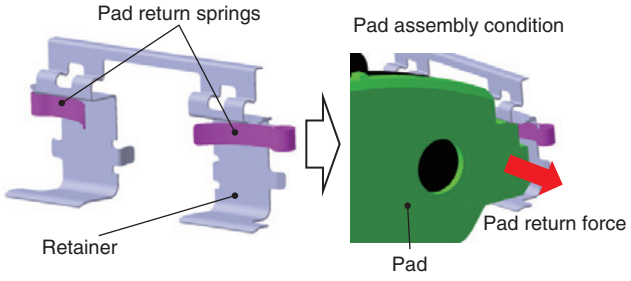


Fig. 3 Example of pad return spring structure

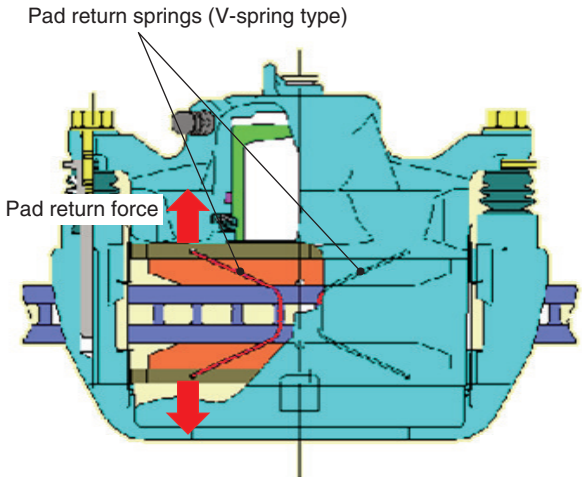


Fig. 4 Example of pad return spring structure (V-spring type)

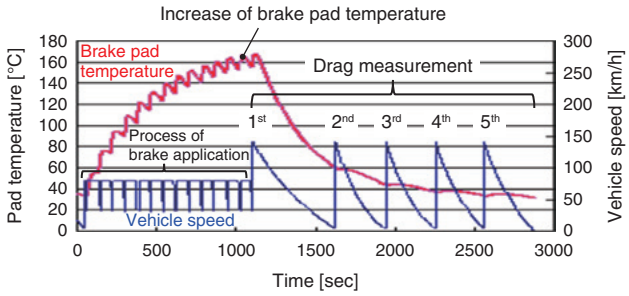


Fig. 5 Bench test condition in C/D mode

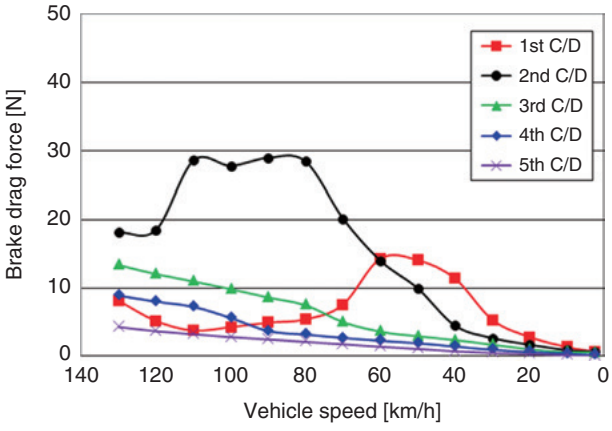


Fig. 6 Brake drag force variability in each C/D

measurement (1st C/D), the drag suddenly increased partway through. There was also instability during the second measurement, but as the drag increased, the vehicle speed decreased and the drag then diminished with it. From the third measurement on, the value decreases gradually and becomes more stable.

The purpose of this research was to identify the causal factors in these phenomena and to propose methods for stabilizing and reducing brake drag.

3. Clarification of the Brake Drag Mechanism

3.1. Confirmation of Drag by Means of a Modified Caliper

Figure 7 shows the test caliper used to clarify the drag mechanism. The purpose of this caliper is to confirm whether drag is occurring from the inner pad or from the outer pad. A mass-production caliper was therefore modified and load cells were arranged so that the resistance force tangential to the direction of rotation could be measured separately on the inner pad and the outer pad.

Figure 8 shows the measurement data for brake drag force during bench testing in C/D mode using the modified caliper. Drag force was not detected on the outer pad; it was detected only on the inner pad.

3.2. Measurement of Displacement

In order to confirm the reason that drag occurred only on the inner pad, mass-production parts were used and displacement was measured at two points each on the caliper body, inner pad, outer pad, and disk while bench testing in C/D mode. Figure 9 shows the measurement points. Figure 10 shows the position of each part measured during those processes of mode testing as obtained from those measurements.

The disk position in the second stage in Fig. 10 indicates that the disk undergoes heat deformation toward the outer pad as a result of the rise in disk temperature from the repeated brake operation process preceding brake drag measurement. Following this disk displacement, the caliper body as well as the inner pad and outer pad move toward the outside. However, as is evident from the third stage in Fig. 10, where brake drag measurement takes place, the temperature of the disk then decreases so that the disk shape, which had been deformed, return toward the inner pad. When this happens, the disk presses against the inner pad, generating drag force. This behavior is thought to be the reason that drag force was not detected except from the inner pad in Fig. 8.

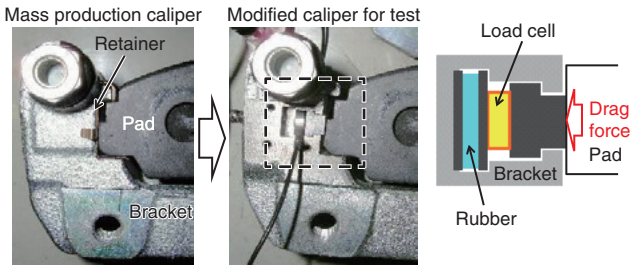


Fig. 7 Test caliper structure

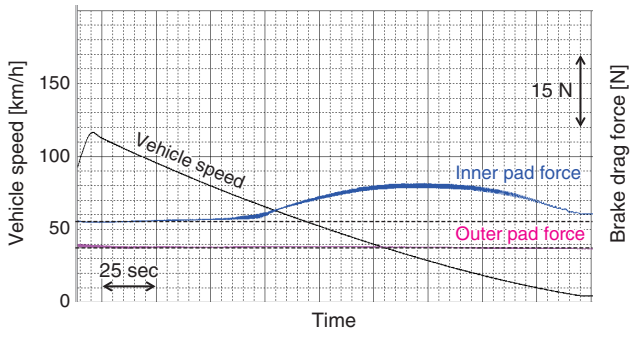


Fig. 8 Brake drag torque of each inner and outer pad in C/D mode

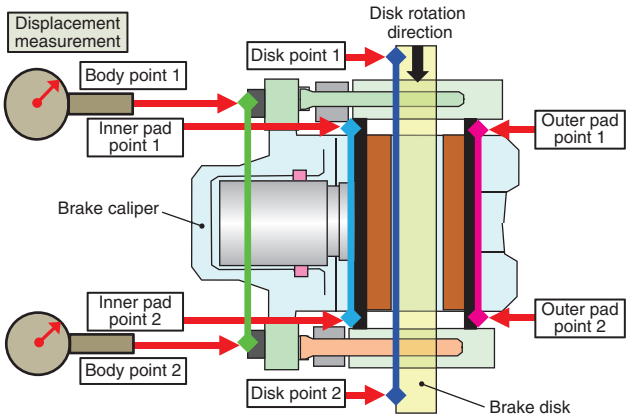


Fig. 9 Measurement points of each part

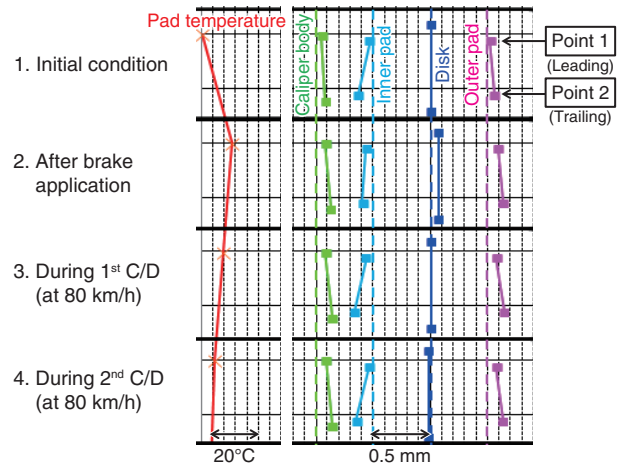


Fig. 10 Position of each part in C/D

Figure 11 shows the displacement over time resulting from heat deformation in the disk during C/D mode testing. The greatest deformation occurs on the outer-pad side of the disk during the repeated braking operation[5]. After that, the disk cools and returns to its original shape while the brake is not being operated. When this happens, some heat expansion of the disk surface in the thickness direction also occurs, and this is one reason why the disk surface is positioned more toward the inner-pad side when the first and second brake drag measurements are made than it was initially. From the third iteration on, further cooling takes place and the disk returns to its initial position. This also clarifies the reason for the drag occurring in the first and second iterations in Fig. 6, where it had been considered variations, as well as the reason why the drag diminished from the third iteration on.

3.3. Vacuum Pressure

Figure 12 shows displacement of the inner pad at the trailing side with respect to the direction of disk rotation (Point 2), displacement of the disk, vehicle speed, and drag force over time during the process of brake drag measurement in C/D mode. It is apparent that when the disk approaches more closely to the inner-pad side during brake drag measurement, the position of the inner pad on the rotation trailing side moves in the direction of the disk so that drag increases. The pad that moves in this way has a tendency to suddenly return to its starting position when the vehicle speed diminishes.

Figures 13 and 14 show the calculation results for fluid analysis of pad inclination and vacuum pressure generation. The rotation leading side of the inner pad is closer to the disk than the trailing side, and when the pad is inclined in this way, a force due to vacuum pressure is generated between the inner pad and the disk. When the pad is inclined in this way but there is sufficient clearance between it and the disk, almost no vacuum pressure is generated (Fig. 13). Figure 15 shows the results for measurement of vacuum pressure made using a pressure sensor actually embedded in the pad. The inner pad inclination was set so that the leading side closes to zero clearance at the equivalent of 160 km/h. This confirmed that drag force

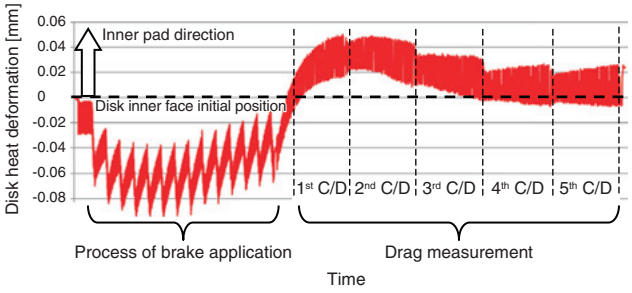


Fig. 11 Disk heat deformation in C/D

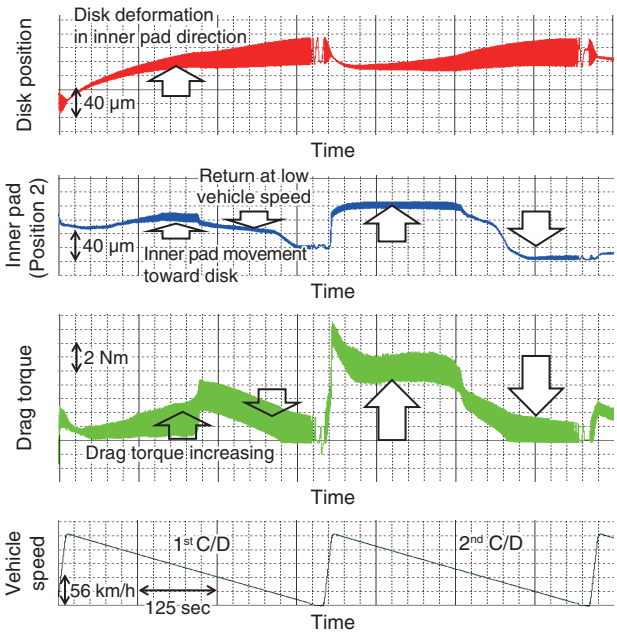


Fig. 12 Displacement behavior of each part in C/D mode

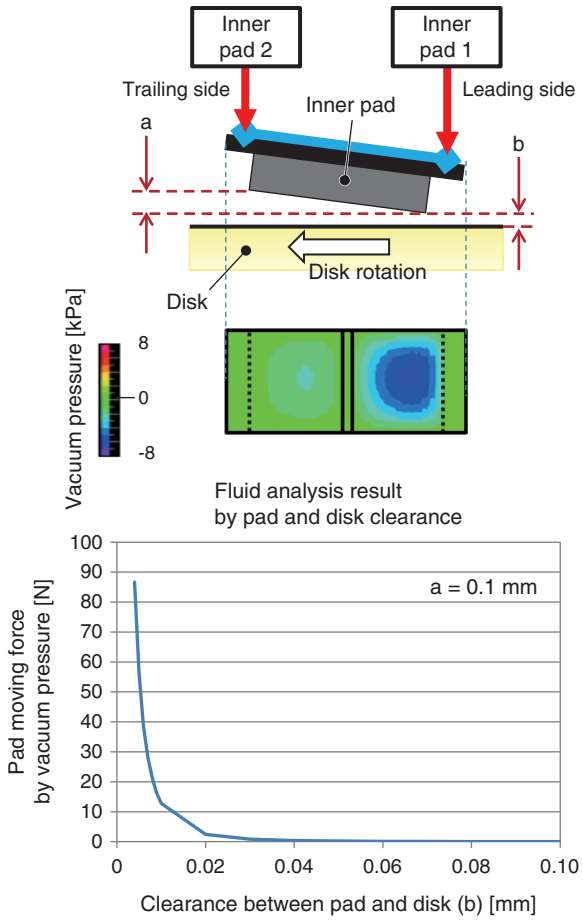


Fig. 13 Vacuum force simulation by pad and disk clearance

was generated at the same time that vacuum pressure was detected. It appears likely that the force of this vacuum pressure draws the inner pad against the disk, triggering the increase in drag.

3.4. Pad Inclination and Drag

Figure 16 shows sample data from the various brake drag measurements made to this point consolidated in terms of the inner pad inclination immediately before brake drag measurement. This shows that even when the inner pad and disk clearance immediately before brake drag measurement is small, drag does not increase except when the pad inclination is such that the clearance is smaller on the leading side than on the trailing side. As the drag tendency in Fig. 16 also shows, the magnitude of the drag values are not in direct proportion to the clearance between the inner pad and the disk or the angle of inclination of the inner pad. This suggests that the phenomenon of sudden increases or decreases in drag of the kind shown by the data in Fig. 6 is a result of the sudden movement of the inner pad shown in Fig. 12, and that the cause is vacuum pressure.

The above findings on the mechanism of brake drag in C/D mode are put into organized form as follows. Heat deformation occurs in the disk in the brake operation process during mode testing. In the state of brake non-operation that follows, the disk cools and returns to its former shape, and when the disk presses against the inner pad, drag force is generated. At that time, the inner pad is inclined to the disk at an angle such that the leading side approaches zero clearance. When this happens, vacuum pressure is generated between the disk and the inner pad, and the inner pad is suddenly drawn against the disk, resulting in the inner pad and disk coming into contact. This is thought to be why the brake drag value suddenly increases.

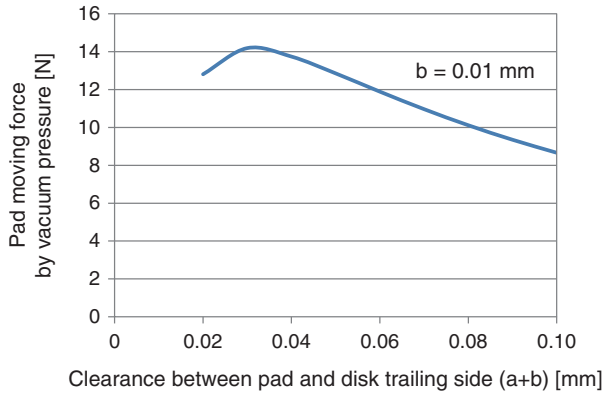


Fig. 14 Vacuum force simulation by pad inclination

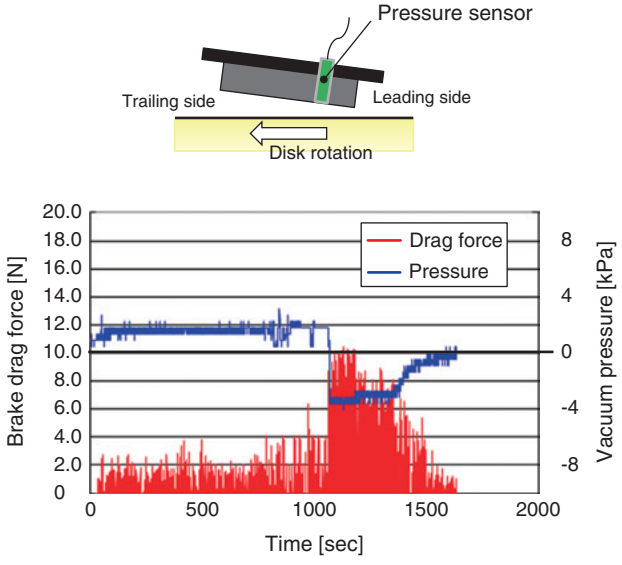


Fig. 15 Vacuum pressure between pad and disk

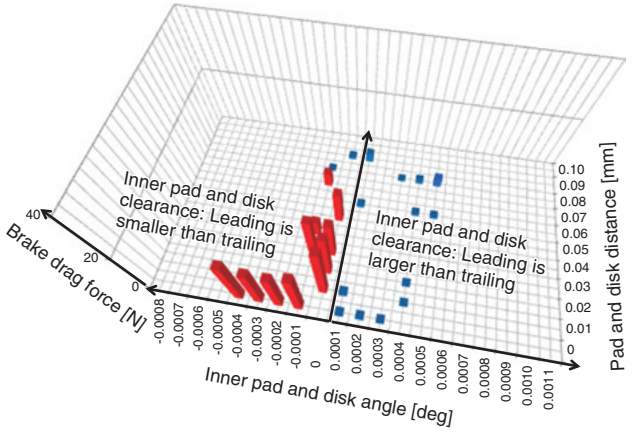


Fig. 16 Brake drag force by inner pad posture

4. Identification of the Main Factors in Drag

A parameter study of caliper component parts was carried out in order to identify the main factors causing drag to increase. This was approached in terms of the mechanism of drag generation described in the preceding chapter, and parameters related to pad inclination and to clearance between the disk and the inner pad were identified. The influence on drag value due to the accuracy of these parts and the differences between specifications were verified. There are also items that vary with the vehicle model, because of the actual vehicle layout and other such reasons, such as the caliper mounting position and the pin clearance in the caliper bracket hole (tight or loose pin configuration). The influence of these items on drag values due to the difference between leading side and trailing side was verified. The verified parameter items are

Table 1 Parameter study items for caliper

Classification	Factor	Items
Accuracy	Pad inclination	Pad return spring force
Specification	Clearance between disk and pad	Piston roll back
		Body deformation
Installation condition	Body position	Car installation position
		Tight and loose pin application
		Car installation angle

shown in Table 1.

Findings obtained by the parameter study are as follows.

The pad return spring has a considerable effect on the inner pad inclination, and the load ratio of the return spring between the leading side and trailing side was varied to confirm the influence on brake drag value (Fig. 17). It can be seen that a higher pad return load on the leading side yields a lower, more stable drag value than it does on the trailing side. The vertical axis shows the inclination of the inner pad with respect to the disk, and a correlation between the pad return spring leading-trailing load ratio and the pad inclination can also be confirmed. This was confirmed using four different types of caliper, and all displayed the same tendency. However, the return spring load must be set at or below the range of the piston rollback load, or the inner pad will push back the piston, which would end up increasing the number of invalid strokes during brake operation.

Next, Fig. 18 shows confirmation of the influence on drag from calipers with different specifications for the differences between piston R/B and caliper body deformation, which are plotted on the horizontal axis. The difference between piston R/B and caliper body deformation is the size of the clearance that can exist between the inner pad and the disk after the brakes are released. Each piston R/B and caliper body deformation value are considered important in terms of determining caliper specifications, and they are carefully managed. Since the disk experiences heat deformation during the C/D mode, further subtracting the disk heat deformation from the difference between the piston R/B and caliper body deformation yields a value that is the remaining clearance between the inner pad and the disk. When the disk heat deformation is taken as a fixed value, as in Fig. 18, the drag will be low and stable as long as a sufficient difference is maintained when caliper body deformation is subtracted from piston R/B. This shows that a greater piston R/B is preferable in order to achieve a lower drag value. When the brake is not operating, however, the piston is in a position more distant from the disk. This means that the piston has a greater distance to travel toward the disk when the brake is operated, increasing the amount of brake pedal operation and causing a reduction in operating feel. A smaller caliper body deformation will also yield lower drag, but reducing caliper body deformation will generally involve increasing its thickness and will require increasing the weight of its parts. In C/D mode operation, where the disk undergoes a process of heat deformation, reducing the heat deformation of the disk contributes to a reduction in drag. However, methods for accomplishing this will generally require increasing the heat capacity, which tends to increase the weight of the parts. What this means, therefore, is that design with an optimal balance of these factors is important for reducing brake drag and for maintaining the competitiveness of brake-part weight and operating feel.

Figure 19 shows how drag is influenced by differences in the angle at which the caliper is mounted on the vehicle with respect to the axis of rotation of the disk. It is clear that varying the angle of installation on the vehicle has little influence on drag.

Figure 20 further shows the results for drag when the caliper is installed in two different positions with respect to the axis of rotation of the disk (installed in front of the axis or behind the axis), and each of these is paired with caliper pins of two different types (tight or loose) in terms of the clearance in a radial direction between the pin and the pin hole at

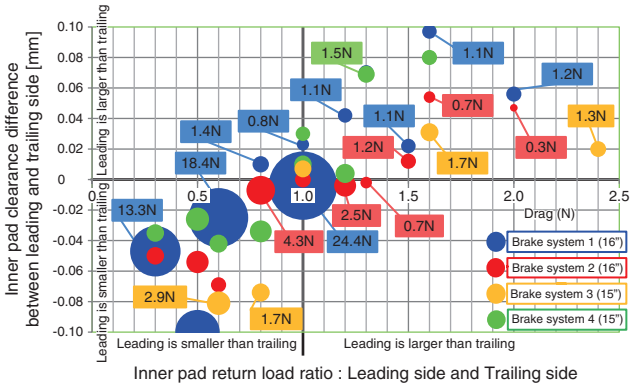


Fig. 17 Brake drag force by pad return spring load balance

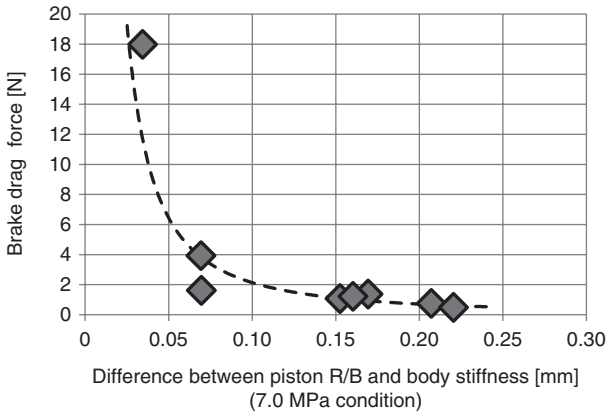


Fig. 18 Brake drag force by piston R/B and body deformation

the leading side and trailing side. The overall drag force is relatively low, at 2 N or less, indicating that these factors have only slight influence on drag. These findings show that the angle of caliper installation on the vehicle and the change in caliper pin type has only slight influence on the drag value. The results here indicate that the caliper installation angle may be varied for layout convenience according to the vehicle model and still make only a slight contribution to the drag value. It is apparent that a greater contribution is made by elements of standalone caliper performance, namely pad return load, piston R/B, and body deformation (stiffness).

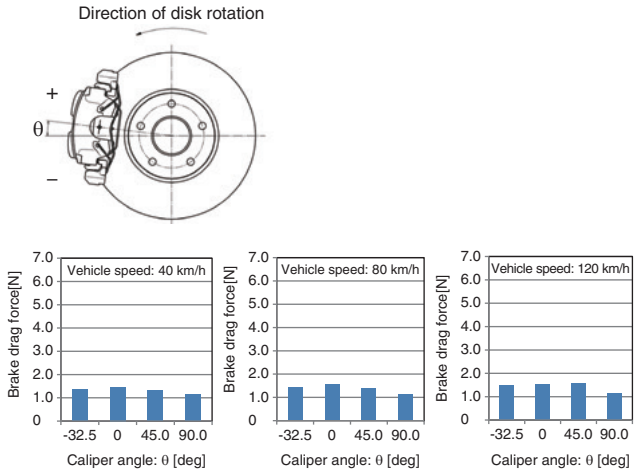


Fig. 19 Brake drag force by caliper installation angle

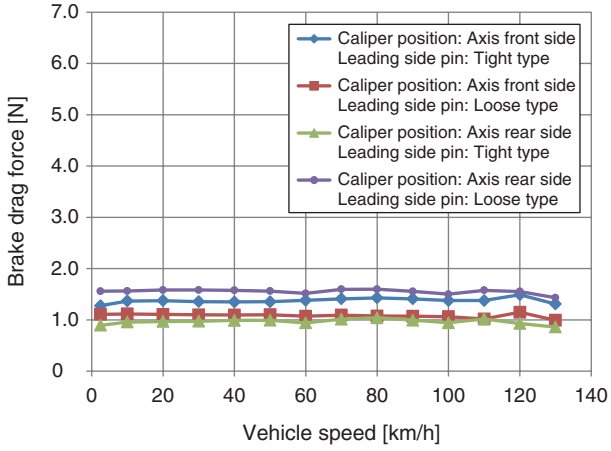


Fig. 20 Brake drag force by caliper position and pin type

5. Proposal of Drag Stabilization and Reduction Methods

In order to realize methods for brake drag stabilization and reduction, design-related guidelines regarding the main causes of drag are formulated as follows.

First, a pad return spring structure was configured. When doing so, it is necessary to configure the inner pad inclination relative to the disk so that it maintains clearance between them while open on the leading side in order not to generate vacuum pressure between the pad and the disk. In order to maintain this inclination in a stable manner, observe the tendency shown in Fig. 21, which presents an organized view of parameter study results on the pad return spring load balance. The pad return load on the leading side of the pad return spring must be greater than on the trailing side. The shaded portion of Fig. 21 is an approximate guide to the target area of configuration. The colors in the graph are blue to indicate a relatively low drag value category of 2 N or less, which is stable; orange to indicate drag from 2 N or greater to 4 N or less; and red to indicate large drag figures at that level or higher. In order to stabilize the pad return load, a coating of grease should be applied between the retainer and pad.

In order to prevent the inner pad and disk from coming into contact while the vehicle is in C/D mode, it is also necessary to assure that the value of the piston R/B with the caliper body deformation subtracted is maintained. The shaded area in Fig. 22 indicates the target for specifications.

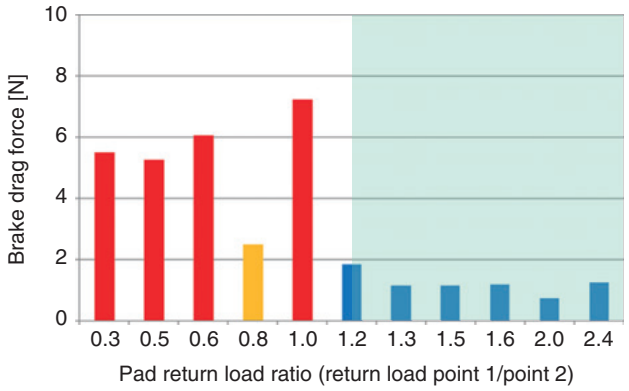


Fig. 21 Design target of pad return load balance

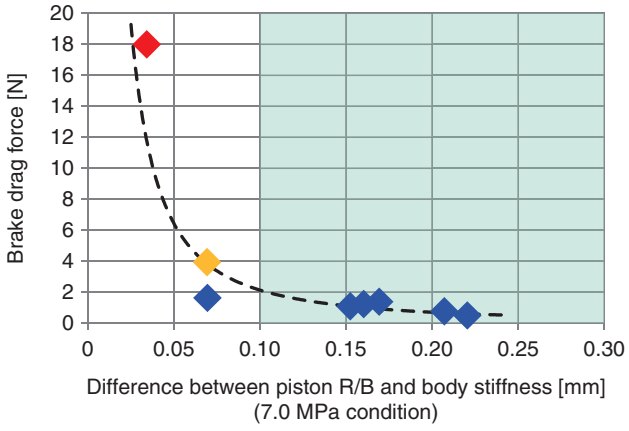


Fig. 22 Design target of piston R/B and body deformation

6. Conclusion

The mechanism of brake drag during C/D mode was clarified in bench testing. When operating in this mode, the brake disk is subject to heat deformation during the process of repeated brake operation. The disk temperature drops during the subsequent drag value measurement process, and its shape returns from its heat deformed state. It was found that drag occurs at this time when the disk and the inner pad come into contact. It was also found that when the inclination of the inner pad relative to the disk surface leaves a smaller clearance between them on the leading side than on the trailing side, vacuum pressure is generated between the inner pad and the disk. This causes the inner pad to be drawn toward the disk, where they come into contact. It was found that this can trigger the phenomenon of suddenly increasing drag values. A parameter study of the caliper was also conducted, and yielded the following findings that contribute to the stabilization and reduction of drag values.

(1) The pad return load setting on the leading side and on the trailing side of the pad return spring should have the load on the leading side higher than on the trailing side, and the inclination of the inner pad with respect to the disk should be such that clearance between them is retained on the leading side.
(2) The remainder when caliper body deformation is subtracted from piston R/B serves as a reference value that should sufficiently be maintained.
(3) The brake disk should be designed to reduce heat deformation of the disk.

References

(1) SAE J2263: Road Load Measurement Using Onboard Anemomentry and Coastdown Techniques (2008)
(2) SAE J2264: Chassis Dynamometer Simulation of Road Load Using Coastdown Techniques (2014)
(3) Gamo, Y., Suzuki, S., Kumemura, Y.: Development of the CLZ type Disk Brake Design Technology, TOKICO review, Vol. 43, No.1, p. 6-13 (2001) (in Japanese)
(4) Gamo, Y., Ishii, H., Suzuki T., Kumemura, Y.: Development of the Technology for Reducing Caliper Drag Torque, TOKICO review, Vol. 42, No.1, p. 20-26 (2001) (in Japanese)
(5) Nakai, K., Nobata, Y., Saito, N.: Dhisuku no Netsuhenkei Teigen niyoru Burekijada Teigenshuho no Kaihatsu , MAE technical report, No.14, p. 27-34 (2005) (in Japanese)

■ Author ■


Yasushi KOBAYASHI


Yuta HIGUCHI


Naoki NAKAMURA

Development of Feedback Active Noise Control Technology for Noise in Multiple Narrow Frequency Bands by Multiplexing of Single-frequency Adaptive Notch Filters

Kosuke SAKAMOTO* Toshio INOUE*

ABSTRACT

When vehicles are in motion, noise made up of noise in multiple narrow frequency bands, originating in input from the road surface, is generated in the cabin. This type of noise is termed low-frequency-band road noise, and it is desirable to reduce it in order to increase occupant comfort. The research discussed in this paper used feedback control technology as a base in the development of an active noise control technology able to simultaneously reduce noise in multiple narrow frequency bands. Methods of connecting multiple single-frequency adaptive notch filters, a type of adaptive filter, were studied. Based on the results, a method of connecting multiple filters that would mitigate mutual interference between controller transfer characteristics was proposed. This method made it possible to realize controllers with amplitude and phase characteristics in multiple narrow frequency bands corresponding to design values, and to obtain the target noise-reduction characteristic.

1. Introduction

When a vehicle is in motion, noise made up of various frequency components is generated in the cabin. Figure 1 shows the in-cabin sound pressure level (SPL) power spectra when a vehicle is driving at a constant speed over two types of rough concrete road surface. Noise of 200 Hz and below that originates in road surface input is termed low-frequency-band road noise, and is made up of noise in multiple narrow frequency bands. This is unpleasant noise that makes vehicle occupants feel uneasy, and it is desirable to reduce it simultaneously in all frequency bands. Active Noise Control (ANC) technology has attracted attention as a technology making it possible to reduce noise without significantly increasing vehicle weight. A variety of types of ANC technologies have been proposed, and a number are already in use, including an ANC technology that reduces drumming noise, a type of low-frequency-band road noise[(1)-(3)]; an ANC technology that reduces engine booming noise originating in combustion[(4)-(7)]; and an integrated ANC technology that simultaneously reduces drumming noise and engine booming noise[(8)]. This integrated ANC technology employs a single-frequency adaptive notch (SAN) filter, a type of adaptive filter, in feedback control to realize a controller that achieves the target noise attenuation performance in relation to noise in a single narrow frequency band. The use of feedback control makes it possible to reduce noise with fewer sensors than feed-forward control, which necessitates a noise source signal. However, there are few examples of the design of controllers able to simultaneously reduce noise in multiple

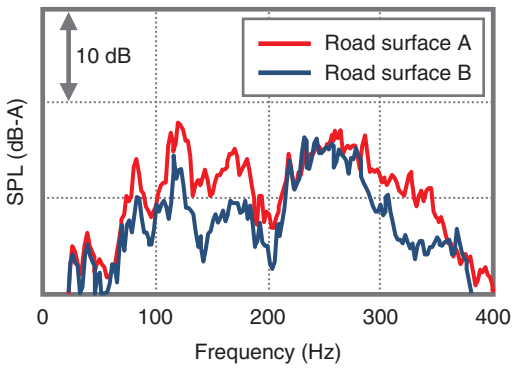


Fig. 1 Characteristics of interior noise

* Automobile R&D Center

narrow frequency bands using feedback control. The research discussed in this paper therefore newly developed a feedback-type ANC technology able to simultaneously reduce noise in multiple narrow frequency bands using multiple SAN filters, and applied the technology in a new model.

2. Control Method

2.1. Basic Principle of Feedback-type ANC

Figure 2 shows a block diagram of the generally applied feedback-type ANC. In terms of control engineering, feedback-type ANC corresponds to disturbance suppression control. With the transfer function from speaker output to microphone as plant C, the base noise as disturbance, d, and residual noise detected by the microphone as the error signal, e, the controller, G, is designed to realize a target value, r, of zero. The relationships between these parameters can be expressed by the following equation:

$$\frac{e}{d} = \frac{1}{1 + C(j\omega) \cdot G(j\omega)} \tag{1}$$

Equation (1) is termed a sensitivity function, and it expresses the frequency characteristic of disturbance suppression. Here, ω is angular velocity. Using the frequency, f, ω can be expressed as $\omega = 2\pi f$. Focusing on the denominator of the right-hand term of Eq. (1), to provide an example, if $G(j\omega)$ is set to make $C(j\omega) \cdot G(j\omega)$ 1, then sensitivity is expressed by Eq. (2):

$$\frac{e}{d} = \frac{1}{2} \tag{2}$$

This shows a 6 dB reduction in noise of frequency f. By contrast, when $C(j\omega) \cdot G(j\omega)$ approaches -1, because the denominator approaches zero,

$$\frac{e}{d} \to \infty \tag{3}$$

This is synonymous with an infinite increase in the amplitude of noise, and means divergence. Generally, $C(j\omega)$ and $G(j\omega)$ each change in response to the frequency, f, but it is desirable to set $G(j\omega)$ to attempt to ensure that the denominator, $1 + C(j\omega) \cdot G(j\omega)$ does not approach zero.

Here, the design of controllers for feedback control using the vehicle's acoustic characteristic as the plant will be considered. The acoustic characteristic of the vehicle will be assumed to include the speaker output characteristic, the microphone detection characteristic, and the acoustic characteristic from the speaker to the microphone. Taking into consideration dead-time, the delay time due to the distance from the speaker to the microphone, the resonance characteristic originating in the structure of the speaker, and reverberation originating in the fact that the vehicle cabin is a closed space, the acoustic characteristic in the cabin is generally a numerous order plant incorporating dead-time. Figure 3 shows an example of a vehicle acoustic characteristic with an audio speaker positioned at the door as the input and a microphone for control use positioned at the roof as the output. The crests and troughs of the amplitude characteristic display a high-frequency order, and the change in the characteristic as frequency increases is delayed by dead-time. A variety of methods are available for the design of controllers for feedback control, including the loop-shaping method, the Smith method, and the H∞ control method[9)-(11)]. However, these methods assume low-frequency-order controllers for low-frequency plants. The reports referenced above focus exclusively on the frequency bands that represent the control targets and approximate the plant in low-frequency-order models, examining the control effect in combination with the controller design methods. As an issue of this method, the reports indicate that while a control effect is obtained in the simulation in the specific frequency band that is focused on, in the actual vehicle modeling error results in a decline in the disturbance suppression characteristic and an increase in the amplitude of disturbance. Given this, it can be considered challenging to expand these methods and realize a controller that would display a design frequency characteristic enabling it to simultaneously respond to multiple narrow frequency bands.

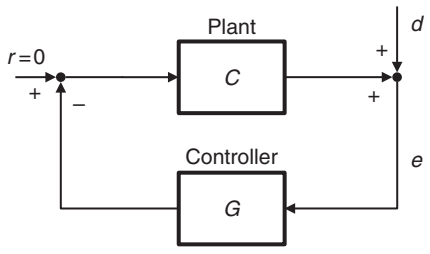


Fig. 2 Block diagram of feedback control

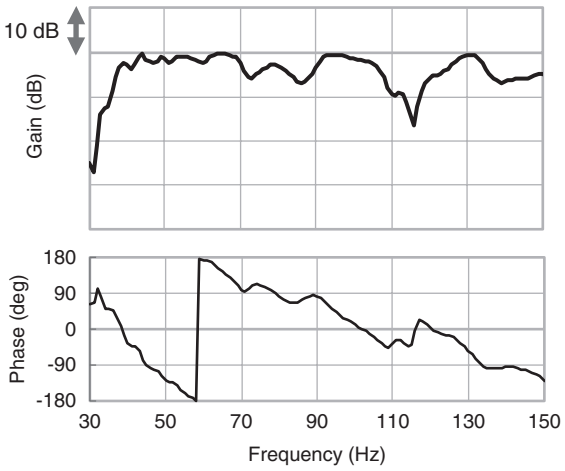


Fig. 3 Acoustic characteristic of automobile audio speaker

2.2. Feedback-type ANC using Multiple SAN Filters

Feedback-type ANC employing single SAN filter has been proposed as a method of reducing noise in a specific narrow frequency band[8]. This system is made up of a signal extractor that focuses on the signal of the specific narrow frequency band, a reference signal generator with conditioned amplitude and phase, and a conditioner that multiplies the adaptive filter coefficient obtained from the signal extractor by the conditioned reference signal to produce output. Figure 4 shows a block diagram of the system.

Here, A and B are the adaptive filter coefficients for signal extraction, ω is the angular velocity of the frequency being focused on, Φ_g is the phase conditioning characteristic, and K_g is the amplitude conditioner.

The update equations for adaptive filters A and B are expressed as follows:

$$A_{n+1} = A_n - \mu \cdot e \cdot \cos(\omega t) \tag{4}$$

$$B_{n+1} = B_n - \mu \cdot e \cdot \sin(\omega t) \tag{5}$$

Here, μ is termed the step size parameter, and is the coefficient that adjusts the degree of updating of the adaptive filters. The merit of this method is that the setting of the target frequency for extraction and the conditioning of phase and amplitude are easy, and these procedures can be realized with low computational load and low delay. Figure 5 shows the frequency response characteristic of a controller using this method. As the figure shows, it is possible to adjust the amplitude of the frequency-passing signal extraction by changing μ. In controller design, the amplitude of the passing frequency is adjusted by μ, the phase characteristic is adjusted by Φ_g, and the amplitude characteristic is independently adjusted by K_g, and Φ_g and K_g are uniquely calculated based on Eq. (1), the acoustic characteristic, and the target amount of reduction of noise.

2.3. Multiplexing Frequencies using Feedback-type ANC employing Multiple SAN Filters

The research discussed here studied a method of simultaneously reducing noise in multiple narrow frequency bands using feedback-type ANC employing multiple SAN filters. The first consideration was that the SAN filter signal extractor and the amplitude and phase conditioner could simply be connected in parallel. For the sake of simplicity, the adaptive filter coefficient for signal extraction will be termed W, the reference signal x, the degree of adjustment of phase Φ_g, the degree of adjustment of amplitude K_g, and the corrected reference signal, x' the phase of which has been adjusted by Φ_g. Figure 6 shows a block diagram.

The relationship between these variables and the variables shown in the block diagram in Fig. 4 is expressed as follows:

$$W = A + \mathrm{j} \cdot B \tag{6}$$

$$x = \cos(\omega t) - \mathrm{j} \cdot \sin(\omega t) = \mathrm{e}^{-\mathrm{j}\omega t} \tag{7}$$

$$x' = \cos(\omega t + \Phi_g) - \mathrm{j} \cdot \sin(\omega t + \Phi_g) = \mathrm{e}^{-\mathrm{j}\omega t - \Phi_g} \tag{8}$$

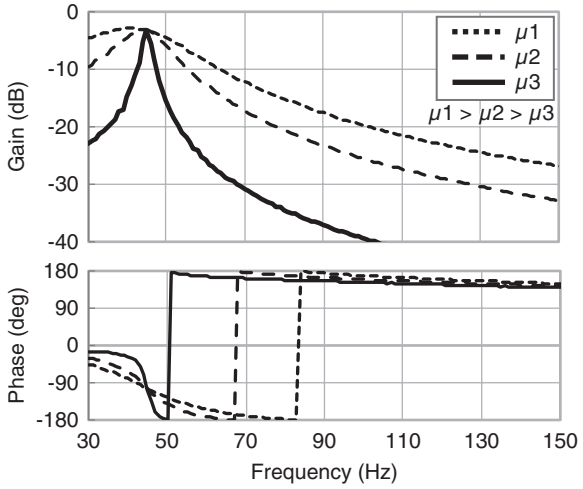


Fig. 5 Frequency response of SAN feedback controller

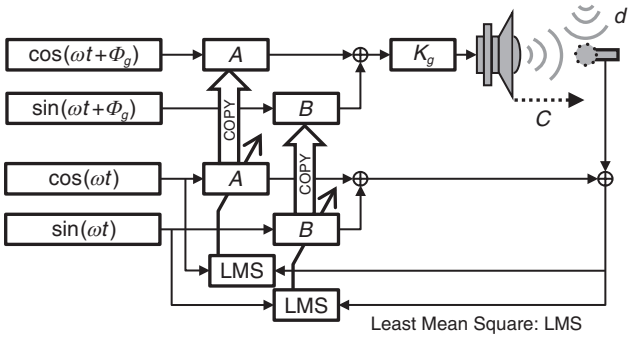


Fig. 4 Block diagram of SAN feedback control

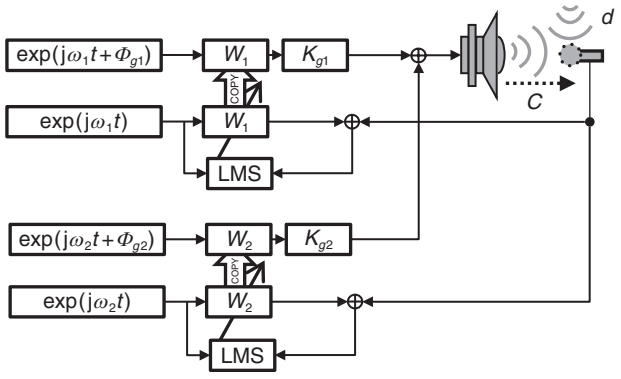


Fig. 6 Block diagram of parallel SAN feedback control

Because the sum of the feedback-type ANC controller characteristics produced by the two SAN filters is the overall controller characteristic in this method, the overall characteristic is simple to calculate. Controllers were designed to reduce the center frequencies of the 45 Hz and 125 Hz frequency bands by 4 dB each, and their frequency response characteristics were calculated. Figure 7 shows the characteristic for the 45 Hz-band controller only, the characteristic for the 125 Hz-band controller only, and the characteristic when the two controllers are connected in parallel.

Figure 7 shows that there is a difference between the frequency response characteristics obtained from the controllers in isolation and the characteristic for the controllers connected in parallel. This is because the characteristic of the 45 Hz-band controller at 125 Hz is added to the characteristic of the 125 Hz-band controller. Similarly, the 125 Hz-band controller changes the controller characteristic in the 45 Hz band. This indicated that a controller with the design frequency characteristic would not be realized, and that as a result the target level of noise reduction would not be achieved. A logic that would mitigate the effect of a controller for a specific frequency band on the characteristics of a controller for another frequency band was therefore necessary. Two methods of employing the characteristic of multiple SAN filters signal extractor to mitigate interference between controllers were proposed. Together with the parallel error connection type discussed above, this represented three control methods. The characteristics and effects of these three control methods were studied, and the results are shown below.

(1) Parallel error connection type: Two controllers based on SAN filters were connected in parallel. This is a simple configuration, because the overall controller characteristic can be calculated as the sum of the characteristics of the two controllers.

(2) Cascade error connection type: A cascade error connection type, in which the residual signal extracted from one SAN filter was employed as the input for the other SAN filter, was used. Because the results of signal extraction for one SAN filter were transmitted to the other filter, the potential for interference between the results of signal extraction between the filters was minimized, indicating that the effect of the characteristic of a controller for one frequency band on the characteristic of the controller for another frequency band would be mitigated.

(3) Common error connection type: The method of integrating the results of signal extraction results for the two SAN filters was termed the common error connection type. There was a possibility of interference between the extraction results for the SAN filters, but prospects seemed good for mitigation of interference between the characteristics of the controllers for each frequency band.

Figure 8 shows a block diagram of the cascade error connection type, and Fig. 9 shows a block diagram of the common error connection type.

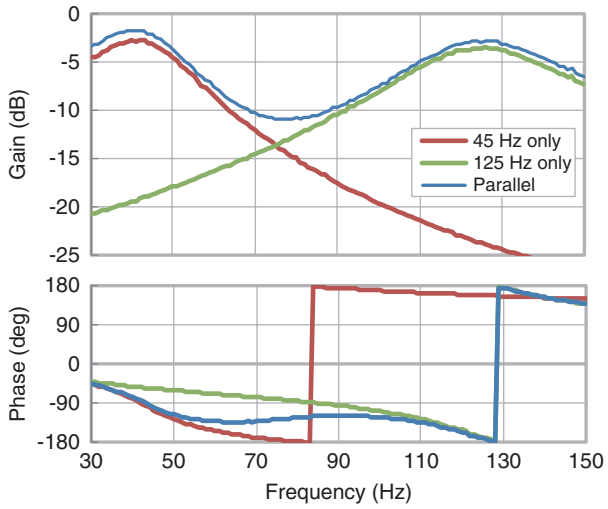


Fig. 7 Frequency response of parallel SAN feedback controllers

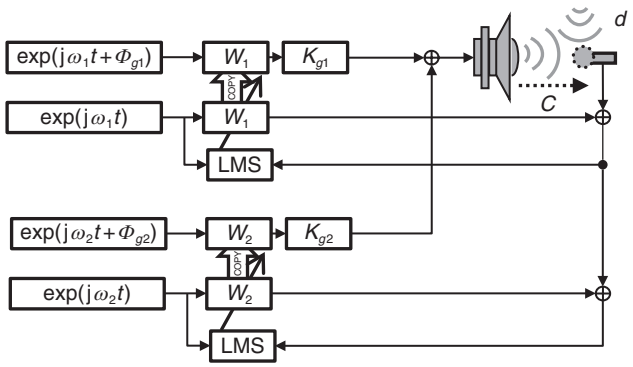


Fig. 8 Block diagram of cascade SAN feedback control

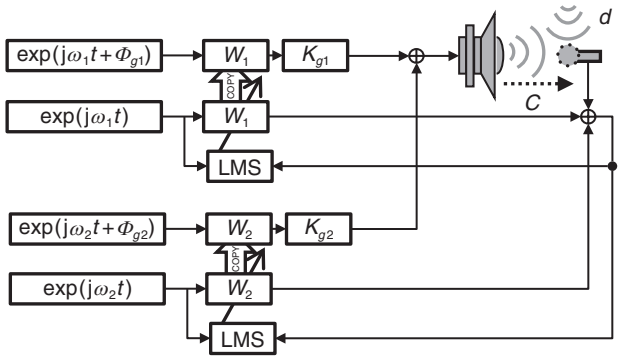


Fig. 9 Block diagram of common SAN feedback control

3. Verification of Controller Characteristics

3.1. Controller Simulation

With the target for the amount of change occurring as a result of the combination of the controllers for the two frequency bands set as within ±0.1 dB, feedback-type ANC controllers were designed using the three connection methods discussed in Chapter 2, based on the same design values as indicated in Chapter 2, and their design values (amplitude characteristics) were calculated. Figure 10 shows the results.

As the results indicate, there is a divergence from design values for the controller characteristic in the case of the parallel error connection type and the cascade error connection type. However, in the case of the common error connection type, a frequency characteristic corresponding to the design values was obtained for both the 45 Hz and the 125 Hz frequency bands. While the design characteristic was realized in the 45 Hz band using the cascade error connection type, there was a divergence in the 125 Hz band. These results indicated that when combining multiple SAN filters, the connection of signal extractors using the common error connection type would help to ensure the realization of a controller characteristic true to design values.

3.2. Detailed Analysis of Common Error Connection Type

In order to verify the effectiveness of the common error connection type, the 45 Hz and 125 Hz controller characteristics were analyzed via simulation, with control gain K_{g1} and K_{g2} set to zero, as shown in Fig. 9. The results were compared with the controller characteristic when control was applied simultaneously to the 45 and the 125 Hz bands. Figure 11 shows the results.

Comparing the 45 Hz and the 125 Hz controller characteristics in the 125 Hz band, there is an attenuation of the amplitude characteristic of more than 40 dB and a difference of less than 1%. This means that the divergence from design values for the controller characteristic has been controlled to within ±0.1 dB. In the case of the parallel error connection type, attenuation was around 20 dB and there was a divergence of around 10% when the controller characteristics were added. In addition to mitigating the mutual effect of controller characteristics in different frequency bands, the common error connection type has the same effect as simply adding the controller characteristics, and it is therefore considered possible to realize a controller characteristic corresponding to the design values.

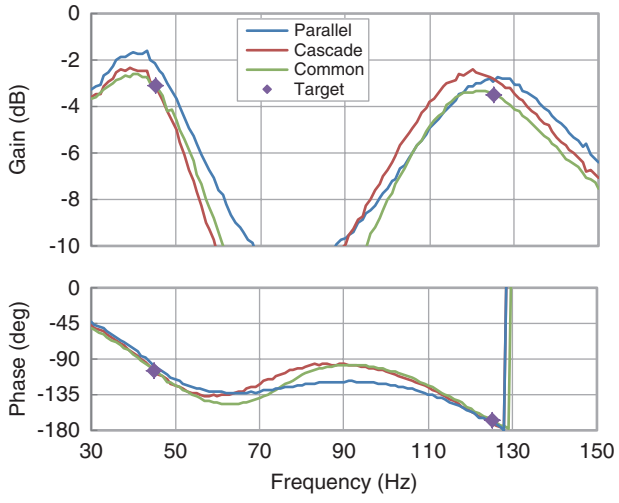


Fig. 10 Frequency response of three connection types

3.3. Study of Feasibility of System using Conventional Methods

The SAN filters were replaced with Finite Impulse Response (FIR) and Infinite Impulse Response (IIR) filters, both digital filter types in standard use, in order to test the feasibility of realizing the system with alternative filters. The least squares method, weighted for the controller characteristic for the common error connection type from 20 Hz to 200 Hz, was used to find the coefficients. Figure 12 shows the results. Even when an 800-tap FIR

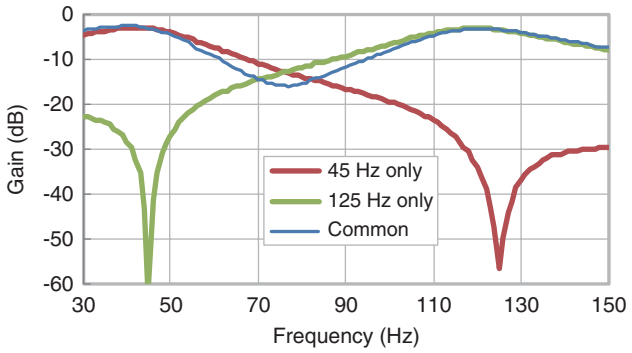


Fig. 11 Frequency response of decomposed common error-type SAN feedback controller

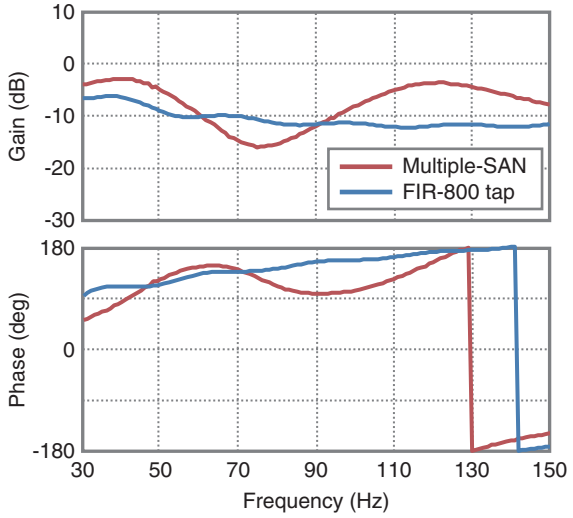


Fig. 12 Frequency response of multiple SAN filters and FIR filter

filter was employed, the characteristic obtained was as shown in the graph, and when an IIR was employed, it was not possible to obtain stable filter coefficients. The method of combining two SAN filters as discussed in this paper makes it possible to obtain a controller characteristic that realizes design values with minimal computation, and can be considered superior to conventional methods.

4. Control Performance

Control performance when the developed method was employed in a vehicle was studied. Feedback controllers were designed based on the acoustic characteristic shown in Fig. 3, with the targets for noise reduction set at -4.5 dB in the 45 Hz band and -3 dB in the 125 Hz band. Figure 13 shows the open loop function determined by simulation. The results show that it was possible to ensure a gain margin, indicating that the controller is stable. Figure 14 shows the sensitivity function. The target noise-reduction characteristic was realized in both the 45 Hz and the 125 Hz bands. The controller realized by the control design was applied in an actual vehicle, and control performance was studied. Figure 15 shows the results of noise measurements taken while driving at 60 km/h over a rough concrete surface and Fig. 16 shows measurements taken while driving at 40 km/h over a rough asphalt surface. The results demonstrate that the proposed method simultaneously reduces noise in the 45 Hz and 125 Hz narrow frequency bands, and realizes control performance equivalent to the sensitivity function.

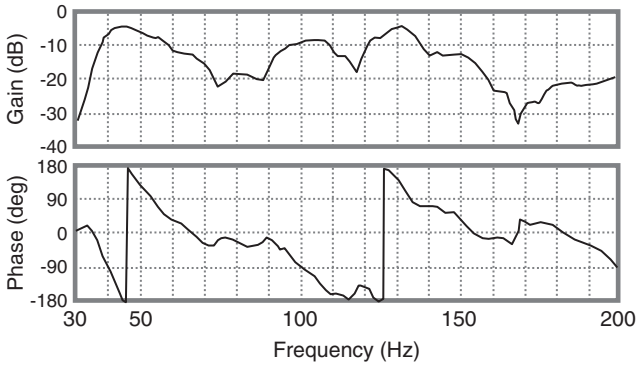


Fig. 13 Open loop function of common error-type SAN feedback controller

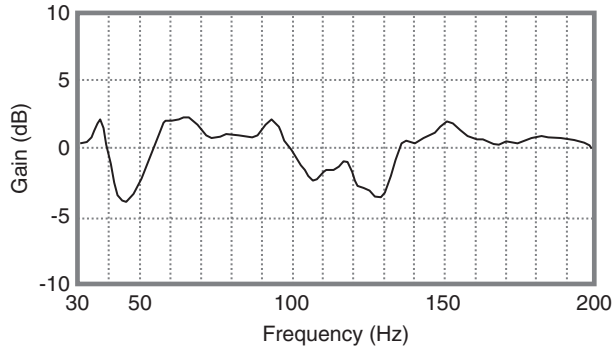


Fig. 14 Sensitivity function of common error-type SAN feedback controller

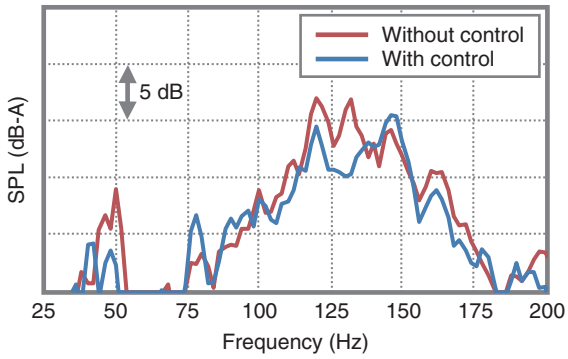


Fig. 15 Control performance 1 of common error-type SAN feedback controller on rough concrete surface

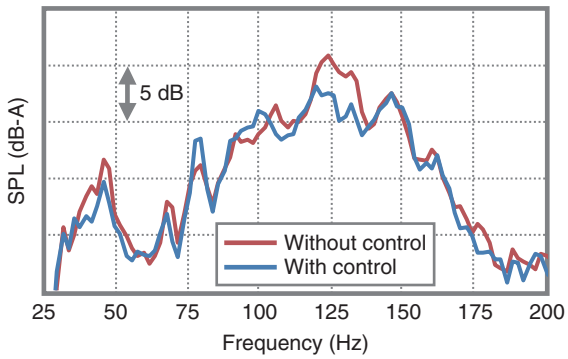


Fig. 16 Control performance 2 of common error-type SAN feedback controller on rough asphalt surface

5. Conclusion

A feedback ANC technology employing SAN filters that is able to simultaneously reduce noise in multiple narrow frequency bands has been developed. It is simple to adjust the controller characteristic for the frequency characteristics and acoustic characteristics of noise in different vehicles, and it is possible to stably obtain the target control characteristic. This paper has discussed results obtained by combining two SAN filters, but it would be possible to reduce noise in three or more narrow frequency bands by combining three or more SAN filters using the common error connection type.

References

(1) Sano, H., Inoue, T., Takahashi, A., Ishihara, D., Yamashita, T., Terai, K.: Active Control System for Low Frequency Road Noise Combined with an Audio System, HONDA R&D Technical Review, Vol. 12, No. 2, p. 71-80

(2) Inoue, T., Sano, H., Takahashi, A., Yamashita, T., Ishihara, D., Nakamura, M., Terai, K., Nakamura, Y.: Development of active control system for low frequency road noise, JSAE Annual Congress Proceedings, No. 111-00, p. 13-16, (2000) (in Japanese)

(3) Sano, H., Inoue, T., Takahashi, A., Terai, K., Nakamura, Y.: Active control system for low-frequency road noise combined with an audio system, Speech and Audio Processing, IEEE Transactions on, Vol. 9, Issue 7, p. 755-763 (2001)

(4) Inoue, T., Takahashi, A., Minowa, S., Sano, H.: Development of Active Noise Control System for Engine Booming Noise, Honda R&D Technical Review, Vol. 15, No. 2, p. 201-208

(5) Inoue, T., Takahashi, A,. Minowa, S., Sano, H., Onishi, M., Nakamura, Y.: Development of Active Booming Noise Control System Applying Adaptive Notch Filter, JSAE Annual Congress Proceedings, No. 84-03, p. 1-4, (2003) (in Japanese)

(6) Inoue, T.: Sharyo no akutibu souon seigyo gijutsu ni tsuite, JSAE Symposium Text, No. 08-10, p. 26-31, (2010) (in Japanese)

(7) Inoue, T.: Active Sound Control Technology in Automobiles, Journal of INCE/J, Vol. 34, No. 5, p. 336-341 (2010) (in Japanese)

(8) Inoue, T., Takahashi, A., Sakamoto, K., Kobayashi, Y.: Integrated Active Noise Control System for Low-frequency Noise in Automobiles, Honda R&D Technical Review, Vol. 23, No. 2, p. 121-128

(9) Widrow, B., Stearns, S. D.: Adaptive Signal Processing, Prentice Hall, Englewood Cliffs, New Jersey (1985)

(10) Adachi, S., Sano, H.: Modeling, control and experiment of a feedback active noise control system for free sound fields, JSME International Journal, Series C, 45-2, p. 409-416 (2002)

(11) Nishida, T., Sakamoto, K., Inoue, T., Adachi, S.: A comparative study of feedback active noise control for low frequency noise, The SICE Annual Conference (2013)

■ Author ■



Kosuke SAKAMOTO



Toshio INOUE

Development of Multiscale Computational Model for Carrier Mobility in GaAs Nanopillars with Twin Boundaries

Mitsumoto KAWAI*

ABSTRACT

A multiscale computational model for the calculation of the effect of (111) twin boundaries on electron mobility in GaAs nanopillars synthesized using the Selective Area Metal Organic Vapor Phase Epitaxy (SA-MOVPE) method has been developed. The Non-equilibrium Green's function method is applied in the calculation of quantum conductance in order to explicitly incorporate the effect of twin defect morphology. Quantum conductance is converted to a thermally-averaged scattering factor to connect quantum conductance to mobility. With this newly introduced factor, electron mobility can be corrected for a twin boundary scattering model. The calculated electron mobility for GaAs nanopillars synthesized under standard SA-MOVPE conditions with a mean twin spacing of 2.48 nm was 1000 $cm^2/V/s$. In addition, the contribution of twin boundary scattering to the reduction of electron mobility was estimated to be 60% of the effect of the scattering factors overall.

1. Introduction

Nanopillar-shaped semiconductor elements of diameters of several tens to several hundreds of nm are manufactured for a variety of applications, including photovoltaic generation devices, sensors, and thermoelectric conversion devices[1]. When heterojunction interfaces are employed in semiconductor elements, misfit dislocation can occur as a result of lattice mismatch[2]. Dislocation results in lattice vacancies, producing significant resistance to the electromigration that is important to device performance. In an attempt to avoid this issue, nanopillars are being synthesized with diameters smaller than the dislocation intervals. Broadly speaking, two methods of synthesis are employed. These are the vapor liquid solid (VLS) method and the selective-area metal-organic vapor phase epitaxy (SA-MOVPE) method[1]. The VLS method uses Au and other catalysts. By contrast, the SA-MOVPE method does not use a catalyst, being a "bottom-up" method of film growth in which the area of deposition of the supplied gas on the substrate is restricted by the application of an amorphous film to sections of the substrate. Whichever method is employed, high-density twin structures have been observed perpendicular to the direction of electromigration (the direction of film growth)[3]. Because these twin structures are stacking faults, they represent electromigration barriers, and this is analogous to a decline in thermal conductivity due to the influence of stacking faults[4]. Devices using compound semiconductors incorporating nanopillar shapes are designed on the basis of an expectation of high electron mobility. It is of concern that the reduction of electron mobility resulting from the effect of twin structures may have a significant effect on device performance. In addition, test measurement of electron mobility in nanopillars is challenging due to the miniscule nature of the parameter, and quantitative analyses are not conducted within the range surveyed in this study.

Focusing on GaAs nanopillars synthesized under standard conditions using the SA-MOVPE method, the research discussed in this paper developed a method of quantifying electron mobility able to explicitly consider the effect of high-density twin structures on mobility. Using this method, the study calculated electron mobility in nanopillars incorporating twin structures and the ratio represented by the effect of twin structures to total scattering factors.

* Fundamental Technology Research Center

2. Twin Structures in GaAs Semiconductor Nanopillars

The subjects of computation in this study, GaAs nanopillars along the [$\bar{1}\bar{1}\bar{1}$] growth direction, were grown epitaxially on a GaAs(111)B substrate using the SA-MOVPE method. In terms of growth conditions, the substrate temperature was 750°C, hydrogen was used as the carrier gas, the Ga source was trimethylgallium, at a partial pressure of P_{Ga} = 1×10^{-6} atm, and the As source was arsine, at a partial pressure of P_{As} = 1×10^{-4} atm. These conditions will be referred to as "standard conditions" below[1), (3)].

Figure 1 shows the results of observation of nanopillars using a scanning electron microscope (SEM). Hexagonal nanopillars have grown on the GaAs(111)B substrate (left), with a growth direction of [$\bar{1}\bar{1}\bar{1}$] and a side orientation of {110} (right).

In order to determine the morphology of the twin structures in these nanopillars, transmission electron microscope (TEM) observations were conducted, and the results were analyzed. Figure 2 shows the results of TEM observation at an incidence of [01$\bar{1}$]. The results show high-density twin faces perpendicular to the [$\bar{1}\bar{1}\bar{1}$] growth direction (upper). A TEM photograph taken at a magnification of 500,000x was subjected to image processing to magnify it to approximately 1,000,000x, revealing rotational twins termed 3C structures (middle) and twins termed 2H structures (AB structures) (lower). However, the repeating continuous ABAB structures termed wurtzite structures were not observed. Here, A, B, and C express the positional relationship of Ga-As atom pairs to the [$\bar{1}\bar{1}\bar{1}$] growth direction.

In order to determine the tendency of the spacing between the twin faces, measurements of spacing were conducted using the results of TEM observations, and the results were subjected to statistical processing. Figure 3 shows a section of a TEM photograph used in the measurement of twin spacing and a histogram showing the results of statistical analysis of measured values (horizontal axis: twin spacing). The mean spacing was 2.48 nm, with a standard deviation of 1.64 nm (total number of measurements: 248). More than 80% of the twins were 3C structures, with less than 20% 2H structures.

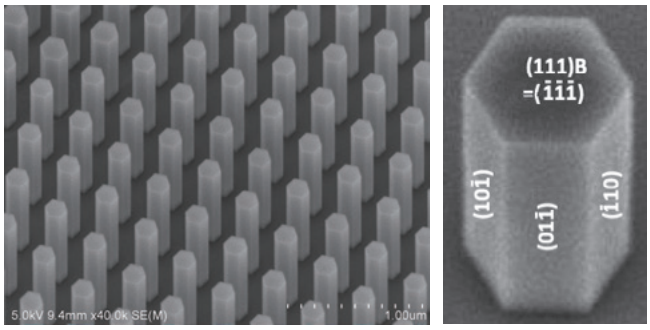


Fig. 1 Macroscopic SEM image (incidence of 30°) of synthesized GaAs nanopillars grown on (111) B GaAs substrate (left) and magnified SEM image of one nanopillar with plane directions (right)

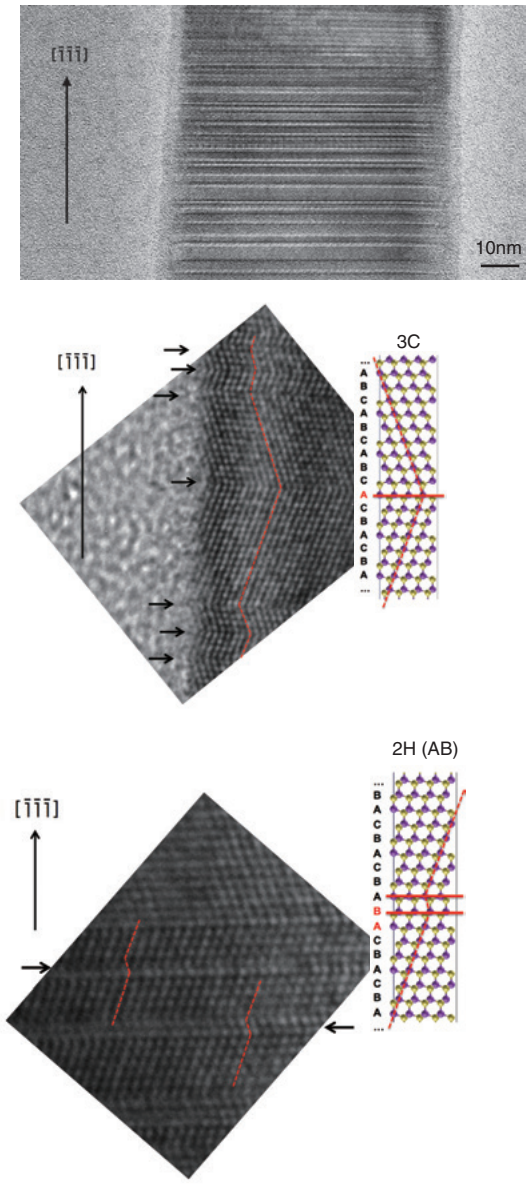


Fig. 2 Cross-sectional TEM image of multi-twinned GaAs nanopillar (upper) 3C-type twin boundaries which have so-called ABCBA stacking sequences from bottom to top (z-direction) (middle), and 2H-type (AB-stacking) twin boundaries which have so-called ABCABABC sequences (lower). Purple and yellow spheres represent Ga and As atoms, respectively.

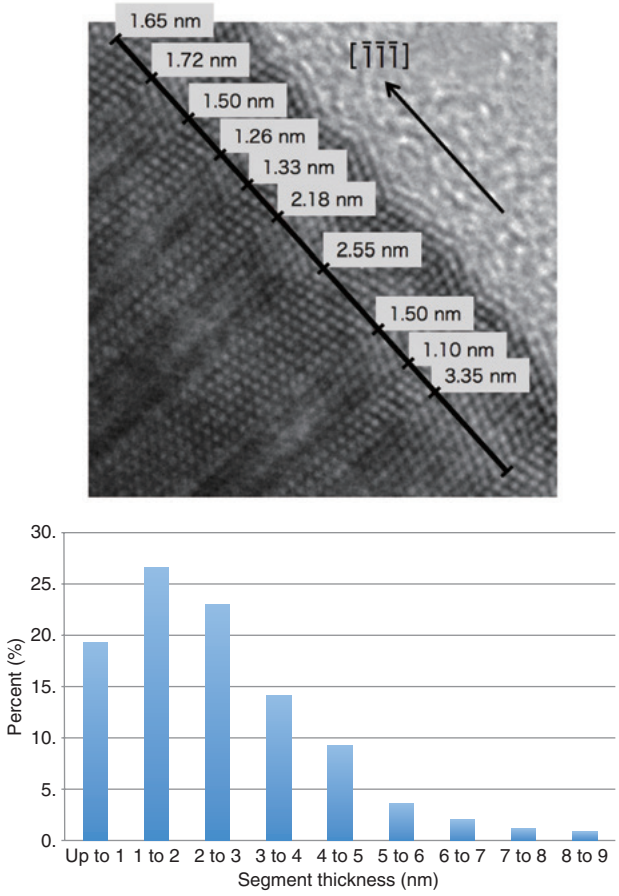


Fig. 3 TEM image of measured twin spacing along [1̄1̄1̄] direction (upper), and histogram of twin spacing with 248 sampling points, average twin spacing of 2.48 nm (lower)

3. Calculation Methods

The classical picture of electron mobility is as a ratio between drift velocity, v_{drift}, and electrical field, E, defined as follows:

$$M \equiv \frac{\langle v_{drift} \rangle}{-E} \tag{1}$$

The effect of twin structures on this indicator of the ease of electron motion was quantified. In establishing the theoretical formula, it was essential to explicitly incorporate the effect of the twin structures. In order to do so, quantum conductance was first determined using first-principle calculations that did not incorporate test values (Section 3.1.), using atomic models with a variety of twin structures. In other words, electron scattering was evaluated with electrons treated as wave motion. Next, quantum conductance was converted to a scattering factor in order to multiscale by incorporating it in the equation for evaluation of mobility (the classical picture)(Section 3.2.).

In addition, Section 3.3. will discuss the relationship between other factors that affect electron mobility and the effect of twin structures.

3.1. Method of Calculation of Quantum Conductance

The non-equilibrium Green's function (NEGF[5]) method based on the density-functional approach was employed in the calculation of quantum conductance. SIESTA[6]-[8] was used as the computation code. In this code, inner shell electrons are treated as norm-conserving pseudopotentials, and the linear combination of the numerical atomic orbital (LCAO) method is used as the basis function. GGA-PBE[9] was used as the exchange-correlation functional, energy cutoff was 300 Rydberg, and the k-point (coordinates on the reciprocal lattice space) division was 31x31x1, based on the Monkhorst–Pack method[10]. The values calculated directly using the NEGF method represent transmittance $T(k, \epsilon)$, a function of the k-points and energy, ϵ. The following relationship holds between transmittance and quantum conductance, $G(k, \epsilon)$[11]:

$$G(k, \epsilon) \equiv \frac{I}{V} \int_k \int_\epsilon T(k, \epsilon)\, d\epsilon dk \tag{2}$$

As an example of the set-ups employed in the computations, Fig. 4 shows a model with a stacking fault in the first layer (a 3C twin structure). In the NEGF method, electrodes are set as sources of electron influx and efflux, and the effects of these phenomena are considered in the form of self-energy in Green's function. Because of this, the atomic models that form the subject of the computations are broadly divided into three sections. These are sections regarded as left and right electrodes, and a section to which the electrons from the electrodes are sent (the section in which the electrons scatter). The difference in electrical potential

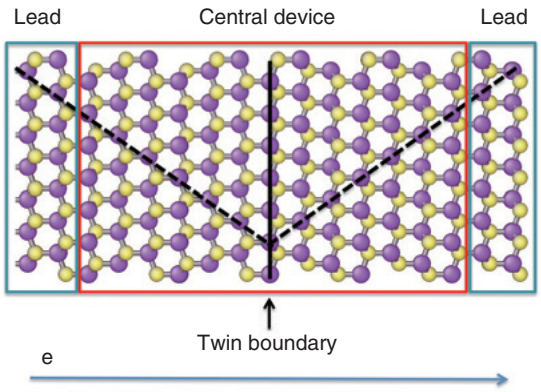


Fig. 4 Configuration of system treated by NEGF method with left and right leads along z-axis (electron transfer direction: [1̄1̄1̄]), under two-dimensional periodic boundary conditions on xy plane. Yellow spheres indicate arsenic, and purple spheres indicate gallium

between these electrodes is considered as a difference in chemical potential between the electrodes. In other words, with ε_f as Fermi energy, a potential difference of $\varepsilon_f \pm {}^{eV}/_{2}$ is imparted to the left and right electrodes.

In this model, in which the twin faces under consideration are in one layer, an atomic model incorporating 13 layers of Ga-As as single pairs in the electron scattering section (the twin section) and two layers of Ga-As in each of the left and right electrode sections, in contact with the 13 layers, was employed. The total number of atoms was 136 (2x2x(13+2+2)x2).

3.2. Method of Conversion of Quantum Conductance to Mobility

This section will first provide an overview of the understanding of the scattering of electrons by twin faces in the classical picture, and next discuss the method of linking it to quantum conductance (multiscaling), the quantum picture.

In the classical picture, twin structures are considered the sole scattering factor, and electrons are temporally accelerated over time, τ from one twin face to the next twin face by the electrical field, E. If the electrical field is assumed to be small, the electron drift velocity, v_{drift}, can be evaluated using the following equation:

$$\langle v_{drift} \rangle = -\frac{1}{2} \cdot \frac{eE\tau}{m} \tag{3}$$

e: Elementary charge
E: Electrical field
m: Mass of electrons
τ: Time between scattering events

The mean is expressed as 1/2 of the coefficients. This is because all of the electrons conducted to the nanopillars necessarily arrive at and are scattered by the twin faces, the scattering sources, and the electron drift velocity immediately following scattering by twin faces can be regarded as basically zero and the electrons can be regarded as accelerating linearly at $v_{drift} \propto E$ until reaching the next scattering body.

Next, time between scattering events, τ, was modeled. Because drift velocity is extremely small compared to heat velocity, time between scattering events is independent of the electrical field, and if time between scattering events is assumed to be rate-controlled by heat velocity, it can be expressed using the following equation:

$$\tau = \frac{\lambda}{\sqrt{\langle v \cdot v \rangle}} = \frac{\lambda\sqrt{m}}{\sqrt{\langle mv \cdot v \rangle}} = \frac{\lambda\sqrt{m}}{\sqrt{k_B T}} \tag{4}$$

λ: Distance between scattering events
k_B : Boltzmann constant
T : Temperature

Here, the nanopillars are regarded as one-dimensional.

Given this, from Eq. (1), (3) and (4), mobility, M[m^2/V/s], can be expressed as follows:

$$M \equiv \frac{\langle v_{drift} \rangle}{-E} = \frac{e\lambda}{2\sqrt{mk_B T}} \tag{5}$$

In addition, terming electron density n, current density, J, can be expressed as follows:

$$J = -en\langle v_{drift} \rangle = \frac{e^2 n\lambda E}{2\sqrt{mk_B T}} \tag{6}$$

Using Eq. (6), electron conductance in the classical picture, σ[Ω^{-1}m^{-1}], can be expressed by Eq. (7), demonstrating that the relationship between mobility and conductance is maintained.

$$\sigma \equiv \frac{J}{E} = \frac{e^2 n\lambda}{2\sqrt{mk_B T}} enM \tag{7}$$

Equation (5), derived as indicated above as the scattering factor for the twin structures incorporated in the nanopillars, corresponds well with the equation for evaluation of electron mobility obtained from tests[12], as will be discussed below. Equation (12) in Reference (12) formularizes mobility, M_l, as shown below, with l as the mean free path (in Reference (12), mobility is expressed as μ).

$$M_l = ({}^{4}/_{3})el\frac{1}{\sqrt{2\pi mk_B T}} \tag{8}$$

The ratio between Eq. (5) and Eq. (8) is 1.064, as shown below (because the twin structures are the only scattering bodies, λ=l.).

$$\frac{M_l}{M} = \frac{{}^{4}/_{3}\sqrt{2\pi}}{{}^{1}/_{2}} \approx 1.064$$

The scattering coefficient $s(k_\perp, \epsilon)$, generated by quantum conductance obtained from NEGF computations, is defined by Eq. (9) below.

$$s(k_\perp, \epsilon) \equiv 1 - \frac{G(k_\perp, \epsilon)}{G_0(k_\perp, \epsilon)} \tag{9}$$

Here, G_0, G are the quantum conductances when twin structures do not exist and do exist, respectively.

The respective quantum conduction values were employed to determine k-point and energy functions using the NEGF method (Section 3.1.). $k_\perp \equiv (k_x, k_y)$ indicates that periodic boundary conditions are maintained on the k_x-k_y plane on the reciprocal lattice space before and after scattering events, because twin faces exist perpendicular to the z-axis, the direction of electron motion. It is therefore possible to designate the state before and after scattering

events using (k_x, k_y).

At the limits of the scattering coefficient defined by Equation (9), $s(k_\perp, \epsilon)$=0 indicates that there is no scattering by twin structures, and $s(k_\perp, \epsilon)$=1 indicates that twin structures are an extremely strong scattering factor.

In the actual computations, average thermal equilibrium was calculated for quantum conductance at each k-point and energy level within the range in which electrons existed, as shown by Eq. (10) below. Because of this, the Fermi distribution function, which expresses the probability of the existence of electrons with energy ϵ in this state of thermal equilibrium, was employed. Temperature, T, was set at 300 K.

$$\langle s \rangle = \frac{\sum_{k_\perp} \int_\mu^{+\infty} f(\epsilon) G_0(k_\perp, \epsilon) s(k_\perp, \epsilon) d\epsilon}{\sum_{k_\perp} \int_\mu^{+\infty} f(\epsilon) G_0(k_\perp, \epsilon) d\epsilon} \quad (10)$$

f(ϵ): Fermi distribution function

$$f(\epsilon) = \left(1 + e^{\frac{\epsilon - \mu}{kBT}}\right)^{-1} \quad (11)$$

μ: Chemical potential

The method of introducing the scattering coefficients calculated using Eq. (10) to electron mobility and conductivity is discussed below. Because the effect of twin structures differs between structures, computations were corrected using scattering coefficients that took into consideration the effect of each structure. In concrete terms, correction was applied to the twin spacing, λ_{TB}, using the scattering factor, $\langle s \rangle$, taking into consideration quantum scattering, to create mean free paths. Equations (12) and (13) below were used for correction in relation to mobility and conductivity.

$$M = \frac{e}{2\sqrt{mk_BT}} \cdot \frac{\lambda_{TB}}{\langle s \rangle} \quad (12)$$

$$\sigma = \frac{e^2 n}{2\sqrt{mk_BT}} \cdot \frac{\lambda_{TB}}{\langle s \rangle} \quad (13)$$

By this means, the model was multiscaled by incorporating the effect of quantum conductance in twin structures in the evaluation equation (the classical picture).

3.3. Relationship with Other Factors Affecting Mobility

Section 3.2. discussed a method of computation of mobility that treated twin structures as the only scattering factor. However, in actuality there are numerous other factors that produce electron scattering. Aggregate mobility, M_{total} , which takes these other factors into consideration, is calculated using Eq. 14[13]. The right-hand term of the equation expresses the individual mobilities that are affected by the respective scattering factors.

$$M_{total}^{-1} = M_{e-TB}^{-1} + M_{e-e}^{-1} + M_{e-phonon}^{-1} + M_{e-dopant}^{-1} + M_{e-surface}^{-1} + \cdots \quad (14)$$

M_{e-TB}^{-1}: Twin structures

M_{e-e}^{-1}: Scattering between electrons

$M_{e-phonon}^{-1}$: Phonon scattering

$M_{e-dopant}^{-1}$: Scattering on dopant

$M_{e-surface}^{-1}$: Surface scattering

With the sum of the terms on the right-hand side, excluding the first term, as the effect of factors other than twin structures, it was possible to use measurement results for a thin GaAs film in which twin structures were not observed[14]. To determine M_{total}^{-1}, M=$M_{e\text{-}TB}$ was first obtained using Eq. (12), following which Eq. (14) was employed, using the abovementioned mobility measurement results. The ratio of the effect of the twin structures to total scattering factors was also determined, as $M_{e\text{-}TB}/M_{total}$.

4. Results and Considerations

This section will discuss the results of calculations conducted by incorporating the quantum conductance obtained from NEGF calculations in the developed method of quantitative analysis of electron mobility [Eq. (12)]. Section 4.1. will discuss the results of calculations of quantum conductance, and Section 4.2. will discuss the conversion of the quantum conductance results into electron mobility.

4.1. Results of Calculation of Quantum Conductance

Figures 5 and 6 show the results of calculations of quantum conductance for 3C and 2H structures, considered as the basic twin structures. In the atomic model, the z-axis (=[$\bar{1}\bar{1}\bar{1}$]) was the direction of electron motion. In the results, the vertical axis shows the ratio between these measurements and conductance when no twin structures exist and the horizontal axis shows energy. Quantum conductance was reduced by both types of twin structure, indicating an effect as a scattering source. However, no systematic effect was observed for either of the twin structures.

Figure 7 shows the results of analysis of quantum conductance for each k-point in a structure with one 3C twin face (the structure on the left in the upper figure in Fig. 5). Scattering behavior on this twin face differs depending on the k-point. Given this, the effect of twin faces on quantum conductance is dependent on the k-points and energy. In other words, even if the spacing between the twin structures is the same, if the structures themselves differ, quantum conductance differs.

Figures 8 and 9 show the results of conversion of the results shown in Figs. 5 and 6 to current-voltage characteristic (I-V characteristic) using Eq. (2). Within the scope of the twin face spacings calculated here, no systematic differences were observed in the spacings of the 3C type (Fig. 8). However, in the case of the 2H type (Fig. 9), a tendency for current flow to be retarded as the number of twin faces increases was observed at the number of faces under study [elec (no twin structures) → 3C → 2H → 2AB → 3AB].

Next, characteristics identified based on the results of the analysis of nanopillars discussed in Chapter 2 were studied with a particular focus on twin spacings, and 14 types of representative nanopillar twin structure model were formulated using two different compositions. Based on the histogram shown in Fig. 3, the ratios of spacings between twin faces were as follows: 40% were 2 nm or less (ABC and AB stacks), 20% were 2-3 nm (ABCx2), 20% were 3-5 nm (ABCx3), and 20% were 5 nm or more (ABCx5). Because AB stacks (2H) were observed in some of the nanopillars, AB stacks were incorporated in the representative models of twin spacings at the above

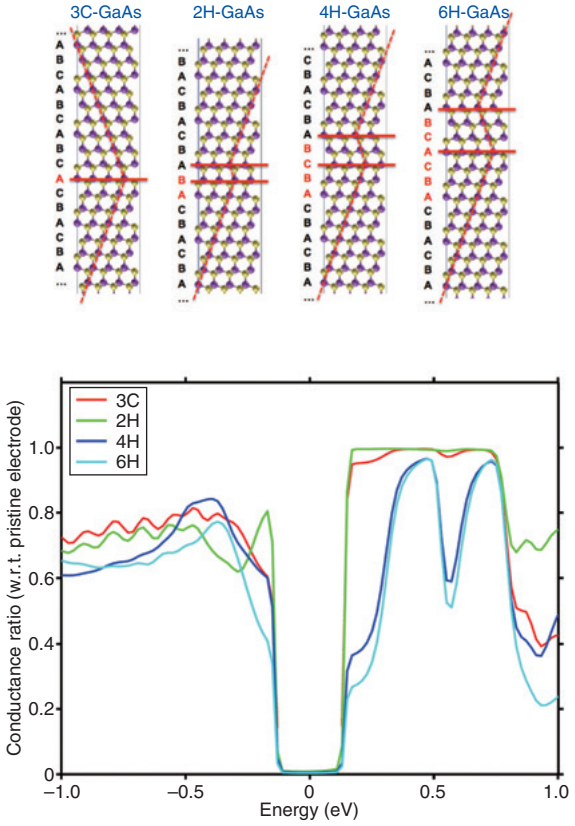


Fig. 5 Quantum conductance calculated using NEGF in different 3C-type structures. Schematic showing GaAs crystals with different types of 3C twin boundaries (upper). Calculated quantum conductance with respect to energy (lower).

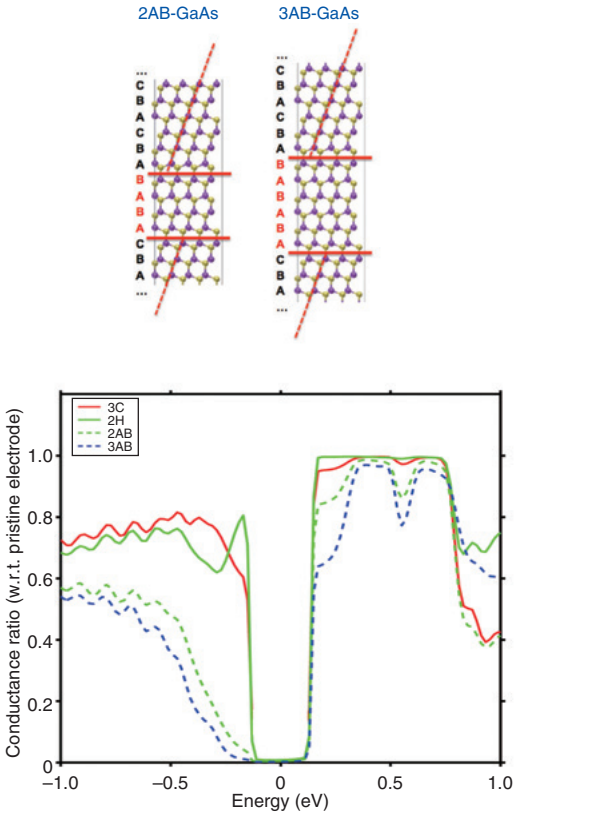


Fig. 6 Quantum conductance calculated by NEGF in different AB-type structures. Schematic showing GaAs crystals with different types of AB twin boundaries (upper). Calculated quantum conductance with respect to energy (lower).

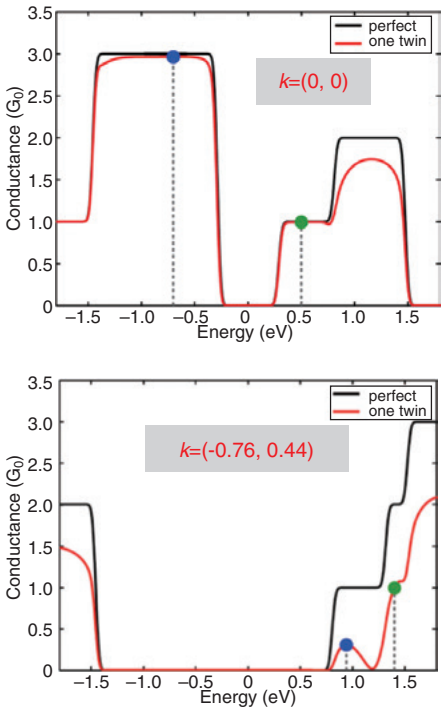


Fig. 7 Quantum conductance with respect to k-points in 3C twin morphology

ratios. The AB stacks were inserted at the respective twin boundaries in each model. Figure 10 shows an example of the representative models of twin structures. The left-hand side shows ordered twin spacings, and the right-hand side shows random twin spacings.

Figure 11 shows the results of calculation of quantum conductance for these arrangements of twin structure spacing. Valence bands were observed as an effect of the arrangement of the twin spacings (shown by the arrows in the figures), but the overall tendency was almost the same. In addition, no conspicuous difference was observed when AB structures were present or absent.

Given these results, the arrangement of the spacing of twin structures can be considered not to have a significant effect on quantum conductance within the scope of the computations conducted in this study.

4.2. Results of Conversion of Quantum Conductance to Mobility

Section 4.1. discussed the computation of quantum conductance using atomic models, with explicit consideration of the effect of twin structures. Figure 12 shows the results, including results for quantum

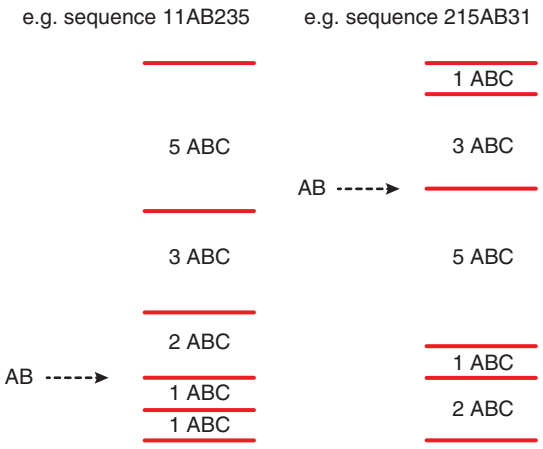


Fig. 10 Examples of representative twin sequence models AB stacks are inserted in 3C boundaries (red line) Ordered twin sequence from bottom to top with AB-stacking between “1ABC” and “2ABC” (left); Random twin sequence with AB-stacking between “5ABC” and “3ABC” (right)

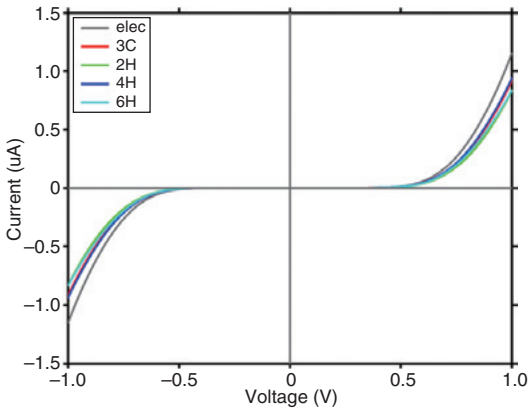


Fig. 8 I-V curve for 3C-type twin boundaries

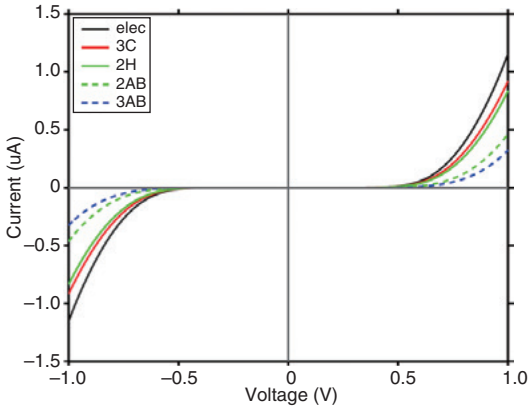


Fig. 9 I-V curve for AB-type twin boundaries

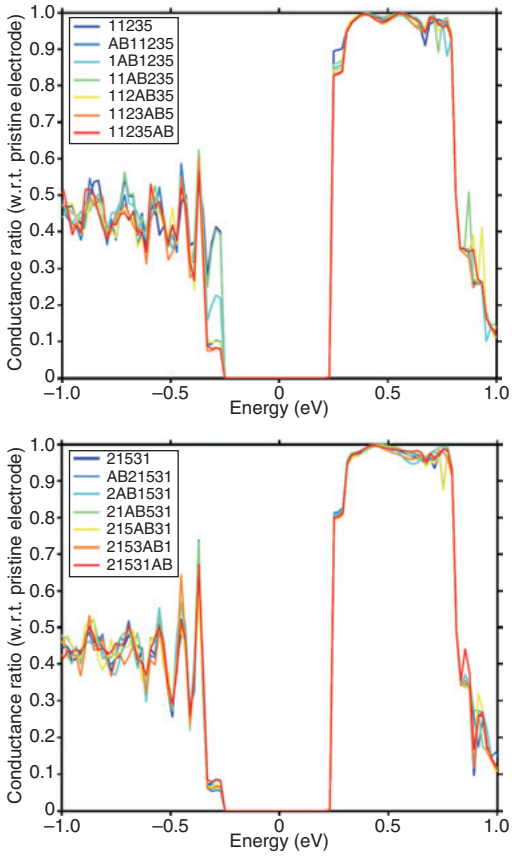


Fig. 11 Quantum conductance with respect to energy in representative models: Ordered twin sequences (upper); Random twin sequences (lower)

conductance computed using different combinations of twin spacings, converted to figures for mobility using Eq. (12). The converted figures for mobility are proportional to the mean twin spacing, matching the intuitive conclusion from the classical picture. Next, the ratio of the effect of twin structures to all scattering factors was computed using Eq. (14). Results obtained from Fig. 12 were used as the first right-hand term of the equation. The other right-hand terms were provided by the results of measurements of electron mobility in a thin GaAs film (without twin structures) [14]. From Fig. 3, the mean twin spacing of nanopillars synthesized under standard conditions is approximately 2.48 nm, indicating from Fig. 12 that it was possible to predict $M_{e\text{-}TB} \approx 1600$ cm^2/V/s . In Reference (14), electron mobility in a thin GaAs film without twin structures is ($n \approx 10^{18}$/cm^3, $T = 300$ K), $M_{e-e}^{-1} + M_{e-phonon}^{-1} + M_{e-dopant}^{-1} + M_{e-surface}^{-1} + \cdots \approx 2500$ cm^2/V/s. Given this, electron mobility following the introduction of twin structures was computed as $M_{total} \approx 1000$ cm^2/V/s. In addition, the effect of twin structures on electron mobility as a percentage of all scattering factors was computed as approximately 60%.

The results discussed above suggest that at a mean twin spacing of 2.48 nm, electron mobility declines by 60% against figures for a GaAs film with no twin structures, indicating that the existence of high-density twin structures is a factor that exerts a significant effect on electron mobility.

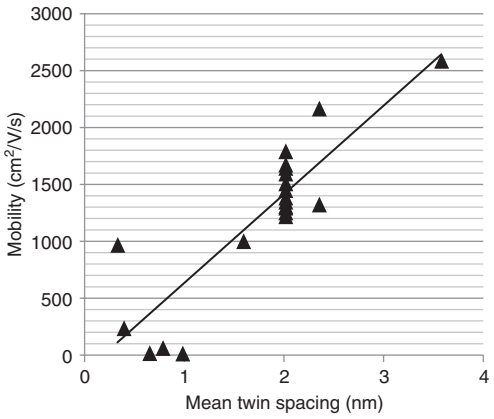


Fig. 12 Predicted mobility as a function of mean twin spacing

5. Conclusion

A method of quantitative prediction of the effect of twin structures on electron mobility has been developed. Twin structures were explicitly considered using the NEGF method based on first-principle calculations. Multiscaling was effected by converting figures for quantum conductance calculated using the NEGF method to scattering coefficients and incorporating these in an equation for evaluation of electron mobility. This made it possible to calculate electron mobility in nanopillars in which twin structures exist.

The results of calculations using the developed method indicated that electron mobility in GaAs semiconductor nanopillars grown using the SA–MOVPE method under standard conditions (twin spacing of approximately 2.48 nm) would be 1000 cm^2/V/s. Given that electron mobility was measured at 2500 cm^2/V/s in a thin GaAs film in which twin structures did not exist, the ratio of the effect of twin structures to the effect of total scattering factors was calculated as approximately 60%. It was therefore possible to separately evaluate the effect of scattering by twin structures.

By means of this research, computational materials science has clarified the mechanism of a phenomenon that has been challenging to study in tests, and the results obtained will find application in a variety of areas, including materials development and device design.

References

(1) Goto, H., Nosaki, K., Tomioka, K., Hara, S., Hiruma, K., Motohisa, J., Fukui, T.: Growth of Core-Shell InP Nanowires for Photovoltaic Application by Selective-Area Metal Organic Vapor Phase Epitaxy, Appl. Phys. Express 2, 035004 (2009)

(2) Kavanagh, K. L.: Misfit dislocations in nanowire heterostructures, Semicond. Sci. Technol. 25, 024006 (2010)

(3) Ikejiri, K., Sato, T., Yoshida, H., Hiruma, K., Motohisa, J., Hara, S., Fukui, T.: Growth characteristics of GaAs nanowires obtained by selective area metal-organic vapour-phase epitaxy, Nanotechnology 19, 265604 (2008)

(4) Guthy, C., Nam, C.-Y., Fischer, J. E.: Unusually low thermal conductivity of gallium nitride nanowires, J. Appl. Phys. 103, 064319 (2008)

(5) Haug, H., Jauho, A.-P.: Quantum Kinetics in Transport and Optics of Semiconductors, Springer Series in Solid-State Science, Springer (1996)

(6) Rocha, A. R., García-Suárez, V. M., Bailey, S., Lambert, C., Ferrer, J., Sanvito, S.: Spin and molecular electronics in atomically generated orbital landscapes, Phys. Rev. B 73, 085414 (2006)

(7) Sánchez-Portal, D., Ordejón, P., Artacho, E., Soler, J. M.: Density-Functional Method for Very Large Systems with LCAO Basis Sets, Int. J. Quantum Chem., Vol. 65, Issue 5, p. 453-461 (1997)

(8) Soler, J. M., Artacho, E., Gale, J. D., García, A., Junquera, J., Ordejón, P., Sánchez-Portal, D.: The SIESTA method for ab initio order-N materials simulation, J. Phys.: Condens. Matter 14, p. 2745-2779 (2002)

(9) Perdew, J. P., Burke, K., Ernzerhof, M.: Generalized Gradient Approximation Made Simple, Phys. Rev. Lett. 77, 3865 (1996)

(10) Monkhorst, H. J., Pack, J. D.: Special points for

Brillouin-zone integrations, Phys. Rev. B 13, 5188 (1976)
(11) Buttiker, M.: Symmetry of electrical conduction, IBM J. Res. Develop., 32(3), p. 317-334 (1988)
(12) Pearson, G. L., Bardeen, J.: Electrical properties of pure silicon and silicon alloys containing boron and phosphorus, Phys. Rev., 75, p. 865-883 (1949)
(13) Li, S. S.: Semiconductor Physical Electronics, Second Edition, Springer, 697 p. (2006)
(14) Levinshtein, M., Rumyanstev, S., Shur, M. S., Handbook Series on Semiconductor Parameters, Vol. 1, p. 85, World Scientific (1996)

■ Author ■



Mitsumoto KAWAI

Honda R&D Co., Ltd.
Honda R&D Technical Paper Committee

Motorcycle R&D Center
Automobile R&D Center
Power Products R&D Center
Aircraft Engine R&D Center
Fundamental Technology Research Center

Editorial Afterword

Honda R&D Technical Review Vol.26 No.2 arrives together with the very latest technology news. On December 13, 2013, the U.S. Federal Aviation Administration (FAA) awarded Type Certificate, as specified by Part 33 of the Federal Aviation Regulations, to the HF120 turbofan engine. Learning of this outcome makes us all the more pleased to have published a special feature on the technologies employed in the HF120. Since its first publication, the Honda R&D Technical Review has served to widely publicize the latest technologies emerging from Honda's research, and I am proud that it has fulfilled this duty so effectively. Based on our clear understanding of the role of the Technical Review, the editorial team will continue to raise the level of technology by promoting mutual communication between engineers.

Recently, a stir was caused by reports that a paper submitted to an overseas academic journal by a well-known Japanese research institute presented issues of quality. Statements made by people involved in the formulation of this paper, taking a variety of positions in relation to the matter, have also been reported. These statements cause me nothing but puzzlement. The highest priority in this case should be to provide a sincere explanation in response to the questions raised concerning the paper, and to clarify the truth behind the events. The vain insistence that this was merely an issue of personal responsibility is regrettable, and one cannot help but feel impatient at the unfolding of the situation. Only papers that have been approved after having been reviewed a number of times by our in-house organizational review system qualify for publication in the Honda R&D Technical Review. If any doubts are raised regarding the content of a paper, we have a system in place that ensures that not merely the author but also the organization must take responsibility and provide an explanation. The creation of this system incorporated the wisdom of our predecessors who worked on the Technical Review from its inception. I can only express my gratitude at being able to edit and publish the journal on the basis of such a reliable system.

Goudo

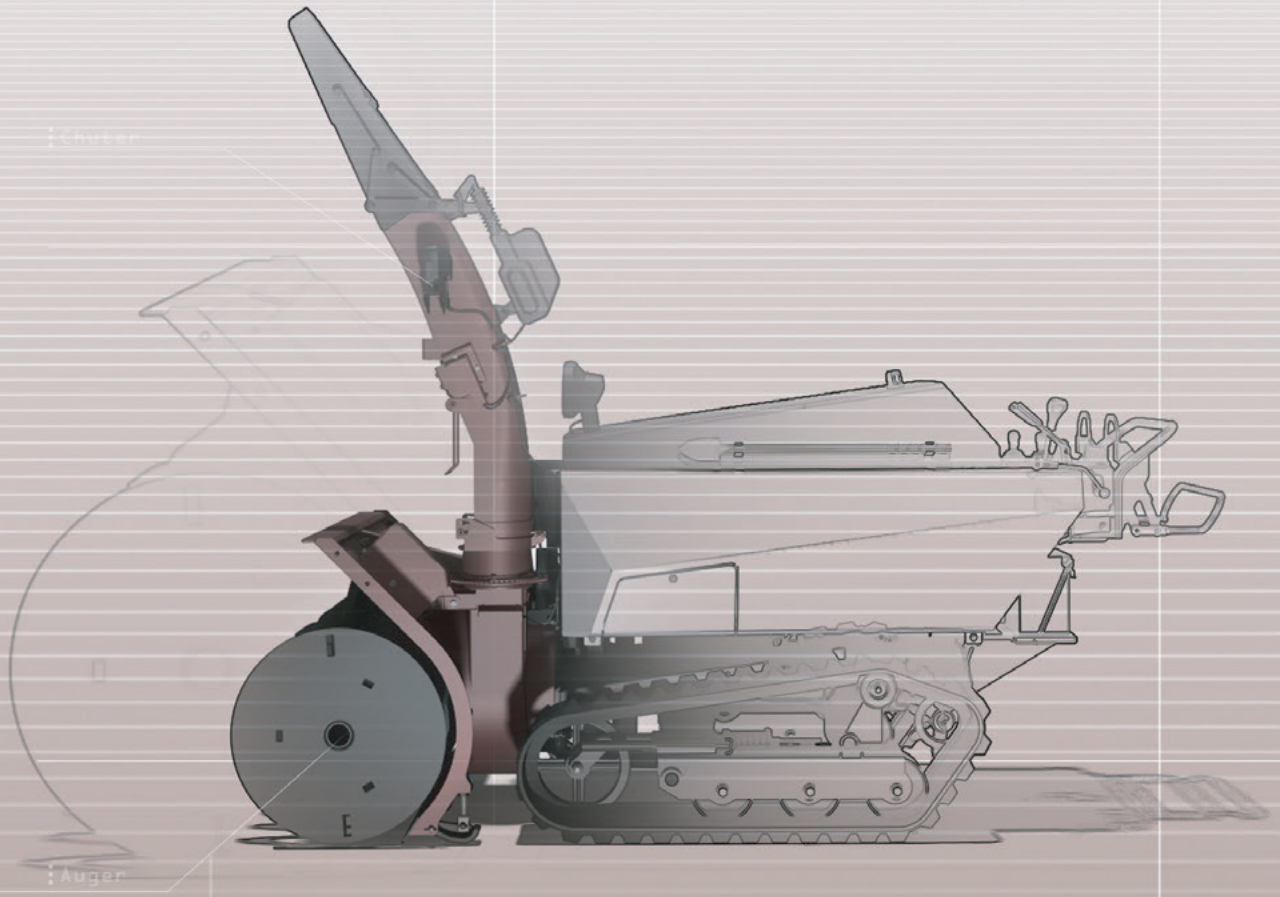
©2014 Honda Motor Co., Ltd. (All rights reserved)

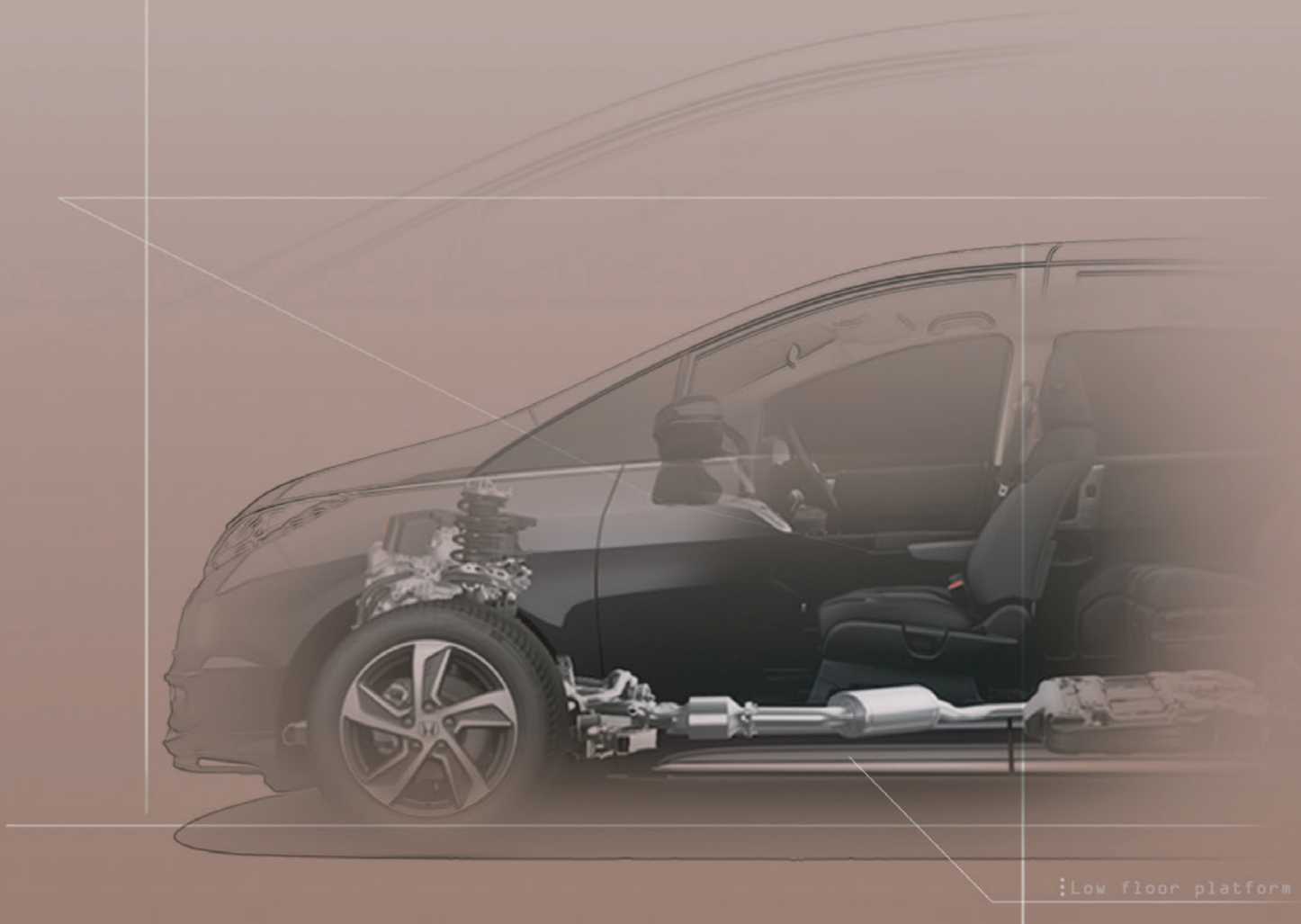
ISSN 1881-6223

Published by:
Honda Motor Co., Ltd.
2-1-1, Minami-Aoyama, Minato-ku,
Tokyo 107-8556, Japan

Edited by:
Honda R&D Co., Ltd.
Honda R&D Technical Paper Committee

Printed:
Sep. 1, 2014


Chute
Auger


Low floor platform